University of New Hampshire

University of New Hampshire Scholars' Repository

Master's Theses and Capstones   Student Scholarship

Spring 2021

Use of Smart Rocks to Improve Rock Slope Design

Bruma Morganna Mendonca Mendonca de Souza
University of New Hampshire, Durham

Follow this and additional works at: https://scholars.unh.edu/thesis

USE OF SMART ROCKS TO IMPROVE ROCK SLOPE DESIGN

By

Bruma Morganna Mendonca de Souza

BS, Federal University of Rio Grande do Norte, 2019

THESIS

Submitted to the University of New Hampshire

in Partial Fulfillment of

the Requirements for the Degree of

Master of Science

in

Civil Engineering

May, 2021

This thesis has been examined and approved in partial fulfillment of the requirements for the degree of Master of Science in Civil Engineering by:

Thesis Director, Dr. Jean Benoît,
Professor of Civil and Environmental Engineering

Dr. Majid Ghayoomi,
Associate Professor of Civil and Environmental Engineering

Mr. Neil Olson, MS,
Hydrogeologist, NH Department of Transportation

Mrs. Krystle Pelham, BS,
Engineering Geologist, NH Department of Transportation

On May 3, 2021

Original approval signatures are on file with the University of New Hampshire Graduate School.

DEDICATION

With all my love and gratitude, I dedicate this work to my parents and sister.

I will never be thankful enough for all the encouragement and endless love.

ACKNOWLEDGEMENTS

First, I want to express my sincere gratitude to my advisor, Professor Jean Benoît, for his enthusiasm, support, dedication, trust, and friendship over the last years.

Second, I would like to thank the New Hampshire Department of Transportation Bureau of Materials and Research, especially Neil Olson and Krystle Pelham, committee members, and Deirdre Nash, for all the interest, support, and collaboration in this research. Thank you also to Professor Majid Ghayoomi for his valuable time being on my thesis committee.

Thank you to Artur Apostolov for the development of the Smart Rocks and for his time helping us whenever necessary. I would also like to thank Noah MacAdam from the UNH Technical Service Center for all the help with the experimental setup anytime I needed (a lot!). Acknowledgments also to the Vermont Agency of Transportation and Ameritech for the cooperation with a portion of our field experiments.

I am very grateful to CEE undergraduate student and friend Hannah Miller for her extensive input in this research. Thank you also to my Geotech. friends Alex Lefebvre, Ian Gates, Oladayo Komolafe, Matthew Turner, Morghan Carr, and Mateus Medeiros for all the help with the research, knowledge, and good moments shared in these two years of grad school.

I am forever grateful to my family, especially my parents Karla and Vladimir, my sister Brenda, my grandmothers Eridante and Núbia, and my love Vinícius. Thank you for the endless love and support, and for always living my dreams as if they were yours too even 6500 km apart.

Finally, I am unconditionally thankful to God for always blessing me and my family with health and protection, especially during such challenging times we are currently facing.

To all my other friends and all cited above: my most sincere ***muito obrigada*** (thank you).

TABLE OF CONTENTS

LIST OF TABLES

LIST OF FIGURES

xvi

LIST OF SYMBOLS

COR   Coefficient of restitution

COR_V Velocity-based coefficient of restitution

COR_E Translational energy-based coefficient of restitution

COR_{TE} Total kinetic energy-based coefficient of restitution

COR_N Normal coefficient of restitution

COR_T Tangential coefficient of restitution

g   Acceleration due to gravity (9.81 m/s²)

h   Height

I   Moment of inertia

KE   Kinetic Energy

m   Mass

μ Coefficient of friction

μ_r Coefficient of rolling friction

ω Rotational (angular) velocity

v   Scalar velocity

LIST OF ACRONYMS

2D	Two-dimensional
3D	Three-dimensional
Caltrans	California Department of Transportation
CRSP	Colorado Rockfall Simulation Program
DEM	Digital Elevation Model
DOT	Department of Transportation
dps	Degrees per second
GIS	Geographic Information System
Lidar	Light Detection and Ranging
NH	New Hampshire
NHDOT	New Hampshire Department of Transportation
RHRS	Rockfall Hazard Rating System
SR	Smart Rock
VT	Vermont
VTrans	Vermont Agency of Transportation

ABSTRACT

USE OF SMART ROCKS TO IMPROVE ROCK SLOPE DESIGN

by

Bruma Morganna Mendonca de Souza

University of New Hampshire, May 2021

For many states, rockfall presents risks of irreversible damage to motorists on highways and roads across the country. Assessing these hazards is difficult as it relies on highly empirical methods based on assumed and/or measured slope and terrain surfaces and rock parameters, which can predict unrealistic trajectories due to unreliable modeling inputs. Research undertaken at the University of New Hampshire over the last decade includes the development of Smart Rock (SR) sensors used to evaluate these events from the perspective of the falling rock. The latest SRs consist of 3D printed capsules 50.8 mm in length and 25.4 mm in diameter, equipped with a ±400 g and a ±16 g 3-axis accelerometer, a ±4000 dps high-rate gyroscope, an altimeter, and a temperature sensor. Approximately 80 field experiments conducted in New Hampshire and Vermont provided SR data on rockfall at 10 different sites with a wide range of topographies and geological conditions. Preliminary laboratory and modeling assessments were also undertaken to compare experimental trajectories with rockfall simulations using different coefficients of restitution. It was concluded that acceleration and rotational velocity data from the rock perspective present a high potential to expand rockfall understanding and modeling. Such broader description of rockfall movements can enhance input parameters in computer rockfall modeling, which often disregards rotational data in kinetic energy estimates and tends to predict overly conservative trajectories.

1.   INTRODUCTION

Rockfall events are an increasing hazard concern, especially near highways and residential areas. Rockfalls are associated with natural phenomena such as weathering, rainfall, freeze-thaw cycles, vegetation growth, activities by animals and the public, and climatic changes. These processes disrupt portions of slopes, which lead to falling rocks and pose a safety hazard to motorists, infrastructure, and buildings nearby—the risk of irreversible damage increases near roads and in areas with significant population density.

Reliable hazard mapping and territory management require reliable predictions of rockfall trajectories, velocities, bounce heights, and kinetic energies. However, the unpredictability of falling blocks turns this task significantly difficult and costly, given their intrinsic randomness and the limited available field instrumentation techniques. Researchers started to instrument test rocks with high-rate sampling acceleration and rotational velocity sensors in field rockfall experiments to address this issue (Caviezel et al., 2018; Disenhof, 2018).

Extensive research conducted at the University of New Hampshire (UNH – Durham, NH, USA) over the last decade developed and improved four generations of Smart Rock (SR) sensors, currently equipped with accelerometers, a gyroscope, altitude and temperature sensors. Previous research conducted by Disenhof (2018) demonstrated the functionality of a Smart Rock for rockfall applications. SRs are capable of instrumenting field and laboratory rockfall experiments from the perspective of the falling rock. The measured acceleration and rotational velocity outputs can be used to validate and improve rockfall computational models and help with mitigation methods, as rotational kinetic energy and impact forces can be assessed more accurately.

In this research, several instrumented rockfall experiments were carried out on ten rock slopes in New Hampshire and one in Vermont, United States. The field tests were conducted with Smart Rock sensors embedded in the center of gravity of local rocks retrieved at each slope location. Preliminary laboratory assessments were performed after the field trials to establish a research methodology capable of evaluating instrumented rock rebounds consistently. Finally, the experimental trajectories and rotation motion were compared with rockfall simulations using default input parameters and energy restitution coefficients estimated in the laboratory.

1.1. Objectives

The main objectives of this research are to characterize rockfall motion over time from the perspective of the falling rock and conduct preliminary laboratory and modeling assessments to evaluate two-dimensional simulated trajectories. Fourth-generation Smart Rock sensors were extensively used to analyze field measurements conducted with several test blocks on slope profiles of different characteristics. The following steps were performed to meet these objectives:

- Experimental rockfalls were performed at eleven locations. The 4th generation Smart Rock sensor was used to describe rock motion in terms of acceleration, rotational velocity, and altitude. The sensor measurements were coupled with video analyses.

- A preliminary laboratory assessment of energy restitution coefficients to calibrate model input parameters was performed. Instrumented tests were conducted, releasing a standard block on sand and rock surfaces.

- Initial two-dimensional modeling assessments were performed to compare the simulated trajectories to field measurements from two slope locations. Default coefficients were initially used and compared with the parameters defined in the laboratory.

1.2. Thesis overview

This thesis is divided into nine chapters and three Appendices that include results from all experiments carried out as part of this research. Chapter 1 discusses the motivation and objectives of the current research. Chapter 2 reviews the definition and basic concepts associated with rockfall events, as well as experimental observations published by other researchers and a summary of rockfall modeling approaches. Previous research findings on the Smart Rock sensors related to rockfall applications are also presented.

Chapter 3 details the methodology followed in all three stages of this research work: field experiments, laboratory tests, and rockfall modeling. Chapter 4 explains the data processing approach followed for the field and laboratory experiments with the Smart Rock. Chapter 5 presents the field data acquired with SR sensors, field measurements, and video measurements. The experimental results presented in Chapter 5 are discussed in Chapter 6, correlating observations established at all site locations.

Chapter 7 presents and discusses the results obtained from the preliminary laboratory assessments of energy restitution. Chapter 8 presents and discusses results for 2D rockfall simulations in two field test locations. Finally, Chapter 9 provides a summary of this research project and offers conclusions and future work perspectives.

Appendix A presents databases of energy restitution results retrieved from the literature. Appendix B provides the rockfall trajectories and Smart Rock data from the field tests not included in Chapter 5, and Appendix C provides the SR data for the laboratory experiments.

2.   BACKGROUND

2.1. Rockfall

Rock slopes often have potentially unstable surfaces subject to mass movements that can negatively impact the environment, transportation, and nearby infrastructure, often resulting in delays or road closures (Bunce et al., 1997; Tavares, 2015). As a result, physical and chemical alterations of the rock along the highway need to be frequently monitored as rockfall risk can be increased (Gomes, 2009).

Rockfalls are an increasingly relevant topic as climatic changes lead to further erosion of slopes, cliffs, and rocky terrains (Caviezel et al., 2018). Several authors highlight the frequent instability of rock slopes in mountainous areas and the high incidence of rockfall events in these regions (Pfeiffer and Bowen, 1989; Pierson, 1992; Bunce et al., 1997; Descoeudres, 1997; Labiouse and Descoeudres, 1999; Chau et al., 2002, 2003; Heidenreich, 2004; Labiouse and Heidenreich, 2009; Turner and Jayaprakash, 2012; Ferrari et al., 2013; Ansari et al., 2015; Wyllie, 2015; Disenhof, 2018; Garcia, 2019). The risk of damage increases in areas with significant population density (Azzoni et al., 1995), such as the French-Swiss Alps, increasing infrastructure demand (Heidenreich, 2004; Garcia, 2019). Therefore, falling blocks present considerable economic importance (Turner and Jayaprakash, 2012), and these regions demand a thorough knowledge concerning rockfall trajectories, consequent hazard mapping, and effective defense systems (Heidenreich, 2004).

Falling blocks are more frequent in older slopes when compared to recently modified and/or fresh rock cuts, which were altered before current design recommendations, and often resulted in significant rock fracture and exposure. Prior to existing knowledge about rockfall risk

and occurrence, it was standard practice to use overly aggressive blasting techniques to modify rock slopes. These methods can potentially weaken the rock mass structure and cause instability along with other factors such as weathering effects with time (Pierson, 1992; Pierson and Van Vickle, 2013; Tavares, 2015; Disenhof, 2018).

Rockfalls are characterized by their high velocities resulting in significant kinetic energies (Descoeudres, 1997; Turner and Duffy, 2012a). Rockfall events may involve more than one rock but usually do not include very large volumes of rock, as observed in rock avalanches and landslides (Chau et al., 2003; Turner and Jayaprakash, 2012). Regions prone to rockfall are typically of large extent and high incidence, increasing the difficulty associated with performing detailed assessments at each location. Such investment is not feasible because of the high cost and time demand for technological control of each area. Therefore, as rockfall incidence, visibility, and consequences increased with time, transportation agencies had an increasing need to optimize rockfall risk assessment in budget and schedule (Pierson, 1992).

The Oregon Department of Transportation (ODOT) recognized the need to create an evaluative method for assessing rockfall hazards. Funded by the Federal Highway Administration, ODOT proposed a Rockfall Hazard Rating System (RHRS). Designed to be simple and easy to implement, the RHRS was widely implemented nationally and internationally. The ratings classify the rockfall hazard levels as A (high), B (moderate), or C (low). While A and B cuts require higher attention levels, C ratings are usually attributed to rocks unlikely to fall or reach an area of risk (e.g., roadway). A and B cuts can become lower priority locations depending on the maintenance conducted (Pierson, 1992; Pierson and Van Vicke, 1993).

Rockfall hazard rating systems are an effective method to rank and classify potentially hazardous rock slopes against rockfall risk through a comparative analysis, thus defining priority

for future investments in maintenance and operation. These systems are primarily qualitative and assess the likelihood of subjective probability of hazardous conditions through scores that contribute to site management (Pierson, 1992; Chau et al., 2003; Turner and Jayaprakash, 2012).

Risk assessments in rockfall mitigation are critical as public and private resources to minimize natural hazards are limited (Bunce et al., 1997). Therefore, it is essential to improve rockfall understanding to define acceptable levels of risk. The appropriate protection measure design requires sufficient knowledge of rockfall behavior at a given site (Pfeiffer and Bowen, 1989), especially in risks of irreversible damage (Azzoni et al., 1995). Reliable hazard mapping and territory management require representative predictions of rockfall trajectories, velocities, bounce heights, and kinetic energies. However, the unpredictability of falling blocks turns this task significantly difficult, given their intrinsic randomness and currently available field instrumentation techniques (Pierson, 1992; Pierson and Van Vickle, 1993; Higgins and Andrew, 2012; Ferrari et al., 2013; Wyllie, 2015; Garcia, 2019).

The rockfall hazard rating system used in the state of New Hampshire, United States, is based on the original RHRS refined by the ODOT. According to Disenhof (2018), there are approximately 375 rock cuts along transportation corridors in New Hampshire tracked and rated in a database maintained by the Bureau of Materials and Research of the NH Department of Transportation (NHDOT). According to the NHDOT (as cited in Disenhof, 2018), the database as of 2018 included rock cuts taller than 8 m, and 11% of the monitored rock slopes in NH were rated A, 27% were rated B, and the remaining 62% were rated C.

A-rated cuts are generally older and modified without controlled blasting techniques, which often result in unstable rock blocks on the slope surface. In contrast, C-rated slopes typically include either short rock slopes, a significant distance to transportation corridors, and/or along

roads with minimal traffic (Disenhof, 2018). Figure 2.1 presents three rock cuts with A, B, and C

ratings near transportation corridors in the state of New Hampshire.
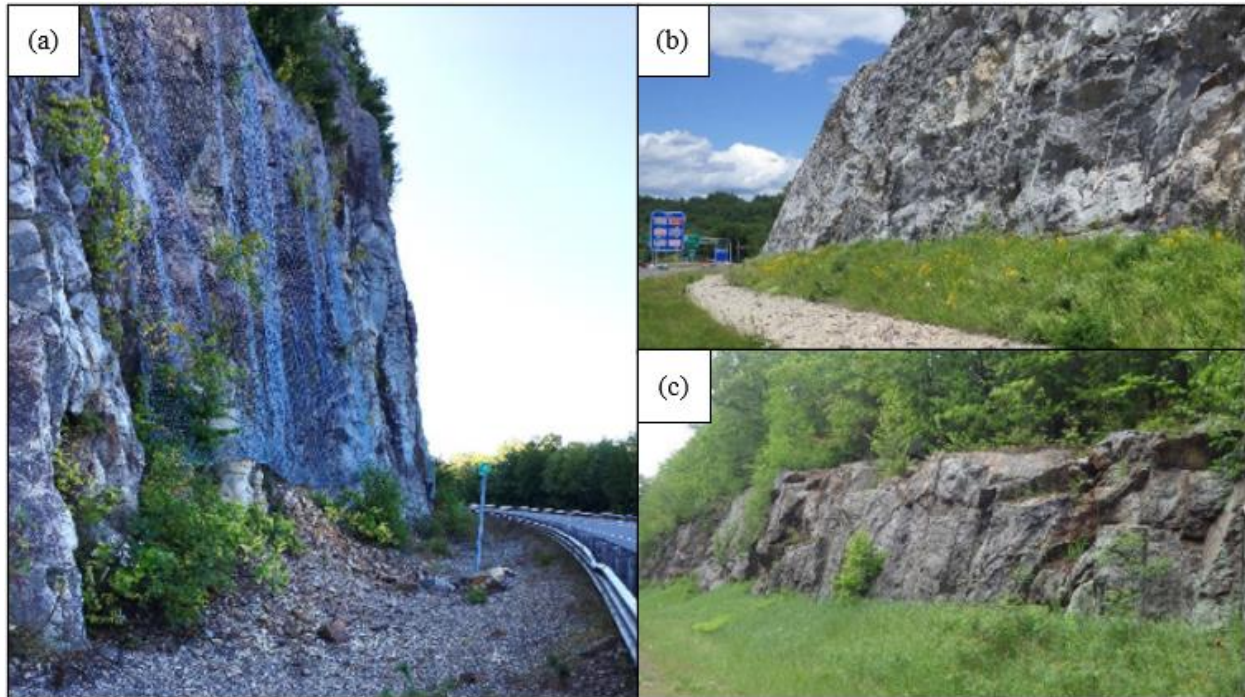
Figure 2.1. Rock cuts in New Hampshire: (a) A-rated in Alton, NH, (b) B-rated in Windham, NH, and (c) C-rated in Sutton, NH (Disenhof, 2018, adapted).

Standard methods of slope stabilization and consequent rockfall mitigation include

removal, reinforcement, and protection. Removal techniques consist of rock scaling and blasting,

while rock reinforcement measures encompass rock bolts, pinned meshes, cables, and rock gluing.

Rockfall protection systems are the most used approaches to minimize rockfall risks and include

draped mesh systems, barriers, attenuator systems, catchment ditches, and other containment forms

(Ardnt and Arpin, 2016).

Proper protection design requires information concerning rockfall energy and trajectory

(Wyllie, 2015). However, the trajectories assumed by falling blocks are complex and still not well-

understood (Chau et al., 2003; Heidenreich, 2004; Labiouse and Heidenreich, 2009; Higgins and

Andrew, 2012; Disenhof, 2018; Garcia, 2019). The present-day mitigation and protective design

are based on kinetic energy estimates, which typically disregard or inaccurately predict inherent and essential aspects of rockfall modeling such as rotational energy and rock rebound (Chau et al., 2003; Turner and Duffy, 2012). In addition to overly conservative simulation models, current rockfall analysis methods typically include field/laboratory measurements, high-frame video recording systems, and detailed event back-analyses. These techniques often do not provide detailed information about rock-surface interaction and translational and rotational rock kinematics (Caviezel and Gerber, 2018).

Rock cuts are often designed with catchment ditches to receive or catch potentially unstable rocks (Disenhof, 2018). Pierson et al. (2001) define rockfall catchment areas as the space between the edge of the pavement and a rock cut base, constructed to impede falling blocks from reaching the road. Catchment ditches are one of the most advantageous and straightforward rockfall mitigation methods and must be designed correctly for potential bounce heights, runout distances, and kinetic energies of rockfall events (Pierson et al., 2001; Disenhof, 2018).

When computer simulation programs were not widely available, it was difficult to obtain slope profiles accurately. Therefore, rockfalls and their resulting mitigation were frequently managed based on previous experience, as knowledge concerning the motion of falling blocks was still limited (Azzoni et al., 1995; Labiouse and Descoeudres, 1999). Finally, empirical approaches to design catchment ditches were also discussed by Pierson et al. (2001), who emphasizes that obsolete techniques commonly lead to unsafe or overly conservative designs.

2.2. Rockfall mechanics

Rockfall events were not systematically investigated until the 1960s. Ritchie (1963) evaluated falling blocks and developed a research program that became one of the most significant rockfall

engineering milestones. Ritchie identified that falling blocks could experience one or more modes of travel, including free fall, bouncing, rolling, and sliding.

Peng (2000) and Duffy and Turner (2012) highlight that locations of interest for rockfall typically reflect observed rockfall behavior identified by Ritchie (1963): upper, steeper slopes as a source location for initial free fall, followed by a transition zone with moderate inclinations where the rocks can bounce, and a final runout zone where the blocks can roll and slide as they decelerate before completely coming to a stop (Figure 2.2).
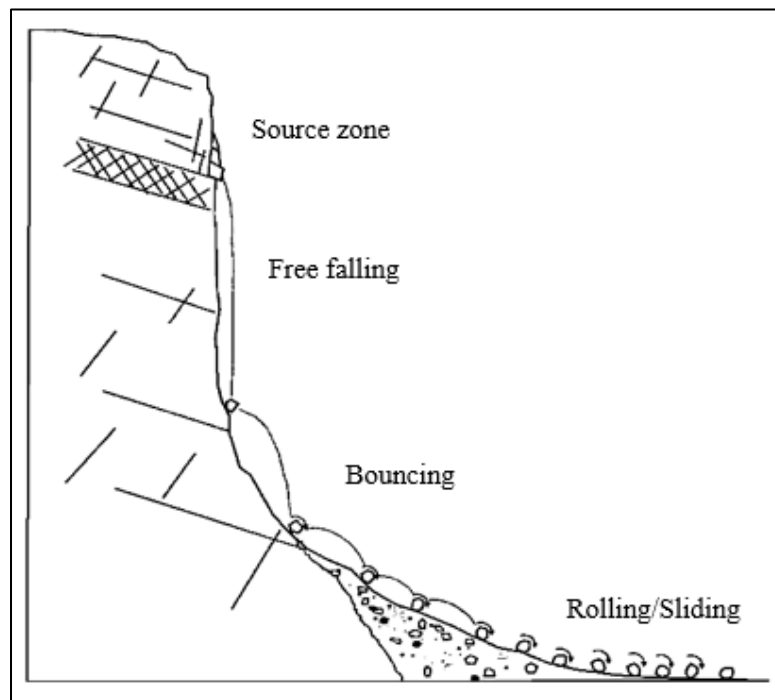
Figure 2.2. Typical rockfall process (Peng, 2000).

The first stage during a rockfall occurrence is the detachment of the block, which generally occurs along discontinuities (e.g., joints, fractures, bedding planes). These discontinuity surfaces must be steep or with low friction resistance such that the block weight can overcome gravity (Higgins and Andrew, 2012). Free fall occurs following an initial rolling or sliding stage, which is usually attributed to a variation in slope angle or motion from a previous impact. Free falling

blocks experience translational (linear displacement of the center of mass) and rotational (angular displacement around the center of mass) movements, which in the field occur three-dimensionally (Azzoni et al., 1995).

The velocity of these falling blocks is related to slope angle and height and time of contact with impact surfaces. If the block comes in contact with the slope, friction decelerates rock movement and consequently decreases kinetic energy. Therefore, higher velocities are usually observed in steeper slopes, and velocity and energy variations are associated with the trajectories. The presence of slope irregularities, commonly called launch features, can significantly influence the remaining trajectory and increasing runout distances near the ground level (Pierson et al., 2001).

Figure 2.3 presents a schematic with typical rockfall paths experienced in steep slopes, as detailed by Pierson et al. (2001). Four general behaviors, indicated as A, B, C, and D, are presented for a rock falling from the top of the slope. Rocks falling along path A impact the rock face just prior to reaching the bottom catchment surface. These rocks will likely have shorter runout distances (measured from the toe of the slope). Rocks following the second path (B) impact the slope face twice but do not develop a significant launch away from the slope, resulting in lower runout. Paths C and D describe broader trajectories, as they impact launch features and the vertical drops are altered to higher dispersions. Horizontal dispersion on the trajectory plane is higher when falling blocks strike launch features at higher translational velocities (Pierson et al., 2001).

Impacts during rockfall occur when a block in aerial trajectory intersects the slope or other surface, resulting in immediate and usually significant energy loss, whose magnitude varies according to the site conditions. Experimental observations suggested that if the block dimensions are smaller than the slope irregularities, the falling rock will likely perform small jumps and slips.

10

On the other hand, if the block dimensions are larger than the slope irregularities, it tends to roll with simultaneous slips at points of contact (Azzoni et al., 1995). Rolling motion after the impact occurs by converting translational kinetic energy into rotational energy, which can potentially increase runout distances (Pierson et al., 2001).
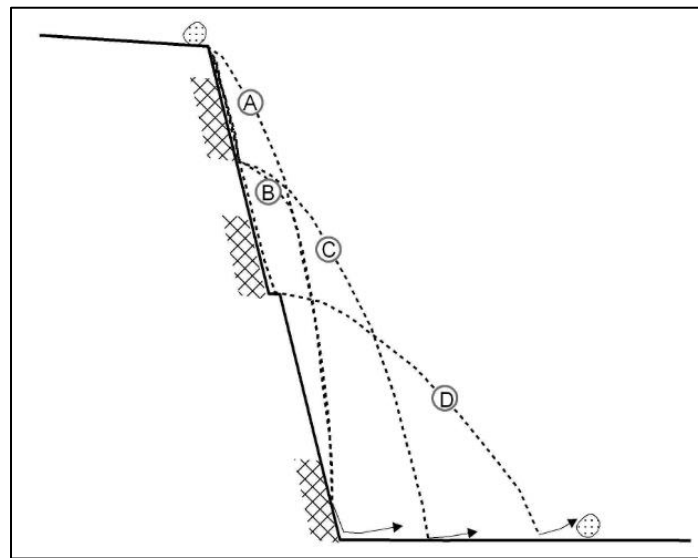
Figure 2.3 Preferred rockfall paths (Pierson et al., 2001).

After impacting the catchment ditch, Pierson et al. (2001) outline two possible outcomes. The block can immediately stop or roll/bounce back, approaching the slope toe (runout distance = impact distance), or roll/bounce towards the road, thus increasing the runout distance (runout distance > impact distance). Additionally, Azzoni et al. (1995) observed that steeper catchment ditches significantly diminish runout distances, and flat ditches and taller slopes generally imply greater and more scattered rock runouts. Sliding is more commonly observed during the initial and final phases of rockfall (Azzoni et al., 1995).

Analysis of falling rocks requires evaluations of trajectories and impacts (Wyllie, 2015). The impact of a falling block on rocks or other typical surfaces comprises physical theories of inelastic shocks and contact forces (Descoeudres, 1977). Although discussions regarding rock

bouncing behavior have dominated research in recent years, this phenomenon is still not fully understood. Several studies identified that the bouncing of blocks depends on several factors that include both impact surfaces and block characteristics, as well as the consequent kinematics produced from such interactions (Ritchie, 1963; Peng, 2000; Heidenreich, 2004; Labiouse and Heidenreich, 2009; Turner and Duffy, 2012a; Wyllie, 2015). Heidenreich and Labiouse (2004) list various factors that influence the rebound response of falling rocks, as shown in Table 2.1.

Table 2.1. Factors influencing rock rebound response (Heidenreich and Labiouse, 2004).

Slope characteristics	Block characteristics	Kinematics
Strength	Strength	Translational velocity
Stiffness	Stiffness	Rotational velocity
Roughness	Weight – Size	Collision angle
Inclination	Shape	Configuration of block

Rock bouncing motion occurs when falling blocks impact the rock slope or other surfaces (sand, grass, gravel, asphalt, etc.). Although the rebound behavior depends on block characteristics that vary for a single site (shape, weight, and size) and the impact surface, the rebound behavior is mathematically governed by one or two coefficients, designated as coefficients of restitution. There are currently multiple definitions and interpretations in the literature, and the lack of consensus on the most accurate analysis approach illustrates the existing gap to achieve the necessary understanding of rockfall impacts against typical surfaces (Chau et al., 2002; Heidenreich, 2004; Turner and Duffy, 2012a).

Rockfall physical analyses are based on the elementary principles of Newtonian mechanics and laws of motion, in which falling blocks describe well-defined parabolic trajectories with assumed zero air resistance (Wyllie, 2015). Turner and Duffy (2012a) and Wyllie (2015) provide a thorough description of the qualitative assessment of falling blocks, whose approach disregards rock fragmentation and applies to all rockfall stages.

In the literature, restitution coefficients are mainly defined in terms of velocities, kinetic energies, and bouncing heights. The kinetic energy developed by a falling block includes both translational and rotational behaviors. Thus, the total kinetic energy is described by the sum of translational (Equation 2.1) and rotational (Equation 2.2) energies (Equation 2.3).

$$KE_T = \frac{1}{2}mv^2$$ (Equation 2.1)

$$KE_R = \frac{1}{2}I\omega^2$$ (Equation 2.2)

$$KE = KE_T + KE_R = \frac{1}{2}mv^2 + \frac{1}{2}I\omega^2$$ (Equation 2.3)

Where: KE_T = translational kinetic energy,

KE_R = rotational kinetic energy,

KE = total kinetic energy,

m = mass of the block,

v = scalar (translational) velocity of the block,

ω = angular velocity of the block, and

I = moment of inertia of the block.

While the translational kinetic energy is solely based on linear displacements and assumes that the falling block is a non-rotating rigid body, the rotational kinetic energy considers angular velocities and the moment of inertia of the falling object. Rockfalls are three-dimensional events, and velocities and moments of inertia of 3D blocks are quantified about three principal axes (X, Y, and Z), which intersect at the center of mass of the rotating body. Therefore, the rotational kinetic energy of a falling block can be rewritten as shown in Equation 2.4, considering the moment of inertia and rotational velocity about each axis.

$$KE_R = \frac{1}{2}(I_{XX}\omega_X^2 + I_{YY}\omega_Y^2 + I_{ZZ}\omega_Z^2)$$ (Equation 2.4)

According to Turner and Duffy (2012a), the moment of inertia of a particular object quantifies the difficulty of changing the rotational motion about that axis. Energy restitution conditions upon rebound include the bounce height, rebound direction, and rotational velocity (Azzoni and de Freitas, 1995; Chau et al., 2002; Heidenreich, 2004; Labiouse and Heidenreich, 2009; Turner and Duffy, 2012a).

The impact and rebound conditions experienced by falling blocks are either plastic or partially elastic collisions. While in plastic impacts, the impact surface fully absorbs the kinetic energy, partial KE restitution occurs immediately after partially elastic collisions. During the impact process, kinetic energy from rockfall motion partially or totally transforms into plastic deformation, heat, and sound. Elastic conditions, which represent complete energy restitution, do not occur in practice (Chau et al., 2002; Turner and Duffy, 2012a; Wyllie, 2015; Garcia, 2019). Coefficients of restitution are defined as dimensionless ratios between velocities, kinetic energies, and/or heights after and before impact and range theoretically between 0.0 (plastic) and 1.0 (elastic) (Turner and Duffy, 2012a; Wyllie, 2015).

An extensive literature review conducted by Turner and Duffy (2012a) concerning empirically determined coefficients of restitution indicated no consensus regarding the terminology used for these parameters. Several authors referred to restitution coefficients as e, R, COR. In this thesis, the terms used will be the same as those used by Turner and Duffy (2012a), as detailed in Table 2.2. The subscripts N and T refer to the normal and tangential components of velocities and energies of incident and rebound trajectories, as named in Figure 2.4. Normal coefficients of restitution are determined perpendicular to the impact surface, while tangential coefficients of restitution are estimated parallel to the impact surface. The incident and reflected angular velocities are also crucial in quantifying energy restitution.
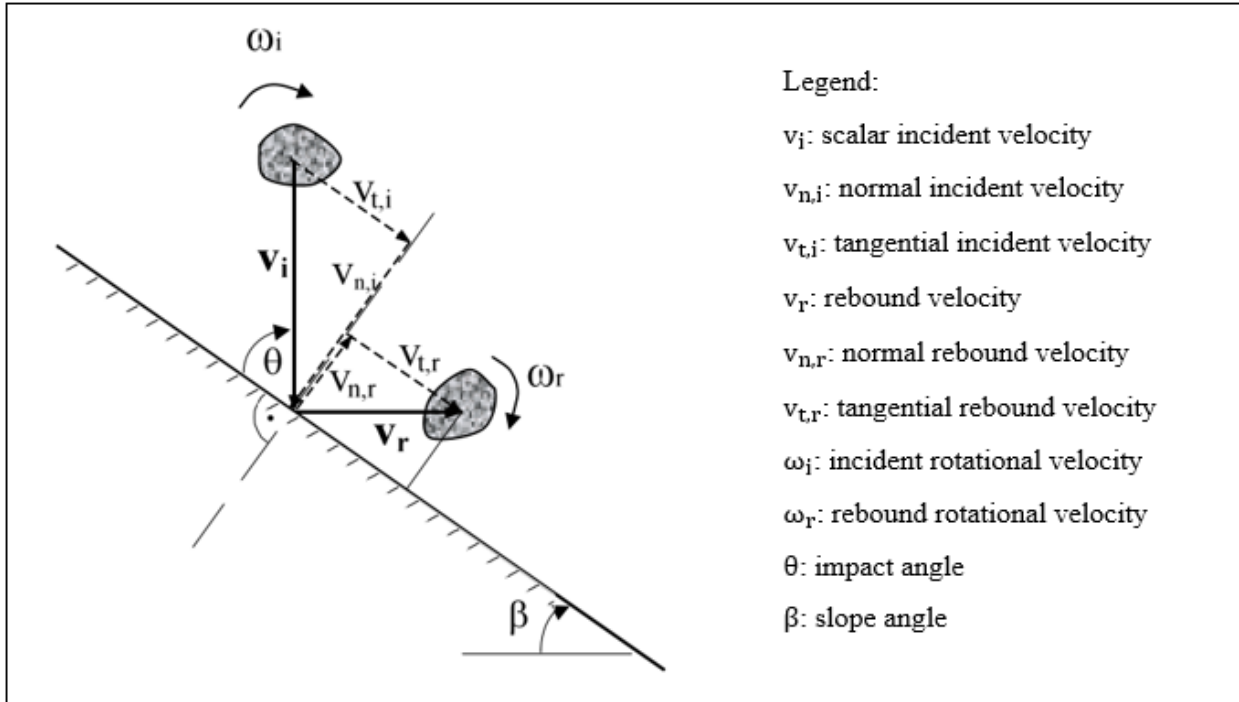
Figure 2.4 Schematic of energy restitution upon rockfall impact (Heidenreich, 2004, adapted).

The restitution coefficients reviewed and outlined by Turner and Duffy (2012a) are detailed in Equations 2.5 to 2.12, as well as revised field and laboratory experimental studies that empirically determined COR values based on these definitions.

The most common set of definitions in the literature and computational modeling regarding the coefficient of restitution is based on velocity ratios. Equation 2.5 considers the scalar incidence and rebound velocities in both normal and tangential directions. The normal and tangential components of COR_V (Equations 2.6 and 2.8, respectively) are based on the normal and tangential block velocities before and after impact. The normal coefficient of restitution can also be defined as a function of the heights of successive bounces (Equation 2.7).

Table 2.2. Definitions of coefficients of restitution.

Basis	Equation		Terms	Used by
	$COR_V = \dfrac{v_R}{v_I} = \sqrt{\dfrac{h_{N+1}}{h_N}}$	(Eq. 2.5)	COR_V = velocity-based coefficient of restitution v_R = scalar velocity of the block after impact v_I = scalar velocity of the block immediately before impact h_{N+1} = height of the current bounce h_N = height of the last bounce or drop height for the first bounce	
	$COR_{VN} = \dfrac{v_{RN}}{v_{IN}}$	(Eq. 2.6)	COR_{VN} = normal component of COR_V v_{RN} = normal translational velocity after impact v_{IN} = normal translational velocity before impact	Wu (1985) Peng (2000) Chau et al. (2002) Giani et al. (2002)
Velocities	$COR_{VN} = \sqrt{\dfrac{h_{N+1}}{h_N}}$, 90° fall	(Eq. 2.7)	h_{N+1} = height of the current bounce h_N = height of the last bounce or drop height for the first bounce	Giani et al. (2004) Dias and Barroso (2006) Asteriou et al. (2012) Giacomini et al. (2012) Saeidi et al. (2014) Ansari et al. (2015) Bar et al. (2016) Wang et al. (2018)
	$COR_{VT} = \dfrac{v_{RT}}{v_{IT}}$	(Eq. 2.8)	COR_{VT} = tangential component of COR_V v_{RT} = tangential translational velocity after impact v_{IT} = tangential translational velocity before impact	Wu (1985) Peng (2000) Chau et al. (2002) Giani et al. (2002) Giani et al. (2004) Asteriou et al. (2012) Giacomini et al. (2012) Saeidi et al. (2014) Bar et al. (2016) Wang et al. (2018)

Table 2.2 (cont.). Definitions of coefficients of restitution.

Basis	Equation		Terms	Used by
	$COR_E = \dfrac{0.5mv_{N+1}^2}{0.5mv_N^2} = \dfrac{v_{N+1}^2}{v_N^2}$	(Eq. 2.9)	COR_E = energy-based coefficient of restitution m = mass of the block v_{N+1} = scalar velocity of the object after impact v_N = scalar velocity of the object before impact	Wu (1985) Peng (2000) Chau et al. (2002) Asteriou et al. (2012) Basson et al. (2012) Saeidi et al. (2014) Arpaz (2015) Wang et al. (2018) Ghana et al. (2019)
Energies	$COR_{EN} = \dfrac{v_{RN}^2}{v_{IN}^2}$	(Eq. 2.10)	COR_{EN} = normal component of COR_E v_{RN} = normal translational velocity after impact v_{IN} = normal translational velocity before impact	
	$COR_{ET} = \dfrac{v_{RT}^2}{v_{IT}^2}$	(Eq. 2.11)	COR_{ET} = tangential component of COR_E v_{RT} = tangential translational velocity after impact v_{IT} = tangential translational velocity before impact	
	$COR_{TE} = \dfrac{0.5[m(v_R^2)+I\omega_R^2]}{0.5[m(v_I^2)+I\omega_I^2]}$	(Eq. 2.12)	COR_{TE} = total energy coefficient of restitution m = mass of the block v_R = scalar velocity after impact v_I = scalar velocity before impact I = moment of inertia of block ω_R = angular velocity of the block after impact ω_I = angular velocity of the block before impact	Wu (1985) Azzoni and de Freitas (1995) Azzoni et al. (1995) Peng (2000) Chau et al. (2002) Asteriou et al. (2012) Wang et al. (2018)

Ratios of kinetic energy define the energy-based coefficients of restitution before and after impact. The rotational kinetic energy is often disregarded in experimental studies due to the difficulty quantifying this parameter about three axes of rotation. Therefore, experimentally determined energy-based restitution coefficients typically only consider the ratio of translational kinetic energies, which can be simplified to the square of the initial and final velocities (Equation 2.9). Similarly, the normal and tangential components of the energy-based coefficient of restitution are calculated through Equations 2.10 and 2.11.

The total energy coefficient of restitution considers both translational and rotational kinetic energies (Equation 2.12). It is essential to include the rotational energy in kinetic calculations, as translational movement converts to rotational motion after impact, which tends to increase in a sequence of bounces (Turner and Duffy, 2012a).

The dynamic friction (μ) and rolling friction (μ_r) coefficients are additional modeling parameters used to address the loss of energy of sliding or rolling blocks during rockfall. The coefficient μ consists of the tangent of the friction angle (Chai et al., 2013), while μ_r is the tangent of the slope angle at which a rolling block travels with constant velocity (critical slope angle). This coefficient is also influenced by both block and surface characteristics. Additionally, the coefficient of kinetic friction is also defined in rockfall motion and addresses the final rockfall runout stages. Rolling motion requires less effort than sliding, and therefore the rolling coefficient is typically higher than the coefficient of dynamic friction (Turner and Duffy, 2012a; Wyllie, 2015).

Rock bouncing and rolling are the least understood trajectory mechanisms (Turner and Duffy, 2012a). According to Chau (2003), the impact and consequent rebound of blocks (when applicable) are the most complex physical processes in rockfall dynamics. The phases of block

impacts are still not fully understood, as well as knowledge concerning rock sliding and rolling (Azzoni and Freitas, 1995; Bourrier et al., 2009; Bozzolo and Pamini, 1986; Descoeudres, 1997; Dorren et al., 2011; Garcia, 2019). Such limited knowledge is mainly attributed to variations in both block and surface shapes.

Several authors conducted experimental studies to determine the coefficient of restitution values for typical surfaces present near rock cuts, including the rock face itself, and better understand rockfall behavior in general. However, as previously discussed, restitution coefficients depend on several parameters, which vary according to the block characteristics and impact conditions. Previous assessments in both the laboratory and the field mostly considered impacts of individual blocks (Wu, 1985; Peng, 2000; Chau et al., 2002; Giani et al., 2002, 2004; Heidenreich, 2004; Dias and Barroso, 2006; Asteriou et al., 2012; Giacomini et al., 2012; Saeidi et al., 2014; Ansari et al., 2015; Asteriou and Tsiambaos, 2016; Wang et al., 2018; etc.). Table 2.3 presents typical ranges of coefficients of restitution observed for different impact surfaces following the velocity-based definitions for normal and tangential restitution. It can be observe how the energy restitution varies depending on material and test conditions.

Table 2.3. Typical ranges of coefficients of restitution.

Material	Default		Literature	
	COR_{VN}	COR_{VT}	COR_{VN}	COR_{VT}
Rock	0.35	0.85	0.12 to 0.88 Peng (2000) Asteriou et al. (2012)	0.44 to 1.26 Peng (2000) Asteriou et al. (2012)
Soil	0.30	0.80	0.00 to 0.32 Peng (2000) Pfeiffer and Bowen (1989)*	0.00 to 0.61 Peng (2000)
Rock talus	0.32	0.85	0.07 to 0.45 Peng (2000) Heierli (1985)*	0.58 to 0.87 Peng (2000) Pfeiffer and Bowen (1989)*
* Cited by Heidenreich (2004)				

2.3. Experimental rockfall

Accurate rockfall hazard assessments demand realistic estimates of potential falling block trajectories. It is widely discussed in the literature how several parameters interfere with selecting representative coefficients to define energy restitution at a given site (Chau et al., 2002; Heidenreich, 2004; Turner and Duffy, 2012a).

There is no standard methodology among published studies to evaluate coefficients of restitution or general rockfall behavior. Different methods in the field, laboratory, and detailed event back analyses have been used to evaluate essential parameters related to rockfall modeling and protective/mitigation design. Such empirical evaluations are broadly used to calibrate parameters concerning rock runout, trajectories, and energy restitution to improve current predictive methods. This section summarizes findings and traditional ways of experimental approaches regarding falling blocks and their behavior.

The empirical approach to be selected depends on the analysis objectives. While laboratory assessments are mainly conducted to evaluate block impact mechanics, field experiments usually encompass a broader number of parameters. Tests on rock slopes allow to obtain runout distance, lateral dispersion, the effectiveness of in-place protective systems, and, when possible, evaluate block impact mechanics. For both laboratory and in situ tests, trajectory and impact mechanics assessments are observational and currently conducted through video analysis. Instrumented tests from the perspective of the falling rock using embedded sensors into a block will be discussed in sections 2.3.3 and 2.4 of this thesis.

Several authors conducted experiments with falling blocks with the aid of video recordings for subsequent quantitative analysis (Wu, 1985; Azzoni and de Freitas, 1995; Azzoni et al., 1995; Chau et al., 2002; Heidenreich, 2004; Asteriou et al., 2012; Arpaz, 2015; Saeidi et al., 2014; Ansari

et al., 2015; Asteriou and Tsiambaos, 2016; Li et al., 2016; Wang et al., 2018; Ghana et al., 2019). The frame rates used vary between 10 and 240 frames per second (fps). Small-scale experiments require higher measurement precision and consequently demand a higher number of frames. Block position and velocities over time are often determined from motion analysis of successive frames from the video recordings with the aid of tracking software.

Marks on the test blocks are used for position tracking and determining translational and rotational velocities. However, it is more complex to decide on rotational velocities as many frames are required, and rocks can rotate about up to three axes simultaneously. Only a few studies determined rotational velocities from video frames, including Chau et al. (2002), Dorren et al. (2006), Giacomini et al. (2012), and Garcia (2019). The difficulty associated with tracking angular velocities was highlighted by Dorren et al. (2006), who conducted experimental rockfalls in the French Alps. Dorren and colleagues determined the angular velocity based on the sequential frames required for one complete revolution about one reference axis.

Additionally, in field experiments, camera positioning depends on both slope and traffic conditions. The difficulty associated with laterally positioning video cameras in the test location had been previously emphasized by Bourrier et al. (2012). Garcia (2019) highlights that the calibration of restitution parameters is a complex task that requires extensive experimental testing and video analysis.

2.3.1. Laboratory experiments

Several authors conducted laboratory experiments to complement information gathered from field tests for rockfall modeling. Most parametric assessments are conducted under controlled conditions, at a small scale in the laboratory. Although highly difficult to obtain in the field, test

repeatability is vital to perform statistical analysis concerning rockfall mechanics. The substantial

variabilities observed in rock slopes (surface inclination, roughness, the variability of material,

climate conditions, etc.) make it very improbable that the same falling block will develop

sufficiently close trajectories in the field (Heidenreich, 2004).

One of the first widely known parametric assessments of coefficients of restitution was

performed by Wu (1985). Wu conducted an extensive experimental evaluation of the coefficient

of restitution at different impact angles. Vertical drop tests were conducted on an inclined wood

platform (3.0 x 3.7 m) and rock cut slopes (Figure 2.5). The wood platform was adjusted at 30º,

40º, 45º, and 60º (α angle) to assess the effect of impact angle (θ) and the drop heights. For normal

drop tests (vertical free fall), the greater the impact angle, the less inclined the surface is.
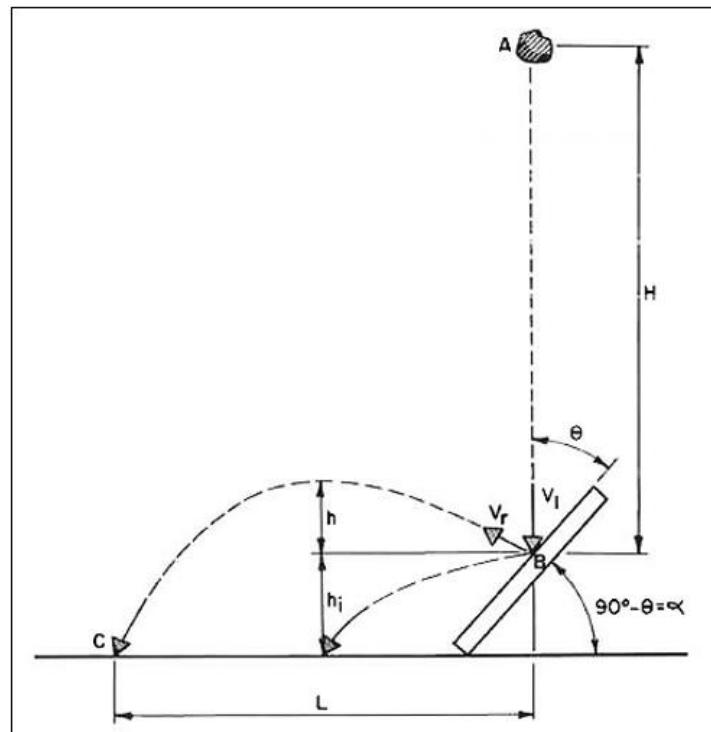
Figure 2.5 Experimental setup by Wu (1985).

Thirteen rocks of different shapes and sizes between 20 and 45 cm in diameter were

dropped at each condition. The experimental data are presented in Figure 2.6. A decrease in normal

restitution (COR_{VN}) was observed with an increase in impact angle θ (decrease in slope angle α), a flatter condition. The trendline for the tangential restitution (COR_{VT}) was not as clearly defined, and not all points seem to follow the assumed linear trend. Although Wu suggests that COR_{VT} slightly increases at higher impact angles (less inclined surfaces), this hypothesis could not be supported by subsequent studies (Chau et al., 2002; Heidenreich, 2004; Heidenreich and Labiouse, 2004; Labiouse and Heidenreich, 2009).
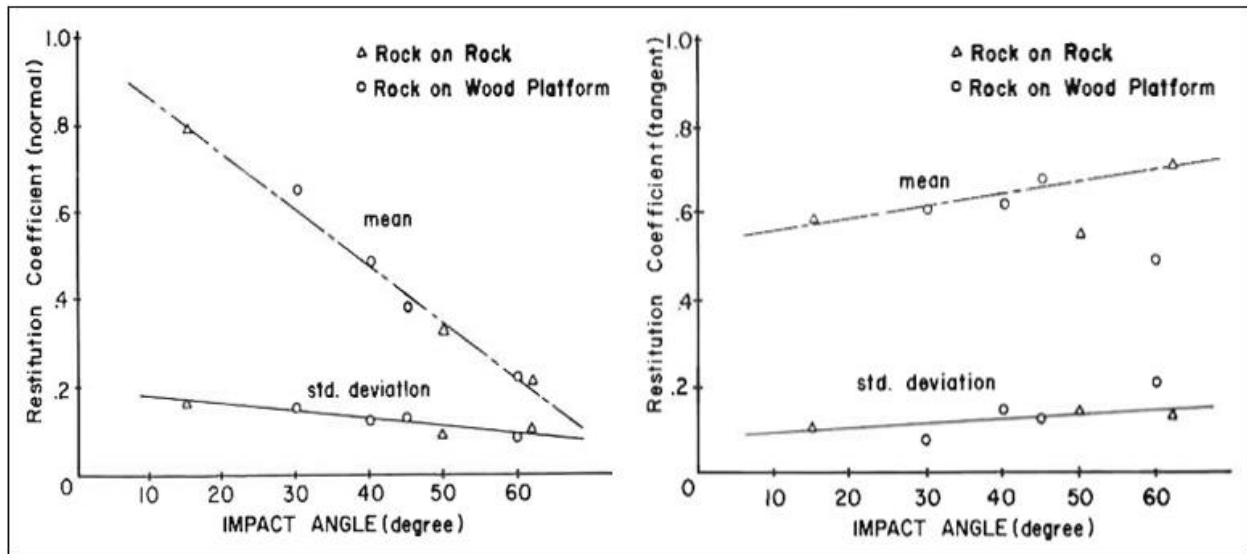
Figure 2.6. Experimental results for the coefficient of restitution obtained by Wu (1985).

The investigation conducted by Chau et al. (2002) is one of the most cited experimental studies in rockfall engineering. Chau and colleagues conducted meticulous parametric testing to evaluate coefficients of restitution under different controlled conditions in the laboratory. Drop tests at different angles were conducted with spherical boulders fabricated with plaster at distinct densities and diameters ranging between 18 and 60 mm. Figure 2.7 shows the test schematic and a combined photograph demonstrating the parabolic trajectory (normal and tangential velocity components) and sphere rotation after impact.

Chau et al. (2002) evaluated both translational and rotational motion of falling blocks. The coefficients of restitution were then estimated based on velocity and energy (kinetic and total energies) ratios. This investigation is one of the most thorough studies developed in energy restitution applied to rockfall engineering.
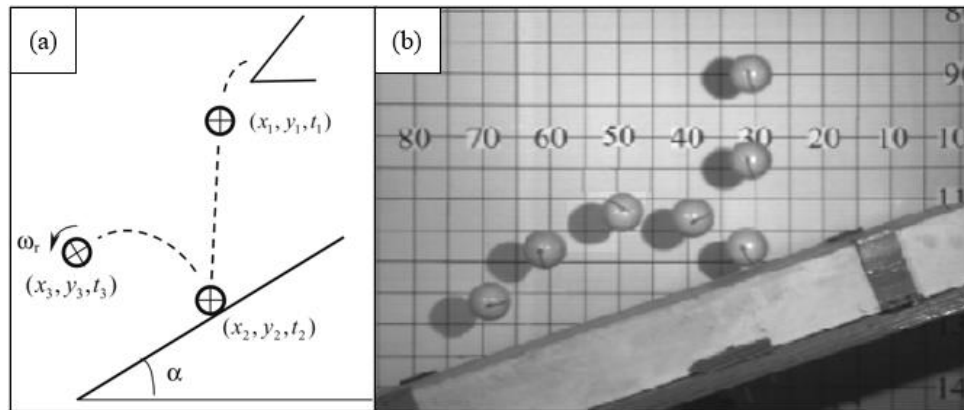
Figure 2.7. (a) Test schematic and (b) combined frames during a test (Chau et al., 2002).

Figure 2.8 presents the results obtained for the normal and tangential coefficients of restitution based on velocity ratios. It was observed that, as the slope angle increases (decrease in impact angle), COR_{VN} also increases slightly. As noted by Wu (1985), no clear correlation could be established between impact angles and the obtained COR_{VT} values.

It was observed that both energy-based coefficients of restitution COR_E and COR_{TE} increase as the slope angle increases (Figure 2.9). Therefore, COR_{VT} is the only parameter that does not demonstrate a clear relationship with changes in surface inclination. Chau et al. (2002) also identified that rotational velocity also depends on the impact angles (Figure 2.10). For the same slope inclination, the ratio between translational and rotational velocity is roughly constant, regardless of the mass of the block or energy levels achieved (Figure 2.10). Observations from the video frames demonstrated that the rotational kinetic energy represented up to 40% of the

24
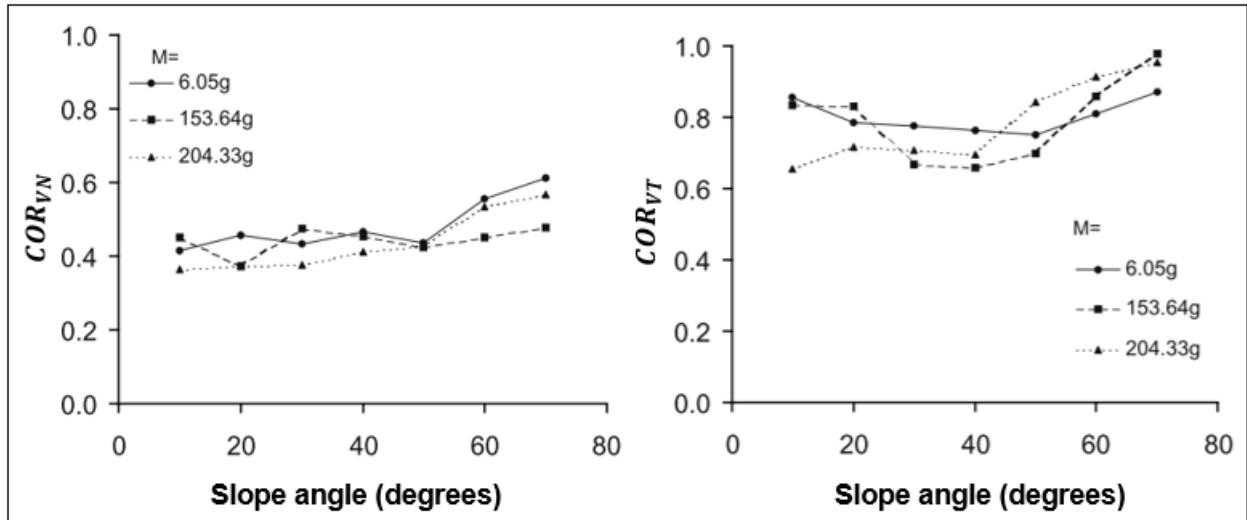
Figure 2.8. Normal and tangential components of COR$_V$ obtained by Chau et al. (2002) for different slope angles.
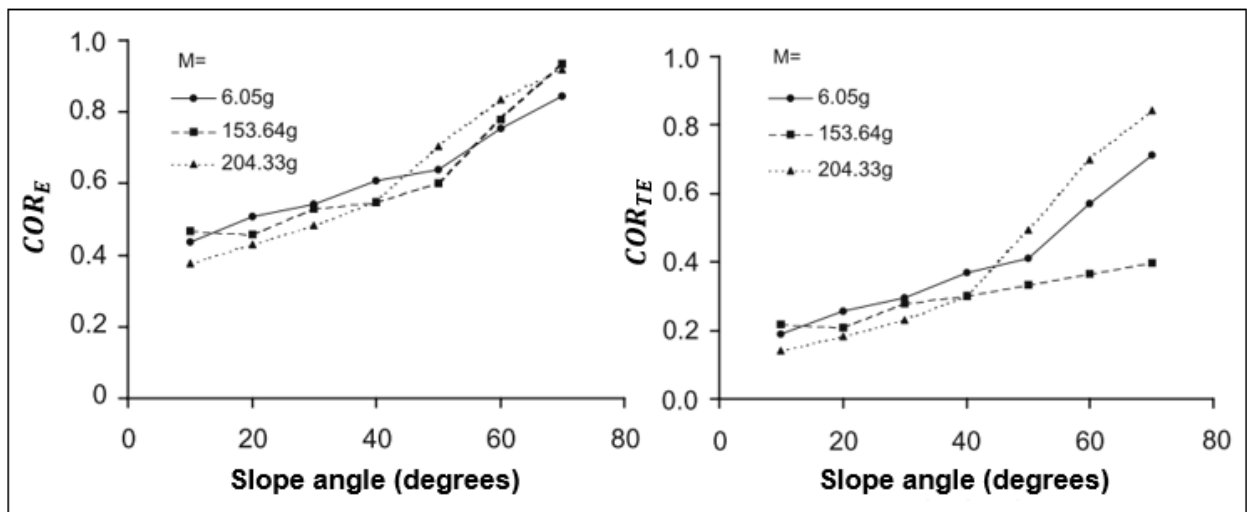
Figure 2.9. Energy-based COR$_V$ obtained by Chau et al. (2002) for different slope angles.

translational kinetic energy. Therefore, rockfall rotational motion cannot be disregarded during trajectory and energy estimates. Rotational velocities are critical during oblique impacts, and it is vital to assess how motion characteristics change during rockfall impacts.

Previous research conducted by Fornaro et al. (1990), cited by Chau et al. (2002), and Heidenreich (2004), evaluated energy restitution upon impacts on rock, debris, and detrital slopes.
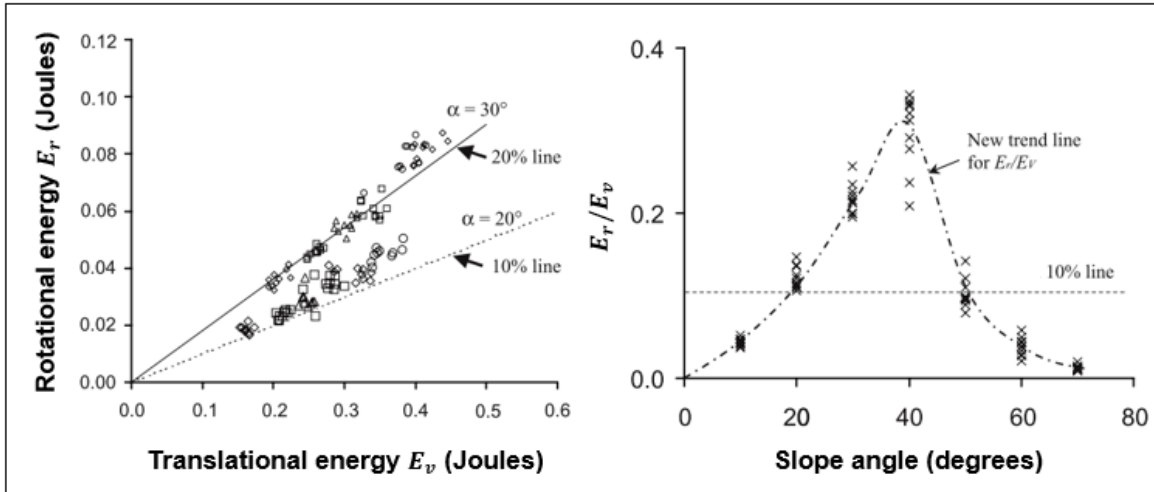
Figure 2.10. Relation between rotation, translation, ratio of energies, and slope angle (Chau et al., 2002).

Fornaro et al. graphically present pairs of normal and tangential coefficients of restitution (COR_{VN} and COR_{VT}) for the three slope materials, demonstrating the variability associated with these modeling parameters and their boundary conditions (Figure 2.11). Experimental data by Wu (1985), Fornaro et al (1990), and Chau et al. (2002) demonstrate that coefficients of restitution of rock slopes are higher in normal and tangential velocities when compared to soil slopes (Figure 2.12). The data corresponding to coefficients of restitution on rock from Fornaro et al. (1990) is presented with a dotted line in the graph.
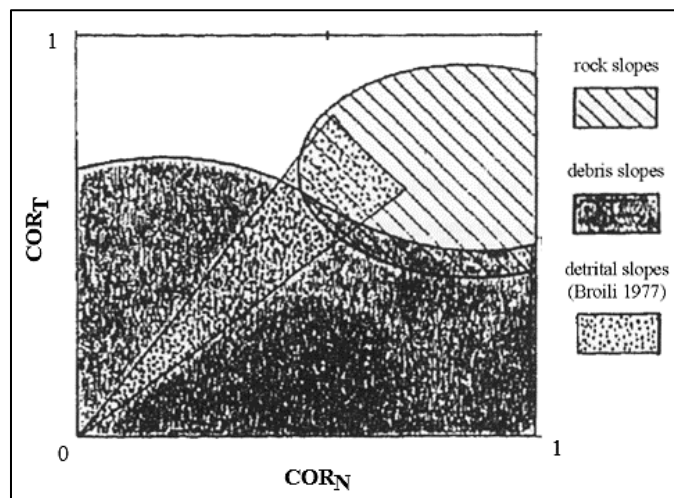
Figure 2.11. Ranges of coefficients of restitution (Fornaro et al., 1990, cited by Heidenreich, 2004).
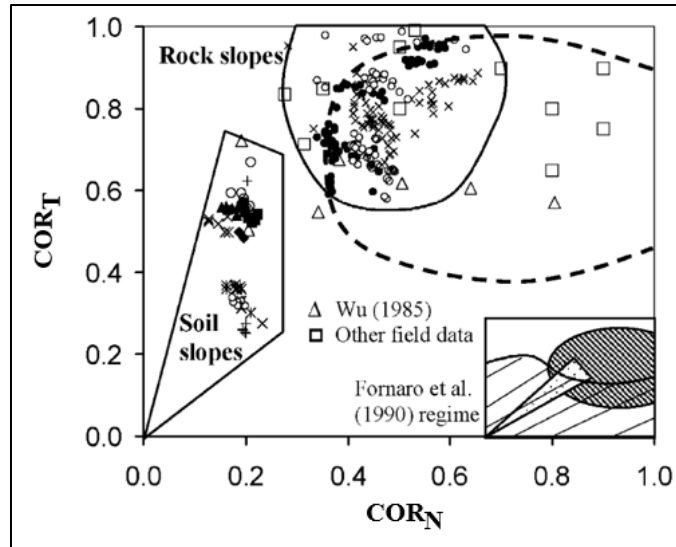
Figure 2.12. Experimental normal and tangential coefficients of restitution from literature for soil and rock slopes (adapted from Chau et al., 2002).

The restitution databases published in the literature show that most experimental studies conducted assess the bouncing phenomenon on rigid surfaces and that there are still few investigations on soft impact surfaces. Heidenreich and Labiouse (Heidenreich, 2004; Heidenreich and Labiouse, 2004; Labiouse and Heidenreich, 2009) conducted detailed small and half-scale parametric experimental campaigns widely cited in rockfall engineering to assess the behavior of falling blocks on sand under controlled conditions. Their research findings suggested that block motion on soft surfaces is complex.

Labiouse and Heidenreich investigated the impact mechanics of falling blocks on granular materials of different properties prepared under various conditions such as relative density, surface inclination, and block releasing mechanism. The block characteristics also varied during these experiments. The small-scale tests were performed on an inclinable box filled with sand of different types and different degrees of compaction (Figure 2.13). Two release mechanisms were used to allow for vertical and parabolic free fall.

27
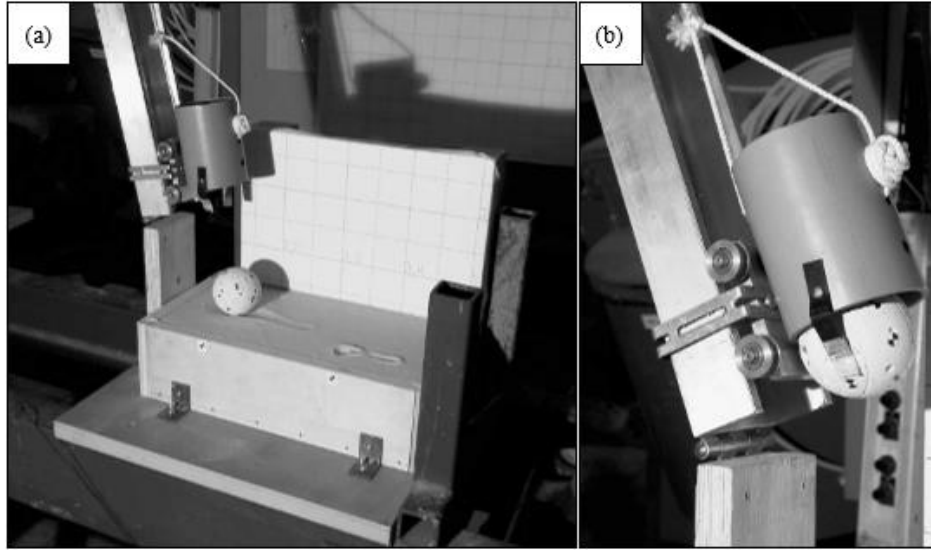
Figure 2.13. Experimental normal and tangential coefficients of restitution from literature for soil and rock slopes (adapted from Chau et al., 2002).

The half-scale experiments were conducted using an overhead crane and a circular shaft 8 m deep. The impact surface consisted of an inclinable container filled with granular material, prepared in surface inclinations between 0º and 40º (Figure 2,14). Blocks with weights between 1 and 10 kN were dropped from heights up to 10 m.

During both stages, Heidenreich and Labiouse demonstrated that block rebound and resulting coefficients of restitution for granular materials depend on the ground characteristics (material, inclination, conditions), block characteristics (weight, geometry), and fall kinematics (impact velocity, angle). Additionally, observations from video recordings show that motion during the impact is also controlled by block penetration, sliding, and rotation. As blocks fall with no rotation, they are quickly slowed down upon impact. The block embedment (penetration depth) and crater shape depend on the surface material properties and in-place conditions. The kinetic energy of solid blocks during impacts with soft ground is too small to produce plastic deformations to the released blocks. Consequently, the ground deforms elastically and plastically (Heidenreich, 2004; Labiouse and Heidenreich, 2009).

28
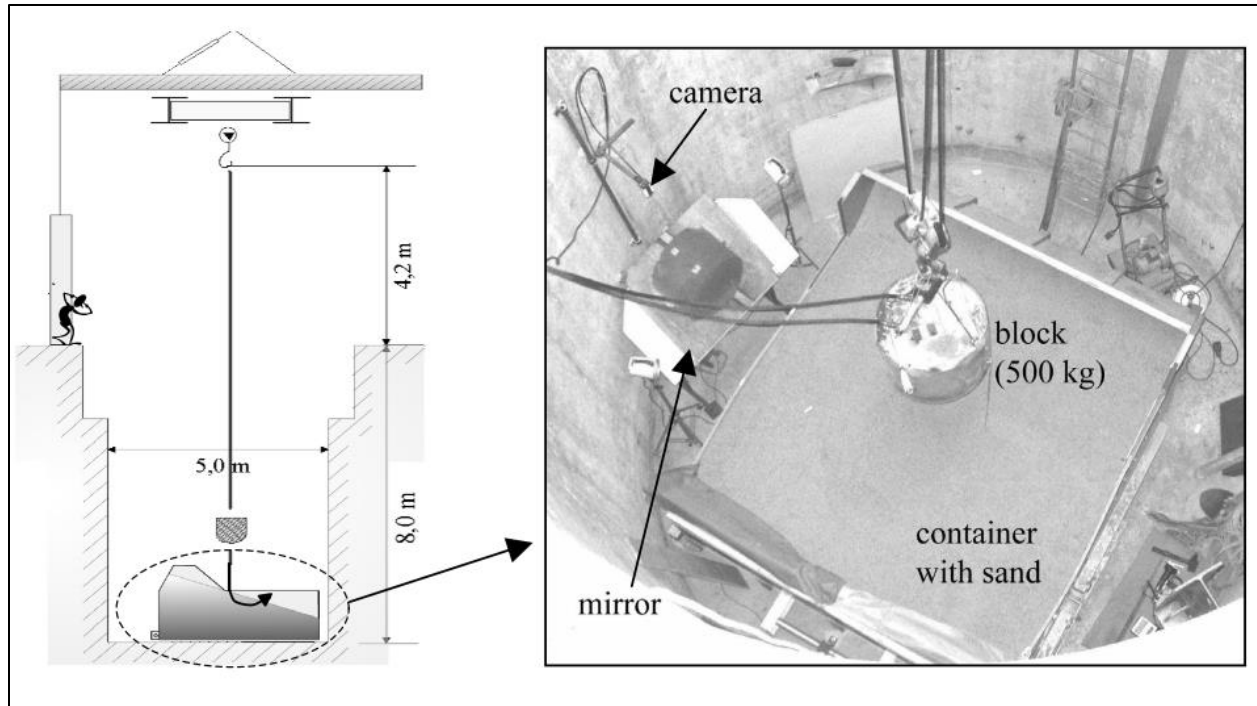
Figure 2.14. Scheme and photo of the test setup in half-scale (Heidenreich, 2004).

Vertical impacts on horizontal, compacted ground material cause very small to no rebound in the vertical direction. Higher impact velocities imply higher embedment depths and consequently lower bounce heights (energy restitution). Higher rebound heights are obtained for higher surface inclinations, and the resulting craters strongly influence the post-impact rotational velocities. Rotation after impact is typically not mobilized unless the falling block already has angular motion before impact. However, vertical impacts on inclined ground generate rotation during block rolling, often accompanied by sliding (Heidenreich, 2004; Labiouse and Heidenreich, 2009).

Laboratory tests demonstrated that denser blocks penetrate deeper into the ground, thus experiencing lower restitution coefficients. Additionally, high impact velocities and less compacted surfaces present higher embedment and energy loss, leading to less visible bounce heights (Heidenreich, 2004; Labiouse and Heidenreich, 2009). Since the penetration depth

influences the rolling motion, lighter blocks will create shallower craters with longer rolling paths. In general, the motion after impact is less prominent for heavier blocks (Heidenreich, 2004; Labiouse and Heidenreich, 2009).

Table 2.4 presents extensive research conducted by Heidenreich (2004) regarding rockfall behavior upon impact. Observations from several studies on different rockfall parameters were compared, as well as how each factor affects COR_{VN}, COR_{VT}, and COR_{TE}. From this data, it is possible to correlate previous observations regarding the normal and total energy coefficients of restitution (Chau et al., 2002) and show that they typically follow the same trends. Also, as noted by several authors (Wu, 1985; Chau et al., (2002); Asteriou et al., 2012; Asteriou et al., 2012; Asteriou and Tsiambaos, 2016), there is seldom a correlation between COR_{VT} and varying boundary conditions. Additionally, these trends also agree with empirical observations from Heidenreich (2004) concerning rock mass, ground compaction conditions, slope angle, and impact velocity previously described.

Extensive analysis of different research methodologies related to laboratory and field energy restitution has been evaluated in this review. For a summary of other experimental laboratory approaches under controlled conditions, the reader is referred to Appendix A, Table A.1 (Peng, 2000; Dias and Barroso, 2006; Asteriou et al., 2012; Basson et al., 2012; Saeidi et al., 2014; Arpaz, 2015; Ansari et al., 2015; Asteriou and Tsiambaos, 2016; Wang, 2018; Ghana et al., 2019).

The uncertainty related to rockfall assessments can also be associated with the different parameters and methodologies to evaluate energy restitution (which typically do not quantify block rotation), with no agreement on what approaches are more accurate and/or better reproduce reality (Asteriou et al., 2012). There exists a significant variety of experimental strategies to address rockfall mechanics. Although assumptions concerning the Newtonian physics of falling blocks are

Table 2.4. Observations related to coefficients of restitution (Labiouse and Heidenreich, 2009).

Parameter	COR_{VN}	COR_{VT}	COR_{TE}	Ground material	Source
Related to rock block					
Increasing rock mass	Decreases	No information	No information	Concrete, rock	Ushiro et al. (2000)
Increasing angularity	Decreases	Increases (slightly)	Decreases	Granite	Wong et al. (2000)
(shape changing from sphere to block)	No change when the impact angle increases from 30º to 60º; increases when the impact angle increases from 15º to 30º	Decreases (slightly)	Decreases (slightly)	Plaster	Chau, Wu, et al. (1999)
Related to ground material					
Increasing Young's modulus	Increases	Increases	No information	Natural slopes	Pfeiffer and Bowen (1989)
	Increases	Increases	No information	Natural slopes	Fornaro et al. (1990)
	Increases	Increases	No information	Plaster, rock, soil	Chau et al. (2002)
Increasing dry density	Increases when density > optimum density; no change when density < optimum density	Increases when density > optimum density; no change when density < optimum density	Increases when density > optimum density; no change when density < optimum density	Soil, plaster	Chau, Wong, et al. (1999)
Related to kinematics					
Increasing impact angle and thus a reduction in the slope angle (impact angle + slope angle = 90º)	Decreases	Increases (slightly)	No information	Wood, rock	Wu (1985)
	Decreases (slightly)	No information	No information	Granite, shotcrete	Wong et al. (2000)
	Decreases	No information	No information	Plaster, soil	Wong et al. (2000)
	Decreases (slightly)	No change	Decreases	Granite, shotcrete	Chau et al. (2002)
	Decreases	No change	Decreases	Plaster, soil	Chau et al. (2002)
Increasing drop height; leads to increasing impact velocity	Decreases	Decreases	Decreases	Limestone	Urciuoli (1988)
	Decreases (slightly)	No change	No information	Concrete, rock	Ushiro et al. (2000)

identical, it has been demonstrated that different test conditions will provide different restitution parameter values, even if the assessed materials are similar. Besides significant differences between test setups, aspects inherent to the test blocks (material composition, mass, shape) and

impact surfaces (material composition, size, presence of irregularities) will affect COR in modeled trajectories (Turner and Duffy, 2012a; Saeidi et al., 2014; Ghana et al., 2019). Also, the rate of video recording and operator dependence of tracking systems (Garcia, 2019) can influence estimated COR values to some extent.

Table A.2 (Appendix A) presents typical coefficients of restitution values for standard surfaces found in literature, compiled by Heidenreich (2004). The variation between test conditions can often result in COR values from experimental studies significantly different from default published values, which typically provide a broad description of the impact materials and generally do not describe their characteristics (Heidenreich, 2004; Asteriou et al., 2012). For example, laboratory tests conducted by Peng (2000) evaluated COR_{VN} values obtained on marl at different slope angles. The results were as low as 0.25 at 0º and as high as 0.88 for the same material at a 45º slope (Peng, 2000). The default COR_{VN} used in two-dimensional modeling is equal to 0.35 for bedrock (Rocscience, 2017).

Due to its high complexity and several influencing factors, Chau et al. (2003) do not recommend restitution coefficients to be defined as material constants but instead established by site-specific evaluations. Azzoni and de Freitas (1995) highlight the importance of conducting standardized field rockfall experiments for more consistent comparisons between models.

2.3.2. Field rockfalls

Rockfall trajectories and expected future events are typically assessed through full-scale experimental campaigns and/or computer simulations, which usually consider restitution coefficients from laboratory tests. Field tests are conducted to measure travel distances and estimate trajectories, bounce heights, and block velocities (Disenhof, 2018).

Turner and Duffy (2012a) highlight the critical importance of full-scale field experiments, especially for the calibration of computational models. Test blocks are selected according to the research objectives and limitations and released down previously characterized slopes. Besides trajectory and rockfall end locations, these experiments can provide more detailed information concerning block motion. The falls are monitored by video cameras and/or measurements of distances of interest, such as the runout distance and known points of impact. In situ tests are essential for a broader rockfall understanding and subsequent calibration of computational models (Duffy and Turner, 2012).

According to Duffy and Turner (2012), preparation measures for field assessments include:

- Select, measure, and weigh representative test rocks to fulfill the research interests,

- Conduct accurate surveys of the test slope,

- Select operational camera positions,

- Install and inspect possible mitigation devices needed,

- Control transportation traffic when applicable, and

- Verify test instrumentation (if applicable).

However, field experiments are time-intensive, and often only a small number of trials can be produced in a day. A limited number of observations can often lead to an apparent lack of a clear relationship between the data (Azzoni and de Freitas, 1995). The low number of experimental tests implies a limitation for statistical and parametric analyses, and it is pertinent to conduct an additional investigation in the laboratory for further parameter validation (Azzoni and de Freitas, 1995; Labiouse and Descoeudres, 1999; Duffy and Turner, 2012). A summary of field rockfall experiments conducted between 1960 and 2010 was compiled by Duffy and Turner (2012) and

presented in Table 2.5. It is possible to observe that all assessments aimed to define rockfall trajectories and/or evaluate protective design systems.

Although only a limited number of tests can be conducted, data analysis is time-consuming and not straightforward. Rockfall assessments with field simulation studies assessed in this research include Ritchie (1963), Wu (1985), Pfeiffer and Bowen (1989), Azzoni and de Freitas (1995), Pierson et al. (2001), Bourrier et al. (2012), Giacomini et al. (2012), Spadari et al. (2012), Bar et al. (2016), Singh et al. (2016), Asteriou and Tsiambaos (2018), Caviezel et al. (2018), Disenhof (2018), and Garcia (2019).

Different authors who conducted field experiments demonstrated that both surface and falling block parameters influence rockfall motion (Ritchie, 1963; Labiouse and Heidenreich, 2009; Duffy and Turner, 2012). Trajectories can be unpredictable during experimental trials, and additional attention is required to ensure that the rocks cannot reach transportation corridors or place research personnel at risk (Duffy and Turner, 2012).

The research report written by Ritchie (1963) and published by the Transportation Research Board (TRB) represented one of the first and most relevant milestones in rockfall engineering. The initial assessment proposed by Ritchie (1963) described a new approach that would subsequently innovate rockfall engineering evaluations and strategies.

Ritchie extensively explored hundreds of experimental rockfalls conducted on highway slopes. The main objective of the study was to diagnose rockfall motion aspects related to boundary conditions. His observations were used to define practical ditch design criteria based on slope height, slope angle, and catchment area depth. It was observed that rockfall motion type is strongly influenced by the slope angle, identifying specific ranges at which a particular behavior usually governs.

Table 2.5. Summary of field rock-rolling experiments performed since the 1960s (Duffy and Turner, 2012).

Test sponsor and approximate date	Reference	Purpose of test	Number or rocks rolled during test
1960s			
Washington DOT, 1963	Ritchie (1963)	Define rockfall trajectories; design fences and ditches	Hundreds
1970s			
City of Lecco, Italy, 1974	Broili (1974)	Define rockfall trajectories	10
North Carolina DOT, 1978	Evans (1989)	Define rockfall trajectories	146
British Columbia Ministry of Highways and Publick Works, 1978	Elston et al. (1978)	Define rockfall trajectories	350
1980s			
North Carolina DOT, 1984	Wu (1984); Evans (1989)	Define rockfall trajectories	Not defined
Caltrans, 1985	McCauley et al. (1985)	Fence, berms, trajectories	223
Golder Associates, British Columbia, Canada, 1987	Wyllie (1991)	Barrier designs	60
Caltrans, 1987	Duffy (1987)	Define rockfall trajectories	12
University of Arizona, Department of Mining and Geological Engineering, Tucson, 1988	Evans (1989)	Define rockfall trajectories	50
Colorado DOT, 1989	Barrett and Pfeiffer (1989)	Barrier designs	13
Caltrans, 1989	Smith and Duffy (1990)	Barrier designs	76
1990s			
Colorado DOT, 1991	Hearn (1991); Hearn et al. (1992)	Barrier designs	70
Caltrans, 1991	Duffy (1991)	Barrier designs	6
Geobrugg Inc., Switzerland, 1991	Duffy (1992)	Barrier designs	90
Geobrugg Inc., Switzerland, 1992	Duffy and Haller (1993)	Barrier designs	18
University of the Pacific, Stockton, California, 1993	Kane and Duffy (1993)	Barrier designs	24
Oregon DOT, 1994	Pierson et al. (1994)	Define rockfall trajectories	2,790
ISMES SpA, Bergamo, Italy; and Department of Geology, Impecial College of Science, Technology and Medicine, London, 1992-1995	Azzoni and de Freitas (1995)	Define rockfall trajectories	60
Caltrans, 1995	Beck (1995)	Define rockfall trajectories	15
Caltrans, 1996	Duffy and Hoon (1996a)	Barrier designs	16
Caltrans, 1996	Duffy and Hoon (1996b)	Barrier designs	25
Chung Cheng Institute of Technology, Taiwan, 1997	Hwu and Spang (1997)	Barrier designs	Not defined
Protec Engineering, Japan, 1998	Hoshida and Nomura (1998)	Barrier designs	9

Table 2.5 (cont.). Summary of field rock-rolling experiments performed since the 1960s (Duffy and Turner, 2012).

Test sponsor and approximate date	Source describing test	Purpose of test	Number or rocks rolled during test
Laboratorio di Fisica Terrestre, Lugano-Trevano, Switzerland, 1998	Bozzolo et al. (1998)	Define rockfall trajectories	7
Chama Valley Productions, LLC, Chama, New Mexico, 1998	Andrew et al. (1998)	Barrier designs	31
Caltrans, 1998	Duffy et al. (1998)	Barrier designs	56
2000s			
Caltrans, 2000	Duffy and Jones (2000)	Barrier designs	25
Oregon DOTm 2001	Pierson et al. (2001)	Define rockfall trajectories	11,250
Geological Survey of Bolzano, Geoproject, Inc., and Bolzano Engineering Office, Bolzano, Italy, 2003	Scweigl et al. (2003)	Define rockfall trajectories	19
Colorado DOT, 2004	Ardnt et al. (2009)	Define rockfall trajectories	10
Department of Civil and Environmental Engineering and Architecture, Università degli Studi di Parma, Parma, Italy, 2003	Giani et al. (2014)	Define rockfall trajectories	83
Colorado DOT, 2005	Ardnt et al. (2009)	Barrier designs	7
Cemagref Grenoble, St. Martin d'Hères, France, 2005 Cemagref Grenoble, St. Martin d'Hères, France, 2005	Dorren, Berger, Le Hir, et al. (2006)	Define rockfall trajectories	202
	Dorren, Berger, and Putters (2006)	Evaluate influence of trees	202
Caltrans, 2006	Whittman and Duffy (2006)	Define rockfall trajectories	56
IGOR, Inc., Trento, Italy, 2007	Badger et al. (2008)	Barrier designs	3
Colorado DOT, 2009	Arndt et al. (2009)	Barrier designs	10
Caltrans, 2009	Salisbury et al. (2009)	Define rockfall trajectories	70

According to Ritchie (1963), blocks tend to roll on slopes with inclinations up to 45º, bounce between 46º and 63º, and fall freely for surface inclinations higher than 63º (Figure 2.15). It was observed that free-falling blocks rarely bounce after impact; alternatively, translational

velocity is converted into rotational velocity. Ritchie also noted that the rebound potential of falling blocks was significantly decreased when embedded in soft sand catchment ditches.

Falling blocks traveling at high velocities often spend most of the rockfall duration in free fall. Ritchie classifies 45° slopes as the most concerning controlling horizontal rock impulse, and blocks falling from very steep slopes are not as concerning as less inclined surfaces. Flatter slopes create higher lateral and rotational motion conditions, which are more challenging to dissipate energy. Field observations also suggested that slopes steeper than 76° required minimal rock motion at the start point for subsequent free fall.
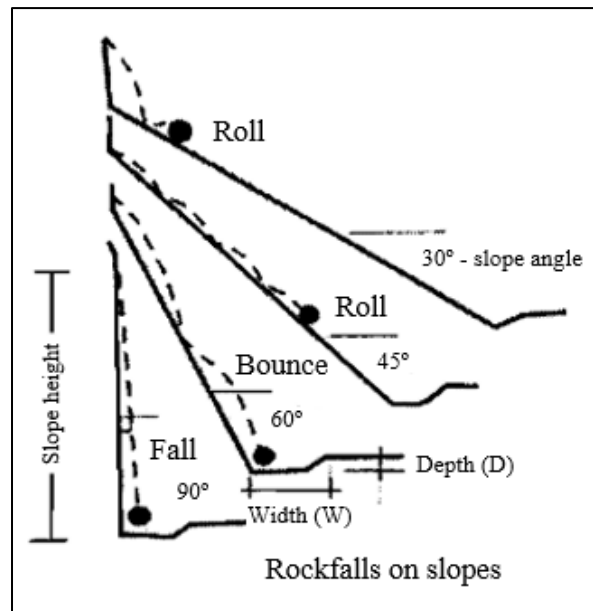
Figure 2.15. Rockfall design criteria (Ritchie, 1963, adapted).

According to Pierson et al. (2001), falling rocks infrequently hits the rock face at nearly vertical slopes, and thus rotational kinetic energy is less developed upon impacts on the catchment ditch. Less rotation consequently implies smaller rock runout. Besides slope angle, vegetation and talus (rock fragments) also play an important role in controlling rock velocities and bounce heights (Duffy and Turner, 2012; Tavares, 2015).

A report prepared by the Japan Road Association, JRA (1983) regarding rotational energy during rockfall experiments provides data from 60 rockfall experiments on slopes with inclinations between 32° and 52°. Although published in Japanese, the paper was cited in relevant rockfall assessments published in the literature (Chau et al., 2002; Heidenreich, 2004; Turner and Duffy, 2012a; Wyllie, 2014). The results obtained demonstrated that the rotational kinetic energy (KE_R) was on average 10% of the translational kinetic energy (KE_T). Additionally, approximately 50% of the data in the KE_R vs. KE_T plot (Figure 2.16) was below the 10% line ($KE_R/KE_T \leq 10\%$), while almost all data was below the 40% line ($KE_R/KE_T \leq 40\%$). Tests with more oblique impacts produced higher ratios and had a more significant rotation. The results obtained by JRA (1983) regarding block rotation were later validated by Chau et al. (2002) in the laboratory.
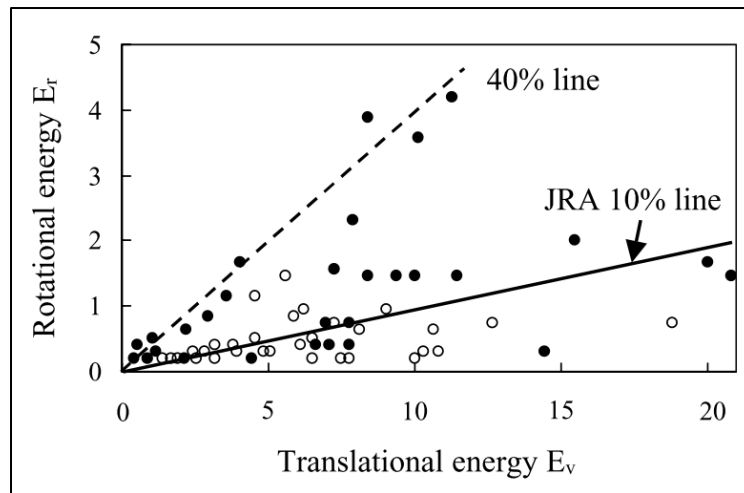
Figure 2.16. Rotational and translational kinetic energies in ton-m (JRA, 1983; modified by Chau et al., 2002).

Wyllie (2015) discusses rockfalls conducted by Ushiro et al. (2006). Experiments were performed on a 42 m tall slope composed of a 26 m tall rock face inclined at 44° and a 16 m talus slope inclined at 35°. High-frame rate cameras captured rockfall motion (Figure 2.17), in which

measured rotational velocities varied between 350 and 1900 degrees per second (dps). Boulders with irregular shapes described rotational velocities typically 300 dps lower.

Giacomini et al. (2012) estimated rotational velocities shortly before and after impact during experimental rockfalls, about a single direction. It was observed that the rotational kinetic energy increases relative to the total energy from 3% to 21% after the impact. The significance of rotational motion has also been assessed during tests conducted by Ferrari et al. (2013). They demonstrated that the rotational energy after impact represents 3% to 16% of the total kinetic energy. Additionally, Ferrari et al. (2013) also observed that tangential velocities after the impact tend to increase (compatible with the increase in rotation) while the normal velocities decrease.
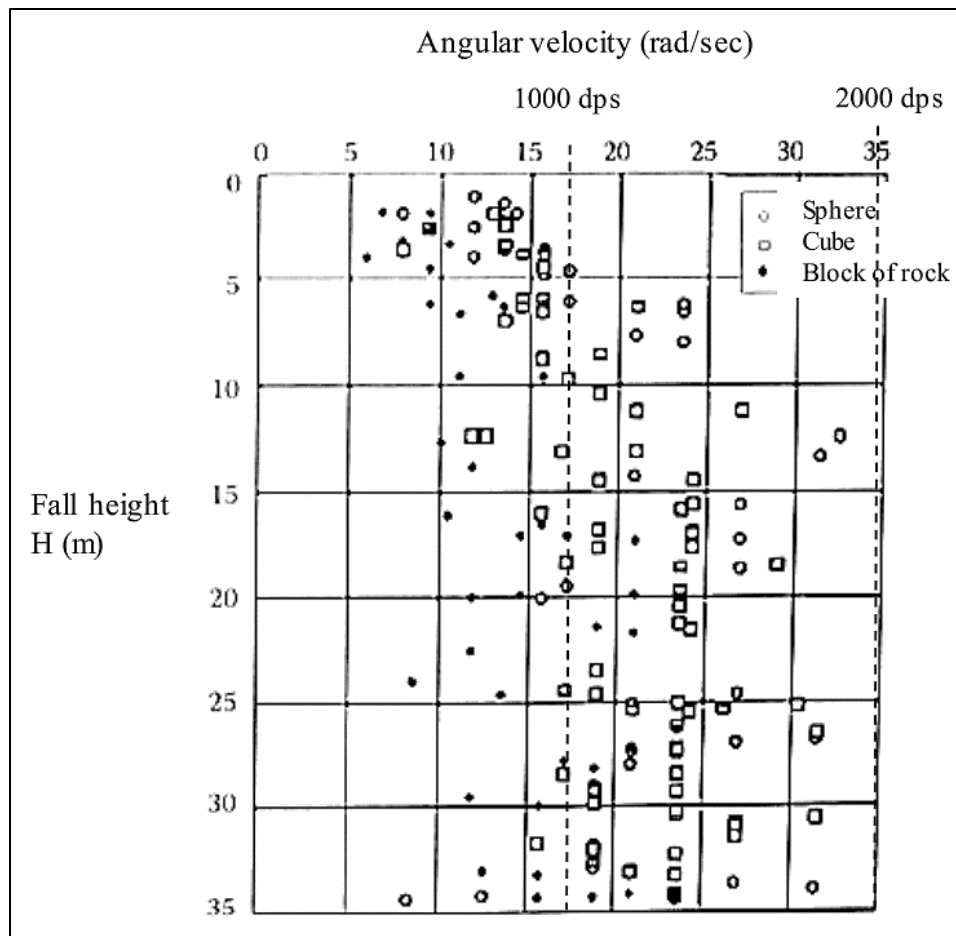
Figure 2.17. Rotational velocities from field rockfalls (Ushiro et al., 2006, cited by Wyllie, 2015).

39

Milestone studies published in rockfall engineering highlight the variability of rockfall trajectories and their respective boundary conditions (Azzoni and de Freitas, 1995; Heidenreich, 2004; Heidenreich and Labiouse, 2004; Labiouse and Heidenreich, 2009). Authors such as Chau et al. (2003) recognize the scarce availability of experimental data at real rockfall sites and do not recommend applying empirical data to areas with different settings.

Azzoni and de Freitas (1995) conducted 60 experimental rockfalls. They assessed their lateral dispersion, defined as the ratio of the horizontal distance between the most diverging rockfall paths (D) and the slope length (L), measured along with the slope profile. Azzoni and colleagues observed that lateral dispersion of rockfalls (D/L) typically varies between 10% and 20%, and the highest distributions commonly occur along longer rock paths.

Rock size is characterized by Pfeiffer and Bowen (1989) as a critical parameter that needs to be analyzed in conjunction with surface roughness. According to Ritchie (1963) and Azzoni et al. (1995), larger blocks have higher moments of inertia and are expected to travel further down slopes, as they are less likely to stop with surface irregularities. However, regarding runout distances, large rocks typically roll and slide at the bottom of slopes and are expected to travel short runout distances and come to a complete stop near the rock face (Evans and Hungr, 1993; Azzoni and de Freitas, 1995). The durability of falling blocks is also a relevant characteristic, as rock types and shapes that are less likely to fragment will consequently present less variability in behavior. Heidenreich (2004) considers the size gradation of talus slopes a natural indicator of energy loss during potential impacts.

Field observations from Azzoni and de Freitas (1995) identified that falling blocks usually start to rotate around their longest axis (smallest inertia). As velocity increases, the blocks begin to spin around their longest axis of inertia, similar to a bicycle wheel. The dispersion of trajectories

was strongly influenced by slope angles, which help define the direction of rebound. Steeper slopes tend to lead to smaller rockfall dispersion. Reliable trajectory and hazard assessments require a preliminary recognition of potential rockfall start locations and likely block sizes.

The farthest distance traveled by a rock from the start location is a relevant parameter for evaluating protective structures (Wyllie, 2015). It is particularly challenging to implement reliable rockfall protective systems in tall rock cuts, typically associated with scattered rock runout (Pierson et al., 2001; Chau et al., 2003). Chau et al. (2003) also indicate the variability of release mechanisms, falling block volumes, kinetic energy, and drop heights as additional factors that need to be considered as they increase trajectory uncertainty in field assessments.

For a summary of other experimental field approaches under controlled conditions, the reader is referred to Appendix A, Table A.3 (Azzoni and de Freitas, 1995; Giani et al., 2002, 2004; Asteriou et al., 2012; Giacomini et al., 2012; Bar et al., 2016). As observed for the laboratory tests, different experimental approaches can result in relatively distinct values between similar materials. Labiouse and Descoeudres (1999) suggest that matching the static characteristics of materials during rockfall on the model is less complicated than accurately modeling the dynamic motion of falling blocks.

Although frequently used as an analysis method of natural rockfalls, it is complex and not often possible to quantify rock kinematics through back analyses of past events. This approach is commonly used to evaluate known start and endpoint locations of falling blocks (Bourrier et al., 2012). Back analyses can be conducted after the occurrence of natural rockfalls for estimating coefficients of restitution. A trial-and-error approach is used to calibrate modeling predictions based on field observations. It is desirable to have as much information as possible regarding

velocities, bounce heights, and runout distances (Labiouse and Descoeudres, 1999; Turner and Duffy, 2012a).

2.3.3. Instrumented rockfalls

Monitoring technologies can be used to provide critical insight into the conception and effectiveness of rockfall protective systems. Instrumentation is used in rockfall engineering as an active process to observe, measure, and evaluate conditions and mechanical properties related to falling rocks and their interaction with impact surfaces (Andrew et al., 2012). Instrumentation can be used in rockfall monitoring to measure displacements and movement rates associated with rock masses and monitor and evaluate protective measures (Andrew et al., 2012).

As previously mentioned, experimental studies demonstrated that video recordings can provide helpful information about the behavior of falling rocks (Wu, 1985; Azzoni and de Freitas, 1995; Azzoni et al., 1995; Chau et al., 2002; Heidenreich, 2004; Asteriou et al., 2012; Arpaz, 2015; Saeidi et al., 2014; Ansari et al., 2015; Asteriou and Tsiambaos, 2016; Li et al., 2016; Wang et al., 2018; Ghana et al., 2019). Frame-by-frame measurements contribute relevant design information such as bounce heights, velocities, kinetic energies, and block spatial changes. When rock motion is relatively simple and complex rotations do not occur, it is possible to estimate translational and rotational velocities through a sequence of frames (Andrew et al., 2012).

Although video monitoring can provide vital information for rockfall assessments, recent researchers highlight the lack of experimental data with instrumentation techniques from the falling rock perspective (Apostolov and Benoît, 2017; Caviezel and Gerber, 2018; Disenhof, 2018). To address this issue, scientists started to instrument rocks themselves with Inertial Measurement Units (IMUs), including triaxial accelerometers and gyroscopes for precise

information regarding rock rotation and impact (Apostolov (2016); Caviezel et al., 2017; Caviezel and Gerber, 2018; Caviezel et al., 2018; Disenhof, 2018). According to Apostolov (2016), accelerometers quantify linear acceleration vectors about three mutually orthogonal axes (X, Y, and Z) and Earth gravity vector, and gyroscopes measure rotational velocities about the same triaxial reference system.

Acceleration and rotation data of instrumented rockfalls provide statistical information that can be used to calibrate current predictive methods and minimize the significant assumptions and uncertainties associated with rockfall assessments (Apostolov and Benoît, 2017). While observational studies present substantial limitations, including camera positions and data extraction, instrumented experiments are easier to set up and do not present constraints besides drilling the rocks to be tested (Caviezel et al., 2018).

This thesis presents experimental methodologies recently conducted at the Swiss Federal Institute for Forest, Snow, and Landscape Research, WSL Institute (Caviezel et al., 2017; Caviezel and Gerber, 2018; Caviezel et al., 2018), and at the University of New Hampshire, UNH, USA (Disenhof, 2018).

Caviezel and colleagues (Caviezel et al., 2017; Caviezel and Gerber, 2018; Caviezel et al., 2018) developed and implemented the StoneNode sensor (Figure 2.18). It consists of a combination of three-axis accelerometers (±400 g) and three-axis gyroscopes (±4000 dps) to measure accelerations and rotational velocities during rockfall experiments with rocks of different shapes at sampling rates between 400 and 500 Hz. These assessments aimed to calibrate their 3D modeling software RAMMS, as further discussed in item 2.5.
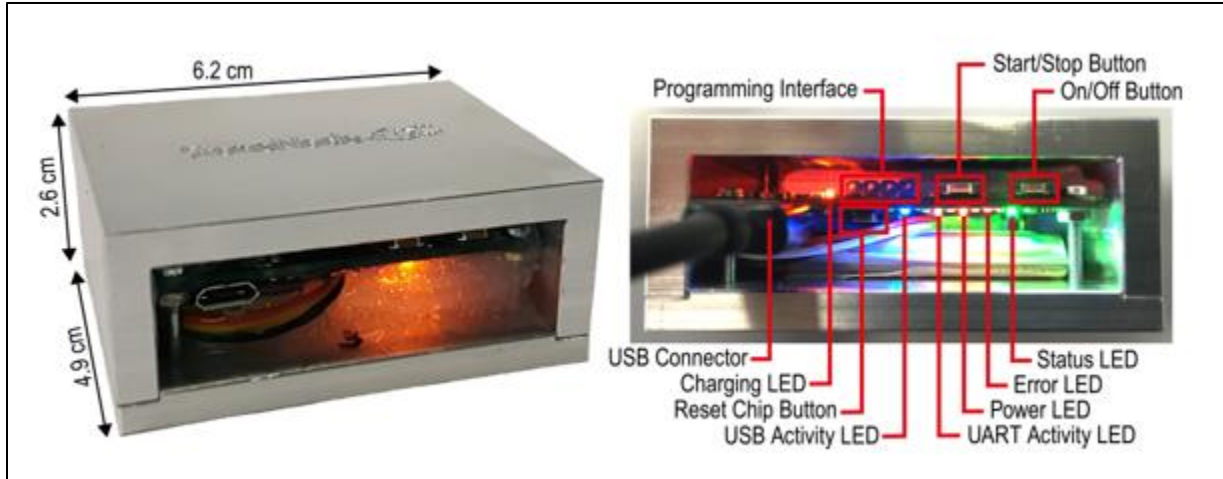
Figure 2.18. StoneNode developed by Caviezel et al. (2017), Caviezel and Gerber (2018), and Caviezel et al. (2018).

More than 50 instrumented tests with rocks of different shapes were conducted on a 50 m tall grassy rocky slope with a maximum inclination of 42º. The shape of each rock was classified according to the particle shape classification diagram developed by Sneed and Folk (1958), based on the length, width, and thickness of the block. Figure 2.19 presents the models of the instrumented rocks and their respective classification according to the Sneed and Folk criteria.
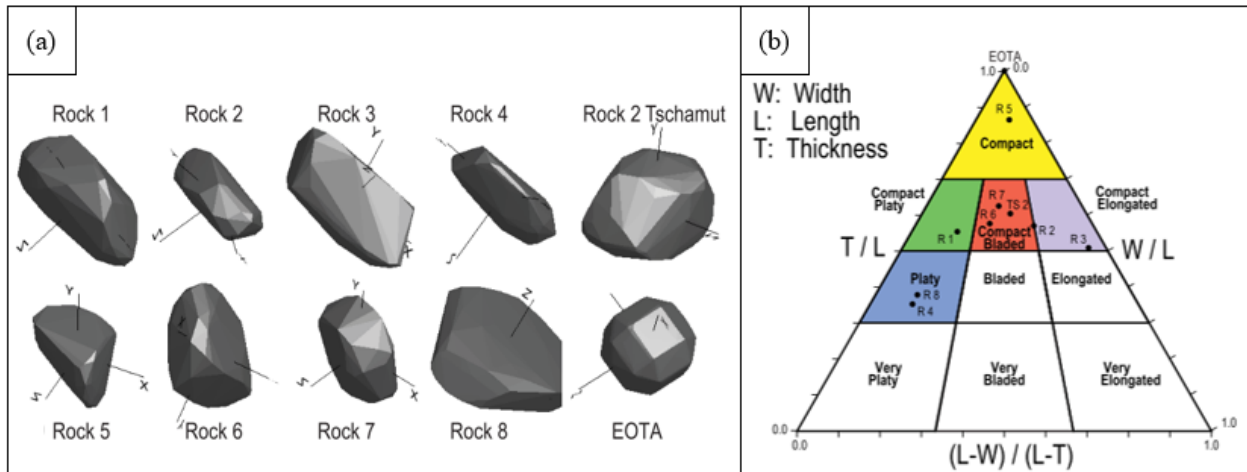
Figure 2.19. (a) Digitized models of the instrumented rocks, and (b) Sneed and Folk (1968) classification diagram of the instrumented rocks (Caviezel et al., 2018).

Each test rock was drilled (68 mm diameter) in its center of gravity (CG) and painted to better visualize rock positions and orientations during video analyses. The CG location was also

marked in black to identify the sensor position through video. The StoneNode was embedded in the test rocks before each experiment, as presented in Figure 2.20. Three-dimensional data were obtained to quantify changes in acceleration and rotation and assess high-impact ground interaction. The sensor is placed in a specific orientation inside each test block. The data for X, Y, and Z can be related to the block characteristics (dimensions, moments of inertia) of the three axes.
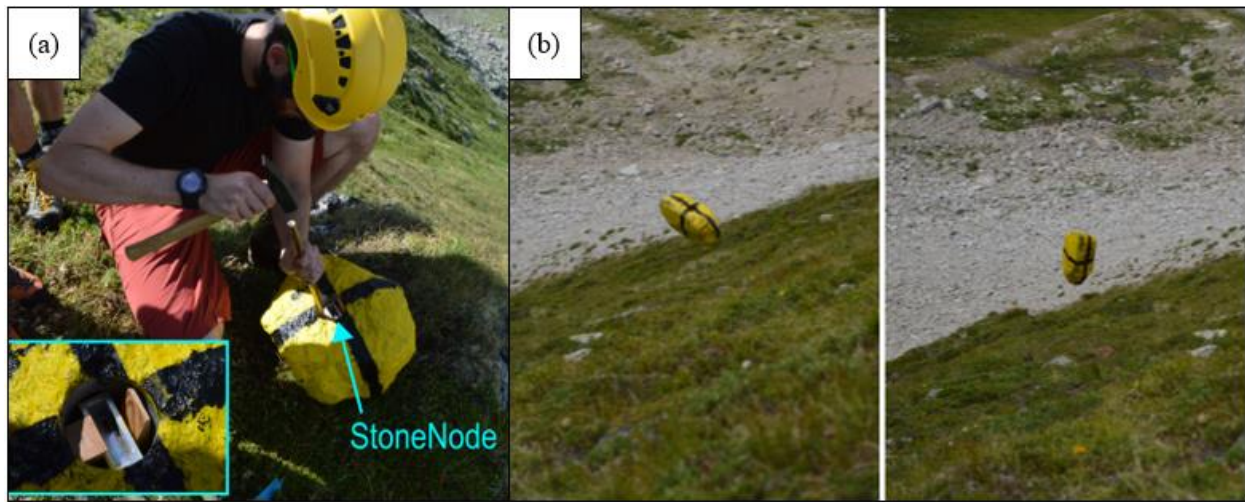
Figure 2.20. (a) StoneNode embedded in a drilled 68 mm hole, and (b) instrumented test (Caviezel et al., 2018).

Data outputs from two field tests conducted by Caviezel et al. (2018) are shown in Figure 2.21. Impacts can be detected through sharp acceleration peaks in the experimental data, immediately followed by rotational velocities changes. Figure 2.21(a) presents acceleration and rotation data for a test whose rotation occurred predominantly about X. The direction of rotation was reversed at about 168 s, immediately after a high impact. Additionally, Figure 2.21(b) displays the data output for a test at which the rock disintegrated upon high impact on the ground. Both trials with rock 7 demonstrated higher rotational velocities, near the sensor capacity of 4000 dps, about the X axis.

Caviezel and Gerber (2018) outline criteria that accelerometers and gyroscopes must follow during experimental rockfalls:

- The measuring range of each sensor should not be exceeded,

- At-rest, the rotational velocity should be 0, and the resultant acceleration should be 1 g,

- During free fall, the resultant rotational velocity should remain constant, with zero absolute acceleration, and

- Constant resultant rotational velocity between two acceleration impacts indicates two separate ground contacts.
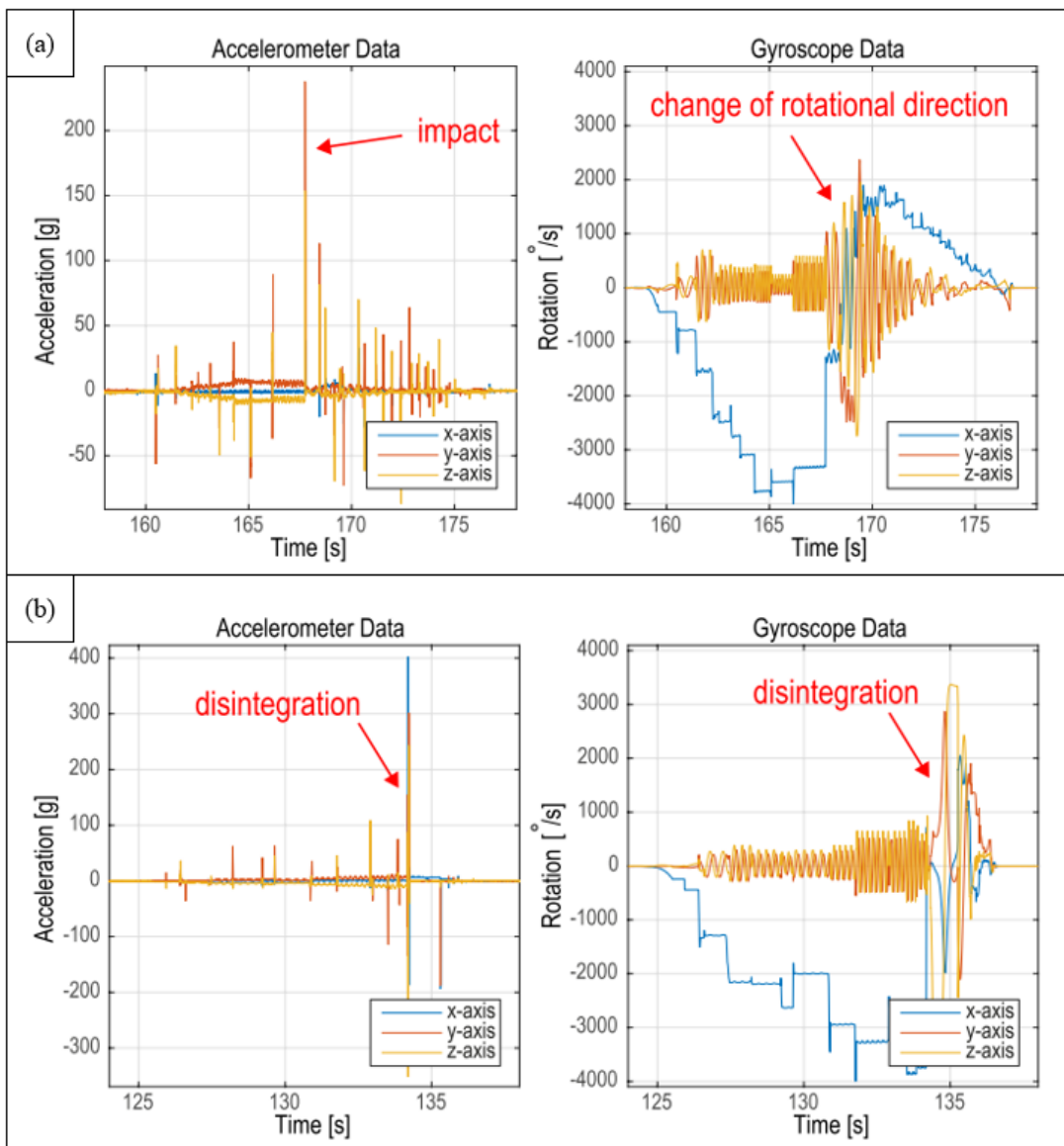
Figure 2.21. Two experimental rockfall tests with a compact bladed rock. It can be observed (a) an abrupt change in the rotational direction and (b) rock disintegration due to a heavy impact on the ground (Caviezel et al., 2018).

Their study confirmed field observations from Ritchie (1963). Higher velocities and higher drop heights in steeper slopes lead to fewer ground contacts than less steep slopes. Also, the data suggest that the test rocks tend to stabilize their rotation about the largest axis of inertia (Caviezel et al., 2018). The obtained data demonstrated that it is possible to gather accurate information on the acceleration and rotation of falling blocks.

The StoneNode sensor was considered a simple but reliable tool to analyze rockfalls (Caviezel and Gerber, 2018; Caviezel et al., 2018). Caviezel et al. (2018) suggest that the chosen measuring limits of the StoneNode are appropriate to capture rockfall motion. The measuring limit of 4000 dps was only exceeded for small rocks. Larger blocks have higher moments of inertia and are expected to result in lower rotational velocities. Acceleration measurements only exceeded the sensor limit of 400 g on rare occasions, such as during rock fragmentation.

Similar to Caviezel et al. in Switzerland, research conducted at the University of New Hampshire (Durham, NH, USA) since the 2000s has developed and improved four generations of Smart Rock (SR) sensors. SRs can instrument field and laboratory rockfall experiments from the falling rock perspective (Harding, 2011; Cassidy, 2013; Gullison, 2013; Harding et al., 2014; Apostolov, 2016; Apostolov and Benoît, 2017; Disenhof, 2018). A summary of previous generations of the Smart Rock sensor and field rockfall experiments conducted by Disenhof is presented in section 2.4.

2.4. Smart Rock sensor

Smart Rock (SR) sensors are sufficiently small, fully autonomous devices designed at the University of New Hampshire (UNH). They are applicable to a wide variety of geotechnical

problems where motion tracking is valuable, such as landslides, debris flow, and rockfalls (Apostolov, 2016; Apostolov and Benoît, 2017).

There are currently four generations of Smart Rock sensors (Figure 2.22), developed and improved by former UNH graduate students (Harding, 2011; Cassidy, 2013; Apostolov, 2016). The first two generations of SRs were initially designed to track the position of soil particles over time during debris-flow flume experiments (Harding, 2011; Cassidy, 2013; Gullison, 2013). Further sensor improvements led to the third- and fourth-generation SRs, applicable to both debris flow and rockfall experiments (Apostolov, 2016; Disenhof, 2018). Previous research conducted with the first three generations of SRs is presented in this chapter. The fourth-generation SR, used in this experimental research, is presented in Chapter 3 (Research Methodology). The obtained data from all SR generations are written to a micro-SD card for easy data processing.
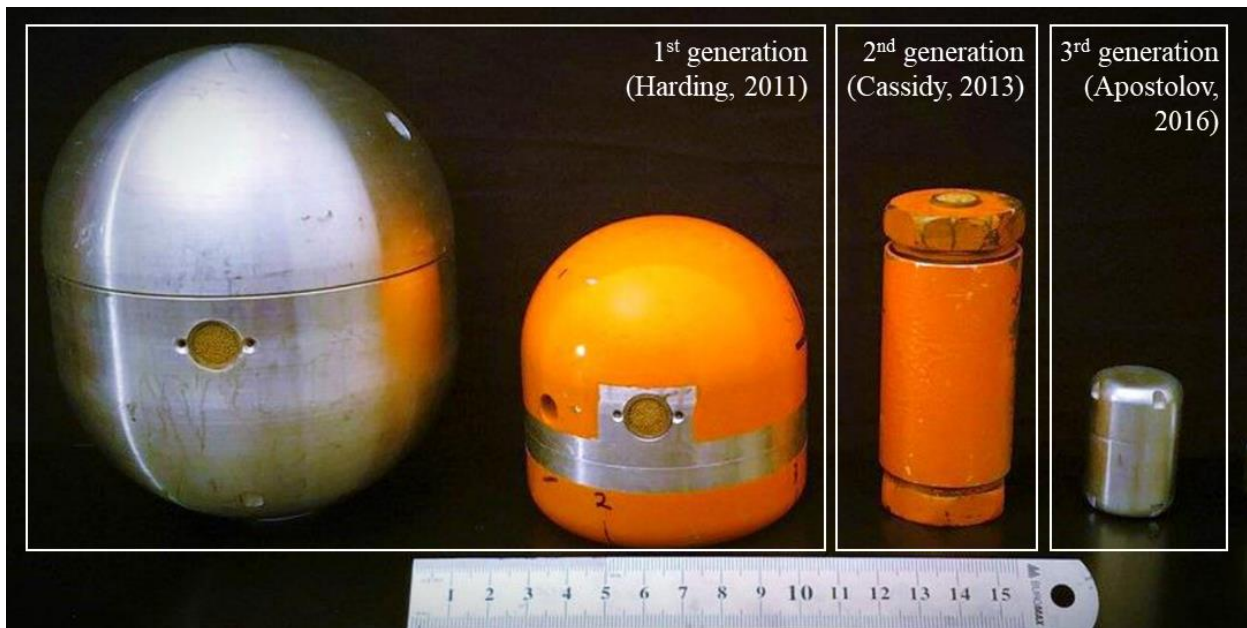
Figure 2.22. Previous generations of Smart Rock sensors (Apostolov, 2016. The reference ruler is in centimeters.

First idealized by Professor Pedro de Alba, Professors Jean Benoît (Civil Engineering) and Barry Fussell (Mechanical Engineering) along with Harding (2011) produced the first-generation

SR which was evaluated in the flume facility of the United States Geological Survey (USGS) by Gullison (2013). It was used to assess and track particle motion during instrumented debris flow experiments. It included a six-degree-of-freedom inertial measurement unit (IMU) formed by a ±18 g triaxial accelerometer, a ±1200 dps triaxial gyroscope. Additionally, the device was also equipped with ±5 psi pore-pressure sensors. Experimental observations demonstrated that the sensor was capable of capturing debris flow motion. However, the signal noise coupled with the absence of a fixed three-axis reference frame (due to sensor rotation) induced significant errors into integrations of acceleration and rotation data for particle position estimates. Therefore, it was concluded that it is nearly impossible to determine the SR position over time with sufficient accuracy with the technology at that time (Harding, 2011; Gullison, 2013).

The second-generation SR was developed at UNH by Cassidy (2013) and was smaller in dimension than the previous design (Harding, 2011). Given previous outcomes in determining the SR position, the IMU was not included in the second version, including a ±16 g triaxial accelerometer, a pore-water pressure sensor, and a temperature sensor.

The third-generation SR was developed by Apostolov (2016) and Professor Jean Benoît. It initially included a ±16 g triaxial accelerometer, a ±2000 dps gyroscope, and a digital magnetometer. It was used to evaluate large-scale experiments of gravity-driven landslides with ceramic particles with diameters ranging between 3 and 25 mm (Figure 2.23). These tests were conducted in collaboration with the Civil Engineering Department of Queens University in Kingston, Canada.

Further development of this version by Apostolov included a third-generation Smart Rock suitable with acceleration, and rotational velocity ranges expected during rockfall experiments. Therefore, the rockfall SR included low-g (±16 g) and high-g (±400 g) accelerometers and a 3-

axis ±4000 dps gyroscope. The measuring ranges were increased as rockfall events are expected to experience higher accelerations and rotational velocities than hazards associated with soil movements. The rockfall SR is contained inside a 25.4 mm diameter, 42 mm long custom 3D printed plastic shell (Figure 2.24) and performs data acquisition at a frequency of 500 Hz, determined in previous research at UNH to be sufficient for rockfall field experiments.
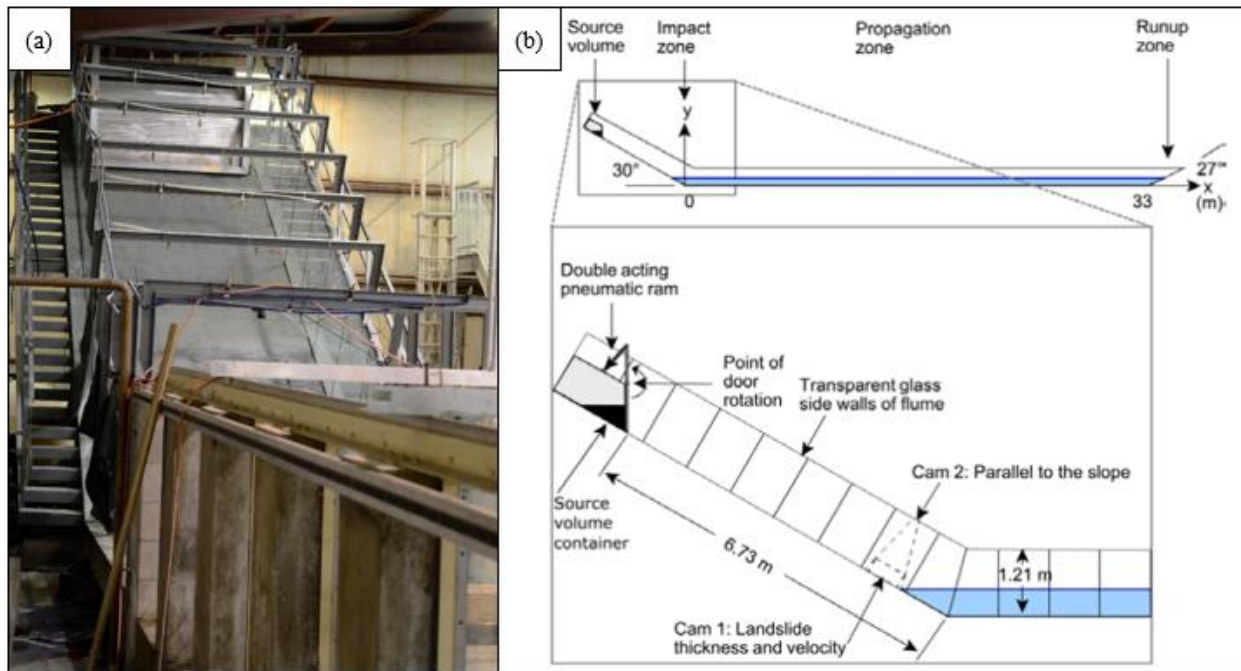
Figure 2.23. (a) Flume at Queens University Coastal Engineering laboratory, and (b) experimental apparatus for gravity-driven landslide-generated tsunamis (Apostolov, 2016).

The dual accelerometers allow the SR to capture the full range of accelerations the tested rock may experience during a rockfall. While the ±400 g accelerometer captures more significant magnitude accelerations produced by higher impacts from a fall or a bounce, the ±16 g accelerometer captures smaller magnitude accelerations not gathered from the high-g accelerometer since accelerations within ±2 g are typically obscured by noise. The ±16 g accelerometer was limited purposely to ±8 g to decrease noise in the acceleration signal; this can
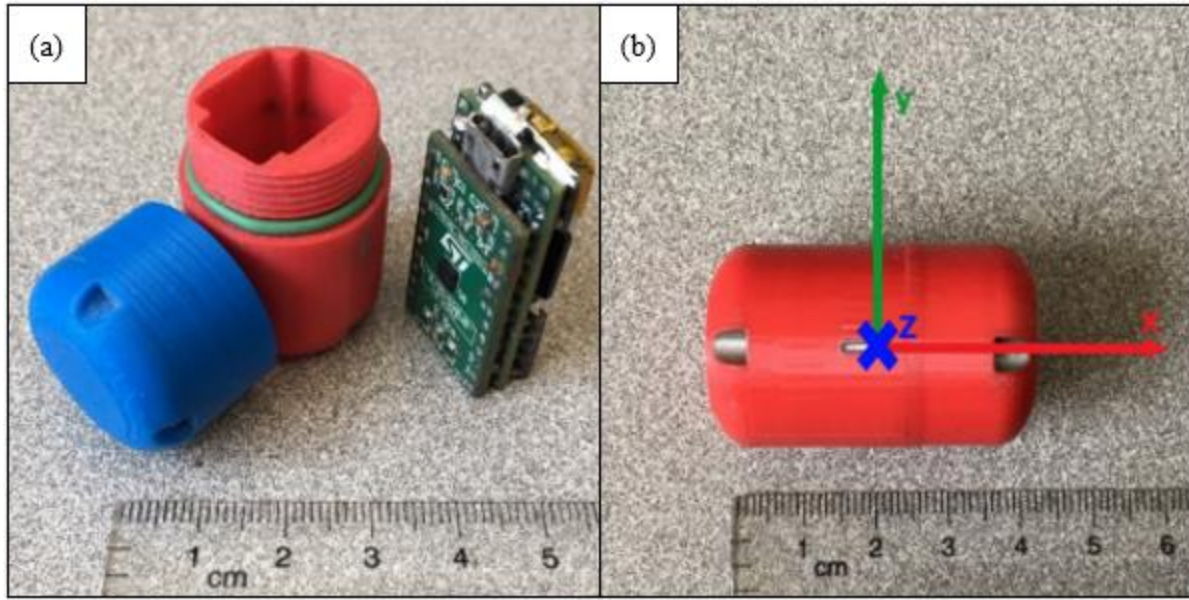
Figure 2.24. (a) 3rd generation Smart Rock sensor and shell, and (b) SR axes orientation (Disenhof, 2018).

be changed to ±2, ±4, ±8, or ±16 g, as desired. The low-g accelerometer presents a significant advantage in evaluating the rock behavior as it allows users to identify whether the rock is in free fall (0 g) or at-rest (1 g). The high-g accelerometer can also be adjusted to ±100, ±200, or ±400 g, and the high-speed gyroscope can be adjusted to ±500, ±1000, ±2000, or ±4000 dps. However, higher measuring ranges also increase inherent noise levels (Apostolov, 2016; Disenhof, 2018).

A test of the rockfall SR conducted by Disenhof (2018) is presented in Figure 2.25. Video frames A through H show when the sensor was held (A), dropped (B), hit the ground (C), and bounced three times (D – G) before rolling and coming to a stop (H). At stage A, while the rock was at-rest, the acceleration reads 1g. In free fall (B, D, and F), the low-g accelerometer reads 0 g. The Smart Rock data output, processed in MATLAB by Disenhof (2018), is shown on the right. Observations from Disenhof (2018) showed that the SR data can be confirmed with video analysis. When the rock was dropped (B), it predominantly rotated about its Y axis (green line) and described a constant rotational velocity of 360 dps. Upon its first impact with the ground (C),

51

Figure 2.25. Results of a drop test with the 3rd generation Smart Rock. Left: progression of the falling SR. Right: SR output (Disenhof, 2018).

it experienced 90 g in deceleration. It bounced while rotating about Y in the opposite direction, with a 780 dps resultant rotational velocity (D) before bouncing two other times with decreasing accelerations (E – G). Last, the SR rolls about X (H) before coming to a stop (Disenhof, 2018).
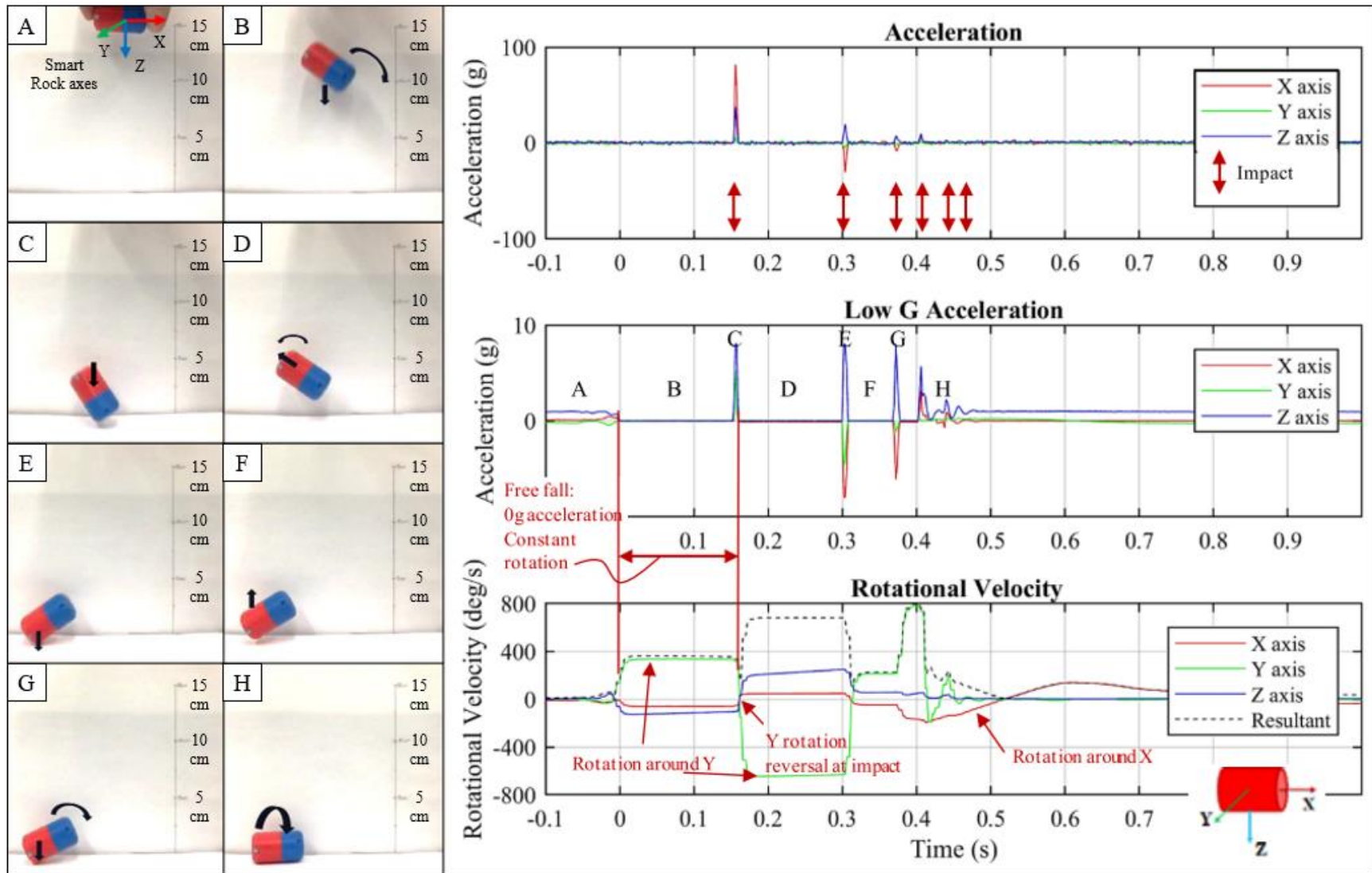
In the research performed by Disenhof (2018), 21 instrumented field rockfall experiments were performed to evaluate the rockfall SR for direct measurement of acceleration and rotation during rockfall that could be used for 2D computer rockfall modeling calibrations. These measurements formed the basis for a preliminary evaluation of a methodology to improve the accuracy of inputs for 2D and 3D rockfall models. The field rockfall experiments were conducted with a sub-angular compact elongated rock and a compact bladed diorite (Figure 2.26), whose properties are presented in Table 2.6. The test rocks were drilled with a 25.4 mm diameter core bit near their centers of gravity (marked in black). The accelerations and rotational velocities were measured while the SR was placed inside the drilled hole. A 25.4 mm diameter rubber plug was inserted to seal and hold the sensor securely in place during these high-energy experiments.

Table 2.6. Characteristics of the test rocks used by Disenhof (2018). The Smart Rock (X, Y, Z) axes correspond to the height, width, and length measurements, respectively.

ID	L	W	H	Mass	Density	Mass moment of inertia (kg.m²)		
	(mm)	(mm)	(mm)	(kg)	(kg/m³)	I_{XX}	I_{YY}	I_{ZZ}
Metamorphic	200	120	120	5.30	2660	0.024	0.024	0.013
Diorite	230	170	125	10.83	2770	0.063	0.051	0.040
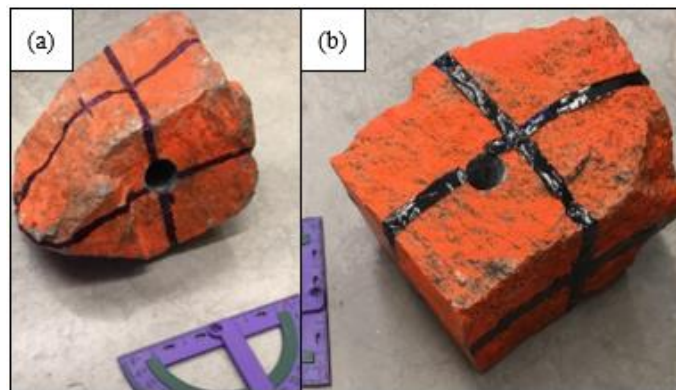
Figure 2.26. (a) 5.30 kg metamorphic rock, (b) 10.83 kg diorite block. The scale is 15 cm wide (Disenhof, 2018).

53

The field experiments were conducted in three different locations in New Hampshire, shown in Table 2.7 and Figure 2.27.

Table 2.7. Slope locations and characteristics of field tests conducted by Disenhof (2018).

Location	Height (m)	Inclination	Slope surface
Durham, NH	6.3	52°	Weathered diorite, topsoil covered with forest debris
Derry, NH	15	70°	Presplit gneiss parallel to NH I-93
Hart's Location, NH	29	65°, 90°	Bedrock with overhanging sections, parallel to roadway

Figure 2.27. Sites investigated by Disenhof (2018): (a) Durham, NH, (b) Derry, NH, and (c) Hart's Location, NH.

Table 2.8 presents the maximum accelerations and average and maximum rotational velocities experienced for each rock at each test location. It was observed that while the 5 kg rock experienced higher rotational rates, the 11 kg block experienced higher accelerations upon impact.

Table 2.8. Smart Rock data summary for experimental trials performed by Disenhof (2018).

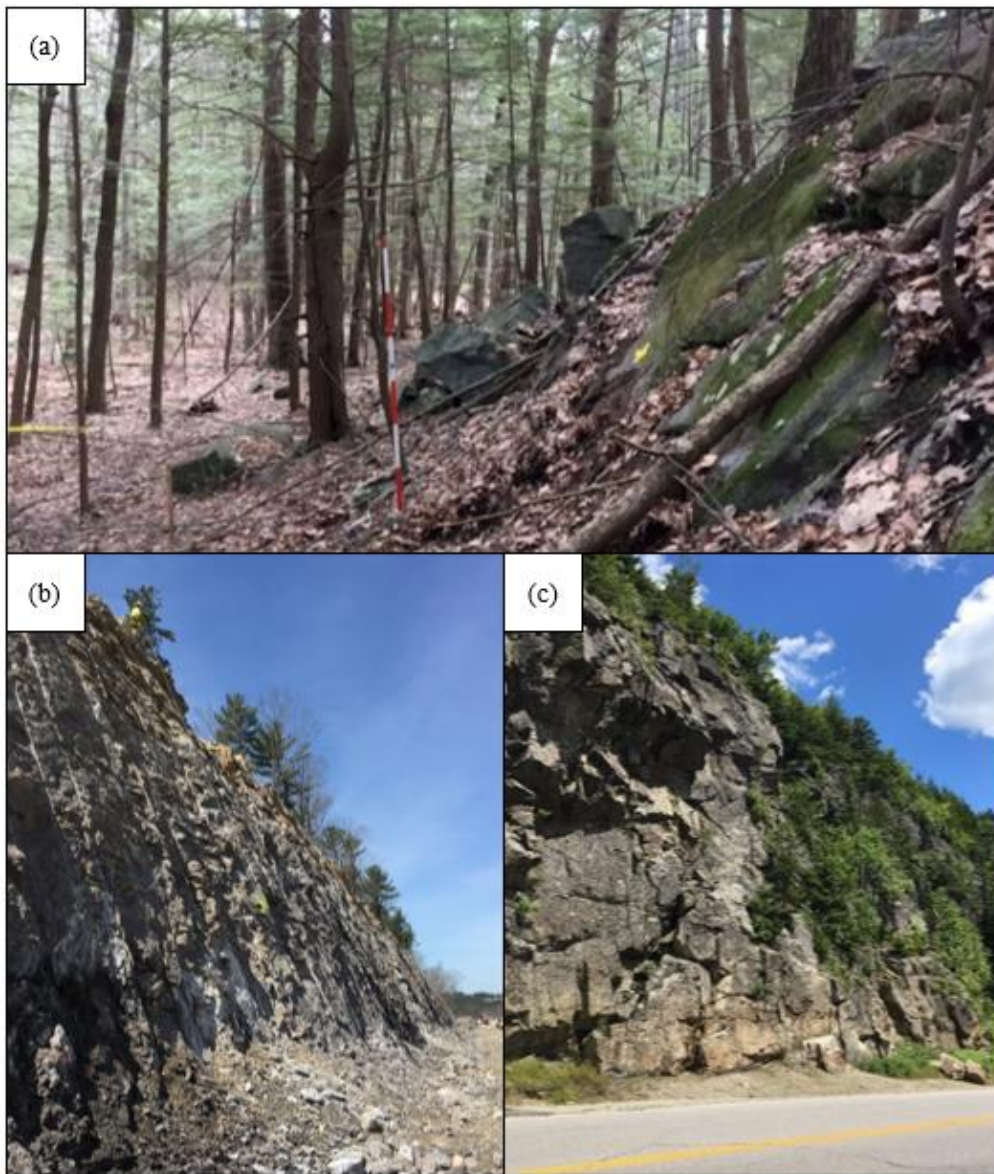| Site ID	Rock ID		Maximum resultant acceleration (g)	Average resultant rotational velocity (dps)	Maximum Resultant rotational velocity (dps)
Durham	5 kg (10 tests)	Mean	167	1017	2767
		SD	93	154	418
	11 kg (5 tests)	Mean	220	928	2214
		SD	114	48	170
Derry	5 kg (3 tests)	Mean	350*	1257	3828*
		SD	49	357	1159
	11 kg (1 test)	Mean	430*	883	3325
		SD	-	-	-
Hart's Location	11 kg (2 tests)	Mean	515*	891	2683
		SD	-	-	-

* One test had an individual data axis recorded at the capacity of the accelerometer or gyroscope.
* Two tests had an individual data axis recorded at the capacity of the accelerometer or gyroscope.

The graphical SR output is presented in Figure 2.28. The SR signal characteristics allow identifying whether the rock is at-rest, free-falling, bouncing, rolling, or sliding. Additionally, the gyroscope data evaluates whether the rock rotates along a principal axis or more than one simultaneously. The most relevant aspects of rockfall motion for each test are detailed on each graph. It was noted that the 5 kg metamorphic rock did not present a principal axis of rotation during free fall.

Caviezel and Gerber (2018) and Caviezel et al. (2018) also observed that impacts during rockfall motion could be clearly distinguished through peaks in the acceleration graphs, especially the high-g accelerometer for high impacts. Rotational motion changes were also noted immediately after impacts, and resultant rotational velocities during free fall were constant.
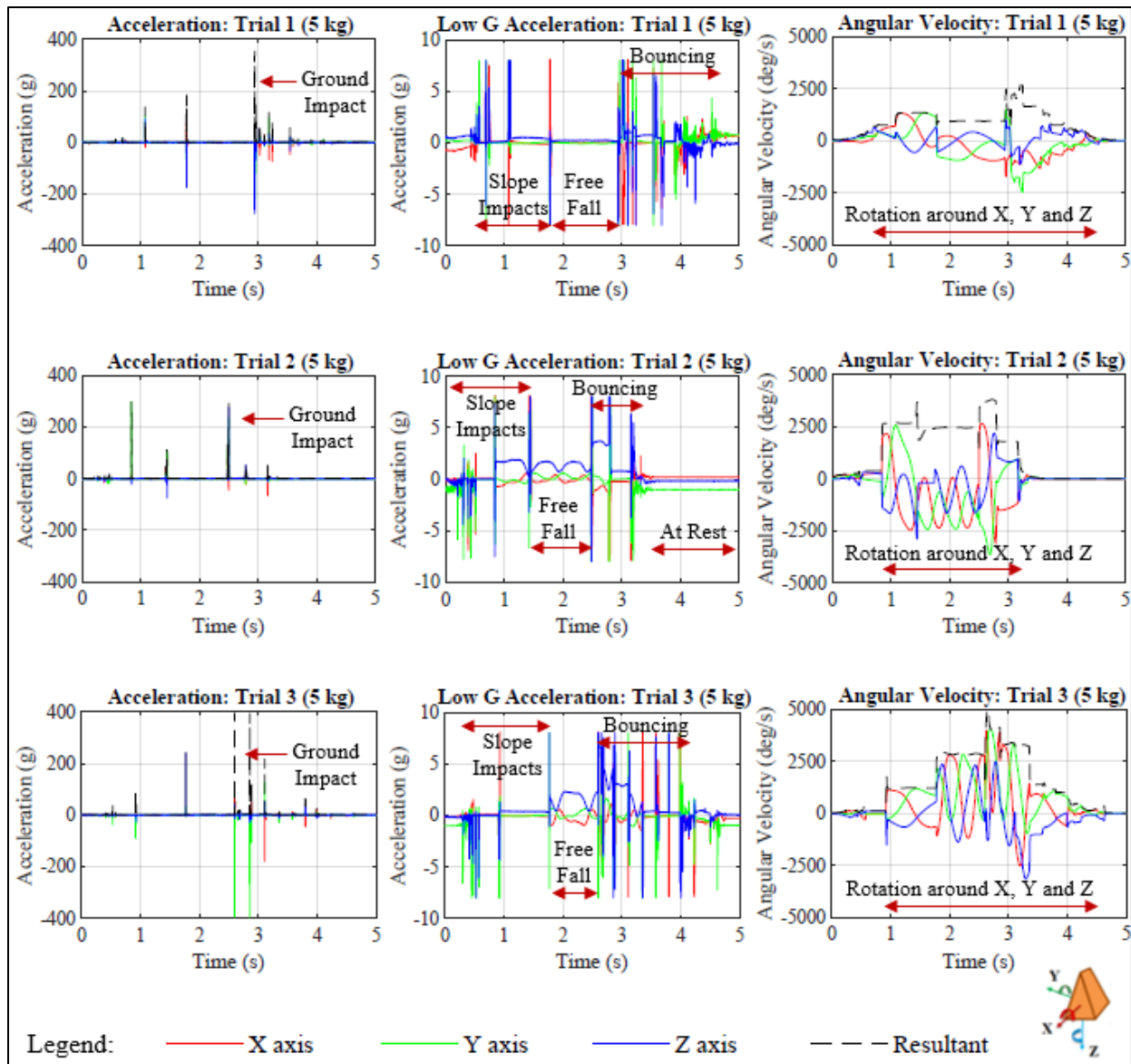
Figure 2.28. Smart Rock output for three experimental tests in Derry, NH conducted by Disenhof (2018).

The findings of this preliminary work led to the conclusion that acceleration and rotational velocity data from the rock perspective present a high potential to expand rockfall understanding and modeling. These parameters can be used to estimate kinetic energy more accurately and better understand the factors influencing runout distances. A broader description of rockfall movements can enhance input parameters in computer rockfall modeling, which often disregards rotational data in kinetic energy estimates.

2.5. Rockfall modeling

Before the aid of computer simulations, rockfall mitigation and protection were managed on an empirical basis (Heidenreich, 2004). With current predictive technologies, computational estimates of trajectories became relevant components of hazard assessments. Potential rockfalls in risk areas must be accounted for in planning land uses in mountainous regions (Turner and Duffy, 2012b).

Rockfall simulations are typically used to investigate block propagation along a slope. As previously discussed, detached blocks can fall freely, bounce, roll, or slide. Falling blocks are modeled according to Newtonian physics, and the rebound characteristics are usually determined by velocity-based normal and tangential coefficients of restitution, which do not account for block rotation (Peng, 2000; Heidenreich, 2004; Turner and Duffy, 2012a; Ferrari et al., 2013; Wyllie, 2015).

Rockfall modeling assessments are conducted to obtain the following parameters (Turner and Duffy, 2012b):

- Potential rockfall trajectories,
- Bounce heights, translational and rotational velocities, kinetic energies, and
- Runout distances to define rockfall hazard areas.

The aid of rockfall simulation programs has significantly increased rockfall knowledge. Risk areas can be determined and assessed by evaluating estimated trajectories and runout distances (Azzoni et al., 1995; Heidenreich, 2004). Computer prediction of rockfall trajectories is commonly associated with experimental campaigns for data comparison and calibration. Duffy and Turner (2012b) suggest that data calibration can effectively analyze how potential slope changes may affect the behavior of falling rocks observed in the field.

The complexity of the models varies according to the defined slope boundaries, which can be two- or three-dimensional, and according to the assumptions made about the falling blocks (Ferrari et al., 2013; Wyllie, 2015). Rockfall modeling can be conducted following two kinematic approaches: lumped mass and rigid body. Lumped mass simulations simplify mathematical assumptions during the calculation process and consider that the falling block is a concentrated, infinitely small point (center of mass), not subjected to rotational motion. On the other hand, rigid body assessments consider the size and shape of the block, rotational velocities, and energies throughout the described trajectory. Lumped mass models are processed faster than rigid body analyses (Azzoni et al., 1995; Turner and Duffy, 2012b; Dadeshzageh et al., 2014; Wyllie, 2015). As block rotation is not considered during lumped-mass models, their trajectories, bounce heights, and estimated runout distances are typically less variable than models accounting for rotational motion (Figure 2.29).
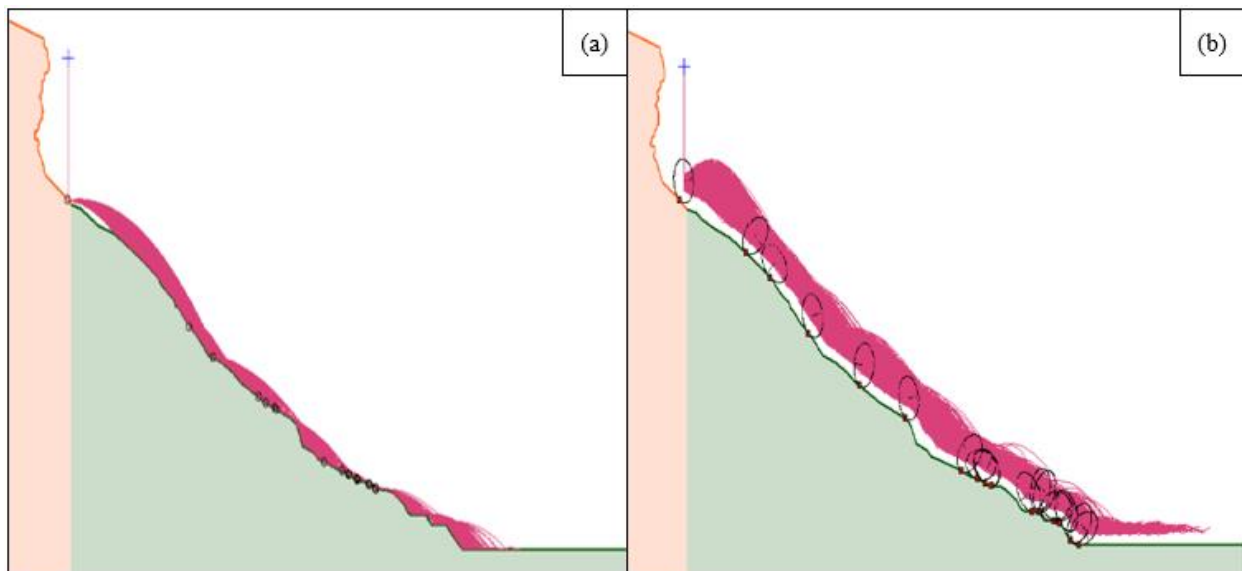

Figure 2.29. (a) Lumped mass, and (b) rigid body rockfall models (Dadeshzageh et al., 2014).

Rockfall modeled trajectories in both kinematic approaches are strongly affected by the assumed input parameters. Small changes in block, surface, or kinematic characteristics can

produce trajectories that may seem reasonable without additional comparison with experimental data. Therefore, it is complex to conduct computational rockfall assessments without previous observation of typical and expected paths in the field (Wyllie, 2015).

Computer simulations must account for the effects of different falling blocks and slope properties (Pfeiffer and Bowen, 1989). The most crucial parameters in rockfall modeling include slope geometry and roughness, coefficients of restitution, coefficients of friction, block geometry, and block density (Ritchie, 1963; Chau et al., 2003; Ansari et al., 2015). According to Dorren et al. (2006), the mitigating effect caused by forest cover on slopes during rockfall motion is usually neglected, leading to overestimated trajectories and protective measures.

As previously discussed, the most complex and least comprehended task in rockfall modeling is to accurately model block kinematics and reproduce impacts and rebounds (Heidenreich, 2004; Ferrari et al., 2013). The bouncing phenomenon is typically simplified using coefficients of restitution, which define the loss of energy upon impact. Energy losses from rolling and sliding are defined through additional friction coefficients (Turner and Duffy, 2012b). Therefore, representative coefficients of restitution are crucial to conduct reliable rockfall assessments (Chau et al., 2002). When experimental rockfalls cannot be performed, restitution coefficients are assumed from back analyses of past rockfall events or typical values published in the literature (Ferrari et al., 2013). The COR values used in rockfall models are typically chosen from literature databases based on rough descriptions of the impact surfaces (e.g., rock, scree, loose soil) (Duffy and Turner, 2012).

Rockfall simulation models require defining boundary conditions of both slope and nearby structures such as catchment ditches, roads, and fences (Wyllie, 2015). Rockfall models are generally obtained to evaluate the least, average, and most conservative trajectories experienced

by falling rocks, as well as their runout trajectories and kinematic parameters (Turner and Duffy, 2012b). Given the high complexity of rockfall events, no computational software can accurately approach all phenomena related to falling blocks (Garcia, 2019). Therefore, modeling assumptions, including slope geometry and falling block kinematics, are generally simplified in rockfall models (Disenhof, 2018). Although local rocks from rock cuts naturally dislodge from rock slopes in a wide variety of shapes and sizes, rockfall modeling typically simplifies falling blocks as regular shapes (Turner and Duffy, 2012a).

Rockfall modeling was typically conducted in two dimensions until the early 2000s. Programs that are widely used include the Colorado Rockfall Simulation Program (CRSP, Colorado Geological Survey) and RocFall (RocScience) (Heidenreich, 2004). Two-dimensional models are defined by a series of (X, Y) coordinates that form sequential straight-line segments. Material properties are assumed to each segment and include normal and tangential coefficients of restitution, surface roughness, and friction angle (Wyllie, 2015).

However, 2D rockfall models present limitations in evaluating the influence of 3D rock block shapes and slope geometry, as falling blocks are represented as 2D objects. This approach tends to estimate overly conservative bounce heights and block velocities than observed in the field, leading to less economical protective designs (Turner and Duffy, 2012b; Wyllie, 2015).

Variations in the slope geometry and lateral displacements are obstacles inherent to two-dimensional slope modeling (Turner and Duffy, 2012b). Rockfall lateral dispersion is one of the barriers during the determination of appropriate 2D slope profiles. As previously discussed, Azzoni et al. (1995) estimated that the lateral distribution of falling blocks is usually within 20% of the slope length. Less significant lateral dispersions are observed for short and steep rocky slopes.

60

Selecting cross-sections for 2D modeling can also be considered a subjective process, as representative slope profiles are required (Disenhof, 2018). The most likely slope cross-sections should be investigated based on field assessments (Heidenreich, 2004; Turner and Duffy, 2012b; Wyllie, 2015) or back analyses of historical data (Ferrari et al., 2013; Khetwal, 2017). Also, Pfeiffer, Bowen, and Higgins (Pfeiffer and Bowen, 1989; Pfeiffer and Higgins, 1990) defend that, since the selected slope profile(s) follow the most likely rockfall paths previously established upon field calibrations, lateral variability does not need to be considered. Despite its limitations, two-dimensional modeling is economically attractive given the lower complexity of the input data (which requires simpler data collection) and a significantly faster computation time (Turner and Duffy, 2012b).

Two-dimensional rockfall simulation programs have been used over the last decades to provide information on the design and analysis of protective measures and consist of a routine procedure in rockfall hazard assessments (Turner and Duffy, 2012b). RocFall software was initially developed at the University of Toronto (Ontario, Canada) and has been supported and improved by Rocscience. RocFall assesses falling blocks along a two-dimensional slope profile defined by a series of segments and generates graphs with average and maximum estimated velocities, kinetic energies, and bounce heights along with the slope profile. Velocity and energy outputs for rigid body analyses include both translational and kinetic motions. The software also provides histograms of endpoint locations which actively contribute to ditch and barrier design.

The coefficients of restitution (COR_{VN} and COR_{VT}) that govern rockfall motion are defined for each line segment, usually based on past studies. Rocscience provides an extensive table with coefficients of restitution found in the literature (Rocscience, 2017). This database is also cited by Turner and Duffy (2012b) and Disenhof (2018) and is commonly used as a reference for two-

61

dimensional assessments in the software. Before each simulation is performed, the start ("seeder") location and the number of tests are specified in the model and the initial kinetic conditions presented by the falling block.

Turner and Duffy (2012b) discuss that advances in computer and site investigation technologies have created conditions for the improvement and feasibility to overcome previous constraints from 2D models through three-dimensional modeling. However, given their higher complexity, 3D models require significantly more information and computation time to characterize rockfalls accurately. 2D modeling programs are readily available and require substantially less expertise than three-dimensional, GIS-based approaches (Disenhof, 2018).

The aid of scanning rock slopes such as lidar and photogrammetry has contributed to developing and improving three-dimensional analyses of potential trajectories (Wyllie, 2015). While 2D models are associated with simplified geometries and ballistic movements to define rock trajectories, 3D approaches are more rigorous and account for more complex block shapes and surface topography (Arpin and Ardnt, 2016; Garcia, 2019). According to Turner and Duffy (2012b), although two-dimensional models only partially reflect conditions of a three-dimensional site, 3D assessments are usually not feasible due to the significantly higher number of input parameters required. In addition, obstacles impeding to obtain representative 3D slope profiles for specific sites limit their analysis to 2D simulations. Therefore, more complex, three-dimensional simulations require more precise field observations than two-dimensional models. The broader availability of technologies does not eliminate the need for rigorous data collection and parameter evaluation (Chau et al., 2003; Crosta et al., 2015).

Both two- and three-dimensional modeling approaches require topographic representations of the evaluated site. Although 2D slope profiles can be simplified with known data points and

angles extracted during field surveying, more accurate slope representations can be obtained extracting cross-sections from 3D data sets, including photogrammetry, lidar, and digital elevation models (DEMs). Different surface models provide different data resolutions, as shown in Figure 2.30 (Disenhof, 2018).
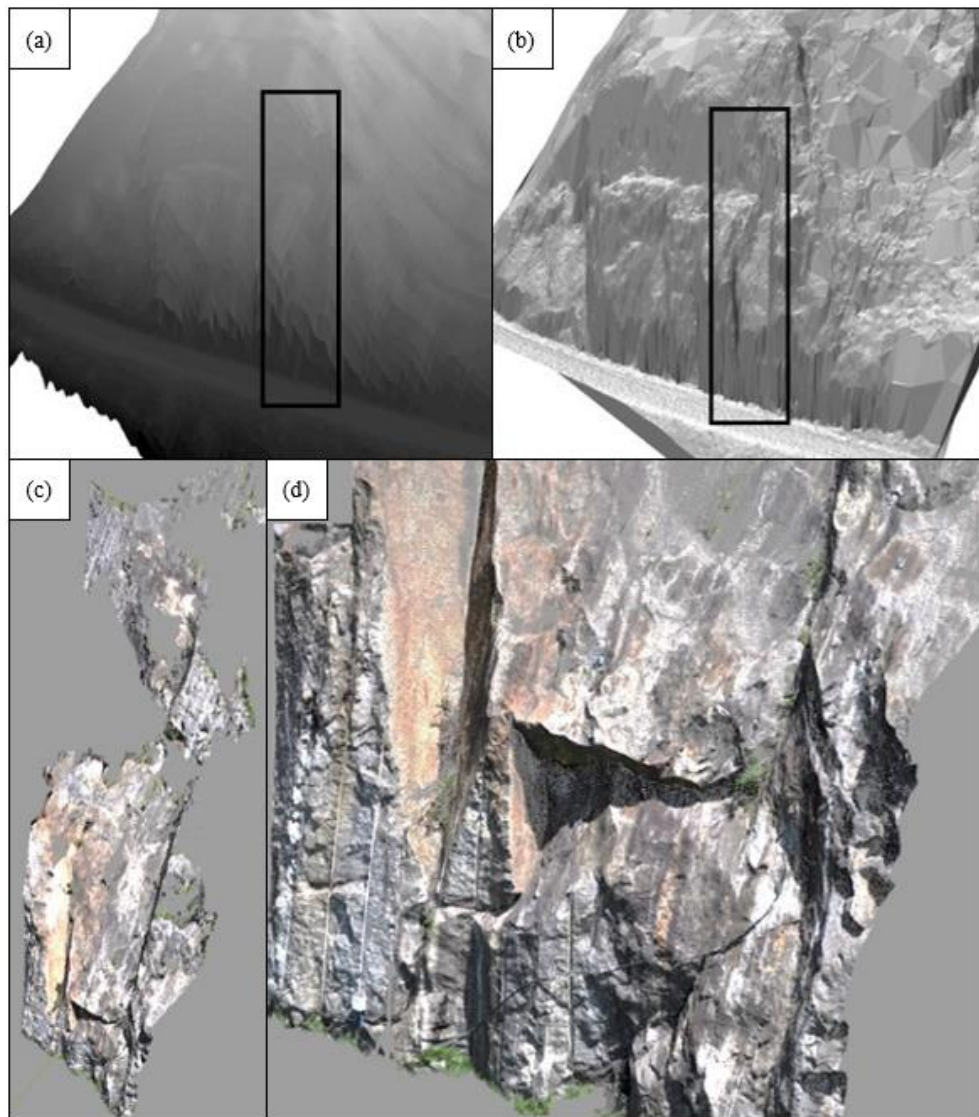

Figure 2.30. Differences in data resolutions for distinct surface models in a rock cut located in Woodstock, NH: (a) 1 m DEM, (b) aerial lidar point cloud, (c) terrestrial lidar point cloud, and (d) Close-up of terrestrial lidar detail. (a) and (b) show the approximate location of (c) (Disenhof, 2018).

Although modeling techniques have been improving for the last decades, the lack of experimental data concerning rockfall motion parameters is still a limiting factor for predicting

and accurately calibrating rockfall trajectories (Ferrari et al., 2013). In this context, the previously presented Smart Rock (Harding, 2011; Cassidy, 2013; Gullison, 2013; Harding et al., 2014; Apostolov, 2016; Apostolov and Benoît, 2017; Disenhof, 2018) and StoneNode (Caviezel et al., 2017; Caviezel and Gerber, 2018; Caviezel et al., 2018) sensors can be considered as promising tools to calibrate experimental rockfalls based on field observations from the perspective of the falling rock. These detailed comparisons between field and model assessments can strongly contribute to enhance the accuracy of existing 2D and 3D rockfall software.

Disenhof (2018) has conducted 2D rockfall models using rigid body analyses using RocFall 6.0 software. Simulations were performed for the same rock slopes in Durham, Derry, and Hart's Location in NH, where experimental rockfall campaigns were previously conducted. The experimental rockfalls were modeled using readily available digital data from photogrammetry point clouds and digital elevation models, whose data resolutions were capable of realistically simulating rockfalls.

The generated slope cross-sections were obtained from the 3D surface models based on field observations of the experimental trajectories. Disenhof (2018) defined the material properties (rock faces, catchment ditches, road) based on default RocFall coefficients found in the literature. The 5 kg compact elongated rock was modeled as a polygon square, and the 11 kg compact bladed rock was modeled as a 5:6 polygon rectangle. The mass and density for both blocks were also provided to RocFall.

It was observed that the modeled trajectories and rotational velocities generally agree with field observations (Figure 2.31). However, bounce heights and runout distances after the first impact with the ground are often overestimated. Figure 2.32 presents the average rotational velocities from the 2D models compared with the measured resultant rotational velocities in the field trials.

The predicted average rotational velocities are compatible with the instrumented tests up to 0 m in the horizontal slope position. The increase in rotational motion suggested by the simulation results from the overly predicted endpoint locations past the catchment ditch limits. Blocks rotating at lower rates stopped closer to the rock cut, causing the average rotation to increase at more distant lateral positions.
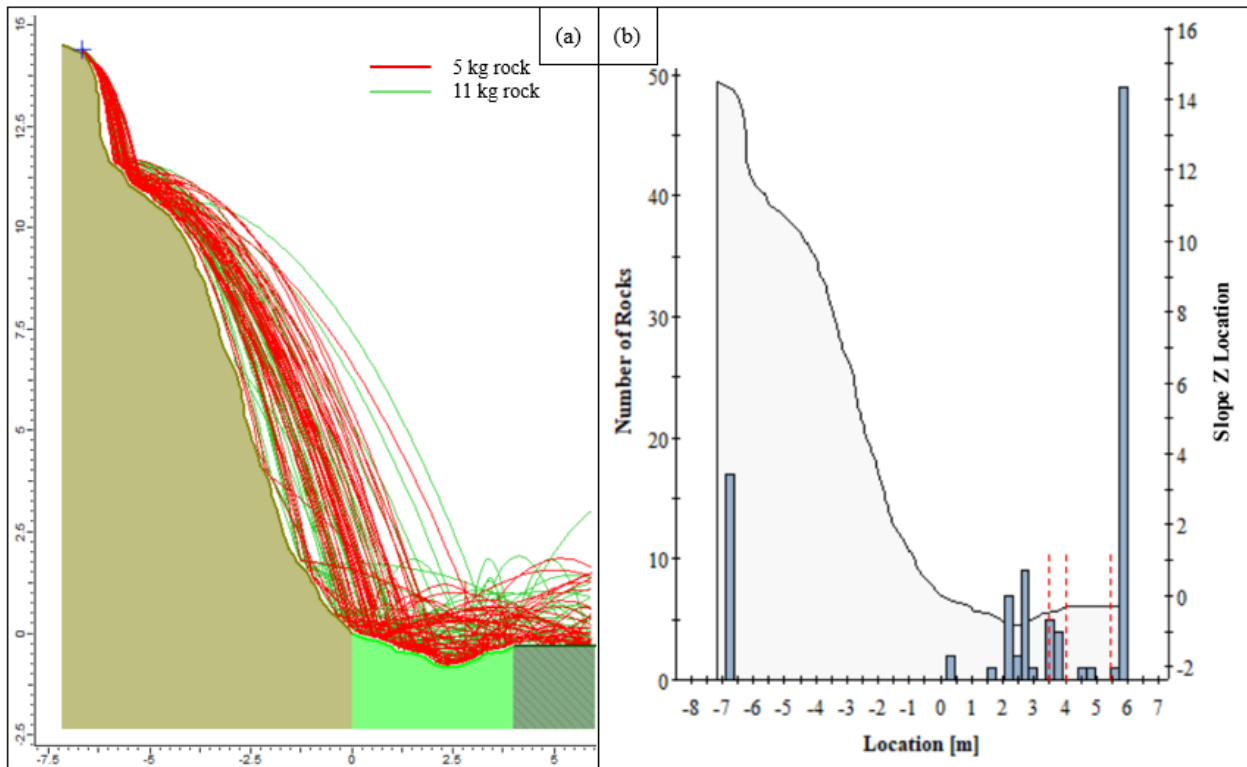
Figure 2.31. (a) Trajectory simulations for the Derry rock cut, and (b) output from RocFall showing rockfall endpoints. The high concentration of endpoint at 6 m indicate that most rocks did not stop before the model boundary. Experimental SR rock endpoints are shown in red (Disenhof, 2018).

The research conducted by Disenhof formed the basis for a new methodology of rockfall modeling assessments, using field calibration from Smart Rock instrumented tests. Therefore, the latest Smart Rock sensors can characterize rockfall experiments and verify modeled rock motion.
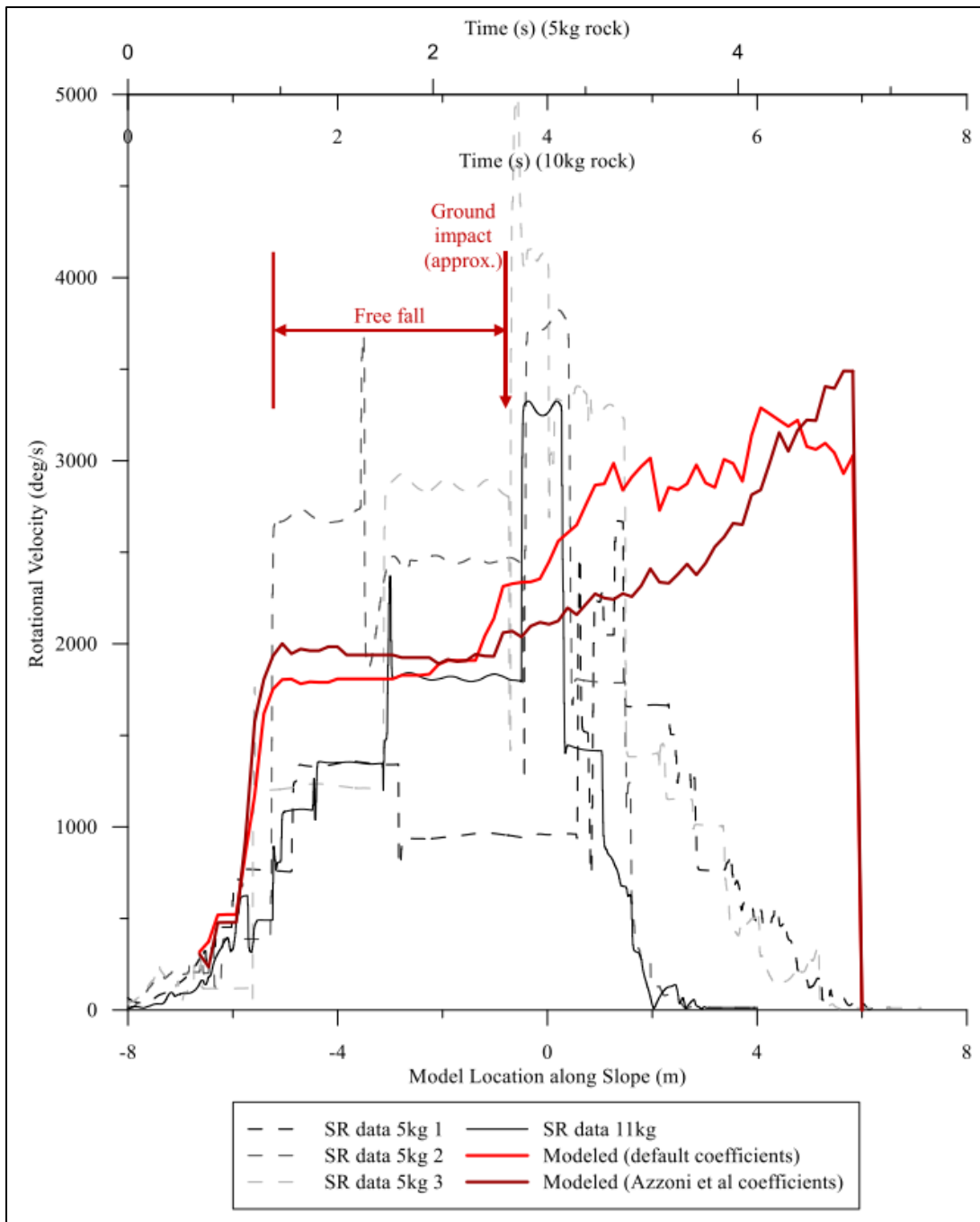
Figure 2.32. Comparison of average modeled values to measured rotational velocities in Derry, NH. The default coefficients represent the data shown in Fig. 2.31, while the Azzoni et al. coefficients are higher (Disenhof, 2018).

2.6. Summary

Rockfalls are associated with natural phenomena such as weathering, rainfall, freeze-thaw cycles, vegetation growth, and activities by animals and the public. These processes disrupt portions of slopes, which lead to falling rocks and pose a safety hazard to motorists, infrastructure, and buildings nearby. Falling blocks experience one or more modes of travel, including free fall, bouncing, rolling, and sliding. The behavior described by a falling rock depends on both block and slope conditions, as well as kinematic parameters such as angle of impact and velocity.

Hazard mapping and territory management require reliable predictions of rockfall trajectories to minimize potential risks. Due to the logistics and difficulty associated with conducting a representative number of rockfalls in the field, expected runout distances and bounce heights are typically simulated through computational modeling to assist in the design of protective structures. The energy restitution in rockfall modeling is defined by one or two coefficients of restitution, with friction parameters that specify impact surface characteristics in these estimates.

In the last two decades, several researchers investigated rockfall behavior using field/laboratory measurements, high-frame video recording systems, and detailed back-analyses to quantify energy losses upon impact with different surfaces. However, the uncertainty related to rockfall behavior and model input parameters is still significantly high, especially concerning the impact and rotational motion from the perspective of the falling rock, which leads to overly conservative and less economical designs.

Research conducted at the University of New Hampshire over the last decade has developed and evaluated a Smart Rock sensor capable of measuring acceleration and rotation data while embedded in test rocks. These sensors present a significant potential for expanding current rockfall knowledge.

3.   RESEARCH METHODOLOGY

The fourth-generation Smart Rock was evaluated in this thesis during field and laboratory rockfall experiments. Improvements include an altitude sensor which has complemented a series of video analyses. The measurements from these experiments were used to evaluate preliminary two-dimensional models comparing the simulations with the field data. The details of the latest SR and research methodology were detailed in this chapter.

3.1. 4th generation Smart Rock

Smart Rock (SR) sensors have been used extensively at the University of New Hampshire to study landslides and more recently characterize rock movement over time (free-fall, bouncing, rolling, sliding). The latest, fourth-generation SRs consist of 3D printed capsules 50.8 mm in length and 25.4 mm in diameter (Figure 3.1), equipped with a ±400 g and a ±16 g 3-axis accelerometers, a ±4000 dps high-rate gyroscope, an altimeter, and a temperature sensor.

The measuring ranges of the low-g accelerometer can be changed to ±2, ±4, ±8, or ±16 g, as desired. Additionally, the high-g accelerometer can also be adjusted to ±100, ±200, or ±400 g, and the high-speed gyroscope can be adjusted to ±500, ±1000, ±2000, or ±4000 dps. However, higher measuring ranges increase inherent noise levels. For that reason, Disenhof (2018) limited the ±16 g accelerometer to ±8 g to decrease noise in the acceleration signal.

The high-rate gyroscope provides instantaneous rotation rates about the three axes simultaneously. Therefore, the measured rotational velocities in degrees per second do not represent constant rotation rates over time.
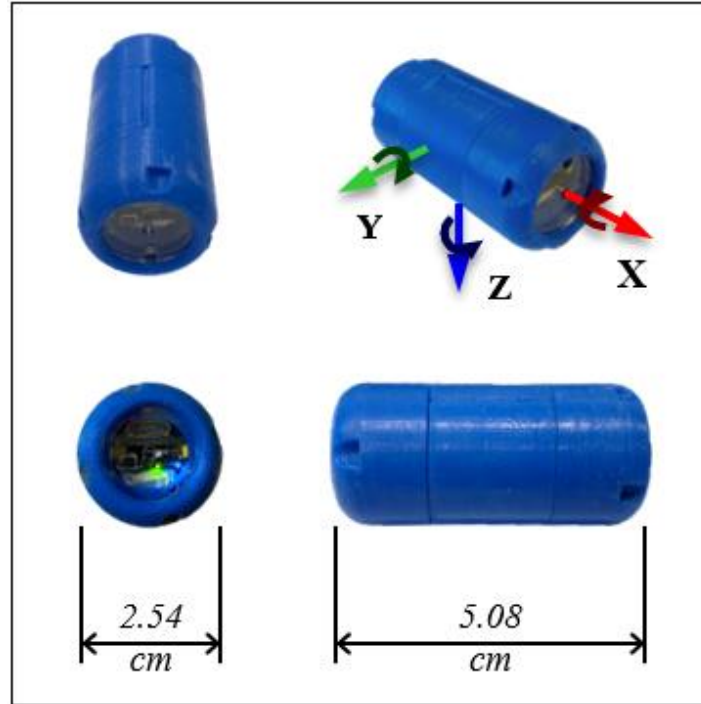
Figure 3.1. Fourth-generation Smart Rock sensor.

The altimeter allows for tracking changes in altitude and requires the sensor to be open to the atmosphere (hence, there is a hole in the SR window). Apostolov (2016) highlights the significant level of inherent noise present in the sensor output signal, which is increased during unsteady rockfall motion.

The latest SRs, also developed by Apostolov, are simple to operate, gather accurate and fast measurements, and process data in real-time. It records acceleration, rotational velocity, altitude, and temperature data at a sampling frequency of 100 Hz, which can be increased to 500 Hz if the altimeter is not used. After the sensor is powered and before data is recorded, the SR initializes all the components and self-calibrates. During this process, several at-rest measurements over 1 second are collected. The device can be prepared for testing in less than a minute and is recharged using a standard micro-USB connection.

A plexiglass window allows the operator to verify if the sensor is turned on and recording data, which is automatically saved to a micro-SD card as a .csv file to be analyzed using MATLAB or spreadsheets such as Microsoft Excel. The sensor is equipped with several indicator LEDs which supply relevant information about its operation status. Two LEDs (green and amber) are controlled by power management and indicate whether the sensor is powered or charging, respectively. Additionally, two other LEDs (blue and pink) are governed by the software and display the mode of operation (self-calibration, data recording, or writing data) or when an error is detected in the system, respectively. For additional information about the latest Smart Rock sensor, the reader is referred to Apostolov (2016) and Apostolov and Benoît (2017).

All Smart Rock data were processed and analyzed in MATLAB. The analysis script was initially adapted from Apostolov (2016) and Disenhof (2018). Additional information about the sensor three-axis output during experimental rockfalls is presented in Chapter 4.

3.2. Experimental rockfall

During this experimental campaign, several field rockfall experiments were carried out on ten rock cuts in New Hampshire and one in Vermont, USA. Each test was conducted with the aid of a Smart Rock sensor embedded in the center of gravity of field-collected rocks, with two of the experiments in Vermont embedded on in place rocks immediately before scaling work. All field trials were conducted with altimeter enabled at a sensor sampling frequency of 100 Hz. In addition, 30 drop tests in the laboratory were conducted to estimate coefficients of restitution under controlled conditions. The laboratory experiments were conducted with the altimeter disabled at a sensor sampling frequency of 500 Hz.

3.2.1. Preparation of the test rocks

The test rocks used in the field experiments were retrieved from each slope location to match the slope composition. For research comparison purposes, the 5 kg metamorphic test rock from Disenhof (2018) was also used in these experiments. Each test rock was drilled in its center of gravity (CG) to avoid eccentricity from SR measurements during the tests. The CG coordinates relative to each block were determined either by hand or through 3D models. The hand-drawn cross-sections were obtained with a plastic contour gauge, and the 3D models were obtained with a 3D scan arm or with a mirror device and an iPhone 11 (Figure 3.2).

Figure 3.2. (a) Plastic contour gauge, (b) Faro 3D ScanArm (https://www.faro.com), and (c) Scandy Pro Lookout (https://www.scandy.co/apps/scandy-pro).

The CG positions of the rocks from the first sites were determined by hand. A set of several hand-drawn cross-sections of each rock, taken in two orthogonal directions with a plastic contour gauge, were used to obtain the desired drilling position. Each block was assumed to have X, Y,

and Z orthogonal axes determined according to the rock geometry. Representative cross-sections with X-Z and Y-Z coordinates were drawn to account for geometry irregularities about all three axes. Each obtained cross-section was drawn to scale in reference X-Z or Y-Z planes and accurately digitized in AutoCAD. The individual cross-section centroid coordinates and areas were used to estimate the center of gravity of the rock, assumed to be a composite body, in which a complex object is divided into simpler shapes. This procedure is presented in Figure 3.3.

Although sufficiently accurate CG coordinates could be obtained by hand, this method is highly time-consuming. The accuracy is directly proportional to the number and location of the cross-sections. Drawing all cross-sections for a single rock could vary between 2 and 10 hours, depending on its geometry, size, and weight. The length and depth of the plastic contour gauges were also a limiting factor for rocks with irregular geometry and dimensions larger than 30 cm.

The 3D coordinates of the CG location of the test rocks were determined through Equation 3.1. Besides the required time to obtain all cross-sections, this method did not correctly estimate the mass moment of inertia of the test rocks required to perform rotational kinetic energy calculations from the sensor data. Therefore, more efficient alternatives to determine the CG location and calculate the 3-axis moment of inertia were necessary.

$$\bar{x} = \frac{\sum A\prime \bar{x}\prime}{\sum A\prime}; \ \bar{y} = \frac{\sum A\prime \bar{y}\prime}{\sum A\prime}; \ \bar{z} = \frac{\sum A\prime \bar{z}\prime}{\sum A\prime} \qquad \text{(Equation 3.1)}$$

Where: $\bar{x}$, $\bar{y}$, and $\bar{z}$: centroid coordinates for a composite body,

$\bar{x}\prime$, $\bar{y}\prime$, and $\bar{z}\prime$: centroid coordinates for the subdivision of a composite body, and

$A\prime$: area of subdivision of a composite body.
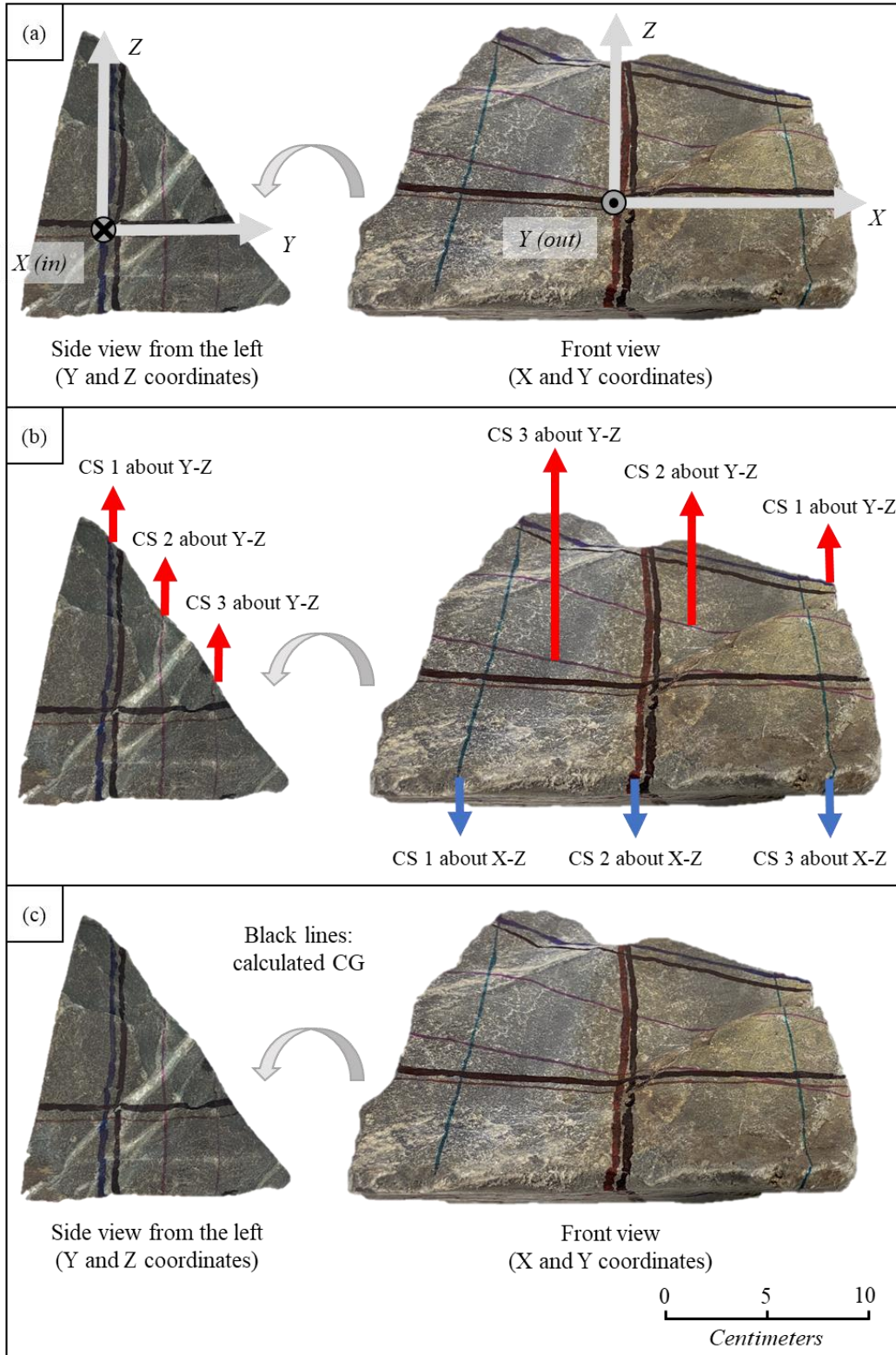
Figure 3.3. Procedure to estimate the CG position of rocks by hand: (a) pre-defined axes of reference (blue and red), (b) hand-drawn cross-sections, (c) CG position in black.

Obtaining 3D models for the test rocks was studied as a possible solution. The first rocks were 3D scanned with a Faro 3D ScanArm, available at the manufacturing center of the University of New Hampshire. The scan output is obtained as a 3D point cloud with X, Y, and Z coordinates. It is converted into a solid using Autodesk Meshmixer after removing any excess points beyond the rock boundary. The 3D solids were then imported to SolidWorks, and the reference coordinate system of the 3D models was defined according to the best drilling position for each rock geometry. It was necessary for the X, Y, Z coordinate system to match the axes orientation of the embedded SR. Last, the mass properties were imported into the model to obtain the three-dimensional CG position and mass moments of inertia.

Upon comparison with hand-calculated locations, it was verified that the 3D models did allow for accurate predictions of the CG position more efficiently, as each model could be processed and analyzed in less than 20 minutes. Although proven efficient, the Faro ScanArm was not available for use during the research duration and cost on average US$ 50/rock.

As an alternative, the remaining 3D models were obtained with an iPhone 11, which could accurately scan the rocks using the iOS application Scandy Pro. The app uses the frontal camera and depth sensor to get a 3D point cloud. A 3D-printed mirror device was used to scan the test rocks more easily. These models were also processed using Autodesk Meshmixer and SolidWorks. As expected, the point clouds generated by the iPhone were less detailed than the models obtained by the scan arm, which provided points with tenths of millimeters of precision. However, such a level of detail is not critical, and the 1.0 mm accuracy of the phone-generated models was proved sufficiently accurate for this experimental research. A comparison between these three methods for a test rock of irregular geometry is shown in Figure 3.4.

Based on the comparative figure, it is possible to observe that the 3D model obtained by the scan arm provides the most accurate representation of the test rock. The output generated by the iPhone 11 does not present the same level of detail but yields a realistic and comparable approximation of the block. The individual hand-drawn cross-sections provide some precision but require several cross-sections about two directions to realistically represent the test block. For this rock, a total of seven cross-sections were drawn by hand. Table 3.1 presents the distances between the calculated center of gravity positions and a known reference point in the measured rock, also shown in the figure.
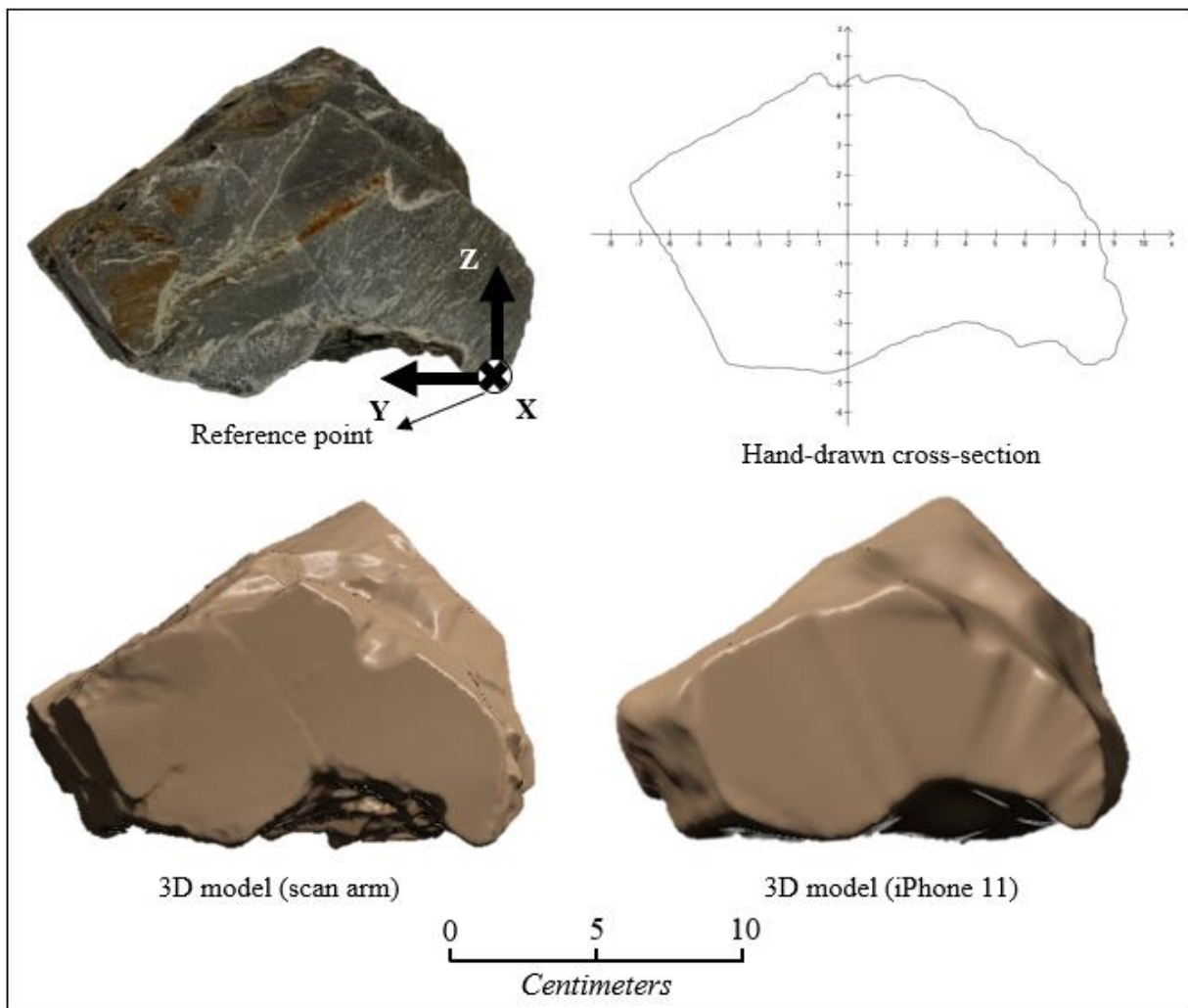
Figure 3.4. Approaches used to estimate the center of gravity position in the test rocks prior to drilling.

Table 3.1. Comparison between the three methods used to estimate CG positions and mass moments of inertia.

Compact elongated block, 4.09 kg Analysis method	Distance from reference point (cm)			Mass moments of inertia (kg.m²)		
	X	Y	Z	X	Y	Z
Hand-drawn cross-sections (7)	6.0	7.5	4.7	-	-	-
FaroArm (3D model)	5.9	7.5	4.2	0.011	0.0073	0.011
iPhone 11 (3D model)	5.8	7.8	4.1	0.012	0.0076	0.011
Average	5.9	7.6	4.3	0.014	0.0083	0.013
Standard deviation	0.1	0.2	0.3	0.005	0.001	0.004

Although there are visible discrepancies in accuracy reproducing the block shape between the three methods, all approaches have estimated similar 3D CG positions, with a maximum standard deviation of 3 mm. This difference is not significant for drilling purposes, and all three methods were considered successful in determining the drilling position. The three-dimensional models are considered more advantageous than the hand-drawn cross-section because the process is less time-consuming and yields more reliable moments of inertia, which account for the irregular shape of the test block.

The test rocks were drilled with a 25.4 mm outer diameter core bit. An adjustable rock borer frame was designed and assembled by the UNH Technical Service Center (TSC) for a higher control drilling location and angle. As shown in Figure 3.5, the structure has openings for pins, allowing for precise control of the test rock position and orientation before drilling.

Each rock was supported on at least three contact points and strapped to ensure that the block was firm and secured against rotation. The position and inclination of the core bit can also be precisely adjusted. The surface of interest needs to be as flush as possible with the core bit in order to avoid excessive torque and undesired rock or core fractures. Positioning and drilling each rock could vary between 10 to 40 minutes, depending on the rock geometry and type. Density measurements were performed using the recovered rock cores.
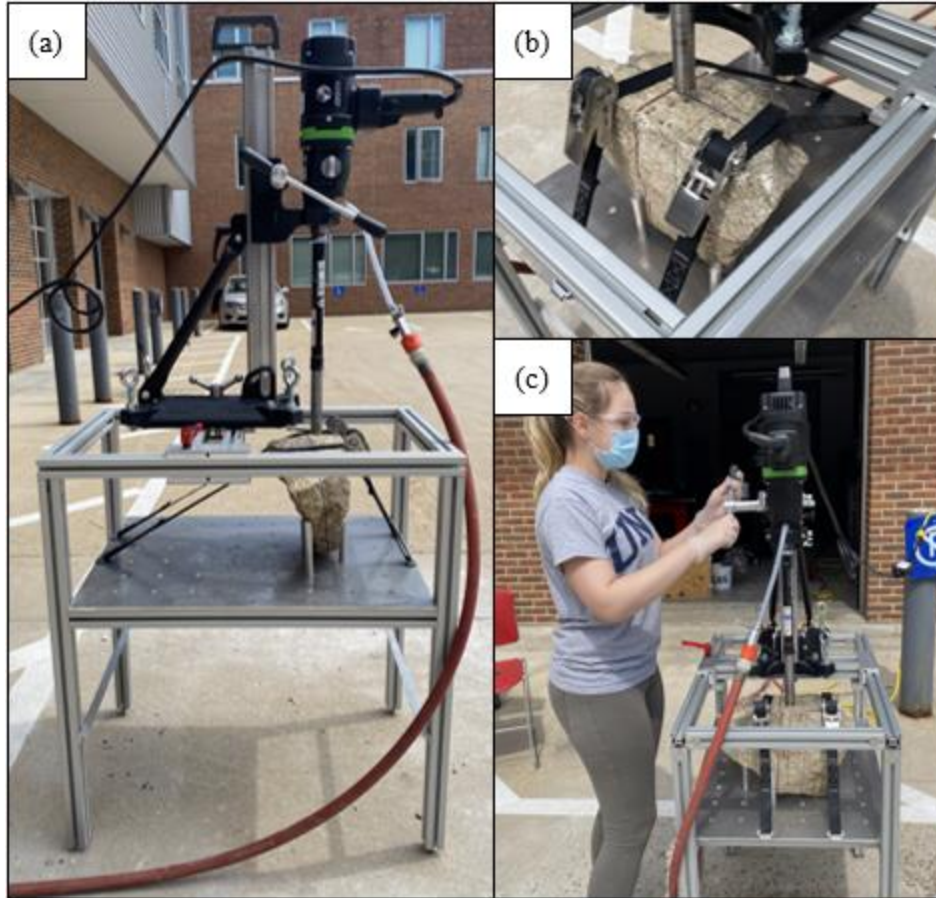
Figure 3.5. (a) Rock borer and adjustable frame, (b) rock adjustment prior to drilling, and (c) rock drilling.

For more efficient video analysis, the center of gravity location was marked on each rock, and the eight resultant quadrants were painted in different colors (Figure 3.6). The SR orientation in each rock was also known during each test, allowing changes in rock motion to be easily identified through video analysis and matched with the sensor data.

As performed by Disenhof (2018) and Caviezel et al. (Caviezel et al., 2017; Caviezel and Gerber, 2018; Caviezel et al., 2018), the shape of each rock was determined based on the particle shape classification diagram developed by Sneed and Folk (1958), shown in Figure 3.7, which takes into consideration the length, width, and height of the block. Due to the irregular geometries of the test rocks, these measurements were performed at the center of gravity location (black lines

in each rock). As detailed in Figure 3.6, the width, length, and height of the test block at the CG

lines (visible in black) were measured in the X, Y, and Z orientations of the Smart Rock embedded

in each block, respectively. These measurements were conducted consistently to relate the block

dimensions and moments of inertia with the 3-axis rotation and acceleration data.
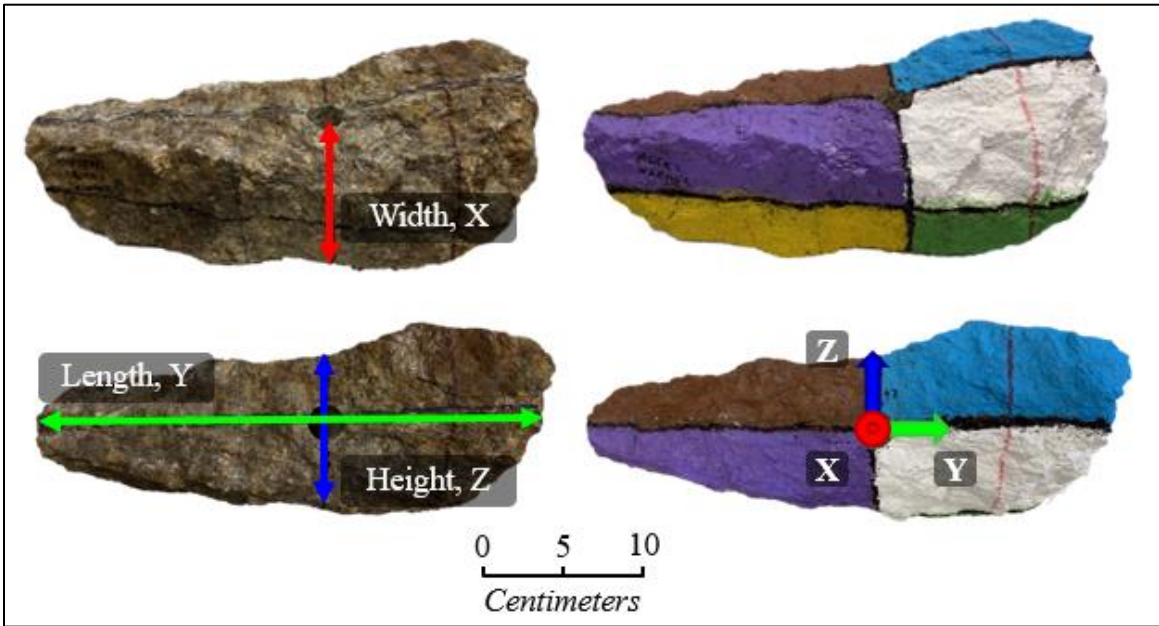
Figure 3.6. Test rock prepared for field experiments in Warner, NH.
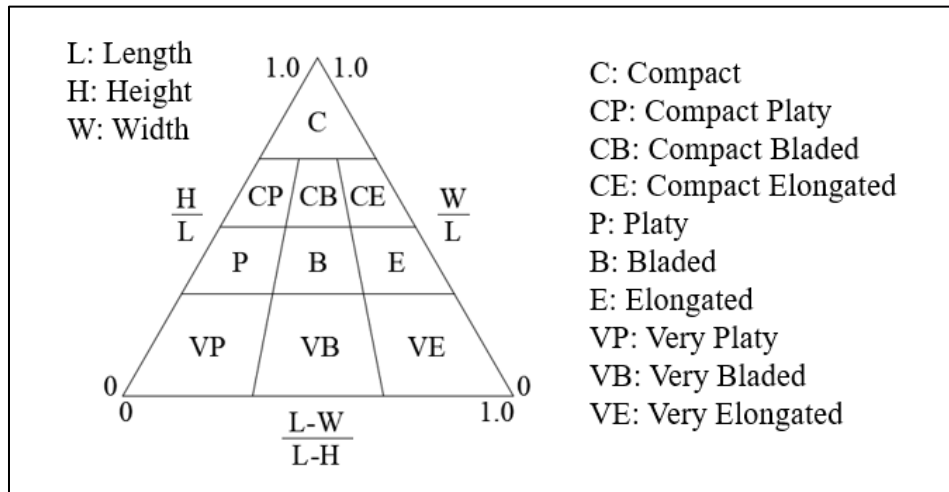
Figure 3.7. Particle shape classification diagram adapted from Sneed and Folk (1958).

3.2.2.1. Test rocks drilled in place

Since the test rocks needed to be manually hoisted or hand-carried to the top of the test slopes, the tested block sizes and weights were the limitations in this preliminary research. To address this issue, two experimental rockfalls with rocks drilled in-place were conducted in Townshend, VT, during ongoing rock scaling performed by the Vermont Agency of Transportation (VTrans). These tests are further detailed in Chapter 5.

3.2.2. Field tests

A total of 85 field rockfall experiments were carried out on 11 rock cuts in the states of New Hampshire and Vermont, whose locations are presented in Figure 3.8. After previous preparation in the laboratory, the drilled and painted rocks were transported to each test site. Before starting each test, the Smart Rock was activated, self-calibrated, and started recording the data. The SR was placed inside the drilled holes, and a 25.4 mm diameter expandable rubber plug with a through-hole screw (Figure 3.9) was used to confine the SR securely. The opening in the screw and the SR window hole allow the altimeter to record data through exposure to atmospheric pressure. The rubber plugs were shortened as needed for holes shallower than 80 mm. Also, for holes deeper than 100 mm, 25.4 mm diameter cylindrical wood dowels with a through-hole drilled were placed between the SR and the rubber plug. A ribbon was also used underneath the SRs to help retrieve the sensor at deeper holes after the tests. After each rock was prepared, a pulley, rope, and bucket were used to hoist them to the top of the slope, while larger rocks were hand-carried.

The test operator tapped the rock onto the slope surface three times to indicate the start of each test in the data signal; then, the rock was released from the slope with the least initial velocity
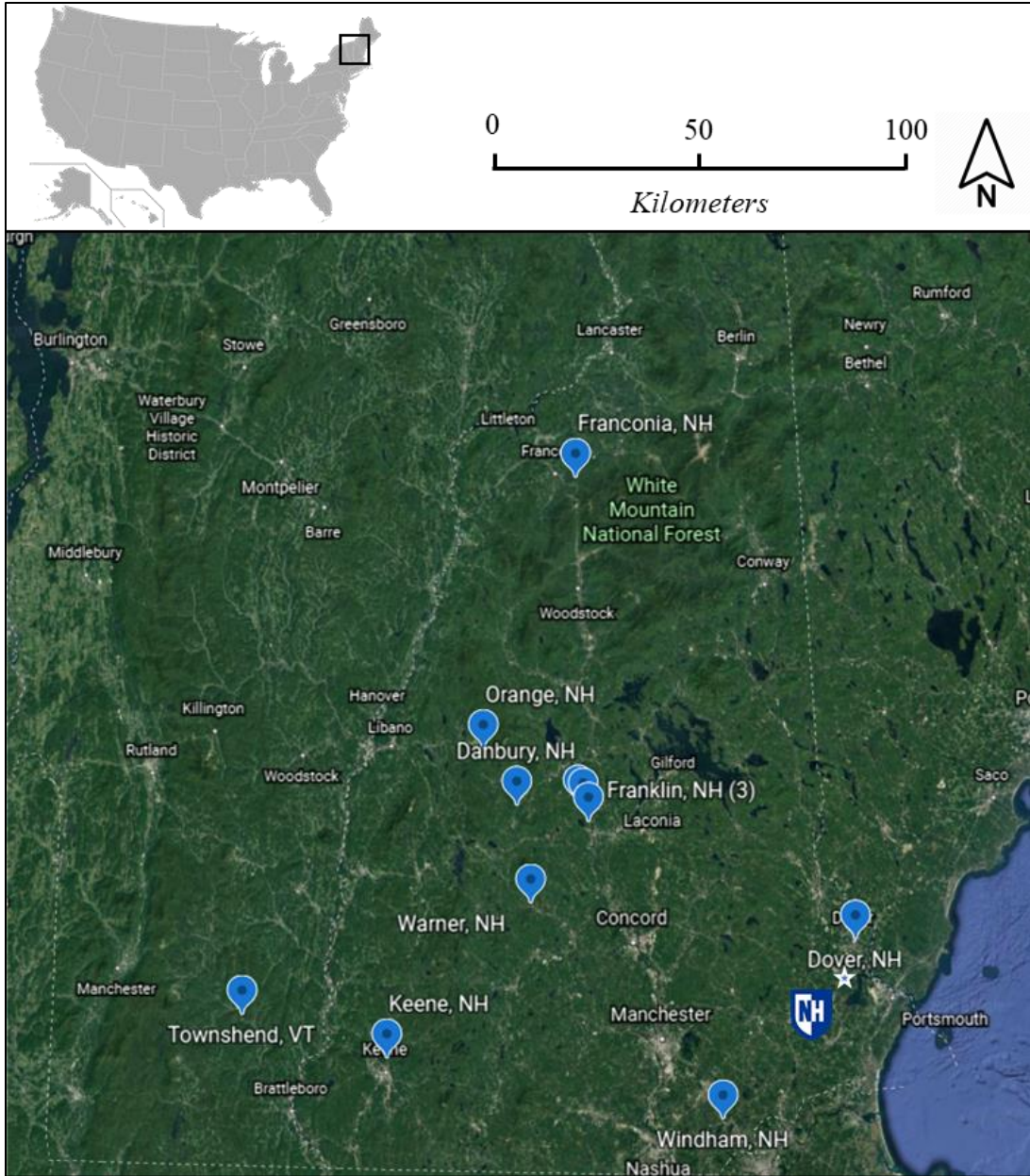
Figure 3.8. Test site locations in New Hampshire and Vermont. UNH is shown with a star.

Figure 3.9. Expandable rubber plugs and through-hole screws: original length (left) and shortened (right).

possible (preferably zero). After rockfall, the runout distance from the slope toe was measured, and the SR was carefully removed from the rock. The sensor data was immediately available for post-processing after data recording. The test data can be easily identified through peaks in acceleration during the initiation taps as well as during the test.

The drop heights were measured in the field with a total station for comparisons with the sensor altimeter data. All field experiments were recorded at 30 fps using a Nikon D3200 semi-professional camera placed perpendicularly to the slope face. When allowed by the slope geometry and road conditions, an additional camera (iPhone 11, 30 fps) was placed parallel to the rock cuts.

The rock movement could be tracked using the application Tracker 5.1.5 by Physlets. The application assumes the camera is stationary and perpendicular to the object in motion and allows the user to obtain vertical and horizontal displacement and velocity data over time by tracking the rock CG position at each frame. A 2D reference axis and a calibration stick for dimension scaling are defined, and the center of gravity position of the block is tracked at each video frame.

The tracking software output was used to evaluate rockfall motion in conjunction with the sensor retrieved data. Figure 3.10 establishes a comparison between the observed trajectory combining selected video frames and using the tracker software. Both analysis methodologies were used to assess rockfall motion during each test: the combined frames complement observations from the sensor measurements. The tracking software provides accurate estimates of the center of gravity position over time. Therefore, the obtained 3D motion data at specific slopes through video were used to estimate translational motion, and the 3D sensor data were used to evaluate rotational motion and impact forces.

The raw data for each rockfall test were processed and plotted using MATLAB. The data for each test were plotted, and resultant, average, and maximum accelerations and rotational

velocities were determined from the sensor data. The acceleration data were used to estimate impact forces experienced by the test blocks upon impact. A detailed analysis of the retrieved test data for different block and site characteristics is presented in Chapters 4 and 5.
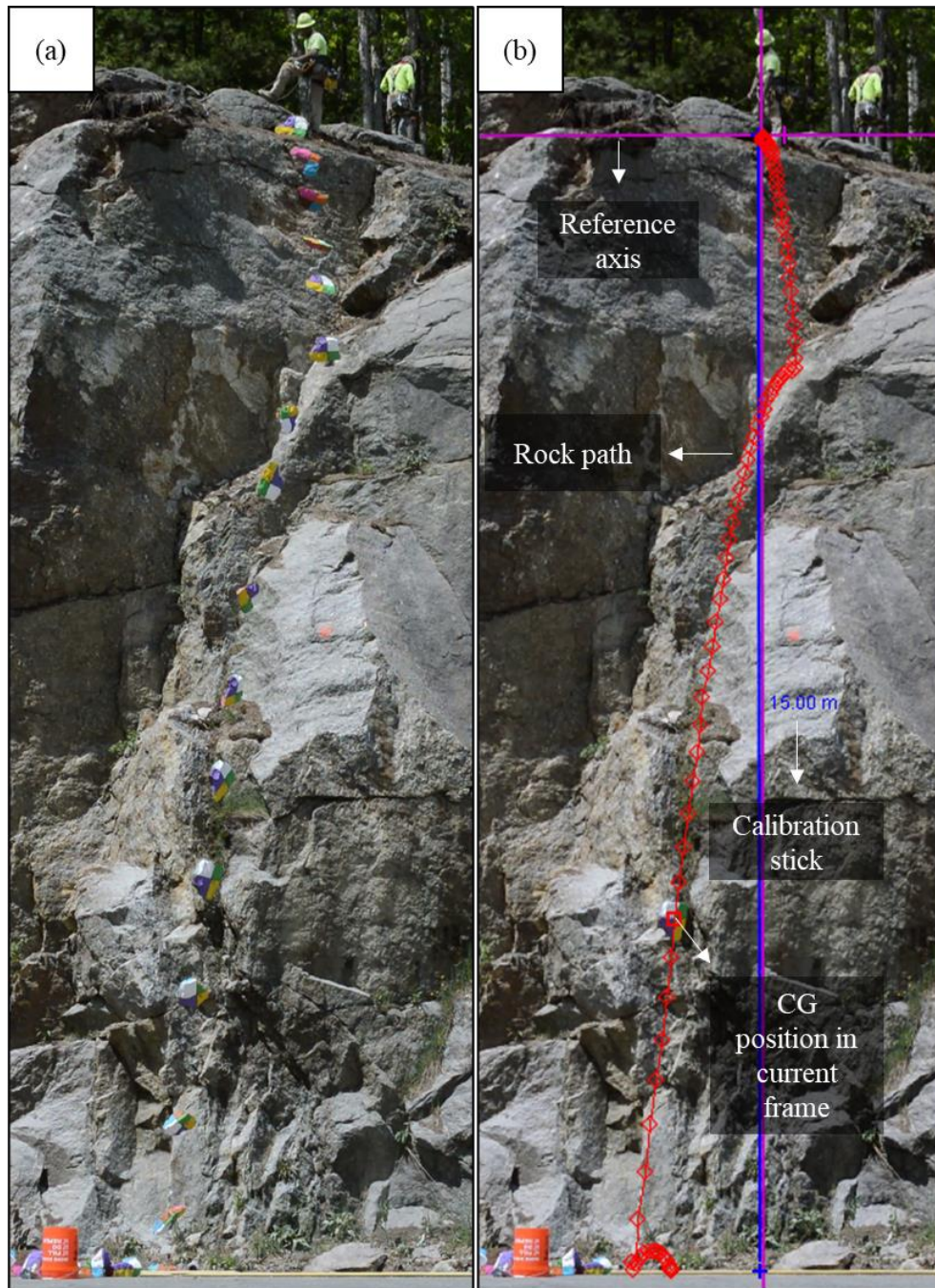
Figure 3.10. (a) Rock trajectory through combined video frames, and (b) rock trajectory using Tracker software. The reference axis is positioned at the rockfall start point, and the video scale is determined by a calibration stick, which is the distance between two known points. The known drop heights were used for video calibration in this research.

3.3. Small-scale drop tests

A preliminary instrumented small-scale experimental campaign was conducted to evaluate coefficients of restitution on granular material and rock in addition to the field tests previously detailed. Energy restitution experiments were carried out in a test pit in the UNH Geotechnical Laboratory to compare with computational models simulated in this research.

A Kinsman Granodiorite test rock from Warner/NH was initially cut into a cubic block with approximately 8 cm sides. Similar to the local rocks from the field tests, the cubic block was also drilled in its center of gravity and painted for video analysis. In a second round of tests, the block edges were cut with a custom 3D printed fixture aid, which aligned the edge position before cutting with the saw. The resulting polyhedron is similar to a cuboctahedron. The results were used to evaluate how rock kinematics during and after impact were affected by shape alteration and consequently weight reduction. The test block and fixture are presented in Figure 3.11, and the properties of both blocks are shown in Table 3.2. The width of the blocks is slightly greater than the other dimensions to ensure that the plug and screw were flush to the rock face.
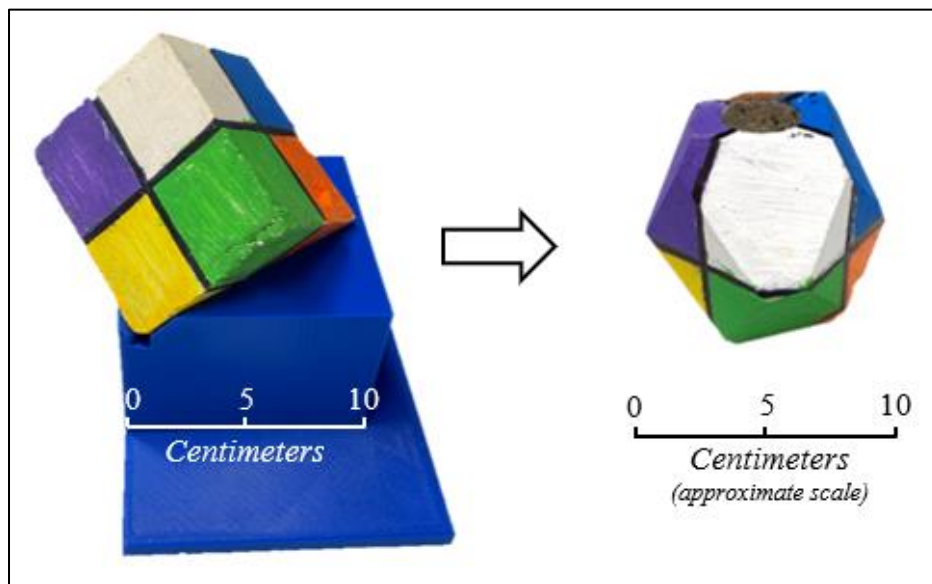
Figure 3.11. Cubic test block and 3D printed fixture (left), and cuboctahedral test block (right).

Table 3.2. Properties of the test blocks used for the laboratory experiments.

| Block | Weight (g) | Density (kg/m³) | Dimensions (cm) | | | Shape | Moments of inertia (kg.m²) | | |
			Length, Y	Width, X	Height, Z		I_{XX}	I_{YY}	I_{ZZ}
Cube	1095	2870	7.4	8.6	7.2	Compact	0.0010	0.0011	0.0012
Cuboc-tahedron	790	2870	7.4	8.6	7.2	Compact	0.0005	0.0006	0.0006

The first tests were conducted on a 50 cm sand layer, compacted using a jack hammer tamper plate. The test block was consistently dropped from a drop device (Figure 3.12a), designed and assembled by the UNH TSC. This device has a trap door mechanism (Figure 3.12b), in which the block is placed between two rectangular doors, opened when a lever is pulled (Figure 3.12c). This mechanism allows the test block to fall with no rotation motion. The box height can be freely adjusted within the frame, allowing tests to be conducted in a consistent manner with different drop heights. For these preliminary tests, the rock dropper was set up at a constant drop height of 2.2 m, from the release surface to the top of the impact surface.

Each experiment was recorded with a frontal (iPhone 11, 240 fps, Figure 3.13a) and an upper camera (GoPro Hero 4, 120 fps, Figure 3.12a), whose field of view is presented in Figure 3.13d. This camera setup allowed recording rock motion about three directions during impact and calculating accurate kinetic energy estimates when matched with the rotation sensor data. As performed during the field tests, Tracker 5.1.5 was used to track the center of gravity of the falling block in each video frame. The video recording scale was calibrated with the aid of prism poles, as shown in Figure 3.13.

The tests were instrumented with Smart Rocks at a sampling frequency of 500 Hz, and the altimeter was disabled due to its significant data noise at high frequencies. Each test signal could be easily identified through a sharp peak in acceleration upon impact, which was used to match the sensor and video data to the same time intervals.
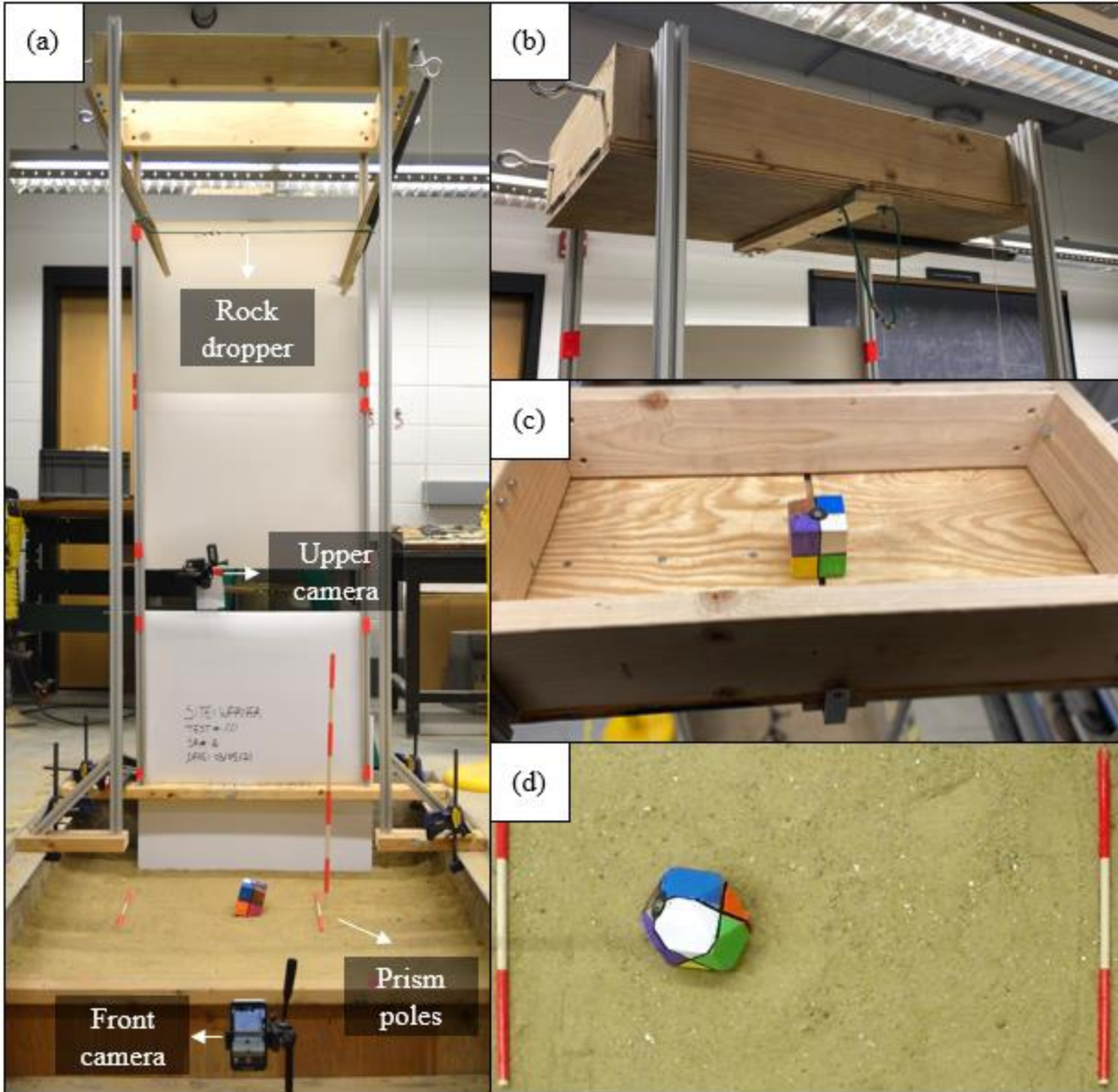
Figure 3.12. (a) Laboratory test set up, (b) rock dropper, (c) block position before testing, and (d) plane view from the upper camera. The reference sections in the prism poles are 10 cm long.

Ten drop tests from a 90° release angle at a flat, granular material surface were conducted for each test block. After each test, the maximum embedment depth was measured with a caliper, and the test surface was leveled, compacted, and prepared for the subsequent trial. The embedment depths are critical to estimate g-forces on known ground deformation and verify how acceleration and rotation measurements vary with changes in shape.
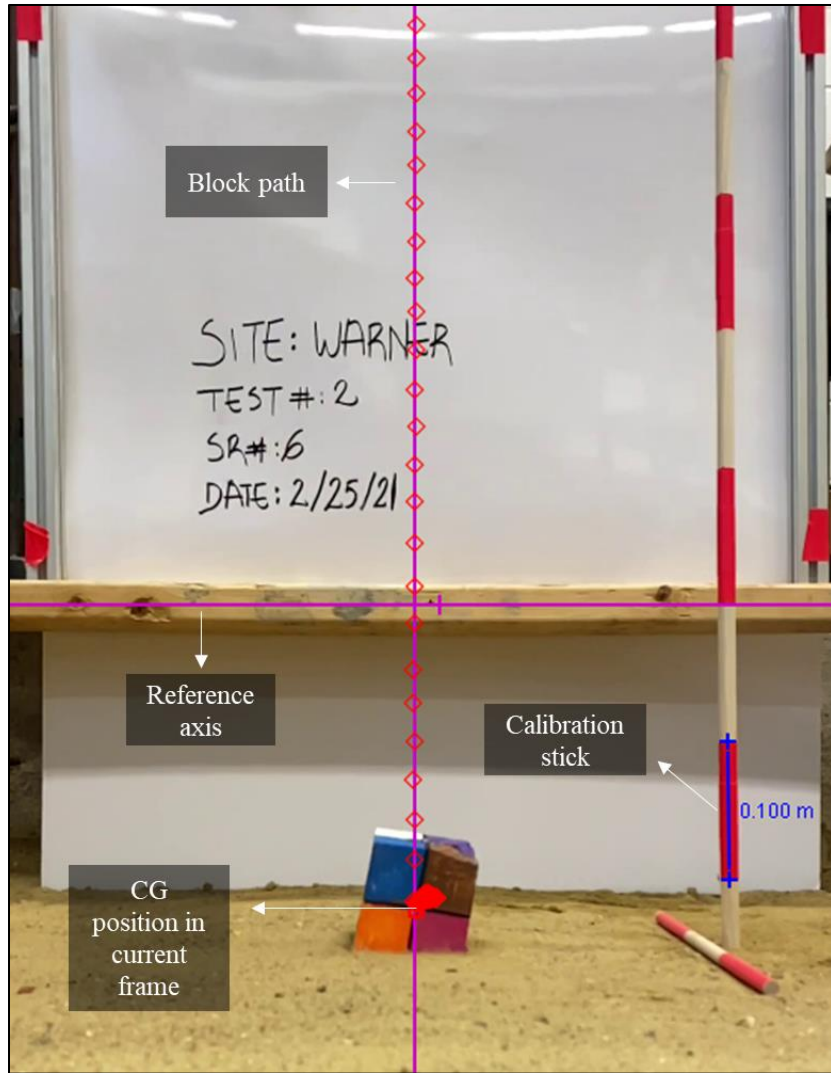
Figure 3.13. Estimated block trajectory through Tracker 5.1.5 software.

In a third stage, 90º drop tests were performed on a 60 cm x 30 cm x 15 cm test block also retrieved at the Warner site, embedded in plaster for a precise adjustment of the surface angle at 0º, as shown in Figure 3.14. In order to conduct the experiments from the same drop height of 2.2 m, approximately 15 cm of sand were removed from the test pit, and the granodiorite block embedded in plaster was placed on compacted sand. The drop tests using the cuboctahedral block on rock were evaluated following the same procedure described for the granular material

assessments. Only two trials could be completed, as the test block split into two halves during the third test.

Figure 3.14. (a) Preparation of the test pit for the drop tests on rock, and (b) experimental setup.

The estimated bounce heights, velocities, and kinetic energies from these experiments were used to calculate velocity- and energy-based coefficients of restitution, whose definitions were previously defined in Chapter 2. These COR values were used for modeling comparisons with default coefficients typically used in the literature and how predictions of trajectories, runout

distances, and block kinematics vary between the two methods. This preliminary experimental campaign has formed a future research methodology that will evaluate impact surfaces such as rock, sand, grass, gravel, and asphalt at different inclinations and drop heights using the same laboratory test setup.

3.4. Rockfall modeling

The field data were compared with digital rockfall models in RocFall 6.0 software by RocScience, which can calculate bounce heights, energies, and velocities for 2D simulated trajectories. The slope cross-sections were imported in the software as coordinates obtained from 3D surface models generated for all test sites by photogrammetry by the NHDOT. Representative cross-sections from each field test, based on video observations, were extracted from the 3D slope models. A 3D point cloud for one of the New Hampshire sites is presented in Figure 3.15.

Figure 3.15. 3D point cloud generated by photogrammetry for a test slope in Warner, NH. The green lines represent the cross-section locations for 2D rockfall modeling.

Each cross-section was defined using 2D (X, Y) coordinates obtained from the 3D point cloud. X corresponds to the lateral direction, and Y corresponds to the slope elevation. The cross-section surface is defined by line segments defined between each pair of consecutive vertices. In order to estimate rockfall behavior, material properties are assigned to each slope segment. As described in Chapter 2, the rock slope and adjacent surfaces (soil and asphalt) are defined based on coefficients of restitution, which will govern rockfall behavior in simulation models.

Rigid body analyses were performed to simulate experimental rockfalls conducted in Warner and Keene, NH. The block mass, shape, and density were imported for each assessment. For more straightforward data processing in 2D, the geometry of each rock was simplified, and all blocks were simulated in two directions to account for rotation about the smallest and largest axes of inertia (Figure 3.16). Each rock cross-section was simulated 50 times from start (seeder) locations approximated from the field tests.
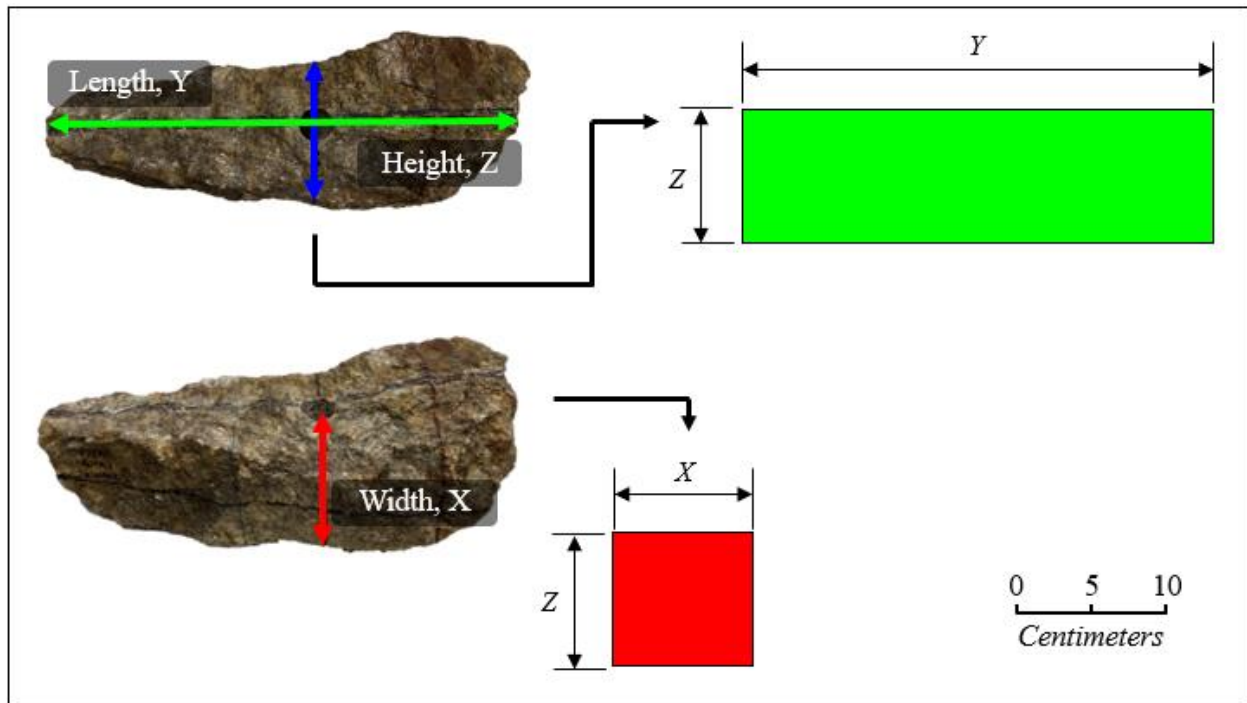
Figure 3.16. Method to simplify cross-sections of a test block using geometric shapes.

As previously discussed, RocFall simulates trajectories and modes of motion (free-fall, bouncing, rolling, sliding) of a pre-defined number of falling blocks. It generates graphs with average and maximum estimated velocities, translational and rotational kinetic energies, and bounce heights along with the slope profile. The software also provides histograms of endpoint locations which actively contribute to ditch and barrier design. Figure 3.17 presents a sample trajectory described by the YZ rock cross-section, shown in Figure 3.16, along the slope profile determined from video observations. Both rockfall start and end locations are visible, and each of the three surface types (rock, sand, and asphalt) was defined by different COR values.
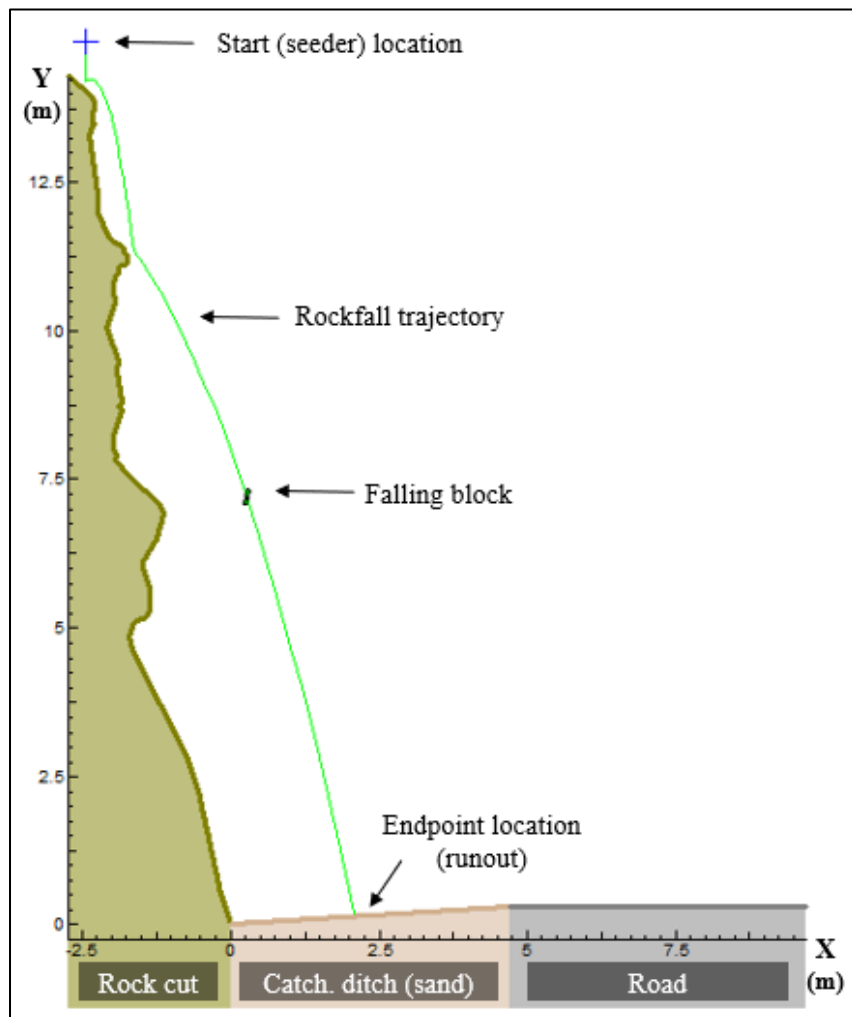
Figure 3.17. Rigid body rockfall simulation performed in RocFall.

The modeling assessments conducted in this research were divided into two main stages:

1. Evaluation of default coefficients of restitution, and

2. Evaluation of laboratory-determined coefficients of restitution.

Default coefficients of restitution previously selected and analyzed by Disenhof (2018) were evaluated in the initial stage of this work. The software output was compared to the field-observed trajectories and rockfall motion measured through video analysis and SR test instrumentation. Based on past comparative rockfall assessments conducted by Disenhof, excessive bounce heights and runout distances were observed in these early models. This behavior was expected because rockfall movements and model input parameters are still not fully comprehended, and current predictions typically disregard block rotation in energy estimates.

In a second stage, additional simulations with the same test blocks and slope profiles were conducted to address this issue, based on the preliminary small-scale energy restitution assessment. These laboratory-estimated coefficients are expected to generate more realistic rockfall trajectories, runout distances, and block kinematics when compared with the field measurements. The input parameters and comparative field analysis of the 2D models performed in this research are further detailed in Chapter 8.

3.5. Summary

Several instrumented rockfall experiments were carried out on ten rock slopes in New Hampshire and one in Vermont, United States. The field tests were conducted with Smart Rock sensors embedded in the center of gravity of local rocks retrieved at each slope location. The acceleration, rotation, and altitude data from the sensor are saved to a micro-SD card for post-processing with MATLAB and Microsoft Excel.

The Smart Rock sensors were also used in a preliminary laboratory assessment to establish a research methodology capable of consistently evaluating instrumented rock rebounds. Experiments on sand and rock were performed to estimate coefficients of restitution using both video and sensor measurements.

Finally, the experimental trajectories and rotation motion were compared with two-dimensional rockfall simulations using default input parameters and energy restitution coefficients estimated in the laboratory. The slope profiles were obtained from three-dimensional point clouds generated by photogrammetry, and representative cross-sections were selected based on previous video observations of the field tests.

4. EXPERIMENTAL DATA PROCESSING

The fourth-generation Smart Rock sensor was extensively used in this research to experimentally characterize rockfall motion from the perspective of the falling block. This chapter discusses one field test performed in Keene, NH, and how the experimental data were processed to analyze the various phases of each rockfall event.

4.1. Plotting the raw data

The accelerometer, altimeter, and gyroscope data measured by the sensor are written to a comma-separated file, processed and analyzed with MATLAB. The sensor records data continuously at a constant sampling frequency of 100 or 500 Hz and is activated before being embedded into the test rock. Recording continues until the SR is removed from the block and instructed to save the data to the SD card. Therefore, the generated raw data requires further processing at specific time intervals of interest to remove extraneous data not related to the actual rockfall experiment. For each event, the following two different time windows were separated for analysis:

- Time interval at which the test rock is manually hoisted to the top of the slope, for comparing the altimeter data during rock hoisting and rockfall (only applicable when the altimeter is enabled), and

- Time interval at which the rockfall experiment occurs.

The field trial from Keene, NH presented in this section had the SRs embedded in a compact elongated, 5 kg metamorphic rock previously used by Disenhof (2018), referred to as "reference rock" in this research. The physical dimensions and inertia properties of this test block are presented in Table 4.1.

Table 4.1. "Reference" Test block characteristics.

ID	Weight (kg)		Density (kg/m³)	Dimensions (m)			Shape	Mass moment of inertia (kg*m²)		
	Before drill.	After drill.		Length, Y	Width, X	Height, Z		I_{XX}	I_{YY}	I_{ZZ}
Ref	-	5.21	2660	0.20	0.12	0.12	Compact Elongated	0.018	0.018	0.011

The SR generates .csv files output columns for time (milliseconds), high-g x, y and z accelerometer (g), low-g x, y and z accelerometer (g), gyroscope x, y and z (dps), and altitude (m). The first 11 measurements after sensor activation are presented in Table 4.2, where:

- time = measured in microseconds,

- hax, hay, and haz = high-g accelerations in X, Y, and Z,

- ax, ay, and az = low-g accelerations in X, Y and Z,

- gx, gy, and gz = rotational velocities about X, Y, and Z,

- t = temperature, and

- alt = altimeter measurements.

Table 4.2. Raw data output from an experimental rockfall in Keene/NH.

time	hax	hay	haz	ax	ay	az	gx	gy	gz	t	alt
(micros)	(g)	(g)	(g)	(g)	(g)	(g)	(dps)	(dps)	(dps)	(C)	(m)
14847828	1.06	0.96	0	0.65	-0.18	0.2	32.71	57.98	-24.05	35.5	1.34
14857828	1.06	-0.01	-0.39	0.63	-0.15	0.2	22.58	37.96	-19.04	35.51	1.49
14867829	0.67	0.57	0.98	0.73	-0.2	0.33	21.12	23.68	-12.82	35.54	1.28
14877826	1.06	-0.79	0.2	0.91	-0.2	0.51	22.58	28.69	-5.13	35.55	1.31
14887827	-0.11	0.57	0.78	0.93	-0.24	0.51	27.1	46.02	1.83	35.57	1.59
14897831	-1.48	0.38	-0.2	0.94	-0.22	0.53	25.88	55.91	1.1	35.58	0.81
14907829	0.28	-0.4	1.37	0.93	-0.22	0.49	24.78	62.5	0.12	35.58	1.87
14917828	0.67	0.96	0	0.88	-0.19	0.36	15.14	58.47	-2.93	35.6	1.57
14927824	0.67	0.77	-0.98	0.79	-0.2	0.31	4.88	47.85	-1.95	35.61	1.35
14937831	1.84	-0.4	0.2	0.79	-0.21	0.32	-5.25	34.06	-0.49	35.63	1.54
14947828	-0.31	0.18	-0.39	0.79	-0.21	0.28	-7.69	16.72	-3.42	35.64	1.98
14957828	1.06	-0.01	0.78	0.82	-0.23	0.24	-8.79	1.59	-1.71	35.66	1.3

The MATLAB script requests the user to select a raw data file and specify the site location and test rock ID, whose properties are searched in a database spreadsheet. Then, the script retrieves all relevant rock characteristics, including mass, dimensions (matching the SR orientation), moments of inertia, and shape. Additional test information such as sensor ID, test date, runout distance, and measured drop height is also provided.

The script normalizes the time (measured in microseconds), converts it to seconds, and calculates the resultant components of acceleration and rotation, estimated from the accelerometers and high-rate gyroscope (Equations 4.1 and 4.2). The resultant acceleration vector is composed of both low- and high-g accelerometers, in which low-g acceleration resultants higher than 8 g were replaced by the high-g resultant acceleration.

$$Acceleration_{RES} = \sqrt{A_X^2 + A_Y^2 + A_Z^2} \qquad \text{(Equation 4.1)}$$

$$Rotational\ velocity_{RES} = \sqrt{R_X^2 + R_Y^2 + R_Z^2} \qquad \text{(Equation 4.2)}$$

Where: $Acceleration_{RES}$ = resultant acceleration,

$Rotational\ velocity_{RES}$ = resultant rotational velocity,

A_X, A_Y, and A_Z = acceleration in X, Y, and Z, respectively, and

G_X, G_Y, and G_Z = rotational velocities about X, Y, and Z, respectively.

After calculating the resultant acceleration and rotation components, the 3-axis and altimeter data are plotted (Figure 4.1). The user is asked to select the time interval corresponding to rock hoisting before the rockfall test. The time window equivalent to manually hoisting the rock to the top of the slope can be easily identified in the altimeter data.
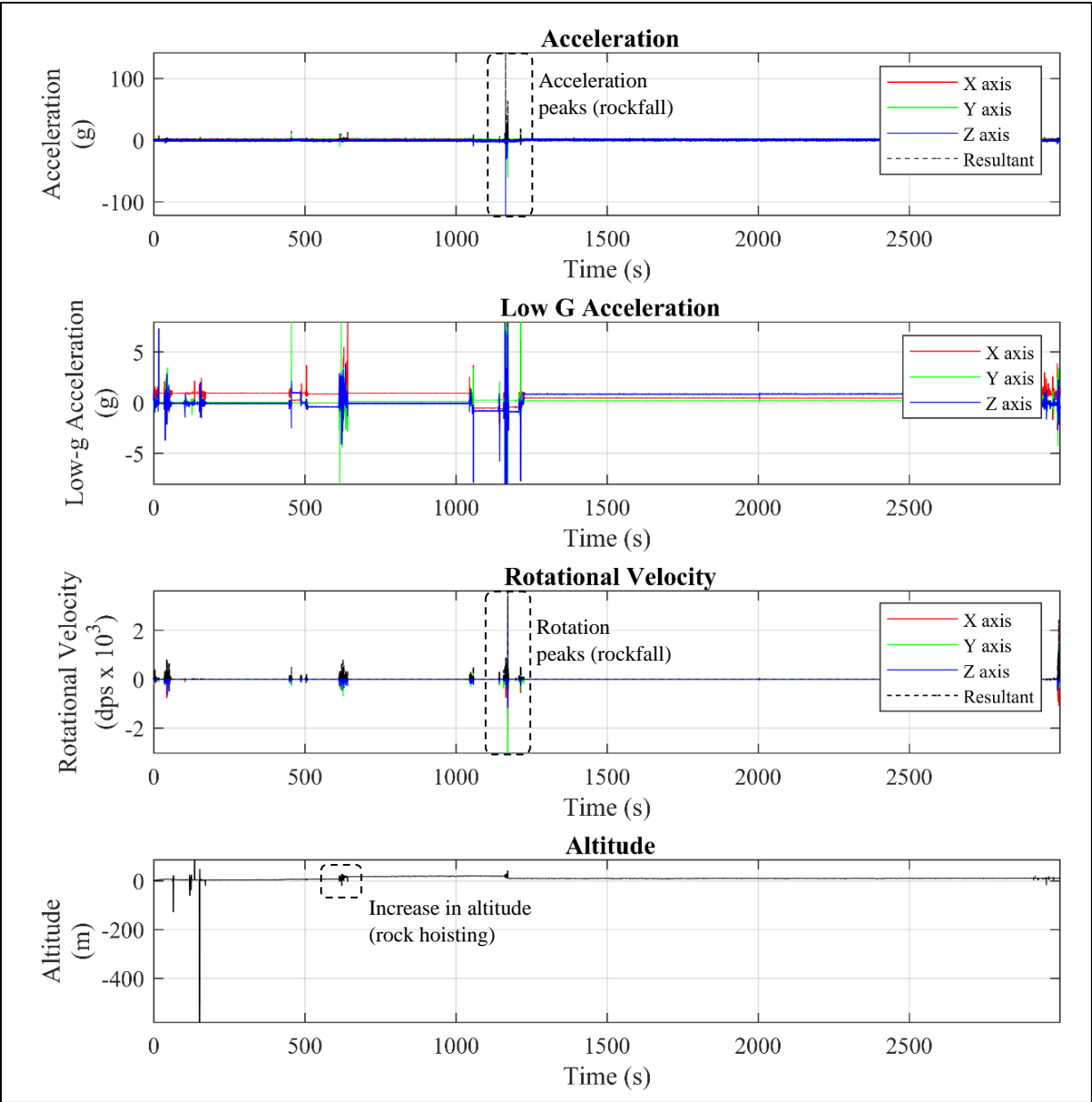
Figure 4.1. Raw data output (reference rock, Keene NH).

4.2. Selecting time intervals of interest

It was observed in the graph that rock hoisting occurs between 600 and 650 seconds, whose experimental data is shown in Figure 4.2. Due to the inherent noise visible in the altimeter data, the hoisting altitude is calculated as the subtraction of the averages of the first and last 100

96

measurements during the selected time interval. Higher levels of noise are observed upon impact and rapid movements, especially during block hoisting and fall. The test discussed in this chapter also presents noisy acceleration and rotation data because the test block was hoisted inside a bucket, in contact with the rock face.
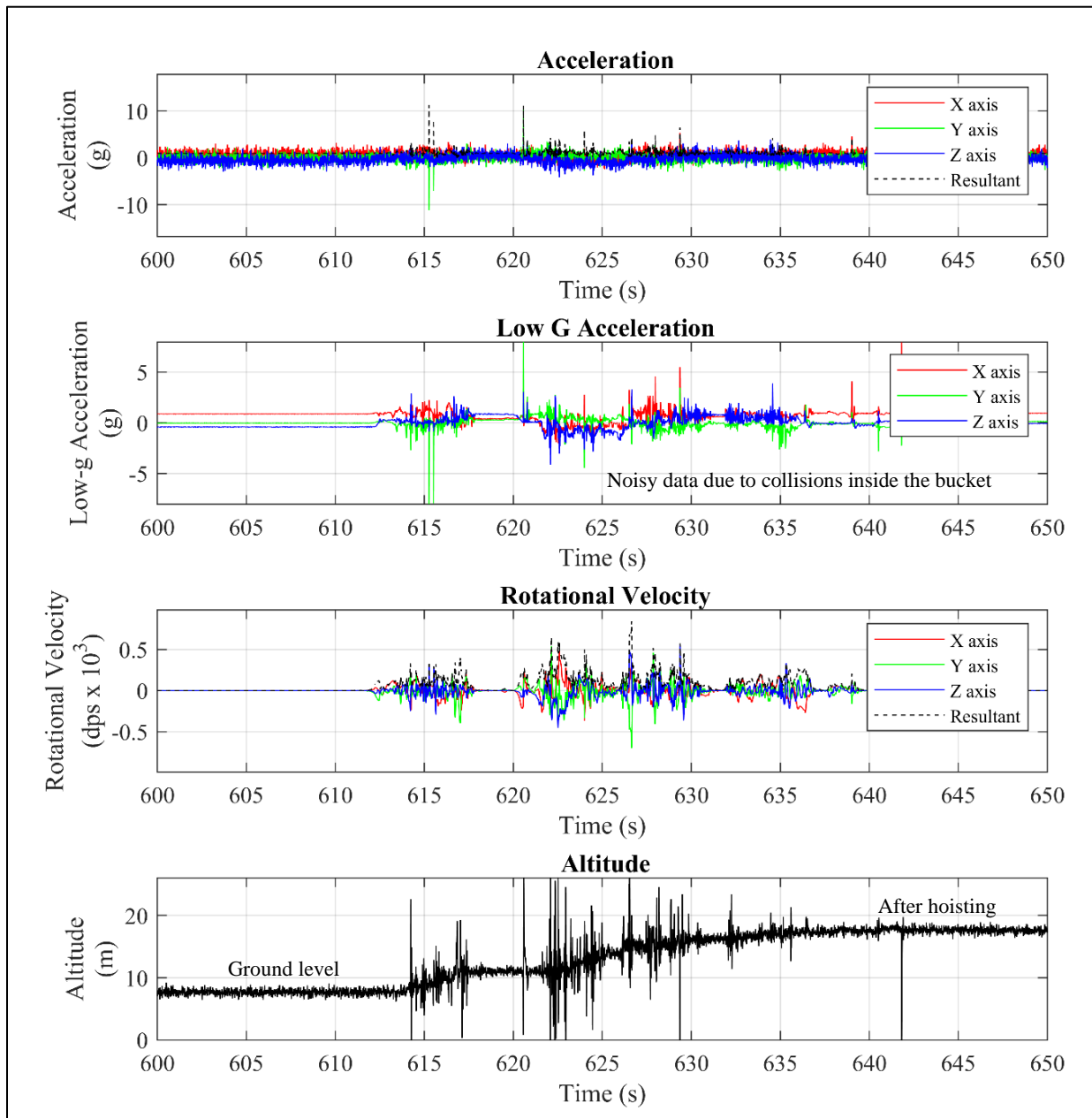
Figure 4.2. Time interval corresponding to rock hoisting (reference rock, Keene NH).

97

The user is then requested to select the time interval corresponding to the rockfall experiment, which can be easily identified in the raw data (Figure 4.1) through the three initiation taps, as well as peaks in the measured high-g acceleration upon significant impacts. As presented in Figure 4.3, the test was performed between 1160 and 1180 seconds.
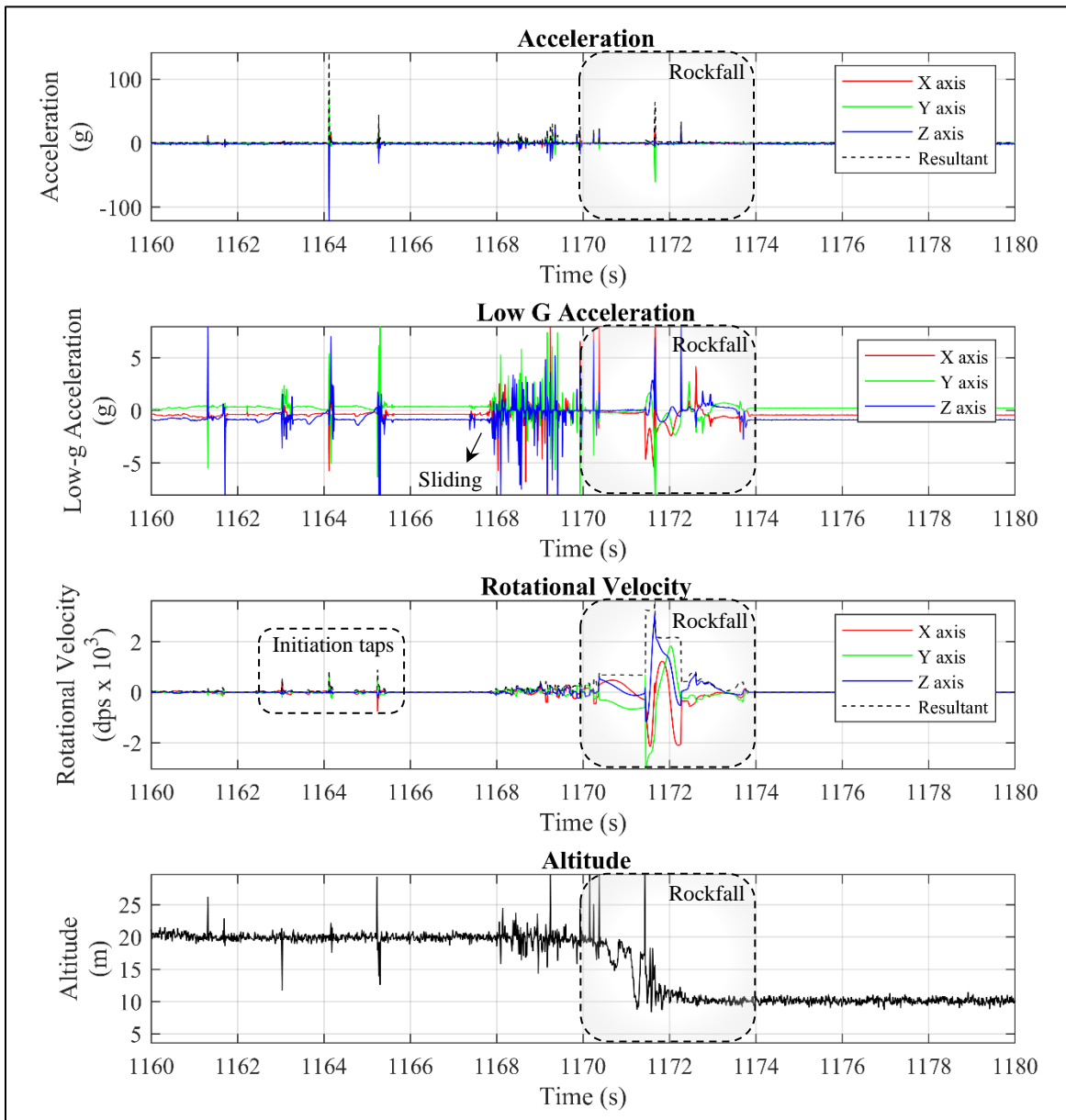
Figure 4.3. Rockfall three-axis and altitude SR data, non-formatted (reference rock, Keene NH).

Due to the slope geometry and height, and safety reasons, it was not feasible for the test operators to drop the reference rock directly from the edge of the rock face in Keene. Therefore, the rock was slowly pushed with a wood dowel, sliding before it could finally fall. The rock sliding motion can be identified through several acceleration peaks accompanied by random changes in rotational motion (1168 to 1170 s) before the abrupt change in altitude at 1170 seconds. The time interval corresponding to the field test (until the rock comes to a complete stop) is highlighted in the figure. For better visualization of rockfall motion in the formatted data and comparison with video recordings, time intervals between 1 to 2 seconds immediately before and after each test were selected. The average and maximum X, Y, Z, and resultant rotation and acceleration components are determined for the time interval corresponding to rock movement (1170 to 1174 s in this test).

4.3. Matching Smart Rock and video measurements

If video analysis was conducted and saved on a separate spreadsheet, the user also has the option to match rockfall motion measurements (displacements and velocities) with the sensor data. Frontal video recordings parallel to the slope face allowed to compare the measured vertical displacement over time with the recorded altimeter data. If the slope geometry allowed video perpendicular to the slope face, a side video was also captured laterally giving a more complete picture of the entire rockfall event. Video recordings from orthogonal perspectives allowed to calculate scalar (resultant) velocities from three different directions. These velocity estimates were used to estimate translational kinetic energy at selected sites, which was added to the rotational kinetic energy (using the Smart Rock data) to estimate total kinetic energies within the video field of view.

Kinetic energy estimates are a future object of study and can be performed from the Keene tests. Figure 4.4 presents the frontal and lateral trajectories described by the reference rock. As previously discussed, the approximate location of the center of gravity was selected in each video frame, and a reference axis was positioned at the rockfall start point for position tracking. The video scale was determined by specifying a known distance between two points. The start and endpoint locations (drop height) were selected in each video analysis from both frontal and lateral perspectives.

Figure 4.4. Frontal and lateral trajectories were determined using Tracker software (reference rock, Keene NH).

Tracker software uses the specified CG positions to calculate the vertical, horizontal, and resultant velocities for each test. The time, displacement, and velocity in both horizontal and vertical directions are saved to a .xlsx file, which is then analyzed by the same MATLAB script, which asks whether the user wants to add video data. If the option is selected, the corresponding video data file is uploaded. Both Smart Rock and frontal video data (vertical displacement and resultant velocity) are then plotted in the same graph, as shown in Figure 4.5, after manually match the video time window with the previously selected SR data interval. It can be noted that the previously selected SR rockfall time of interest has been normalized to start at zero seconds.

As discussed and shown in previous graphs, the altimeter presents a significant noise level, especially during rapid movements and substantial impacts. Because of the data noise, it can be challenging to accurately match the video measurements if only the vertical displacements are compared. On the other hand, acceleration peaks and abrupt changes in rotational velocity can be easily compared with sharp decreases in velocity in the video measurements. The user can adjust the video time frame unlimited times until a satisfactory match is obtained.

If applicable to the test in analysis, the user can select a lateral video data file matched with both SR and frontal video data (Figure 4.6). It is possible to observe that the velocity plots for both frontal and lateral video data do not follow smooth lines over time (even in free fall between 2 and 3 seconds). This characteristic is attributed to the approximate location of the rock CG in the video frames. This task was particularly challenging during rock rotation, with rocks of greater size, motion behind or inside vegetation, and blurry video frames. Therefore, the obtained velocities should be considered as estimates in these rockfall assessments.
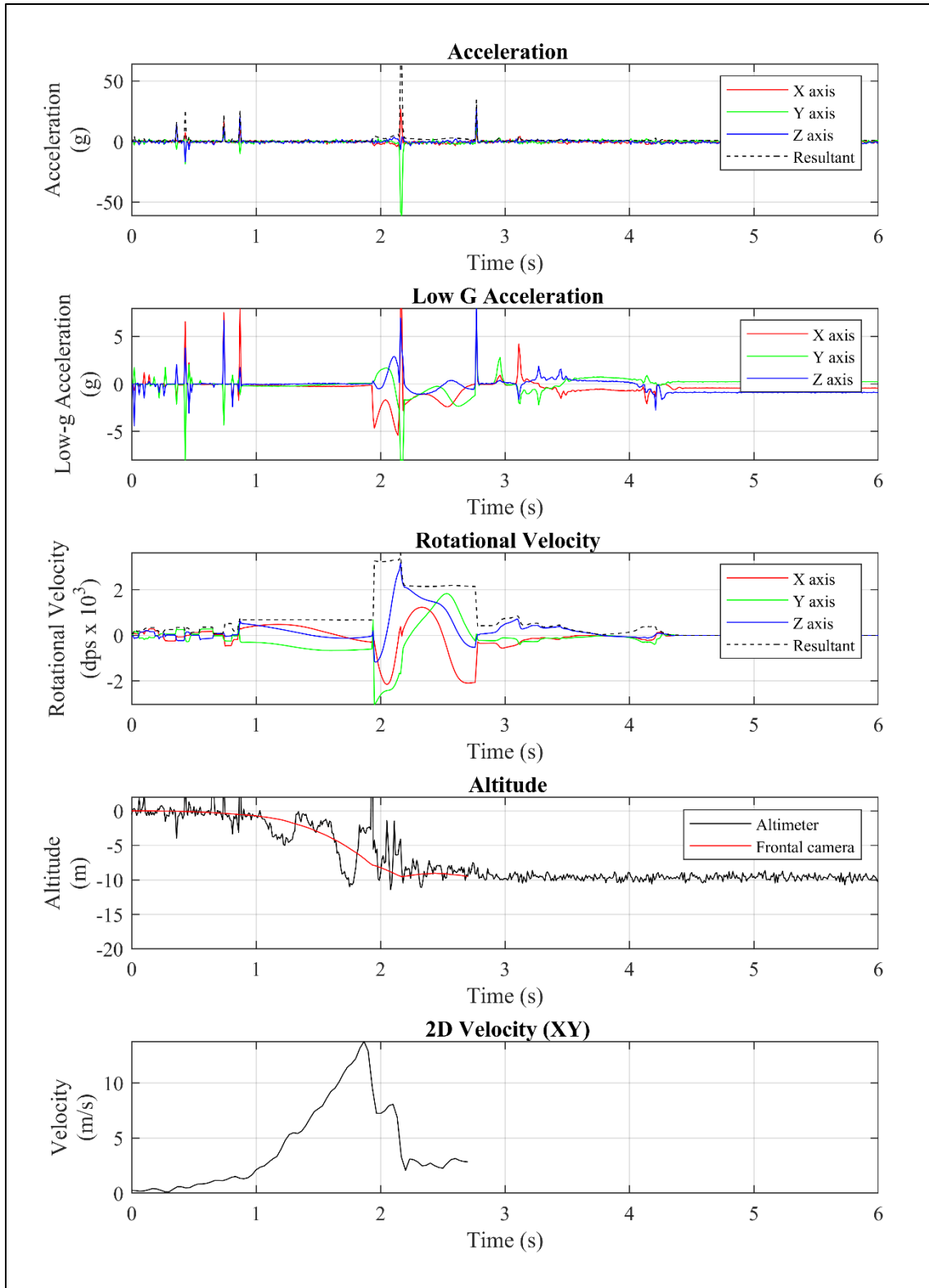
Figure 4.5. Smart Rock and frontal video data after matching their time intervals (reference rock, Keene NH).
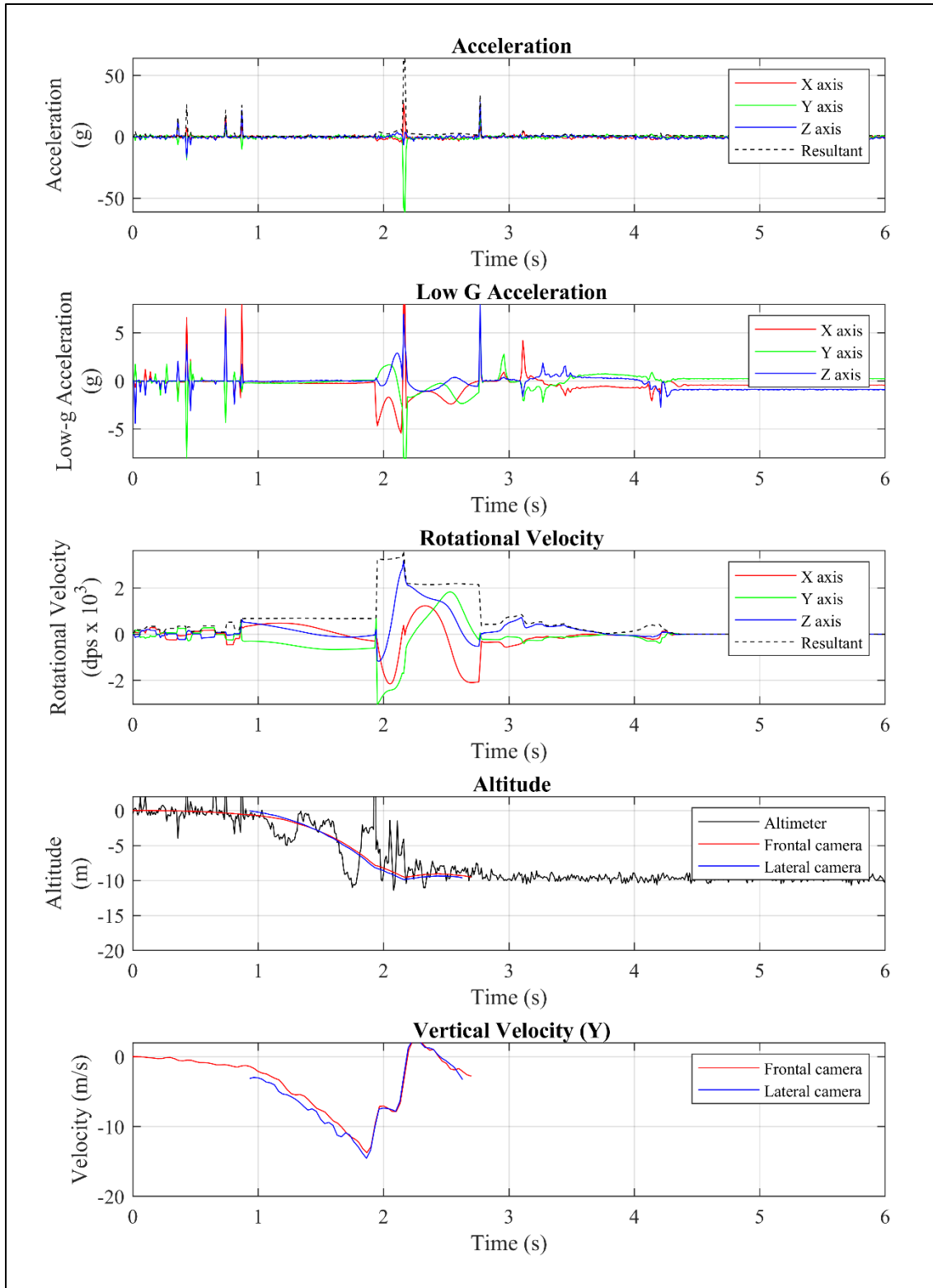
Figure 4.6. SR, frontal, and lateral video data after matching their time intervals (reference rock, Keene NH).

4.4. Plotting and interpreting the processed data

All sensor, test, block, and video data are written to a new .xlsx file, which can be re-processed by the MATLAB script for re-plotting the data. The script can also combine multiple pre-processed .xlsx files into a single spreadsheet to analyze numerous test data. Finally, the sensor output and video displacement data are plotted in a single figure with all acceleration, rotation, altitude plots, and all relevant test information previously provided by the user. The compatibility between both SR and video data is presented in Figures 4.7 and 4.8.

Figure 4.8 details the rockfall trajectory with a combination of video frames that identify rock rotation. The axis orientation of the Smart Rock sensor in the test rock is also presented in the upper left corner. The letters A through G in both graph and combined figure indicate the different rockfall stages, matched through both SR and video recording times. The reference rock experienced a wide range of rockfall motion, which could be clearly identified in video and sensor signal. The flat acceleration (1 g) and rotational velocity (0 dps) lines indicate that the rock is at-rest and helps identify the start and end times of each test.

After being released from the top of the rock cut at 0 s, the rock initially slid (A) and bounced four times (B) on a roughly 50º initial inclined surface about 1 meter tall. Block impacts can be easily identified in the sensor signal through acceleration peaks captured by the high-g accelerometer, immediately followed by visible changes in rotational velocity kept constant in free fall until the next bounce.

At about 1 meter of vertical displacement (immediately after the bouncing behavior), the inclination of the rock face increases to 70º, and the block falls freely for 1 s (C). It is possible to observe in both sensor and video data that the block initially rotates about its shortest axes (X and Z, 12 cm), and gradually starts to rotate strictly about its Y axis (longest axis, 20 cm, shortest axis

of inertia). Although visible changes in each axis occur during free fall, the sensor measures a constant rotational velocity until an external force acts on the test block at approximately 2 s (D).
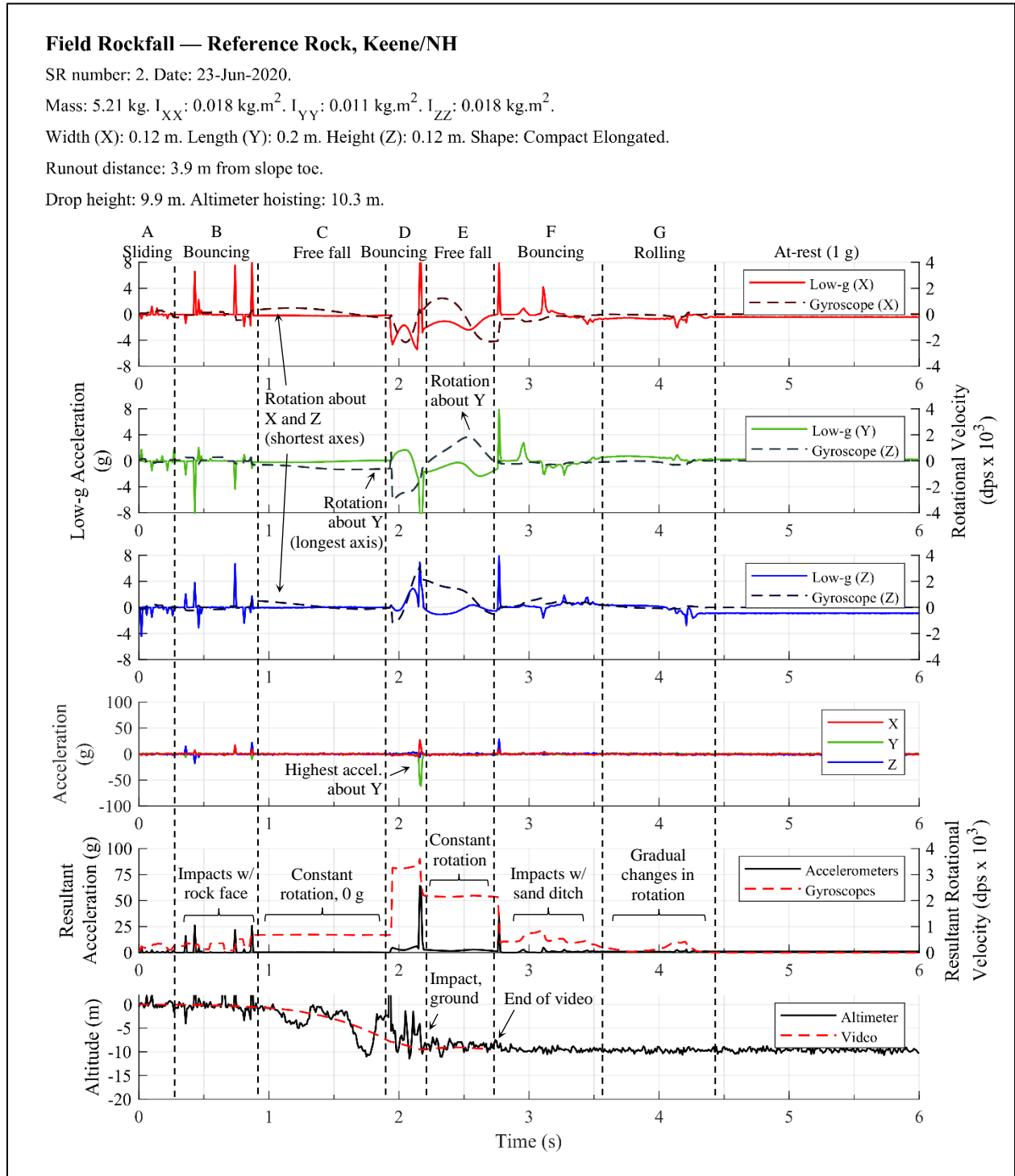
Figure 4.7. Smart Rock test data: reference rock, Keene NH.

105
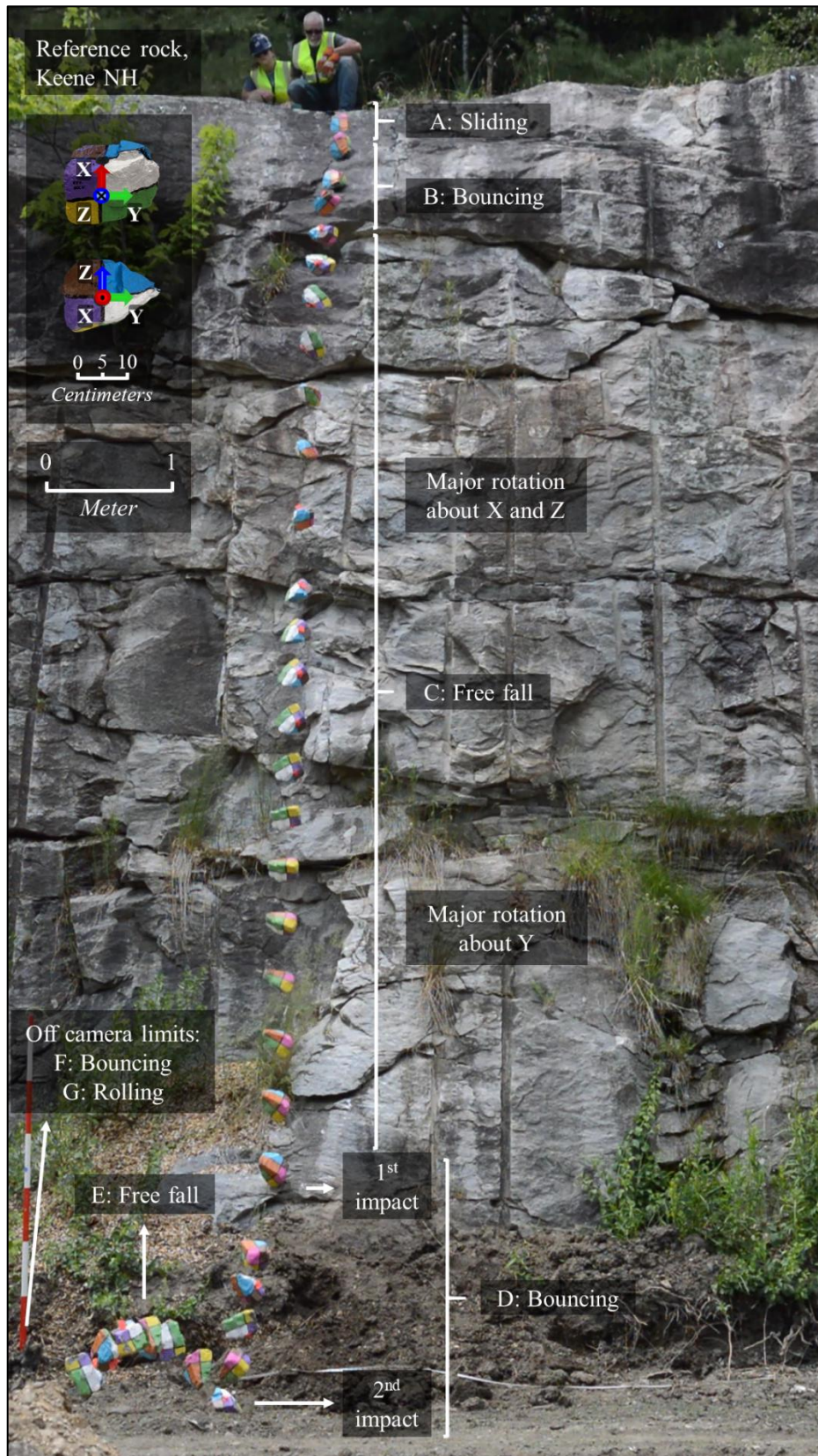
Figure 4.8. Rockfall trajectory: reference rock, Keene NH.

At D, the test rock bounces two times, with accelerations of 5 g and 64 g, at about 7.8 m (rock face) and 9.9 m (ground surface) vertical displacement, respectively. The first bounce occurred nearly parallel to the rock face, and, even though a low g-force was recorded, the resultant rotational velocity increased from 675 dps to 3230 dps, an increase of 480%. The block rotated about all three axes after the initial bounce at D, and the highest resultant rotational velocity occurred immediately before the second impact (3624 dps).

The test rock bounced approximately 50 cm upon impact with the ground surface and describes a parabolic trajectory also observed in the videos for about 0.6 s (E). The resultant rotational velocity decreases to 2145 dps during free fall and drops to 425 dps after a 34g impact on granular material at 2.8 s. Although not possible to confirm with video data due to its limited field of view, the block describes smaller bounces with accelerations between 3 and 5 g (F). The rotational velocity gradually decreases until the rock starts rolling and comes to a complete stop (G).

The resultant acceleration data provides information to estimate impact forces to a surface or barrier, which are relevant for protective design against rockfall. The metamorphic block has experienced resultant impact accelerations ranging from 3 to 34 g (bouncing) to 64 g upon impact with the ground. These respected resulting g-forces can be converted to intensities of 0.2 to 1.7 and 3.3 kN using the rock mass (5.21 kg) and gravity acceleration (g = 9.81 m/s²) in Equation 4.3. Estimating impact forces is fundamental in the design of protective structures.

$$Impact\ force = (Resultant\ G - force) * g * (rock\ mass) \qquad \text{(Equation 4.3)}$$

In addition to the maximum rotational velocity of 3624 dps, this rockfall test described an average resultant rotational velocity of 954 dps. The measured data demonstrates that block

rotation is an essential component of rockfalls and should not be disregarded in kinetic energy estimates.

4.4. Estimating kinetic energies during rockfall

To better understand the influence of rotation in the total kinetic energy (KE), energy calculations for the Keene tests were performed for this test. As previously mentioned, the total kinetic energy is subdivided into translational and rotational components. While the translational KE is governed by the rock mass and scalar velocity (Equation 2.1), the rotational KE is governed by the mass moment of inertia and rotational velocity (Equations 2.2 and 2.4).

Field experiments with video recordings parallel and perpendicular to the rock trajectory can provide fair estimates of scalar velocity during the test. Also, the Smart Rock sensor embedded inside the test rock provides rotation data from the perspective of the falling block. Therefore, the scalar velocities obtained from the video data were used to estimate the translational KE of selected tests. In contrast, the measured rotational velocities were used to calculate the rotational KE. Consequently, the total kinetic energy could be estimated by summing both KE components (Equation 2.3). In order to match the video frame rate (30 fps) and sensor sampling frequency (100 Hz) to calculate the total kinetic energy, three-point moving averages were calculated from the rotational KE at 100 Hz.

As shown in Figure 4.9, a second MATLAB code plots the estimated kinetic energies, previously calculated in Microsoft Excel, following the same format with relevant test information. It can be observed that the test block presents its maximum total kinetic energy (0.53 kJ) immediately before the first impact at C.
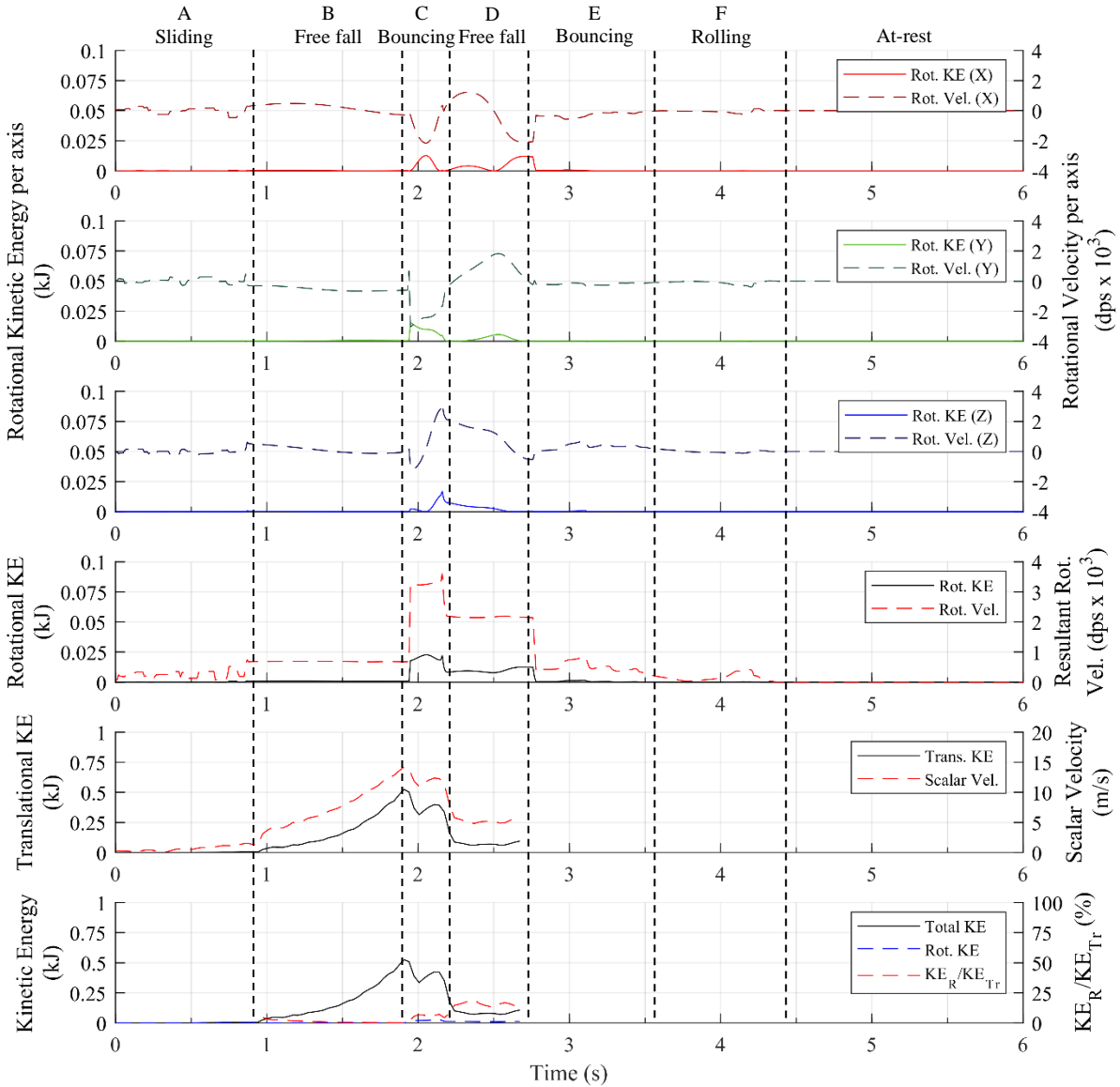
Figure 4.9. Kinetic energy data: reference rock, Keene NH.

The graph also shows how the rotational KE contribution significantly increases after the

first bounce at approximately 2 s. While the total and translational KE decrease with time, the

KE_{Rot}/KE_{Trans} ratio gradually increases with translational energy dissipation, increasing from nearly 0% to 7% immediately after the first impact at 1.9 s and reaching a maximum ratio of 19% at 2.3 s. Therefore, although the rotational kinetic energy is nearly negligible compared to the translational KE before the first significant impact, the contribution of the rotational kinetic energy should not be disregarded in rockfall modeling applications.

4.5. Calculating rockfall lateral dispersion

The test discussed in this chapter was performed with a 5.21 kg, compact elongated, metamorphic test rock, dropped from 9.9 meters from the ground surface (measured with a total station). Although the described trajectory was not captured by the video recordings in totality, as shown in Figure 4.4 and subsequent displacement and velocity plots, a lateral displacement of about -2.5 meters was observed (to the left of the start point). In addition, the runout distance was measured at 3.9 meters from the slope toe. The lateral test dispersion, previously defined in Chapter 2, can be calculated using Equation 4.4.

$$Lateral\ dispersion = \frac{Lateral\ displacement}{Slope\ length} \qquad \text{(Equation 4.4)}$$

The slope length can be estimated based on the cross-sections obtained for each slope profile, where the trajectory has occurred. The correspondent slope length for the test with the reference rock is shown in red in Figure 4.10. Therefore, the lateral test dispersion can be calculated as follows:

$$Lateral\ dispersion = \frac{2.5\ meters}{11.8\ meters} \times 100\% \cong 21\%$$
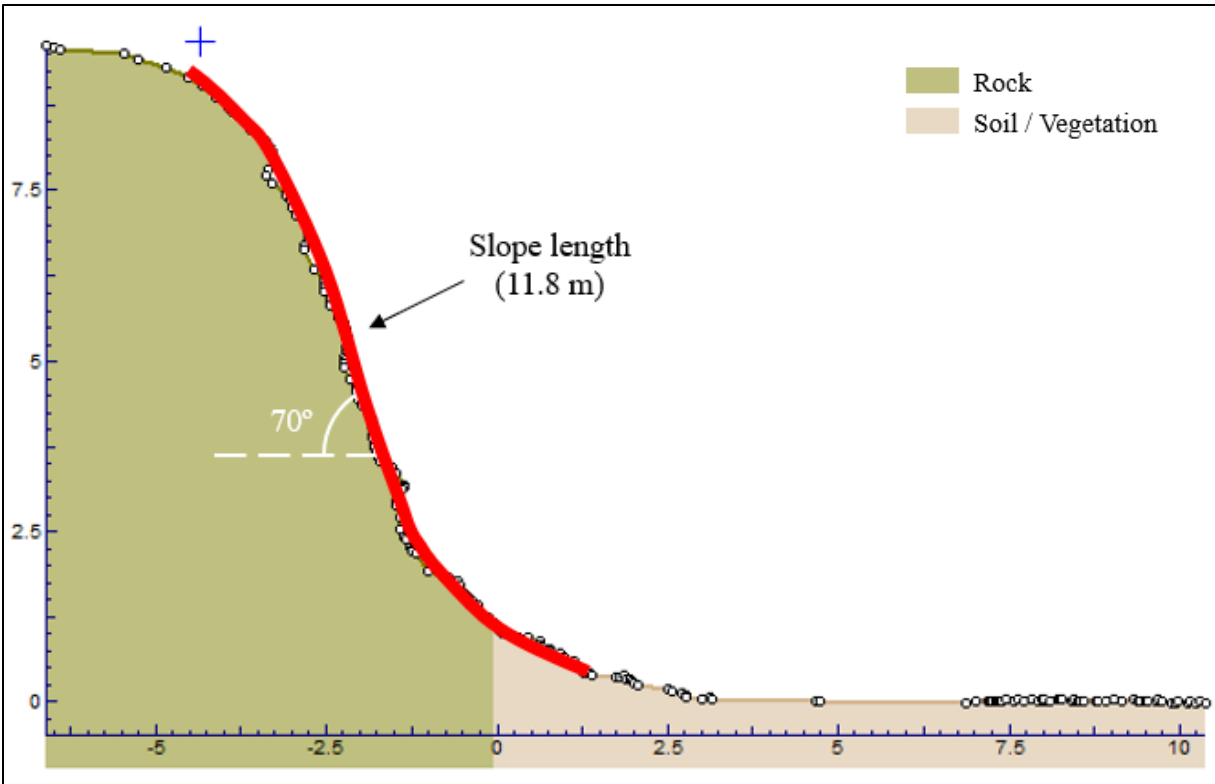
Figure 4.10. Correspondent slope profile for the reference rock (Keene, NH). Dimension units are in meters.

A lateral dispersion of approximately 21% was observed for this test. This percentage is comparable to the lateral dispersion range of 10 to 20% previously reported by Azzoni and de Freitas (1995).

4.6. Identifying rock motion from the Smart Rock data

The rockfall motion data recorded by the fourth-generation Smart Rock were compatible with previous experimental studies. As previously observed by Disenhof (2018), Caviezel et al. (2017), Caviezel and Gerber (2018) and Caviezel et al. (2018) during instrumented rockfalls with accelerometers and gyroscopes, block motion as free fall, bouncing, rolling, and sliding, and their exact times can be identified through the sensor output without the need for video recordings. The SR data output patterns to distinguish rockfall motion were consistent for most experimental trials:

111

- At-rest: zero rotational velocity, constant 1 g acceleration,

- Free fall: 0 g acceleration, constant resultant rotational velocity, the rock is free to rotate in all three directions, and the gyroscope graphs are smooth lines,

- Rolling: changes in rotational velocity accompanied by small peaks in acceleration (which typically do not exceed the capacity of the low-g accelerometer, < 8 g),

- Sliding: small acceleration peaks (which usually do not exceed the low-g sensor limits, $<$ 8 g) accompanied by zero or small rotational velocities,

- Impact: sharp peak in acceleration, typically captured by the high-g accelerometer, which can be followed by additional impacts, rolling, sliding, or a complete stop (at-rest), and

- Bouncing: one or more impacts, followed by free fall, typically captured by the high-g accelerometer, followed by visible rotational velocity changes.

Figure 4.11 presents the trajectory described by a rockfall test in Franconia/NH that experienced all modes of motion, as detailed in the SR output shown in Figure 4.12.
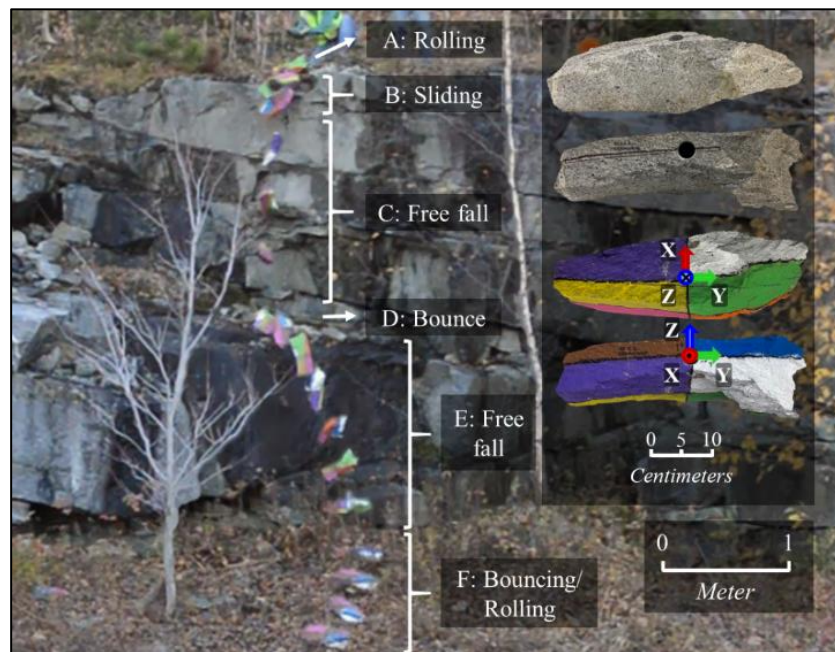
Figure 4.11. Rockfall trajectory: rock 2 (slope 1), Franconia NH.

112

Field Rockfall — Rock 2 (slope 1), Franconia/NH

SR number: 5. Date: 23-Oct-2020.

Mass: 10.41 kg. I_{XX}: 0.113 kg.m^2. I_{YY}: 0.024 kg.m^2. I_{ZZ}: 0.119 kg.m^2.

Width (X): 0.15 m. Length (Y): 0.4 m. Height (Z): 0.08 m. Shape: Very Elongated.

Runout distance: 3 m from slope toe.

Drop height: 9.6 m. Altimeter hoisting: 11.7 m.
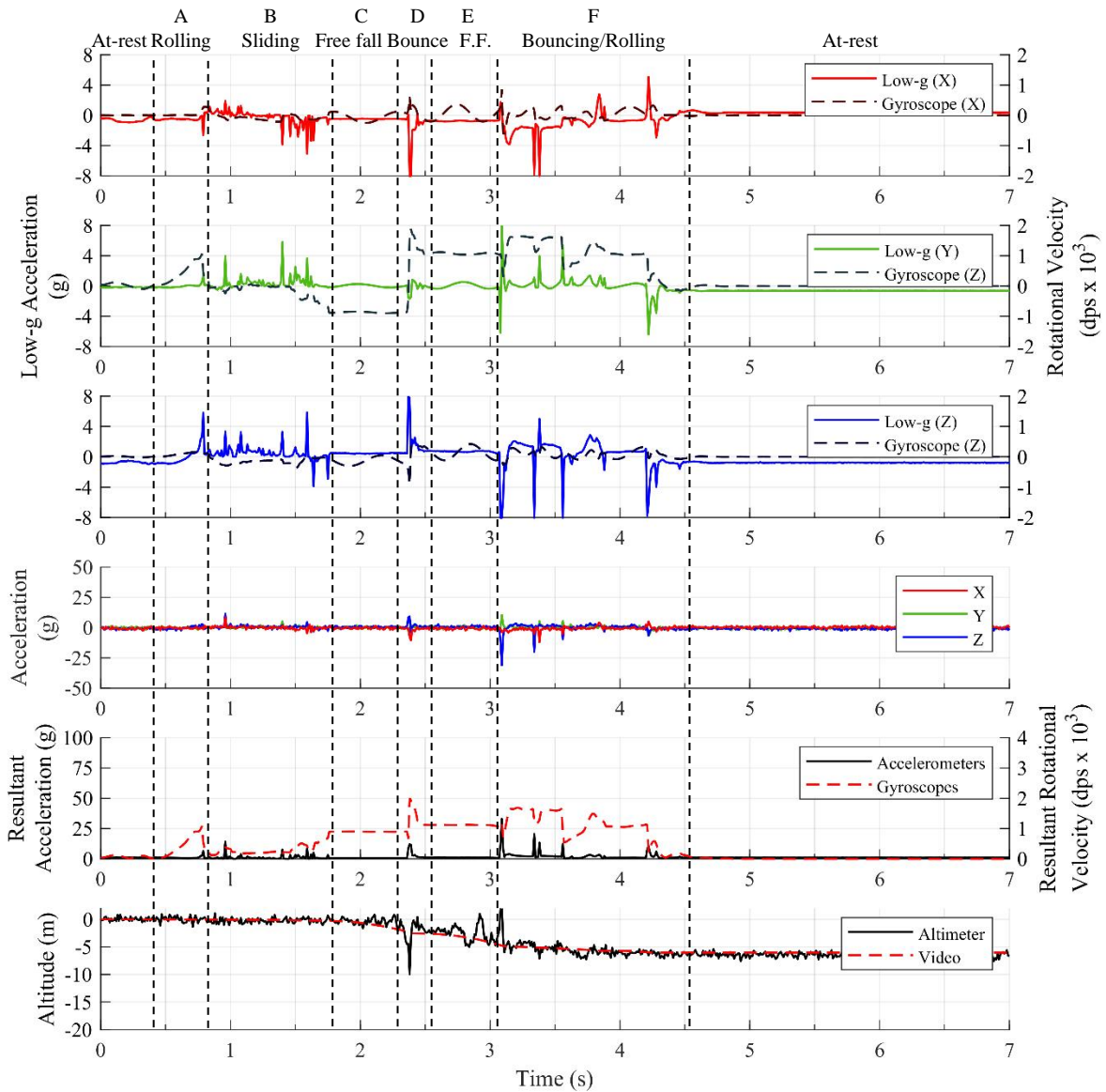
Figure 4.12. Smart Rock test data: rock 2 (slope 1), Franconia NH.

The 10 kg elongated block predominantly rotated about its longest axis, Y (smallest moment of inertia). The SR output allows the identification of modes of motion even when video
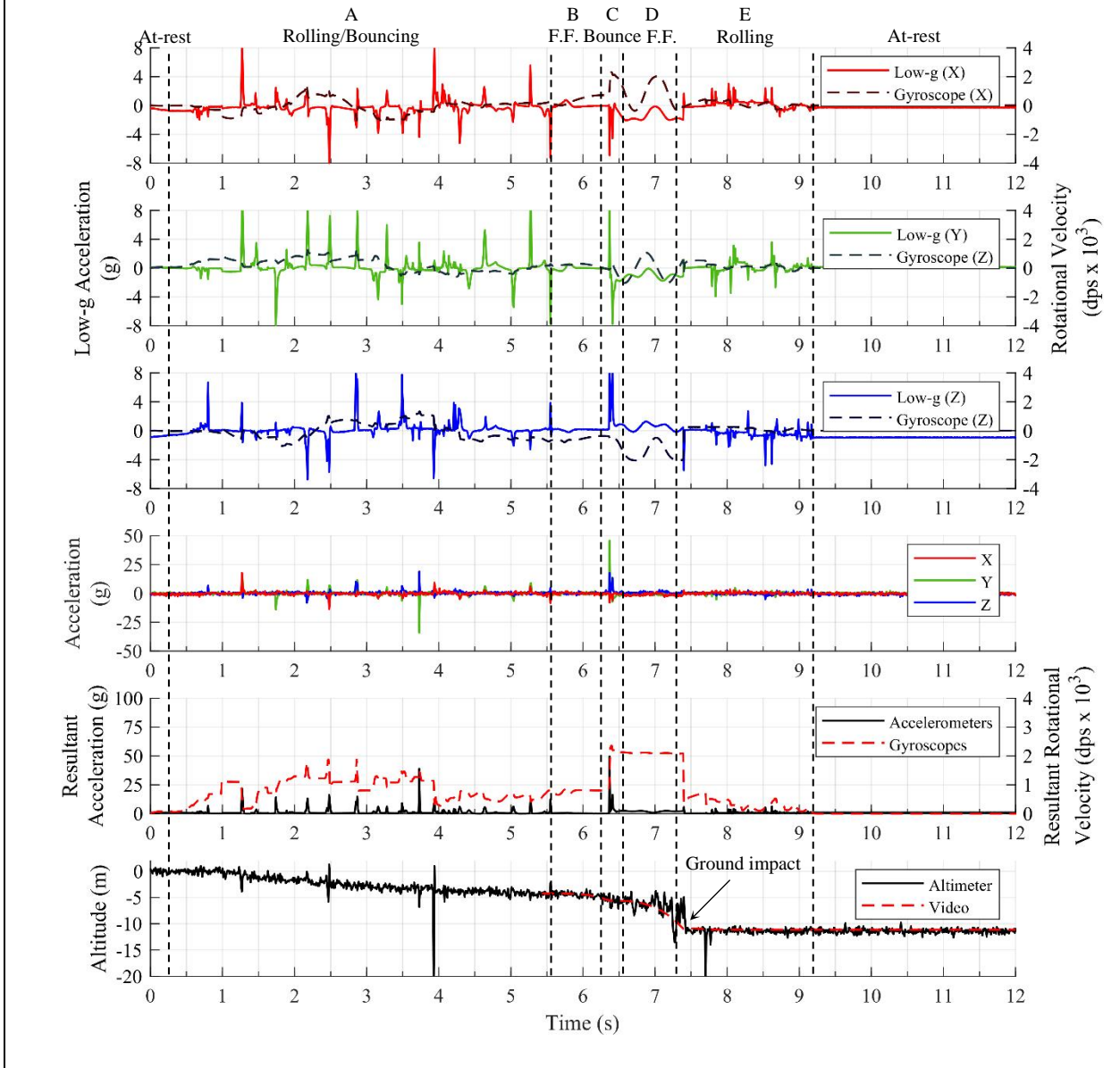
tracking is not feasible, while recording relevant aspects of rockfall that cannot be obtained through observational methods for model calibrations. The altimeter measurements could be verified with video analysis and are a promising tool for rockfall analyses. However, the recorded signal shows a significant noise level and needs additional digital signal processing to provide reliable estimates on rock position over time. The altimeter data noise increases during rapid movements and upon impacts exceeding the low-g accelerometer limit of 8 g.

As seen in Figure 4.11, rock 2 bounces on a launch feature at the middle of the rock face, and the predominant rockfall behavior for this test consisted of free fall at the rock face and bouncing and rolling after impact on the grass slope.

4.7. Summary

The Smart Rock records data continuously over time at a constant sampling frequency of 100 or 500 Hz, and therefore requires post-processing after all experiments. An analysis script was written in MATLAB in order to process the sensor data in this research. The time intervals relative to rockfall assessments can be easily identified in the sensor signal through high acceleration peaks.

After selecting the time intervals of interest for data analysis, the script calculates relevant aspects from the sensor data, such as resultant acceleration and rotation and maximum impact forces. If applicable, the sensor data can be matched with video measurements in one or two directions. Finally, the SR data are plotted along with additional relevant test information such as rock properties, video measurements, and runout distance. The SR data can be used to readily identify modes of motion experienced by falling blocks, such as free fall, bouncing, rolling, and sliding. Kinetic energy calculations can also be performed using sensor measurements.

5.   EXPERIMENTAL ROCKFALLS

During this experimental campaign, several field rockfall experiments were carried out on ten rock cuts in New Hampshire and one in Vermont, USA. The characteristics of the test sites, including location, geology, slope height and inclination, ditch geometry, and existing road conditions, are shown in Table 5.1.

A total of 83 experiments were conducted with 56 local rocks previously prepared in the laboratory. Each rockfall was performed with one Smart Rock sensor, embedded with a specific axis orientation in the center of gravity of the test block. Two additional tests with multiple SRs were performed in Vermont. The sensors were embedded directly on the e rocks to be scaled. For all tests, the altimeter was enabled and compared to video tracking, and data were recorded at a sampling frequency of 100 Hz (except for one test in Vermont, where the frequency was set at 500 Hz for comparison with the 100 Hz data). Each SR used was securely embedded in the test block using an expandable rubber plug.

As previously detailed in Chapter 4, the raw data for each rockfall test were processed and plotted using MATLAB. Acceleration, rotation, altitude, and video measurements were plotted, and resultant, average, and maximum accelerations and rotational velocities were determined from the sensor data. Relevant test information and block characteristics were also included in the graphs.

The following sections present the experimental field campaign results and selected data outputs for each site. Additional photos and graphs for each slope are included in Appendix B. Access to the site locations (except Dover and Townshend, VT) was provided by the Bureau of Materials and Research of the New Hampshire Department of Transportation.

Table 5.1. Test site information.

| Slope ID, rating | Latitude | Rock formation | Rock type | Drop heights (m) | Slope angle | Catchment ditch | | | Road present? | Protective structure? | Number of tests |
						Type	Geometry	Width (m)			
Dover, NH (preliminary)	N 43.19° W 70.87°	Kittery Formation, Metasandstone	Metamorphic	9.0	50° to 60°	Talus	Flat	-	No	No	4
Danbury, NH (A-rated)	N 43.50° W 71.88°	Kinsman Granodiorite	Igneous	7.5 10.5	70° to 75°	Grass	Flat	2.0	Yes	No	9
Franconia, NH (B-rated)	N 44.21° W 71.68°	Bethlehem Granodiorite / Kinsman Granodiorite / Littleton Formation	Igneous / Igneous / Metamorphic	9.5	25° to 90°	Grass / soil	Inclined / Flat	10.0 / 1.5	Yes	No	12
Franklin, NH (1) (A-rated)	N 43.46° W 71.66°	Rangeley Formation, Metasandstone	Metamorphic	11.5 12.5	45° to 90°	Soil with grass	Flat	1.3	Yes	No	8
Franklin, NH (2) (A-rated)	N 43.50° W 71.68°	Rangeley Formation, Metasandstone	Metamorphic	8.0 10.0	50° to 60°	Soil with vegetation	Trapezoidal	2.5	Yes	No	7
Franklin, NH (3) (A-rated)	N 43.50° W 71.69°	Rangeley Formation, Metasandstone	Metamorphic	18.0	40°	Soil with vegetation	Trapezoidal	3.0	Yes	No	7
Keene, NH (C-rated)	N 42.96° W 72.27°	Ordovician Dome, Granodiorite / Tonalite	Igneous	10.0	70° to 75°	Soil	Flat	-	No	No	8

Table 5.1 (cont.). Test site information.

Slope ID	Latitude	Rock formation	Rock type	Drop heights (m)	Slope angle	Catchment ditch		Width (m)	Road present?	Protective structure?	Number of tests
						Type	Geometry				
Orange, NH (B-rated)	N 43.63° W 71.98°	Bethlehem Granodiorite / Littleton Formation	Igneous / Metamorphic	9.0	65° to 75°	Soil with vegetation	Flat	5.0	Yes	No	7
Townshend, VT (A-rated)	N 43.05° W 72.70°	Moretown Formation Amphibolite and Greenstone	Metamorphic	18.0 19.0	30° to 80°	Boulders	Inclined downwards, irregular	2.5	Yes	Yes	8
Warner, NH (A-rated)	N 43.29° W 71.84°	Kinsman Granodiorite	Igneous	15.0	70° to 85°	Soil	Flat	3.5 to 5.0	Yes	No	8
Windham, NH (B-rated)	N 42.81° W 71.28°	Merrimack Group, Berwick Formation	Metamorphic	11.0 12.5	60° to 65°	Talus	Trapezoidal	2.0	No	No	7
Total number of tests											85

Table 5.2. Weather conditions at each test site.

Slope location	Test date	Temperature °C	Wind (km/h)	Weather	Slope location	Test date	Temperature °C	Wind (km/h)	Weather
Dover, NH	5/25/2020	12	9	Sunny	Orange, NH	10/16/2020	13	0	Rainy
Danbury, NH	10/16/2020	13	0	Cloudy	Townshend, VT	11/11/2020	20	13	Cloudy
Franklin, NH	7/15/2020	20	13	Sunny	Warner, NH	6/2/2020	21	13	Sunny
Franconia, NH	10/23/2020	19	30	Sunny	Windham, NH	10/29/2020	7	7	Rainy
Keene, NH	6/23/2020	34	22	Sunny					

5.1. Dover, NH

Prior to the start of the experimental campaign, the fourth-generation Smart Rock sensor was evaluated using a 9 m tall metasandstone cut in Dover, NH. These early experiments were performed with the reference rock (Figure 5.1) used by Disenhof (2018), whose properties are presented in Table 5.3. It was evaluated at all slope locations due to its durability and as a "standard" rock for comparison from site to site.
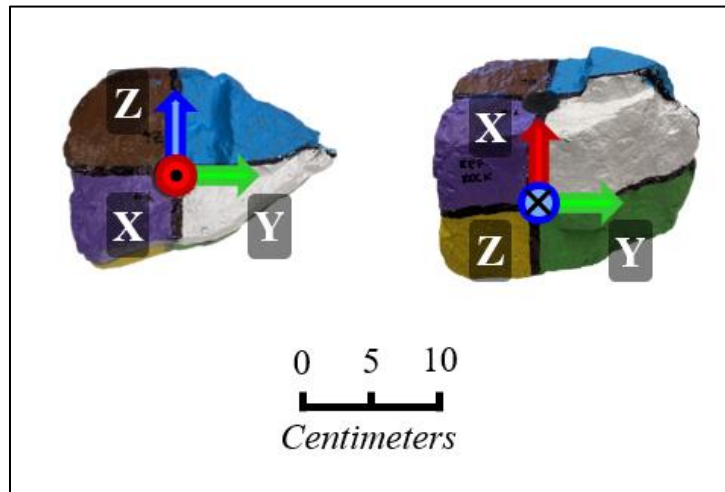
Figure 5.1. 5 kg metamorphic reference rock used by Disenhof (2018). The SR orientation is also indicated.

Table 5.3. Test block characteristics: Dover NH.

| ID | Weight (kg) | | Density (kg/m³) | Dimensions (m) | | | Shape | Mass moment of inertia (kg*m²) | | |
	Before drill.	After drill.		Length, Y	Width, X	Height, Z		I_{XX}	I_{YY}	I_{ZZ}
Ref	-	5.21	2660	0.20	0.12	0.12	Compact Elongated	0.024	0.024	0.013

The rock face has an average inclination between 50º and 60º. As shown in Figure 5.2, the test slope has numerous discontinuities and is severely fractured due to recent blasting activity. The lower portion of the slope is mostly composed of rock talus (fragments) and the adjacent

gravel ground surface. The rock cut did not have a catchment ditch or other rockfall protective structures as it was not located near transportation corridors or infrastructure.

Figure 5.2. The preliminary test site in a recently blasted rock cut in Dover, NH. The white circle shows the test block position in the captured video frame.

Figure 5.3 presents the Smart Rock output for the first test at the Dover site. As previously discussed in Chapter 4, acceleration peaks represent block impacts, typically followed by bouncing, rolling, or sliding motion, and can be identified based on the sensor output signal. The start of the test is represented by the three initiation taps against the top of the rock face, highlighted at approximately 1, 2, and 3 seconds.

The block is then released from the top of the slope. After sliding and rolling from 3.8 to 5 s, the rock bounces until finally stopping on the ground surface. Rock bounces can be identified between 5.3 and 10.5 s, through rapid acceleration peaks exceeding the ± 8 g low-g accelerometer limit, alternated with time intervals with constant resultant rotational velocity. The bouncing behavior was expected due to the slope inclination and surface irregularity/roughness shown in Figure 5.2.

Lower acceleration impacts varied between 5 and 30 g. Three impacts exceeded 50 g and recorded 52, 84, and 105 g, which are equivalent to 3, 4, and 5 kN impacts with the 5.21 kg test block. Due to the significant slope irregularity, the block rotated about X, Y, and Z and did not stabilize rotation over a principal axis. The lowest rotation measured at free fall was equal to 850 dps, and the highest revolution rate recorded was 3100 dps. Overall, it is possible to observe that block rotation increases as the rock falls down the slope. The rotation rate starts to decrease upon impact with the nearly flat ground surface and comes to a complete stop within 2.5 s.

Although the drop height of these experiments was not measured at the site, the video recordings could be verified based on the drop height measured by the SR altimeter. Figure 5.3 demonstrates the existing compatibility between both video and altimeter measurements of vertical displacement over time, despite the altimeter data noise increases upon impact.

Table 5.4 presents the maximum resultant accelerations and maximum and average accelerations experienced by the test block on all four field trials. The maximum accelerations varied between 61 and 402 g, resulting in impact forces between 5 and 21 kN. Also, all maximum rotational velocities were higher than 2400 dps (6.7 rotations per second). As for the previous test, the rock position estimated by both video tracking and sensor altimeter were compatible. Therefore, it was observed that the frontal camera system to track rock displacement was suitable

for subsequent field trials. These preliminary tests demonstrated that all 4th generation Smart Rock sensors were fully operational.
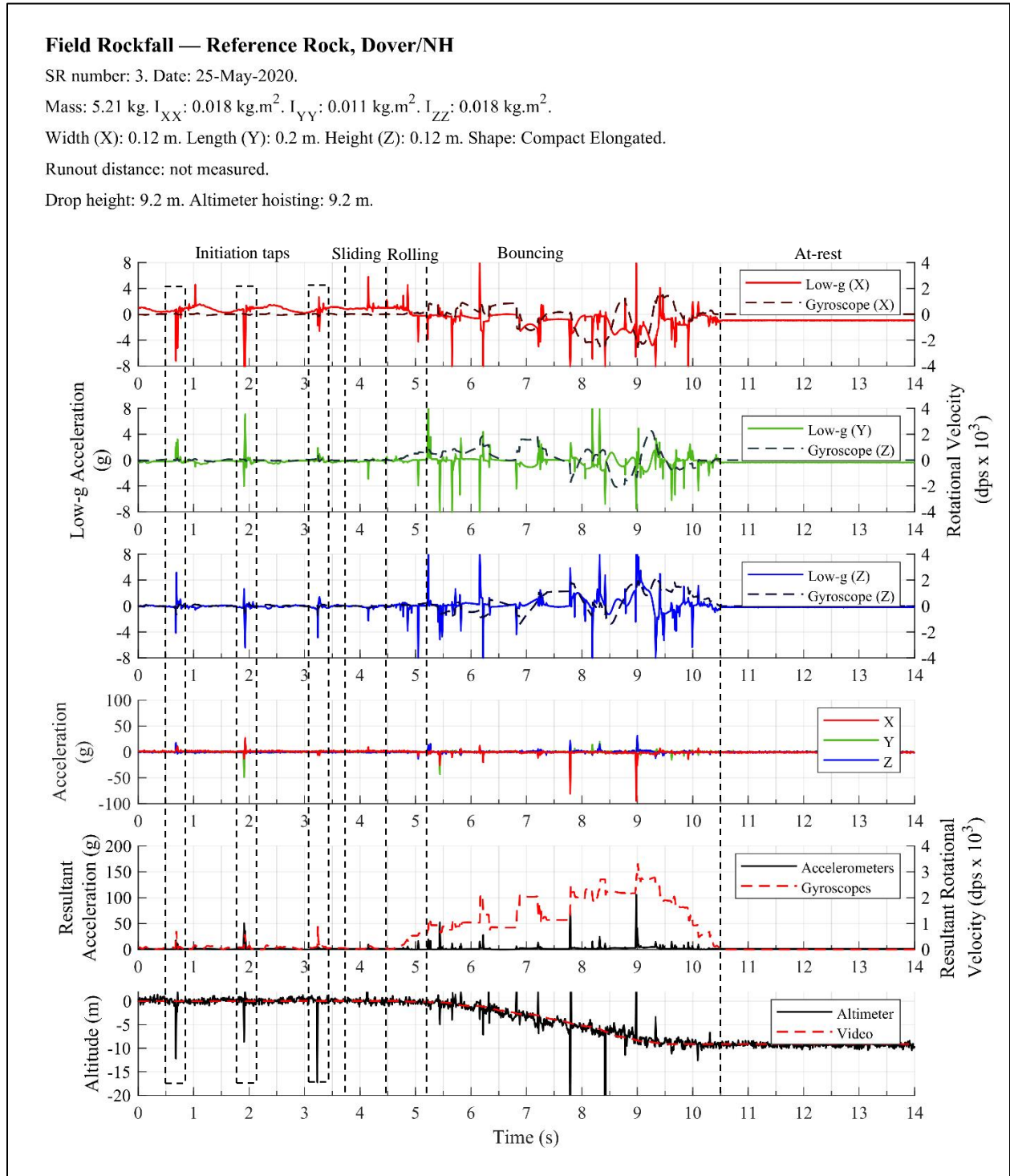
Figure 5.3. Smart Rock test data: reference rock (SR 3), Dover NH.

Table 5.4. Smart Rock data summary: Dover NH.

Rock ID	Smart Rock resultant data			Maximum impact force (kN)
	Maximum acceleration (g)	Maximum rotational velocity (dps)	Average rotational velocity (dps)	
Reference (SR3)	106	3320	1488	5
Reference (SR4)	109	2415	978	6
Reference (SR5)	402*	3578	1131	21
Reference (SR6)	61	3717	1302	2
Average	170	3258	1225	9
Standard deviation	157	585	220	9

* The high-g accelerometer measuring limit was exceeded for the X axis.

5.2. Danbury, NH

Nine experimental rockfalls were conducted on a 10.5 m tall, A-rated granodiorite road rock cut in Danbury, NH. The slope is located along NH Route 4 and formed by a 7.5 m tall rock face, with a 2 m wide flat catchment ditch constructed with soil and covered with vegetation (Figure 5.4a).
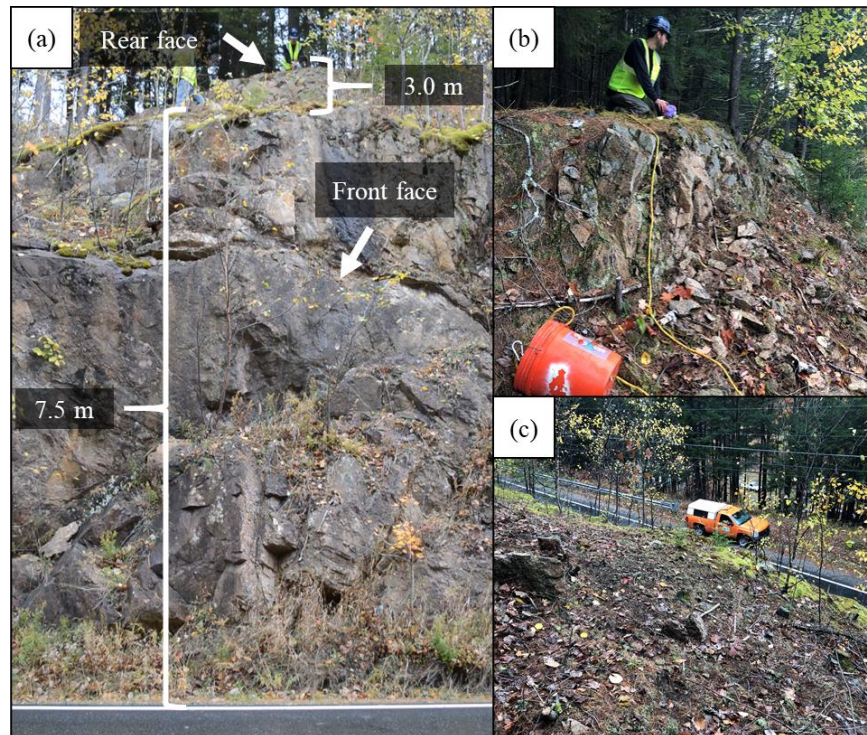
Figure 5.4. Test slope in Danbury NH: (a) front face, (b) rear face, and (c) soil slope covered with vegetation.

An additional 3.0 m tall rock face is above the main slope with a grass slope between both rock faces (Figure 5.4b, c). The 7.5 m tall rock slope has an average inclination between 70º and 75º (Figure 5.5). The proximity of the test slope to the road required traffic control to conduct the tests and video recordings.
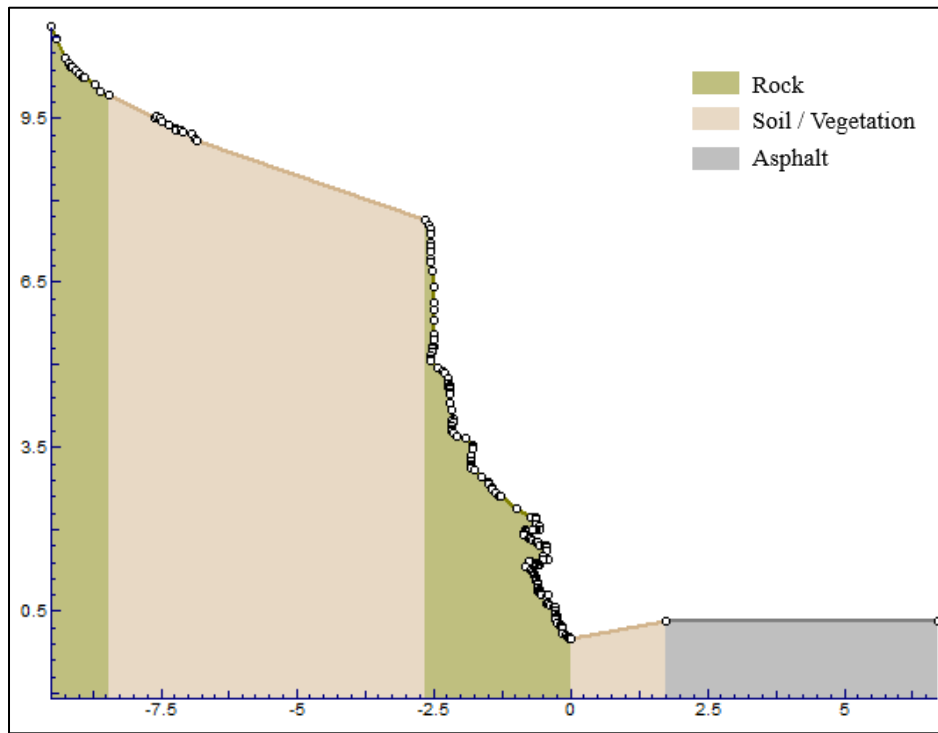
Figure 5.5. Sample cross-section of the test slope in Danbury imported in RocFall. Units in meters.

In addition to the reference rock, three other metasandstone blocks from the Dover slope location (D1, D2, and D3) were also evaluated in Danbury. The characteristics of the test blocks are presented in Table 5.5. The trajectories described by the test blocks are presented in Figure 5.6. Rocks dropped from the taller portion of the slope (rocks 3, D1, D3, and reference) generally showed more significant lateral displacements due to the rolling motion on an inclined plane between the two rock faces. Rock bouncing on the 7.5 m rock face can also be easily identified through abrupt changes in trajectory, which also deviated the rockfall paths laterally.

Table 5.5. Test block characteristics: Danbury NH.

ID	Weight (kg)		Density (kg/m³)	Dimensions (m)			Shape	Mass moment of inertia (kg*m²)		
	Before drill.	After drill.		Length, Y	Width, X	Height, Z		I_{XX}	I_{YY}	I_{ZZ}
Ref	-	5.21	2660	0.20	0.12	0.12	Compact Elongated	0.024	0.024	0.013
1	13.85	13.73	2690*	0.37	0.13	0.17	Elongated	0.152	0.040	0.144
2	7.38	7.22	2690	0.22	0.25	0.07	Platy	0.036	0.029	0.056
3	12.23	12.11	2690*	0.28	0.22	0.10	Bladed	0.081	0.049	0.101
4	4.48	4.35	2690*	0.29	0.10	0.09	Elongated	0.025	0.007	0.022
5	3.58	3.47	2690*	0.22	0.10	0.10	Elongated	0.013	0.006	0.015
D1	4.09	3.972	2990	0.20	0.11	0.13	Compact Elongated	0.011	0.007	0.011
D2	3.65	3.52	3020	0.10	0.18	0.13	Compact	0.006	0.012	0.012
D3	12.37	12.16	3070	0.23	0.22	0.15	Compact Platy	0.065	0.051	0.077

* Estimated density, rock cores were too small and/or fractured after drilling.
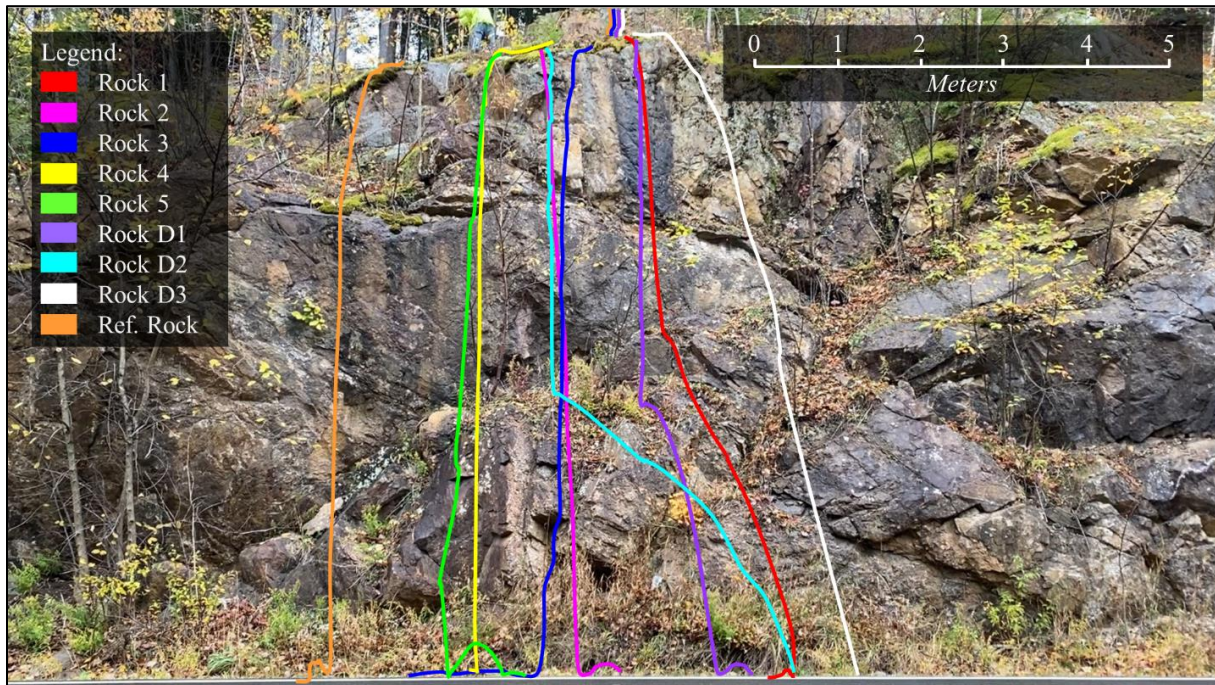
Figure 5.6. Rockfall trajectories: Danbury NH.

Figures 5.7 and 5.8 present the trajectory and SR data output, respectively, for the reference

rock at the Danbury site. It was released from the upper slope, 10.5 m tall, from where it alternated

Reference rock, Danbury NH

A: Rolling
Bouncing

B: Free fall

C: Bounce

D: Free fall

E: Rolling

0 5 10
Centimeters

0 1
Meter
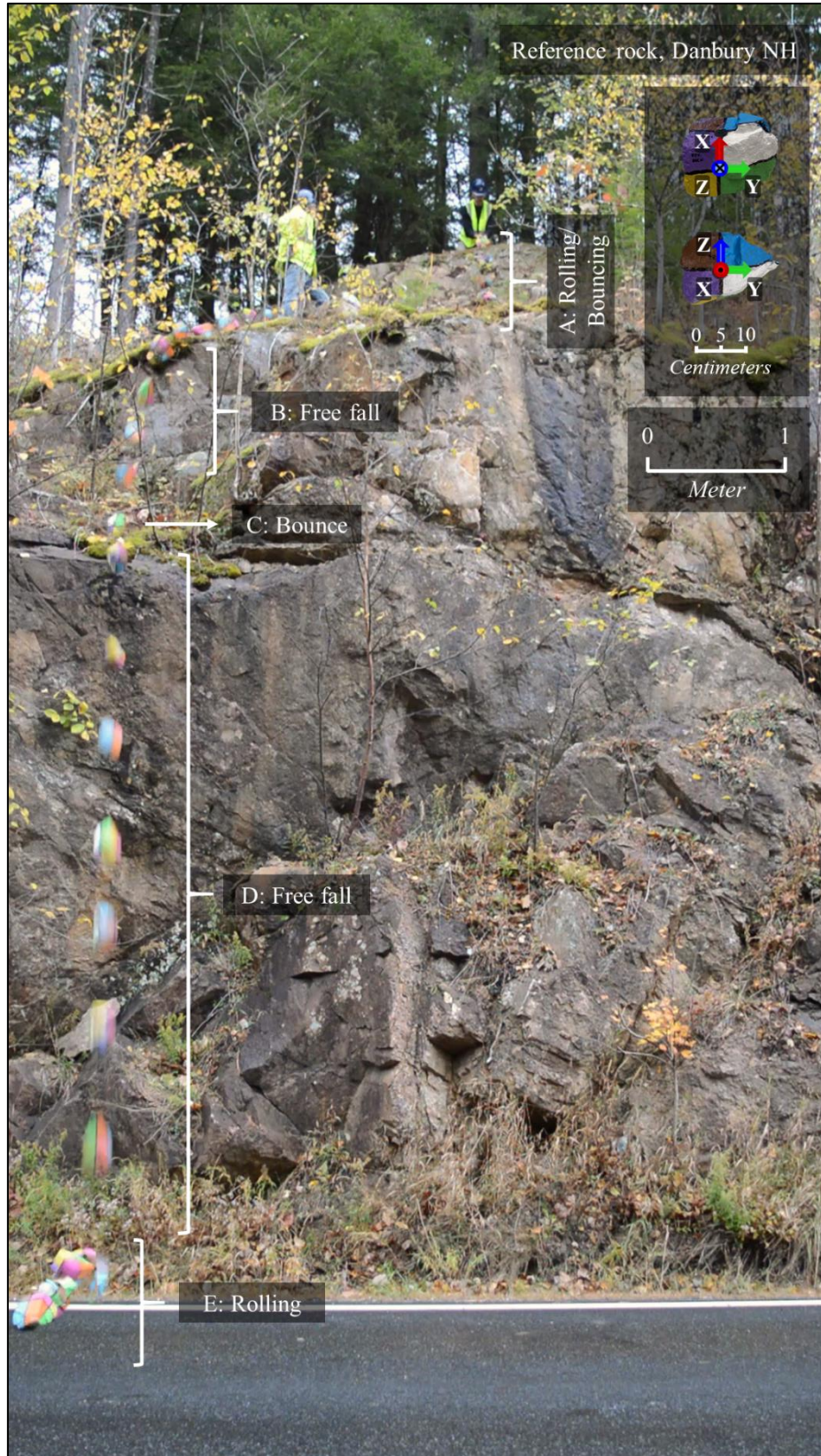
Figure 5.7. Rockfall trajectory: reference rock, Danbury NH.

125

Figure 5.8. Rockfall trajectory: reference rock, Danbury NH.

between bouncing (acceleration peaks between 5 and 40 g) and rolling until reaching the front rock

face at 5.5 s (A). The rock initially experienced an average rotation of 1000 dps until 4 s, with no

predominant revolution about a single axis while moving towards the front face in a straight line. This rotation rate decreased to approximately 600 dps with significant rotation about X between 4 and 5.5 s, when the block started to move laterally towards the left portion of the 7.5 m rock face.

The reference rock went into free fall while revolving about X and Y (axes of highest inertia) between 5.6 and 7.4 s. The rotation rate increased from 800 dps (B) to 2120 dps (D) after bouncing from about 5.3 m from the ground surface (C). The highest impact force (3 kN for 50 g) occurred while bouncing on the rock face at C. A significantly lower acceleration of 5 g and force magnitude of 0.3 kN was measured upon impact with the catchment ditch at the ground surface, formed by soil covered with vegetation.

A predominantly rolling motion was observed after the initial impact with the catchment ditch. The rock rolled towards the road (E) at approximately 700 dps with major rotation about Y (longest axis, shortest inertia). The reference rock came to a complete stop 1.2 m beyond the road shoulder, with a runout distance of 3.2 m from the toe of the slope. Therefore, the existing catchment ditch was not effective during this experimental trial and could have posed a significant hazard to motorists during actual rockfall conditions.

A second test, performed with rock 5, is presented in Figures 5.9 and 5.10. Released from a 7.5 m drop height, the 3.6 kg block initially rolled towards the rock face (A) and experienced free fall (B, C, D) until impacting the bottom of the rock face at 3 s (E).

Two visible increases in the rotation occurred at C after impacts with tree branches adjacent to the rock face. The block initially fell at 270 dps (0.75 rotation/second) for 0.8 s. The rotation rate increased to 2100 and 2300 dps after the first and second impact, respectively, representing an approximate increase in rotation of 800%. Although the block initially rotated mostly about its

highest axes of inertia (Z and X), rock 5 progressively started to revolve about its axis of shortest

inertia, Y (largest dimension).
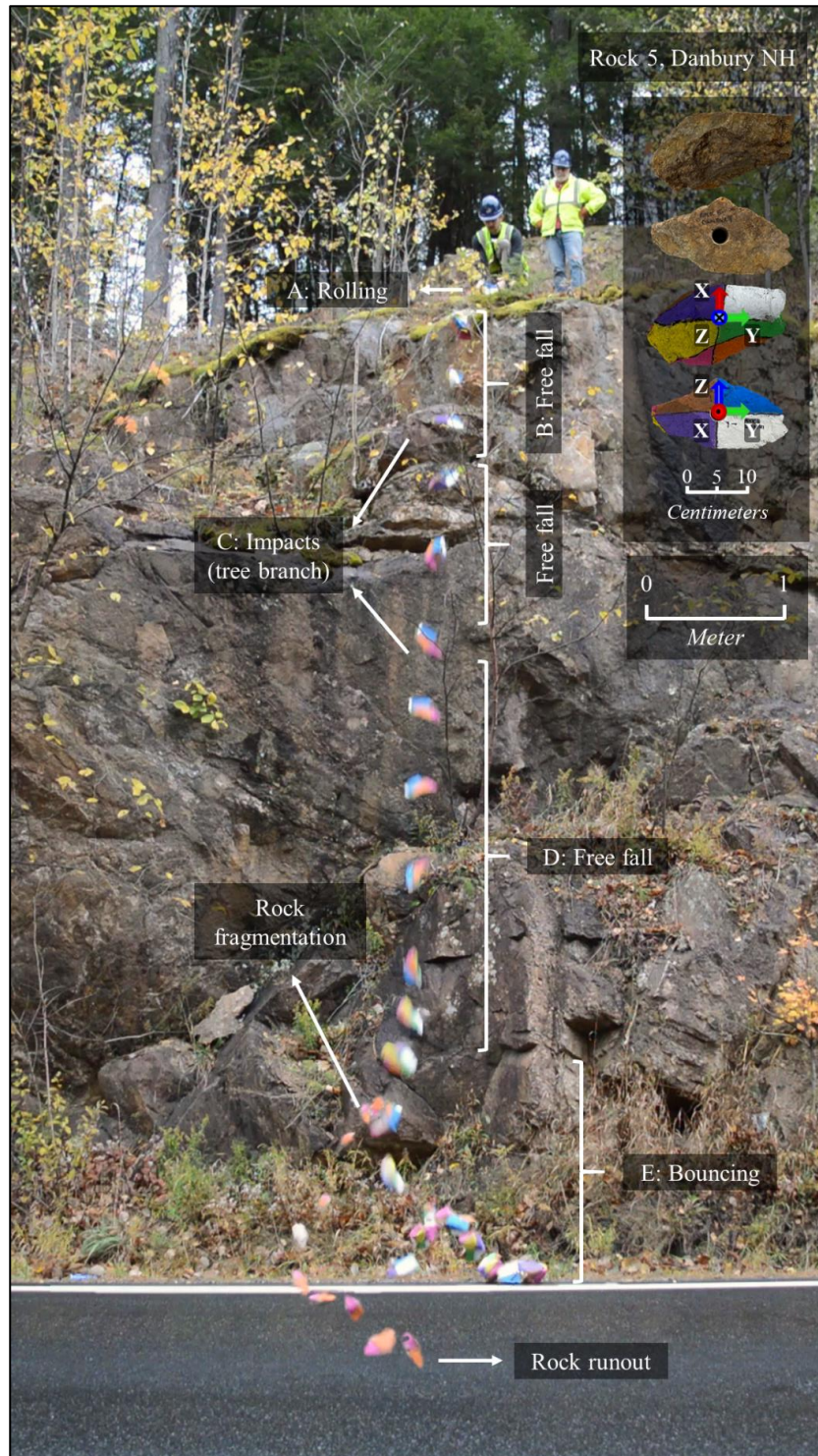
Figure 5.9. Rockfall trajectory: rock 5, Danbury NH.
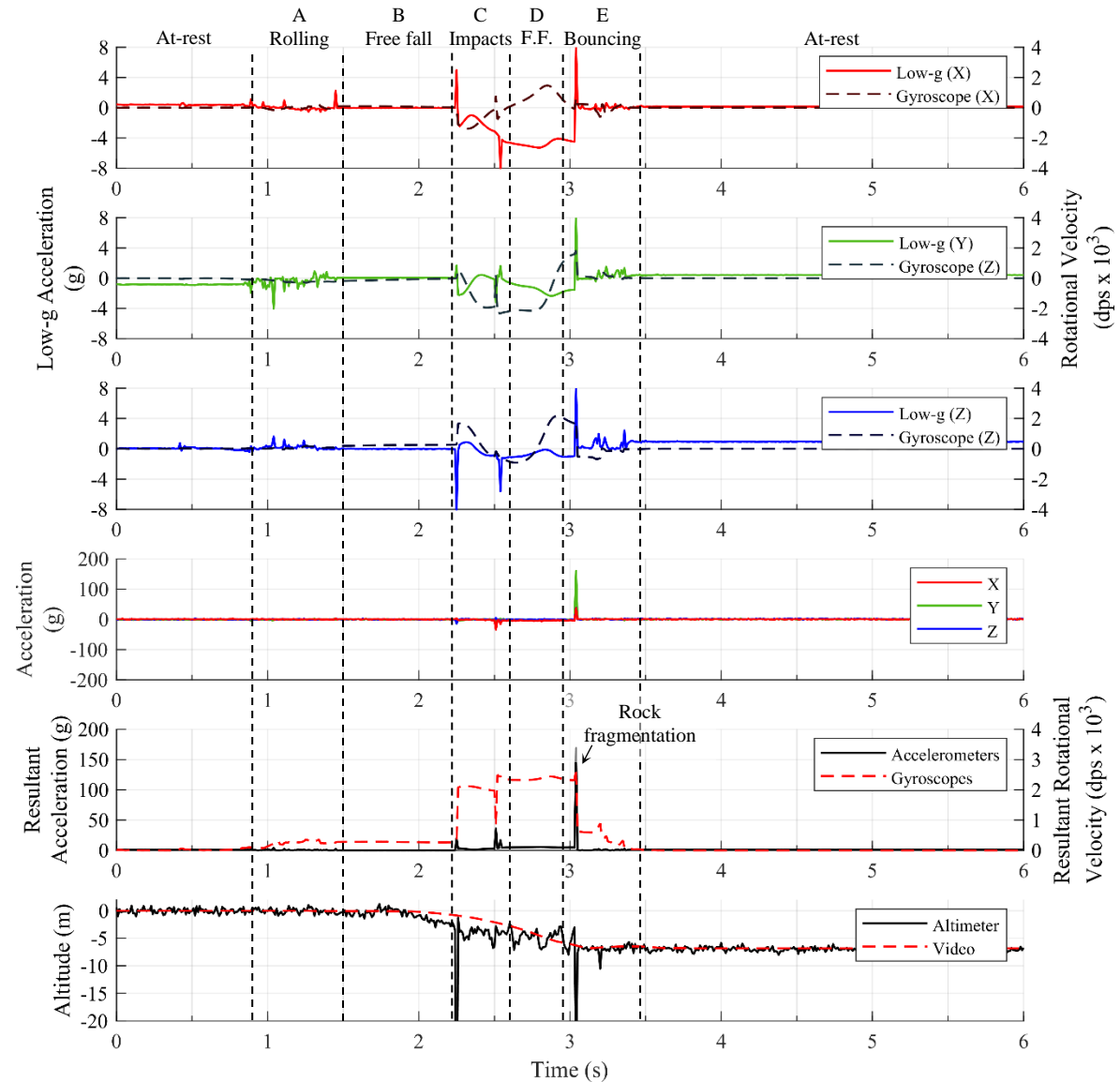
Figure 5.10. Smart Rock test data: rock 5, Danbury NH.

As observed in the previous test, the highest accelerations experienced by the test block

(20 g, 36 g, 169 g, progressively increasing with downward movement) occurred upon impacts

129

with the rock face, rather than the ground surface covered by vegetation. Although lighter than the reference rock, the most significant impact force experienced by rock 5 at D was two times the highest impact force felt by the reference block. Figure 5.9 shows that the rock fragmented upon its first impact at D. Although the largest portion of the test block stopped at the edge of the pavement, the smaller rock fragment bounced towards the road and stopped 2.1 m away from the road shoulder (4.1 m runout distance).

A third test is presented in Figures 5.11 and 5.12. Rock 1 is a 14 kg elongated block that showed similar rockfall motion but stopped within the catchment ditch limits. Following an initial rolling motion (A), rock 1 falls freely (B) parallel to the 7.5 m rock face at 340 dps, strictly about its X axis (highest inertia). After a 76 g impact with the slope face (C), major rotation occurs about its shortest axis of inertia (Y), at about 1200 dps resultant rotational velocity (D). Peak acceleration of 107 g was measured upon impact with the edge of the pavement (E), from where it bounced towards the rock face and stopped within the catchment ditch limits (0.9 m runout).

The video tracking measurements were compatible with the altimeter data despite its inherent noise, especially during free fall and rock bouncing. A summary of the results obtained at the Danbury site is presented in Table 5.6. It can be observed that, for an average slope angle between 70 and 75º, the test rocks experienced an average maximum resultant acceleration of 84 g, during impacts with the rock face or pavement. Except for the heaviest block (rock 1), all impact forces were inferior to 10 kN. Impact forces upon granular material covered by vegetation were significantly smaller than on stiffer surfaces such as rock and asphalt. This behavior was expected as the damping effect on soil and vegetation promote higher plastic ground deformation and energy absorption. The detailed trajectories and data output for the remaining tests presented in the table are provided in Appendix B.2.
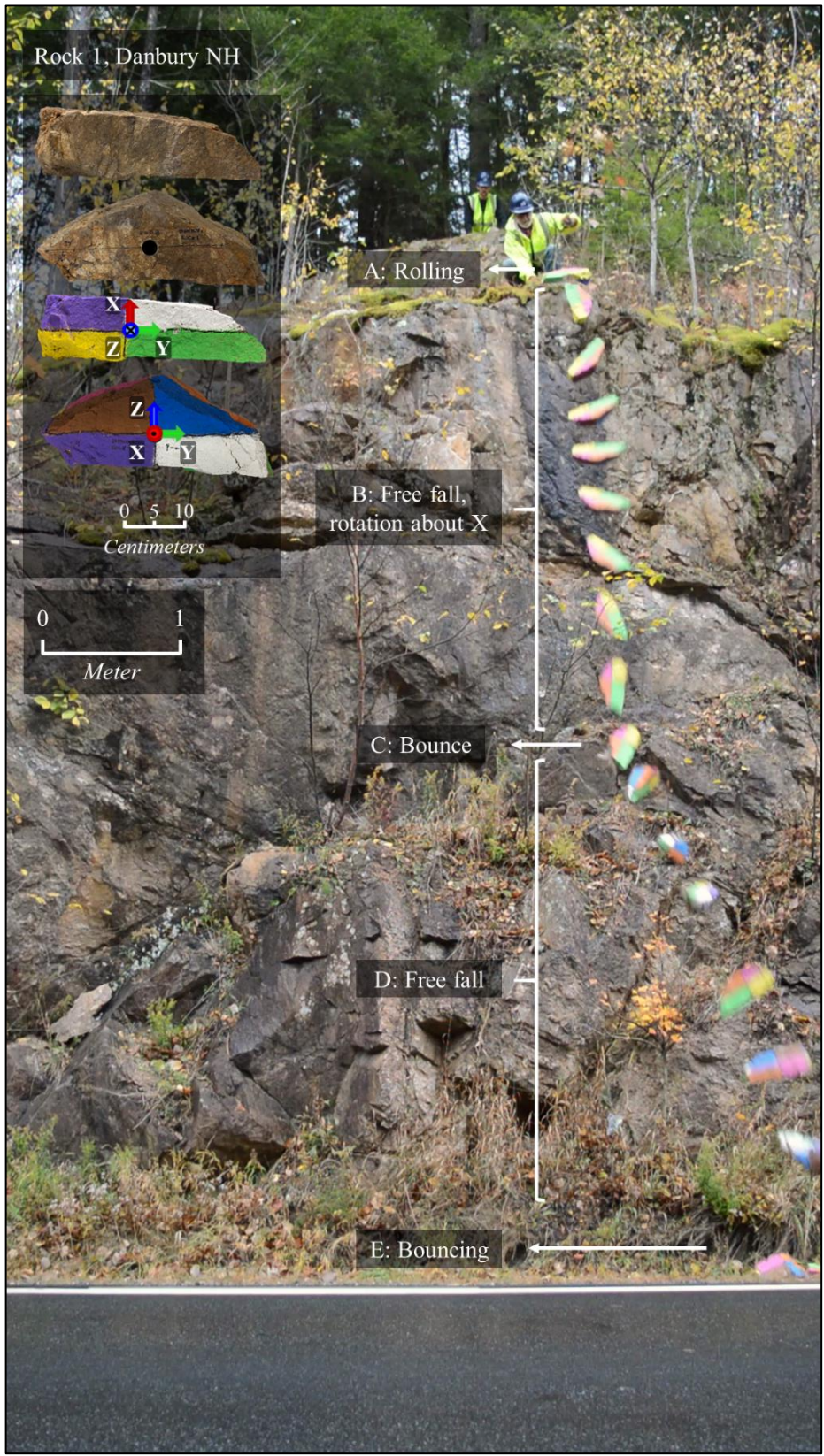
Figure 5.11. Rockfall trajectory: rock 1, Danbury NH.

Field Rockfall — Rock 1, Danbury/NH

SR number: 1. Date: 16-Oct-2020.

Mass: 13.85 kg. I_{XX}: 0.152 kg.m^2. I_{YY}: 0.04 kg.m^2. I_{ZZ}: 0.144 kg.m^2.

Width (X): 0.13 m. Length (Y): 0.37 m. Height (Z): 0.17 m. Shape: Elongated.

Runout distance: 0.9 m from slope toe.

Drop height: 7.3 m. Altimeter hoisting: 10.7 m.
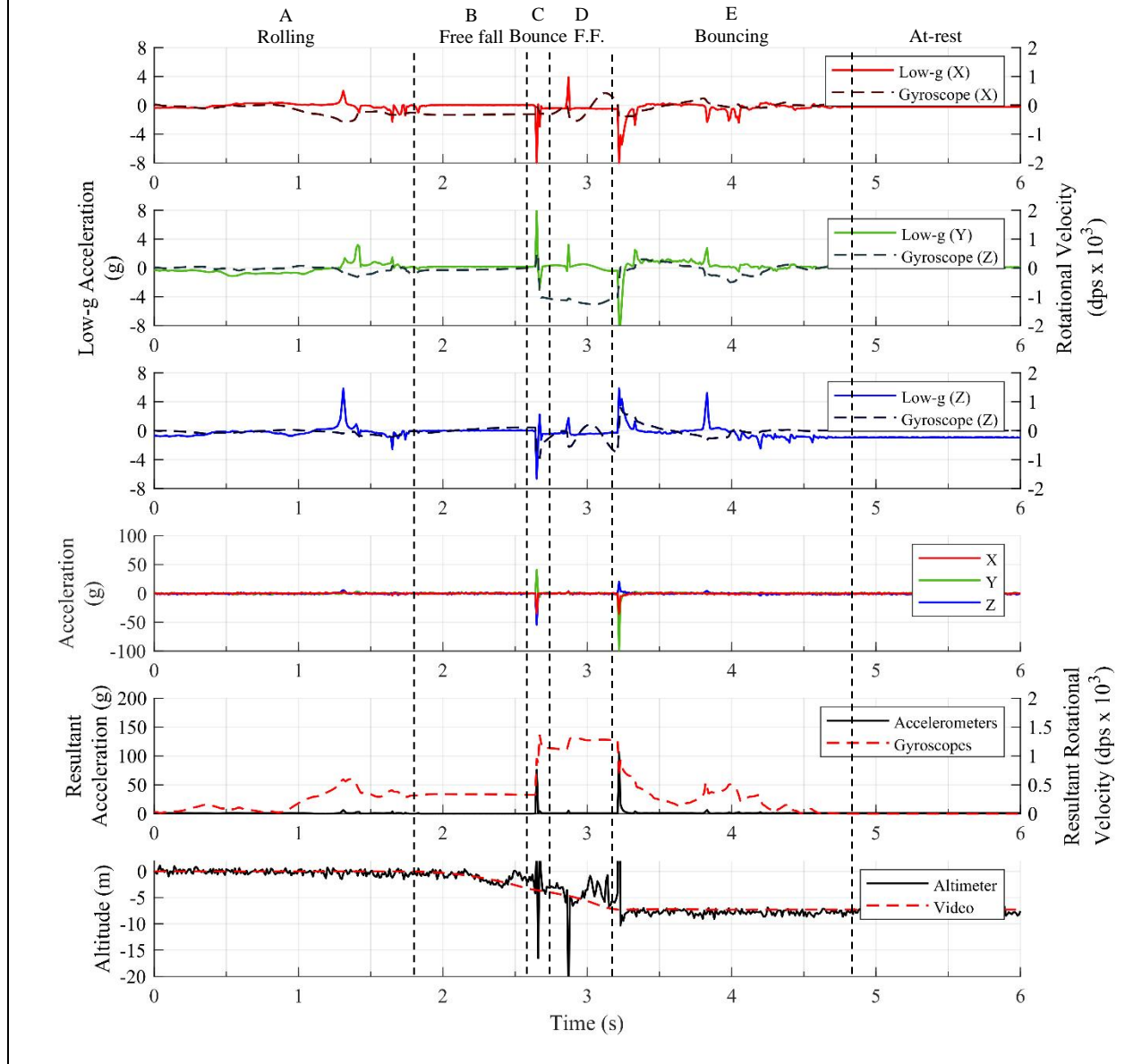
Figure 5.12. Smart Rock test data: rock 1, Danbury NH.

Due to the steep angle of the rock face, free fall was the predominant rockfall motion during these field tests. All test blocks (regardless of trajectory start point) originally showed constant

132

Table 5.6. Field rockfall summary: Danbury NH.

Rock ID	Slope angle	Drop height (m)	Displacements			Smart Rock resultant data			Maximum impact force (kN)
			Lateral (m)	Lateral dispersion (%)	Runout from toe (m)	Maximum acceleration (g)	Maximum rotational velocity (dps)	Average rotational velocity (dps)	
Ref	75°	10.6	-3.1	20	3.2	50	2362	900	3
1	70°	7.3	1.6	10	0.9	107	1370	451	15
2	75°	7.3	0.9	12	1.0	111	1721	617	8
3	75°	10.6	-0.2	1	1.0	69	3975	862	8
4	75°	7.3	-0.9	12	1.2	53	2632	602	2
5	75°	7.3	0.3	4	4.1	169	2713	905	6
D1	70°	10.6	-1.8	11	0.9	99	3086	875	4
D2	75°	7.3	2.8	38	1.8	49	4925*	1260	2
D3	70°	10.6	2.2	14	0.3	51	1769	812	6
		Average	1.5	14	1.6	84	2728	809	6
	Standard deviation		1.9	11	1.2	41	1142	233	4

* The gyroscope measuring limit was exceeded for the Y axis.

rotational velocities under 1000 dps before the first impact during free fall, generally about their highest axes of inertia. The rotation rate tends to increase with subsequent bounces. The SR recorded an average maximum resultant rotation of 2728 dps, which occurred immediately after bounces and impacts while on free fall parallel to the rock face.

The Danbury tests had an average lateral dispersion of 1.5 m, or 14% of the slope length. Rock bouncing against the rock face has significantly increased lateral displacement of blocks, especially at resultant rotational velocities higher than 3000 dps. The runout distances presented in the table are summarized in a histogram in Figure 5.13. It is possible to observe that, although seven rocks stopped within the catchment ditch limits, two blocks reached the road and would undoubtedly pose a risk of hazard to motorists. Therefore, the catchment ditch in Danbury was not fully adequate to prevent rockfall runout.
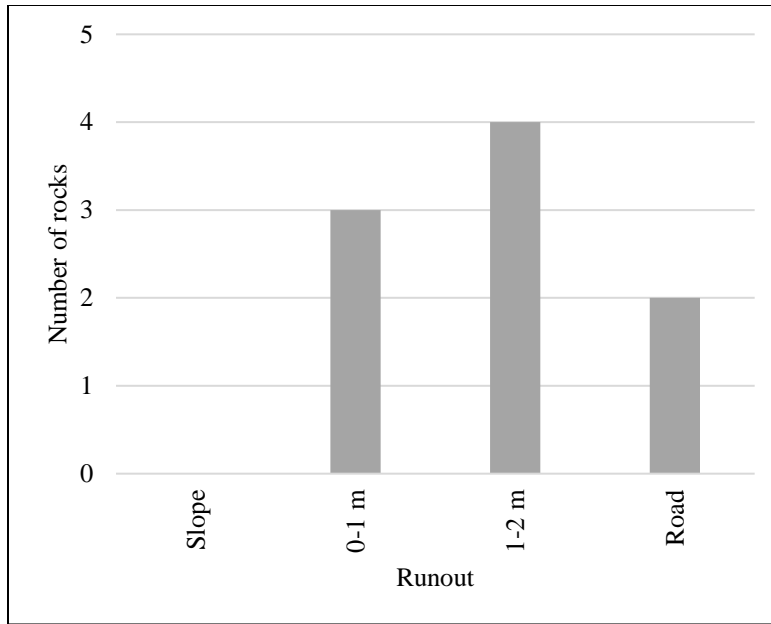
Figure 5.13. Runout histogram: Danbury NH.

5.3. Franconia, NH

Twelve experimental rockfalls were conducted on a 9.5 m tall, B-rated road rock cut in Franconia, NH along NH Route 3. The slope is formed by a roughly 4 m tall granodiorite rock face 11 m away from the road, followed by an additional 5.5 m tall, 10 m wide consisting grassy slope with inclinations between 25º and 30º. The road cut has a flat, 1.5 m wide catchment ditch constructed with soil and covered with grass between the grassy slope and the road shoulder. The proximity of the test slope to the road required traffic control to conduct the tests safely.

The test rocks were retrieved from two slope locations in Franconia. Besides the test slope previously described, rockfall tests were also going to be performed at another road rock cut nearby (N 44.1798º, W 71.6910º, Figure 5.14) of similar geological composition. However, the slope access conditions did not allow the tests to be conducted safely. For this reason, the test blocks from both locations were evaluated on the rock and grass slope along Route 3.

Figure 5.14. Road cut with low safety conditions to conduct rockfall tests in Franconia NH.

The road cut where the tests could not be performed was denominated "slope 1", and the slope where the tests were conducted was named "slope 2". A sample cross-section from slope 2 is presented in Figure 5.15. The test block characteristics and their respective site locations are presented in Table 5.7.
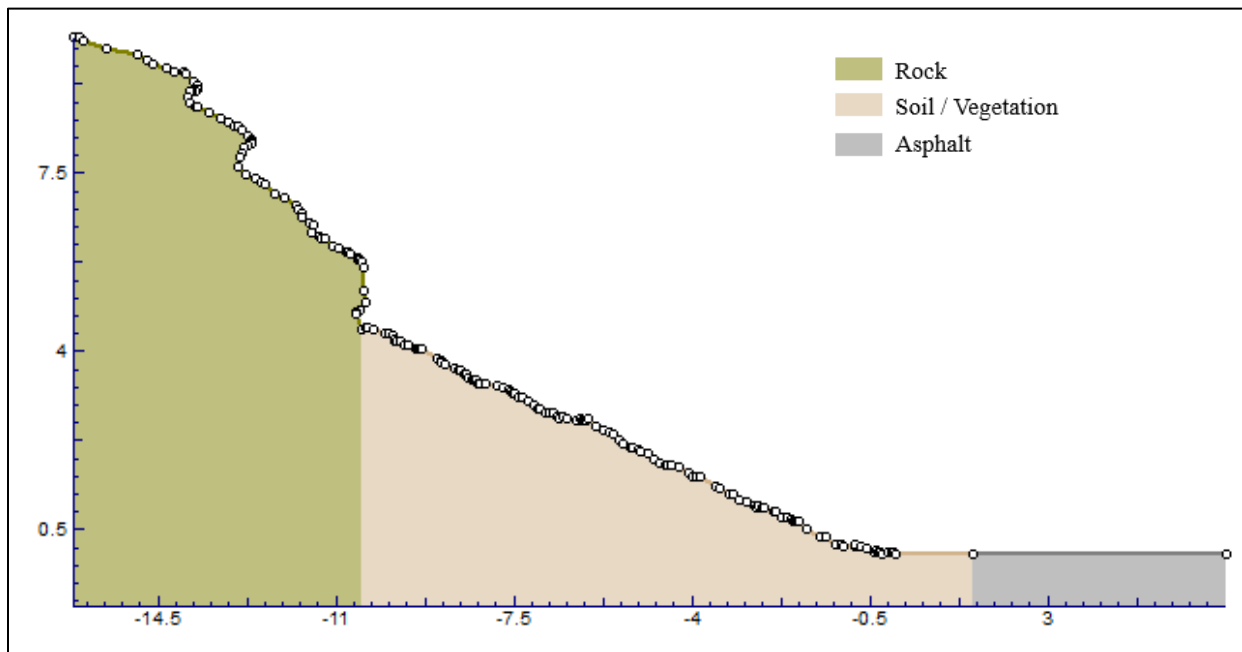
Figure 5.15. Sample cross-section of the test slope in Franconia imported in RocFall. Units in meters.

135

Table 5.7. Test block characteristics: Franconia NH.

ID	Weight (kg)		Density (kg/m³)	Dimensions (m)			Shape	Mass moment of inertia (kg*m²)		
	Before drill.	After drill.		Length, Y	Width, X	Height, Z		I_{XX}	I_{YY}	I_{ZZ}
Ref	-	5.21	2660	0.20	0.12	0.12	Compact Elongated	0.024	0.024	0.013
1-2	10.41	10.30	2610	0.40	0.15	0.08	Very Elongated	0.113	0.024	0.119
1-3	3.75	3.64	2600	0.18	0.10	0.14	Compact	0.009	0.007	0.013
1-4	4.18	4.08	2600*	0.20	0.10	0.10	Elongated	0.013	0.007	0.015
1-6	6.95	6.77	2610	0.29	0.19	0.07	Very Bladed	0.049	0.018	0.062
1-7	9.01	8.90	2600*	0.34	0.10	0.20	Compact Elongated	0.081	0.022	0.069
1-9	27.27	27.16	2600*	0.42	0.25	0.18	Elongated	0.416	0.153	0.369
1-10	9.38	9.26	2600*	0.32	0.34	0.08	Very Platy	0.026	0.041	0.062
2-2	7.37	7.51	2700*	0.23	0.18	0.19	Compact	0.034	0.021	0.032
2-3	9.14	9.13	2690	0.28	0.24	0.08	Very Platy	0.039	0.034	0.063
2-5	4.88	4.74	2750	0.12	0.15	0.11	Compact	0.014	0.013	0.015
2-6	5.50	5.38	2710	0.24	0.20	0.09	Platy	0.019	0.015	0.029

* Estimated density, rock cores were too small and/or fractured after drilling.

1- slope 1; 2- slope 2.

Except for one test (rock 6, slope 1), all experimental rockfalls were successfully recorded with the SR. The trajectories described by the test blocks are presented in Figure 5.16. Although most of the blocks stopped on the grassy slope, 3 of the 12 tests reached the catchment ditch limits, and one rock stopped adjacent to the road shoulder.

Two pairs of modes of motion were generally observed. After an initial rolling motion on the rock face, the rocks free fell and frequently bounced. On the grassy slope, the rocks have predominantly bounced and rolled. The following test information describes the measured Smart Rock output for these field experiments.
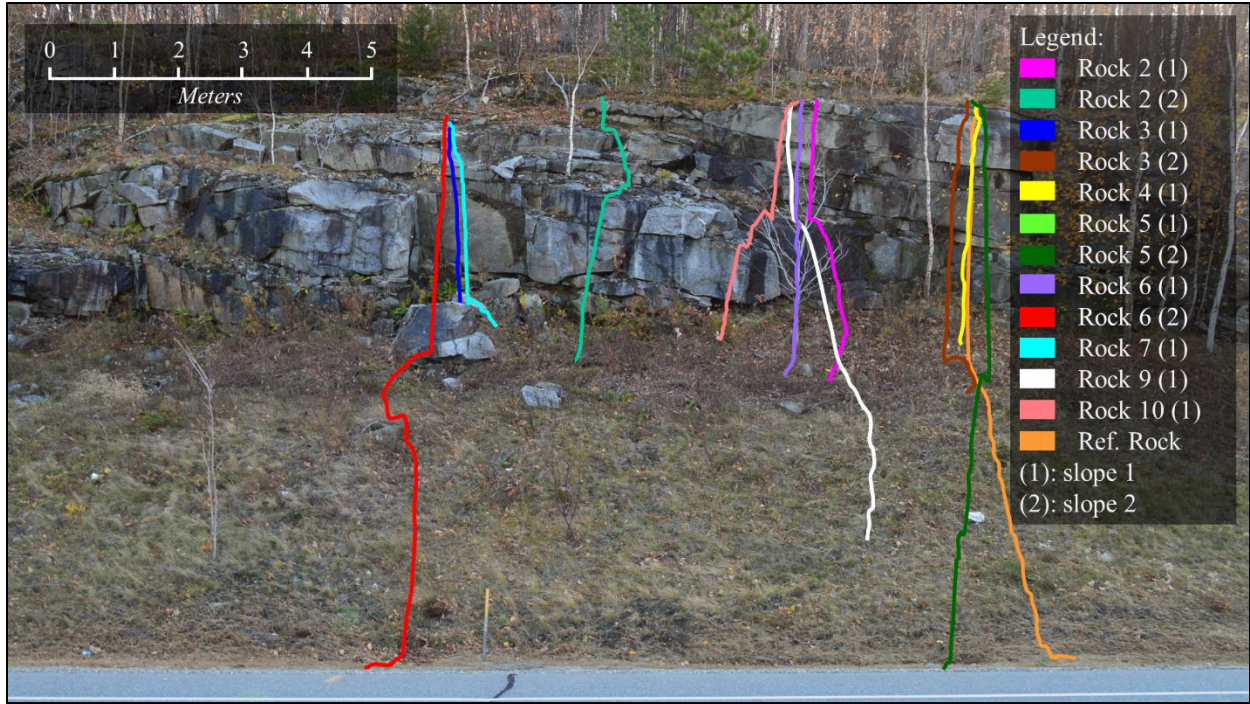
Figure 5.16. Rockfall trajectories: Franconia NH.

Figures 5.17 and 5.18 present the trajectory and sensor output for the reference rock,
released 9.6 m from the ground surface. After rolling at the top of the rock face (A), the block
bounced on rock (B) and fell freely for 1 s (C) at 850 dps before impacting the grass slope with 73
g at 2.5 s (D). The initial rotation predominantly occurs about the highest axes of inertia (X and
Z), and the rotational velocity about Y gradually increases with vertical displacement. The peak
acceleration of 255 g experienced by the test rock resulted in a 13 kN impact force.

As opposed to the Danbury tests, in which block rotation significantly increased during fall
and decreased upon impact with the catchment ditch, the rotation rate of the reference block at
Franconia increased after the first bounce on the grass slope. Block rotation increased on average
to 2220 dps, and gradually decreased while rolling and bouncing for 4 s until the block reached
the catchment ditch and came to a complete stop (D). The subsequent acceleration peaks between

2.5 and 6 seconds gradually decrease from 73 g to 6 g. The rock stopped 10.0 m away from the

rock face and 1.5 m away from the road.

Figure 5.17. Rockfall trajectory: reference rock, Franconia NH.

Field Rockfall — Reference Rock, Franconia/NH

SR number: 5. Date: 23-Oct-2020.

Mass: 5.21 kg. I_{XX}: 0.018 kg.m^2. I_{YY}: 0.011 kg.m^2. I_{ZZ}: 0.018 kg.m^2.

Width (X): 0.12 m. Length (Y): 0.2 m. Height (Z): 0.12 m. Shape: Compact Elongated.

Runout distance: 1.5 m from road shoulder.

Drop height: 9.6 m. Altimeter hoisting: 10.6 m.
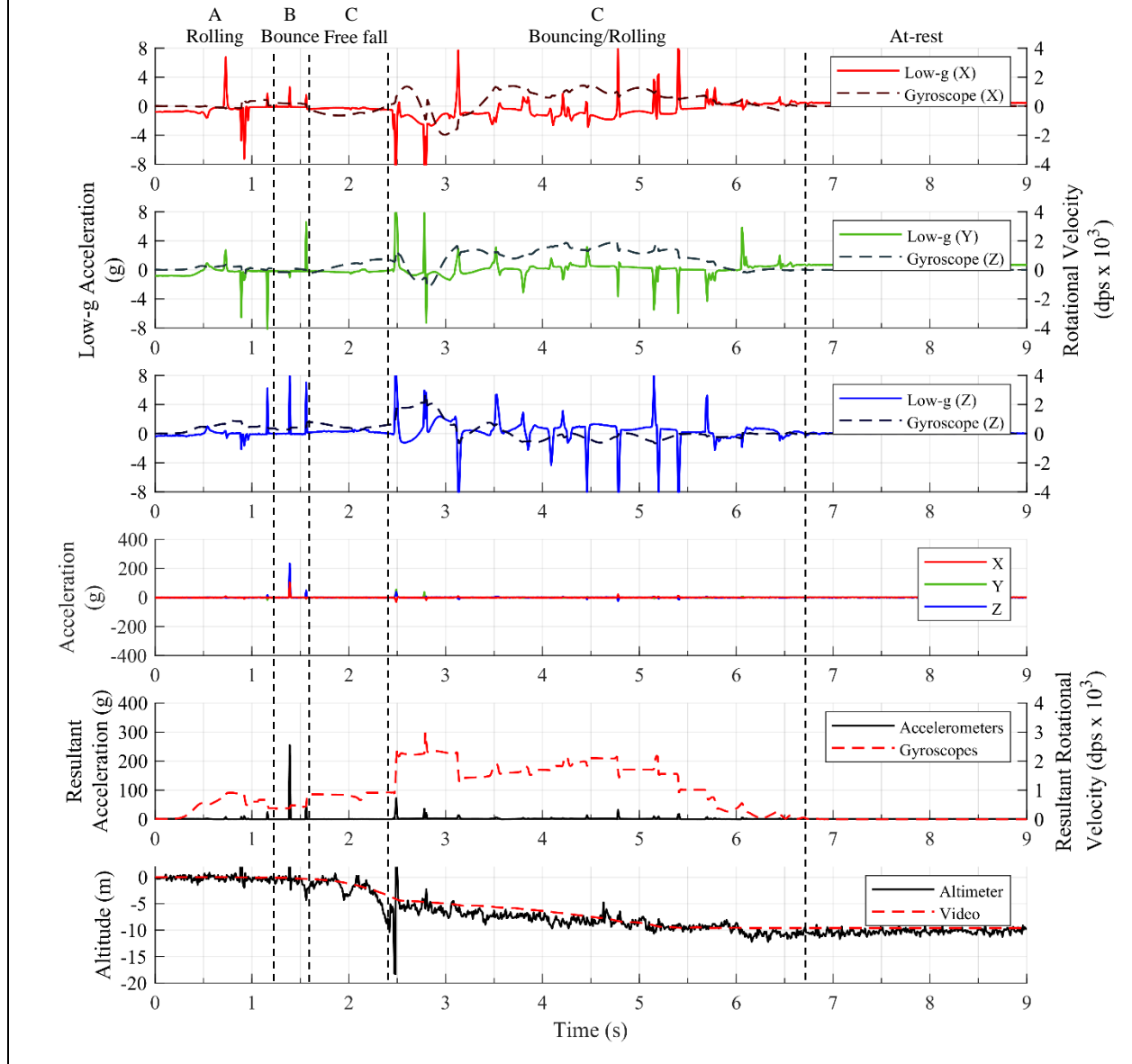
Figure 5.18. Smart Rock test data: reference rock, Franconia NH.

In contrast with the reference rock, the trajectory described by rock 2 (slope 2), a 7.4 kg compact block, is presented in Figure 5.19. The SR output is shown in Figure 5.20. Although both

139
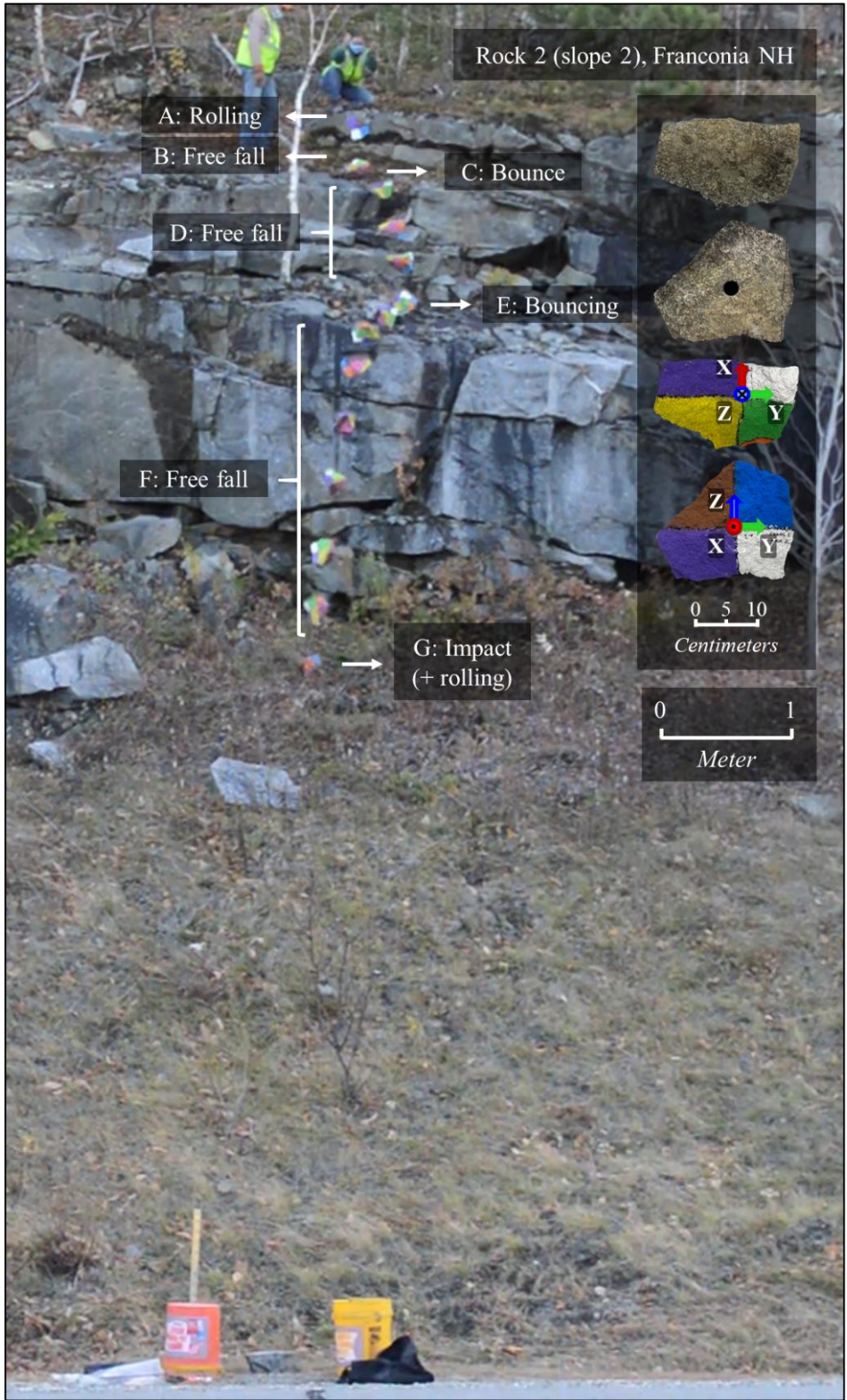
Figure 5.19. Rockfall trajectory: rock 2 (slope 2), Franconia NH.
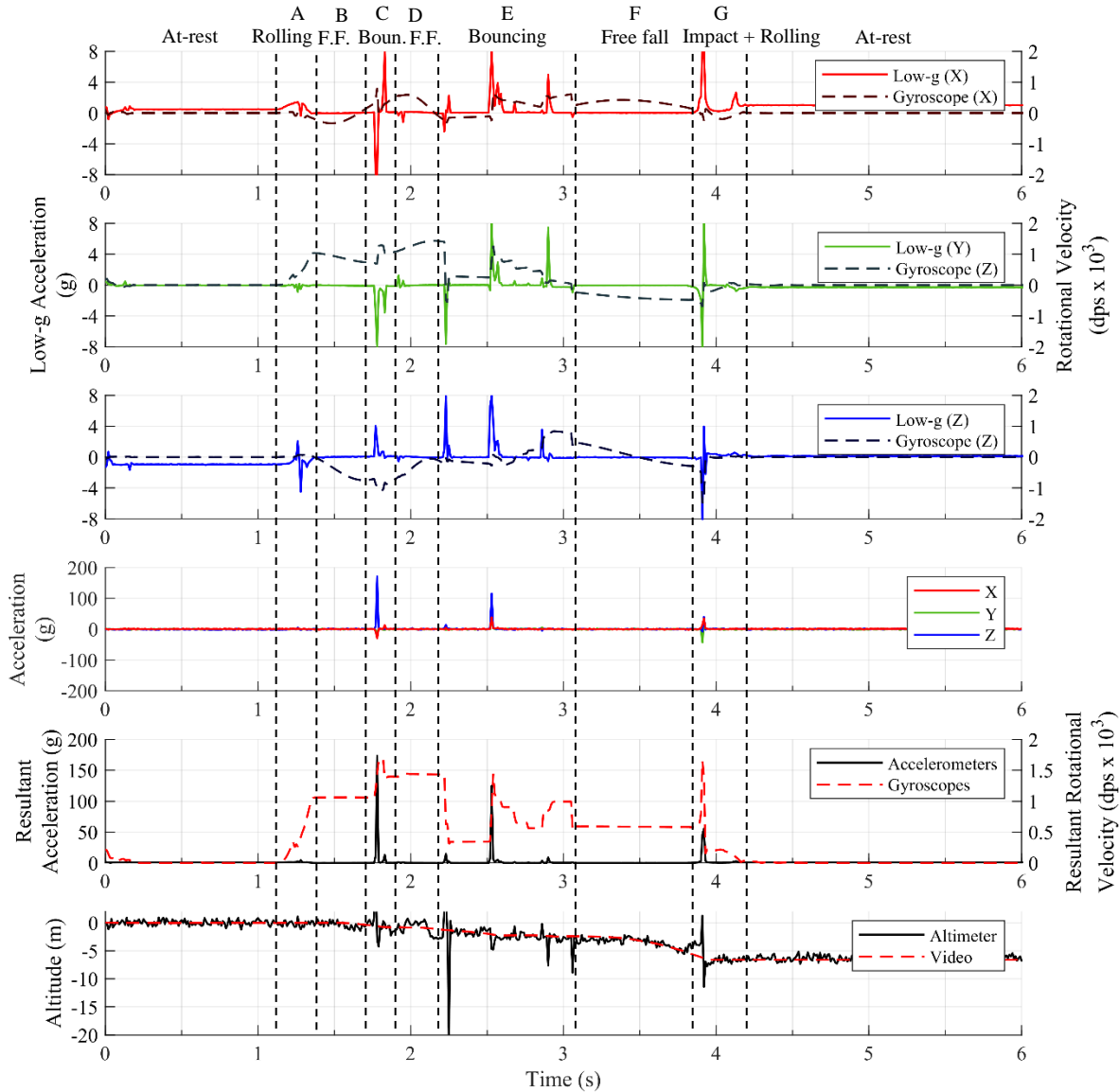
Figure 5.20. Smart Rock test data: rock 2 (slope 2), Franconia NH.

test blocks have similar weights, the runout distance after the impact with vegetation was only 1.8 m from the toe of the slope. Natural slope changes from the top to the middle of the rock face

141

caused rock 2 (slope 2) to bounce four times against the slope, experiencing two peak accelerations of 173 g and 125 g at C and E (converted to impact forces of 13 and 9 kN, respectively). The block rotation initially increased from 1000 dps (B) to 1450 dps (D) after the first bounce but decreased to 340 dps upon impact with a nearly flat discontinuity at the rock face at E. During the free fall motion between B and E, the block predominantly revolved about its lowest axis of inertia (Y).

On the lower half of the slope cross-section, the test rock had a continuous free fall motion while rotating about X, Y, and Z at a resultant rate of 540 dps (F) until bouncing against the grass slope at 3.9 s (G). As opposed to the peak accelerations from rock-on-rock impacts between 1 and 3 s, the SR recorded a 55 g acceleration upon impact with vegetation (4 kN). The test block immediately decelerated in rolling motion and came to a complete stop 0.2 s after the impact on grass.

A third test, conducted with the heaviest block is presented in Figures 5.21 and 5.22. Rock 9, retrieved at slope 1, is a 27.3 kg elongated block that experienced a lower peak impact force than the two previously described rocks despite its significant mass. An intermediary runout distance of 6.3 m from the rock face was observed.

After the initial rolling motion (A), visible through acceleration peaks captured by the low-g accelerometer (lower than 8 g) accompanied by irregular changes in rotation, the rock bounced against the rock face and experienced a peak acceleration of 37 g upon ground contact (10 kN impact at B). Rock 9 predominantly rotated about its shortest axis of inertia (Y) during free fall at 780 dps before ground impact. Y was also the principal axis of rotation during rolling motion on the grassy slope (C). Small divergences between the altimeter and video tracks were observed due to the significant slope depth towards the camera direction due to the 25° grass slope.
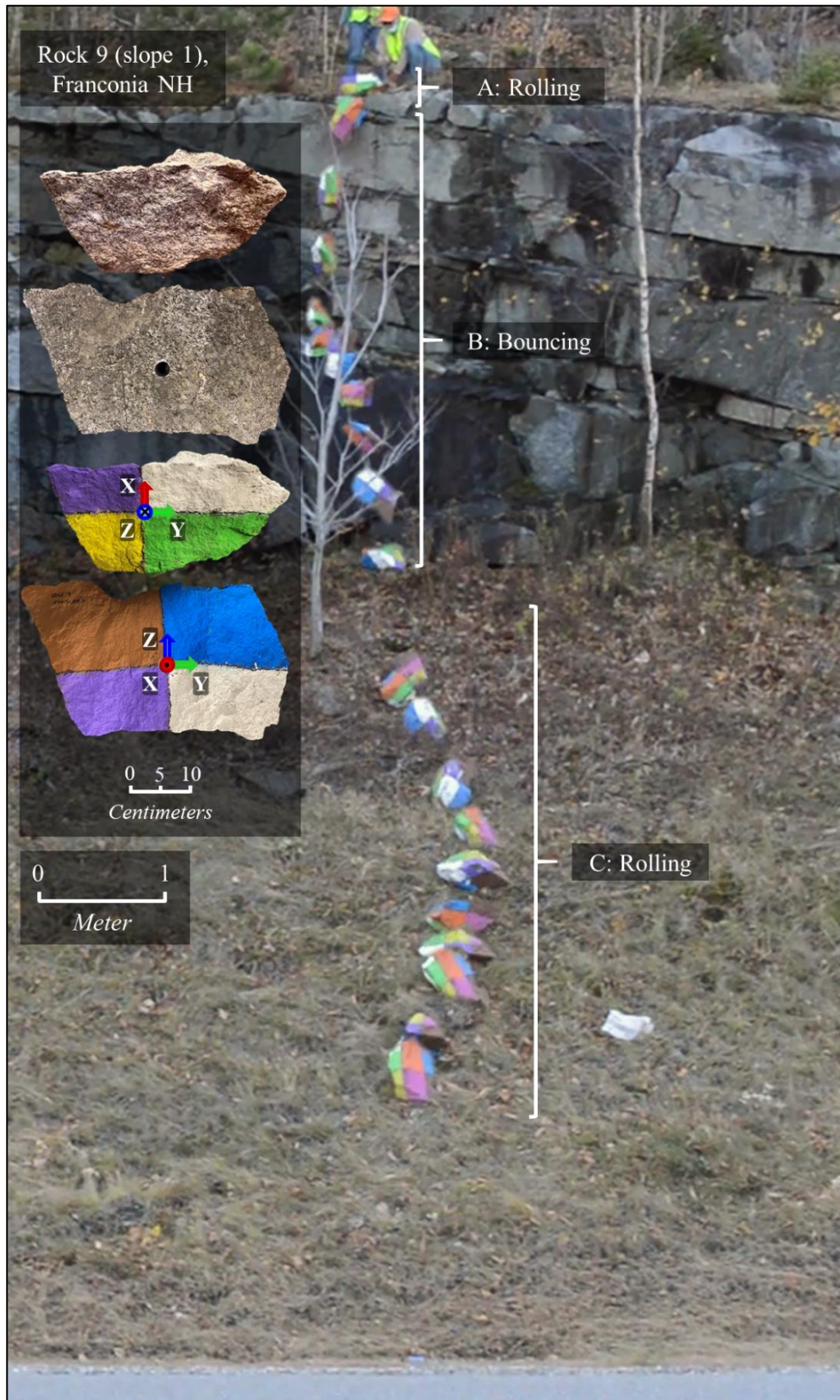
Figure 5.21. Rockfall trajectory: rock 9 (slope 1), Franconia NH.

143
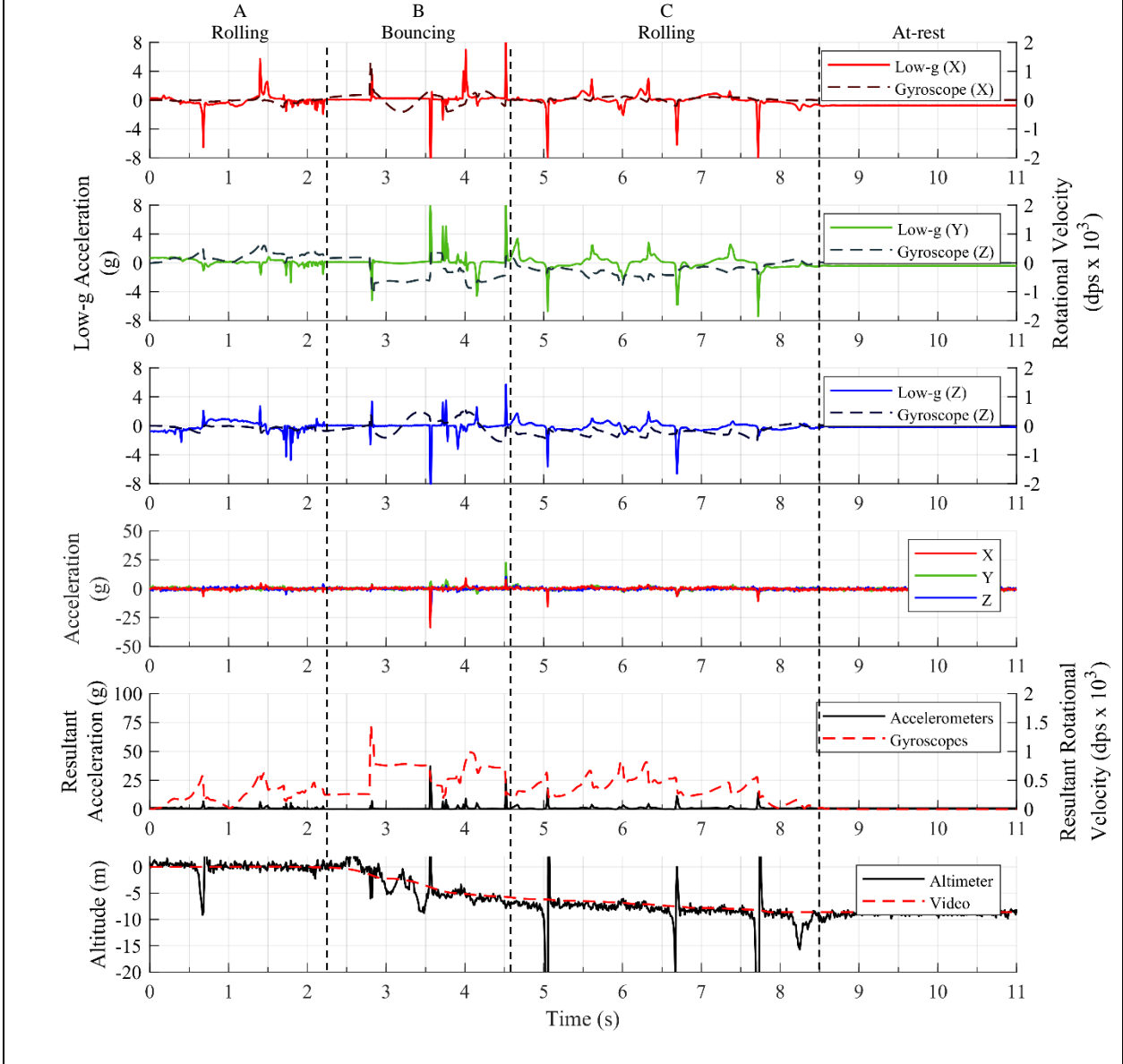
Figure 5.22. Smart Rock test data: rock 9 (slope 1), Franconia NH.

A summary of the results obtained at the Franconia site is presented in Table 5.8. Most test blocks experienced rolling motion before free fall and bouncing behavior against the rock face.

144

The distinct slope profile conditions at the rock face caused specific test blocks to bounce more or less against the rock slope. Therefore, the rocks experienced a wide range of maximum resultant accelerations, which varied between 37 and 255 g. Such variability can be attributed to the fact that specific test blocks interacted more with the rock face rather than the vegetation surface, or vice-versa.

Table 5.8. Field rockfall summary: Franconia NH.

Rock ID	Slope angle	Drop height (m)	Displacements			Smart Rock resultant data			Maximum impact force (kN)
			Lateral (m)	Lateral dispersion (%)	Runout from toe (m)	Maximum acceleration (g)	Maximum rotational velocity (dps)	Average rotational velocity (dps)	
Ref rock	90º/30º	9.6	2.0	11%	10.0	255	2985	1143	13
2 (sl. 1)	50º/25º	9.6	0.2	1%	3.0	33	2004	787	3
3 (sl. 1)	65º/30º	9.3	1.4	8%	0.0	214	2382	483	8
4 (sl. 1)	90º/30º	9.6	-0.2	1%	1.9	99	1105	572	4
6* (sl. 1)	50º/25º	9.6	-0.2	1%	2.0	-	-	-	-
7 (sl. 1)	65º/30º	9.3	1.1	6%	1.3	81	1788	371	7
9 (sl. 1)	50º/25º	9.6	-0.4	2%	6.3	37	1430	389	10
10 (sl. 1)	50º/25º	9.6	-1.9	10%	0.8	71	2359	537	7
2 (sl. 2)	50º/25º	9.6	-3.9	21%	1.8	173	1698	788	13
3 (sl. 2)	90º/30º	9.6	-0.1	1%	7.7	110	2134	496	10
5 (sl. 2)	90º/30º	9.6	-1.3	7%	10.5	81	5396*	1621	4
6 (sl. 2)	65º/30º	9.3	-1.0	5%	10.1	422**	3364	997	23
Average			1.1	6%	4.6	143	2422	744	9
Standard deviation			1.6	6%	4.0	116	1181	383	6

* * The gyroscope measuring limit was exceeded for the Z axis.

** The high-g accelerometer measuring limit was exceeded for the Y axis.

The test rocks experienced an average maximum resultant acceleration of 143 ± 116 g, demonstrating a wide range of g-forces measured for the slope conditions. The highest impact force of 23 kN, experienced by rock 6 (slope 2), occurred during bouncing on rock. The majority of the test blocks predominantly rotated about their shortest axes of inertia. Bouncing behavior did not significantly increase rotation in most tests. The detailed trajectories and data output for the remaining tests are provided in Appendix B.3.

Except for one test (rock 2, slope 2), all rocks had lateral displacements inferior to 2 m (20% of the slope height). The runout distances presented in the table are summarized in a histogram in Figure 5.23. Only 25% of the tests reached the catchment ditch, demonstrating that the presence of vegetation helps reduce the effect of rock bouncing and often shorten runout distances.
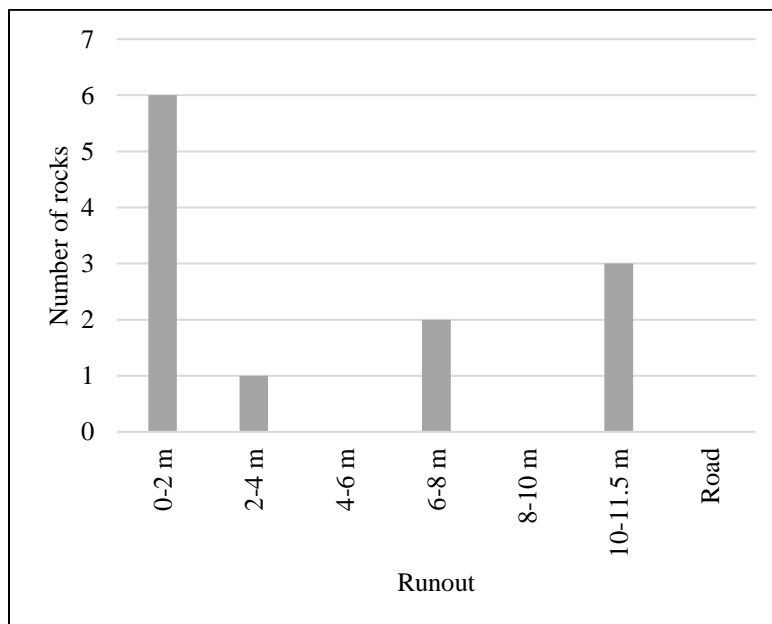
Figure 5.23. Runout histogram: Franconia, NH.

146

5.4. Franklin, NH

Experimental rockfall tests were conducted on three consecutive slopes along NH Route 3A, a relatively busy, two-lane road that lacks shoulder on both sides of the pavement. All three road cuts consist of metamorphic rocks, and the same local blocks were used at all three sites (Table 5.9). The numbering gaps between the rock IDs indicate that rocks 6 and 7 broke during preparation in the laboratory. The lack of road shoulder required traffic control to release the test blocks and record the experiments.

Table 5.9. Test block characteristics: Franklin NH.

ID	Weight (kg)		Density (kg/m³)	Dimensions (m)			Shape	Mass moment of inertia (kg*m²)		
	Before drill.	After drill.		Length, Y	Width, X	Height, Z		I_{XX}	I_{YY}	I_{ZZ}
Ref	-	5.21	2660	0.20	0.12	0.12	Compact Elongated	0.024	0.024	0.013
1	9.39	9.25	2710	0.34	0.13	0.15	Elongated	0.055	0.023	0.060
2	8.44	8.30	2630	0.24	0.16	0.09	Bladed	0.056	0.030	0.064
3	9.45	9.30	3070	0.25	0.14	0.17	Compact Elongated	0.057	0.028	0.053
4	11.35	11.21	2800*	0.22	0.18	0.16	Compact	0.067	0.042	0.055
5	14.24	14.04	2820	0.23	0.16	0.14	Compact	-	-	-
8	15.88	15.65	2600	0.35	0.21	0.11	Bladed	0.131	0.070	0.161
9	10.52	10.38	2780	0.21	0.16	0.25	Compact	0.062	0.049	0.053

* Estimated density, rock cores were too small and/or fractured after drilling.

5.4.1. Franklin 1, NH

The first slope in Franklin is a 12.5 m tall, A-rated, severely weathered road cut with overhanging fractured portions towards the road. The slope profile typically has a 45º inclination at the top and nearly 90º at the bottom portion of the slope (Figure 5.24). The catchment ditch is flat, 1.3 m wide, constructed with soil, and covered with vegetation. Eight tests were performed at this slope location, whose trajectories are presented in Figure 5.25.
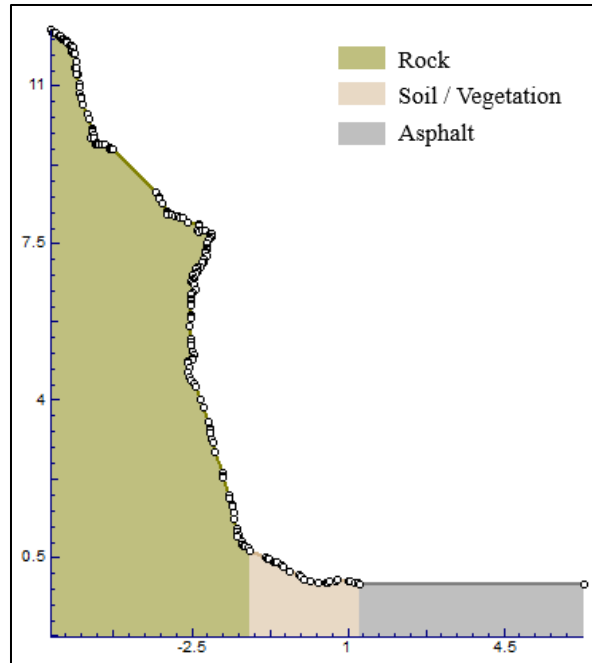
Figure 5.24. Sample cross-section of the test slope in Franklin 1, imported in RocFall. Units in meters.
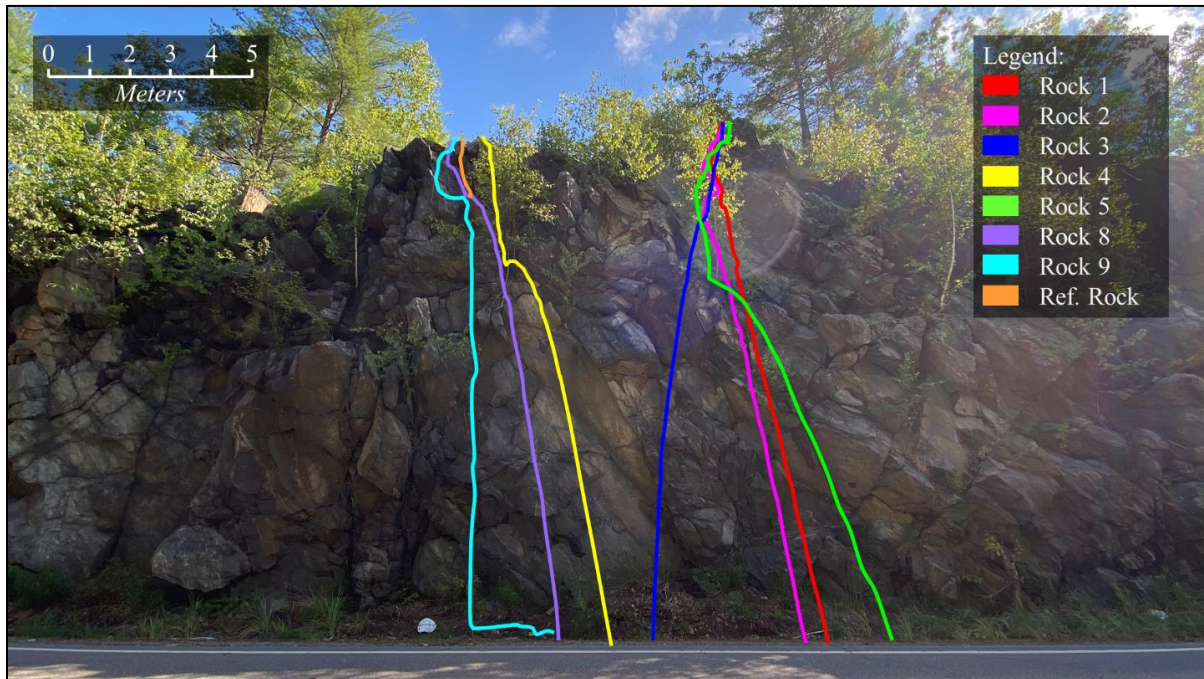
Figure 5.25. Rockfall trajectories: Franklin 1 NH.

All blocks reached the ground surface, except for the reference rock (Figures 5.26 and 5.27), which needed to be manually removed at the end of the test. After initial sliding (A) and

148

bouncing (B) stages against the rock face, the block experienced free fall (C), bounced against a flat portion of the slope, and stopped (D). Figure 5.25 clearly shows the nearly 300 g acceleration

Figure 5.26. Rockfall trajectory: reference rock, Franklin 1 NH.

Field Rockfall — Reference Rock, Franklin 1/NH

SR number: 3. Date: 15-Jul-2020.

Mass: 5.21 kg. I_{XX}: 0.018 kg.m^2. I_{YY}: 0.011 kg.m^2. I_{ZZ}: 0.018 kg.m^2.

Width (X): 0.12 m. Length (Y): 0.2 m. Height (Z): 0.12 m. Shape: Compact Elongated.

Runout distance: 0 m from slope toe.

Drop height: 11.5 m. Altimeter hoisting: 10.9 m.
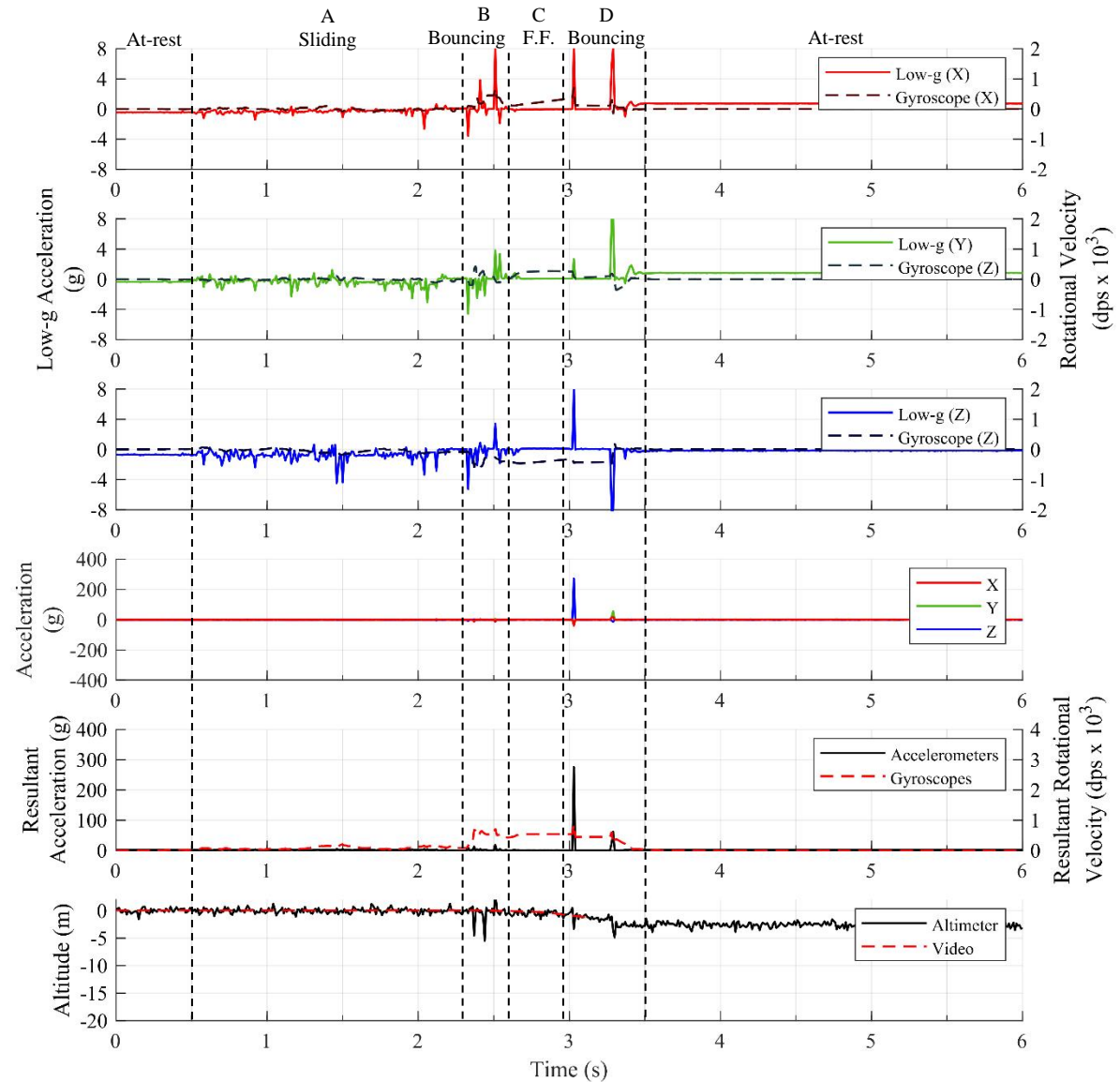
Figure 5.27. Smart Rock test data: reference rock, Franklin 1 NH.

peak experienced by the reference rock at D, resulting in an impact force of 14 kN. A second test,

performed with a 9.4 kg elongated rock, is presented in Figures 5.28 and 5.29.

150
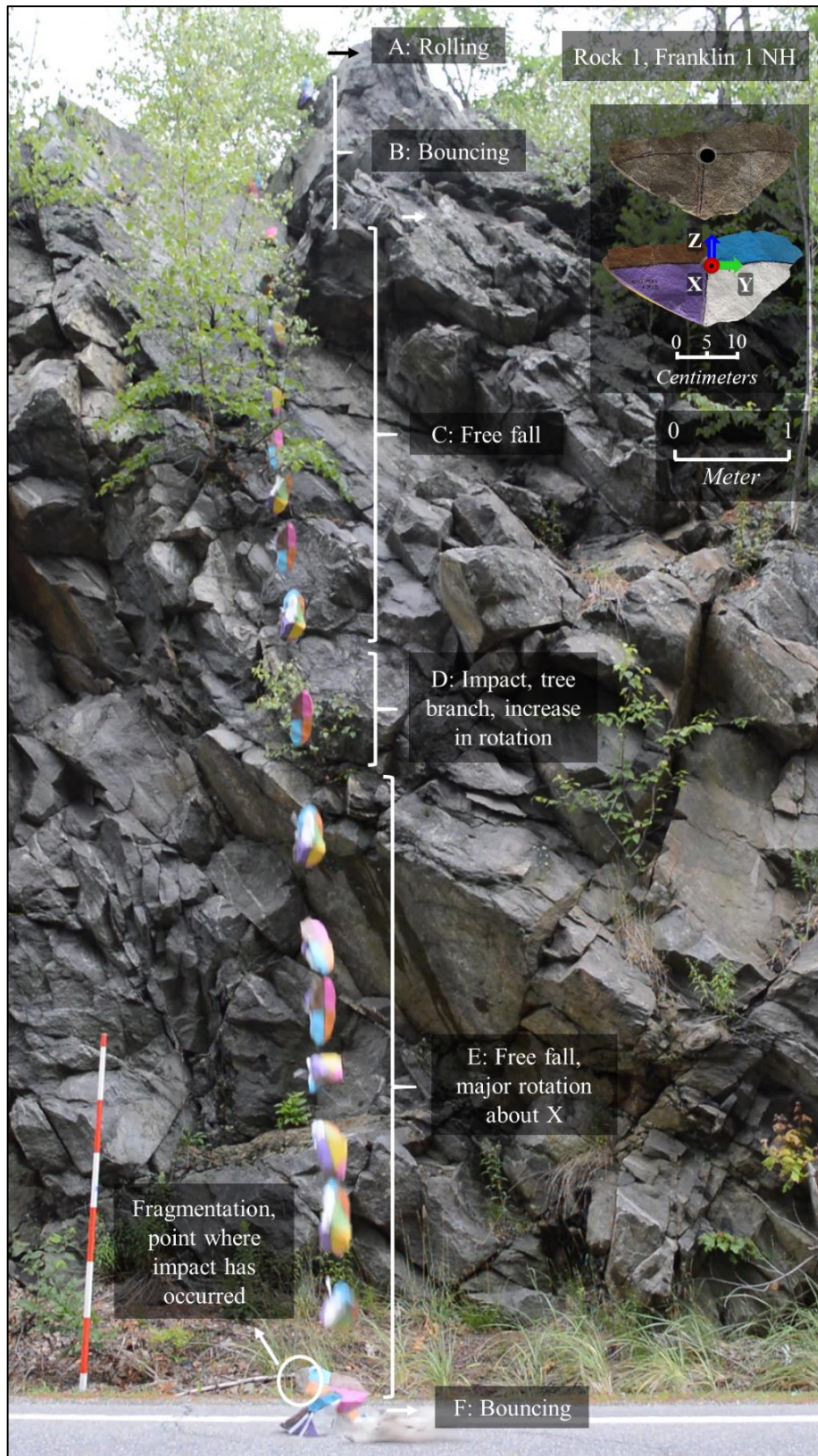
Figure 5.28. Rockfall trajectory: rock 1, Franklin 1 NH.

151
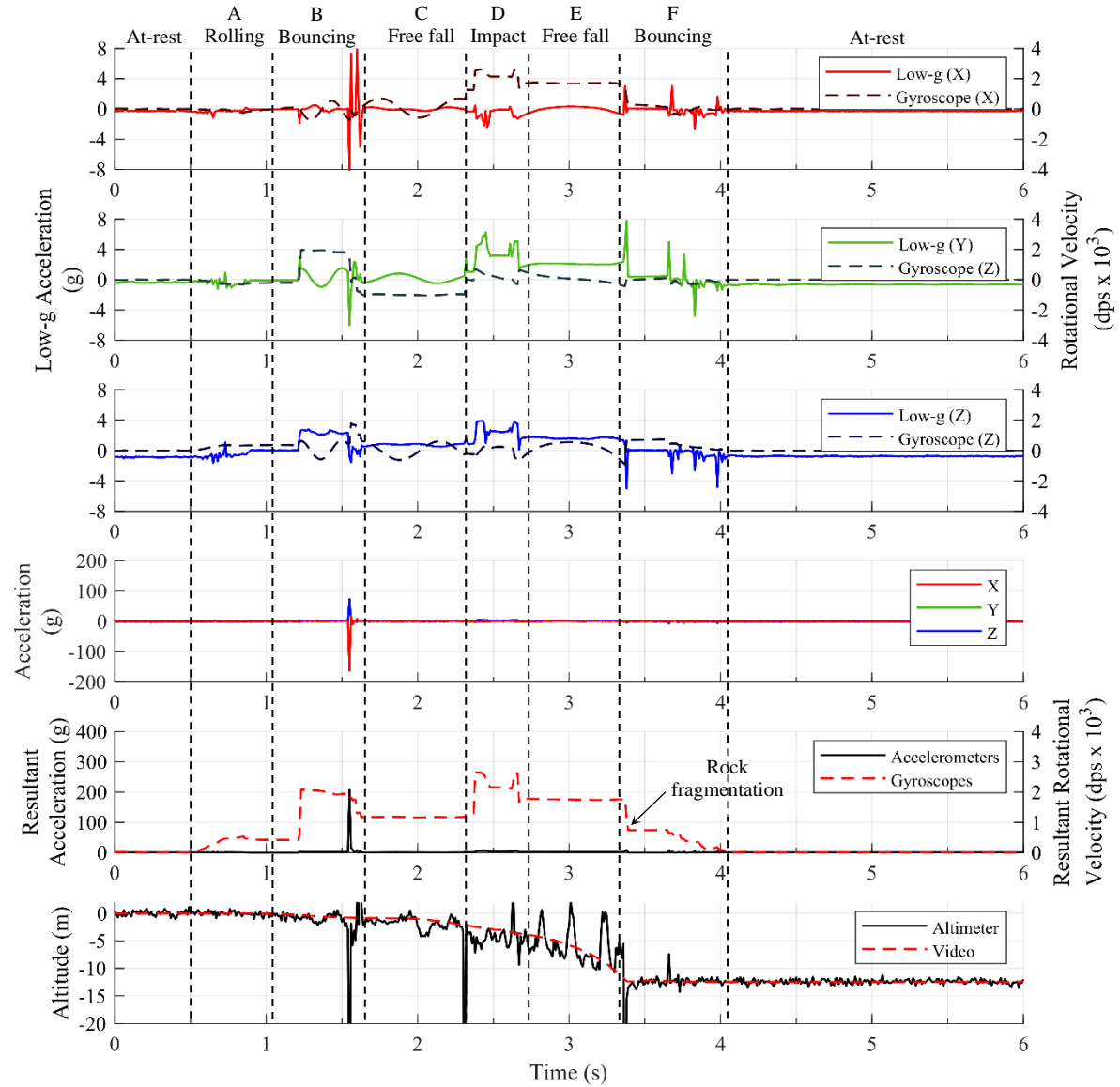
Figure 5.29. Smart Rock test data: rock 1, Franklin 1 NH.

Rock 1 initially rolled (A) with predominant rotation about Z (most significant axis of inertia) and bounced (B) against a flat section on the upper portion of the slope. A small-magnitude

bounce of 5 g at 1.2 s increased rock rotation from 420 dps to 2000 dps, and the block developed its significant rotation about the shortest axis of inertia (Y). During free fall between C and E, the block rotated simultaneously about all three axes with a resultant average rate of 1800 dps. The test block bounced on the road and immediately fragmented during impact. Even though the rock bounced against a stiff surface, only 10 g resultant acceleration was captured by the SR at 3.4 s.

The rock bounced with major rotation about Z (most significant axis of inertia) and came to rest at 4 s. As seen in Figure 5.26, the rock stopped on the road with a measured runout distance of 2.9 m from the toe of the slope. It would represent a significant hazard to motorists, especially considering the absence of a road shoulder.

A third test performed at the first Franklin site is shown in Figure 5.30, in which rock 5, a 14 kg compact block, fractured at the drilled hole after bouncing against the rock face (C). The sensor fell out unprotected, the 3D printed shell was damaged during the impact on the road, and SR data were not recorded. Both resulting portions of rock 5 bounced (E) after the initial impact at the ground surface, and the furthest runout distance was equal to 10.6 m from the rock face. The remaining half of the block also stopped on the road. The runout distance developed in this test was the most significant endpoint location of all tested sites.

A summary of the results obtained at the first Franklin slope is presented in Table 5.10. The test rocks experienced an average maximum resultant acceleration of 138 g, and the highest acceleration was experienced by the reference rock, which did not bounce past the rock face. Rocks predominantly rolled/slid and bounced against the top of the slope profile and experienced free fall from the middle of the rock face to the ground surface. The measurements suggest that acceleration magnitudes as low as 5 g can result in significant increases in rotation.
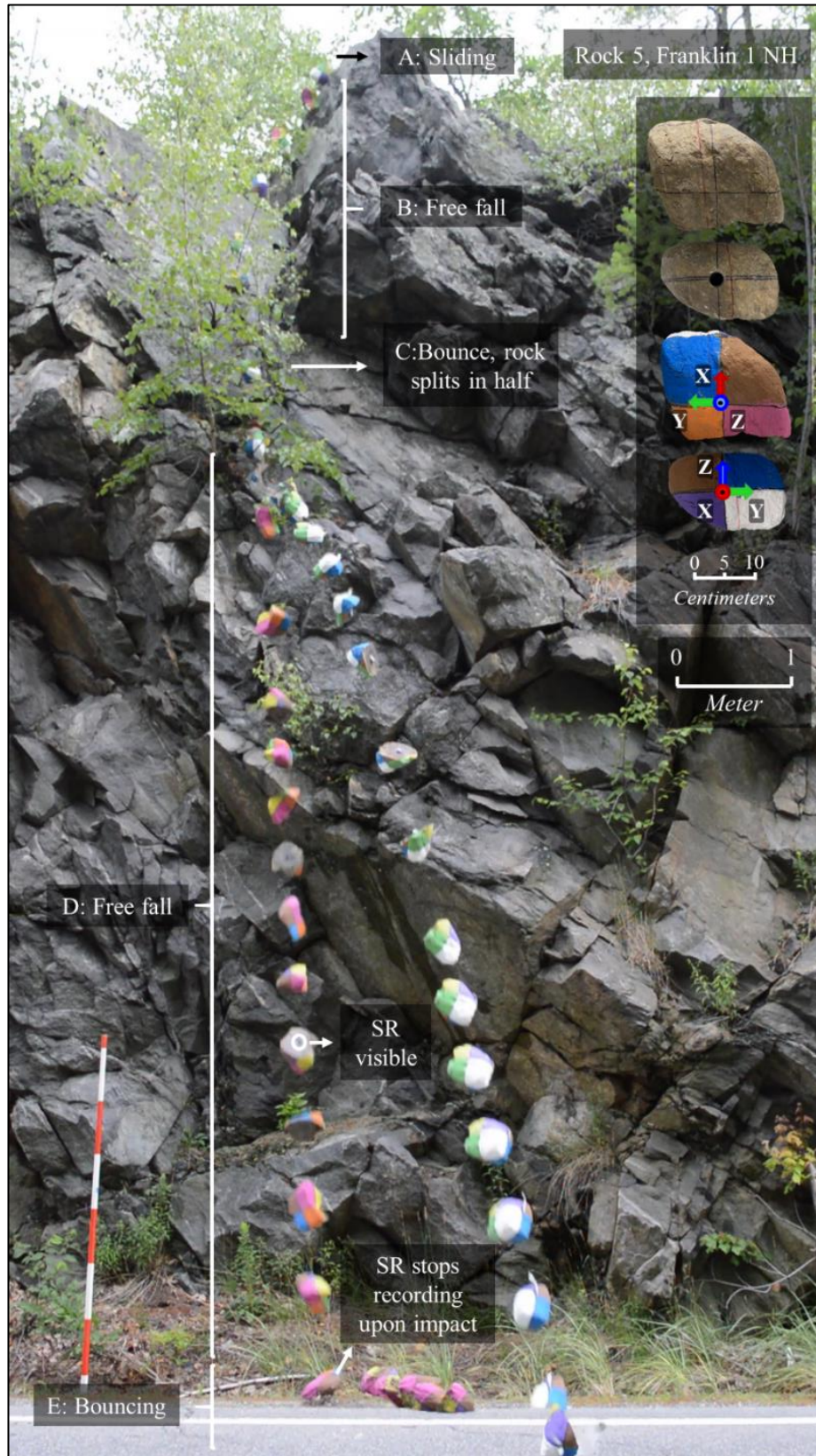
Figure 5.30. Rockfall trajectory: rock 5, Franklin 1 NH.

154

After bouncing motion, the test rocks generally tended to rotate about their shortest axes of inertia, even if it previously described greater rotation about their longest axis of inertia. The average resulting block rotation was equal to 905 dps. Except for the reference rock and rock 4, all test blocks experienced a maximum rotation rate higher than 2000 dps (5.6 rotations/s). The detailed trajectories and data output for the remaining tests are provided in Appendix B.4.1.

Table 5.10. Field rockfall summary: Franklin 1 NH.

Rock ID	Slope angle	Drop height (m)	Displacements			Smart Rock resultant data			Maximum impact force (kN)
			Lateral (m)	Lateral dispersion (%)	Runout from toe (m)	Maximum acceleration (g)	Maximum rotational velocity (dps)	Average rotational velocity (dps)	
Ref*		11.5	0.2	1	0.0	276	861	483	14
1	90°	12.5	-0.1	1	2.9	207	2658	1193	19
2	90°	12.5	0.4	4	1.1	114	2841	1289	9
3	90°	12.5	-2.9	25	8.1	90	2960	1332	8
4	45° / 75°	11.5	3.0	21	2.5	155	1377	701	17
5**	90°	12.5	2.6	23	10.6	-	-	-	-
8	45° / 75°	11.5	4.1	29	0.9	83	2494	541	13
9	45° / 75°	11.5	3.6	25	1.5	43	2508	793	4
	Average		2.1	16	3.5	138	2243	905	12
	Standard deviation		2.4	12	3.8	81	800	360	5

* Rock stopped in outcrop and did not reach the road or the catchment ditch.

** Rock split in two halves after impact with the road and damaged the sensor shell. No SR data.

The lateral dispersion ranged from 1% to 29% of the slope length and had an average of 16% or 2.1 m. Higher lateral displacements occurred during free fall after bouncing against the rock face, or while rolling/bouncing on the road. As shown in the table, significant runout distances were measured in this site. Five of the eight blocks reached and stopped on the road. The highest runout distances were equal to 8.1 and 10.6 m. The runout histogram is shown in Figure 5.31, in which only two rocks stopped on the catchment ditch, and one block stopped at the rock face.
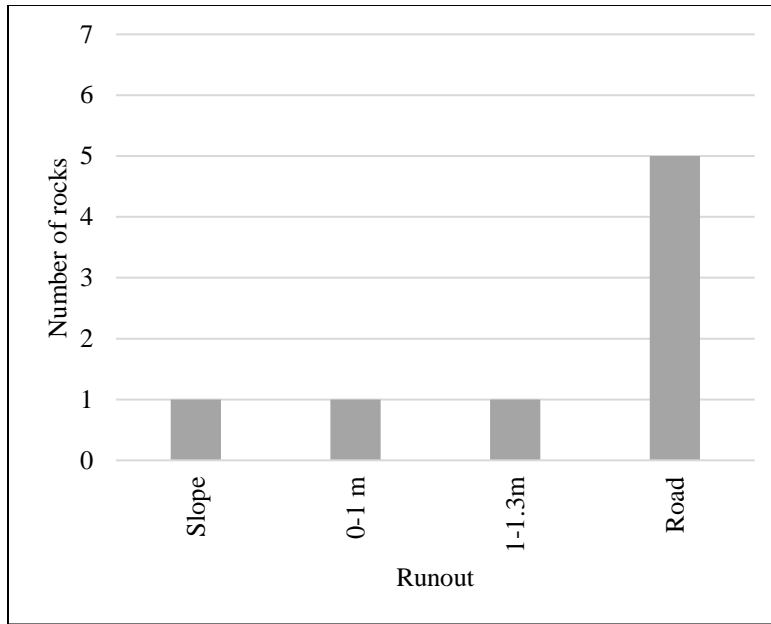
Figure 5.31. Runout histogram: Franklin 1 NH.

5.4.2. Franklin 2, NH

The second slope in Franklin is a 10 m tall, A-rated road cut with two major cross-section types. The slope profile angles vary between 50º and 70º (Figure 5.32), and the catchment ditch is trapezoidal and 2.5 m wide, constructed with soil and covered with vegetation. Seven tests were performed at this slope location, whose trajectories are presented in Figure 5.33.

The predominant mode of motion depended on the slope inclination. The four trajectories on the left of Figure 5.33 mainly included rock bouncing, while the three rockfalls on the right mostly experienced free fall. It can be observed that, for the same start point at each location, the steeper slope on the right presented significantly less lateral dispersion when compared to the less inclined surface on the left.
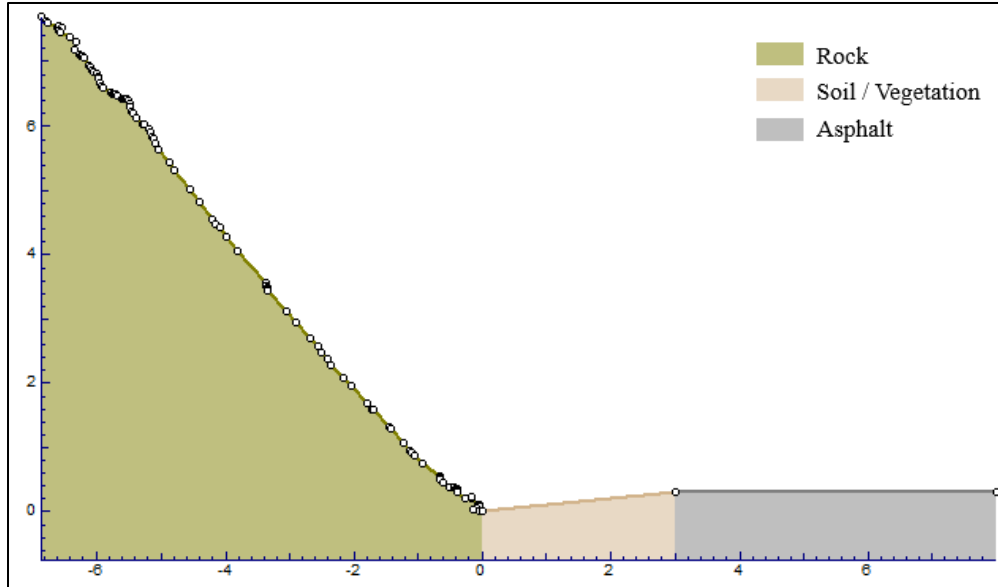
Figure 5.32. Sample cross-section of the test slope in Franklin 2, imported in RocFall. Units in meters.

Figure 5.33. Rockfall trajectories: Franklin 2 NH.

Figure 5.34 presents the rockfall test conducted at the left side of the rock slope, inclined at approximately 50º. Predominant bouncing behavior occurred after an initial rolling motion (A).

157
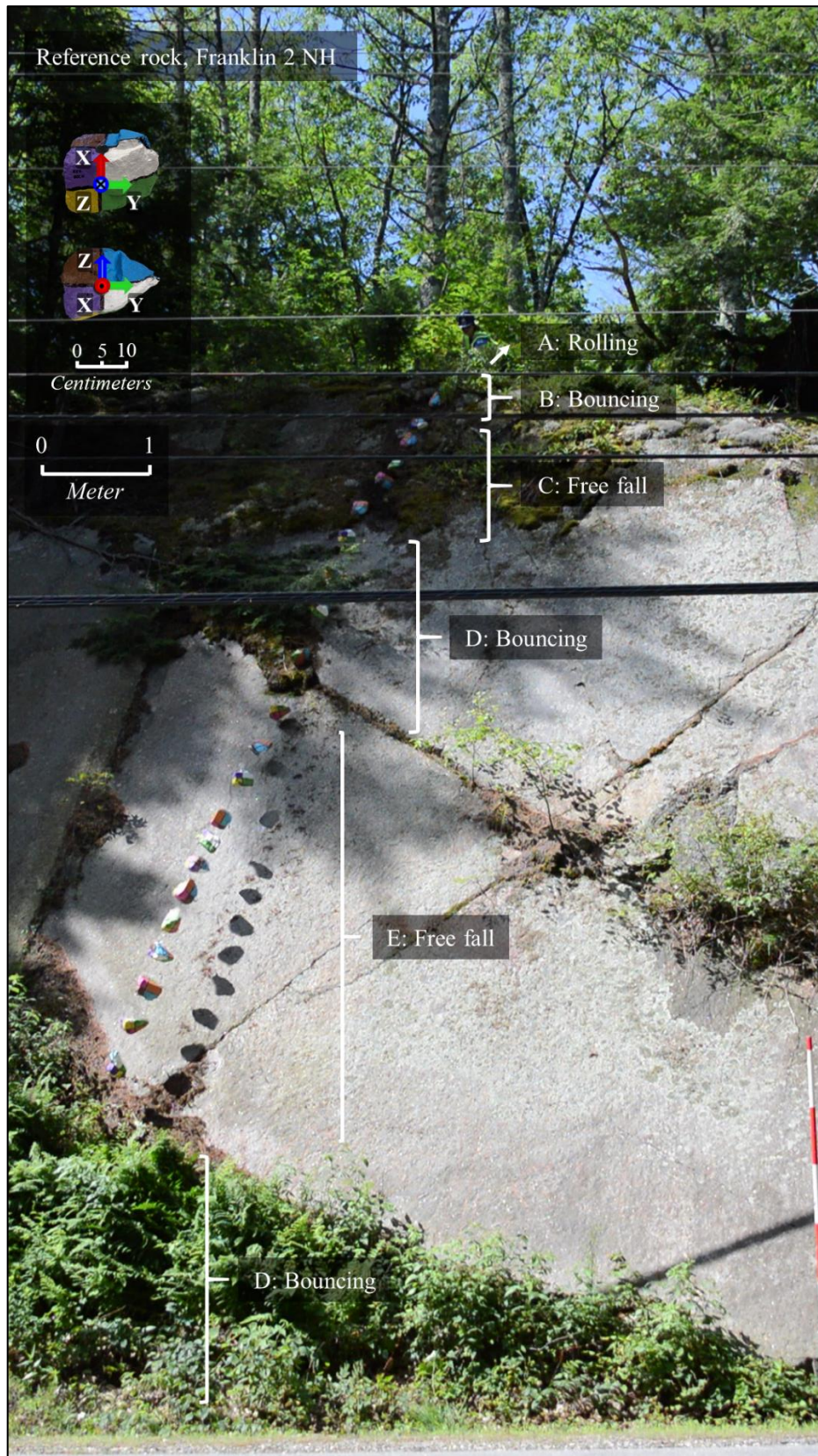
Figure 5.34. Rockfall trajectory: reference rock, Franklin 2 NH.

Field Rockfall — Reference Rock, Franklin 2/NH

SR number: 4. Date: 15-Jul-2020.

Mass: 5.21 kg. I_{XX}: 0.018 kg.m^2. I_{YY}: 0.011 kg.m^2. I_{ZZ}: 0.018 kg.m^2.

Width (X): 0.12 m. Length (Y): 0.2 m. Height (Z): 0.12 m. Shape: Compact Elongated.

Runout distance: 0.2 m from slope toe.

Drop height: 9.9 m. Altimeter hoisting: 10.9 m.
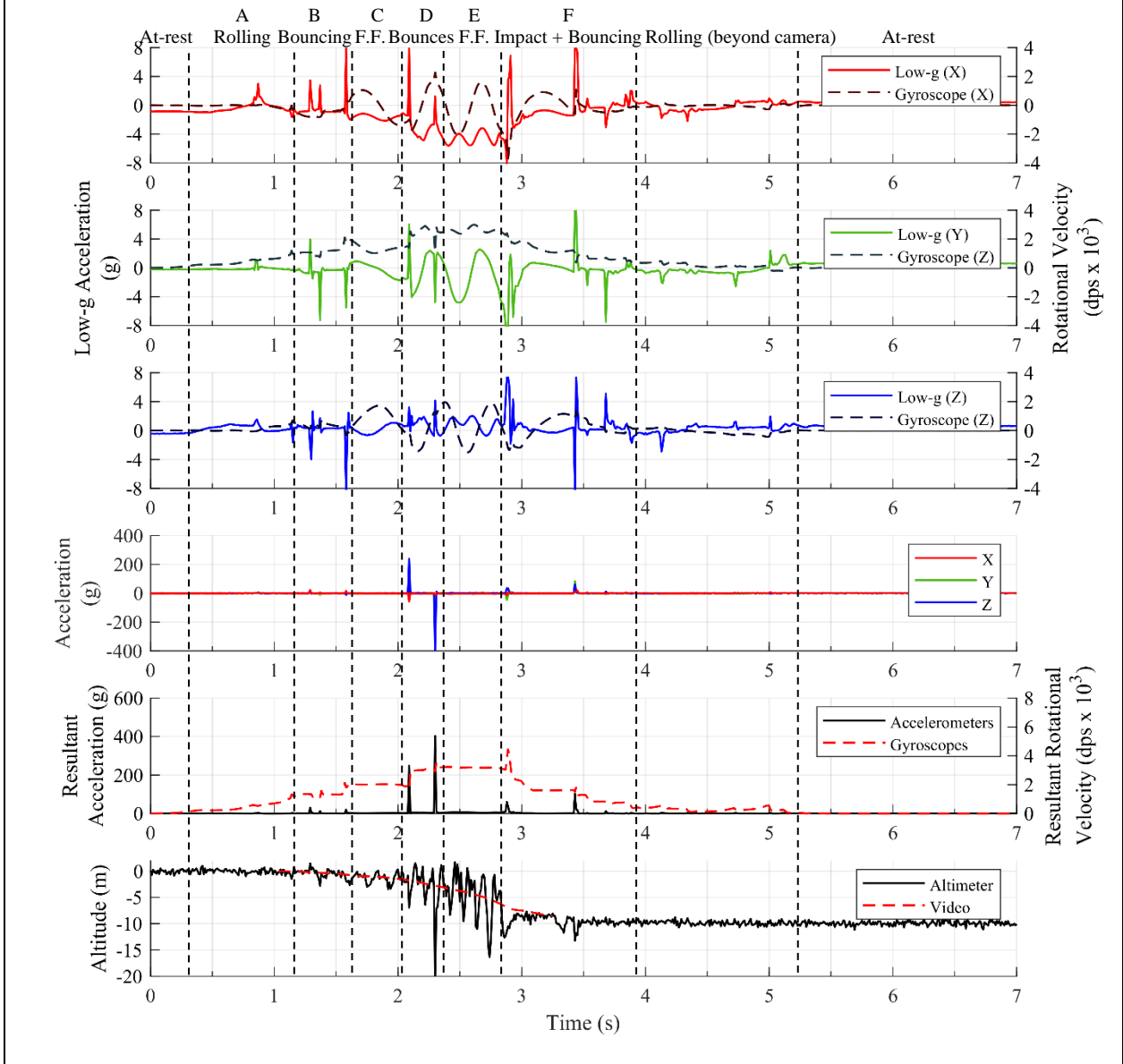
Figure 5.35. Smart Rock test data: reference rock, Franklin 2 NH.

The rotation rate was gradually increased with vertical displacement from 1300 dps (B) to

3180 dps (E), and significant rotation occurred about the Y axis (shortest axis of inertia). The most

159

significant impact magnitudes happened upon two successive bounces on rock and recorded 250 g and 400+ g at D, where the measuring limit of the high-g accelerometer was exceeded about the Z axis during impact on a discontinuity at the slope mid-section.

A maximum block rotation of 4483 dps was recorded upon contact with the bottom of the slope, covered with vegetation. Although the maximum resultant rotational velocity exceeded the measuring limit of the gyroscope, the rotations recorded for each axis did not exceed the maximum 4000 dps rate. The block bounced inside the catchment ditch with a resultant acceleration of 103 g and ended 0.2 m from the toe of the slope. Figure 5.35 shows how the block rotation gradually decreased while bouncing and rolling in the catchment ditch.

A second test performed from the same start point at the Franklin slope is presented in Figures 5.36 and 5.37. Rock 4 is a compact block that developed similar modes of motion as the reference rock. The rock bounced against the rock face with acceleration peaks between 35 and 70 g. The block reduced rotation upon impact with vegetation on the rock face at D. Rock 4 rotated simultaneously about all three axes on the rock face and developed predominant rotation about X (intermediate axis of inertia).

Due to the slope angle, rock 4 experienced a higher horizontal motion towards the road during the fall when compared to steeper slopes. For this reason, it bounced on the catchment ditch and reached the edge of the road. It is essential to highlight that NH Route 3A does not have a large shoulder at the test location, and rocks on the edge of the road can pose a higher hazard.
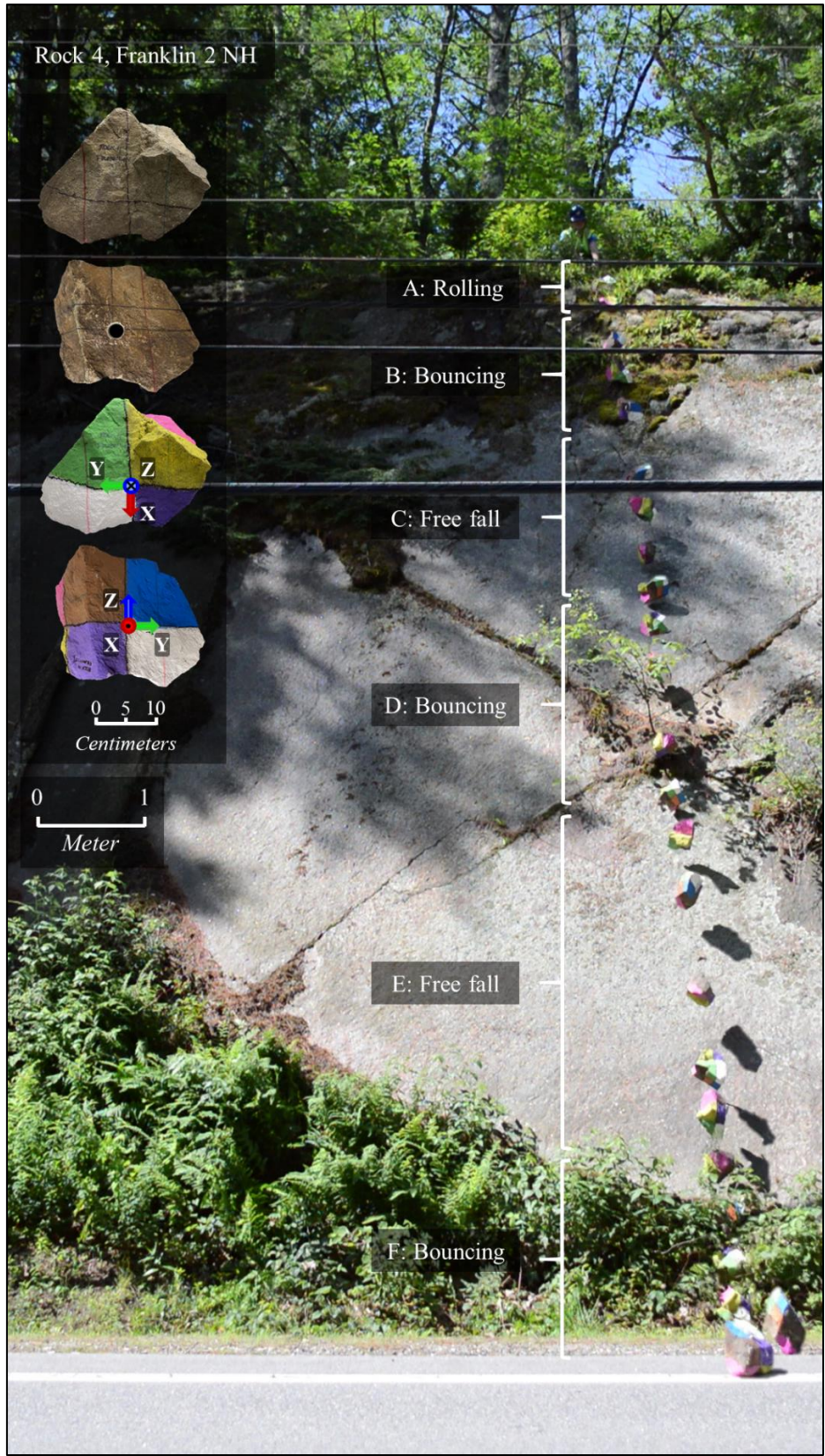
Figure 5.36. Rockfall trajectory: rock 4, Franklin 2 NH.
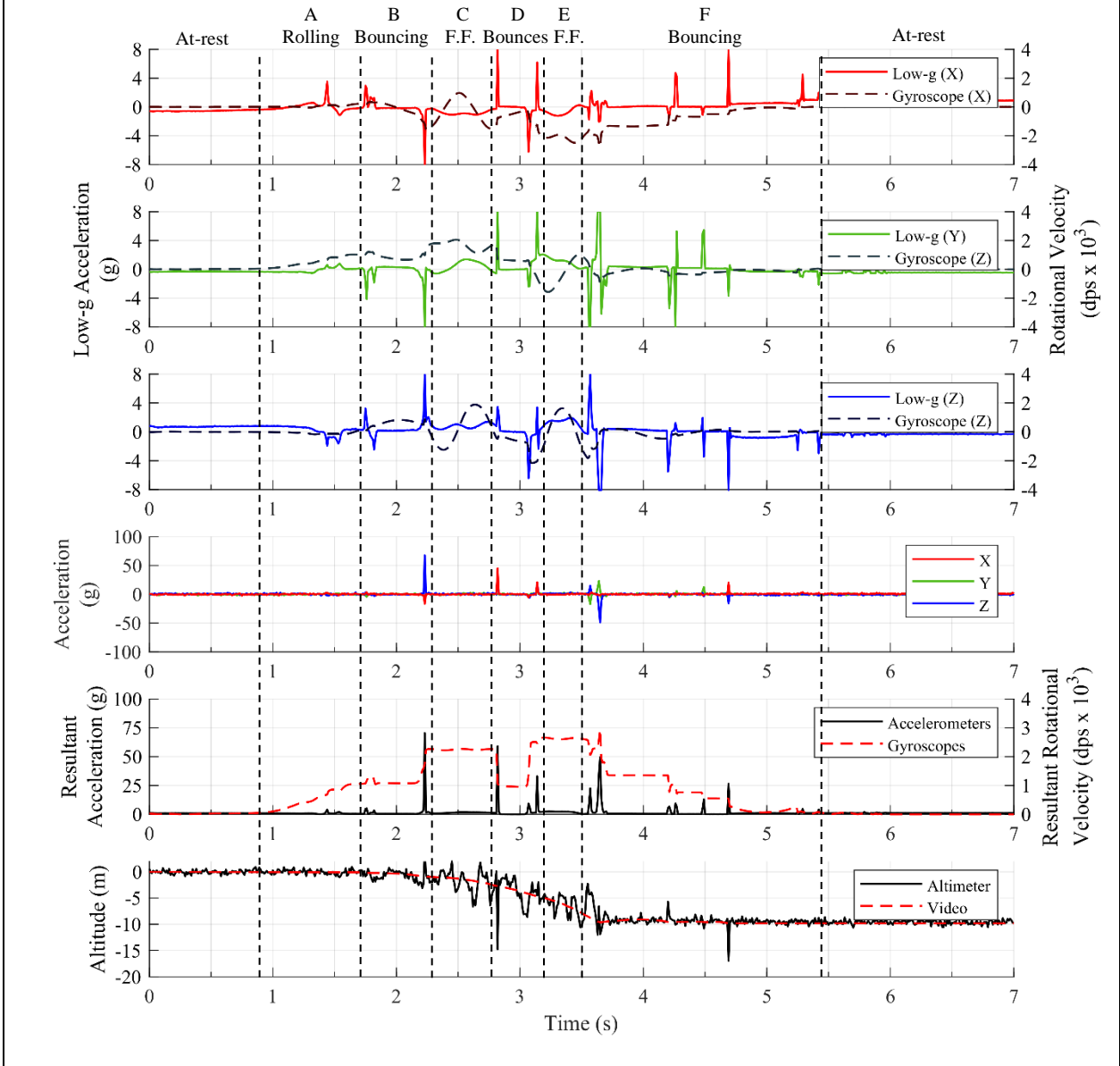
Figure 5.37. Smart Rock test data: rock 4, Franklin 2 NH.

Finally, one experimental rockfall performed at the second start location is shown in Figures 5.38 and 5.39. Due to the higher inclination of the rock face (70°), rock 8 mostly reached

the ground in free fall mode. The maximum acceleration of 70 g occurred during an impact against

the slope face (B, 2.3 s), and changes in rotation were not observed after this bounce.
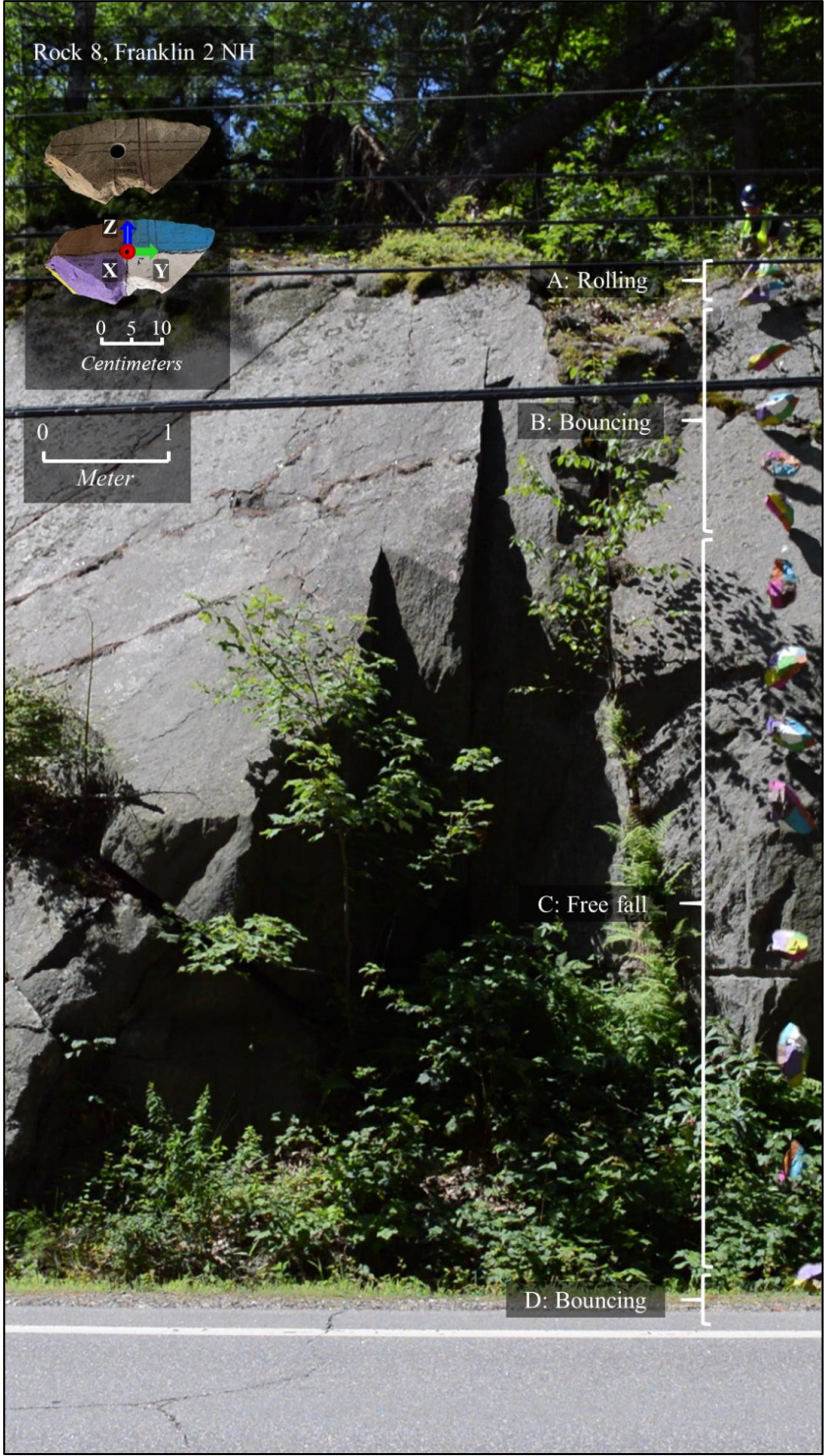
Figure 5.38. Rockfall trajectory: rock 8, Franklin 2 NH.

Field Rockfall — Rock 8, Franklin 2/NH

SR number: 4. Date: 15-Jul-2020.

Mass: 15.88 kg. I_{XX}: 0.131 kg.m^2. I_{YY}: 0.07 kg.m^2. I_{ZZ}: 0.161 kg.m^2.

Width (X): 0.21 m. Length (Y): 0.35 m. Height (Z): 0.11 m. Shape: Bladed.

Runout distance: 1.5 m from slope toe.

Drop height: 7.8 m. Altimeter hoisting: 7.8 m.
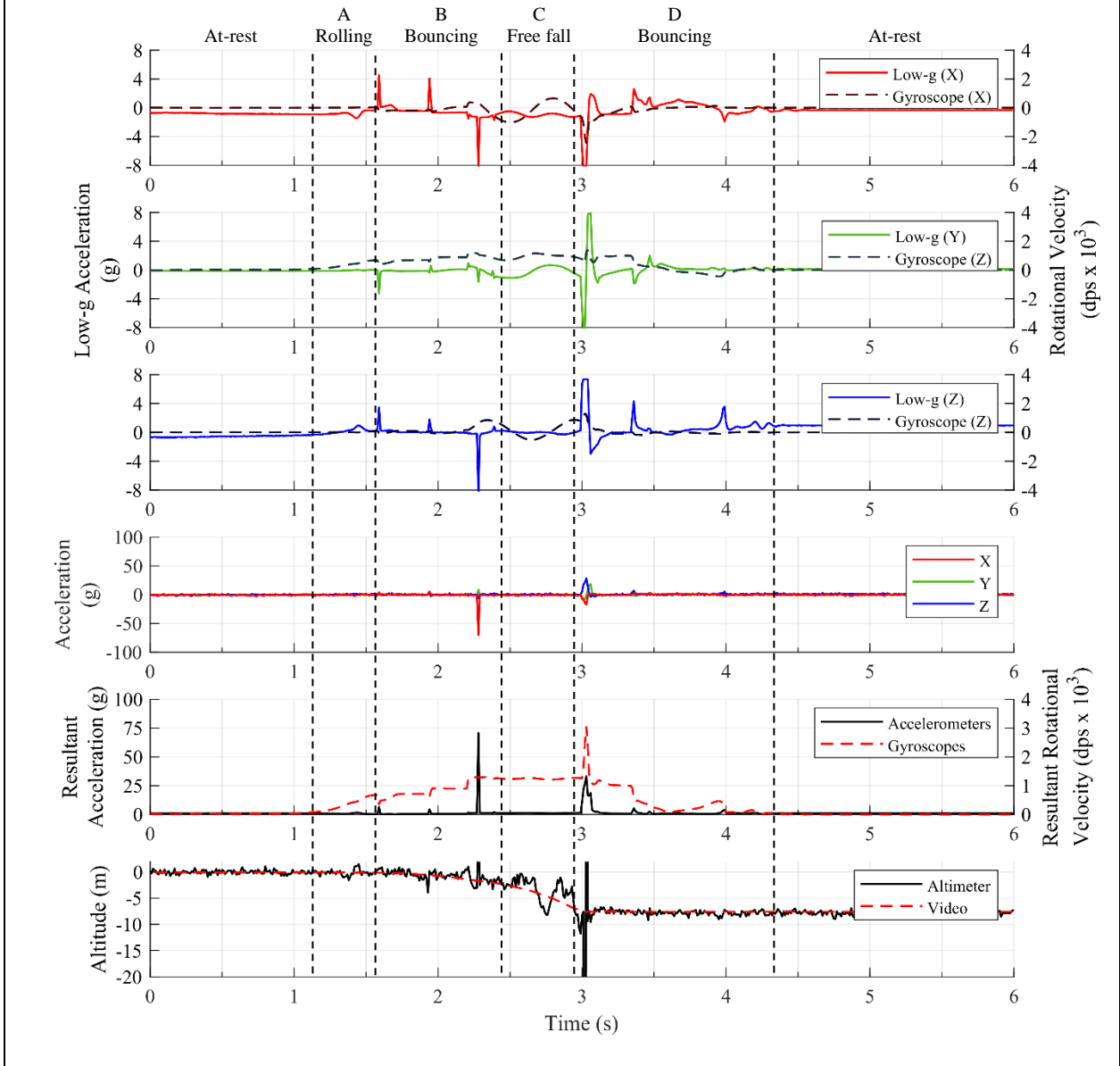
Figure 5.39. Smart Rock test data: rock 8, Franklin 2 NH.

During this experiment, block rotation remained approximately constant, near 1000 dps from the beginning of the trajectory until the second bounce at the catchment ditch at D (3.4 s).

164

The test block stopped within the catchment ditch limits even after bouncing. The maximum rotation experienced by rock 8 was equal to 3050 dps.

A summary of the results obtained at the second Franklin slope is presented in Table 5.11. Five of the seven experiments were successfully recorded with the Smart Rock sensor and experienced maximum resultant accelerations between 60 and 75 g, mostly during contacts with the rock face.

Table 5.11. Field rockfall summary: Franklin 2 NH.

| Rock ID | Slope angle | Drop height (m) | Displacements | | | Smart Rock resultant data | | | Maximum impact force (kN) |
			Lateral (m)	Lateral dispersion (%)	Runout from toe (m)	Maximum acceleration (g)	Maximum rotational velocity (dps)	Average rotational velocity (dps)	
Ref	50°	9.9	-5.1	39%	0.2	403*	4483	1327	21
1	50°	9.9	-5.3	40%	3.5	62	2791	1097	6
2**	70°	7.8	-0.3	4%	1.1	-	-	-	-
3**	50°	9.9	-0.8	6%	2.7	-	-	-	-
4	50°	9.9	1.5	11%	2.9	71	2940	878	8
8	70°	7.8	0.5	6%	1.5	71	3055	791	11
9	70°	7.8	-0.3	4%	1.5	73	2549	563	7
		Average	2.0	16%	1.9	136	3164	931	11
	Standard deviation		2.7	17%	1.2	149	761	292	6

* The high-g accelerometer measuring limit was exceeded for the Z axis.

** SR battery died during the test. The sensor data were not recorded.

The reference rock experienced the highest acceleration and rotation motions, whose bounces of 250 g and 400+ g (Z-limit exceeded) produced rotations higher than 3000 dps. The lowest average rotations occurred on both SR data recorded at the steeper slope profile, demonstrating that bouncing behavior tends to increase block rotation. Although the reference rock experienced the highest resultant rotation upon impact with the catchment ditch (4483 dps), it was

the only test block released from the 50º slope profile which stopped within the catchment ditch limits.

The second slope in Franklin showed the highest mean average and maximum rotational velocities compared to the Danbury, Franconia, and Franklin 1 slopes. On the other hand, except for the reference rock, some of the lowest peak accelerations occurred at Franklin 2. The detailed trajectories and data output for the remaining tests are provided in Appendix B.4.2.

As shown in the table, while all rocks tested on the steeper slope profile stopped within the catchment ditch limits, three of the four rocks released on the 50º slope reached the road. This behavior demonstrates how, for the same catchment ditch, blocks with higher horizontal velocities (developed in shallower slope angles) towards the road tend to develop further runout distances. Figure 5.40 presents the runout histogram obtained at Franklin 2.
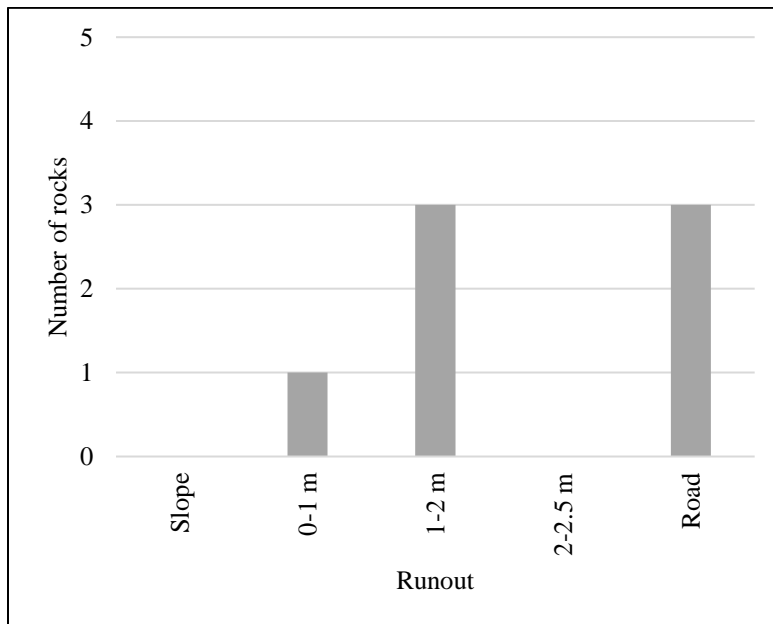
Figure 5.40. Runout histogram: Franklin 2 NH.

5.4.3. Franklin 3, NH

The third slope in Franklin is an 18 m tall, A-rated road cut with uniform geometry, partially covered with vegetation, and a 40° slope angle (Figure 5.41). The catchment ditch is trapezoidal, 2.5 m wide, constructed with soil, and covered with vegetation.
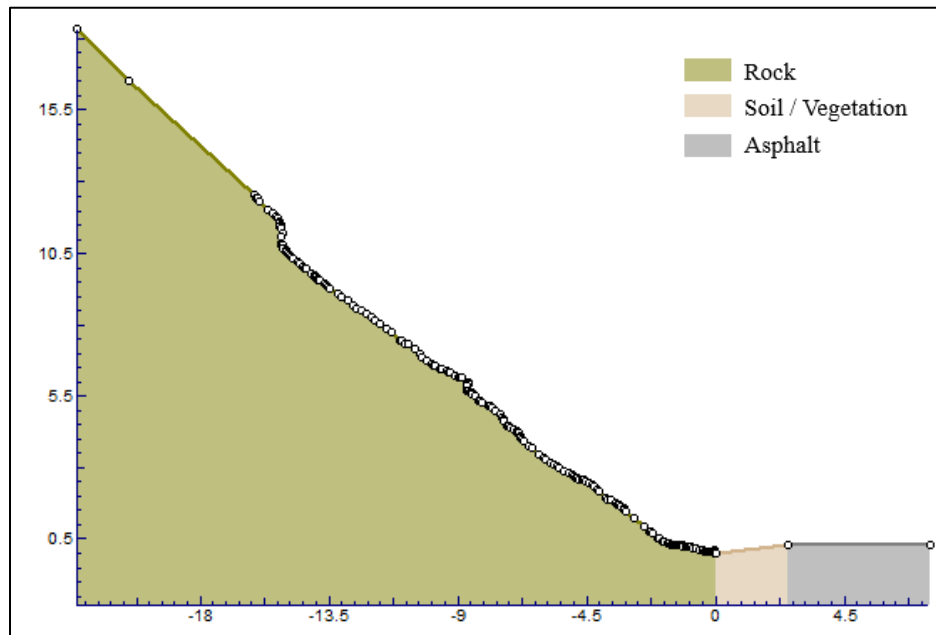
Figure 5.41. Sample cross-section of the test slope in Danbury imported in RocFall. Units in meters.

Seven tests were performed in this slope location, whose trajectories are presented in Figure 5.42. The test rocks predominantly bounced against both rock face and catchment ditch due to the slope angle. The significant height and relatively shallow inclination of the test slope result in a horizontal distance of approximately 21 m between the rockfall start location and the catchment ditch. For this reason, video tracking with a single frontal camera was not feasible, and cameras could also not be positioned laterally due to the slope geometry. Therefore, the video recordings were only used to delineate the described trajectories, as shown in the figure.
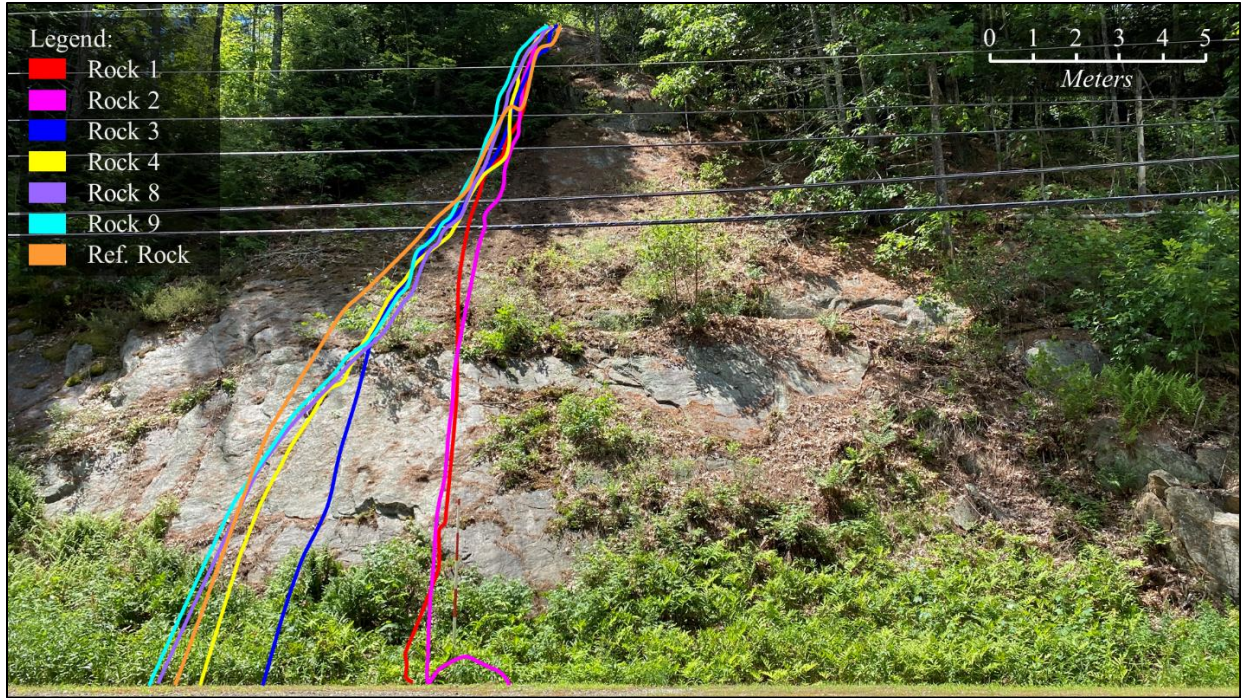
Figure 5.42. Rockfall trajectories: Franklin 3 NH.

Figure 5.43 presents the SR data for the reference rock, which experienced small acceleration peaks between 10 and 20 g at the beginning of the trajectory. A major resultant acceleration peak of 500+ g was measured in the middle of the slope profile, whose 400 g maximum acceleration limit was exceeded, producing an impact force of at least 26 kN.

Although block rotation occurred about the largest axes of inertia at the early rockfall stages (B), the test block rotated simultaneously about X, Y, and Z. The rotational velocity increased even after the maximum impact and only started to decrease after bouncing within the catchment ditch. The block rotated at about 2450 dps after ground impact and came to a complete stop on the road (3.0 m runout distance from the toe of the slope).

Figure 5.43. Smart Rock test data: reference rock, Franklin 3 NH.

In a second test (Figure 5.44), a 9.4 kg elongated block also demonstrated a bouncing

behavior. Average block rotation until mid-slope at 2.7 s was equal to 1000 dps and increased to

169

Figure 5.44. Smart Rock test data: rock 1, Franklin 3 NH.

approximately 1700 dps until ground impact (4.5s). Unlike the reference rock, rock 1 experienced

a maximum acceleration of 61 g upon ground impact, producing a force of 6 kN (nearly 25% of

170

the maximum force exerted by the reference block). The rock bounced in the catchment ditch with a resulting runout distance of 3.5 m (on the road). The block developed significant rotation about its shortest axes of inertia (X and Z) shortly before and after impact.

Although video tracking was not possible, it is possible to identify the moment of ground impact from the altimeter and accelerometer data (4.4 s for the reference rock and 4.5 s for rock 1). However, the noise level was significant during these experiments and cannot be used for position tracking without previous data processing. The data noise also decreases significantly when the rock is nearly at-rest (after 5 s).

A summary of the results obtained at the third Franklin slope is presented in Table 5.12. All rocks bounced against both rock face and catchment ditch. Although similar trajectories were observed, as shown in Figure 5.45, the maximum resultant accelerations (and consequently, impact forces) did vary significantly, between 61 and 504 g (the latter had its measuring limit exceeded on the Z axis). Franklin 3 was the test site that experienced the highest mean maximum block rotation even with such high variability.

Franklin 3 was also the test site whose test blocks gave the highest maximum and average block rotation rates. The field results on this test slope indicated that, although the trajectories can be fairly similar due to the slope geometry, rockfall characteristics such as runout, acceleration, and block rotation can vary significantly. The detailed trajectories and data output for the remaining tests are provided in Appendix B.4.3.

The runout histogram for the third Franklin slope is presented in Figure 5.45. Four tests stopped on the road, and the remaining trials stopped between 2 and 3 m from the toe of the slope (close to the ditch limit).

Table 5.12. Field rockfall summary: Franklin 3 NH.

Rock ID	Slope angle	Drop height (m)	Displacements		Smart Rock resultant data				Maximum impact force (kN)
			Lateral (m)	Lateral dispersion (%)	Runout from toe (m)	Maximum acceleration (g)	Maximum rotational velocity (dps)	Average rotational velocity (dps)	
Ref*	40°	18.2	-	-	3.5	504	4017	1886	26
1	40°	18.2	-	-	3.0	61	3775	1173	6
2	40°	18.2	-	-	2.4	67	2683	1330	6
3	40°	18.2	-	-	3.2	401	4247	1440	37
4	40°	18.2	-	-	2.7	159	2550	1212	18
8	40°	18.2	-	-	7.6	353	2939	1226	55
9	40°	18.2	-	-	3.0	167	3965	1424	17
	Average		-	-	3.6	244	3454	1384	24
	Standard deviation		-	-	1.8	174	705	245	18

* The high-g accelerometer measuring limit was exceeded for the Z axis.
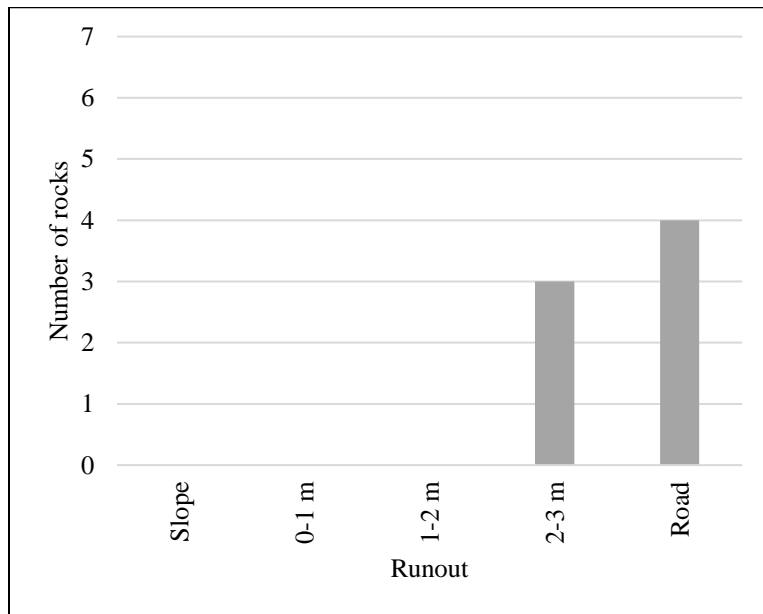
Figure 5.45. Runout histogram: Franklin 3 NH.

5.5. Keene, NH

Eight experimental rockfalls were conducted on a pre-split 10 m tall, C-rated granodiorite and tonalite rock cut in Keene, NH. The rock face is on a closed transportation corridor, and therefore there was no protective ditch against rockfall, only a flat soil surface at the ground level. The slope profile has an average inclination of 70º to 75º (Figure 5.46).
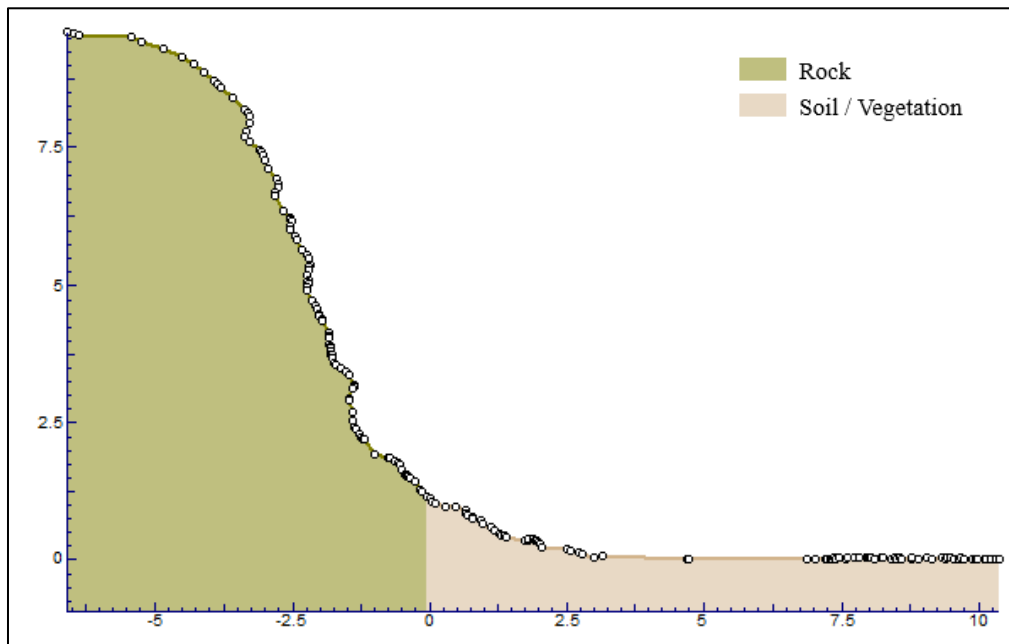
Figure 5.46. Sample cross-section of the test slope in Keene imported in RocFall. Units in meters.

The characteristics of the test blocks used in these tests are presented in Table 5.13. The trajectories described are shown in Figure 5.47, in which the test blocks generally bounced one to two times against the slope face. Unlike observed in tests in Danbury and Franklin 1, the trajectory was not significantly affected after bouncing behavior, and most lateral dispersion occurred upon ground contact.

Table 5.13. Field rockfall summary: Keene NH

ID	Weight (kg)		Density (kg/m³)	Dimensions (m)			Shape	Mass moment of inertia (kg*m²)		
	Before drill.	After drill.		Length, Y	Width, X	Height, Z		I_{XX}	I_{YY}	I_{ZZ}
Ref	-	5.21	2660	0.20	0.12	0.12	Compact Elongated	0.024	0.024	0.013
1	6.73	6.53	2840	0.19	0.26	0.07	Platy	0.016	0.033	0.042
2	11.70	11.58	2790	0.22	0.20	0.18	Compact	0.056	0.056	0.056
3	16.21	16.06	2800*	0.32	0.25	0.33	Compact	0.128	0.072	0.162
4	21.05	20.87	2860	0.25	0.22	0.20	Compact	0.150	0.125	0.150
5	7.66	7.55	2810	0.27	0.13	0.19	Compact	0.043	0.018	0.038
6	20.81	20.62	2630	0.24	0.17	0.24	Compact	0.144	0.148	0.146
7	13.54	13.12	2520	0.27	0.27	0.13	Platy	0.075	0.066	0.118

* Estimated density, rock cores were too small and/or fractured after drilling.

Figure 5.47. Rockfall trajectories: Keene NH.

Figures 5.48 and 5.49 present the trajectory and test data for rock 4, a 21 kg compact block that initially slid (A), fell with no rotation (B), and developed a resultant rotation of 540 dps upon impact at C, where a small rock fragmentation occurs. The block is in free fall (D) until bouncing

174
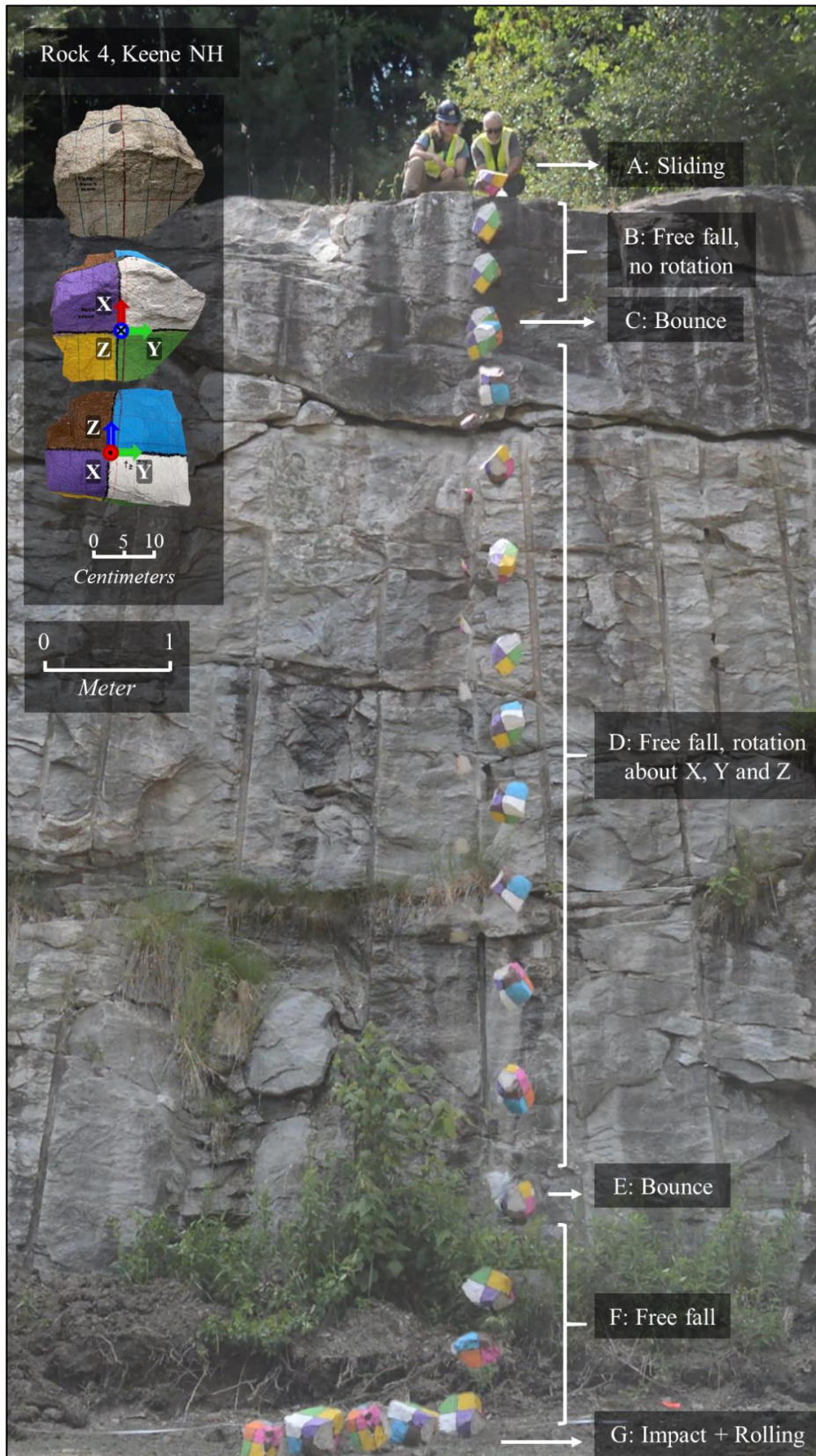
Figure 5.48. Rockfall trajectory: Rock 4, Keene NH.

175
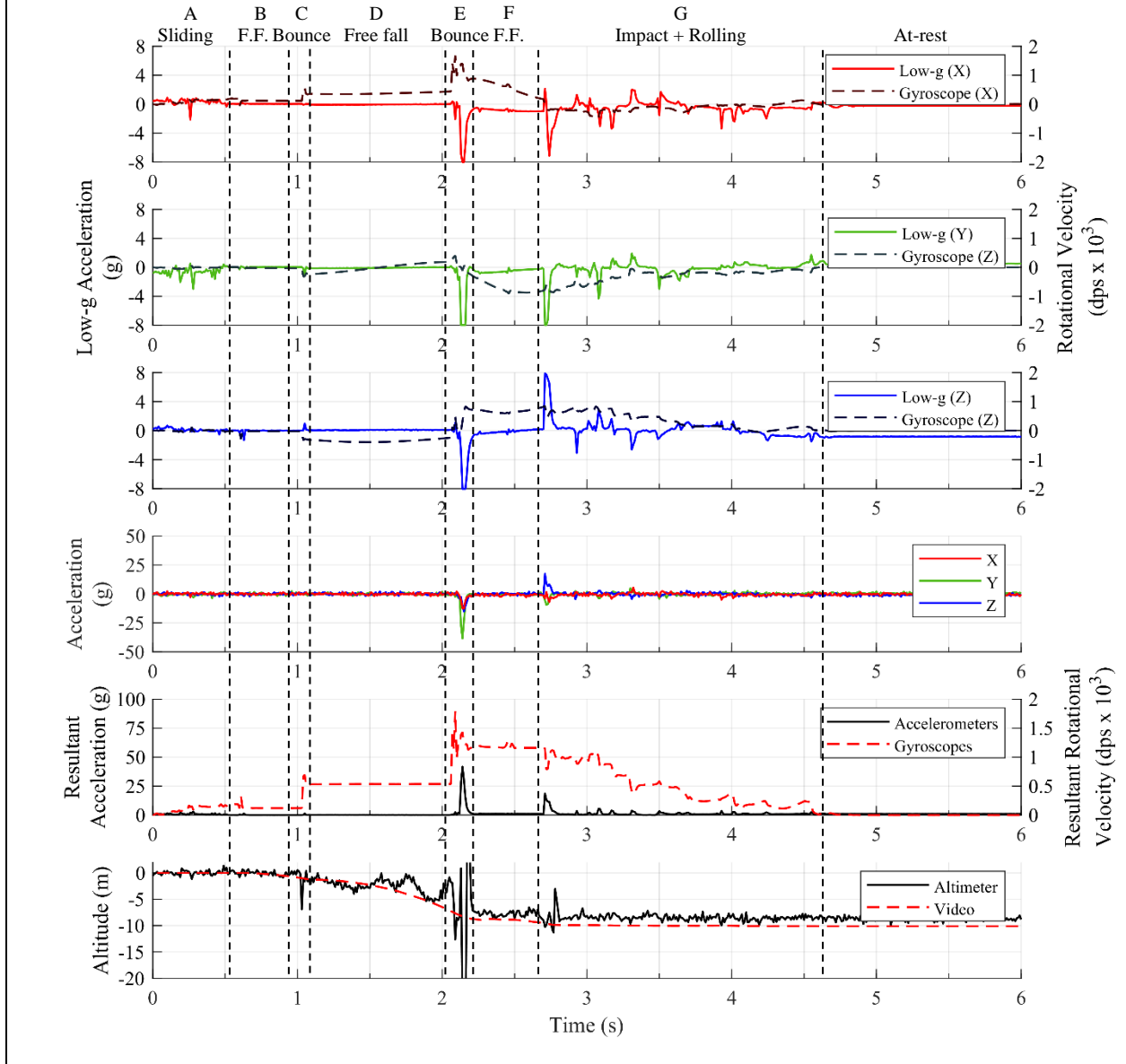
Figure 5.49. Smart Rock test data: rock 4, Keene NH.

bouncing against the bottom of the rock face (E), bouncing at the ground surface, and rolling before

coming to a complete stop (F). The block rotation was increased upon the second impact with the

slope face at E, and the motion was gradually reduced while rolling on granular material. The peak acceleration experienced by the test block was equal to 42 g during the impact at the bottom of the rock face.

Although the deceleration of the test block during rock-on-rock impact was not significant compared to other maximum accelerations previously recorded, the test block exerted an impact force of 9 kN due to the greater block mass. The test block did not develop major rotation about a specific axis, and a runout distance of 3.0 m from the toe of the slope was measured.

Figures 5.50 and 5.51 present a test performed with rock 1, a 6.5 kg platy block, which, while sliding and bouncing, experienced four acceleration peaks at the top of the rock face (A). The initial bouncing recorded the maximum acceleration experienced during the test, equal to 166 g and an impact force of 11 kN. Rock 1 was in free fall (B) at a constant rotation rate of 300 dps about the X axis (shortest moment of inertia). During sliding, rock 1 experienced four clear acceleration peaks. The block bounced after 3.2 m of vertical displacement at C, and the rotation rate increased to a resultant rate of 2000 dps about X, Y and Z, with predominant rotation about the X axis. The acceleration at C was equal to 91 g.

The block impact at the bottom of the slope occurs in a region covered with soil and vegetation. A second acceleration peak at 3.3 s represents the impact of the block with the prism pole at the lower left in Figure 5.50.
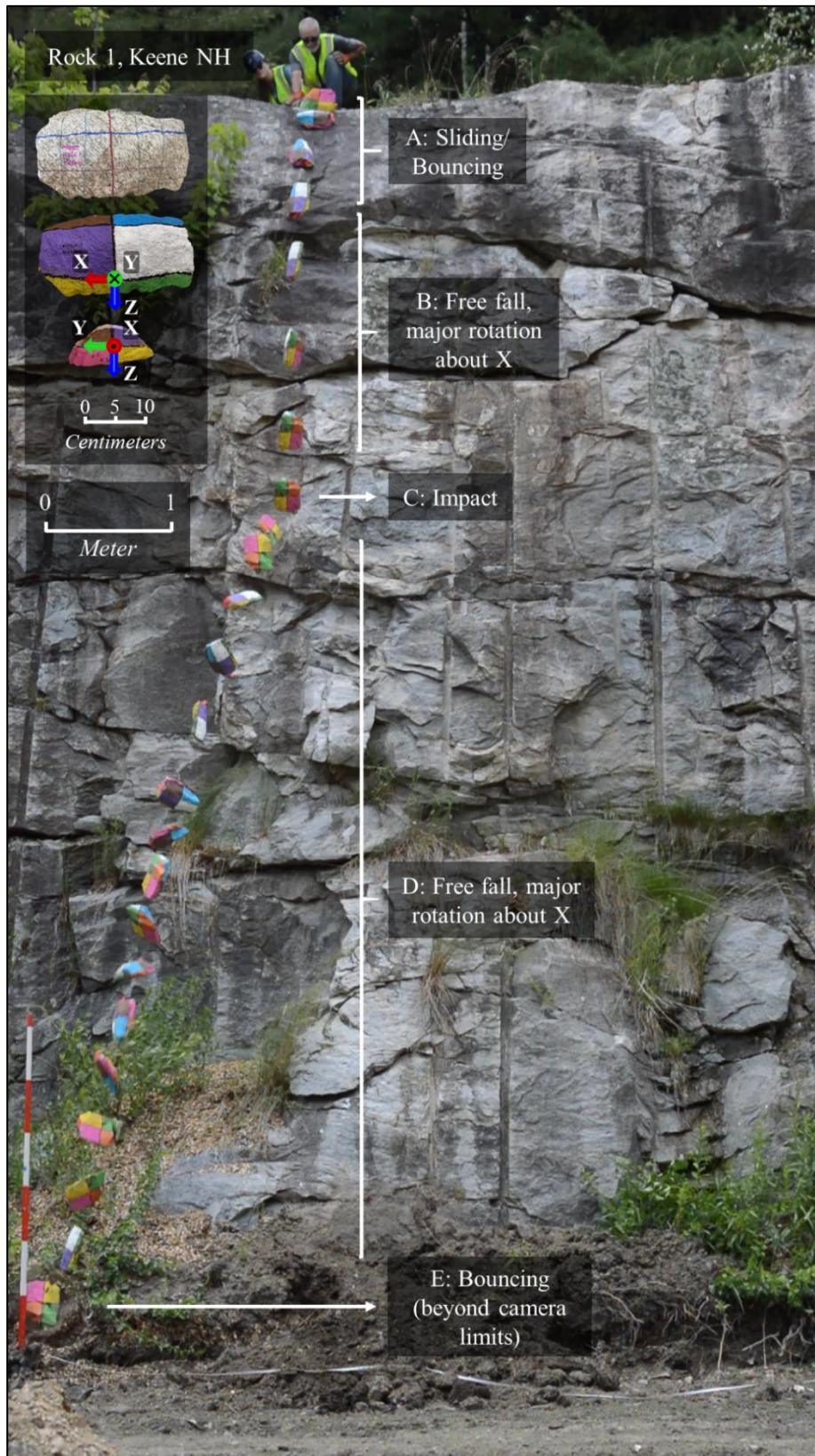
Figure 5.50. Rockfall trajectory: Rock 1, Keene NH.
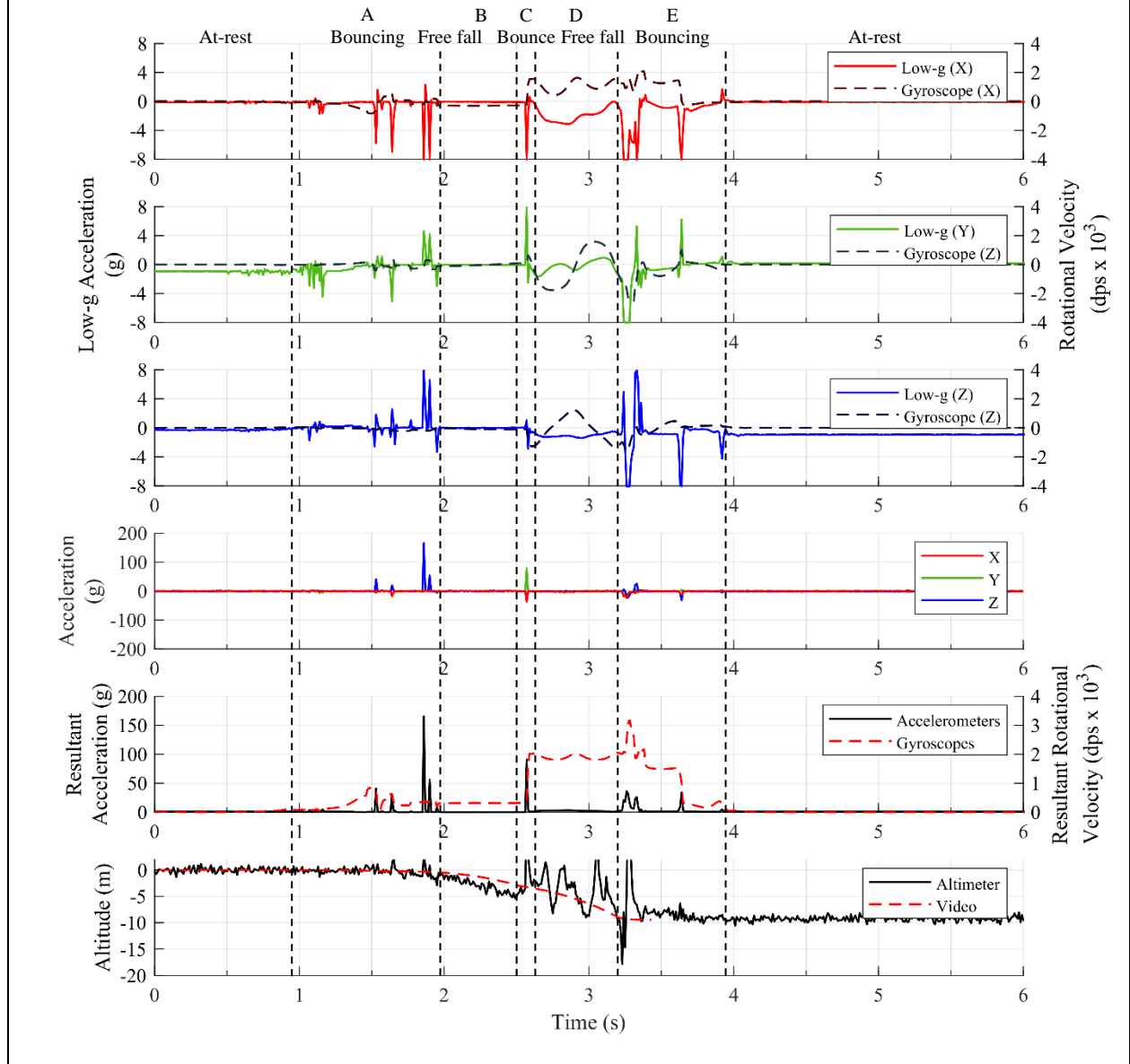
Figure 5.51. Smart Rock test data: rock 1, Keene NH.

Table 5.14 presents a summary of the results obtained at the Keene slope. Test rocks released from the same start location described similar trajectories and modes of motion as

previously shown. Even though the blocks had different shapes and sizes, similar peak accelerations were measured for all eight experimental trials, and occurred upon rock-on-rock contact. The average maximum acceleration was equal to 82 g, with a standard deviation of 44 g. Low variability has also been observed for the estimated impact forces, and the test blocks experienced, on average, a maximum impact force of 9 ± 3 kN. The rockfall tests performed in Keene yielded the lowest average peak acceleration and the second-lowest maximum and average block rotation. The detailed trajectories and data output for the remaining tests are provided in Appendix B.5.

Table 5.14. Field rockfall summary: Keene NH.

Rock ID	Slope angle	Drop height (m)	Displacements			Smart Rock resultant data			Maximum impact force (kN)
			Lateral (m)	Lateral dispersion (%)	Runout from toe (m)	Maximum acceleration (g)	Maximum rotational velocity (dps)	Average rotational velocity (dps)	
Ref	75°	9.9	-2.4	20%	3.9	64	3624	954	3
1	75°	9.9	-0.7	6%	2.6	166	3195	854	11
2	75°	9.6	-1.4	12%	0.0	74	2500	1076	8
3	75°	9.6	-1.8	16%	3.0	43	1866	748	7
4	70°	9.6	-1.8	15%	1.1	42	1793	622	9
5	75°	9.9	-0.5	4%	3.0	124	1709	563	9
6	70°	9.9	-2.1	18%	2.4	49	1492	544	10
7	75°	9.6	-1.9	16%	1.3	91	808	425	12
		Average	1.6	13%	2.2	82	2123	723	9
	Standard deviation		0.7	6%	1.3	44	927	224	3

In Keene, the maximum lateral dispersion measured was equal to 20% of the slope length, or 1.6 m. The runout histogram for these tests is presented in Figure 5.52. The maximum runout distance measured at the site was equal to 3.9 m, and most test blocks stopped within 1 and 3 m from the slope face. It is important to highlight that this test location did not have a catchment ditch or protective structures as the risk of rockfall in the area does not pose a hazard to the public.
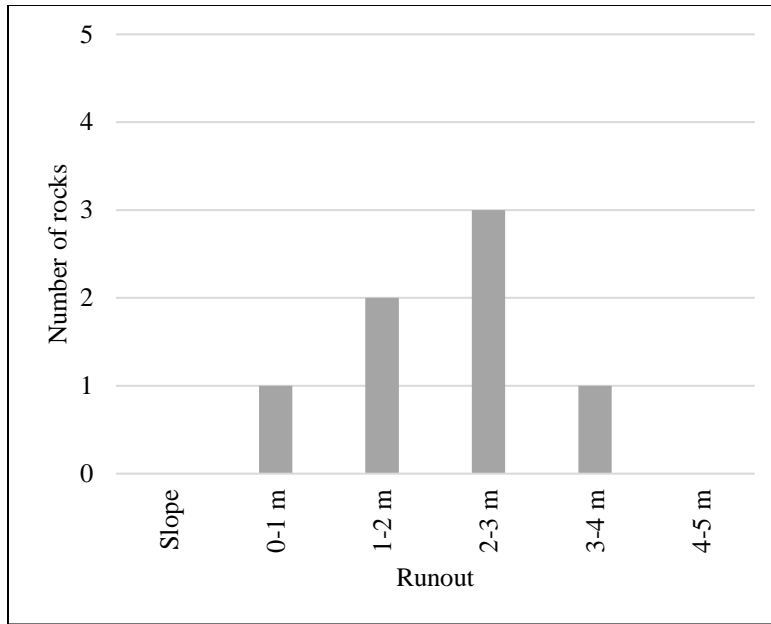
Figure 5.52. Runout histogram: Keene NH.

5.6. Orange, NH

A total of 8 experimental rockfalls were conducted on a 9 m tall, B-rated granodiorite road rock cut in Orange, NH. The rock face is located parallel to NH Route 4 and has a 5.0 m wide flat catchment ditch constructed with soil and covered with vegetation. The slope has an average inclination between 65º and 75º (Figure 5.53).

Only five local rocks could be retrieved, and one rock fractured during drilling. In addition to the reference rock, three other metasandstone blocks from the Dover slope location were also evaluated in Orange. The characteristics of the test blocks are presented in Table 5.15.

The trajectories described by the test blocks are shown in Figure 5.56. All field trials were performed from the same start point and had linear paths with low lateral dispersion after an initial rolling and/or sliding phase at the top of the rock face.

181
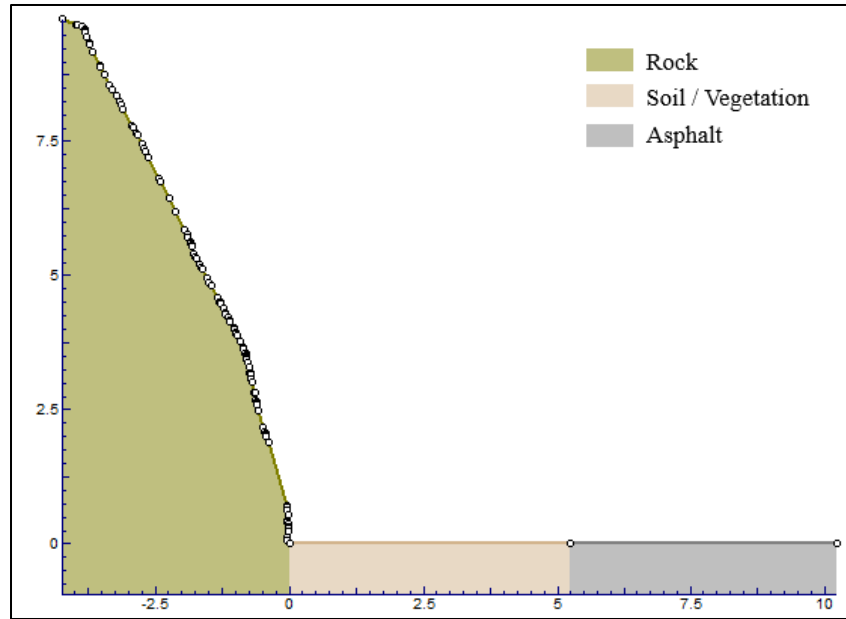
Figure 5.53. Sample cross-section of the test slope in Orange imported in RocFall. Units in meters.

Table 5.15. Test block characteristics: Orange NH.

ID	Weight (kg)		Density (kg/m³)	Dimensions (m)			Shape	Mass moment of inertia (kg*m²)		
	Before drill.	After drill.		Length, Y	Width, X	Height, Z		I_{XX}	I_{YY}	I_{ZZ}
Ref	-	5.21	2660	0.20	0.12	0.12	Compact Elongated	0.024	0.024	0.013
1	13.96	13.83	2710	0.32	0.14	0.20	Compact Elongated	0.093	0.054	0.082
2	10.39	4.60	2750	0.19	0.17	0.15	Compact	0.030	0.027	0.028
4	18.06	17.91	2720	0.36	0.20	0.13	Elongated	0.271	0.084	0.284
5	16.13	15.99	2770	0.41	0.15	0.17	Elongated	0.211	0.056	0.231
D1	4.09	3.972	2990	0.20	0.11	0.13	Compact Elongated	0.011	0.007	0.011
D2	3.65	3.52	3020	0.10	0.18	0.13	Compact	0.006	0.012	0.012
D3	12.37	12.16	3070	0.23	0.22	0.15	Compact Platy	0.065	0.051	0.077

In Orange, as observed in Figures 5.57 and 5.58, the reference rock initially bounced at a constant rotational velocity of approximately 800 dps (A) and experienced the highest acceleration peak of 160 g during an impact at the top of the slope face. The rotation of the block increased to

182
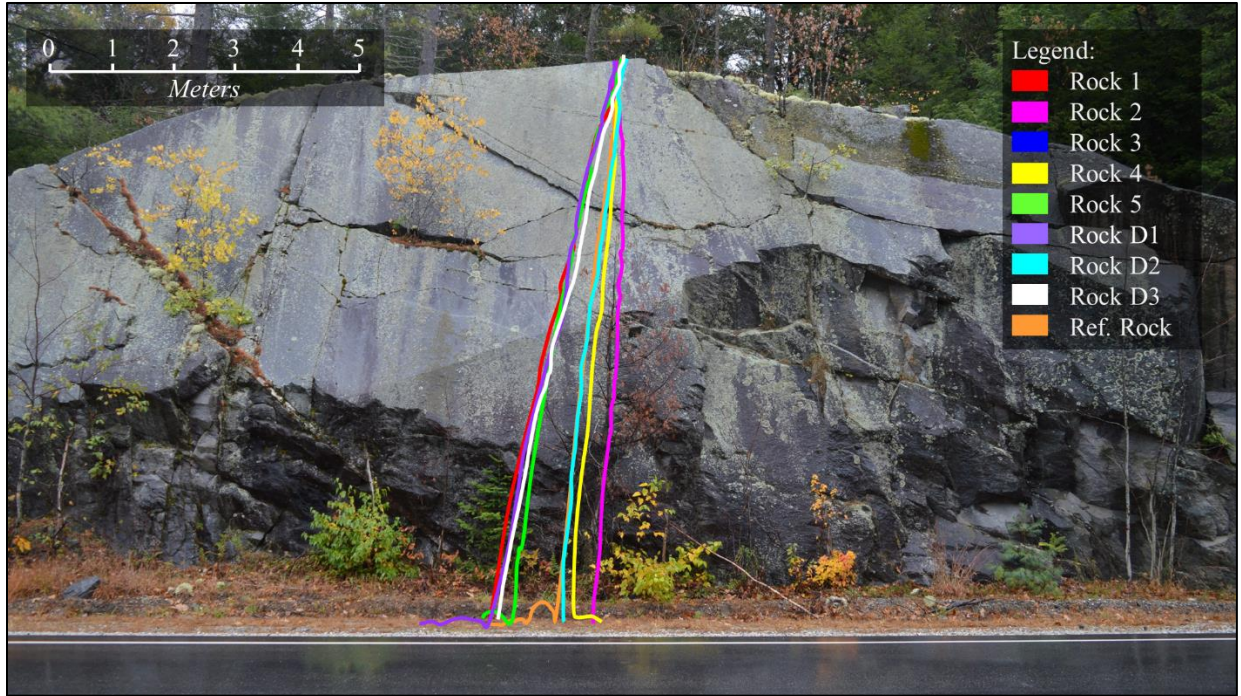
Figure 5.54. Rockfall trajectories: Orange NH.

1200 dps (B) after a 6 g bounce at 2.2 s, with major rotation about the X and Z axes (highest inertia). The block bounced on the catchment ditch with a deceleration of 65 g, followed by an increase in rotational velocity until a second bounce on the ground surface.

The scalar velocity measured at the bottom of the slope was approximately 20 m/s, and the rapid block movement increased the data noise during the fall. Although the time instants of start and end of block motion match the video measurements, the altimeter recorded slightly higher vertical positions than during video analysis.

Figures 5.57 and 5.58 present the results for rock 5, a 16 kg elongated block. It described an initial rolling motion (A), followed by free fall at 760 dps (B) with major rotation about Y (smallest moment of inertia), and experienced two 30 g bounces (C) and nearly stopped rotating before describing free fall at 800 dps with significant rotation about X and Z (largest moments of inertia). The peak acceleration of 125 g (impact force of 20 kN) occurred against the ground (E),
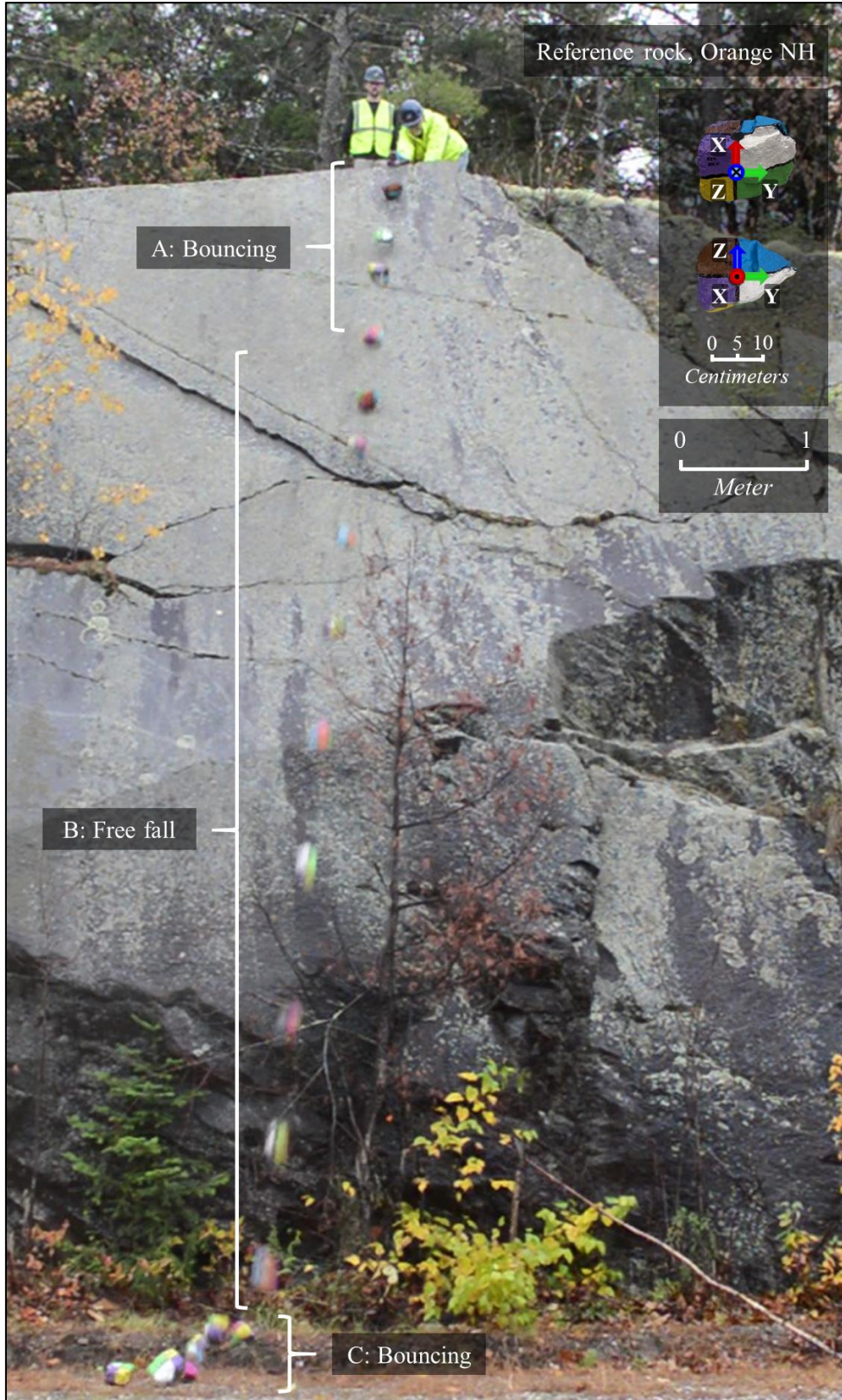
Figure 5.55. Rockfall trajectory: reference rock, Orange NH.
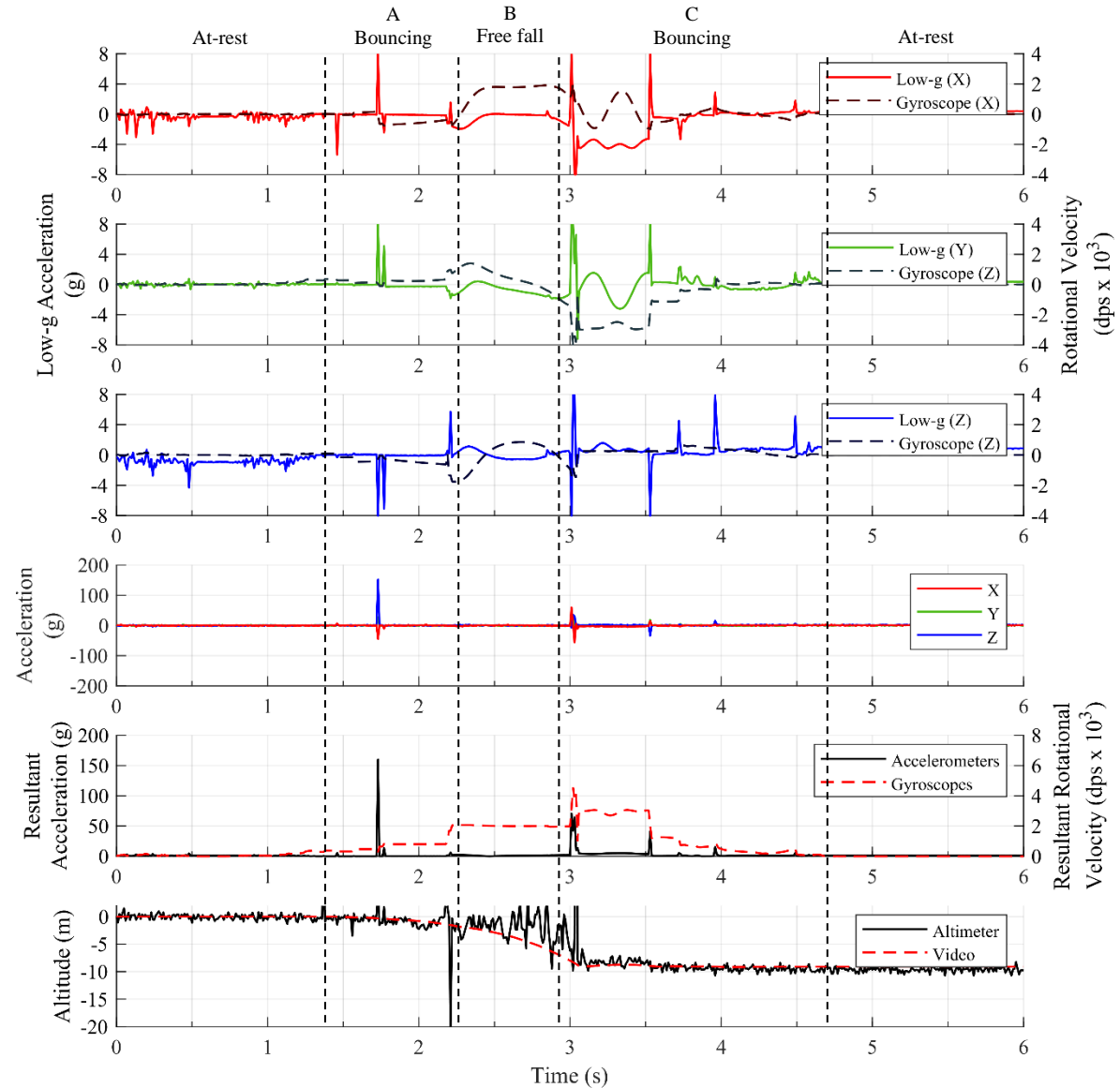
Figure 5.56. Smart Rock test data: reference rock, Orange NH.

where the rock bounced until coming to a complete stop. Unlike most field tests, the peak impact

force has not occurred upon ground contact.

185
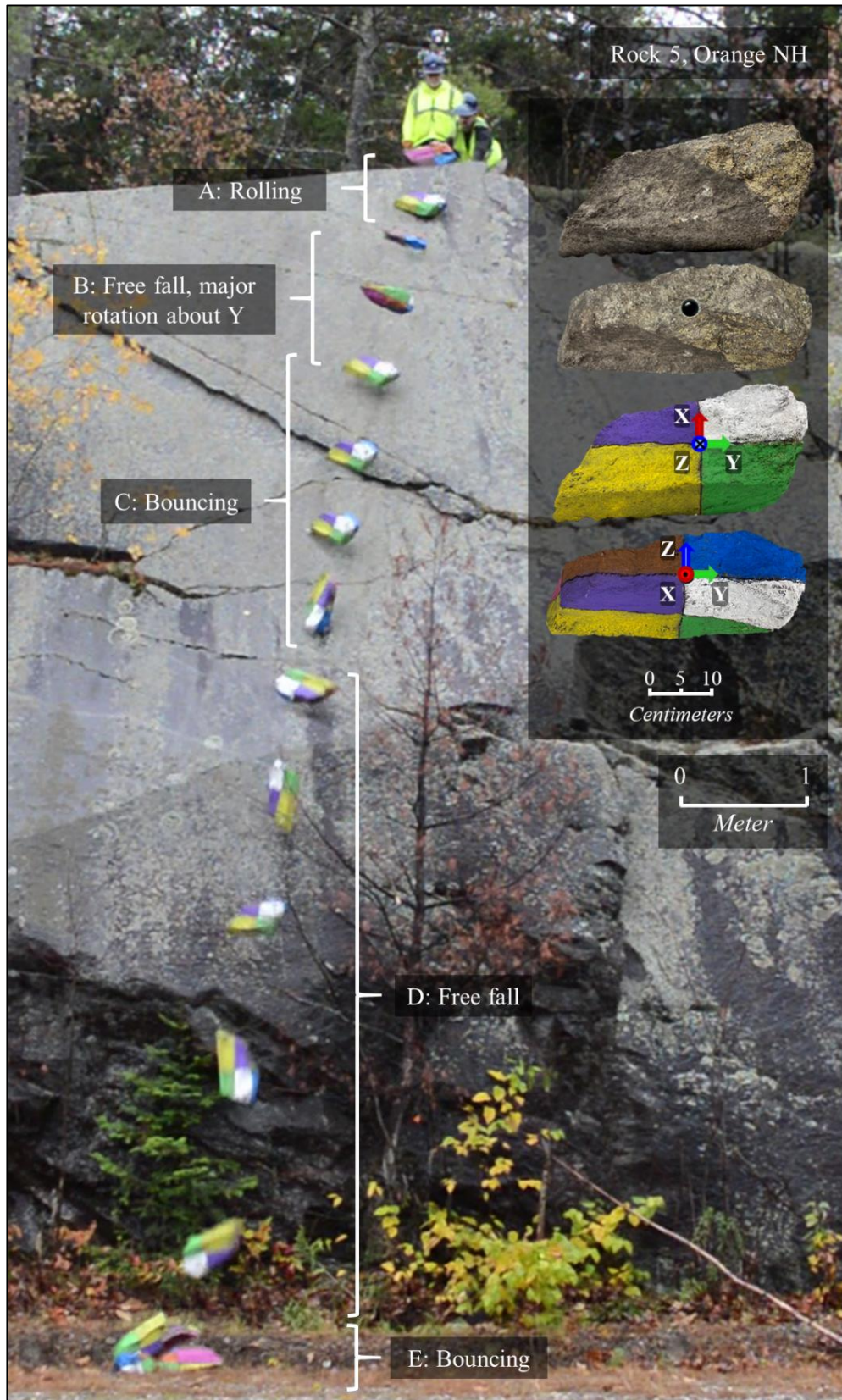
Figure 5.57. Rockfall trajectory: rock 5, Orange NH.
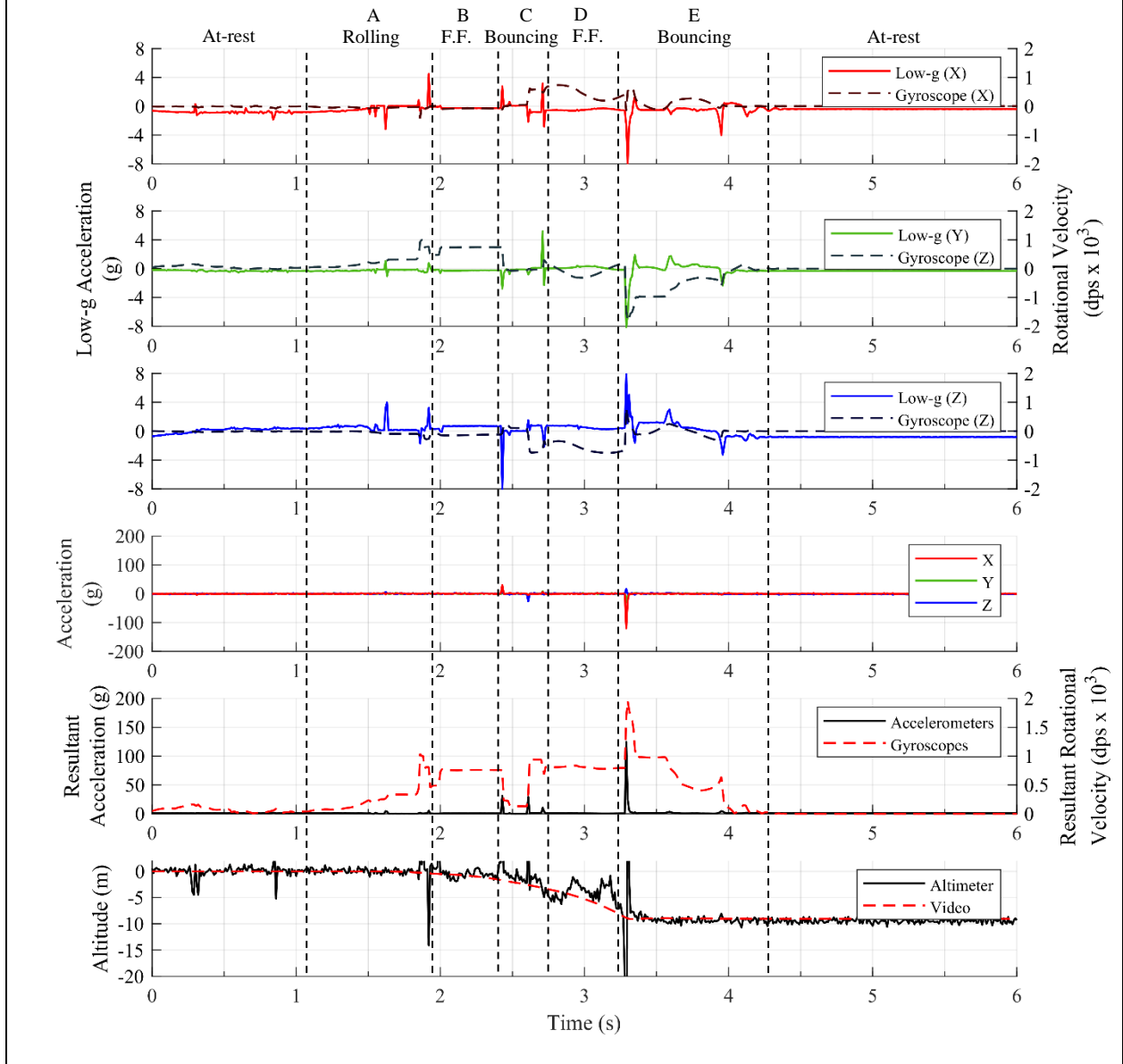
Figure 5.58. Smart Rock test data: rock 5, Orange NH.

A second test is shown in Figures 5.59 and 5.60. Rock D1 from Dover is a 4 kg compact elongated block, whose peak acceleration of 165 g also occurred during ground contact. The test
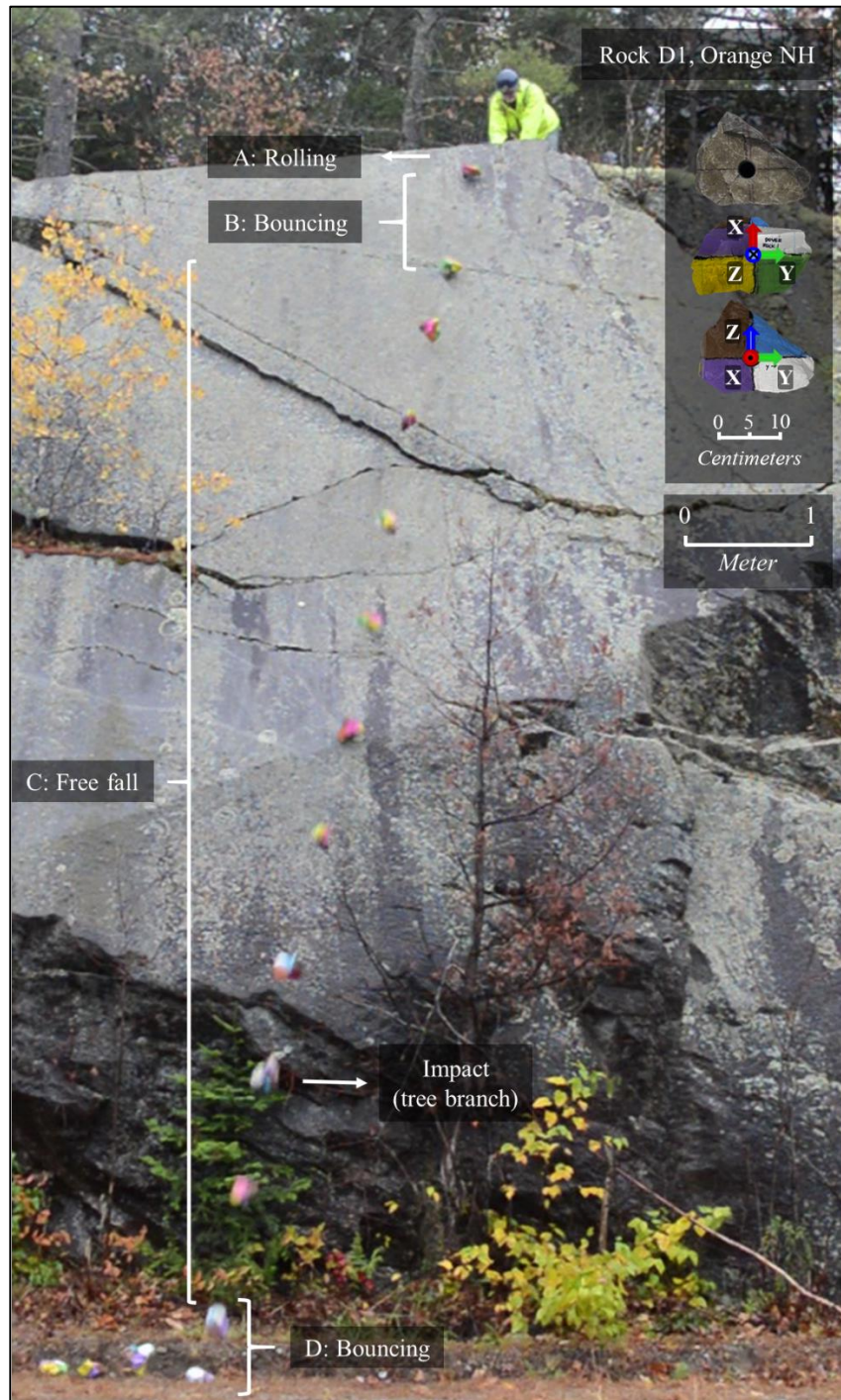
Figure 5.59. Rockfall trajectory: rock 5, Orange NH.

block experienced initial rolling (A) and bouncing (B) motions at the top of the slope face and, as

rock 5, also goes into free fall (C) until ground impact (D). The block described major rotation

about its most significant axes of inertia (X and Y) after an increase in rotation from580 dps to

1700 dps during an impact on a tree branch. Major rotation at D, however, occurred about the shortest axis of inertia (Y).
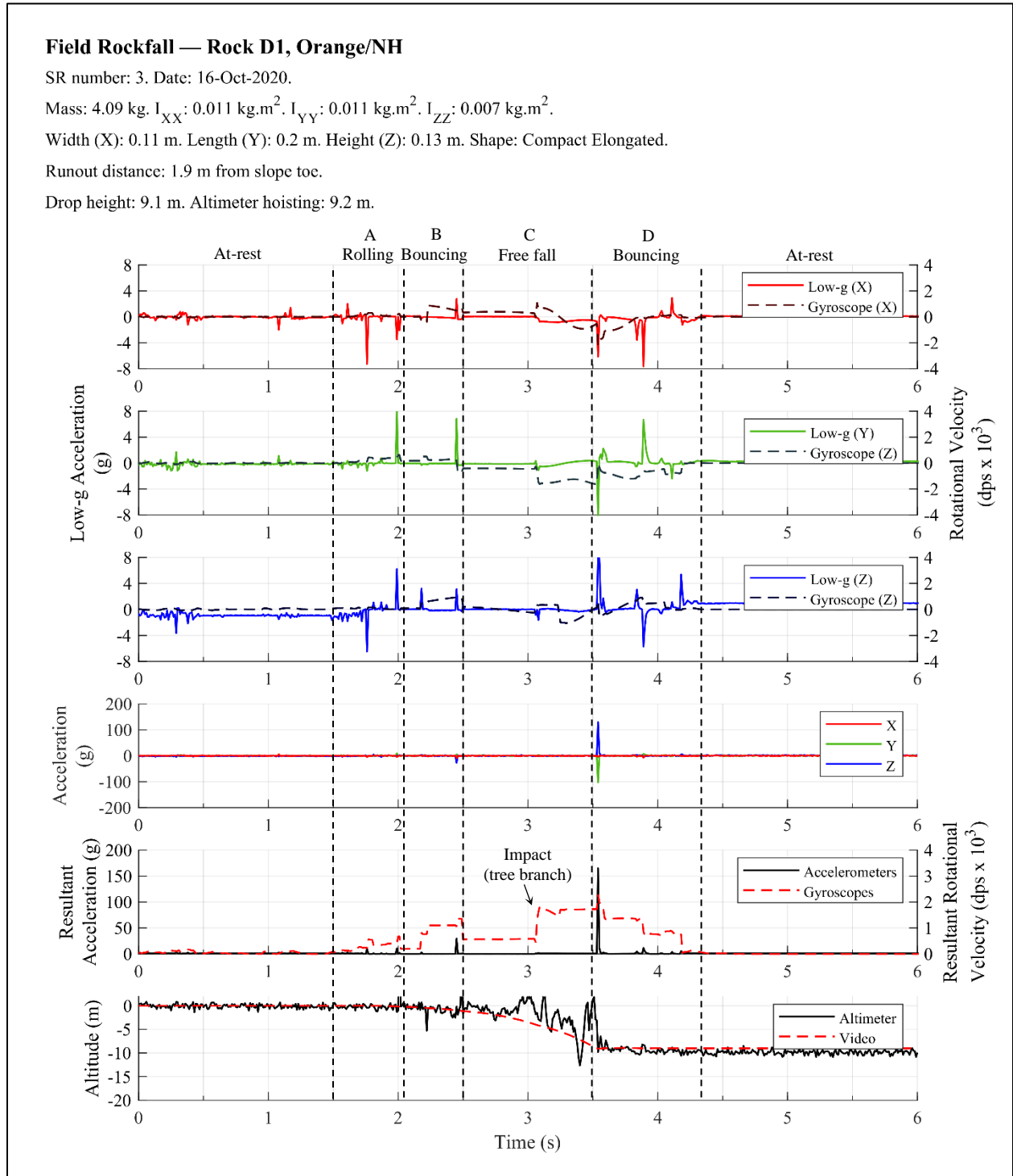
Figure 5.60. Smart Rock test data: rock D1, Orange NH.

Table 5.16 presents a summary of the results obtained at the slope in Orange. As previously shown, test rocks released from the same start location had similar trajectories and modes of motion. Even though the blocks presented different shapes and sizes, similar peak accelerations were measured for all experimental trials with recorded SR data. The average maximum acceleration was equal to 123 g. Although the maximum impacts occurred at different locations (rock face or catchment ditch), these tests presented the lowest variability (standard deviation) among all test sites.

Table 5.16. Field rockfall summary: Orange NH.

Rock ID	Slope angle	Drop height (m)	Displacements			Smart Rock resultant data			Maximum impact force (kN)
			Lateral (m)	Lateral dispersion (%)	Runout from toe (m)	Maximum acceleration (g)	Maximum rotational velocity (dps)	Average rotational velocity (dps)	
Ref	65° / 75°	9.1	-2.2	20	3.4	160	4568	1235	8
1	65° / 75°	9.1	-2.2	20	2.0	151	1742	830	21
2	65° / 75°	9.1	-0.5	5	1.8	110	3220	1207	11
4	65° / 75°	9.1	-0.4	4	1.6	66	1799	362	12
5	65° / 75°	9.1	-2.3	21	2.1	125	1959	562	20
D1	65° / 75°	9.1	-3.3	31	1.9	165	2288	822	7
D2*	65° / 75°	9.1	-3.2	30	1.5	-	-	-	-
D3	65° / 75°	9.1	-2.1	19	2.5	85	1982	789	10
		Average	2.0	19	2.1	123	2508	830	13
		Standard deviation	1.1	10	0.6	38	1038	316	6

The maximum lateral dispersions occurred because of rock bouncing on the catchment ditch after ground impact. However, such dispersion is not concerning given the uniform ditch conditions and significant distance of the farthest endpoint locations from the road. The runout histogram for these experimental trials is shown in Figure 5.61. All test blocks stopped at least 1 meter away from the road shoulder, indicating that the catchment ditch has been effective against the rockfalls evaluated at this location.
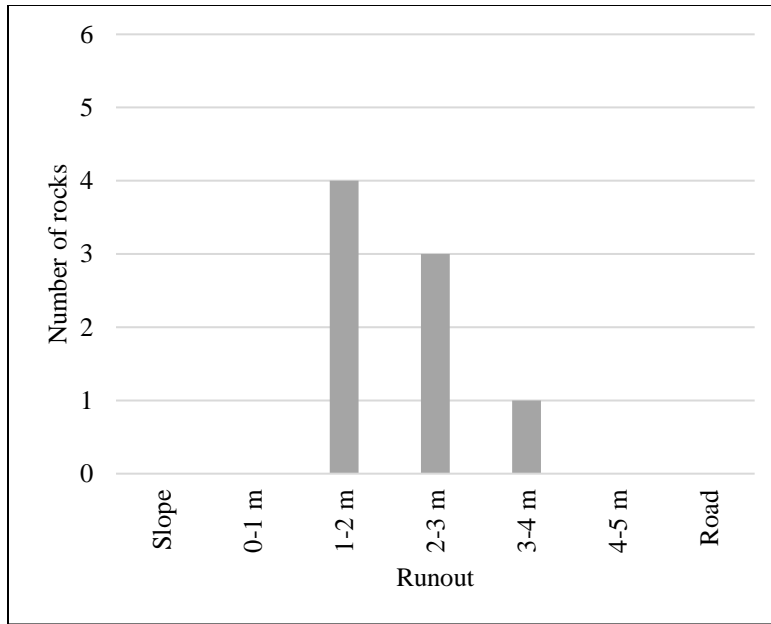
Figure 5.61. Runout histogram: Orange NH.

5.7. Townshend, VT

Eight experimental rockfalls were conducted in two sections of a two-lane amphibolite and greenstone A-rated rock cut in Townshend, VT. These tests were performed during scaling work conducted for the Vermont Agency of Transportation (VTrans) by Ameritech. During ongoing work, the high rockfall risk required one lane to be temporarily closed, and a concrete barrier was placed between both lanes in the middle of the road. Six experiments were carried out with local rocks (and the reference rock) previously prepared in the laboratory. Two additional rockfalls were performed with rocks drilled in place during scaling work.

5.7.1. Rocks prepared in the laboratory

Five local rocks (and the reference rock), whose characteristics are presented in Table 5.17, were evaluated in a 19 m tall portion of the road cut. The density values were estimated because all drilled cores were laminated, and specimen lengths larger than 5 mm could not be retrieved.

191

Table 5.17. Test block characteristics: Townshend NH.

ID	Weight (kg)		Density (kg/m³)	Dimensions (m)			Shape	Mass moment of inertia (kg*m²)		
	Before drill.	After drill.		Length, Y	Width, X	Height, Z		I_{XX}	I_{YY}	I_{ZZ}
Ref	-	5.21	2660*	0.20	0.12	0.12	Compact Elongated	0.024	0.024	0.013
1	11.72	11.58	2660*	0.27	0.13	0.14	Compact Elongated	0.089	0.031	0.086
2	5.85	5.75	2660*	0.29	0.10	0.12	Elongated	0.032	0.009	0.030
3	6.27	6.14	2660*	0.20	0.11	0.12	Compact Elongated	0.039	0.140	0.035
4	6.87	6.76	2660*	0.30	0.09	0.13	Elongated	0.045	0.011	0.042
5	11.51	11.40	2660*	0.39	0.12	0.14	Elongated	0.118	0.029	0.115

* Estimated density

The rockfall trajectories for the six tests performed are presented in Figure 5.62. Due to ongoing scaling work, the catchment ditch was covered with boulders and rock talus. The toe of the slope is inclined towards the road and located 2.5 m away from the road shoulder. In addition,

Figure 5.62. Rockfall trajectories: Townshend VT. Please note some horizontal distortion in the trajectories due to the camera position and wide lenses to capture the entire slope. The detailed trajectories show accurate positions.

the slope angles during the scaling work varied between 30º and 80º in the generated cross-sections (Figure 5.65). The angle reduction in the slope cross-section at approximately 9 m above the ground level led to block trajectories to bounce and affect horizontal dispersion, as observed in Figure 5.63. Certain portions of the 30º section in the slope profile were covered with soil.
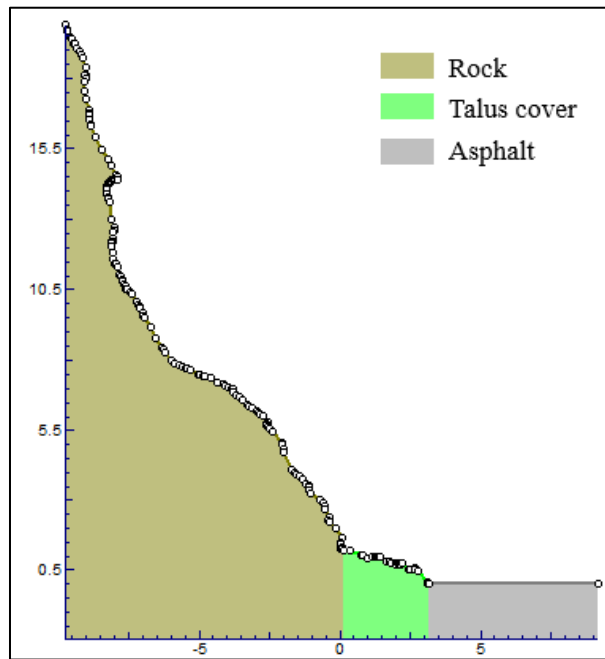
Figure 5.63. Sample cross-section of the test slope in Townshend imported in RocFall. Units in meters.

During the Townshend tests, the reference rock experienced a wide range of motion between rolling, free fall, and bouncing, as shown in Figures 5.64 and 5.65. The initial rolling motion experienced (A) developed an 1100 dps resultant rotational rate in 0.5 s, with major rotation about its shortest axis of inertia (Y), and described free fall with a similar rotation rate of 900 dps. The reference rock gradually started to rotate strictly about its X and Z axis (highest moments of inertia) and bounced after approximately 10 m of vertical displacement at C. The bounce at mid-slope measured a peak g-force of 206 g, leading to an impact force of 11 kN. A bounce height of 1 m was observed in the video measurements. The block then fell freely (D) at a constant rotation rate of 2000 dps with a predominant rotation about its X and Z axes. It stopped immediately after

impact at E near 5.5 s, indicating that the rock talus catchment ditch fully absorbed the kinetic

energy. A runout distance of 0.8 m from the toe of the slope was measured.
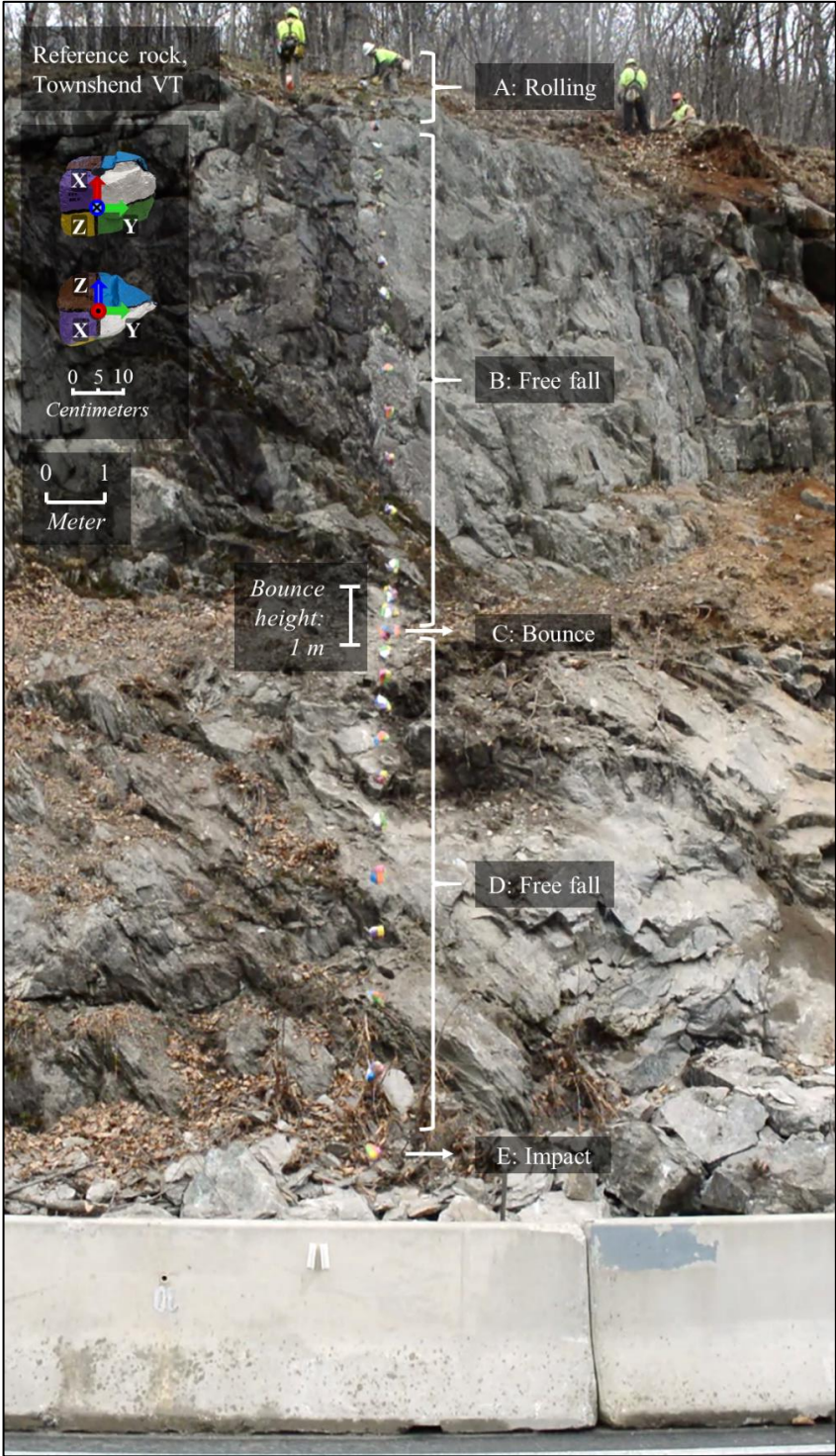
Figure 5.64. Rockfall trajectory: reference rock, Townshend VT.
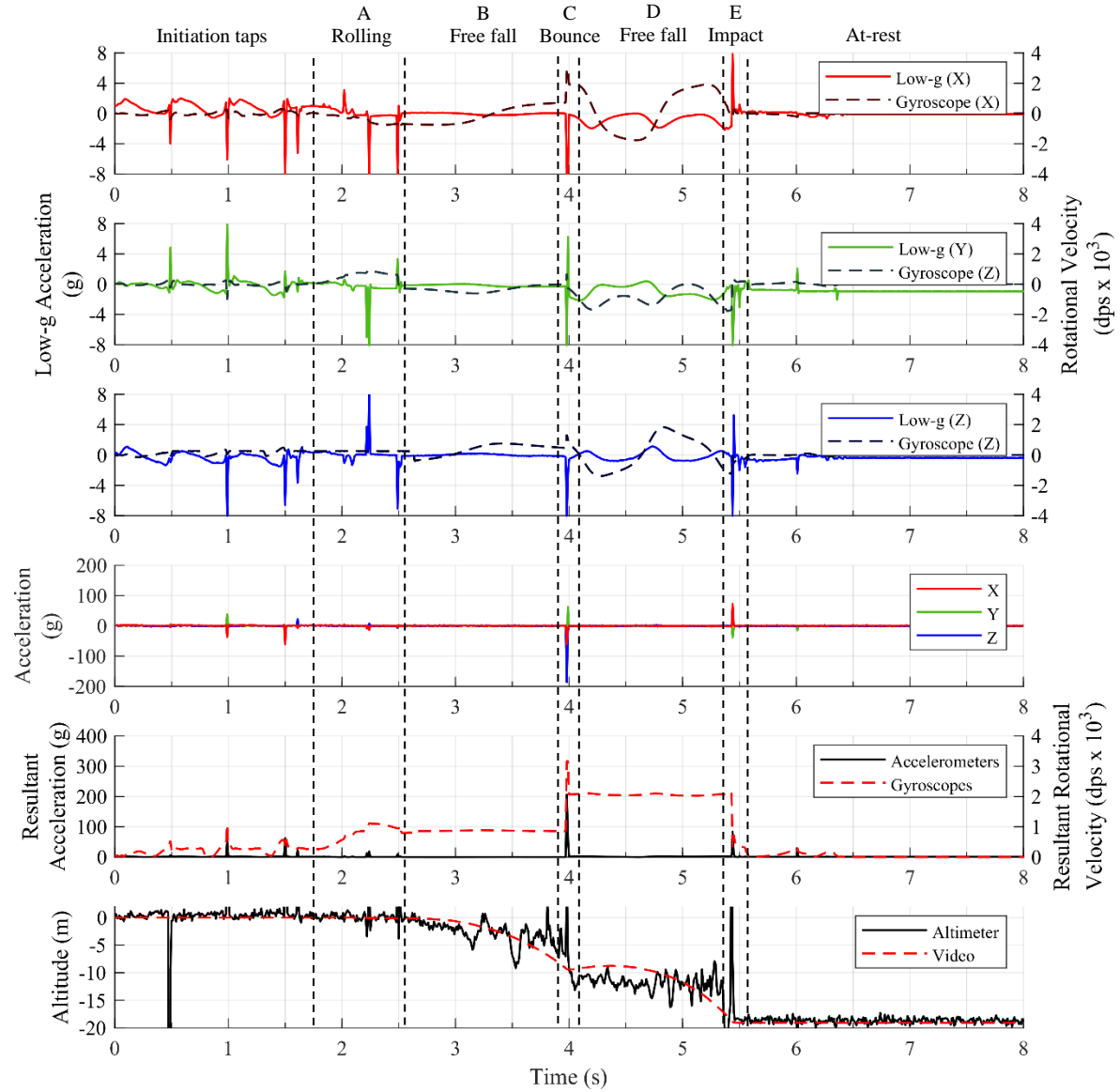
Figure 5.65. Smart Rock data: reference rock, Townshend VT.

Rock 1, an 11.7 kg compact elongated block, was released from a 19 m drop height (Figures 5.66 and 5.67). Rock 1 rotated at an approximate rate of 1200 dps (A) until a peak acceleration of
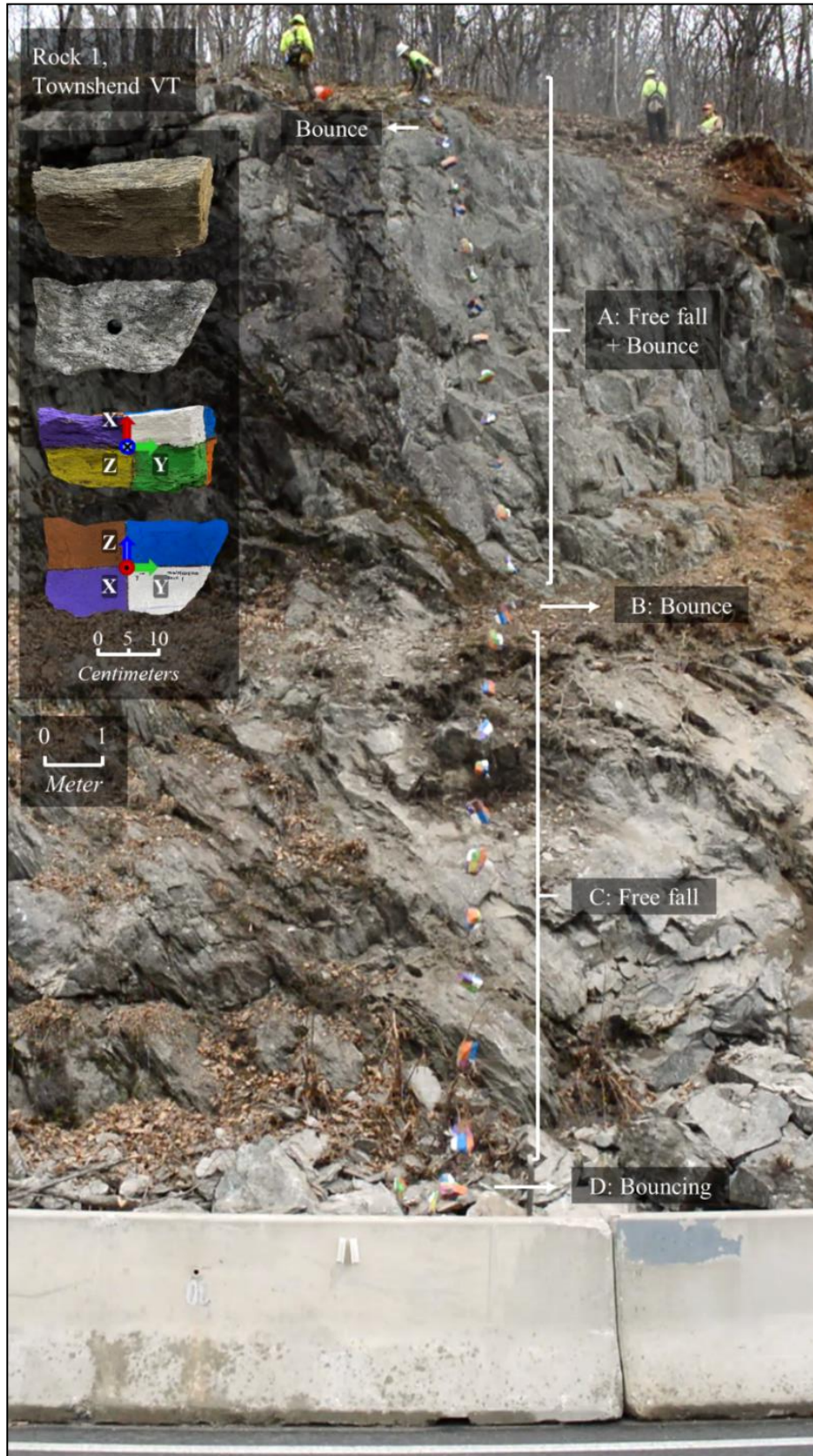
Figure 5.66. Rockfall trajectory: rock 1, Townshend, VT.
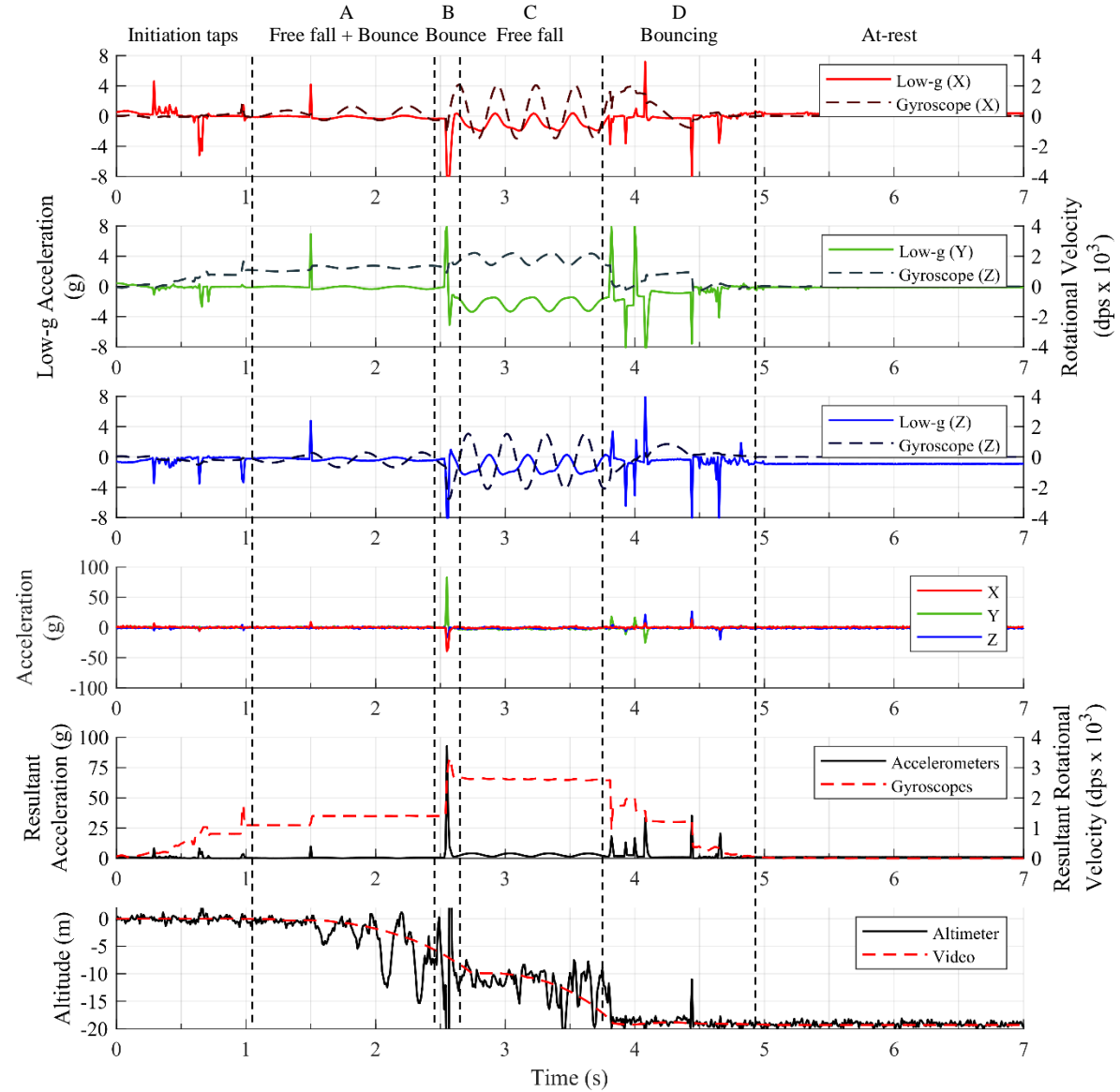
Figure 5.67. Smart Rock data: rock 1, Townshend VT.

93 g (11 kN force) at mid-slope (B). The block rotation increased to 2640 dps at a second free fall

(C) before bouncing against the talus catchment ditch and reaching the road (D). Due to the barrier

197

positioned for rockfall protection, video measurements could not be obtained at the lower portion of the trajectory that reached the road. Rock 1 rotated about all three principal axes, but predominant rotation about its shortest axis of inertia (Y) was observed during the entire trajectory.

Rock 3 is a 6 kg compact elongated rock that bounced two times against the rock face before ground contact (Figures 5.68 and 5.69). An initial rotation rate of 960 dps about Y (smallest inertia) at A was followed by a similar rotation rate in free fall (B) and predominant rotation about Y. Two consecutive impacts at C and E recorded impact accelerations of 92 g and 295 g, producing 6 and 18 kN impact forces, respectively. The rotation rate of nearly 1000 dps stayed constant between C and E, although the block described predominant rotation about the X and Z (largest axes of inertia).

The resultant rotational velocity of the block increased to 2800 dps after the second bounce, and rotation occurred about all three axes. Major rotation, however, happened about Y. There is a sharp decrease in rotational velocity after ground impact at G, whose measured deceleration was equal to 106 g. Rock 3 completely stopped at the base of the toe of the slope (0 m runout). During the fall, the significant block motion considerably affected the noise level in the altimeter measurements, especially during impacts. The start and end times of rockfall, however, match the video measurements.

Significant data noise in the altimeter measurements visually suggest that the video data is displayed inaccurately. However, as previously described in Chapter 4, each video measurement is matched with the sensor data primarily based on the acceleration and rotation plots. Therefore, although the altimeter is a promising tool to better assess vertical displacements during rockfalls, it was not reliable in these field experiments. The initial and final altitude data (at slower rock motion), however, do reproduce reality.
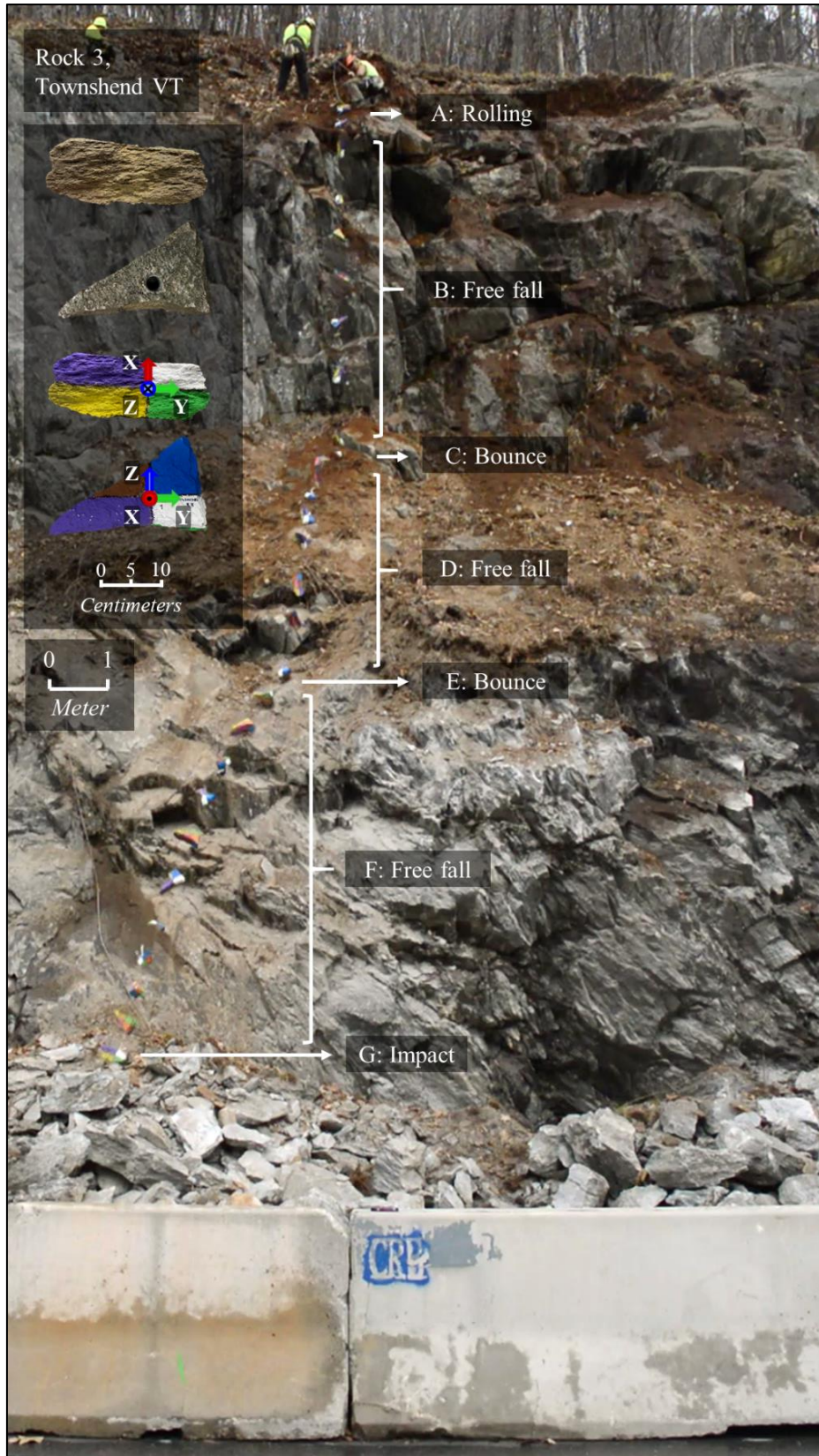
Figure 5.68. Rockfall trajectory: rock 3, Townshend VT.
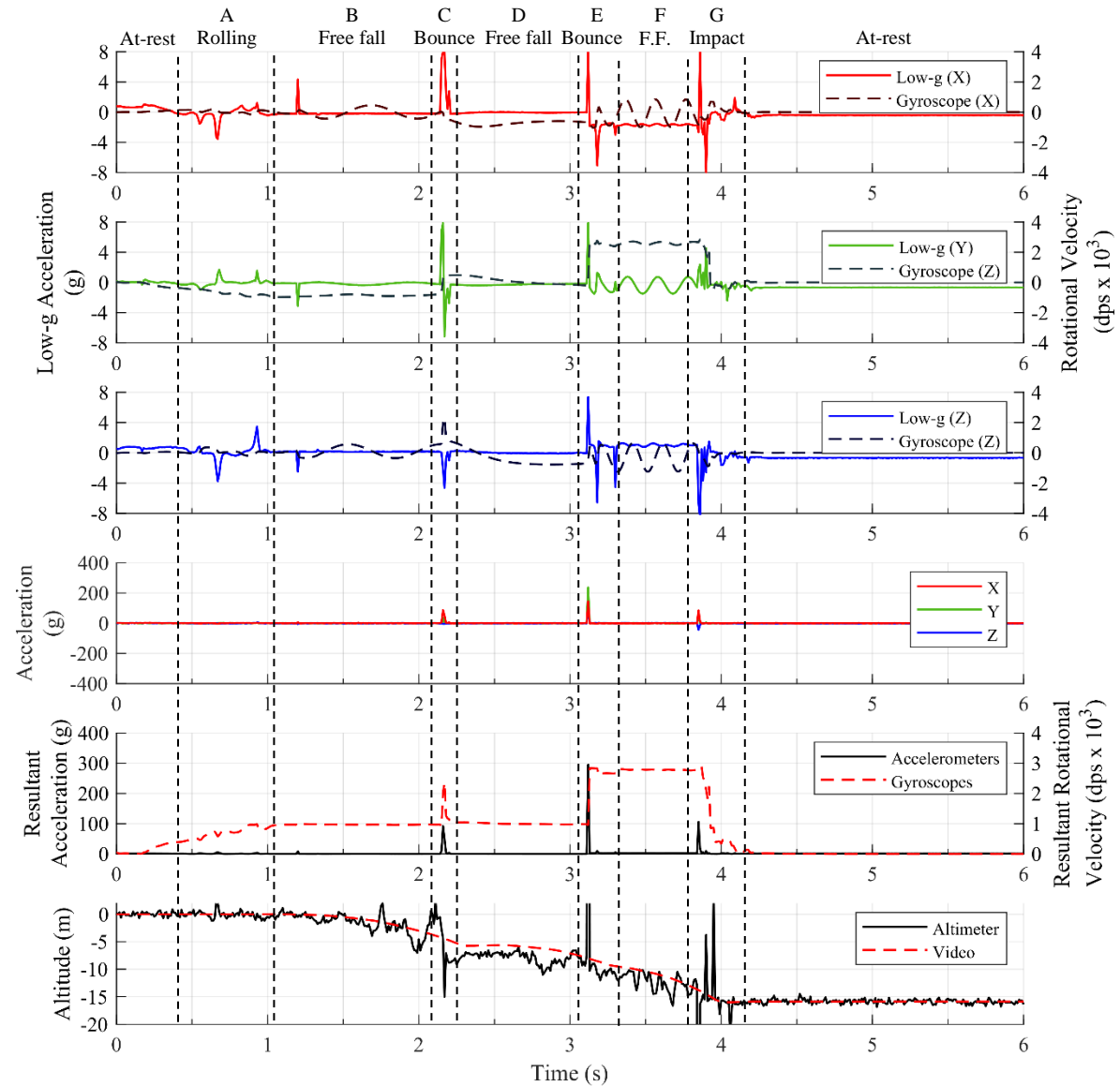
Figure 5.69. Smart Rock test data: rock 3, Townshend VT.

Table 5.18 presents a summary of the test results from the locks previously prepared in the laboratory. All test blocks experienced similar modes of motion, with one or two impacts at mid-

slope separating two major free-falls. The maximum resultant acceleration was equal to 165 g, and the test blocks produced an average maximum impact force of 11 kN. Except for rock 5, which experienced the lowest peak acceleration, all remaining rocks exerted peak impact forces above 10 kN.

Table 5.18. Field rockfall summary: Townshend VT.

Rock ID	Slope angle	Drop height (m)	Displacements			Smart Rock resultant data			Maximum impact force (kN)
			Lateral (m)	Lateral dispersion (%)	Runout from toe (m)	Maximum acceleration (g)	Maximum rotational velocity (dps)	Average rotational velocity (dps)	
Ref	75° / 55°	19.0	0.2	1%	0.8	206	3172	869	11
1	75° / 55°	19.0	0.9	4%	6.6	93	3304	1424	11
2	75° / 55°	19.0	0.4	2%	3.2	182	3825	1448	10
3	80° / 45°	17.0	-4.0	16%	0.0	295	2901	1209	18
4	80° / 45°	17.0	-2.0	8%	1.6	147	3929	1342	10
5	80° / 45°	17.0	-2.1	8%	0.3	66	3063	690	7
		Average	1.4	6%	2.8	165	3366	1164	11
	Standard deviation		1.9	6%	2.9	83	419	314	4

The location of the maximum impact force varied between the experimental tests. Three tests experienced their peak g-forces during bouncing at mid-slope (1, 3, reference rock), while the remaining blocks had their peak accelerations measured upon impact on the catchment ditch (2, 4, 5).

All test blocks had an increase in rotational velocity after bouncing in the middle of their trajectories and had predominant rotation about their shortest axis of inertia, Y, except for the reference rock. This difference in behavior probably occurs because the local rocks from Townshend are more elongated than the 5 kg metamorphic block. All tests except rock 3 had

maximum rotation rates higher than 3000 dps (8.3 rotations/s). The remaining test trajectories and sensor data at this site location can be found in Appendix B.7.

An average lateral dispersion of 6% was measured. The runout histogram for these field trials is presented in Figure 5.70. Two of the three tests (except for the reference rock) released from the 19 m tall cross-section reached the road, and all three tests dropped from the 17 m tall cross-section stopped within the ditch limits. The measured endpoint locations demonstrate the need for the scaling work performed and suggest that significant bounce heights do not necessarily imply concerning lateral dispersions or endpoint locations.
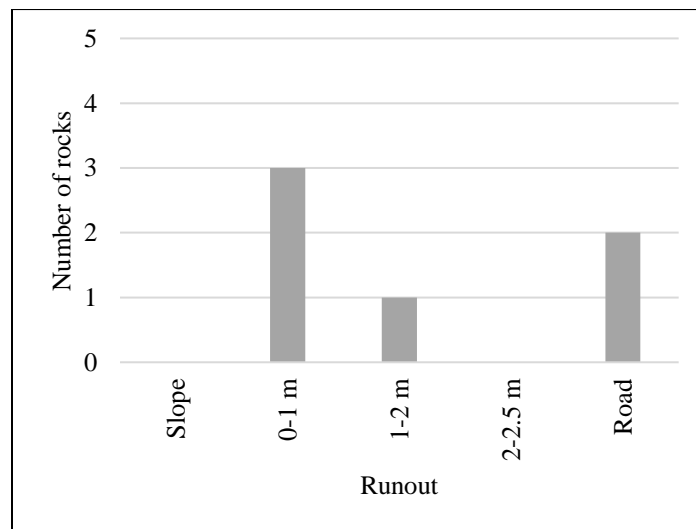
Figure 5.70. Runout histogram: Townshend VT.

5.7.2. Rocks drilled in-place

Two additional rockfall experiments were performed at a different portion of the Townshend site. Rocks in place were drilled prior to scaling, and the Smart Rock sensors were inserted for instrumentation of large-scale rockfalls. Due to the significant size of the scaled blocks, whose estimated characteristics are presented in Table 5.19, the holes could not be drilled at the center of gravity of these blocks. The SRs were placed by the rock scalers in holes that they drilled with the

202

portable hand drill used in the laboratory, and the sensor orientations inside the scaled blocks were not known. The locations of the SRs were spray painted for visual tracking since video tracking was not possible in these experiments due to the difficulty in accurately estimating the SR position.

The first test was conducted with a single SR on a roughly 2000 kg "compact" block (Figure 5.71), and data were recorded at a sampling frequency of 100 Hz. The scaled block trajectory and SR data are presented in Figures 5.72 and 5.73.

Table 5.19. Scaled block characteristics: Townshend VT.

ID	Weight (kg)		Density (kg/m³)	Dimensions (m)			Shape	Mass moment of inertia (kg*m²)		
	Before drill.	After drill.		Length	Width	Height		I_{XX}	I_{YY}	I_{ZZ}
1	2300	2300	2660*	1.20	0.60	1.20	Compact	550	350	350
2	9600	9600	2660*	3.00	1.00	1.20	Elongated	8350	1950	8000
* Estimated density										

Figure 5.71. First scaled rock (a) during preparation, and (b) before scaling (the pink dot marks the SR location).

Figure 5.72. Rockfall trajectory: first scaled block, Townshend VT.

Field Rockfall — Scaled Rock 1, Townshend/VT

SR number: 5. Date: 11-Nov-2020.

Mass: 2300 kg. I_{XX}: 550 kg.m^2. I_{YY}: 350 kg.m^2. I_{ZZ}: 350 kg.m^2.

Width (X): 0.6 m. Length (Y): 1.2 m. Height (Z): 1.2 m. Shape: Compact.

Runout distance: 4.7 m from road shoulder.

Drop height: not measured. Altimeter hoisting: 10.8 m.

* The sensor orientation was not known, and the moment of inertia estimates about X, Y, and Z are relative to the width, length, and height of the block.
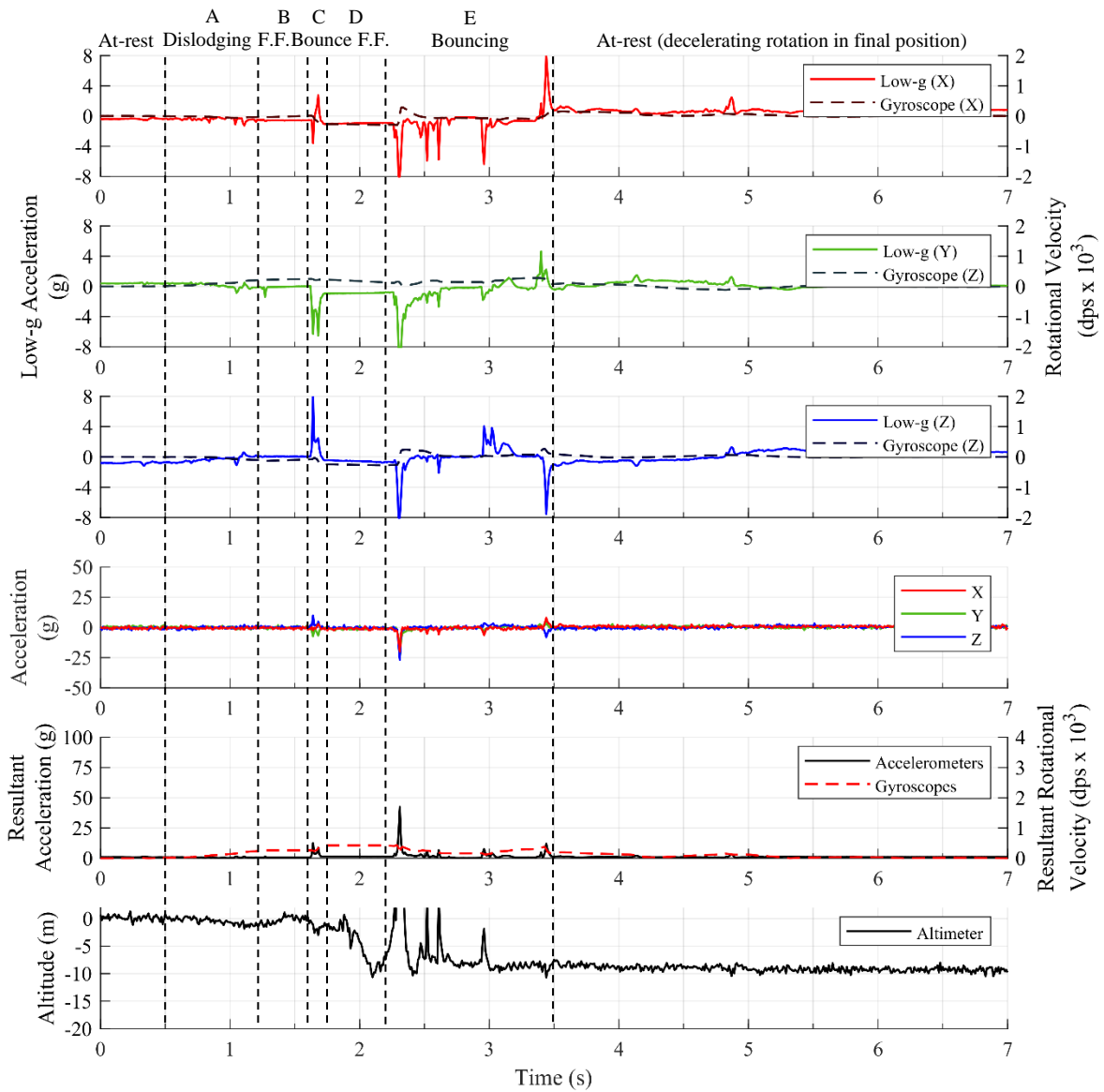
Figure 5.73. Smart Rock test data: first scaled rock, Townshend VT.

After the block was manually dislodged by the scalers (A), it went into free fall (B, D) with an intermediate bounce at mid-slope (C) and a second bounce upon ground contact (E). The peak

205

acceleration of 42 g occurred at C, and an impact force of approximately 1 MN was experienced. The maximum resultant rotation of 425 dps was developed during the second free fall (D).

A second test was conducted with an elongated block of minimum dimension equal to 1 m. Due to the significant length of the scaled rock, three SRs were positioned inside the block (Figure 5.74). The top and bottom sensors had the altimeter enabled and recorded data at 100 Hz. The middle SR had the altimeter disabled and recorded data at 500 Hz. The rock was scaled using air pillows placed inside the discontinuity on the upper left side of the block and pry-bars.
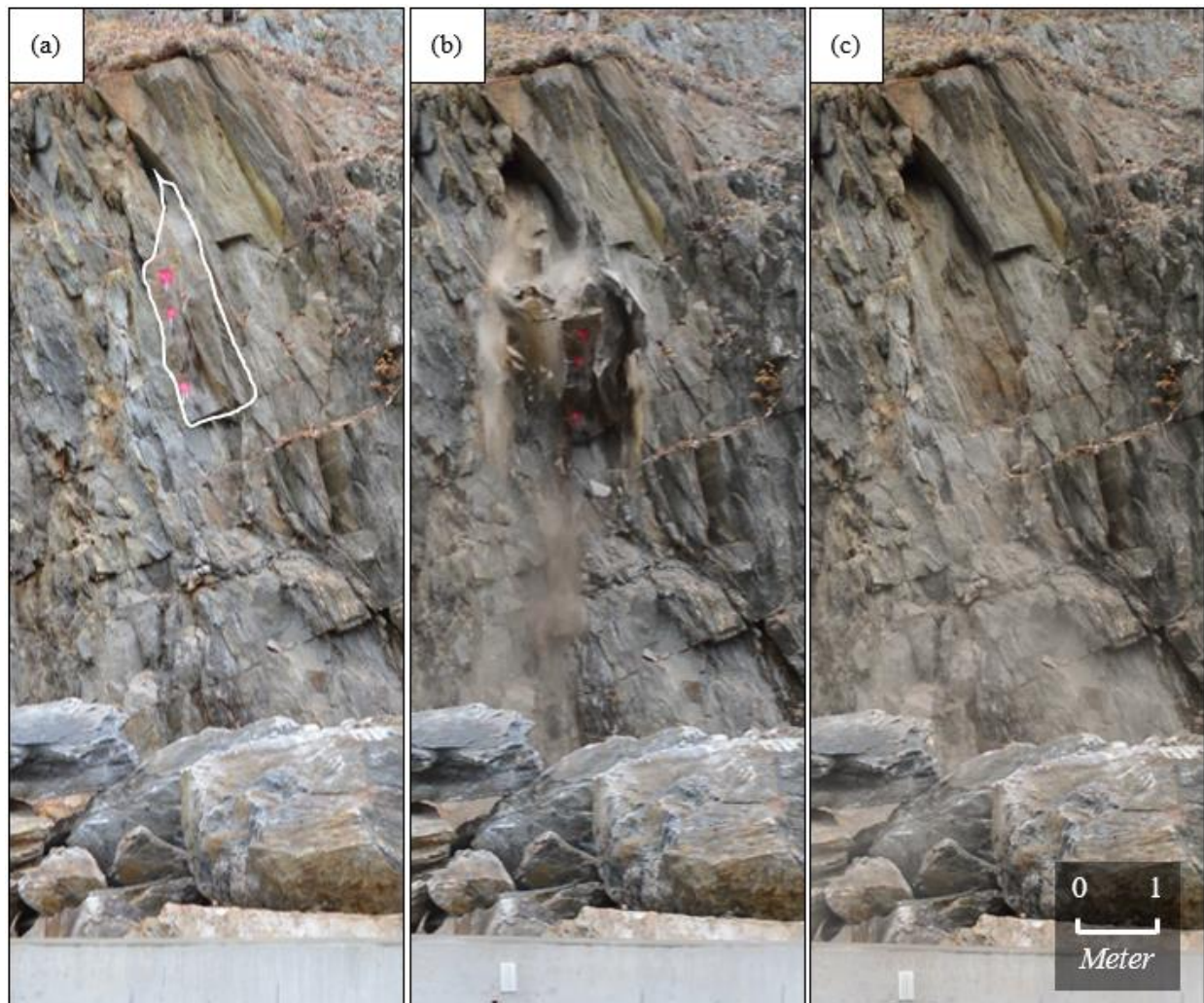
Figure 5.74. Second scaled rock (a) prior to rockfall, (b) during rockfall, and (c) after rockfall.

From frontal and lateral video recordings, although position tracking was not possible, it was observed that the block starts dislodging from the top and describes free fall. The top of the block then impacts the ground surface, and the scaled rock bounces while rotating about the point of impact on the ground (near the top SR), until completely stopping.

Figure 5.75 presents the SR data output for the sensor placed at the top of the scaled block where the movement first started due to the location of the mat and where the block first impacts the ground. Before a peak acceleration of 148 g upon ground impact, the block free fell at a recorded rotational velocity of 100 dps. The maximum impact force estimated for this sensor was equal to 14 MN. The altimeter noise does not allow clear visualization of rock position but allowed to easily identify the test in the sensor data and the moment of ground impact, as the three initiation taps before the beginning of the test could not be performed. Block rotation is significantly lower than 1000 dps until ground impacts and shows a clear peak when the block rotates about the top SR (3.7 s).

The data recorded with the 500 Hz SR in the middle of the scaled block is presented in Figure 5.76. As seen in the top SR, the middle Smart Rock also described a resultant rotational velocity of 100 dps during free fall. A smaller peak acceleration of 27 g was recorded upon impact, implying an impact force of approximately 2.5 MN. The rotation rate measured during rock bouncing was smaller than recorded with the top SR, and a peak resultant rotation of 190 dps was observed.

Finally, the data output for the sensor placed at the bottom of the scaled rock is displayed in Figure 5.77. A lower acceleration of 17 g was recorded during ground impact, exerting an impact force of approximately 1.6 MN. The block rotation during free fall was also equal to 100 dps, and

block rotation during bouncing behavior was very similar to the measured data with the middle sensor.
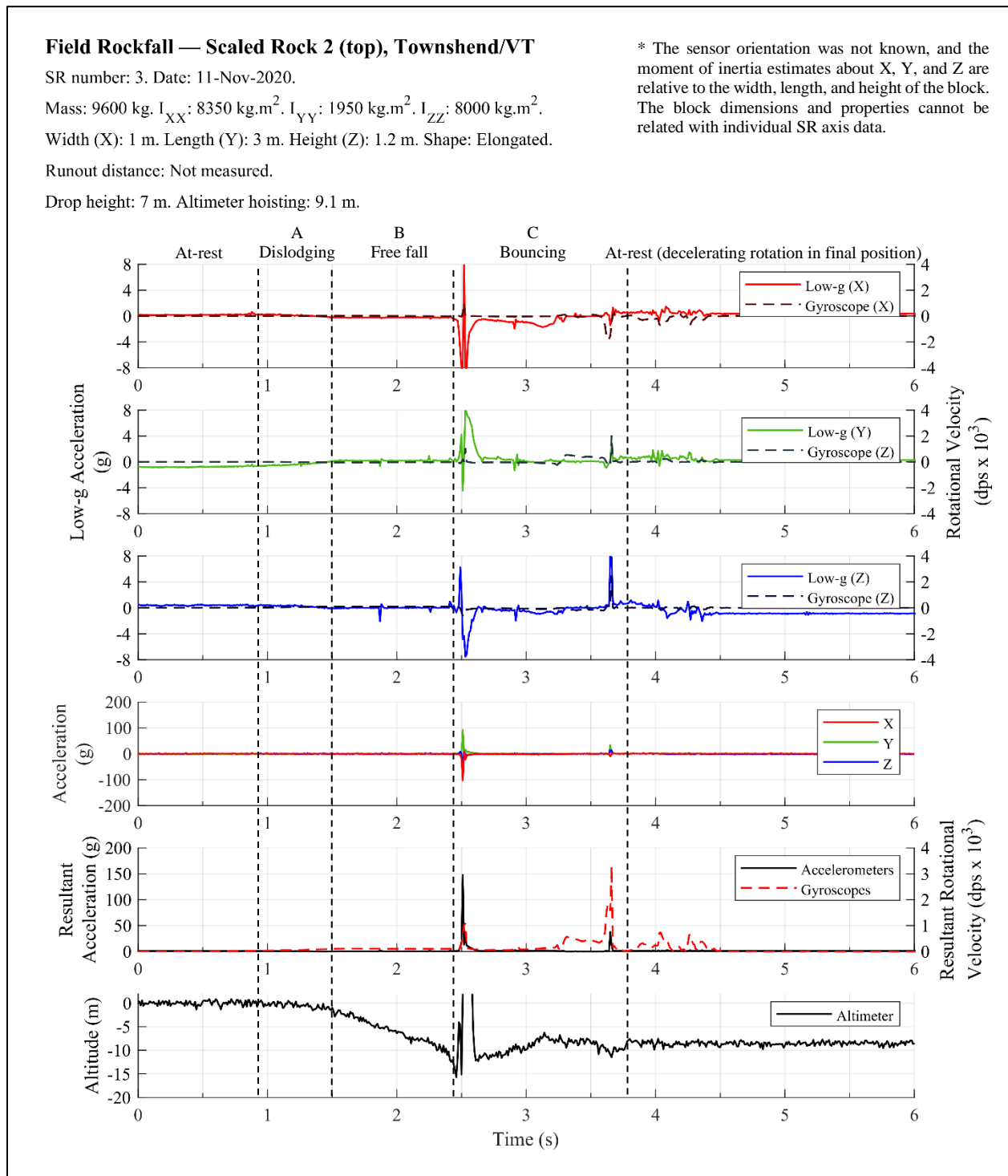
Figure 5.75. Smart Rock test data: second scaled rock (top), Townshend VT.

Field Rockfall — Scaled Rock 2 (middle), Townshend/NH

SR number: 6. Date: 11-Nov-2020.

Mass: 9600 kg. I_{XX}: 8350 kg.m^2. I_{YY}: 1950 kg.m^2. I_{ZZ}: 8000 kg.m^2.

Width (X): 0.086 m. Length (Y): 0.074 m. Height (Z): 0.072 m. Shape: Compact.

Runout distance: Not measured.

Drop height: 7 m.

* The sensor orientation was not known, and the moment of inertia estimates about X, Y, and Z are relative to the width, length, and height of the block. The block dimensions and properties cannot be related with individual SR axis data.
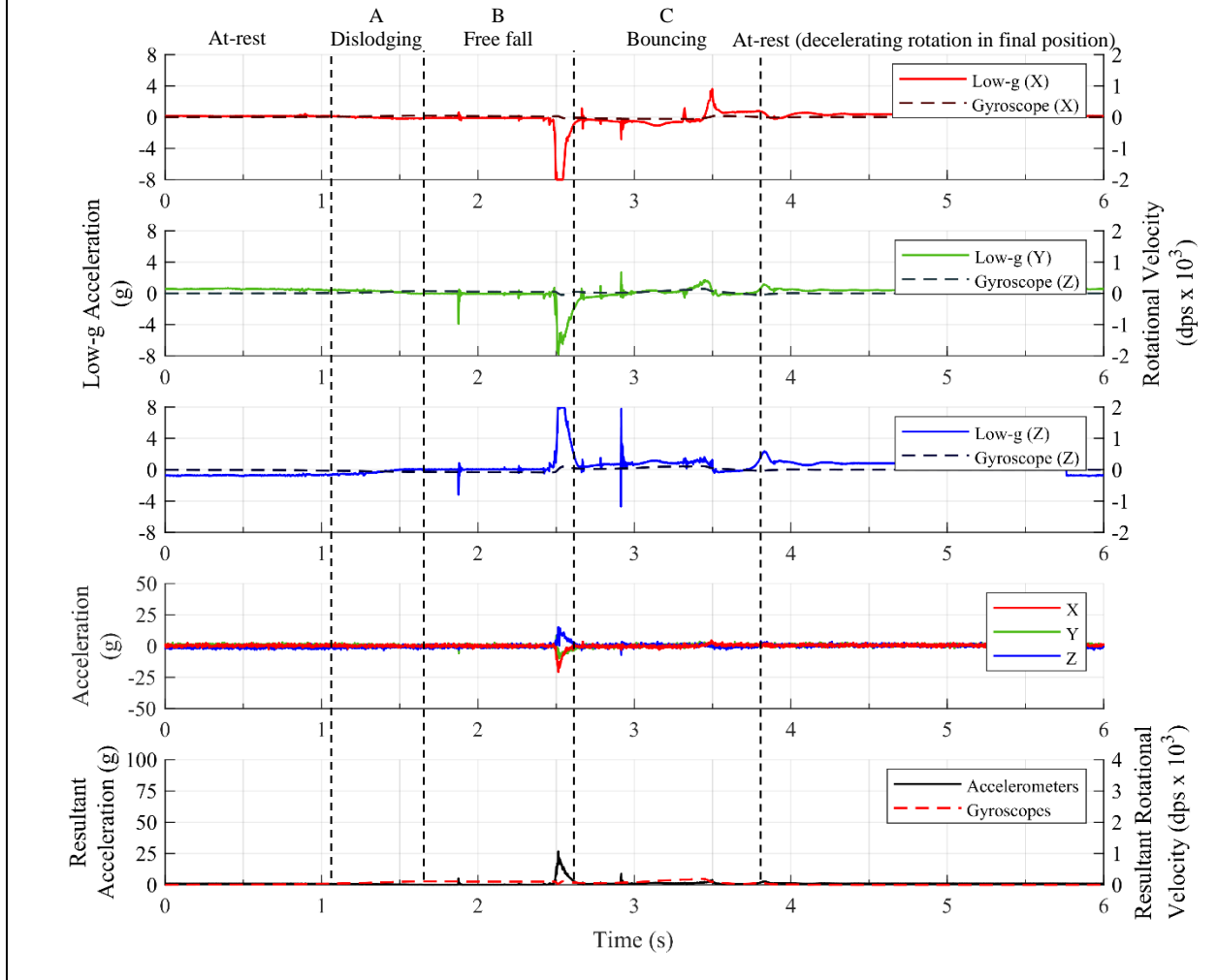
Figure 5.76. Smart Rock test data: second scaled rock (middle), Townshend VT.

A comparison between the experimental data measured from three Smart Rocks positioned in three distinct positions of a 3 m long scaled block is presented in Figure 5.78. Since the sensor rotation was not known, only the resultant data were compared. The graph demonstrates how the resultant rotation rates during rock dislodging were similar, and how the acceleration peak for the

209

top sensor stands out compared to the other two SRs. As expected, higher rotational motion was measured about the top Smart Rock, where ground contact initially occurred.

Field Rockfall — Scaled Rock 2 (bottom), Townshend/VT

SR number: 4. Date: 11-Nov-2020.

Mass: 9600 kg. I_{XX}: 8350 kg.m^2. I_{YY}: 1950 kg.m^2. I_{ZZ}: 8000 kg.m^2.

Width (X): 1 m. Length (Y): 3 m. Height (Z): 1.2 m. Shape: Elongated.

Runout distance: Not measured.

Drop height: 7 m. Altimeter hoisting: 8.9 m.

* The sensor orientation was not known, and the moment of inertia estimates about X, Y, and Z are relative to the width, length, and height of the block. The block dimensions and properties cannot be related with individual SR axis data.

Figure 5.77. Smart Rock test data: second scaled rock (bottom), Townshend VT.
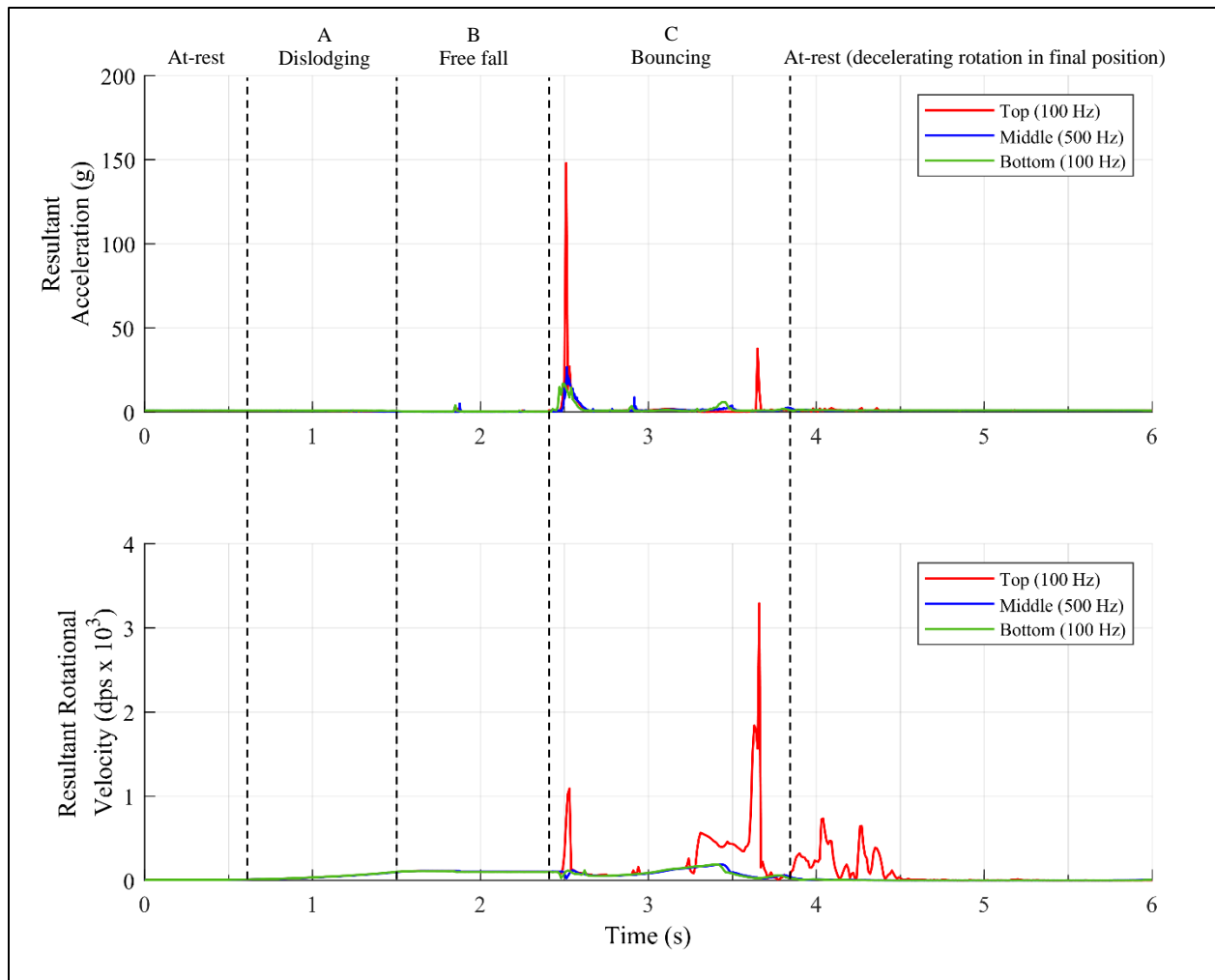
Figure 5.78. Combination of the resultant data for the three SRs in the second scaled block, Townshend VT.

The plotted accelerations and rotation for the bottom (100 Hz sampling frequency) and middle (500 Hz sampling frequency) were similar and indicate that a sampling frequency of 100 Hz is sufficient to capture rockfall motion. Further experiments will be conducted in the shake table in the laboratory to compare the 100 and 500 Hz sensors at controlled conditions. Smart Rock measurements at 100 Hz are advantageous due to the aid of the altimeter measurements to help identify rock position. Although modes of motion are also readily identified in the 500 Hz data, it is easier to relate rockfall motion with visual observations and video measurements if the altimeter is enabled.

A summary of the SR test data is presented in Table 5.20. The instrumented rockfalls performed at the Townshend site demonstrated that larger blocks tend to experience lower peak accelerations and lower rotational velocities. The lower rotational rates can be related to the significantly higher inertia of large-scale rockfalls, representing a greater difficulty in rotating the block about their principal axes. Although these rotation rates are less than in small-scale events, the rotational KE component is still expected to be considerable due to the naturally higher moments of inertia. Besides, although lower accelerations are observed, the impact forces and potential risk of damage produced are significantly greater than in small-scale rockfalls.

Table 5.20. Field rockfall summary (scaled blocks): Townshend VT.

Rock ID	Smart Rock resultant data			Maximum impact force (MN)
	Maximum acceleration (g)	Maximum rotational velocity (dps)	Average rotational velocity (dps)	
Scaled 1	42	429	171	1.0
Scaled 2 (bottom)	17	189	85	1.6
Scaled 2 (middle)	27	189	60	2.5
Scaled 2 (top)	148	3292	200	14

Table 5.20 also displays how the peak accelerations gradually decrease according to the block position, demonstrating that sensor eccentricity is a crucial factor that can strongly bias rockfall results if the drilling position is unknown.

5.8. Warner, NH

Eight experimental rockfalls were conducted on a 15 m tall, A-rated granodiorite rock cut in Warner, NH. The rock face is located parallel to NH Route 103 and has a 3.5 to 5 m wide flat catchment ditch constructed with granular soil. The slope has an average inclination between 70º and 85º (Figure 5.79). Traffic control was required during the rockfall experiments due to the proximity of the slope to the road.
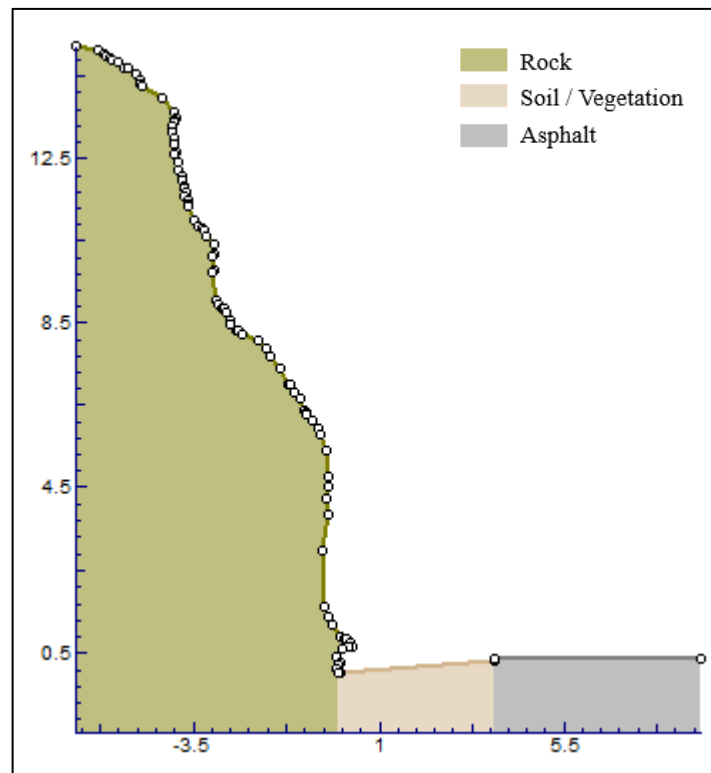
Figure 5.79. Sample cross-section of the test slope in Warner imported in RocFall. Units in meters.

The characteristics of the test blocks used are presented in Table 5.21. All eight rockfall tests were successfully recorded with the SR, including cases when the rock split and the sensor was ejected. The trajectories described by the test blocks are presented in Figure 5.80. Bouncing motion can be easily identified through changes in the rockfall paths.

Table 5.21. Test block characteristics: Warner NH.

ID	Weight (kg)		Density (kg/m³)	Dimensions (m)			Shape	Mass moment of inertia (kg*m²)		
	Before drill.	After drill.		Length, Y	Width, X	Height, Z		I_{XX}	I_{YY}	I_{ZZ}
Ref	-	5.21	2660	0.20	0.12	0.12	Compact Elongated	0.024	0.024	0.013
1	8.66	8.53	2870	0.39	0.10	0.11	Very Elongated	0.081	0.015	0.080
2	7.03	6.90	2990	0.15	0.11	0.16	Compact	0.011	0.010	0.012
3	6.79	6.67	2870	0.26	0.07	0.12	Elongated	-	-	-
4	28.85	28.64	2970	0.25	0.25	0.21	Compact	0.269	0.193	0.296
5	10.45	10.32	2910	0.35	0.16	0.07	Very Elongated	0.111	0.027	0.129
6	18.26	18.08	2940	0.37	0.18	0.27	Compact	0.152	0.080	0.134
7	24.61	24.52	2940	0.44	0.08	0.33	Platy	0.416	0.190	0.272
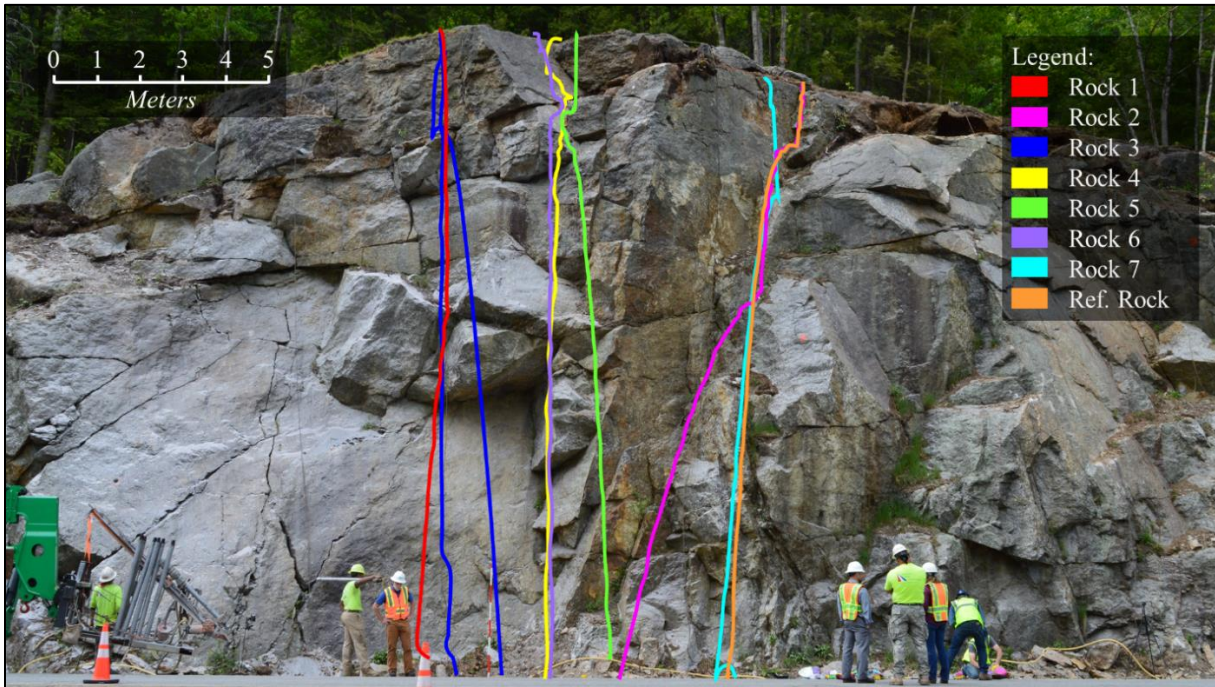
Figure 5.80. Rockfall trajectories: Warner NH.

Rock 3 shows two trajectories because it split into two halves during the initiation taps, and both rock fragments fell independently. In Warner, the reference rock (Figures 5.81 and 5.82)

initially experienced small bounces against the rock face between 3 and 33 g (A) before free falling

at 1200 dps with major rotation about the Y axis (longest axis of inertia).

Figure 5.81. Rockfall trajectory: reference rock, Warner NH.

Field Rockfall — Reference Rock, Warner/NH

SR number: 2. Date: 02-Jun-2020.

Mass: 5.21 kg. I_{XX}: 0.018 kg.m^2. I_{YY}: 0.011 kg.m^2. I_{ZZ}: 0.018 kg.m^2.

Width (X): 0.12 m. Length (Y): 0.2 m. Height (Z): 0.12 m. Shape: Compact Elongated.

Runout distance: 2.6 m from slope toe.

Drop height: 14.7 m. Altimeter hoisting: 15.1 m.
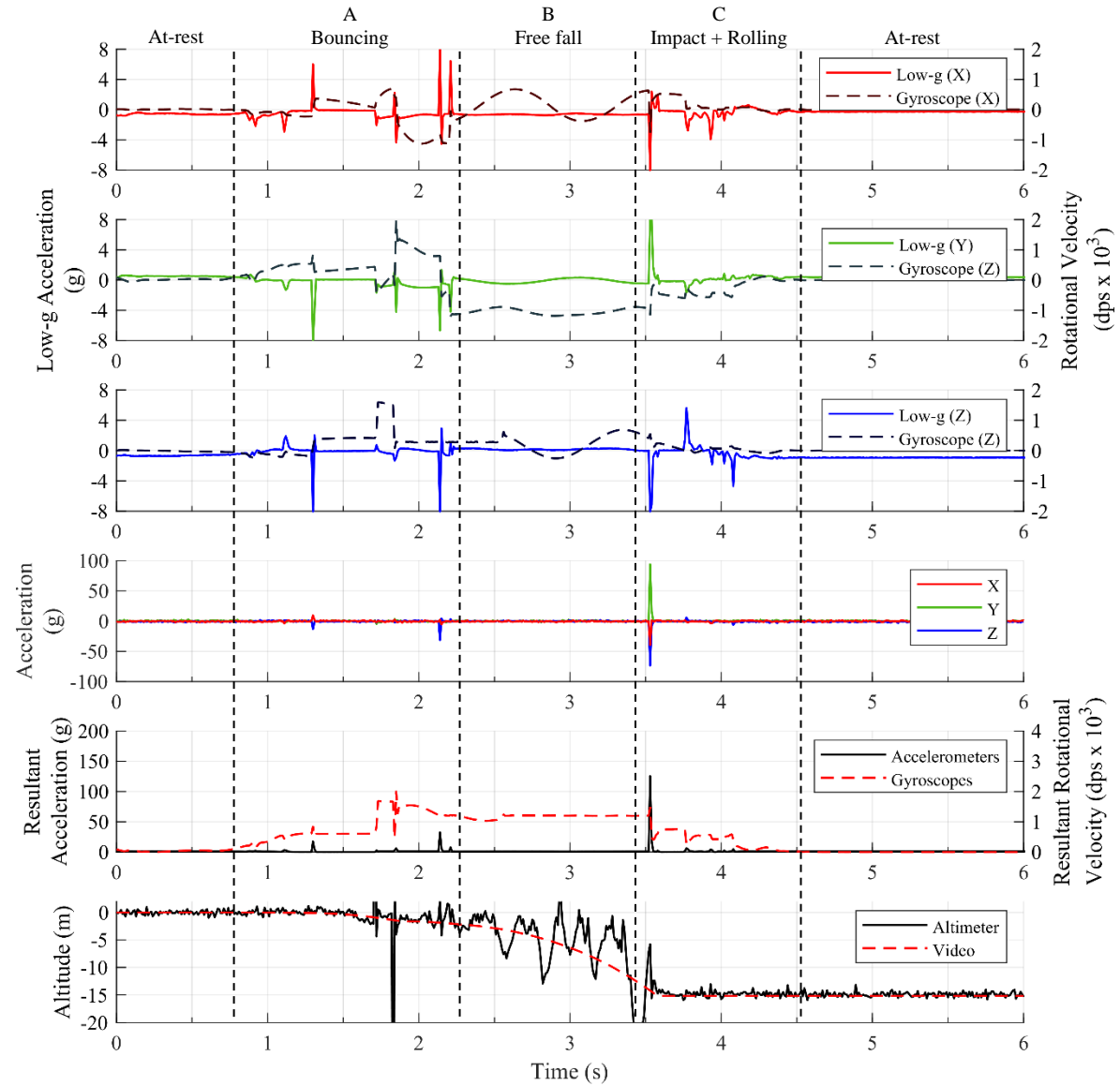
Figure 5.82. Smart Rock test data: reference rock, Warner NH.

The peak acceleration of 126 g occurred during ground contact, and the block bounced against the catchment ditch before coming to rest with a gradual decrease in rotational velocity. The maximum block rotation was described during bouncing at the early stages of rockfall.

Figures 5.83 and 5.84 describe the rockfall trajectory and sensor data for rock 6, an 18 kg compact block. After being released from the top of the rock cut at 0.8 s, the rock initially rolled down a roughly 60° inclined surface (A), with major rotation about Y, its longest axis, and the smallest moment of inertia. It is possible to observe an increase in rotation with the downward movement and small acceleration peaks that do not exceed ±8 g, likely due to surface roughness and irregular rock shape.

The rock then bounced four times in the rock face (B), with visible changes in rotation after each impact, and fell freely for 2 s (C) while rotating about X, Y, and Z at 0 g. During free fall, it was observed that major rotation occurred around the X-axis (largest moment of inertia). The test rock then hit the ground surface at 3.7 s (D) and experienced its maximum acceleration in the Y-axis. After the impact on the ground, the rock was embedded 10 cm in the soil, and no rotational velocities were experienced. Therefore, no kinetic energy was restituted.

Rock 6 experienced impact resultant accelerations that varied from 50 to 100 g (bouncing) to 382 g upon its impact with the ground. These respective resulting g-forces can be converted to intensities of 9 to 18 kN and 68 kN.
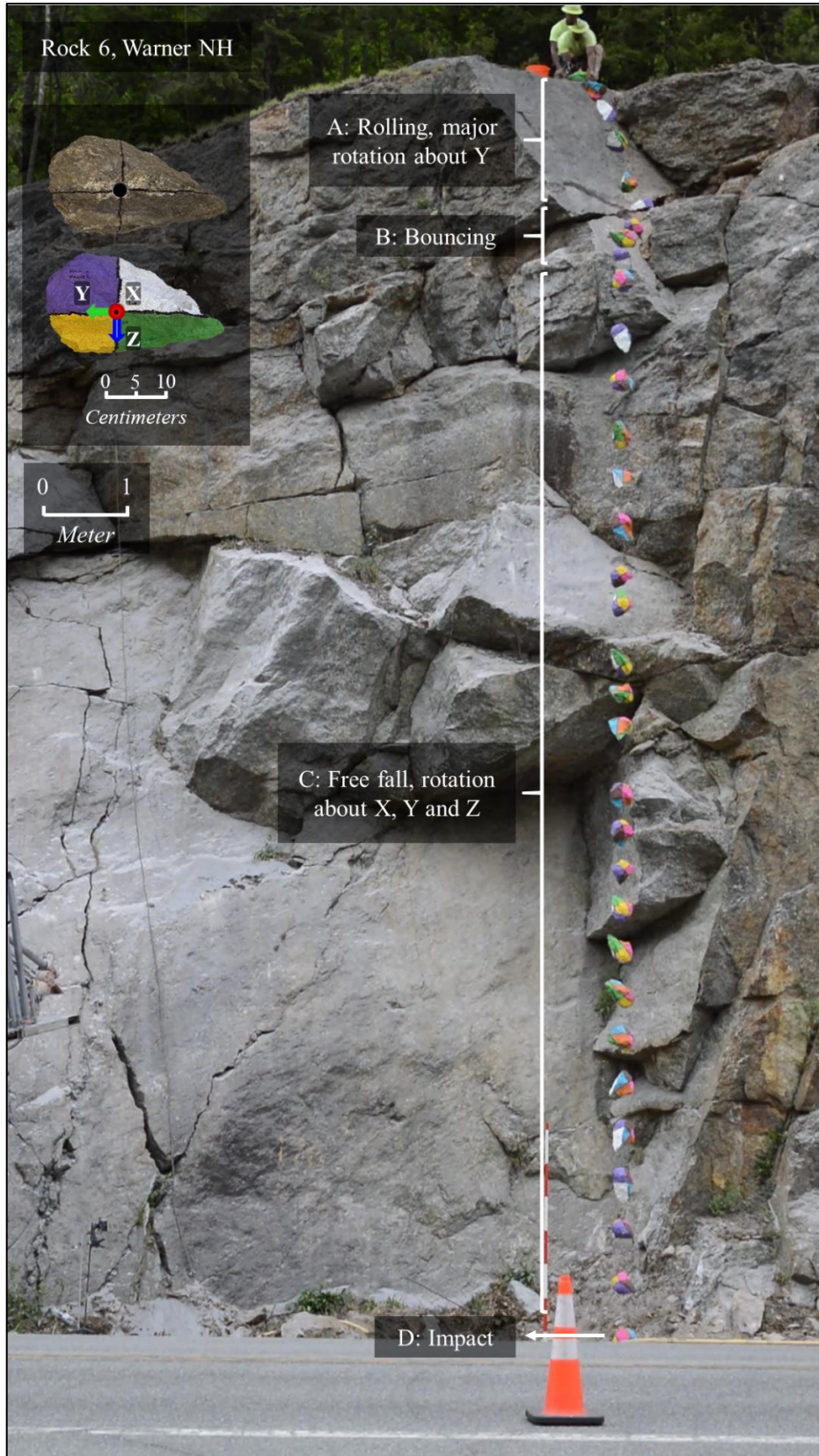
Figure 5.83. Rockfall trajectory: rock 6, Warner NH.

218
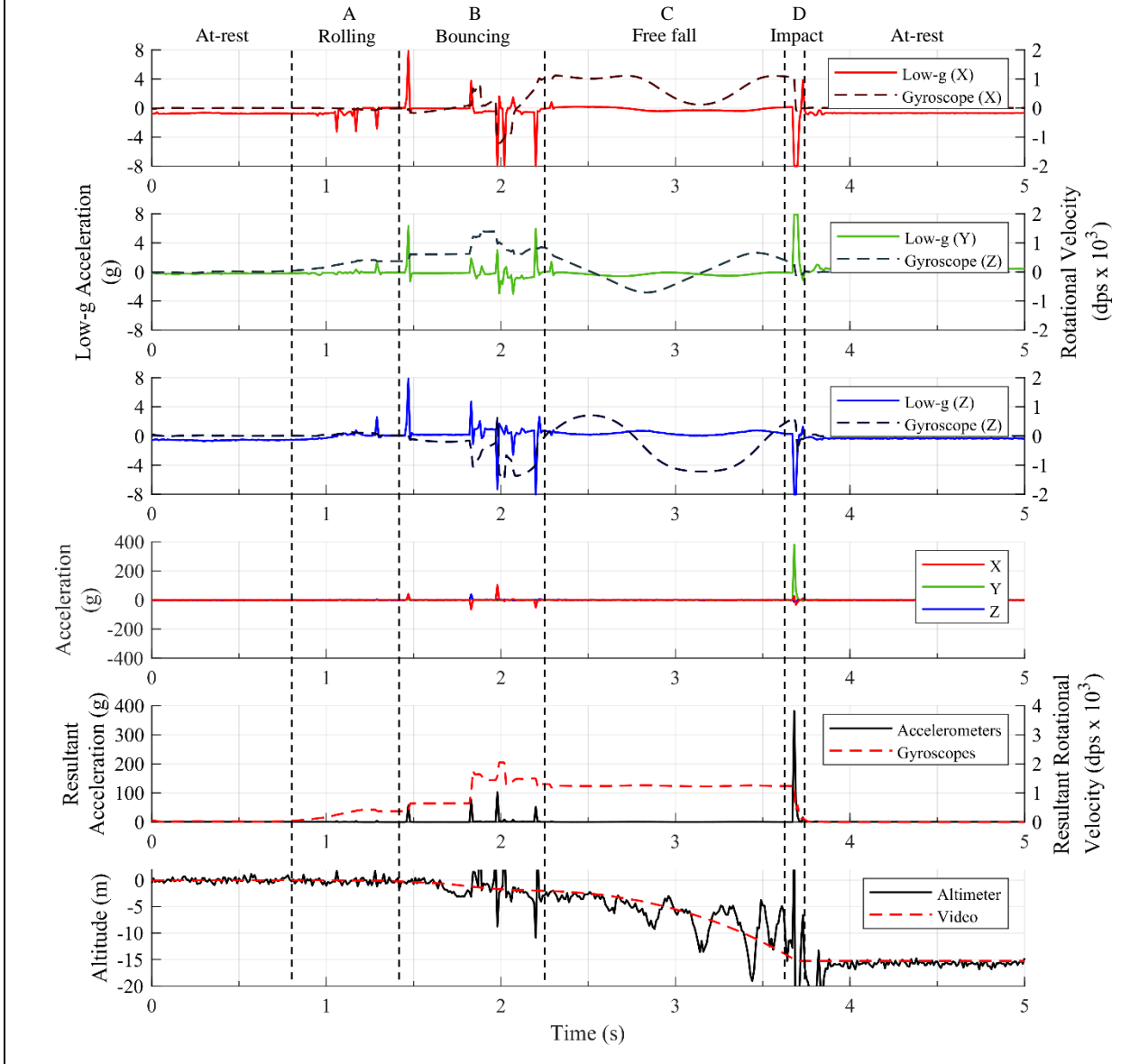
Figure 5.84. Smart Rock test data: rock 6, Warner NH.

A second test performed at the Warner site is presented in Figures 5.85 and 5.86. Rock 7 is a 25 kg platy block that described nearly all types of rockfall motion: sliding (A), free fall (B,

D), and bouncing (C, E). During its initial rolling action, the block experienced small acceleration

peaks and approximately 100 dps of resultant rotation.
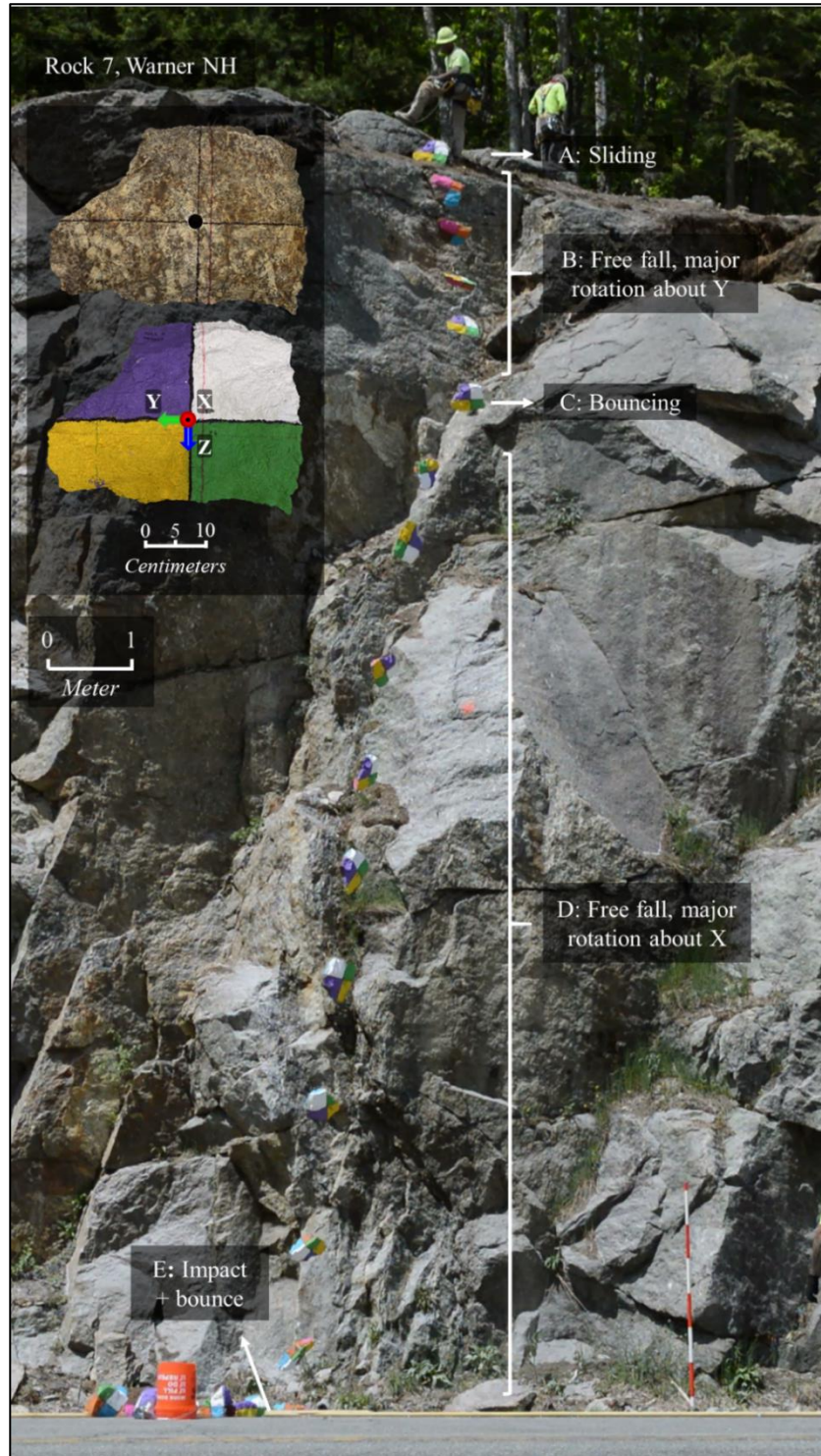
Figure 5.85. Rockfall trajectory: rock 7, Warner NH.
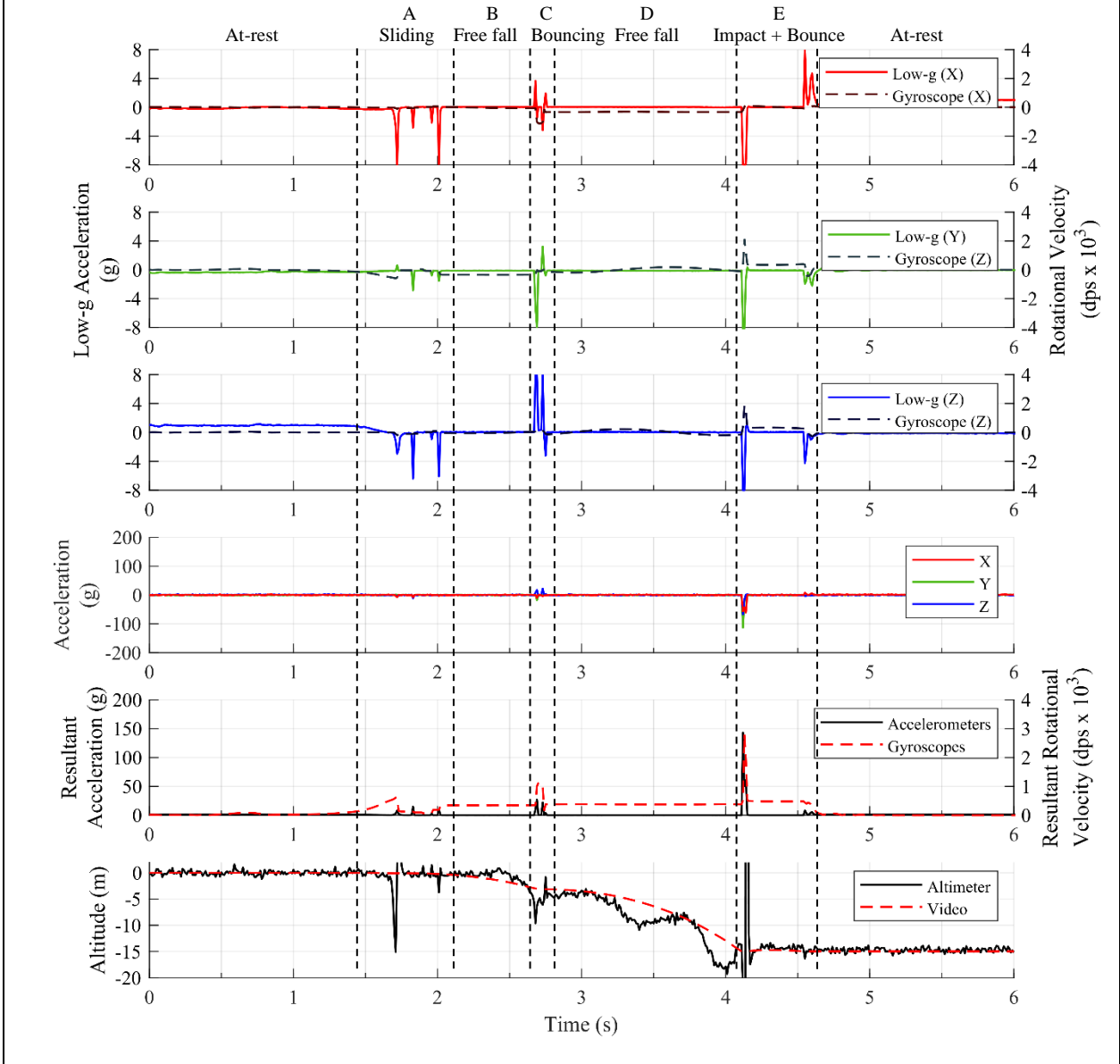
Figure 5.86. Rockfall trajectory: rock 7, Warner NH.

The rotational velocity increased to 350 dps during free fall, rotating strictly about its Y axis (lowest moment of inertia), and experienced two small successive bounces of 25 g. The second

free fall experienced at D describes nearly the same rotation rate but with a predominant rotation about the X axis (most significant inertia). Rotation about Y also gradually increases as the rock nears the catchment ditch. The peak acceleration of 143 g occurred during ground impact, resulting in an impact force of 35 kN. Rock 7 bounces once against the soil.

Table 5.22 presents a summary of the test results from the Warner site. The test blocks produced an average maximum impact force of 26 kN, with a significant standard deviation of 25 kN due to block mass differences. In Warner, lighter blocks laterally displaced more after impact than heavier blocks. These tests achieved the highest average and variability in impact forces when compared to the other sites. The remaining test trajectories and sensor data at this site location can be found in Appendix B.8.

Table 5.22. Field rockfall summary: Warner NH.

Rock ID	Slope angle	Drop height (m)	Displacements			Smart Rock resultant data			Maximum impact force (kN)
			Lateral (m)	Lateral dispersion (%)	Runout from toe (m)	Maximum acceleration (g)	Maximum rotational velocity (dps)	Average rotational velocity (dps)	
Ref	70°	14.7	-2.9	20	2.6	125	2023	834	6
1	85°	15.2	-0.3	2	0.0	88	2604	782	8
2	70°	14.7	-5.3	37	1.1	99	1598	688	7
3*	85°	15.2	1.5	-	4.3	36	6053	776	-
4	80°	15.2	-0.4	2	0.4	166	1468	682	47
5**	85°	15.2	2.0	12	1.7	187	1667	286	8
6	80°	15.2	0.4	2	1.3	382	2053	947	68
7	70°	14.7	-1.2	7	2.3	143	2820	349	35
		Average	1.8	12	1.7	170	2033	653	26
	Standard deviation		2.4	13	0.9	100	515	247	25

* Rock split in two halves during initiation taps, SR left the rock at the beginning of the drop. Not considered in avg and stdev.

** Rock broke in several pieces after hitting the toe of the slope, SR left the rock during that impact.

The runout histogram presented in Figure 5.88 summarizes the rockfall endpoint locations shown in the table. It was observed that all test rocks, including fragments, stopped within the catchment ditch limits.
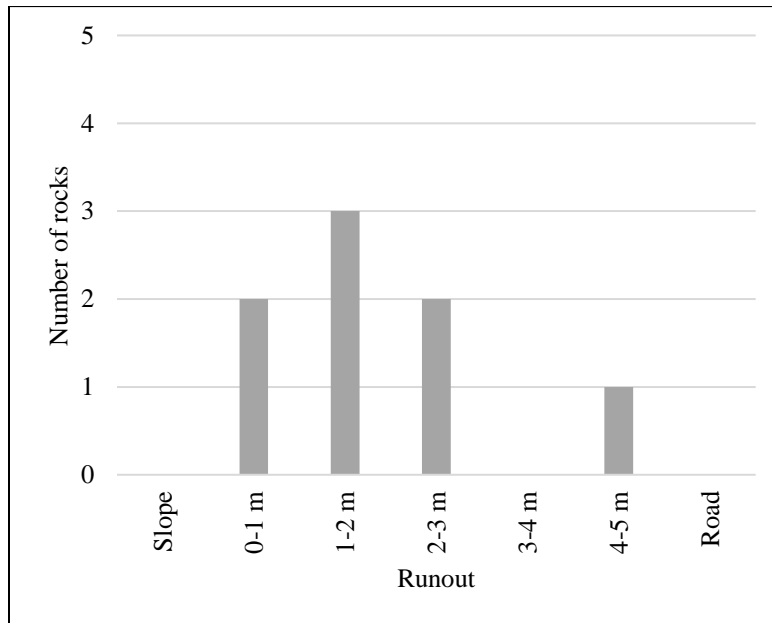
Figure 5.87. Runout histogram: Warner NH.

5.9. Windham, NH

Finally, seven experimental rockfalls were conducted on a pre-split 11 to 12.5 m tall rock cut in Windham, NH, consisting of metamorphic rock. This slope was rated as medium hazard (B) because it is an extension of a road cut. The rock face evaluated in this research is not located near transportation corridors or infrastructure, and the ground surface at the bottom of the slope was formed by a 2.0 m wide trapezoidal ditch composed of rock talus. The remaining ground surface is granular material covered with some vegetation. The slope profile presents an average inclination of 60º to 65º (Figure 5.89).

The characteristics of the test blocks are presented in Table 5.23. Due to the significant width of the test slope, the tests were conducted at two distinct sections of the rock cut, as shown

223

in Figure 5.90. The trajectories of the experimental rockfalls at each slope section are presented in Figures 5.88 and 5.89. As previously observed in the Keene tests, the uniform conditions of the slope cross-sections led to similar trajectories of the falling blocks.
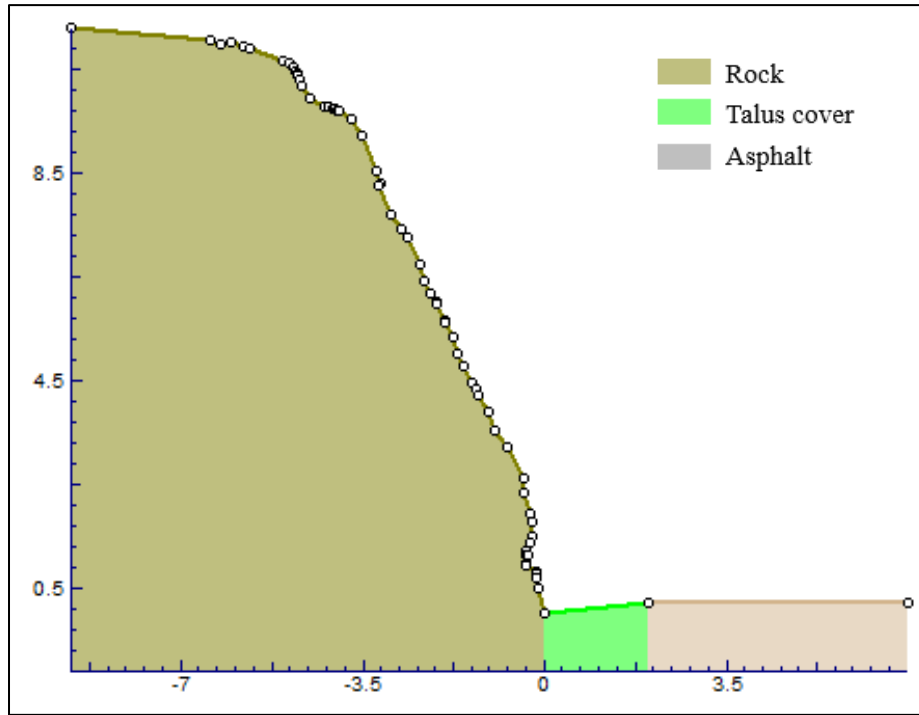
Figure 5.88. Sample cross-section of the test slope in Windham imported in RocFall. Units in meters.

Table 5.23. Test block characteristics: Windham NH.

| ID | Weight (kg) | | Density (kg/m³) | Dimensions (m) | | | Shape | Mass moment of inertia (kg*m²) | | |
	Before drill.	After drill.		Length, Y	Width, X	Height, Z		I_{XX}	I_{YY}	I_{ZZ}
Ref	-	5.21	2660	0.20	0.12	0.12	Compact Elongated	0.024	0.024	0.013
1	5.09	4.96	2650*	0.20	0.16	0.09	Bladed	0.015	0.011	0.019
2	7.14	7.03	2630	0.23	0.18	0.11	Bladed	0.033	0.023	0.039
3	9.26	9.24	2650*	0.30	0.13	0.13	Elongated	0.057	0.025	0.058
4	9.46	9.34	2730	0.17	0.12	0.15	Compact	0.059	0.026	0.059
5	6.71	6.59	2610	0.25	0.16	0.09	Bladed	0.034	0.015	0.041
6	10.40	10.22	2650*	0.21	0.17	0.22	Compact	0.052	0.043	0.051

* Estimated density, rock cores were too small and/or fractured after drilling.
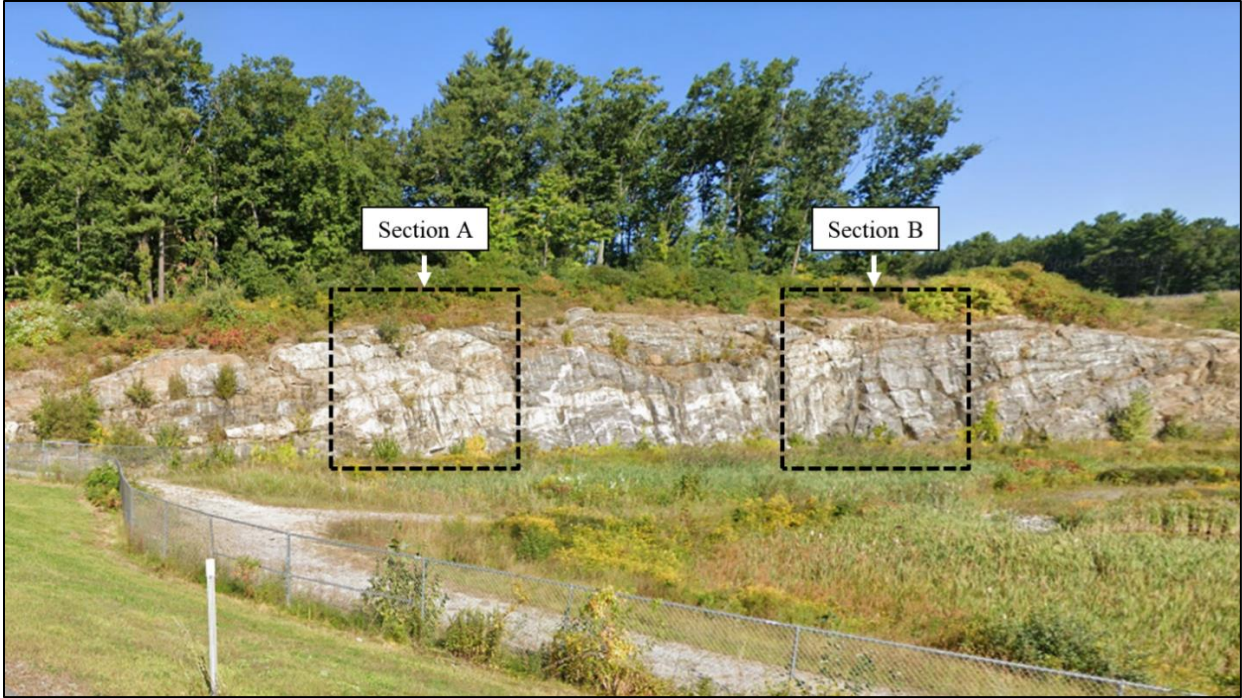
Figure 5.89. Rock cut in Windham NH (Google Maps, 2020).
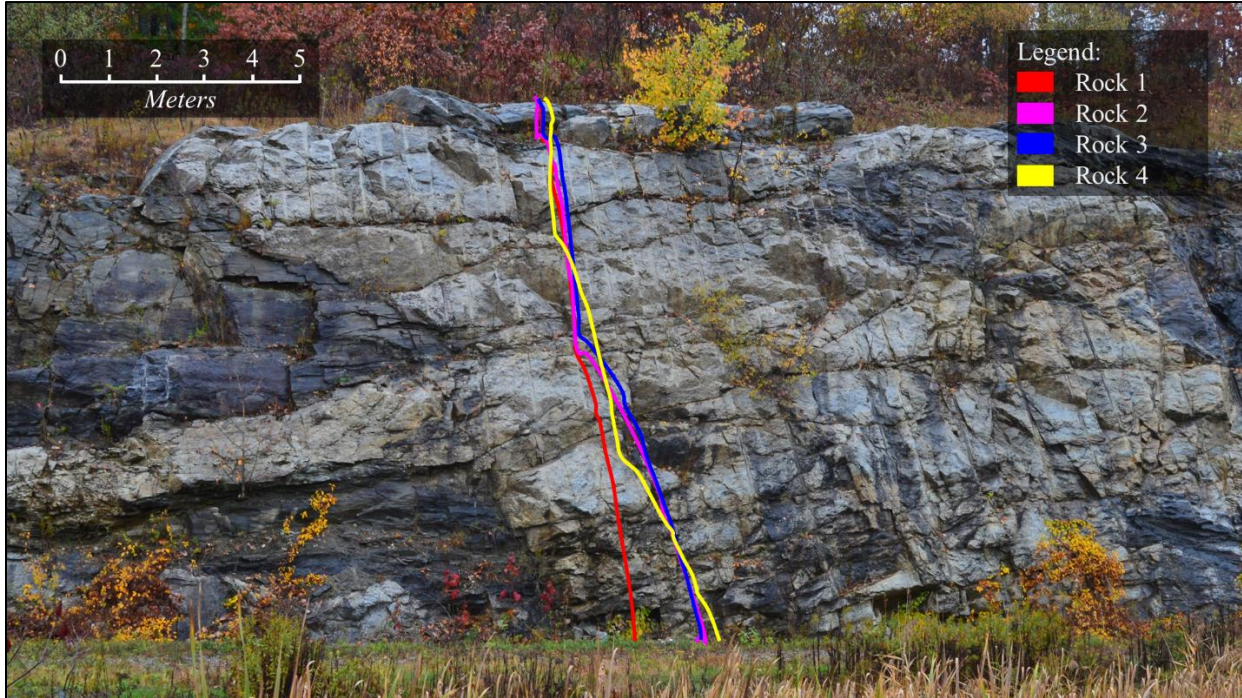
Figure 5.90. Rockfall trajectories: section 1, Windham NH.
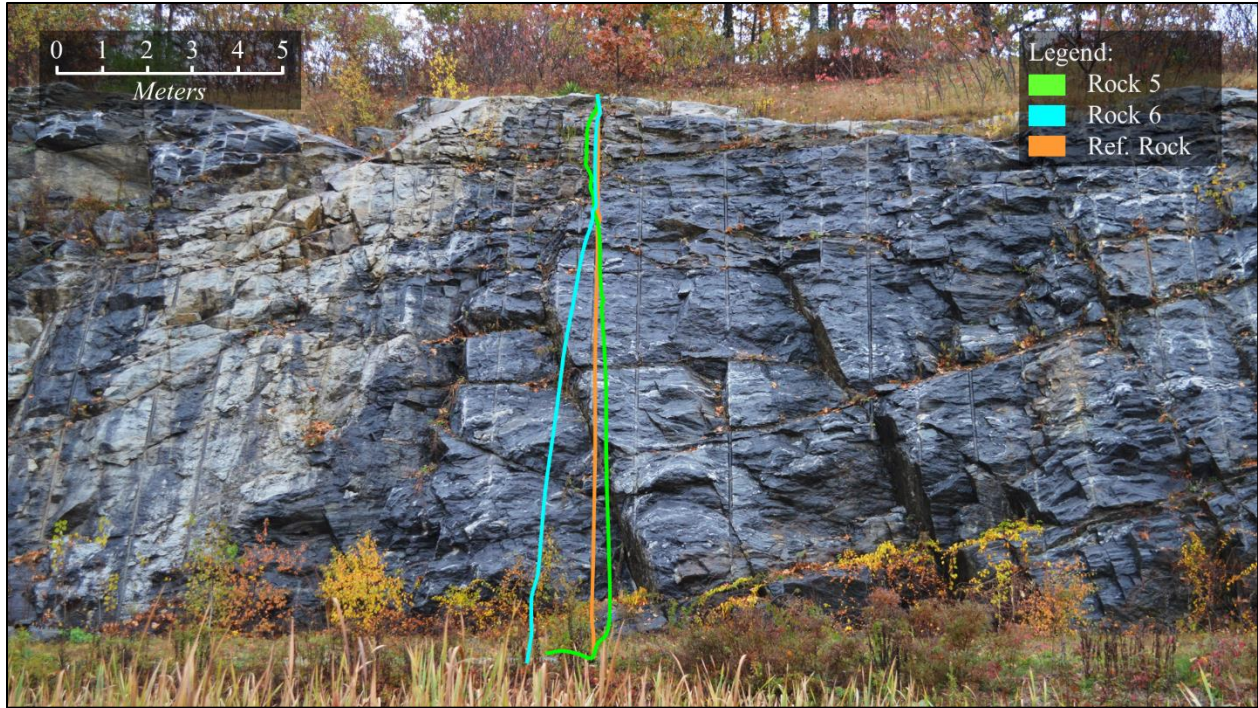
Figure 5.91. Rockfall trajectories: section 2, Windham NH.

The data for the reference rock in Windham are presented in Figures 5.92 and 5.93. Released from section 2, the reference rock initially bounced against the top of the rock face (A), and after a 61 g acceleration impact, the block rotation increased from 1200 to 3700 dps (B). Majorrotation developed about the Y axis until a bounce mid-slope at C, when the altimeter data noise significantly increased. The rock starts to rotate about all three axes at a lower resultant rate of 2180 dps. The maximum acceleration was experienced upon ground impact when the measured 93 g can be estimated as an impact force of 5 kN. The rock then experienced a bounce of lower acceleration (not visible in the video).

A second test presented in Windham, conducted on section 1, is detailed in Figures 5.94 and 5.95. Rock 4 is a 9 kg compact block that experienced approximately eight bounce peaks against the rock face before the peak acceleration at E, at the lower slope profile. Rock rotation
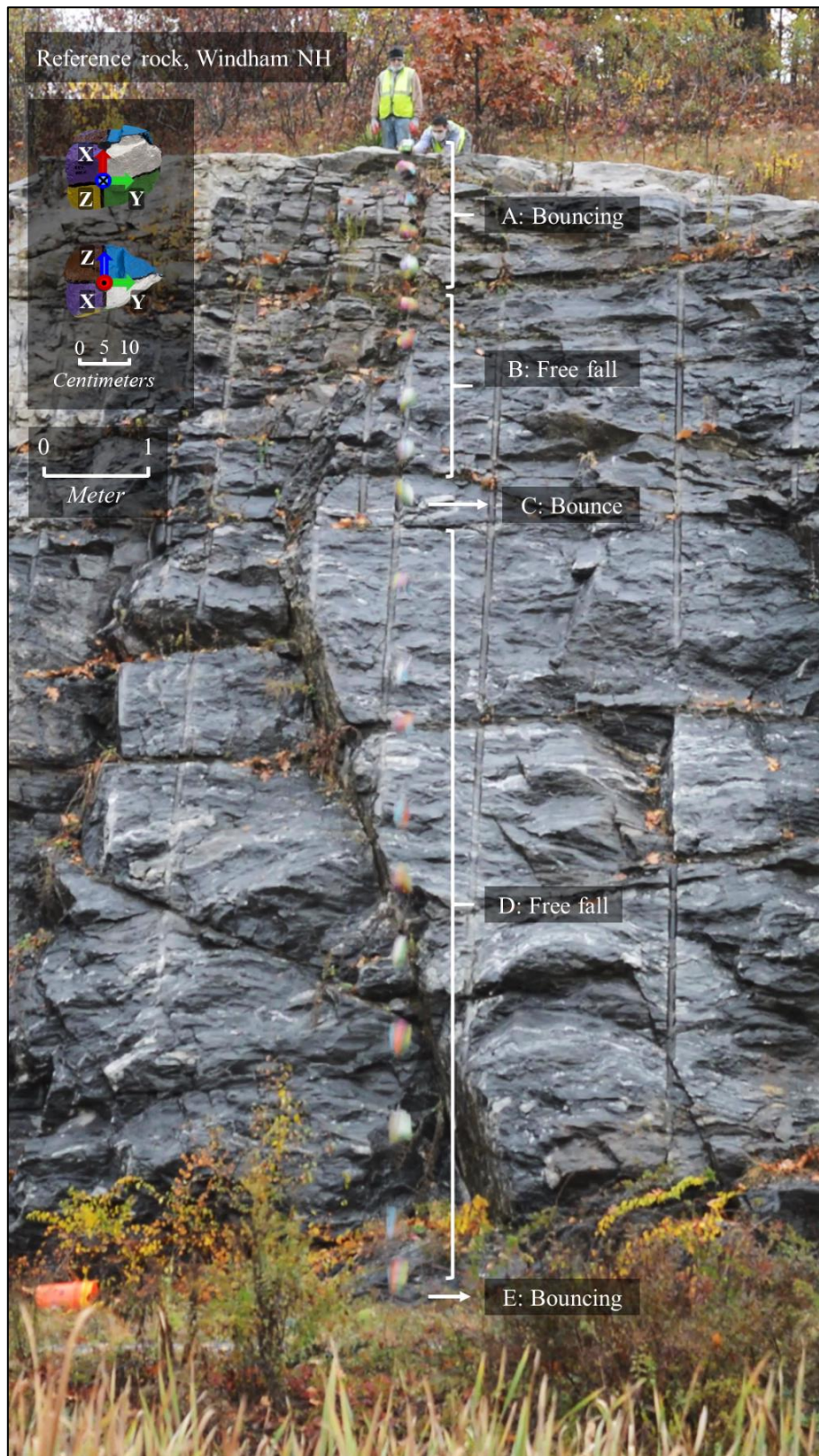
Figure 5.92. Rockfall trajectory: reference rock, Windham NH.
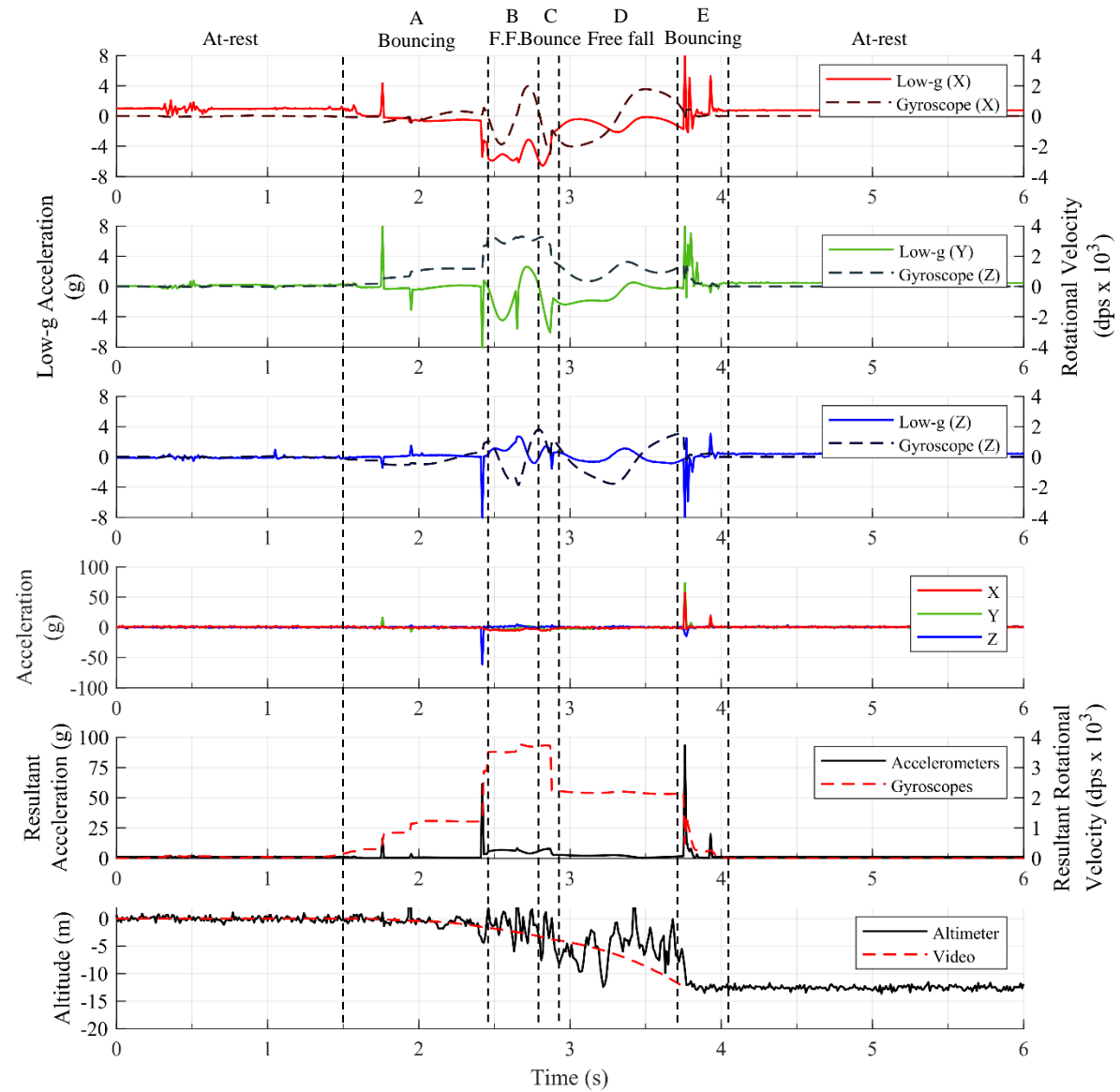
Figure 5.93. Smart Rock test data: reference rock, Windham NH.

gradually increased from A to E, at 1460 dps. The test rock initially rotates about its shortest axes

(X and Z, highest moments of inertia), and after 2.5 s starts to revolve about its shortest axis of

inertia, Y. The maximum acceleration measured had its measuring limits almost exceeded about the X axis during the test and experienced a resultant acceleration of 399 g (37 kN impact force). The block then impacted the talus ditch with a resultant acceleration of 44 g. Three minor bounces occur against the catchment ditch, and the block came to a complete stop.
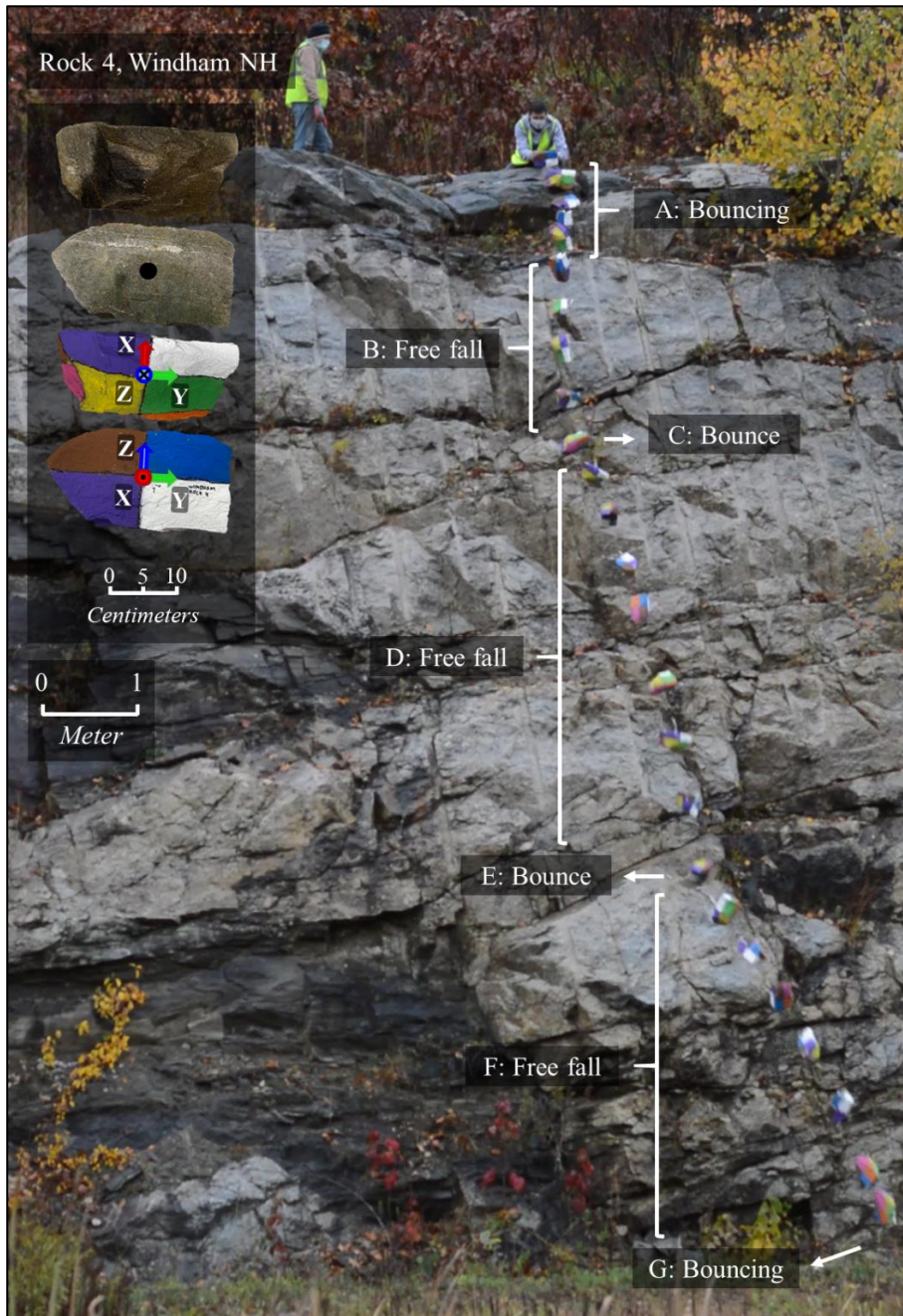
Figure 5.94. Rockfall trajectory: rock 4, Windham NH.
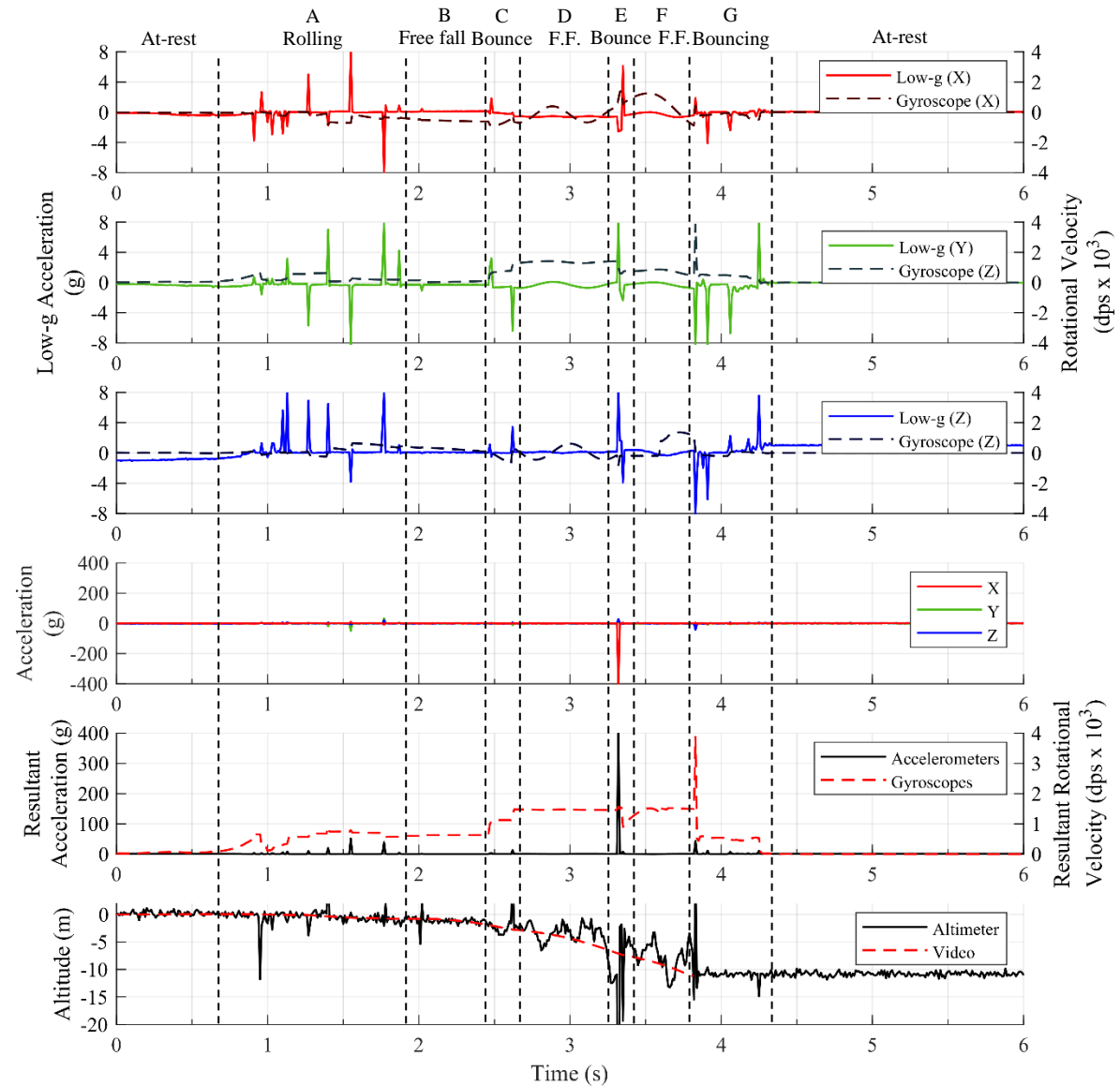
Figure 5.95. Smart Rock test data: rock 4, Windham NH.

Table 5.24 presents the test summary for the experimental rockfalls conducted at the Windham site. Significant variability of impact accelerations was observed during these trials.

230

Lateral displacements as high as 29% or 3.7 m were measured because of the bouncing motion against the rock face. The runout distances of the test rocks, summarized in Figure 5.96, demonstrate how most rocks stopped beyond 3 m from the toe of the slope. The remaining trajectories and SR data are displayed in Appendix B.9.

Table 5.24. Field rockfall summary: Windham NH.

Field rockfall data - Windham/NH - 29 October 2020									
			Displacements			Smart Rock resultant data			
Rock ID	Slope angle	Drop height (m)	Lateral (m)	Lateral dispersion (%)	Runout from toe (m)	Maximum acceleration (g)	Maximum rotational velocity (dps)	Average rotational velocity (dps)	Maximum impact force (kN)
Ref	60°	12.6	-0.1	1	1.7	93	3765	1692	5
1	65°	11.2	2.0	16	4.4	254	2583	1005	13
2	65°	11.2	3.3	26	3.0	71	4007	1168	5
3	65°	11.2	3.3	26	3.2	95	2030	810	9
4	65°	11.2	3.7	29	4.4	399	3906	846	37
5	60°	12.6	-1.2	9	4.4	91	4244	1127	6
6	60°	12.6	-1.5	11	1.9	175	2267	1138	18
		Average	2.2	17	3.3	168	3257	1112	13
	Standard deviation		2.2	11	1.2	120	927	293	11
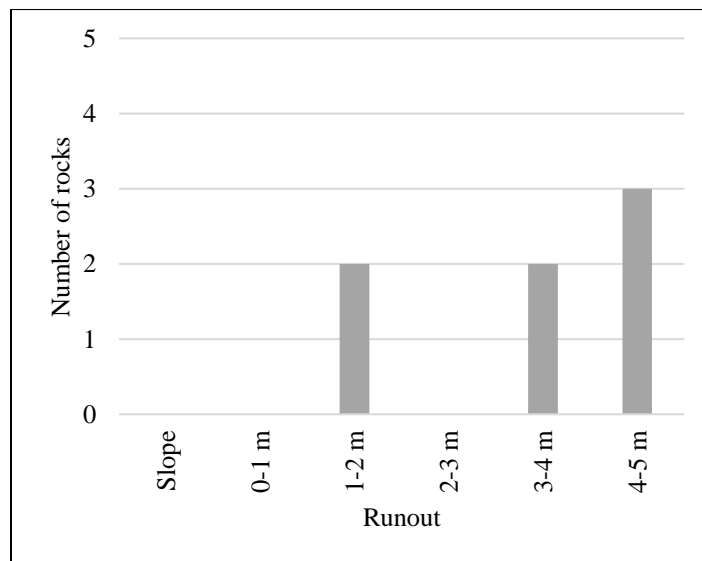
Figure 5.96. Runout histogram: Windham NH.

5.10. Summary

A total of 85 field experiments performed on different rock cuts with distinct block characteristics were used to characterize rockfall behavior from the perspective of the falling rock. Video recordings were captured during each test in order to better correlate and understand the sensor data with the modes of motion discussed in the literature since the 1960s (free fall, rolling, bouncing, and sliding).

The video tracking measurements were compatible with the altimeter data in spite of its inherent noise, especially during rapid movements such as free fall and rock bouncing. It was observed that higher noise levels occur at higher rotation rates, especially about all three axes. The altimeter measurements are helpful to identify rock position and identify time intervals of interest in the raw sensor data.

The tests performed demonstrated that rockfall behavior can vary under different, or even similar, slope conditions. Rock kinematics is influenced by the characteristics of both block and impact surfaces and also influences subsequent rockfall behavior. General observations could be established concerning changes in measured acceleration, impact force, and rotation for different test block and slope characteristics are further discussed in Chapter 6.

6. DISCUSSION OF EXPERIMENTAL ROCKFALLS

A total of 83 instrumented experimental rockfalls were carried out with local rocks from 10 rock cuts in the states of New Hampshire and Vermont. The test slopes encompassed a wide variety of characteristics, including slope height, slope inclination, irregularities in geometry, geology, protective ditch, and presence of road nearby. These field trials were conducted to evaluate how rock motion occurs at different site conditions. The comparisons included block rotation, runout distances, and resulting accelerations and impact forces. In this chapter, observations from the field experiments are compared to current rockfall knowledge published in the literature.

The test blocks were selected for each site based on their size. They needed to be large enough to house the SRs and small enough to be hand-carried to the top of the slopes. As presented in Table 6.1, the maximum and minimum dimensions of the tested rocks varied between 7 and 44 cm, with an average side of 19 ± 9 cm. The masses of the blocks ranged between 3.6 and 28.8 kg and averaged 10.6 ± 5.8 kg.

Table 6.1. Test block characteristics for all 11 slope locations.

Site	Number of rocks	Rock mass (kg)				Dimensions (m)			
		Min.	Max.	Avg.	SD	Min.	Max.	Avg.	SD
Dover, NH	1	5.21	5.21	5.21	-	5.21	5.21	5.21	-
Danbury, NH	9	3.6	13.9	7.8	4.3	0.07	0.37	0.17	0.07
Franconia, NH	12	3.8	27.3	8.6	6.3	0.07	0.42	0.19	0.09
Franklin, NH	8	5.2	15.9	10.6	3.3	0.09	0.35	0.19	0.07
Keene, NH	8	5.2	21.1	12.9	6.2	0.07	0.33	0.21	0.07
Orange, NH	8	3.7	18.1	10.5	5.6	0.10	0.41	0.19	0.08
Townshend, VT	6	5.2	11.7	7.9	2.9	0.09	0.39	0.17	0.09
Warner, NH	8	5.2	28.8	13.7	9.0	0.07	0.44	0.20	0.11
Windham, NH	7	5.1	10.4	7.6	2.1	0.09	0.30	0.17	0.06
All slopes	56	3.6	28.8	10.6	5.8	0.07	0.44	0.19	0.09
Scaled rocks (Townshend, VT)	2	2300	9600	5950	5162	0.6	3.0	1.4	0.8

6.1. Identifying rock motion

The Smart Rock sensor designed at UNH has demonstrated that it is a simple and reliable instrument capable of accurately measuring rockfall motion (Apostolov, 2016; Apostolov and Benoît, 2017; Disenhof, 2018). The measured acceleration and rotational velocity outputs from these various experiments are the first step in validating and improving rockfall computational models and ultimately help with mitigation methods. A broader description of rockfall movements can improve input parameters in computer rockfall modeling, which often disregards rotational data in kinetic energy estimates (Turner and Duffy, 2012a).

Predominant rockfall motion identified at different ranges of slope angles at the different sites is presented in Table 6.2. The table does not include observations from the scaled blocks in Vermont. In general, prevalent rolling behavior during rockfall was only identified at soil slopes covered with vegetation. Block motion parallel to the rock face varied between bouncing and free fall, with a transition zone between 60º and 65º. These observations can be related to conclusions from Ritchie (1963), in which blocks tend to roll on slopes up to 45º, bounce between 46º and 63º, and fall freely for surface inclinations higher than 63º. Ritchie also observed that rockfalls at high scalar velocities spend most of their durations in free fall.

The described rockfall behavior was compatible with previous milestone studies in rockfall engineering (Ritchie, 1963; Azzoni et al., 1995; Pierson et al., 2001). Therefore, as the rock falls along the slope profile, the following sequence was typically observed:

1. Rolling and/or sliding,

2. Bouncing (at slope profiles with inclinations lower to 65º),

3. Free fall with bouncing against launch features (at slope profiles steeper than 60º), and

4. Bouncing against the ground surface, followed by additional bounces or subsequent rolling

motion, until a complete stop.

Table 6.2. Predominant rockfall behavior at each site.

Site	Surface inclination	Predominant motion	Remarks
Dover, NH	50º to 60º*	Bouncing	Significant surface roughness and rock mass discontinuities
Danbury, NH	20º	Bouncing / Rolling	Soil covered with grass and leaves
	70º to 75º	Free fall	Isolated bounces on launch features
Franconia, NH	25º to 30º	Bouncing / Rolling	Grass slope
	50º to 65º	Bouncing	Slope cross-section formed by "steps"
	65º to 90º	Free fall	Bounces on launch features
Franklin 1, NH	45º	Bouncing	Early stages of rockfall, upper portion of the slope
	80º to 90º	Free fall	Isolated bounces on launch features
Franklin 2, NH	50º	Bouncing	Free fall from the middle to the slope bottom, at higher velocities
	70º	Free fall	Rolling/bouncing only on the upper portion of the slope
Franklin 3, NH	40º	Bouncing	Slope with a most significant bouncing motion
Keene, NH	70º to 75º	Free fall	Blocks usually bounced one time
Orange, NH	65º	Free fall / Bouncing	Early stages of rockfall, upper portion of the slope
	75º	Free fall	
Townshend, VT	30º	Bouncing	Abrupt change of surface angle in the middle of the slope profile
	80º	Free fall	
Warner, NH	45º	Bouncing	Early stages of rockfall, upper portion of the slope
	70º to 85º	Free fall	Bounces on launch features
Windham, NH	60º to 65º	Free fall / Bouncing	One or two bounces on the rock face

Table 6.3. Predominant rockfall behavior at different ranges of slope angles.

Slope angle	Predominant behavior
20º to 30º (soil + vegetation)	Rolling / Bouncing
40º to 60º	Bouncing
60º to 65º	Bouncing / Free fall
65º to 90º	Free fall

6.2. Measured block displacements

After rockfall, the test blocks predominantly bounced and rolled after the initial impact with the

catchment ditch. A small number of tests completely stopped immediately after impact,

235

demonstrating a complete dissipation of the kinetic energy. Past observations from Ritchie (1963) were confirmed during the experimental trials in Warner, NH. The rebound potential of falling blocks is significantly decreased when embedded in soft sand catchment ditches.

Although significant bounce heights after ground impact were not observed in the field trials, 25% of the rockfall tests performed near transportation corridors reached the road. This behavior occurred especially in all three Franklin slopes. In general, rockfalls on slopes between 40 and 50º caused the test blocks to develop higher horizontal velocities and more significant runouts due to the bouncing behavior on these inclined surfaces during a rockfall. According to Ritchie (1963), less inclined surfaces near 45º are more concerning in rockfall risk mitigation, as they create higher lateral and rotational motion conditions, which are more challenging to dissipate energy.

Excessive runout distances occurred on the first Franklin location due to the proximity of the rock face and its overhanging portions to the road, leading a few rocks to initially bounce against the pavement instead of the catchment ditch. In addition, the absence of rockfall protective structures caused the test blocks to bounce on the soil with grass ditch and move towards the road. The lack of a pavement shoulder on NH Route 3A increases the risk of hazards in the area. Therefore, the effectiveness of catchment ditches near less inclined rock surfaces must be demonstrated during field rockfall assessments.

As previously discussed by Pierson et al. (2001), bouncing behavior on launch features (horizontal irregularities in the 2D slope profile) is also a factor to increase runout distances and block lateral dispersion. This behavior was observed in slopes in Danbury and Townshend, where rockfall endpoints on the road were also measured. Table 6.3 displays the minimum, average, and maximum runout distances for each catchment ditch configuration.

Table 6.4. Catchment ditch characteristics for each site and measured runout distances. The percentage in the ditch effectiveness represents the percentage of rocks that have not reached the road. Slopes assigned with "N/A" were not located near transportation corridors.

Site/Slope angle	Rating	Catchment ditch			Runout (m)				Ditch effectiveness
		Material	Width (m)	Geometry	Min.	Max.	Avg.	Stdev.	
Franconia, NH 25° to 90°	B	Grass / soil	10.0 / 1.5	25° / Flat	0.0	10.5	4.6	4.0	100%
Franklin 3, NH 40°	A	Soil covered with grass	3.0	Trapezoidal	0.2	7.6	3.6	1.8	43%
Franklin 2, NH 50° to 70°	A	Soil covered with grass	2.5	Trapezoidal	0.2	3.5	1.9	1.1	57%
Windham, NH 60° to 65°	B	Talus	2.0	Trapezoidal	1.7	4.4	3.3	1.2	N/A
Orange, NH 65° to 75°	B	Soil covered with grass	5.0	Flat	1.5	3.4	2.1	0.6	100%
Danbury, NH 20° to 75°	A	Soil covered with grass	2.0	Flat	0.3	4.1	1.6	1.2	78%
Keene, NH 70° to 75°	C	Soil	-	Flat	0.0	3.9	2.2	1.3	N/A
Townshend, VT 30° to 80°	A	Talus	2.5	Irregular downward	0.0	6.6	2.8	2.9	67%
Warner, NH 70° to 85°	A	Soil	3.5 to 5.0	Flat	0.0	4.3	1.7	0.9	100%
Franklin 1, NH 45° to 90°	A	Soil covered with grass	1.3	Flat	0.0	10.6	3.5	3.8	38%

Besides lower inclination slopes and bounces on launch features along the rock face, longer runouts were also observed after impact on stiffer ground surfaces (e.g., pavement, talus ditches). In turn, shorter runout distances occurred when the test blocks experience less bouncing against the rock face or impact on catchment ditches formed by softer material (e.g., granular soil). Runout distances were also potentially increased in test sites where rolling and/or bouncing motion occurred after ground contact, as previously observed by Pierson (2001) and Disenhof (2018). The significant dispersion of the measured runouts can be attributed to the flat or descending geometry of the catchment ditch in most test locations, as noted by Azzoni et al. (1995).

In this experimental campaign, lateral rockfall dispersion (maximum lateral displacement divided by the slope length) was also estimated during video analyses of the field trials. The

minimum, maximum, and average percentages of lateral dispersion for each site are presented in Figure 6.1.
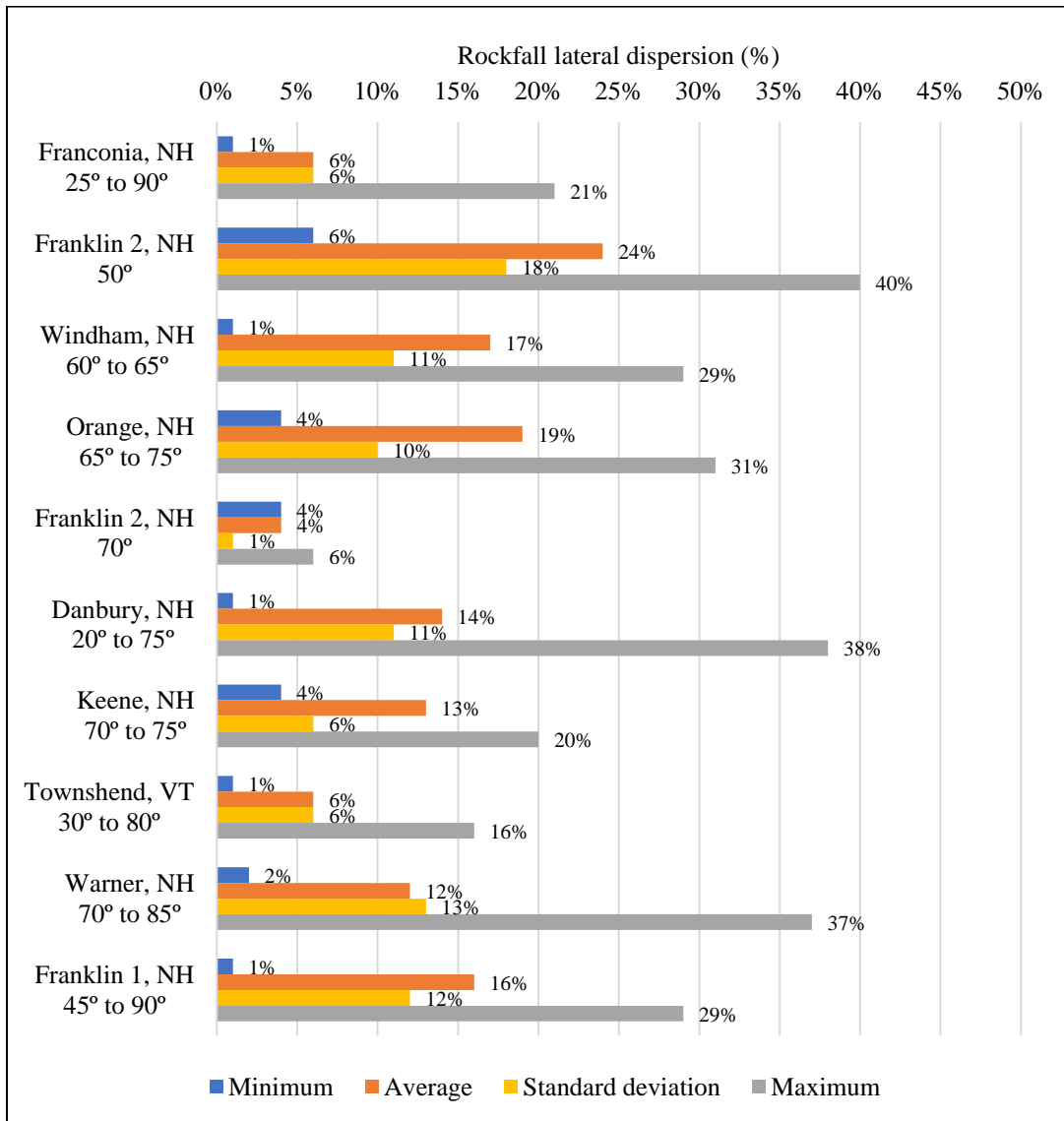
Figure 6.1. Lateral dispersion statistics for experimental rockfalls in NH and VT.

The third Franklin site is not included in the chart because video analysis could not be performed for these tests. Except for the 50º slope in the second Franklin location, all remaining average dispersions were less than 20%. The maximum lateral dispersion and data variability (standard deviation) has also occurred at Franklin 2, at the least inclined rock face where video

tracking was conducted. The 70º slope also in Franklin 2 presented a maximum lateral dispersion of 6%, demonstrating that the slope geometry on the same site strongly affects rockfall displacements laterally and towards the road. Figure 6.3 also suggests that the average lateral dispersion tends to decrease when the slope angle increases.

Similar to the runout distances, rock bouncing on both slope face and catchment ditch can increase lateral dispersion. As previously discussed, rock bouncing typically led to a significant increase in block rotation, which Pierson et al. (2001) considered a factor that strongly affects horizontal displacements during rockfalls.

Figure 6.2 presents a histogram with ranges of lateral dispersion estimated for the slopes. The obtained results indicate that nearly 80% of the tested rocks came to a complete stop with lateral displacements between 0 to 20% of the slope length. These ranges agree with previous observations from Azzoni and de Freitas (1995), in which the lateral dispersions of 60 rockfalls primarily varied between 10 and 20% of the slope length.
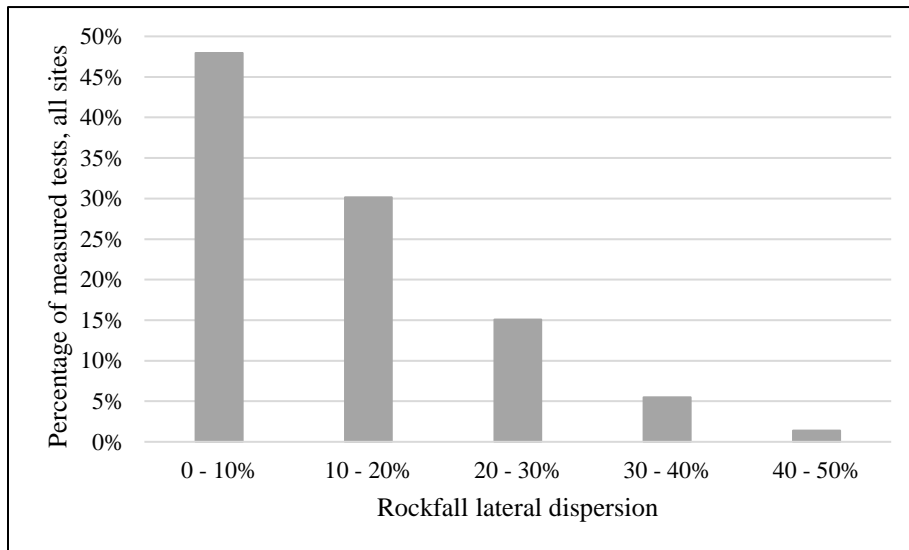
Figure 6.2. Histograms with lateral dispersions for experimental rockfalls in NH and VT.

Disenhof (2018) performed past experiments with two blocks of different mass (5 and 10

kg) and suggested that the block mass does not influence runout distances on flat catchment ditches. On the other hand, tests conducted in Durham/NH at a 4 m tall, 52º rock slope followed by a 2 m tall descending slope formed by topsoil and debris demonstrated that the 10 kg block developed longer runout distances than the reference rock.

Other authors as Evans and Hungr (1993) and Azzoni and de Freitas (1995) have also suggested that larger blocks are expected to stop at farther endpoint locations than smaller rocks. However, the experimental rockfalls performed in this research indicated that there is no apparent correlation between runout distances and block mass in nearly flat catchment ditches. The tests performed in Franconia have not suggested a similar runout behavior compared to Disenhof's tests in Durham. As shown in Figure 6.5, there is no clear trend between block mass and runout distance from the rock face in Franconia/NH, measured along the grass slope.
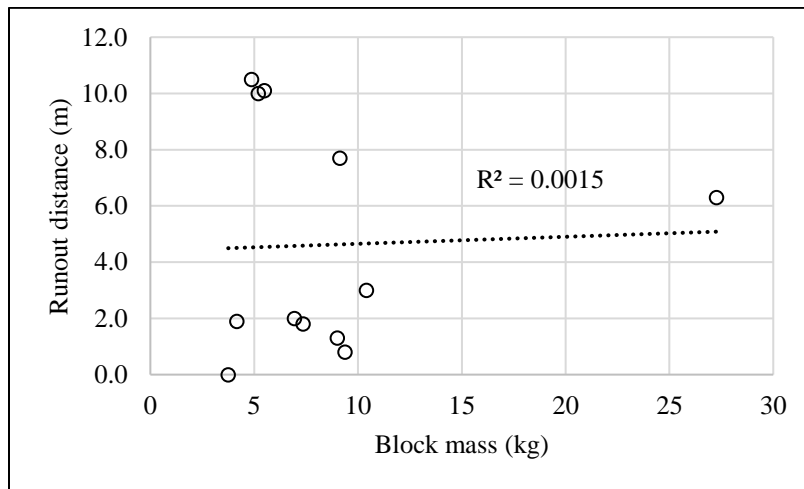
Figure 6.3. Relationship between block mass and runout distances in Franconia NH.

6.3. Block accelerations upon impact

The field rockfall tests conducted in this research measured 3-axis of acceleration and rotation data from the perspective of the falling rock. Acceleration measurements are captured by low- and high-g accelerometers, which can capture the full rockfall motion.

Previous experiments conducted by Disenhof (2018) and Caviezel and colleagues (Caviezel et al., 2017; Caviezel and Gerber, 2018; Caviezel et al., 2018) demonstrated that the ±400 g measuring limits were sufficient to capture rockfall motion while the sensor is embedded in the test rocks. Only a small number of experimental rockfalls exceeded this limit in cases of rock fragmentation and impact on rigid surfaces (e.g., rock and asphalt) at high translational and rotational velocities.

The acceleration data about the X, Y, and Z axis of the Smart Rock can be used to calculate resultant acceleration magnitudes, which can estimate impact forces experienced by the test rocks. This information is particularly relevant in designing protective structures, especially at less inclined slopes where higher horizontal motion is likely to be developed.

Objects dropped onto rigid and less deformable surfaces can achieve remarkably high levels of acceleration. According to Leonhardt (2001), the acceleration experienced by a dropped object can be estimated using Equation 6.1.

$$a = \sqrt{\frac{E \, A \, g \, d_1}{h \, m}} \qquad \text{(Equation 6.1)}$$

Where: a = acceleration,

A = area of the object being compressed,

E = modulus of elasticity of the dropped object,

g = acceleration of gravity (9.81 m/s²),

d_1 = drop height,

h = compressed height of the object, and

m = mass of the object.

From Equation 6.1, Leonhard (2001) presents the following circumstances in which greater acceleration levels can be achieved:

- When the surface area (A) is increased – impacts on a flat face of an object will experience a higher acceleration than if the impact occurs on a sharp corner,

- At higher drop heights (d_1),

- With lower mass objects (m), and

- With stiffer objects (higher modulus E) and harder impact surfaces (lower penetration h).

As presented in Chapter 5, the SRs embedded in the test rocks measured higher acceleration magnitudes during impacts on rock, compared to most impacts on less stiff material as granular soil, covered with grass or not. Therefore, nearly all test rocks experienced their maximum resultant accelerations upon impacts against the rock face or stiff material at the ground level (asphalt and rock talus).

Figure 6.4 presents the resultant peak accelerations for the recorded SR data versus the mass of each rock. It can be observed that rocks of lower mass have, in general, experienced higher acceleration magnitudes, as noted by Leonhardt (2001). However, data correlation could not be established given the different conditions at which each test was performed, and researchers highlight the different behavioral responses of rock rebound influenced by slope and rock characteristics, as well as block kinematics (Heidenreich, 2004; Heidenreich and Labiouse, 2004; Labiouse and Heidenreich, 2009). In addition, most peak accelerations experienced by the test blocks are significantly higher than for the tests with rocks drilled in place.

In turn, although the sensor has generally recorded higher accelerations inside lighter blocks, heavier blocks typically exert higher impact forces. The impact force caused by a rockfall can be estimated based on the measured g-force, block mass, and acceleration of gravity (Equation 6.2). Figure 6.5 displays the impact forces estimated for test rocks ranging from approximately 4 to 28 kg.
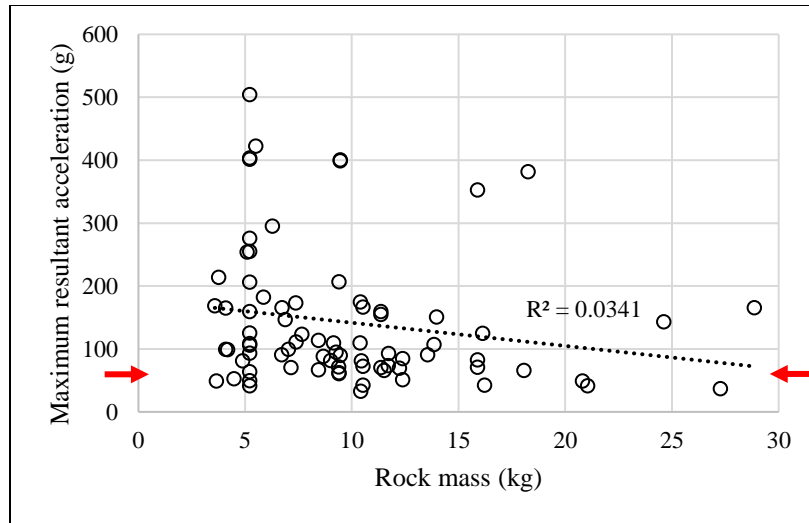
Figure 6.4. Relationship between block mass and peak resultant acceleration in all test sites. The red line marks the average maximum resultant acceleration experienced by the scaled blocks, equal to 66 g.

$$Impact\ force = (Resultant\ G - force) * g * (rock\ mass) \qquad \text{(Equation 6.2)}$$
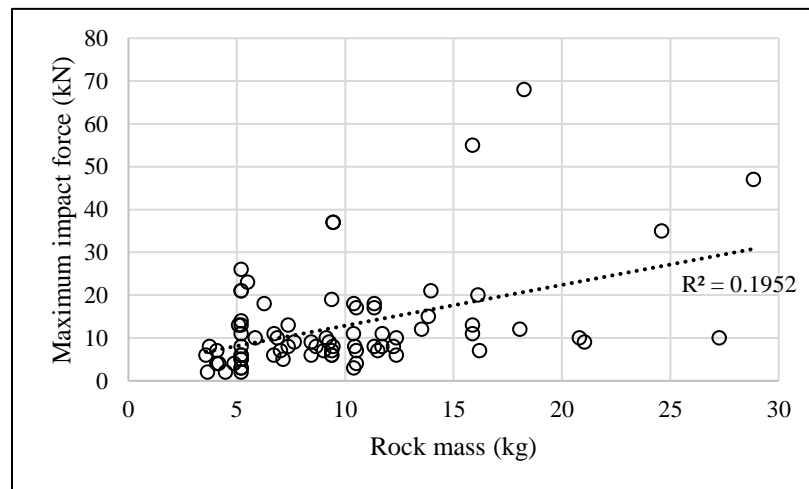
Figure 6.5. Relationship between block mass and peak impact force in all test sites.

Higher acceleration magnitudes were measured on taller slopes with predominant free fall behavior (Franklin 1, Townshend, Warner) and less inclined slopes where significant bouncing has occurred (Dover, Franklin 2, Franklin 3, Windham). However, significant impact forces can also be achieved with higher rotation rates or abrupt changes in the slope profile, such as launch

features. Figure 6.6 presents the minimum, maximum, and average peak accelerations measured at each site presented in increased order for predominant slope angle. It can be noted that data variability is increased in less steep slopes and decreases in slopes steeper than 65º.
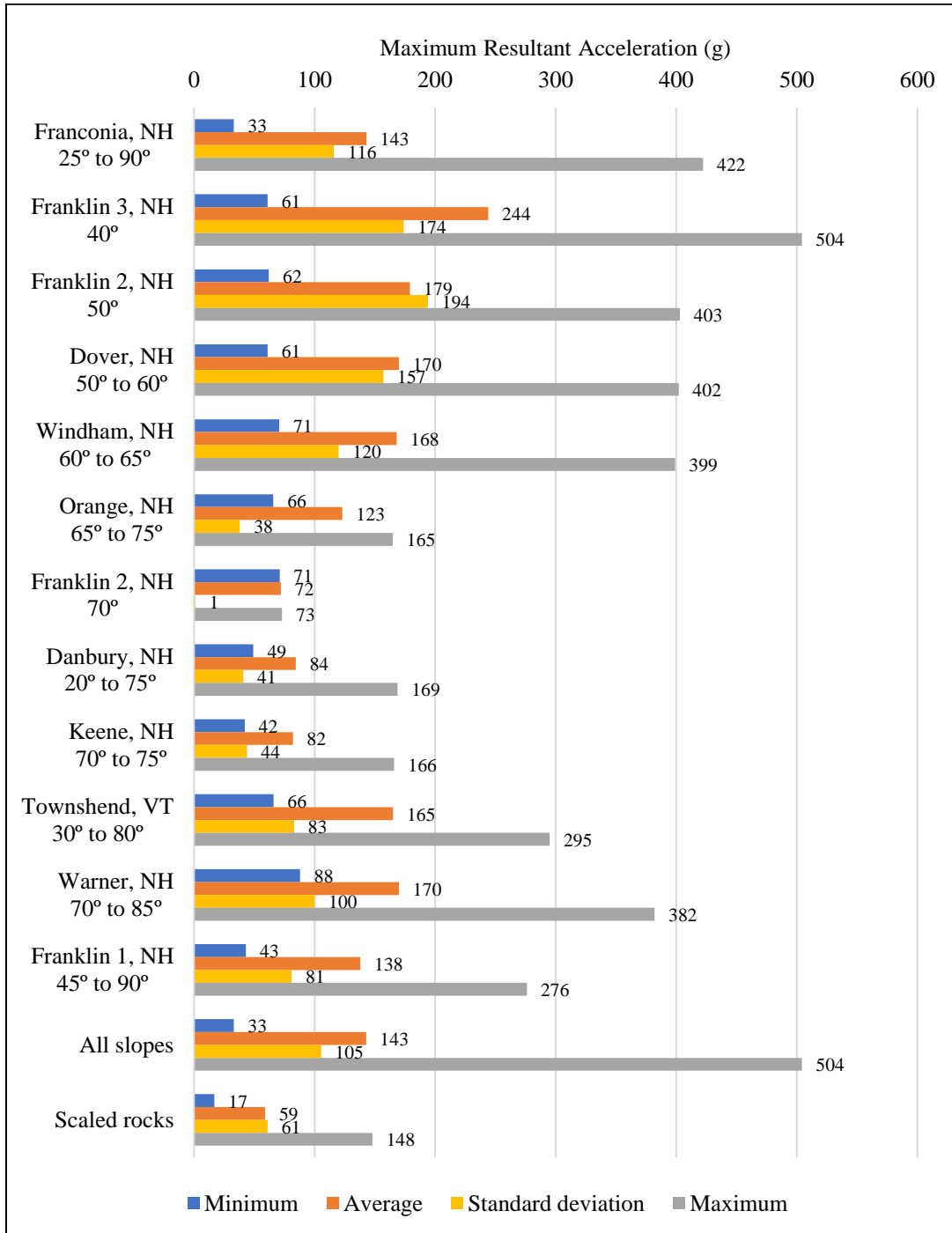
Figure 6.6. Maximum resultant acceleration data for the 11 test sites.

In turn, the impact force data for all the sites are displayed in Figure 6.7. It can be observed how the maximum acceleration experienced in Franklin 3 did not produce the highest impact force. The highest average, maximum, and variability of impact forces occurred during the Warner tests, which evaluated the most significant variability in block weights (5 kg to nearly 30 kg). The maximum impact force produced by the tests was significantly higher than the average force of 13 kN for all sites, which is still significant and can represent a high hazard if not properly contained.
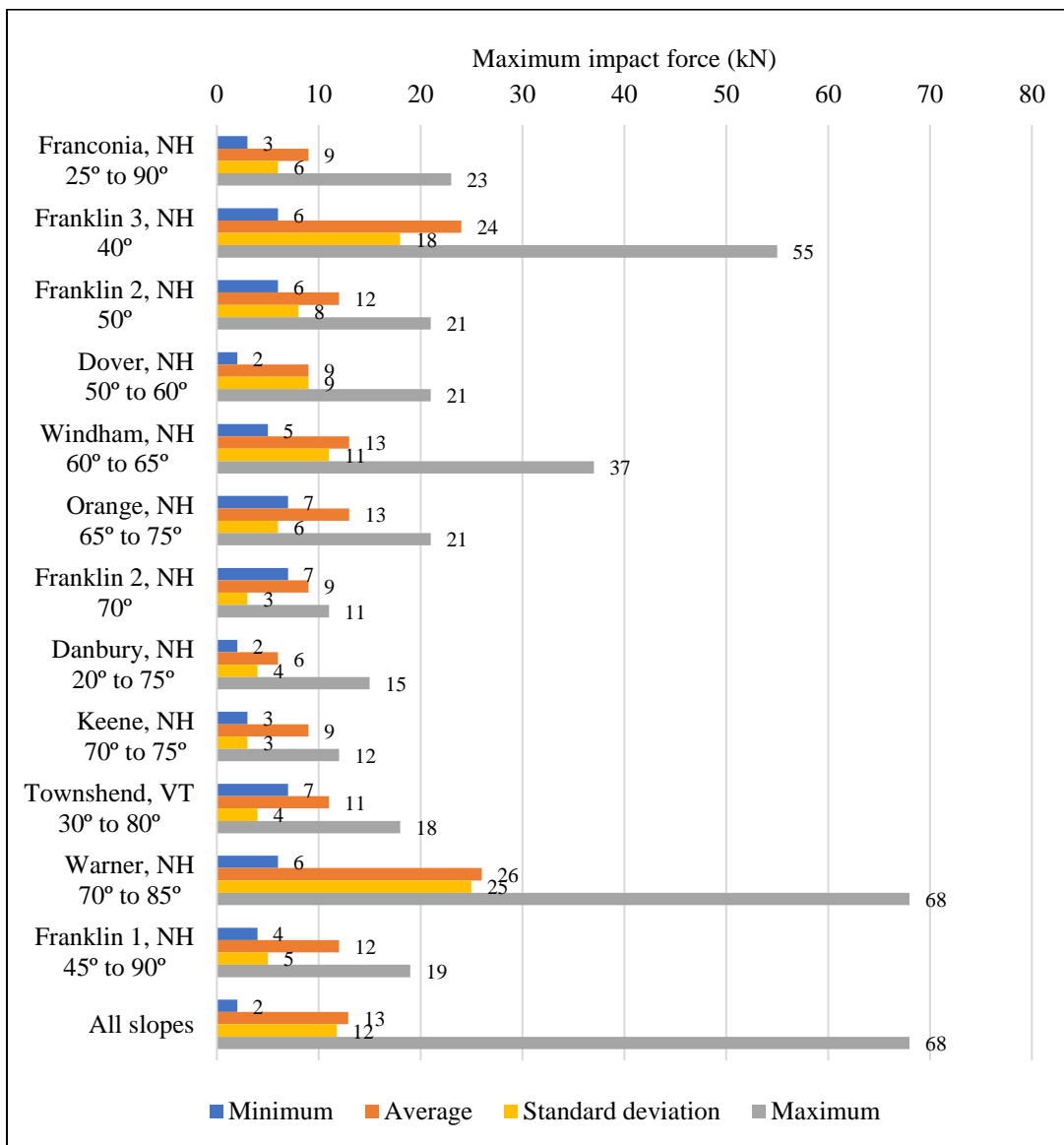
Figure 6.7. Maximum impact force data for the 11 test sites. The scaled blocks were not included.

In the research conducted by Caviezel et al. (2018), the highest acceleration was experienced by the test block with the lowest mass. In the tests performed by Disenhof (2018), the 10 kg block presented higher acceleration magnitudes and impact forces than the reference rock. However, a lower number of tests was evaluated. In Durham/NH, 10 experimental trials with the reference rock experienced an average peak acceleration of 167 ± 93 g. In contrast, 5 tests with the heavier block measured an average peak acceleration of 220 ± 114 g. In Derry/NH, only one test was performed with the 10 kg rock, and the measuring capacity of the accelerometer was exceeded. In the three tests conducted with the reference rock in Derry, one trial exceeded the high-g capacity. The other two trials experienced accelerations of 299 and 355 g. Disenhof also observed that higher acceleration magnitudes were obtained at slopes with higher drop heights.

6.4. Block rotation during rockfall

Coupled with the accelerometer data, the measured rotational velocities in a rockfall experiment can be used to readily identify changes in rock motion, especially during bouncing and free falling periods, through constant resultant rotation or abrupt changes in rotational motion, respectively. The sensor data presented in Chapter 5 demonstrated how block rotation is sensitive to changes in boundary conditions. Factors as simple as contact with thin tree branches can significantly increase the rotation rate of a free-falling block. The rotational velocities are defined as instantaneous values of revolution rates about X, Y, and Z, and are measured in degrees per second (dps). In order to better visualize the rotational motion in each rockfall experiment, resultant rotational velocities were calculated from the three-axis data.

The Smart Rock data have demonstrated that, in general, blocks of smaller mass (and smaller moments of inertia) are more easily subjected to changes in rotation for the same drop

height. Figure 6.8 presents the maximum and average resultant rotational velocities experienced for each test, plotted against the mass of the released blocks.
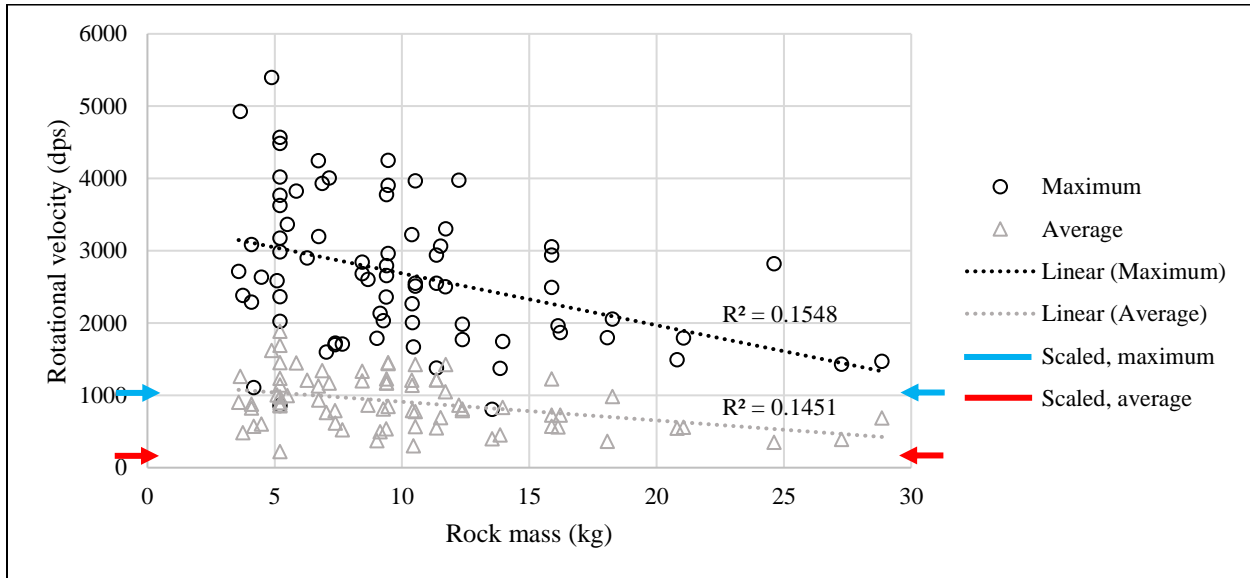
Figure 6.8. Maximum and average resultant rotational velocities for the 11 test sites. Comparison with block mass.

Although correlations between rock mass and the rate of revolution cannot be established for rockfall tests performed at different conditions, Figure 6.10 demonstrates how heavier test blocks generally described less scattered, and lower rotational velocities than the significant data spread for block masses lower than 15 kg. The graph also illustrates the mean average and maximum rotational velocities measured during the scaled tests and demonstrates that significantly lighter blocks present higher rotation rates. This behavior can be associated with the difficulty in rotating blocks with higher mass (higher moments of inertia) for shorter slopes normally encountered in New Hampshire.

As shown in Figure 6.10, the maximum rotation rates experienced by the test blocks had a significant variability, and a similar behavior was observed between test sites. The SR data plots presented in Chapter 5 and Appendix B display how the maximum rotational velocities generally occur instantaneously, immediately after an acceleration peak, and are usually not sustained for a

significant time interval. For this reason, although the maximum block rotation is essential in estimating rotational kinetic energies and block runout for protective structures, the average resultant rotational velocity is more representative of the duration of the rockfall behavior and can be better associated with test block and slope characteristics.

Figure 6.9 displays a bar chart with the minimum, mean, and maximum average rotation rates for each test site. The figure suggests that, while similar data variabilities (standard deviations) were calculated for each site, higher minimum, average, and maximum rotation rates are generally observed at less inclined slopes. This observation is reasonable given the known increase in horizontal velocity at rock cuts where bouncing motion was predominant (angle < 65°). Similarly, a correlation with such increase in rotation at less steep slopes can also be established between the low-efficiency of certain road catchment ditches.

Rotation rates tend to increase with subsequent bounces (especially in fewer steeper slopes or rotating about the shortest axis of inertia) and generally only decrease upon impact at the ground level (nearly horizontal surfaces, implying higher impact angles between the rock path and the surface).

As presented in Chapter 5, most test blocks stabilized their rotation about one or two principal axes. Most test blocks (especially those with a more elongated dimension) have initially rotated about their shortest axis of inertia and gradually increased rotation about the longest axis of inertia as the scalar velocity increased. This pattern had been previously noted by Azzoni and de Freitas (1995) and Turner and Duffy (2012a). They state that blocks usually start to rotate around their longest dimension axis and begin to spin around their longest axis of inertia (bicycle wheel analogy). Alternatively, test blocks with similar dimensions have also primarily rotated
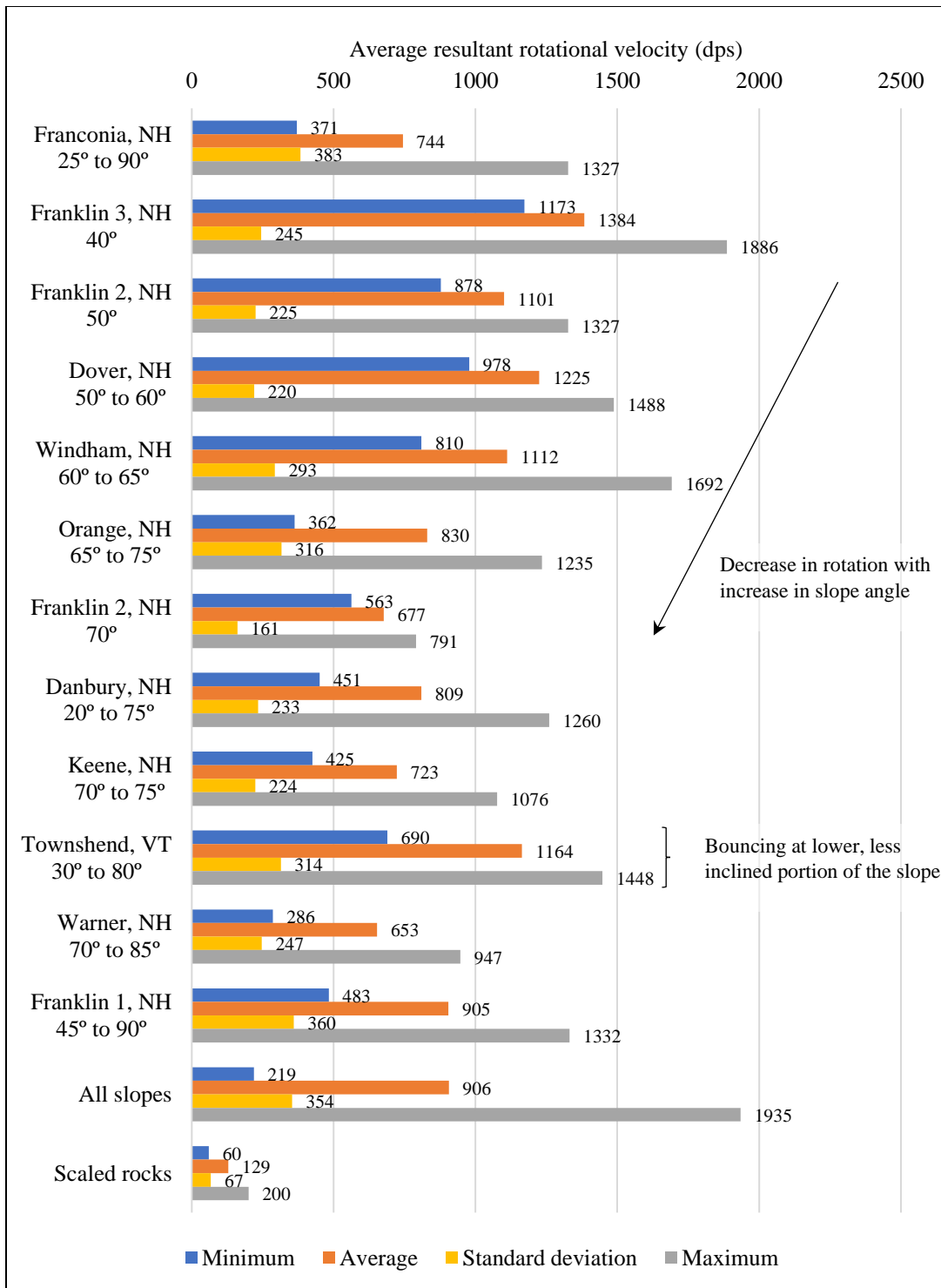
Figure 6.9. Average resultant rotational velocities for the 11 test sites.

about their longest axis of inertia or multiple axes. This behavior was observed by Caviezel and

Gerber (2018) and Caviezel et al. (2018). Therefore, in this experimental research, a single

stabilization axis during block rotation was not observed for all test rocks.

The measured ranges of maximum and average block rotation agree with field measurements from the instrumented tests performed by other authors. The maximum resultant rotational velocities obtained by Disenhof (2018) varied between 2000 dps at a 4.0 m tall slope to nearly 5000 dps (gyroscope capacity exceeded) at a 15.0 m rock face. Similarly, Caviezel and Gerber (2018) and Caviezel et al. (2018) measured maximum resultant rotational velocities ranging from 2500 dps to 4500 dps. The rotation rates obtained in this experimental campaign were higher than rotational velocities published by Ushiro et al. (2006), which varied between 350 and 1900 dps (Wyllie, 2015).

6.5. Comparisons with the reference rock

As previously discussed, the reference rock from Disenhof (2018) was evaluated at each test site to establish a preliminary correlation between the measured rockfall behavior and changes in slope conditions. Each trajectory and sensor output for the experimental rockfalls conducted with the reference rock were detailed in Chapters 4 and 5. After the preliminary testing in Dover with four trials with the reference rock, the 5 kg block was only evaluated once at each of the other ten sites. Therefore, test repeatability could not be evaluated in this research due to time restrictions at each slope location.

A summary of the test results obtained with the reference rock is shown in Table 6.5. It could be observed that there were no clear trends to correlate the sensor data or the measured displacements with the slope characteristics. The experimental data presented in the table demonstrates the wide range of rockfall motion regarding acceleration, rotation, and displacements that a single test block can experience under different slope conditions.

Table 6.5. Test data summary for the reference rock at ten different slope locations.

Site ID	Slope angle	Drop height (m)	Displacements		Smart Rock resultant data			Maximum impact force (kN)
			Lateral dispersion	Runout (m)	Maximum acceleration (g)	Maximum rotational velocity (dps)	Average rotational velocity (dps)	
Danbury, NH	75º	10.6	20%	3.2	50	2362	900	3
Franconia, NH	90º / 30º	9.6	11%	10.0	255	2985	1143	13
Franklin 1, NH	45º	11.5	1%	0.0	276	861	483	14
Franklin 2, NH	50º	9.9	39%	0.2	403	4483	1327	21
Franklin 3, NH	40º	18.2	-	3.5	504	4017	1886	26
Keene, NH	75º	9.9	20%	3.9	64	3624	954	3
Orange, NH	65º / 75º	9.1	20%	3.4	160	4568	1235	8
Townshend, VT	75º / 55º	19.0	1%	1.7	206	3172	869	11
Warner, NH	70º	14.7	20%	2.6	125	2023	834	6
Windham, NH	60º	12.6	1%	1.7	93	3765	1692	5
	Average	12.5	15%	3.0	214	3186	1132	11
	Standard deviation	3.6	13%	2.8	149	1168	421	8

The results obtained for the reference rock suggest that a test block can describe distinct trajectories and consequently pose different levels of hazard at different site conditions. In natural rockfall conditions, the reference rock would have posed a risk of danger to motorists in the Danbury and Franklin 3 rock cuts since it stopped beyond the road shoulder in both tests.

The reference rock described lateral displacements as low as 1% in Orange and Windham even with bouncing behavior and as high as 39% after a predominantly bouncing motion at a 50º rock face in Franklin 2. Also, the resultant peak accelerations and rotations varied significantly. The maximum impact forces varied between 3 and 26 kN, and the maximum resultant rotations ranged between 861 and 4568 dps.

A lower variability was observed for the average rotational velocities in these experimental trials. As opposed to the predominant rotation behavior observed in this research for blocks with a more elongated dimension, the reference rock has primarily rotated about the longest axes of inertia (X and Z) before developing significant rotation about the shortest axis of inertia (Y). In

the tests conducted by Disenhof (2018), the reference rock trials did not stabilize rotation about a single axis.

Table 6.6. Axes of predominant rotation during rockfall, reference rock.

Site ID	Axis of major rotation
Dover, NH	X, Y, Z
Danbury, NH	X and Z, then Y
Franconia, NH	X and Z, then Y
Franklin 1, NH	X, Y, Z, then Z
Franklin 2, NH	Y
Franklin 3, NH	X, Y, Z
Keene, NH	X and Z, then Y
Orange, NH	X and Z, then Y
Townshend, VT	X and Z, then Y
Warner, NH	Y
Windham, NH	Y, then X Y Z

Although assessing repeatability was not in the scope of this research, the initial tests performed in Dover/NH with the reference rock have demonstrated that even released from the same start location, rockfalls can experience a wide range of accelerations, impact forces, and rotation rates. Such data variability highlights the need for a realistic estimate of rockfall trajectories in computational models. Time constraints associated with field experiments do not allow for a significant variability of trajectories and test block characteristics in a timely fashion for a given number of slopes.

6.6. Summary

The rockfall motion data recorded by the fourth-generation Smart Rock were compatible with previous experimental studies conducted by Caviezel et al. (2018) and Disenhof (2018). The findings of this preliminary work demonstrated that acceleration and rotational velocity data from the rock perspective present a high potential to expand rockfall understanding and modeling. The

instrumented rockfalls discussed in the previous chapters were analyzed for different test blocks and test slopes. The Smart Rock data and field measurements acquired in this experimental campaign yielded the general observations presented in Table 6.7. It is essential to highlight that the general trends observed for the discussed test sites do not represent all obtained results and should not be used for design applications.

Table 6.7. General observations of rockfall behavior during the experimental campaign.

Change in parameter	Acceleration	Impact force	Block rotation	Lateral dispersion	Runout distance
Increase block mass	↓ Decreases	↑ Increases	↓ Decreases	✕ Correlation not established	✕ Correlation not established
Decrease slope angle	↑ Increases	↑ Increases	↑ Increases	↑ Increases	↑ Increases
Increase slope height	↑ Increases	↑ Increases	✕ Correlation not established	✕ Correlation not established	✕ Correlation not established
Increase in block rotation	✕ Correlation not established	✕ Correlation not established	-	↑ Increases	↑ Increases
Presence of launch features in the rock face	↑ Increases	↑ Increases	↑ Increases	↑ Increases	↑ Increases
Impacts on stiffer ground surface/ditch	↑ Increases	↑ Increases	↓ Decreases	↑ Increases	↑ Increases

As previously discussed by several authors, rockfall behavior is a complex phenomenon that depends on numerous parameters, including block and surface characteristics and block kinematics (Ritchie, 1963; Peng, 2000; Heidenreich, 2004; Labiouse and Heidenreich, 2009; Turner and Duffy, 2012a; Wyllie, 2015). Although general trends could be observed, data variability is still significant and numerical relationships could not be established for rockfall influencing parameters. Further assessments of isolated parameters are still necessary to quantify any possible correlations.

7.   LABORATORY TESTS

The rockfall tests discussed in Chapters 4 to 6 were followed by preliminary laboratory experiments to evaluate coefficients of restitution under controlled conditions. As previously presented in Chapter 3, these experiments consisted in dropping a test block using a "rock dropper" device into a test pit filled with various ditch landing materials. A total of 23 instrumented drop tests (20 on sand and three on rock) were conducted with a single test block from Warner/NH, released from a constant drop height of 2.2 m.

The first ten trials on sand were performed with a cubic-shaped test block. The following ten trials, also on sand, were conducted with the same test block but reshaped to a cuboctahedron. Finally, the test pit was prepared with a local rock from Warner/NH, and three tests were conducted on this flat rock. The ten proposed tests could not be completed at this stage because the cuboctahedric block split in tension during the third trial. The characteristics of the test blocks previously presented in Chapter 3 are shown in Table 7.1.

Table 7.1. Properties of the test blocks used for the laboratory experiments.

| Block | Weight (g) | Density (kg/m³) | Dimensions (cm) | | | Shape | Moments of inertia (kg.m²) | | |
			Length, Y	Width, X	Height, Z		I_{XX}	I_{YY}	I_{ZZ}
Cube	1095	2870	7.4	8.6	7.2	Compact	0.0010	0.0011	0.0012
Cuboc-tahedron	790	2870	7.4	8.6	7.2	Compact	0.0005	0.0006	0.0006

Figure 7.1 displays that the test blocks did not rotate during the initial free fall. This was verified by both Smart Rock and video measurements. This chapter presents the preliminary results

obtained with this laboratory setup, whose observations will be used to adjust the parameters used

in the analyses and to perform a detailed parametric study of rock bouncing phenomenon.
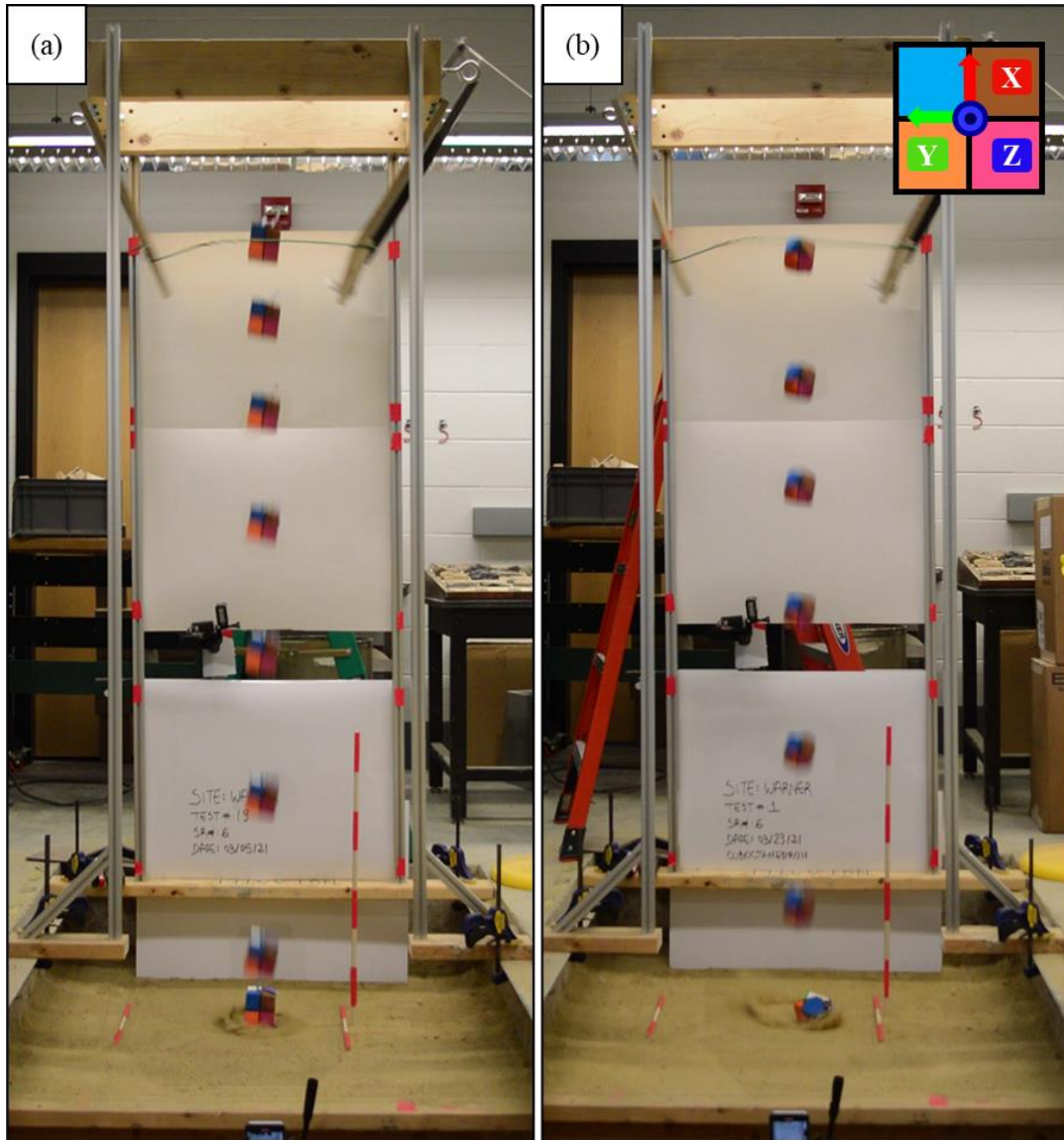
Figure 7.1. Test blocks released from the rock dropper during the laboratory tests: (a) cube and (b) cuboctahedron. The reference lines in the prism poles are 10 cm long.

Each experiment was recorded with a frontal (iPhone 11, 240 fps) and an upper camera

(GoPro Hero 4, 120 fps). This camera setup allowed recording the rock motion about three

directions during impact and calculating accurate kinetic energy estimates when matched with the

rotation sensor data. The video recording scale was calibrated with the aid of prism poles, as shown in the figure. The tests were instrumented with Smart Rocks at a sampling frequency of 500 Hz, and the altimeter was disabled due to its significant data noise at high frequencies. The drop took approximately 0.7 seconds from release to hitting the soil or rock surface.

7.1. Coefficients of restitution

The coefficients of restitution estimated in these laboratory tests were assessed using the expressions detailed in Table 7.2. Tangential coefficients of restitution were not evaluated because the test block was released at a horizontal velocity equal to zero.

Table 7.2. COR definitions used in the laboratory experiments.

Basis	Equation		Terms
Velocities	$COR_{VN} = \frac{v_{RN}}{v_{IN}}$	(Eq. 7.1)	COR_{VN} = normal component of the velocity-based coefficient of restitution
			v_{RN} = normal translational velocity immediately after impact
	$COR_{VN} = \sqrt{\frac{h_{N+1}}{h_N}}$; 90º fall	(Eq. 7.2)	v_{IN} = normal translational velocity immediately before impact
			h_{N+1} = height of the current bounce
			h_N = height of the last bounce or drop height for the first bounce
Energies	$COR_E = \frac{0.5mv_{N+1}^2}{0.5mv_N^2} = \frac{v_{N+1}^2}{v_N^2}$	(Eq. 7.3)	COR_E = energy-based coefficient of restitution
			m = mass of the block
			v_{N+1} = scalar velocity of the object after impact
			v_N = scalar velocity of the object before impact
	$COR_{TE} = \frac{0.5[m(v_R^2)+I\omega_R^2]}{0.5[m(v_I^2)+I\omega_I^2]}$	(Eq. 7.4)	COR_{TE} = total energy coefficient of restitution
			m = mass of the block
			v_R = scalar velocity after impact
			v_I = scalar velocity before impact
			I = moment of inertia of block
			ω_R = angular velocity of the block after impact
			ω_I = angular velocity of the block before impact

Velocity parameters were estimated based on video measurements using Tracker 5.1.5 software, and rotation parameters were selected from the measured Smart Rock data. The procedure to match the sensor data with the video measurements was identical as previously detailed for the field experiments in Chapter 4.

The theoretical scalar velocity of free-falling blocks can be estimated through Equation 7.5 and used to calculate the expected kinetic energy prior to impact at each experimental trial (Equation 7.6). The rotational energy can be disregarded until immediately before impact, as the block does not develop initial rotation, and no external forces act on it during the fall.

$$v = \sqrt{2\,g\,h} \qquad \text{(Equation 7.5)}$$

$$KE = KE_T + KE_R = \frac{1}{2}mv^2 + \frac{1}{2}I\omega^2 \qquad \text{(Equation 7.6)}$$

Where: v = scalar (translational) velocity of the block,

              g = acceleration of gravity (9.81 m/s²),

              h = drop height,

              KE_T = translational kinetic energy,

              KE_R = rotational kinetic energy,

              KE = total kinetic energy,

              m = mass of the block,

              ω = angular velocity of the block, and

              I = moment of inertia of block.

Therefore, for a 2.2 m drop height, as demonstrated in the following calculations, the test block is expected to develop a peak velocity of 6.6 m/s. The estimated velocity implies 23.8 J of total KE for the cubic block, and 17.2 J for the cuboctahedron due to its reduced mass.

$$v = \sqrt{2\,g\,h} = \sqrt{2 * 9.81\frac{m}{s^2} * 2.2\,m} = 6.6\,m/s$$

$$KE = \frac{1}{2}mv^2 + \frac{1}{2}I\omega^2 = \frac{1}{2} * 1.095\,kg * \left(6.6\frac{m}{s}\right)^2 + 0 = 23.8\,J \text{ (cube)}$$

$$KE = \frac{1}{2}mv^2 + \frac{1}{2}I\omega^2 = \frac{1}{2} * 1.095\,kg * \left(6.6\frac{m}{s}\right)^2 + 0 = 17.2\,J \text{ (cuboctahedron)}$$

The rotational KE after impact was calculated considering the moment of inertia and rotational velocity about each axis, as displayed in Equation 7.7.

$$KE_R = \frac{1}{2}(I_{XX}\omega_X^2 + I_{YY}\omega_Y^2 + I_{ZZ}\omega_Z^2) \qquad \text{(Equation 7.7)}$$

In addition, g-forces on sand can be estimated from physics theory and the approximate maximum embedment depths measured after each test. These estimates were used to compare the measured resultant g-forces captured by the SR sensor during the experimental trials. The rate of deceleration of a falling object, calculated in Equation 7.8, is used to estimate the g-force of a given impact using Equation 7.9 (Nelson and Snowden, 2010). The estimated g-forces are presented in section 7.2.

$$a = \frac{v^2}{2d} \qquad \text{(Equation 7.8)}$$

$$G = \frac{a}{g} \qquad \text{(Equation 7.9)}$$

Where: a = deceleration rate,

d = deceleration distance, equal to the embedment depth in sand,

G = g-force, and

g = acceleration of gravity (9.81 m/s²).

7.2. Tests on sand

The initial tests of the experimental laboratory campaign were conducted on a 50 cm sand layer, compacted using a jack hammer tamper plate. Sections 7.2.1 and 7.2.2 detail the results for the cubic block and cuboctahedron, respectively. The different responses of both shapes on the granular material surface yielded significantly distinct coefficients of restitution, demonstrating the variability of restitution parameters cited in the literature for different test conditions in rockfalls.

7.2.1. Cubic block

All cubic test blocks followed a perfectly vertical (90º angle) trajectory prior to impact (Figure 7.2). Small bounce heights followed all impacts, and a small horizontal displacement prior
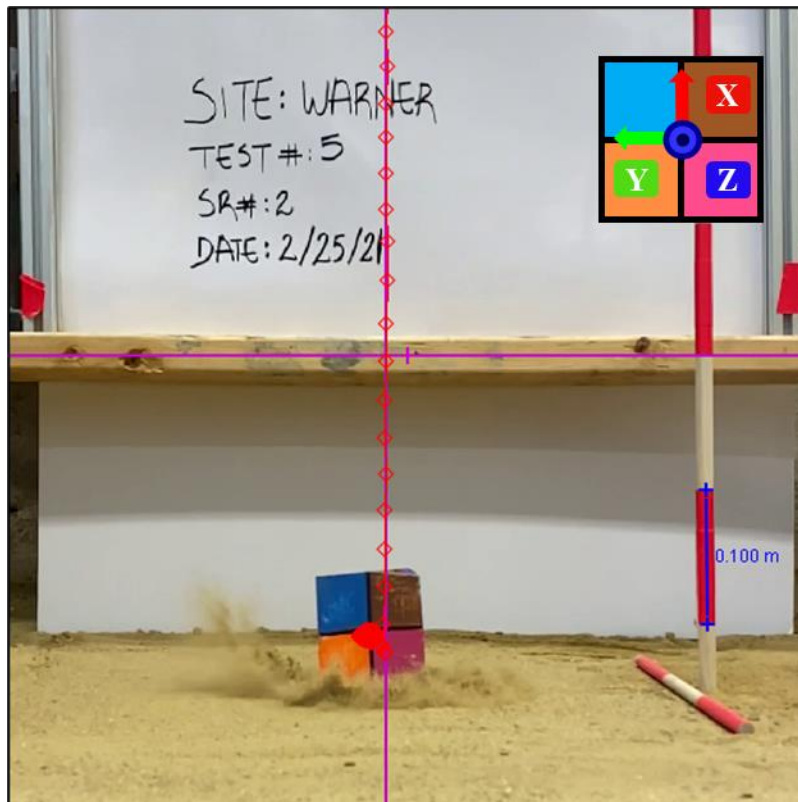
Figure 7.2. Laboratory drop test on sand: cubic block, test 5 (frontal camera).

to a complete stop. The upper camera recordings (Figure 7.3) were used to estimate the horizontal velocity towards the frontal video camera, which cannot be captured from the angle displayed in Figure 7.2.
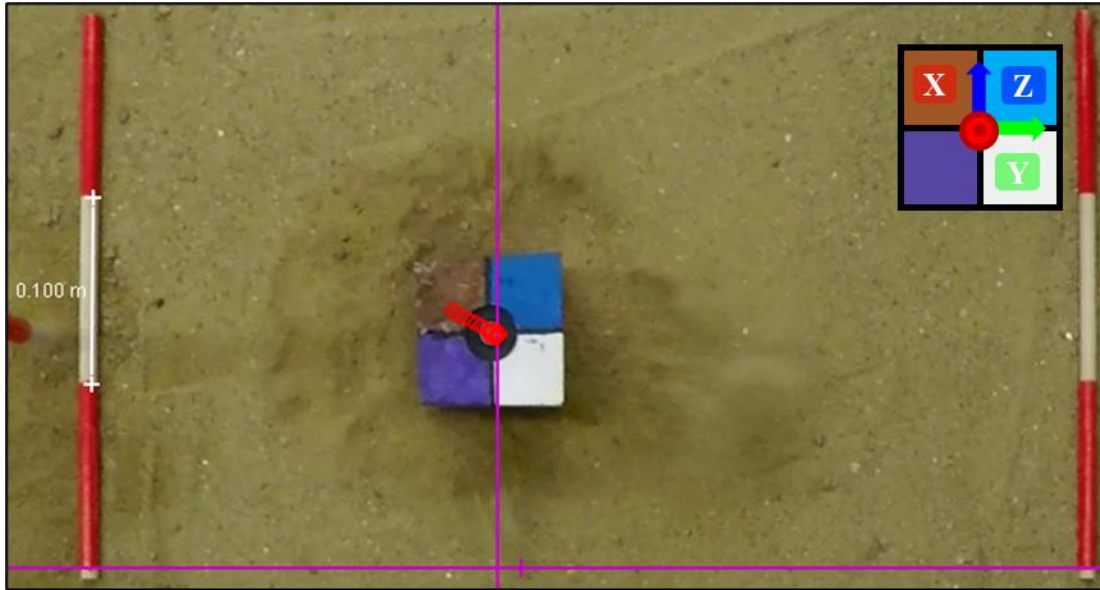
Figure 7.3. Laboratory drop test on sand: cubic block, test 5 (upper camera).

Given the difference in the number of video frames for each camera, the resultant horizontal velocity was estimated from the horizontal velocity obtained from the frontal camera at 240 fps, coupled with the average velocity in the plane, from the upper camera, towards the frontal camera immediately after impact (Equation 7.10). Average values were used from the upper measurements due to the difficulty in precisely estimating the center of gravity position from the camera angle, which could not be perpendicular to the trajectory because the test block was released above it.

$$v_{hor.} = \sqrt{v^2_{x\,(frontal\,camera)} + v^2_{y\,(upper\,camera)}} \qquad \text{(Equation 7.10)}$$

Where: $v_{hor.}$ = resultant rotational velocity in the horizontal direction, parallel to the impact surface,

$v_{x\ (frontal\ camera)}$ = horizontal velocity, parallel to the impact surface, obtained from the frontal camera measurements, and

$v_{y\ (upper\ camera)}$ = horizontal velocity, parallel to the impact surface and towards the frontal camera, obtained from the upper camera measurements.

Finally, the resultant scalar velocity about all three directions after rebound can be calculated using Equation 7.11.

$$v_R = \sqrt{v_{hor.}^2 + v_{vert.}^2} \qquad \text{(Equation 7.11)}$$

Where: v_R = scalar rebound velocity,

$v_{hor.}$ = scalar horizontal velocity, and

$v_{vert.}$ = scalar vertical velocity.

As previously observed during the field experimental rockfalls, the modes of motion could also be easily identified and matched with video observations during the laboratory tests. The SR output for test 5 is presented in Figure 7.4. The test block was positioned at-rest about the X axis (SR window faced up), with the Z axis facing the frontal camera, and the Y axis parallel to the frontal camera.

The sensor data indicates that the test block stayed at-rest until 0.55 s (A) with a resultant acceleration of 1 g (measured about the X axis) and described free fall for 0.65 s (B). A resulting acceleration of 233 g (with the highest acceleration measured about the X axis), yielding an impact force of 2.5 kN, was then recorded upon impact at C. The cube bounced with a resultant rotational velocity of 250 dps, with rotation about Y and Z axes. The lack of rotation about the X axis indicates that the cubic rock did not rotate parallel to the granular material surface, and the Z axis

stayed aligned and facing the frontal camera during the entire test. After bouncing, the rotation

rate gradually decreases and completely stops at 1.5 s.

A bounce height of approximately 17 mm was observed for this test. An impact velocity

of 7.1 m/s was estimated through video, with vertical and horizontal rebound velocities of 0.7 and

0.3 m/s, respectively, resulting in a scalar velocity of 0.75 m/s after impact. The rotational

velocities immediately after impact about X, Y, and Z were equal to 3, 133, and 217 dps,

respectively, which can be converted to 0.05, 2.32, and 3.79 rad/s. Finally, the four definitions of

coefficients of restitution can be estimated as follows:

- Velocity-based COR:

$$COR_{VN} = \sqrt{\frac{h_{N+1}}{h_N}} = \sqrt{\frac{1.7 \, cm}{220 \, cm}} = 0.09$$

$$COR_{VN} = \frac{v_{RN}}{v_{IN}} = \frac{0.7 \, m/s}{7.1 \, m/s} = 0.10$$

- Energy-based COR:

$$COR_E = \frac{0.5 m v_{N+1}^2}{0.5 m v_N^2} = \frac{v_{N+1}^2}{v_N^2} = \frac{(0.7 \, m/s)^2}{(7.1 \, m/s)^2} = 0.011$$

$$COR_{TE} = \frac{0.5[m(v_R^2) + (I_{XX}\omega_{X\,Rebound}^2 + I_{YY}\omega_{Y\,Rebound}^2 + I_{ZZ}\omega_{Z\,Rebound}^2)]}{0.5 \, m(v_I^2)}$$

$$= \frac{\left[1.095 \, kg \left(0.75 \frac{m}{s}\right)^2 + \left(0.0010 \, kg \, m^2 \left(0.05 \frac{rad}{s}\right)^2 + 0.0011 \, kg \, m^2 \left(2.32 \frac{rad}{s}\right)^2 + 0.0012 kg \, m^2 \left(3.79 \frac{rad}{s}\right)^2\right)\right]}{1.095 \, kg \left(7.1 \frac{m}{s}\right)^2}$$

$$COR_{TE} = \frac{0.3 \, J}{27.6 \, J} = 0.011$$

Using the velocity definition of COR_{VN}, the value of 0.10 was obtained for test 5. This

result is compatible with the alternative definition of COR_{VN}, specified from the ratio of bounce

heights (measured bounce/drop height), which was equal to 0.09. In contrast, both kinetic energy-

based COR definitions (COR_E and COR_{TE}) were equal to 0.011. This test yielded total kinetic

energies before and after impact equal to 27.6 and 0.3 J, representing a significant loss of kinetic
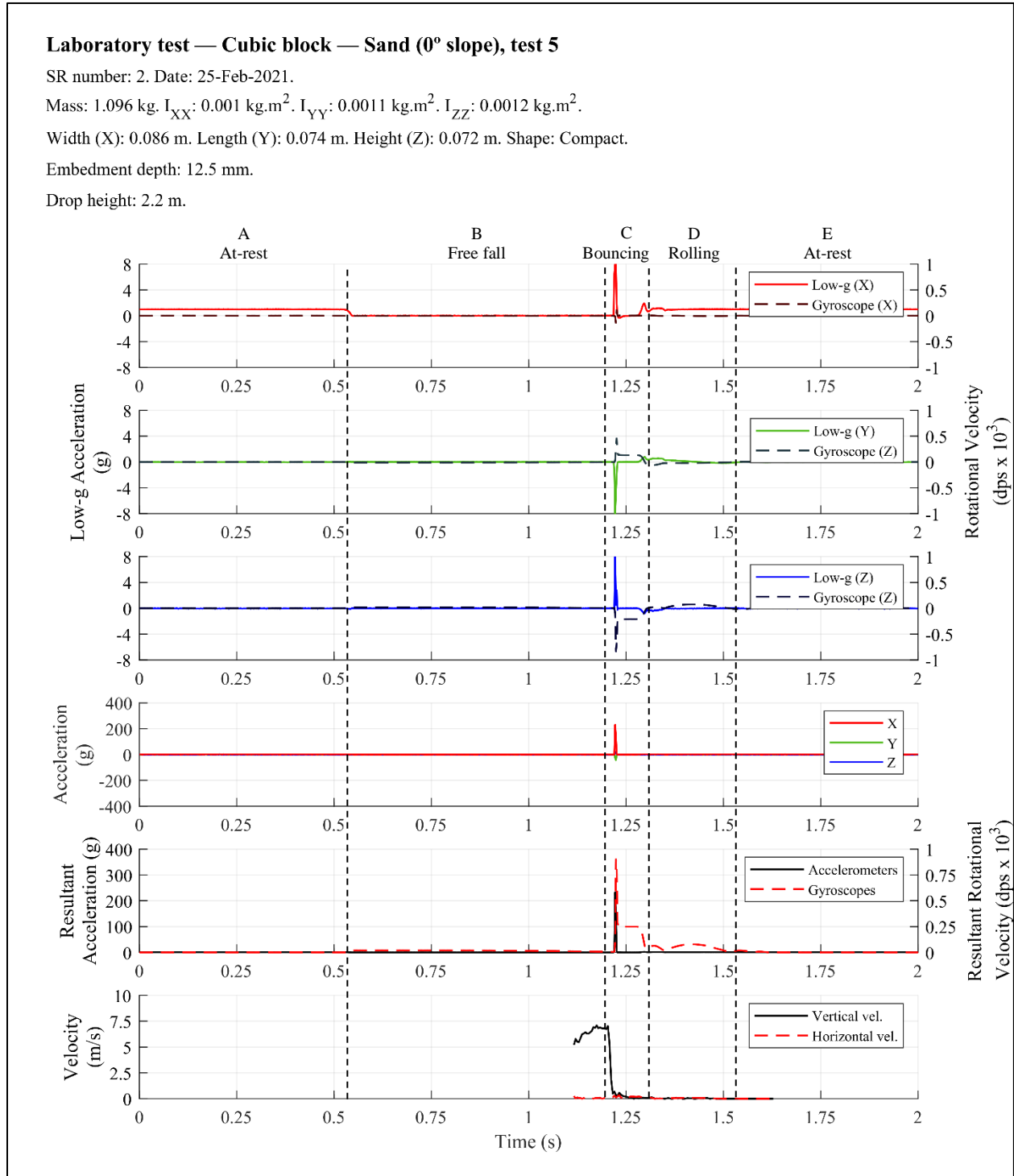
Figure 7.4. Smart Rock test data: test 5, cubic block (sand).

energy after free fall. Slight rotation was developed due to the angle of impact, and the rotational

KE only represented 4% of the translational KE immediately after impact.

The maximum embedment measured after the test was equal to 12.5 mm, yielding a

theoretical G-force of 206 g using the measured velocity in Equations 7.8 and 7.9. Therefore, the

sensor measurements can be verified with theoretical calculations in this test. Table 7.3 presents a

summary of the SR data results for the ten trials with the cubic block. The maximum accelerations

measured by the sensor ranged from 185 to 417 g. The theoretical g-forces ranged from 176 to 229

g and were similar to the peak accelerations below 300 g recorded with the sensor. This difference

indicates that the maximum embedment depths measured at the test are likely not an accurate

reference for the deceleration distance. It represents the point of maximum deflection in the soil

surface after impact. Deceleration distances lower by 30% yield theoretical forces as high as 300

g.

Table 7.3. Smart Rock data summary: sand tests, cubic block, 2.2 m drop height.

Test ID	Block embedment (mm)	Theoretical g-force (g)	Smart Rock resultant data			Maximum impact force (kN)
			Maximum acceleration (g)	Maximum rotational velocity (dps)	Average rotational velocity (dps)	
1	10.6	261	231	675	39	2.5
2	12.1	218	417	354	43	4.5
3	12.0	229	272	1294	76	2.9
4	15.1	176	362	894	41	3.9
5	12.5	206	233	907	43	2.5
6	12.5	217	382	740	34	4.1
7	7.8	345	369	742	26	4.0
8	13.7	210	385	491	27	4.1
9	13.1	199	403	458	23	4.3
10	12.1	220	185	556	27	2.0
Average	12.1	228	324	711	38	3.5
S. Dev.	1.9	47	85	275	15	0.9

Table 7.4 presents a summary of the 10 tests with the cubic block. In spite of the variations between bounce heights and velocities, both definitions of COR_{VN} were equal to an average of 0.08. As noted for test 5, the rotational KE contribution of all tests was minimal due to the 90° impact angle. Therefore, both kinetic-based coefficients of restitution were equal to 0.008, governed by the translational kinetic energy of the block before and after impact. Higher block rotation and tangential velocities are expected on inclined impact surfaces and/or stiffer materials such as rock.

Table 7.4. COR results for the drop tests on sand using the cubic block.

| Test number | Before impact | | | After impact | | | | Coefficients of restitution | | | |
	V_{vert} (m/s)	V_{hor} (m/s)	Rot. vel (dps)	Bounce height (cm)	V_{vert} (m/s)	V_{hor} (m/s)	Rot. vel (dps)	COR_{VN} (bounce heights)	COR_{VN}	COR_E	COR_{TE}
1	7.4	0.1	5	1.3	0.7	0.3	208	0.08	0.09	0.009	0.009
2	7.2	0.1	6	1.4	0.6	0.3	107	0.08	0.09	0.010	0.010
3	7.4	0.1	5	1.2	0.5	0.4	379	0.07	0.06	0.007	0.008
4	7.2	0.0	2	1.9	0.7	0.2	240	0.09	0.09	0.009	0.009
5	7.1	0.1	5	1.7	0.7	0.3	255	0.09	0.10	0.011	0.011
6	7.3	0.0	7	1.8	0.6	0.1	153	0.09	0.08	0.007	0.007
7	7.3	0.1	2	1.6	0.6	0.1	159	0.09	0.09	0.007	0.008
8	7.5	0.1	2	1.8	0.6	0.1	88	0.09	0.08	0.007	0.007
9	7.2	-0.1	1	1.6	0.6	0.1	97	0.09	0.08	0.006	0.006
10	7.2	-0.1	4	1.4	0.6	0.1	96	0.08	0.08	0.006	0.006
Avg.	7.3	0.1	4	1.6	0.6	0.2	178	0.08	0.08	0.008	0.008
S. Dev.	0.1	0.1	2	0.2	0.1	0.1	93	0.01	0.01	0.002	0.002

The normal coefficients of restitution obtained from the trials with the cubic block are in close agreement with previous assessments on granular material performed by Peng (2000) (COR_{VN} between 0.10 and 0.12 for soil), and in the lower limit of the COR_{VN} range between 0.10 – 0.20 specified by Jones et al. (2000, cited by Heidenreich, 2004) for soft soil slopes. In addition, the estimated normal coefficients of restitution are significantly lower than default coefficients

used in two-dimensional modeling, published by Hoek (1987, cited by Heidenreich, 2004) and Pfeiffer and Bowen (1989, cited by Heidenreich, 2004), equal to approximately 0.30.

7.2.2. Cuboctahedron

As opposed to the tests with the cubic block, the cuboctahedric block did not bounce during the experimental trials. Higher block embedment was measured in all trials and equal to approximately double the ground deformations measured in the previous series of tests. The lower energy restitution observed in the video recordings caused the test block to tilt diagonally upon impact with increasing depth instead of experiencing small bounces noted for the cubic blocks.

The higher embedment depth and loss of energy also caused a higher volume of granular material to be disturbed in the surroundings of the test blocks, turning video tracking after impact into a difficult test to estimate the CG position after impact (Figure 7.5). The block rotation with the tilting behavior was also an obstacle during video tracking. For this reason, the tests with the cuboctahedron were only position-tracked immediately after impact, and the block was not tracked until it completely stopped. During all experiments, bouncing behavior was not visually observed resulting in bounce heights equal to zero. The horizontal displacement of the test block was more significant than before cutting the edges of the cubic block as shown in Figure 7.6.

The SR output from test 1, presented in Figures 7.5 and 7.6, is shown in Figure 7.7. After being released at 0.35 s, the test block falls freely (B) and impacts the ground surface at C. The sensor recorded a maximum resultant acceleration of 224 g (1.7 kN impact force), followed by a resultant rotation of approximately 530 dps, double the rotation experienced with the cubic block. As observed in the previous test, the block has not rotated about the X axis and decreases its
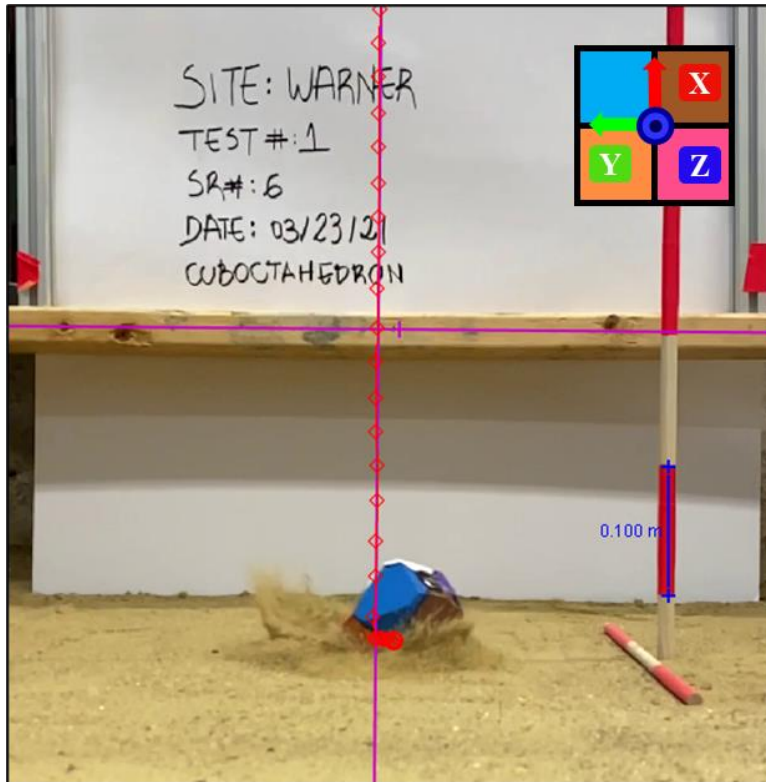
Figure 7.5. Laboratory drop test on sand: cuboctahedron, test 1 (frontal camera).
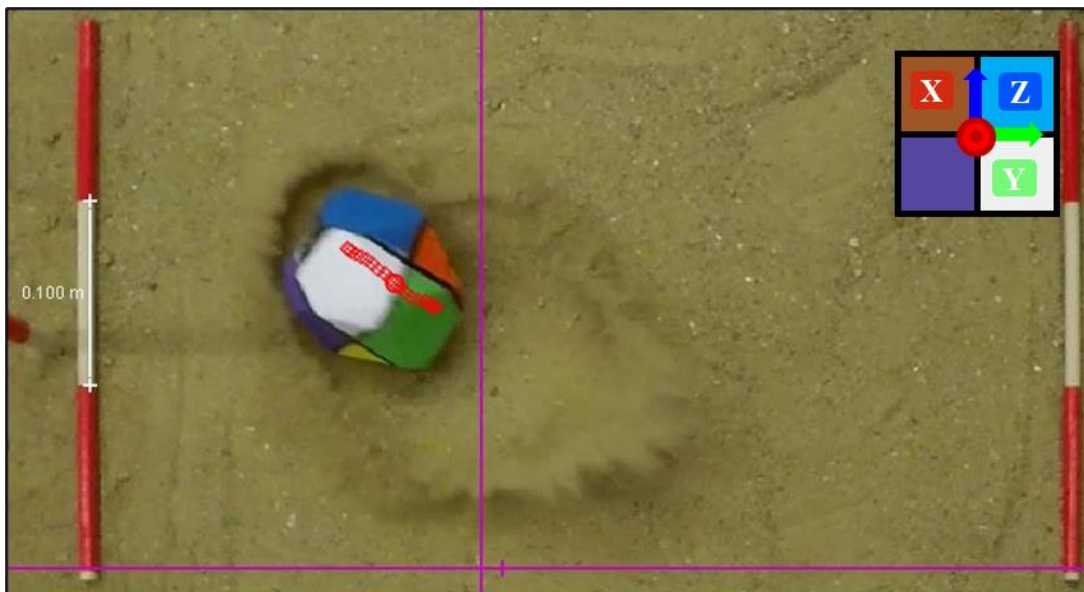
Figure 7.6. Laboratory drop test on sand: cuboctahedron, test 1 (upper camera).

rotation rate until completely stopping at 1.5 s. An impact velocity of 7.1 m/s was estimated through video, with vertical and horizontal rebound velocities of 0.1 and 0.5 m/s, respectively.

Therefore, as suggested by the images, the horizontal motion was more significant than the vertical motion during the test.
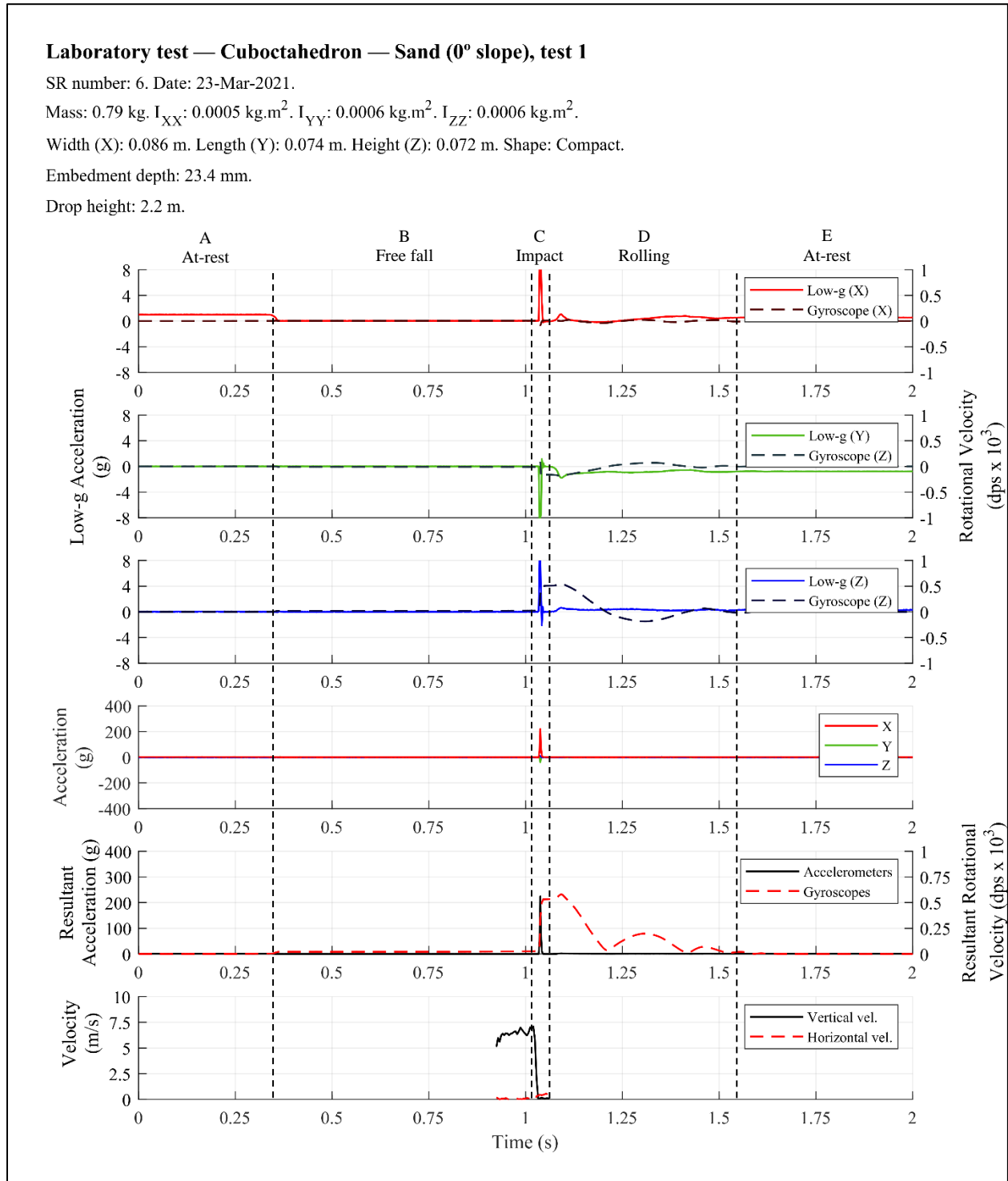
Figure 7.7. Smart Rock test data: test 1, cuboctahedron (sand).

Test 1 yielded total kinetic energies before and after impact equal to 19.8 and 0.13 J, representing a significant loss of kinetic energy after free fall. The higher rotation developed due to the block shape led to a ratio between rotational and translational energies equal to 24%, a significantly higher contribution than the test presented in section 7.1.1 for the cubic block, even though the total energy restitution was smaller. The maximum embedment measured after the test was equal to 23.4 mm and yielded a theoretical g-force of 109 g. Comparing the theoretical and the measured g-forces, it is suggested that block embedment immediately upon impact was lower than the measured depth of 23.4 mm. For this experimental trial, the restitution coefficients COR_{VN}, COR_E and COR_{TE} were equal to 0.014, 0.005, and 0.006, respectively.

Table 7.5 presents a summary of the SR data results for the 10 trials with the cuboctahedric block. The maximum accelerations measured by the sensor ranged from 144 to 225 g, lower than the trials with the cubic block. The theoretical g-forces ranged from 92 to 120 g and were lower than all sensor peak measurements.

Table 7.5. Smart Rock data summary: sand tests, cuboctahedron, 2.2 m drop height.

| Test ID | Block embedment (mm) | Theoretical g-force (g) | Smart Rock resultant data | | | Maximum impact force (kN) |
			Maximum acceleration (g)	Maximum rotational velocity (dps)	Average rotational velocity (dps)	
1	23.4	109	224	580	86	1.7
2	24.9	103	222	417	60	1.7
3	25.8	99	165	593	54	1.3
4	24.8	92	225	620	81	1.7
5	23.2	118	165	557	59	1.3
6	25.7	104	180	597	58	1.4
7	26.4	99	152	735	68	1.2
8	23.5	120	144	852	93	1.1
9	25.9	104	161	683	87	1.2
10	24.7	123	214	724	80	2.0
Average	24.8	107	185	636	73	1.5
S. Dev.	1.1	10	33	119	14	0.3

Table 7.6 presents a summary of the COR for the 10 tests performed with the cuboctahedron. The higher energy dissipation observed in these tests yielded lower COR values and increased the variability in results. The obtained range of velocity- and energy-based COR values are comparable to results obtained at the small-scale parametric experimental campaign conducted by Heidenreich (2004). However, the results obtained by Heidenreich were used for evaluating pertinent parameters for subsequent medium-scale tests and were not used as modeling parameters in rockfall simulations.

Table 7.6. COR results for the drop tests on sand using the cuboctahedron block.

Test number	Before impact			After impact			Coefficients of restitution		
	V_{vert} (m/s)	V_{hor} (m/s)	Rot. vel (dps)	V_{vert} (m/s)	V_{hor} (m/s)	Rot. vel (dps)	COR_{VN}	COR_E	COR_{TE}
1	7.1	0.1	27	0.1	0.5	517	0.014	0.005	0.006
2	7.1	0.0	25	0.1	0.4	278	0.014	0.004	0.004
3	7.1	0.1	23	0.2	0.1	555	0.03	0.001	0.003
4	6.7	0.0	27	0.1	0.4	401	0.015	0.004	0.004
5	7.3	0.1	26	0.1	0.2	302	0.014	0.001	0.002
6	7.2	0.0	28	0.2	0.2	477	0.03	0.001	0.002
7	7.2	0.0	26	0.5	0.2	665	0.06	0.005	0.007
8	7.4	0.1	25	0.4	0.3	749	0.05	0.004	0.006
9	7.3	0.0	28	0.2	0.4	592	0.03	0.003	0.005
10	7.7	0.1	28	0.2	0.4	612	0.02	0.003	0.004
Avg.	7.2	0.0	26	0.2	0.3	515	0.03	0.003	0.004
S. Dev.	0.3	0.1	1	0.1	0.1	153	0.02	0.001	0.002

Peng (2000) performed tests with spherical blocks released on coarse sand which yielded normal coefficients of restitution equal to zero. However, assuming zero restitution on sand slopes potentially underestimates rockfall trajectories and can increase the risk of hazards to the public.

7.3. Tests on rock

Finally, the tests on a rock surface described significantly distinct trajectories and energy restitution compared to the tests on sand. Bouncing behavior could be identified in the video, and rock displacement occurred in all three directions (vertical, parallel to the frontal camera, and towards the frontal camera). High impacts were experienced upon block bouncing, and the cuboctahedric test block split into two halves during the third trial (of 10 trials initially planned). The significant block rotation was also an obstacle in identifying the CG position during each video frame. For this reason, only the velocities before and immediately after impact were estimated with reliability.

Figure 7.8 shows the trajectory described by the test block in the first trial on rock. Compared to the tests on granular material, a clear bounce can be visualized, and significant energy restitution was estimated compared to the previous trials. The direction of the bounce was expected
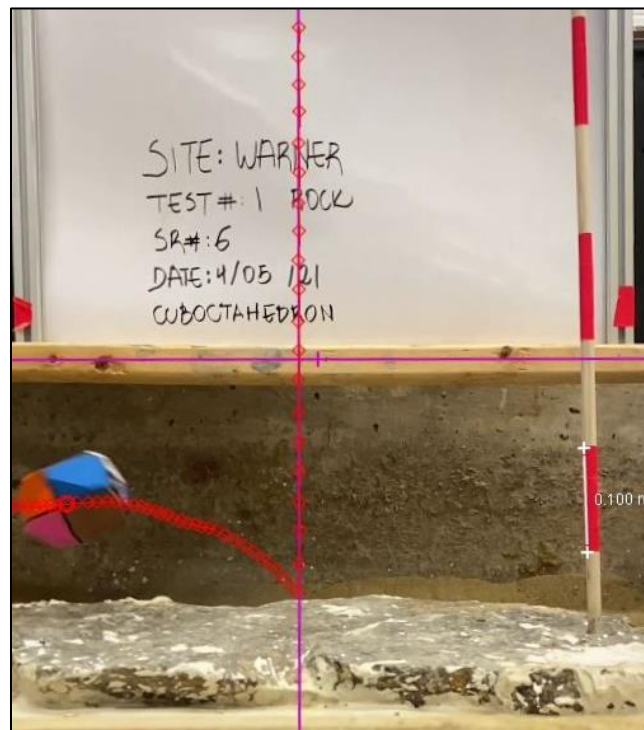
Figure 7.8. Laboratory drop test on rock: cuboctahedron, test 1 (frontal camera).

due to a small slope at the landing point on rock, as shown in Figure 7.9. Figure 7.10 displays the plan view of the drop test. The lateral dispersion perpendicular to the frontal camera was nearly zero. The video frame shown in the figure is the approximate location of the image presented in Figure 7.8.

Figure 7.9. Small inclination of the natural rock at the pont of contact (below the spirit level).
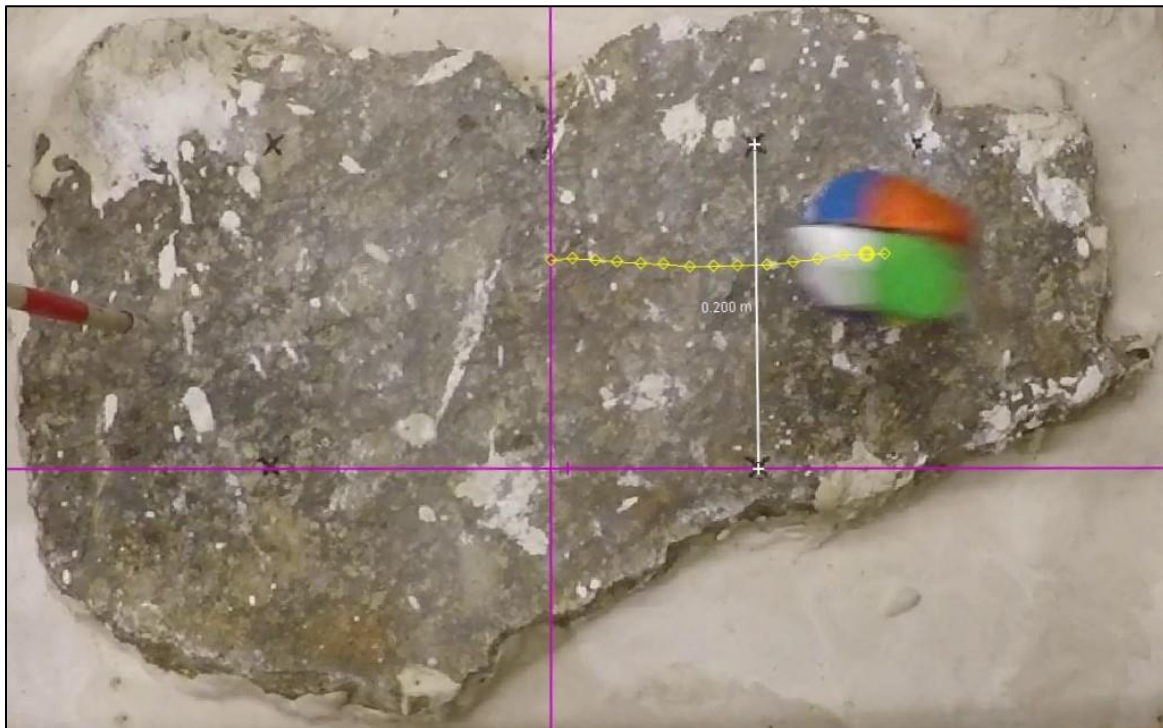
Figure 7.10. Laboratory drop test on rock: cuboctahedron, test 1 (upper camera).

The sensor output for the first test is displayed in Figure 7.10. The impact against the rock face at 1.15 s has exceeded the high-g measuring limit about X, and a peak acceleration of 567 g was recorded (4.4 kN force). As shown in Figures 7.8 and 7.9, the block bounces and deviates its trajectory laterally towards the wall of the pit. It impacts against the wall, exceeding the high-g limit, and stops after 0.5 s of free fall. The second bounce at D was not used for kinetic energy restitution purposes. The second high-impact acceleration demonstrates the difference in behavior after impacts on sand and rock at a 90º fall. The rotational rate described by the test block during the first bounce is equal to the rotational velocity of the cubic block after the impact on sand (500 dps).

An impact velocity of 7.2 m/s was estimated through video, with vertical and horizontal rebounds velocity of 1.5 and 2 m/s, respectively. This test yielded total kinetic energies before and after impact equal to 20.2 and 2.5 J, representing a loss of 78% of the kinetic energy after free fall. Slight rotation was developed due to the angle of impact, and the rotational KE only represented 1% of the translational KE immediately after impact.

During the rebound behavior, a bounce height of approximately 88 mm was measured. Using the velocity definition of COR_{VN}, a value of 0.21 was obtained for test 1. This result is compatible with the alternative definition of COR_{VN}, specified from the ratio of bounce heights (measured bounce/drop height), which was equal to 0.20 for the same test. Both kinetic energy-based COR definitions (COR_E and COR_{TE}) were equal to 0.12.

Table 7.7 presents a summary of the SR data results of the drop tests on rock. All three trials (including when the block split) experienced higher acceleration than the sand tests and exceeded the measuring limits of the high-g accelerometer. As discussed in previous chapters, smaller mass objects with less contact area are subject to feel higher accelerations upon impact on
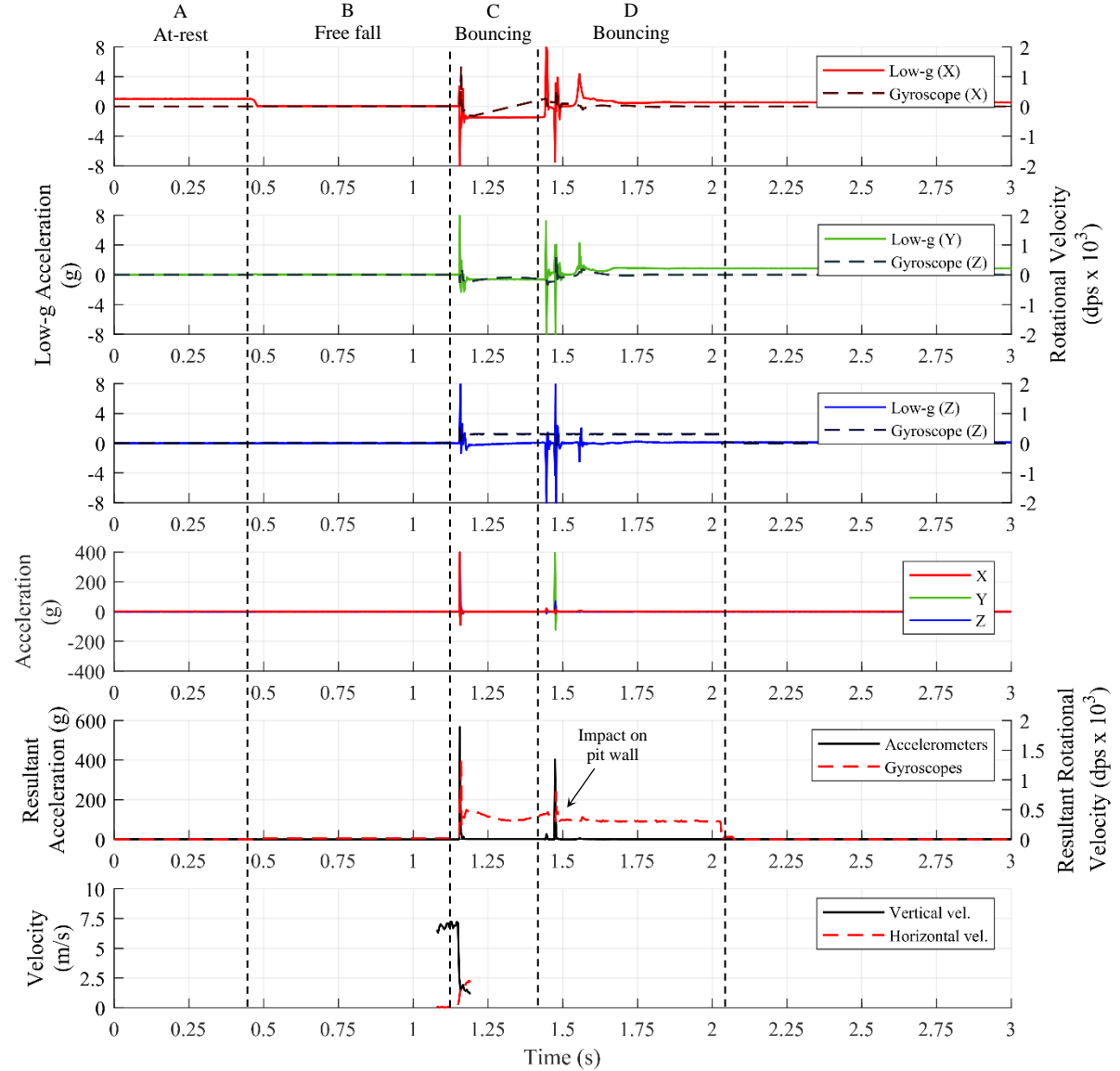
Figure 7.11. Smart Rock test data: test 1, cuboctahedron (rock).

274

stiffer surface (Leonhardt, 2001). The rotational velocities during bouncing motion were also significantly higher than the previous tests. However, rotation motion was negligeable in the tests on rock due to the restitution of translational energy.

Table 7.7. Smart Rock data summary: rock tests, cuboctahedron, 2.2 m drop height.

Test ID	Smart Rock resultant data			Maximum impact force (kN)
	Maximum acceleration (g)	Maximum rotational velocity (dps)	Average rotational velocity (dps)	
1	567*	1365	201	4.4
2	455*	4008	465	3.5
3**	445*	3310	468	3.4
Average	489	2894	378	3.8
S. Dev.	68	1370	153	0.5

* High-g accelerometer measuring limit exceeded for one or more axes.

** Block split in half upon impact, not included in the average calculations.

The trajectory for the second test is presented in Figures 7.12 and 7.13. It demonstrates the significant variability observed for impacts on rock, contrasting with the repeatable and smaller block dispersion during the previous tests on sand. Test 2 deviated from the plane parallel to the front camera and had a maximum bounce height of 170 mm. Despite the trajectory variability, both tests on rock had similar coefficients of restitution, as displayed in Table 7.8.

Table 7.8. COR results for the drop tests on rock using the cubic block.

Test number	Before impact			After impact				Coefficients of restitution			
	V_{vert} (m/s)	V_{hor} (m/s)	Rot. vel (dps)	Bounce height (cm)	V_{vert} (m/s)	V_{hor} (m/s)	Rot. vel (dps)	COR_{VN} (bounce heights)	COR_{VN}	COR_E	COR_{TE}
1	7.2	0.0	21	8.8	1.5	2.0	432	0.20	0.21	0.12	0.12
2	7.2	0.0	25	17	1.5	1.6	395	0.28	0.21	0.09	0.09
Avg.	7.2	0.0	23	13	1.5	1.8	413	0.24	0.21	0.11	0.11
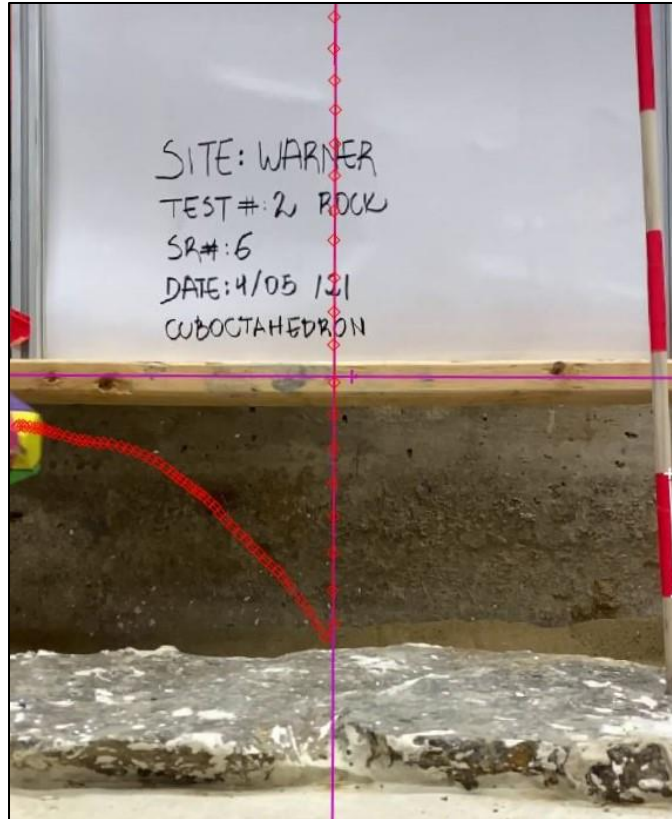
Figure 7.12. Laboratory drop test on rock: cuboctahedron, test 2 (frontal camera).
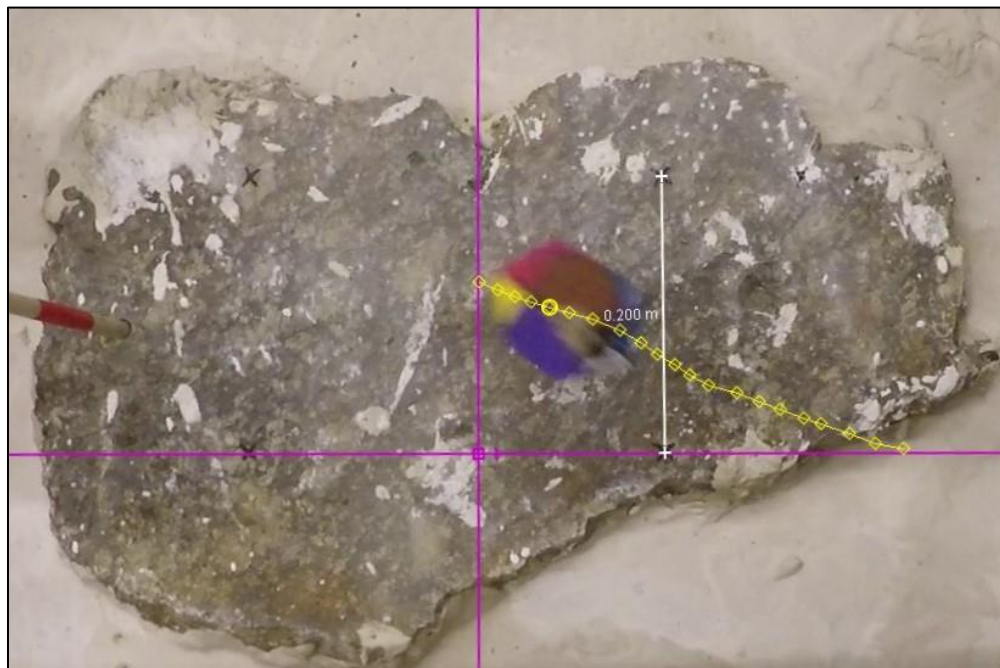
Figure 7.13. Laboratory drop test on rock: cuboctahedron, test 2 (upper camera).

Finally, the trajectory variability of impacts on rock is also attested by the fragmentation on test 3, as shown in Figure 7.14.
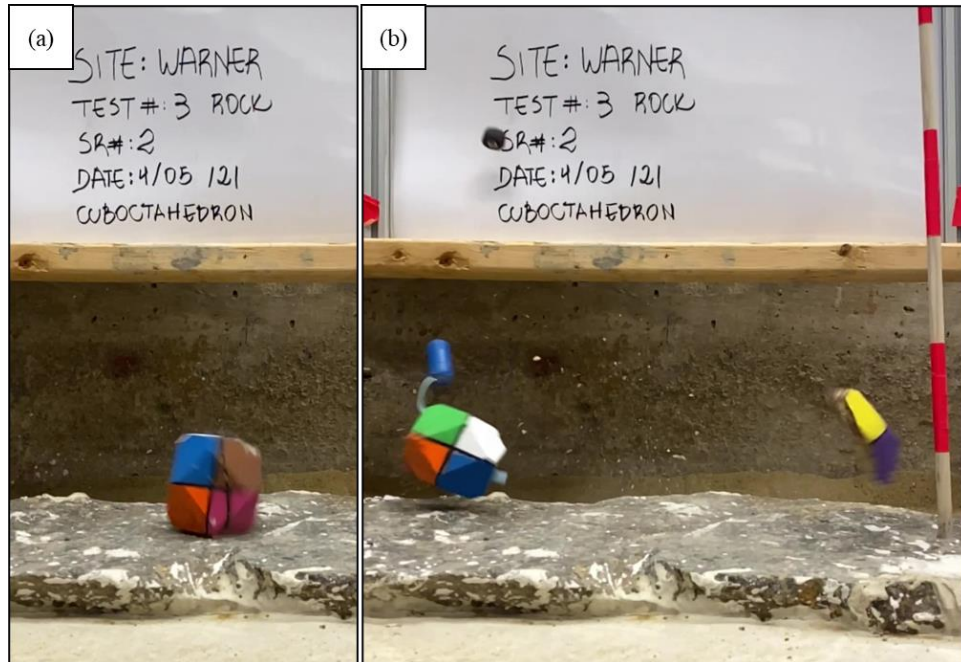
Figure 7.14. Laboratory drop test on rock: cuboctahedron, test 3 (frontal camera). (a) Fragmentation during ground contact, and (b) trajectory dispersion. Both SR and rubber plug are released.

Although only two tests could be performed in the laboratory, impacts on rock tend to present a higher scatter of endpoint locations and higher energy restitution when compared to softer ground. The coefficients of restitution estimated from both tests on rock are compatible with field and laboratory results from Urciuoli (1988, cited by Heidenreich, 2004), Peng (2000), Ushiro et al. (2000, cited by Heidenreich, 2004), and Asteriou et al. (2012). However, most of the energy assessments published in the literature present higher restitution values, including default coefficients used in modeling software.

7.4. Summary and comparisons

This chapter presented a preliminary laboratory assessment of coefficients of restitution, expressively used to model experimental rockfalls, during instrumented tests with the Smart Rock. In these tests, an 8 cm side block from Warner/NH was evaluated upon impact on sand and rock retrieved at the same site. The first tests were performed with the specimen in a cubic shape on sand. The low bounce heights and measured rotational energies (compared to the field data) led to the assumption that a smaller sample with a more rounded shape would experience higher energy restitution on sand for the same drop height of 2.2 m. The effects of surface inclination and drop height were not evaluated in these test conditions.

The video and sensor measurements demonstrated that the cubic block, which had a larger surface contact area during impact, presented a distinct behavior compared to the cuboctahedron. Table 7.9 displays the differences in behavior observed in both samples under identical release and impact surface conditions. It was identified that the block penetration in the sand governs the rebound and energy restitution behavior. Higher embedment depths (ground deformation) implied higher rotation and a rolling behavior instead of block bouncing. Past rebound assessments on plaster performed by Chau, Wu et al. (1999), cited by Heidenreich (2004), have also shown higher normal coefficients of restitution for cubic blocks than spherical blocks.

Table 7.9. General observations of rockfall behavior during the experimental campaign.

Change in parameter	Acceleration	Block rotation	Lateral dispersion	Block embedment	Block rebound
Flat contact area	↑ Increases	↓ Decreases	↓ Decreases	↓ Decreases	↑ Increases
"Rounded" contact area	↓ Decreases	↑ Increases	↑ Increases	↑ Increases	↓ Decreases

The change in behavior with the alteration of the shape of the test follows observations from Heidenreich (2004) and Labiouse and Heidenreich (2009), who did a meticulous study of block impacts on soft ground. They defend that the rebound behavior is controlled by block penetration, sliding, and rotation, as impacts on soft ground typically do not have enough KE to deform the released blocks plastically. Labiouse and Heidenreich also state that vertical impacts on soft horizontal ground, even if compacted, produce very small to no rebound in the vertical direction. More significant rebound behavior can be observed upon impact at inclined conditions.

The investigation conducted by Heidenreich and Labiouse demonstrated that there is a high complexity associated with block bouncing on soft ground, which produces a significant variability in restitution coefficients with different surface conditions. Heidenreich and Labiouse reiterated that default coefficients of restitution published in the literature are prone to inaccurate predictions if applied to another site and/or test conditions. This affirmation brings to question the validity of coefficients databases for general rockfall evaluation with no field calibration data. Incorrect predictions may result in improper mitigation designs. Therefore, it is challenging to select representative parameters for trajectory predictions upon impacts on soil. In this context, Heidenreich and Labiouse recommend the verification of rockfall models with field trials for protective assessments of potential areas at risk.

Finally, the tests on rock presented a significantly distinct behavior compared to the sand tests. As observed by authors such as Pfeiffer and Bowen (1989, cited by Heidenreich, 2004), Fornaro et al. (1990, cited by Heidenreich, 2004), and Chau et al. (2002), impact surfaces with higher Young's modulus will also increase energy restitution in both normal and tangential directions. Although the described trajectories were different while bouncing, the test blocks presented similar velocity- and energy-based coefficients of restitution.

The three series of tests confirmed observations from previous authors that the rebound behavior of falling blocks depends on a wide variety of simultaneous factors. The ground characteristics (material, inclination, conditions), block properties (weight, geometry), and fall kinematics (impact velocity, impact angle, block rotation) exert a crucial role in the developed bounce heights and runout distances. This way, distinct responses can be produced for the same block if the test conditions are altered. Coefficients of restitution in rockfall modeling need to account for several impact conditions and provide the most probable responses for subsequent sizing of protective structures.

Smart Rocks are promising tools capable of quantifying changes in rotation and providing accurate rotational KE estimates during block rebound, as previously observed in the field tests. Although the effect of block rotation was nearly negligeable in most tests, the contribution of block rotation tends to increase at steeper impact surfaces. As observed by different authors, coefficients of restitution generally increase at steeper slope angles and smaller impact angles (Wu, 1985; Peng, 2000; Chau et al., 2002, Asteriou et al., 2012; Saeidi et al., 2014; Wang et al., 2018). Future research perspectives following this experimental approach and considering a higher variability of parameters and impact surfaces are presented in Chapter 9.

8. MODELING EXPERIMENTAL ROCKFALLS

A preliminary two-dimensional modeling assessment of field rockfalls was performed using RocFall 6.0 by Rocscience. Two sets of digital models were used to compare the field data from the Keene and Warner sites to 2D simulated trajectories. Representative slope cross-sections from both sites were imported in the software as coordinates, obtained from three-dimensional surface models generated by the NHDOT. The results of the rigid-body analyses conducted are presented in the following sections. As detailed in Chapter 3, each test block was simulated in two directions (X-Z and Y-Z coordinates) with simplified geometries (Figure 8.1). Each rock cross-section was simulated 50 times from locations approximated from the field tests, resulting in a total of 100 simulations for each model. The number of successful trials was often not equal to 100 because of simulations which exceeded the maximum computation time of the software.
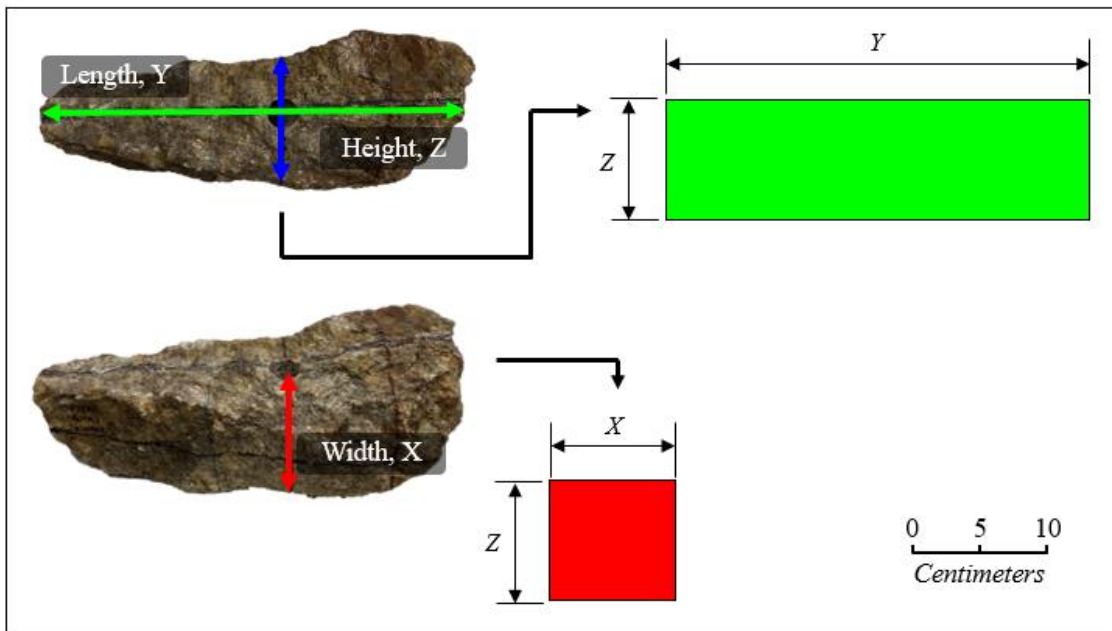
Figure 8.1. Method to simplify cross-sections of a test block using geometric shapes.

The modeling assessments were performed in two stages, in which default coefficients from the literature previously evaluated by Disenhof (2018) were used. Next, the COR values determined in the laboratory for the tests on sand and rock were compared to the initial simulations. The coefficients and standard deviations used in this modeling effort are shown in Table 8.1. Coefficients of friction were not evaluated in this research, and default values were used in both stages.

Table 8.1. Coefficients of restitution (respectively): normal coefficient of restitution, dynamic coefficient of friction, and rolling coefficient of friction. Source: Rocscience, Coefficient of Restitution table.

Source	Color	Description	COR_{VN}	μ	μ_r
Default coefficients		Bedrock outcrops	0.35±0.04	0.55±0.04	0.15±0.04
		Soft soil, some vegetation	0.30±0.04	0.55±0.04	0.30±0.02
		Asphalt	0.40±0.04	0.55±0.04	0.10±0.01
Laboratory coefficients		Bedrock outcrops	0.21±0.04	0.55±0.04	0.15±0.04
		Soft soil, some vegetation	0.08±0.02	0.55±0.04	0.30±0.02

RocFall 6.0 software considers a probabilistic approach during trajectory estimates, in which a normal distribution of the coefficients of restitution is used to estimate rockfall kinematics. Therefore, the specified standard deviations are considered up to three times their original magnitude. For normal distributions:

- 99.74% of the tests are within ± (3 × standard deviation),

- 95.44% of the tests are within ± (2 × standard deviation), and

- 68.27% of the tests are within ± (1 × standard deviation).

Since the laboratory COR value for rock was only based on the average of two tests, a standard deviation could not be estimated from these measurements. For this reason, the same standard deviation used in the default COR for rock was assumed. For the sand tests, the

coefficient of restitution obtained in the tests with the cubic block was used. Although these tests presented a standard deviation of 0.01, significant variability was measured when the cuboctahedron was dropped. For this reason, the sand surface was defined with the highest standard deviation possible, equal to 0.02 due to limitations from the normal distribution.

8.1. Keene, NH

As presented in Chapter 5, the rock cut located in Keene, NH is a 10 m tall C-rated slope located away from transportation corridors or constructions. The 3D point cloud used to generate the slope cross-sections is shown in Figure 8.2. Most vegetation seen in the figure had been removed before the test date, and excess points due to vegetation in the cross-sections were deleted. The base of the rock slope was formed mainly by soil and any remaining small bushes and foliage.
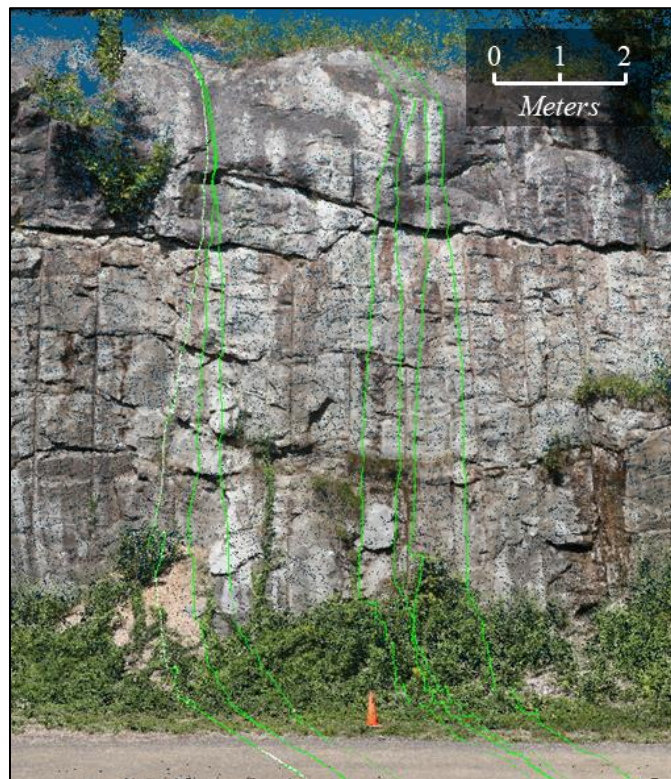
Figure 8.2. Three-dimensional digital model for the rock cut in Keene, NH. The green lines indicate the cross-sections obtained from the model.

Simulations were performed for all test blocks using the two sets of COR values. The results are shown for the reference rock and rock 4, whose trajectories and sensor data were previously discussed in Chapters 4 and 5. From the field tests, it was observed that the test block initially slid and bounced against the top of the rock face before free falling until the base of the slope. The first impact near the ground surface occurred on rock, and a clear rebound was seen until a second impact against the sand ditch. A second bounce was also observed before the block rolled and completely stopped. The approximate field trajectory described by the reference rock is shown in black in Figure 8.2. The red trajectories represent the cross-section with X and Z dimensions, while the green trajectories represent the cross-section with the Y and Z dimensions. Although probably excessive runout distances were calculated, the models correctly predict the modes of motion observed during the field experiment (bouncing, free fall, bouncing/rolling).

A visual comparison between the default (Figure 8.3a) and laboratory (Figure 8.3b) coefficients suggests that the default coefficients predict higher bounce heights that are not quickly dissipated with the increase in distance from the toe of the slope. On the other hand, the laboratory coefficients describe a smaller variability in trajectories during free fall. The damping effect on soil reduces the bounce heights at shorter distances from the toe when compared to the default COR_V, whose value (0.30) is nearly the same as rock (0.35). This behavior was expected due to the decrease in normal restitution in sand equal to almost 75%. The rebound behavior obtained by the laboratory-based simulations yielded more realistic bounce heights than the default coefficients, even though the runout distances were overestimated.

Figure 8.4 presents the resultant rotational velocities measured with the Smart Rock in the field compared with the average rotational rates calculated in the models. Similar comparisons were performed by Disenhof (2018), and the SR time was used as a proxy for the block position
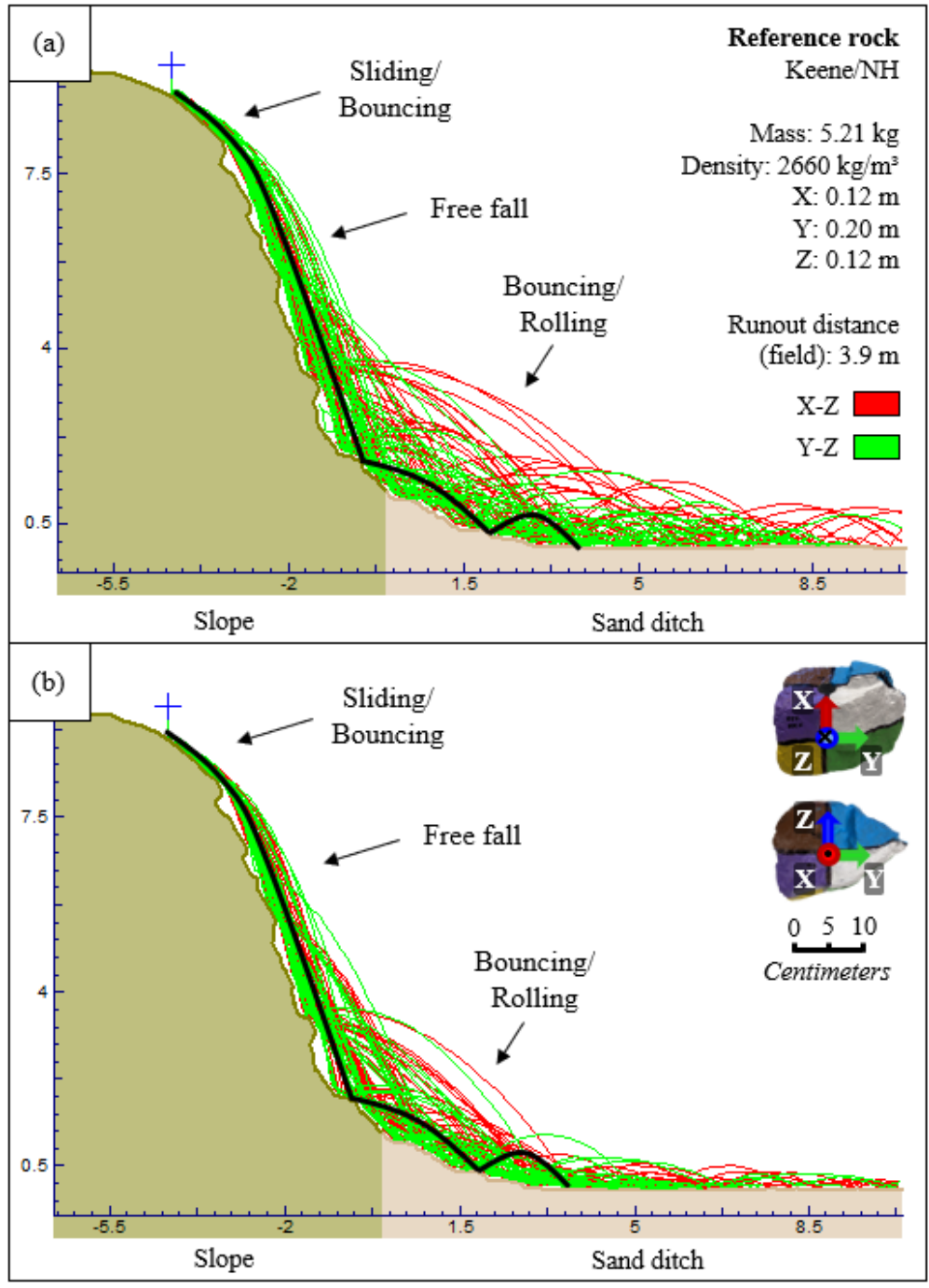
Figure 8.3. RocFall trajectories for the reference rock in Keene NH: (a) default coefficients and (b) laboratory coefficients. The black trajectory was approximated from the field experiment. Dimension units are in meters.

on the slope. The simulation data were plotted for the X-Z and Y-Z cross-sections and a combination of both. The X-Z trials have rotated around the Y axis (smallest moment of inertia),

while the Y-Z simulations have revolved around the X axis (largest inertia). Free fall behavior can be identified in the flat lines between 1 and 2 s for the SR, and -4 and -2 m in the horizontal position for the RocFall simulations. The graph indicates that the estimated rotation rate of 700 dps for the laboratory coefficients correlates well with the field data during the initial free fall stage between -4 and -2 m.
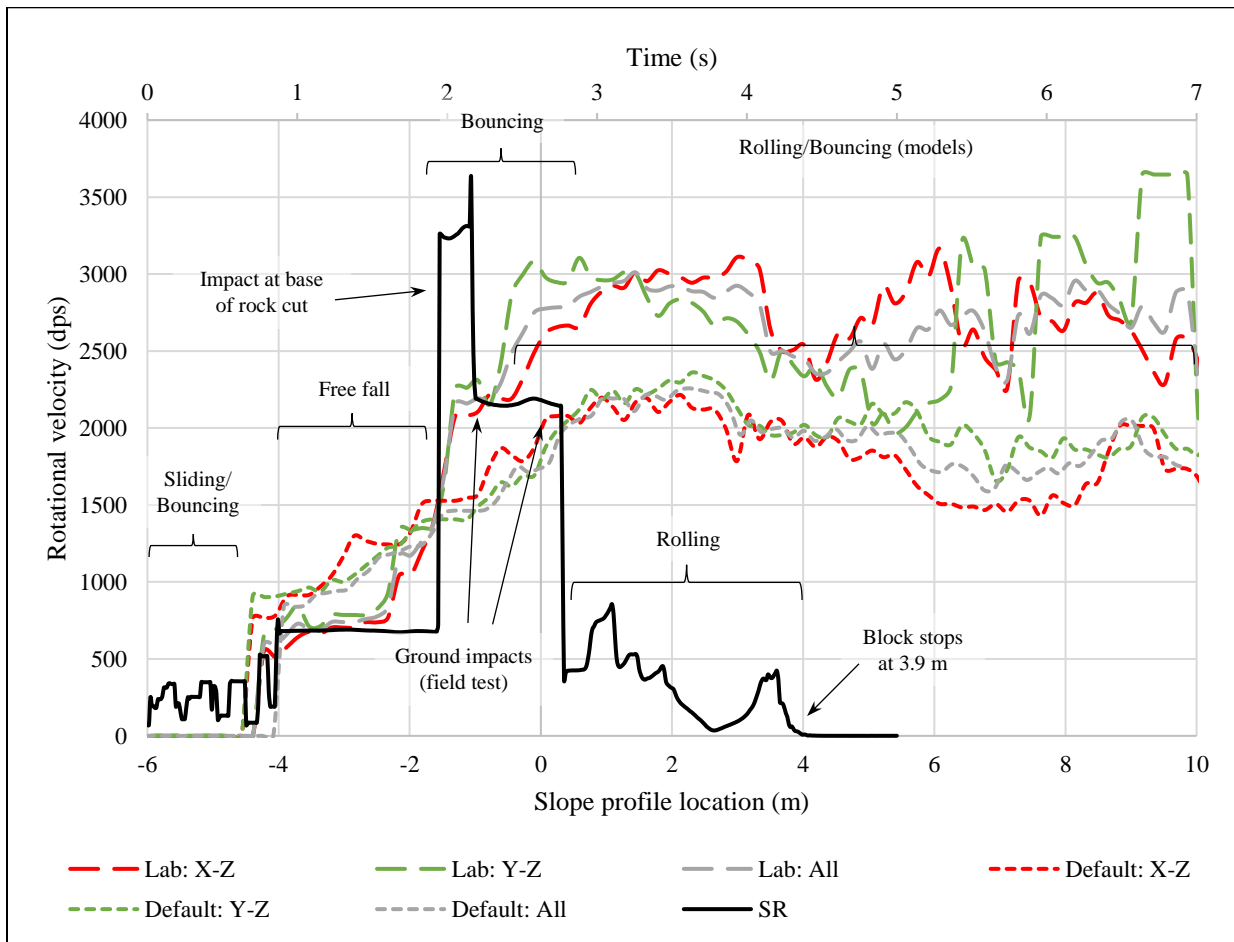
Figure 8.4. Comparison of average modeled values to measured rotational velocities: reference rock, Keene NH.

The rotation rate of models is increased to a range between 1500 and 3000 dps during the modeled bouncing behavior. The sudden rise in rotation to 3250 dps in the field test is initially higher than the models. It can be attributed to potential differences between the actual slope and block and the modeled slope profile and test rock, which consist of simplified representations of

the field conditions. Also, the sensor data recorded rotation data about three simultaneous axes, while each modeled block can only rotate about a single axis. Still, this rate is rapidly decreased upon ground contacts and this behavior was not observed in the simulations. During the field test, the final rolling motion contrasts with the predicted rotations, which do not gradually reduce as the horizontal displacement decreases. Consequently, higher runout distances were estimated.

A second test, performed with rock 4, is displayed in Figure 8.5. The block is four times heavier than the reference rock and described a rolling motion upon ground impact in the field. While the runout measured in the field is close to the slope toe, significantly higher endpoint locations were also estimated in the models for this rock. Unrealistic bounce heights (due to the higher mass of the block) are identified mainly when the default coefficients are used.

A similar comparison between measured and estimated rotation rates is displayed in Figure 8.6. As suggested by the modeled trajectories and increased bounce heights and endpoint locations, the rotation data calculated by the software was higher than the SR rotation at all positions on the slope profile, including in free fall. As observed for the reference rock, the sensor data shows how the motion of the block was rapidly decreased after the impact on the ground. In turn, the rotation rates of the models were not significantly dissipated for the blocks in motion at each slope profile location. Higher rotational velocities were measured, especially during the simulations with the default coefficients.

A summary of the measured and estimated endpoint locations for all Keene rocks is presented in Figure 8.7. The numbers on top of each test series display the number of test rocks that stopped within the specified range. The histogram displays the overestimated runout distances predicted by the simulations, especially using default coefficients. The nearly 90% of rock runouts after 5 m past the toe of the slope, observed in the first simulations, are decreased to approximately
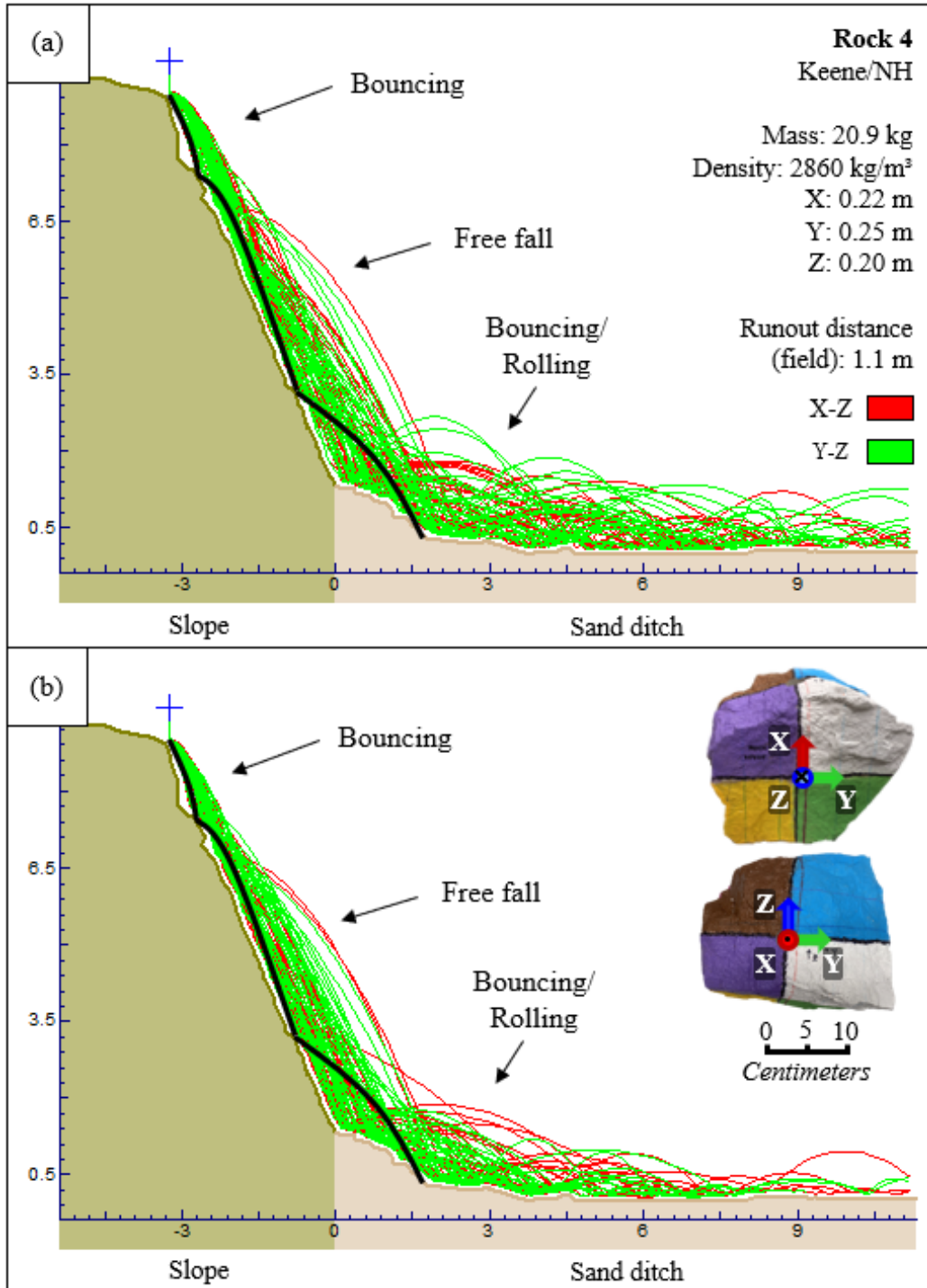
Figure 8.5. RocFall trajectories for rock 4 in Keene NH: (a) default coefficients and (b) laboratory coefficients. The black trajectory was approximated from the field experiment. Dimension units are in meters.

40% using the laboratory-based coefficients. However, it is important to highlight that the tested

blocks were not evaluated for repeatability in the field, and were only released once at each site.
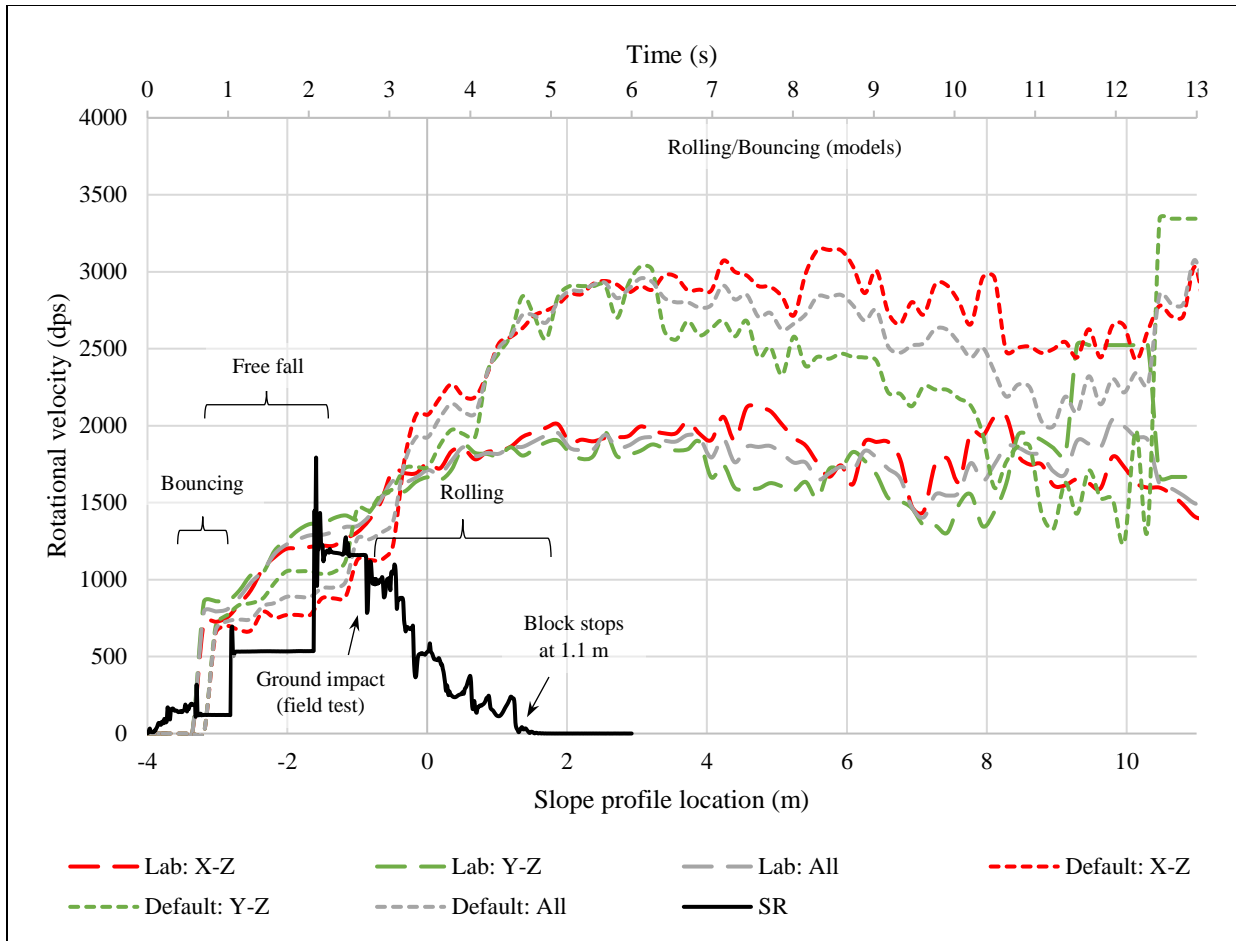
Figure 8.6. Comparison of average modeled values to measured rotational velocities: rock 4, Keene NH.
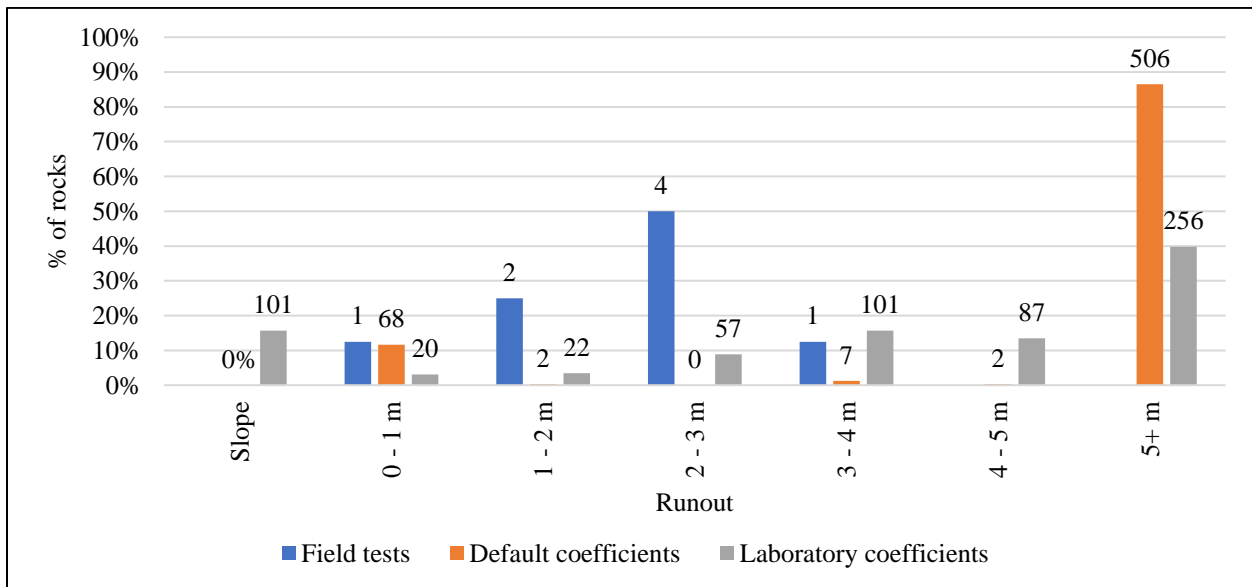
Figure 8.7. Comparative histogram between field measurements and rockfall models: Keene NH.

8.2. Warner, NH

The road cut in Warner/NH consists of a 15 m tall A-rated slope that is 3.5 to 5 m away from NH Route 103. Figure 8.8 shows the 3D point cloud used to extract the approximate slope cross-sections for each trajectory measured in the field. The tests with rocks 3 and 5 from Warner fractured and were not included in the models and runout histogram as RocFall software does not account for block fragmentation.

Figure 8.8. Three-dimensional digital model for the rock cut in Warner, NH.

A comparison between the simulated and field-measured trajectories for the reference rock at the Warner site is presented in Figure 8.9. As observed for the Keene models, the modes of motion (bouncing, free fall, bouncing/rolling) were correctly estimated, but the runout distances and bounce heights were higher than the field test. The trajectory dispersion, bounce heights, and runout distances were reduced using the laboratory coefficients but are still overestimated. Very little bouncing motion was observed for all test rocks in Warner.
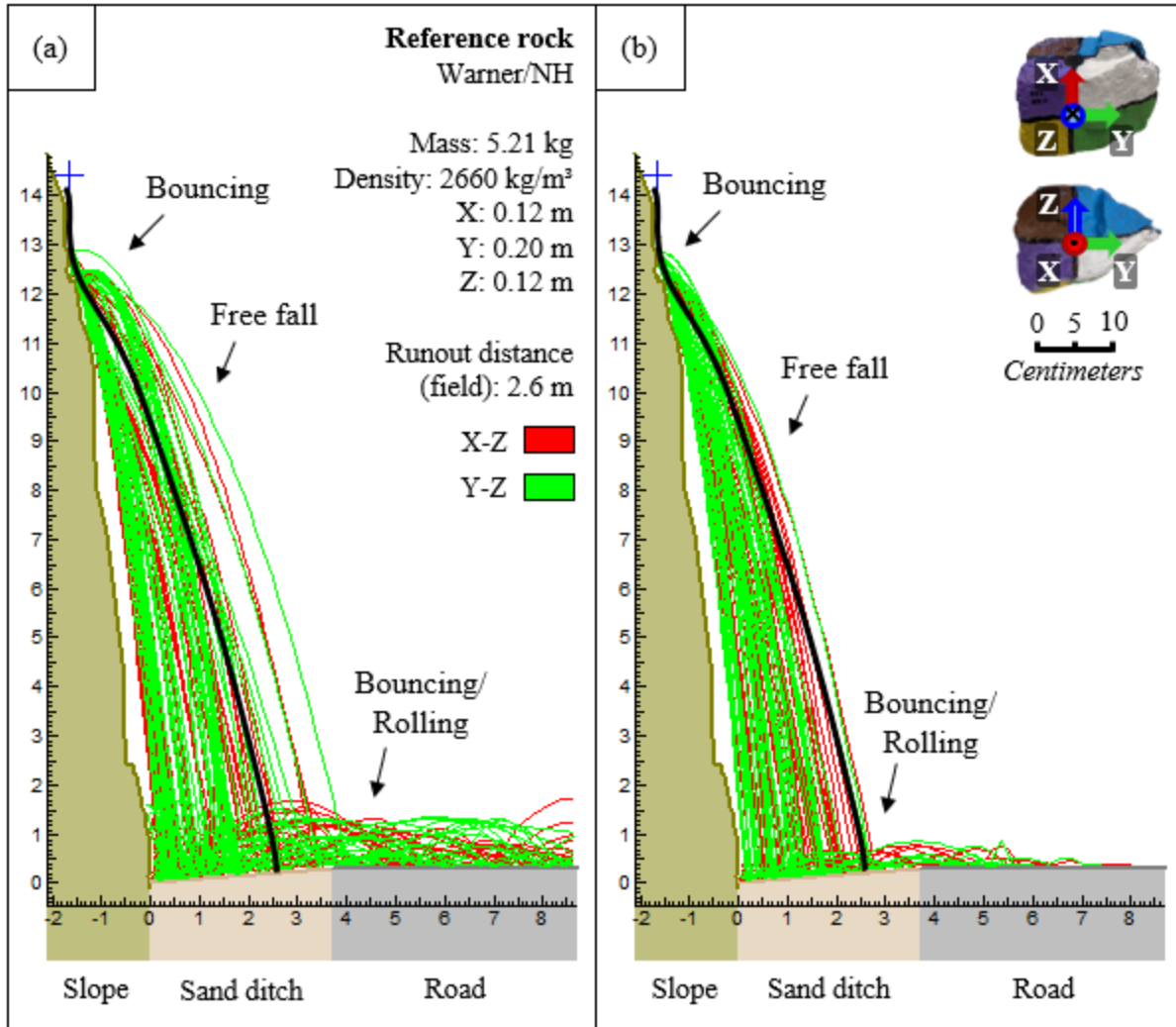
Figure 8.9. RocFall trajectories for the reference rock in Warner NH: (a) default coefficients and (b) laboratory coefficients. The black trajectory was approximated from the field experiment. Dimension units are in meters.

Figure 8.10 displays the measured and estimated rotation data. Although the rotation range for the models is comparable to the Smart Rock data near the upper slope (between 12 and 14 m in the vertical position), higher rotation rates were calculated after the bouncing behavior at the height of 12 m. A significant number of trials have reached the road after 3.8 m. Higher rotation rates were estimated for the default coefficients, which initially revolved around the X axis (shortest inertia) and presented slightly higher rotation around the Y axis after bouncing. The same behavior was identified in the measured field data previously detailed in Chapter 5.
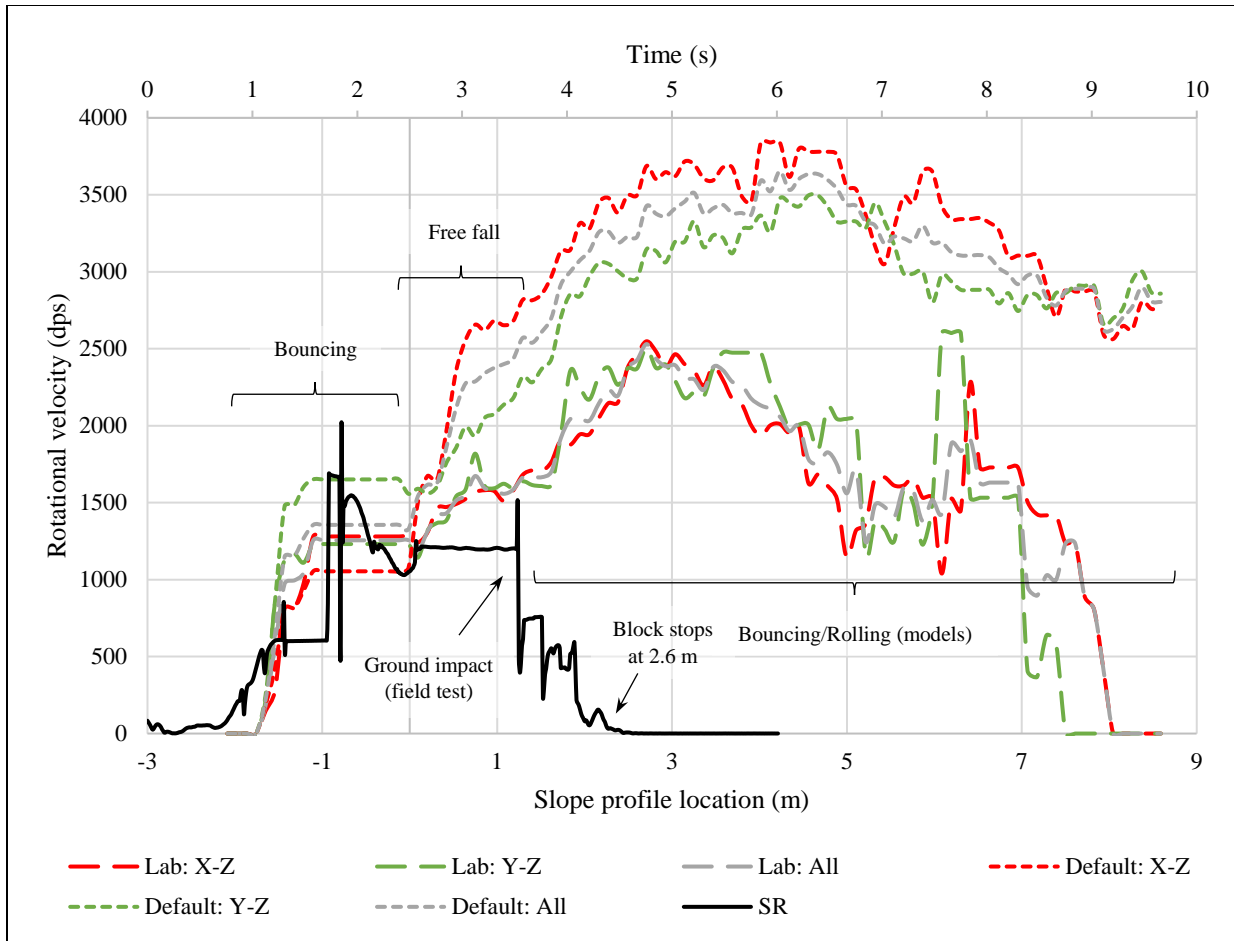
Figure 8.10. Comparison of average modeled values to measured rotational velocities: reference rock, Warner NH.

The field trajectory described by rock 6 is presented with the correspondent simulations in Figure 8.11. The test rock had kinetic energy fully absorbed upon ground impact, and no further rockfall motion was recorded (zero bounce height). From both modeled cross-sections, it is possible to observe that unrealistic bounce heights and runout distances were predicted, considering that the experimental test did not roll after reaching the catchment ditch. However, the initial rock behavior (rolling/bouncing and free fall) was correctly predicted by the software. Similar lateral dispersions were calculated before ground contact using both sets of default and laboratory coefficients. The bounce heights and runout distances estimated by the default coefficients were higher than the laboratory-based assessments.
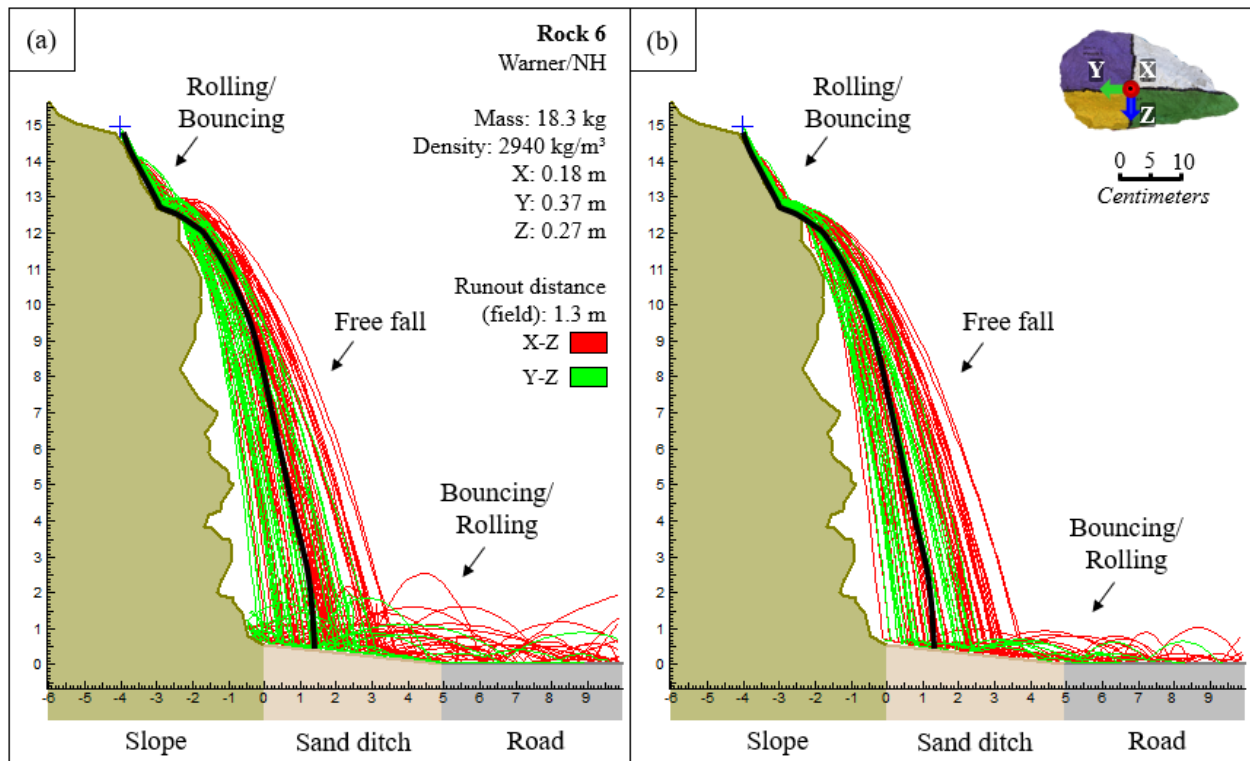
Figure 8.11. RocFall trajectories for rock 6 in Warner NH: (a) default coefficients and (b) laboratory coefficients. The black trajectory was approximated from the field experiment. Dimension units are in meters.

The comparison between rotational velocities from the SR and the computational models is displayed in Figure 8.12. As opposed to the previous tests, the rotation motion described by the block during free fall was underestimated by the models compared to the experimental data. However, the calculated rotation is increased after ground contact, while it immediately stops in the field.

The estimated rotational velocities about both X (green) and Y (red) axes were similar, comparing the default and laboratory coefficients. A clear distinction in rotation for each axis is observed during the entire trajectories for both COR_{VN} values. Higher revolution rates were calculated about the shortest axis of inertia (Y), and the same simulations shown in red have developed the farthest runout distances. In the field, rock 6 had significant rotation about Y at the

top slope and developed predominant revolution about the X axis (largest inertia) during free fall while simultaneously rotating about all three axes.
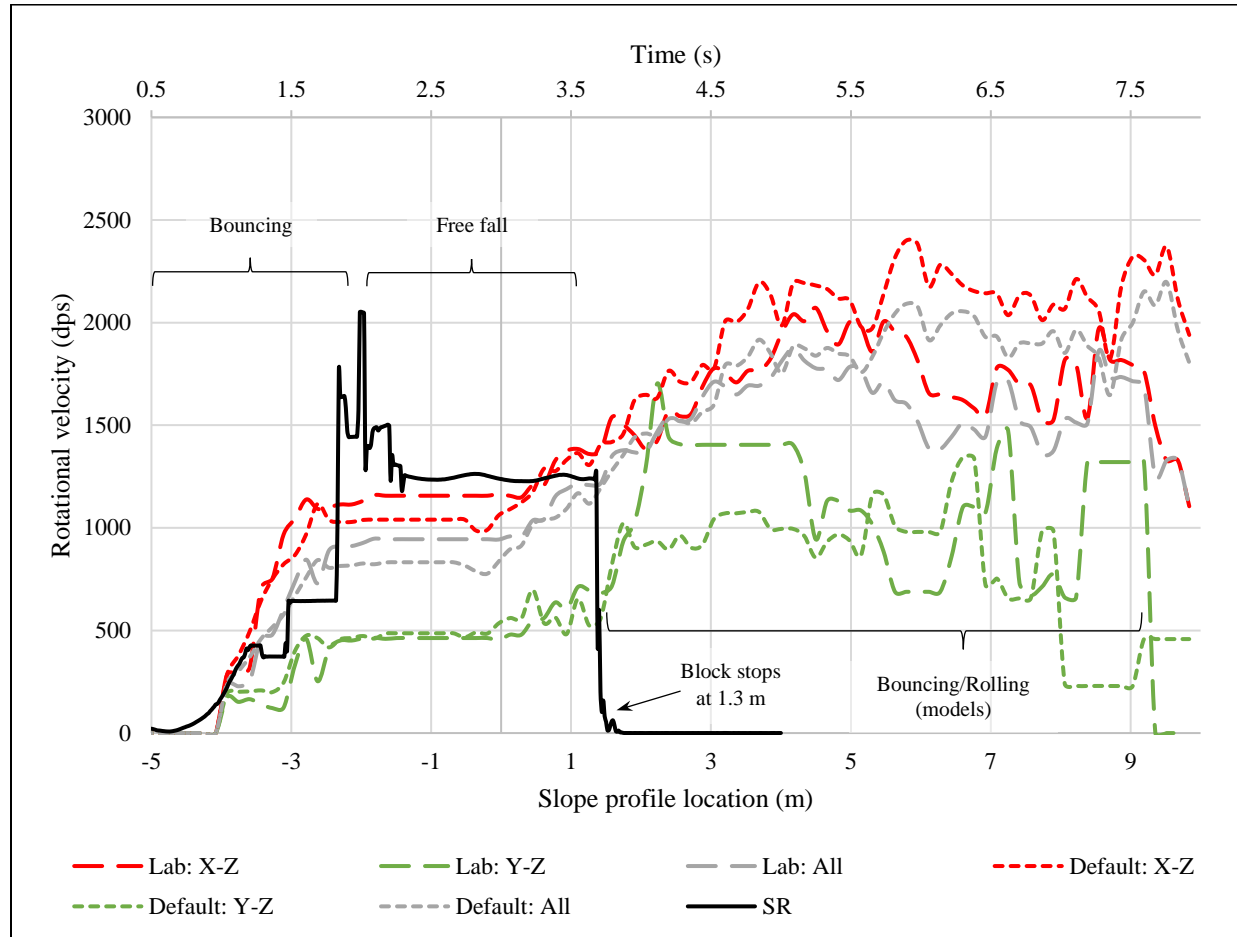
Figure 8.12. Comparison of average modeled values to measured rotational velocities: rock 6, Warner NH.

A combined comparative histogram is shown in Figure 8.13. Almost 50% of the computer models stopped either on the rock face surface or the road using default coefficients, and this proportion reduces to near 35% for the laboratory-based coefficients. Both possibilities are improbable in high frequencies given the slope geometry, the rock weight, and the low energy restitution in the catchment ditch. In addition, while all field trials in Warner did not stop near the road shoulder (including fragmented blocks not considered in these models), a significant number of blocks did reach the pavement in the 2D simulations.
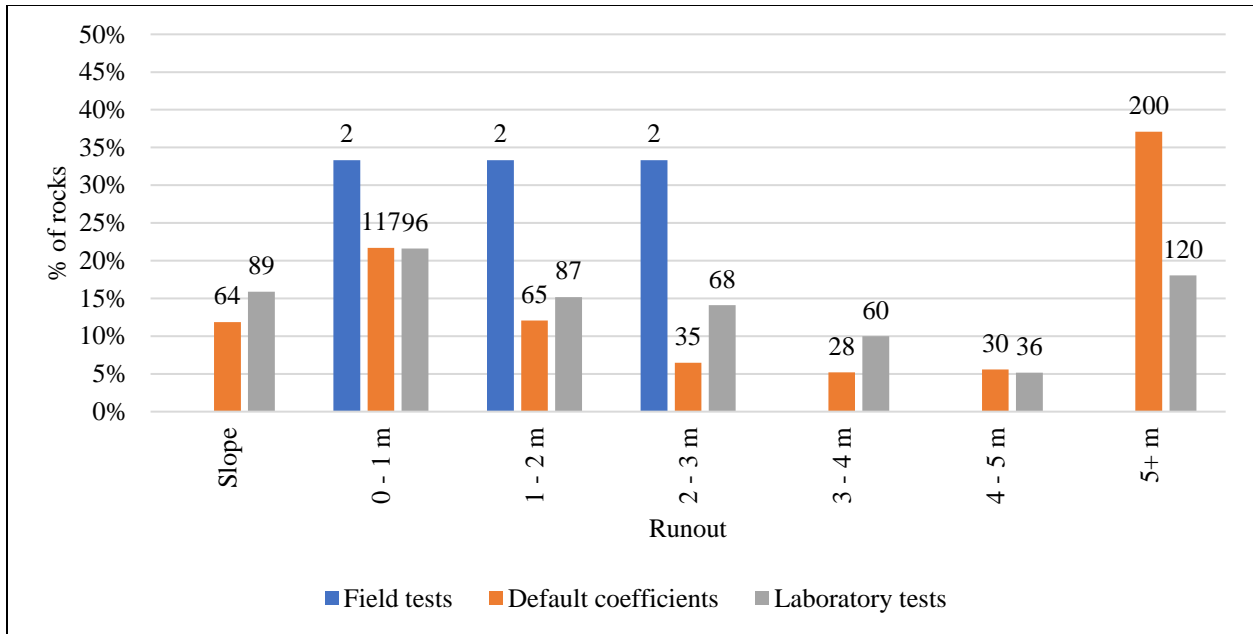
Figure 8.13. Comparative histogram between field measurements and rockfall models: Warner NH. The road is located between 3.5 and 5.0 m from the slope toe, depending on the slope profile.

8.3. Summary and discussion

Two-dimensional rockfall models were compared with measurements in two of the ten evaluated slopes during the experimental field campaign. In general, it was observed that the modeled rockfall motion type (free fall, rolling, bouncing) before ground impact typically agrees with the field experiments. However, the quantitative data (bounce heights, runout, and rotational velocities) were often overly overestimated, especially after the test blocks reached the sand catchment ditches. Although the laboratory-based coefficients estimated smaller bounce heights more compatible with the field behavior, the rotational motion was not significantly decreased after the first impacts with the ground as observed in the field.

Heidenreich (2004) highlights that coefficients of restitution retrieved from the literature typically do not reproduce local site conditions are likely to yield inaccurate results when used at other slopes. The excessive energy restitution predicted by the models consequently increased the predicted rotational velocities, which were significantly higher than the Smart Rock

measurements. The same behavior was obtained by Disenhof (2018) using default coefficients, where the quantitative aspects of rockfall motion anticipated by most models did not produce results comparable to the field measurements. Therefore, additional kinetic energy assessments are necessary to improve these models. The Smart Rock is a promising tool to help calibrate current predictive methods using realistic rotation measurements from instrumented tests. The effect of different coefficients of friction was not investigated in this research, and changes in surface friction should also be evaluated for changes in rotation.

As discussed by Azzoni et al. (1995) and Heidenreich (2004), rockfall models are widely used to identify risk areas. Unrealistic trajectories and bounce heights often result in overly conservative and thus costly designs (Wyllie, 2015), representing an issue as resources to minimize natural hazards are limited (Bunce et al., 1997). However, conducting field rockfalls is not always feasible due to budget, schedule, restrict access to hazardous areas, and risk near transportation corridors and infrastructure (Ferrari et al., 2013; Disenhof, 2018).

9. SUMMARY, CONCLUSIONS, AND FUTURE WORK

9.1. Summary

The objectives for this research were to characterize rockfall motion over time from the perspective of the falling rock and conduct preliminary laboratory and modeling assessments to evaluate two-dimensional simulated trajectories. Fourth-generation Smart Rock sensors were extensively used to analyze field measurements performed with several test blocks on slope profiles of different characteristics. In order to achieve these objectives, this research examined:

- How acceleration, rotation, altitude from a Smart Rock sensor can be used to characterize the motion of a falling rock, coupled with video observations.

- How the measured rockfall behavior can vary under different, or even similar, slope conditions and falling block characteristics.

- How velocity- and energy-based coefficients of restitution can be evaluated with Smart Rock data using an experimental laboratory setup.

- How trajectories, runout distances, and rotational velocities differ from the field measurements using default and laboratory-based input parameters.

A total of 85 instrumented field experiments was conducted on 10 medium-to-high hazard rock cuts in New Hampshire and one high-hazard slope in Vermont. The Smart Rock sensor was embedded in the center of gravity of natural rocks collected at each site and prepared in the laboratory. The Smart Rock data allowed more in-depth evaluations of acceleration magnitudes, rotation rates, and modes of motion with precise time intervals, which cannot be captured in high-rate video recording systems and other instrumentation techniques. The sensor data were evaluated with video recordings of the rockfall trajectories at each site. In addition, field measurements of

297

runout distances were used to evaluate the effectiveness of catchment ditch systems under different slope conditions.

The Smart Rock sensor was also used to instrument small-scale energy restitution experiments. A preliminary laboratory experimental campaign was carried out, dropping a standard block on sand and rock from a constant drop height of 2.2 m. A frontal and upper camera system was implemented to estimate the scalar velocity of the released block in three directions. Bounce heights, scalar velocity estimates, and rotational velocity measurements were used to estimate velocity- and energy-based coefficients of restitution for sand and rock. These experiments have formed the basis of a detailed parametric assessment of rock bouncing parameters.

The field experiments conducted at two of the New Hampshire test sites were compared with two-dimensional simulations. The slope profile for each model was obtained from three-dimensional point clouds of the test slopes, whose cross-sections were extracted based on video observations of the field trajectories. Default coefficients of restitution typically used in 2D simulations were evaluated, as well as the coefficients obtained in the laboratory for sand and rock.

Finally, this research addresses limitations of previous field research conducted at the University of New Hampshire (Disenhof, 2018) and the Swiss Federal Institute for Forest, Snow, and Landscape Research (Caviezel et al., 2017; Caviezel and Gerber, 2018; Caviezel et al., 2018), which have evaluated rockfall motion with a more limited number of slope configurations and test block characteristics. The addition of the altimeter to the fourth-generation SR provides additional information on rock position which may eventually remove the need for video tracking.

9.2. Conclusions

The following conclusions can be made or confirmed with this research:

Experimental rockfalls with the Smart Rock sensor were successful at the ten proposed test sites:

- The fourth-generation Smart Rock accurately recorded acceleration, rotational velocity, and altitude from the perspective of the falling rock. The video tracking measurements were compatible with the added altitude sensor, whose measurements were useful to identify the time intervals of the rockfall experiments precisely.

The Smart Rock measurements were used to evaluate rockfall modes of motion under different test characteristics:

- Falling block behavior:
  - Acceleration and rotational velocity measurements from a Smart Rock were used to describe the modes of motion of a falling block. The results show that Smart Rock data output patterns could be used to successfully distinguish rockfall motion over time (free fall, bouncing, rolling, sliding).
  - The video measurements validated the SR data and were used to help identify patterns for modes of motion in the Smart Rock data. The colors used at each test rock allowed to visualize changes in rotation direction along the rockfall trajectory.
  - Predominant rockfall modes of motion were identified at different ranges of slope angles. Blocks tended to roll and bounce at grassy slopes between 20º and 30º, bounce on rock slopes between 40º and 60º, describe a transition between bouncing and free falling between 60º and 65º, and predominantly free fall at rock slopes steeper than 65º. These ranges were compatible with field and model observations published in the literature since the 1960s.

- Block displacements:

  o Rock bouncing against the rock face typically increased lateral displacements and runout distances, especially at higher rotation rates. In addition, blocks with higher horizontal velocities towards the road (developed in shallower slope angles) tended to develop further runout distances.

  o Except for one test slope in Franklin (50° inclination), all tests had average lateral dispersions less than 20% of the slope lengths. The measured dispersions agree with ranges published in the literature. While trends could not be observed for runout distances, the data measurements suggest that lateral dispersion increases at less inclined slope angles. Both runout distances and lateral dispersion can increase after impact on slope irregularities (launch features). Significant bounce heights do not necessarily imply longer runout distances.

  o The most concerning rock cuts were those with shallow slopes (below 50°) and narrow catchment ditches. The experiments have shown that most A-rated cuts were not fully effective to prevent rockfalls from reaching the road, while the B- and C-rated slopes were successful in mitigating rockfall hazard.

- Accelerations and impact forces:

  o Acceleration magnitudes as low as 5 g resulted in significant increases in rotation.

  o The maximum impact force on a rockfall typically occurs upon impact against the rock face or stiffer material at the ground level (asphalt and rock talus). The acceleration measurements can be described using physics principles. Objects dropped onto rigid and less deformable surfaces are expected to achieve higher acceleration levels than softer materials.

- o Rocks of lower mass experienced higher acceleration magnitudes in both field and laboratory experiments. Higher acceleration magnitudes occurred on taller slopes with predominant free fall behavior and less inclined slopes where significant bouncing occurred.

- Block rotation:
  - o The Smart Rock data demonstrated how block rotation is sensitive to changes in boundary conditions. Factors as simple as contact with thin tree branches or accelerations as low as 5 g can significantly increase the rotation rate of a falling block.
  - o Blocks of smaller mass were more easily subjected to changes in rotation. This behavior could be associated with the difficulty in rotating blocks with higher mass (higher moments of inertia).

The experimental setup in the laboratory was successful in developing a preliminary methodology for energy assessments of falling blocks using a Smart Rock sensor:

- Experiments on sand and rock were successfully conducted to obtain energy- and velocity-based coefficients of restitution for subsequent modeling assessments.

- Impacts on rock have experienced higher acceleration levels compared to sand.

- The results suggest that block dispersion increases as the stiffness of impact surfaces increase. It was observed that a slight inclination at the point of contact on rock influenced the bouncing direction in the three tests performed.

- The alteration in block shape during the tests on sand produced significant differences in energy restitution between the cubic blocks and the cuboctahedron. The cubic block had lower embedment depths compared to the cuboctahedron, thus experiencing higher

301

acceleration levels. Along with deeper embedment, the cuboctahedron experienced a higher lateral dispersion and rotation after impact. While small bounce heights could be measured for the cubic block, the cuboctahedron did not describe visible rebound.

- Higher coefficients of restitution were obtained for the cubic block compared to the cuboctahedron, which displayed nearly zero restitution. The estimated COR values for both sets of tests agree with previous studies but are significantly lower than default modeling coefficients. Although past studies in the literature have been published with nearly zero restitution, the author advises against using restitution coefficients approximately equal to zero without previous field assessments, as they can lead to underestimated trajectories.

- Energy restitution on deformable grounds is complex and requires further investigation. Observations from the tests on sand agree with results obtained by Heidenreich (2004), in which the block rebound behavior on granular material is governed by block penetration, sliding, and rotation.

- Based on a limited number of drop tests on rock, the estimated coefficients of restitution were found lower compared to those published in the literature.

- The designed laboratory methodology has a high potential to evaluate bouncing behavior through instrumented tests on different impact surfaces at a range of surface inclinations and drop heights.

The preliminary two-dimensional modeling assessments were successfully compared to the experimental measurements:

- The rockfall simulations performed with both default and laboratory-based coefficients of restitution demonstrated that the modeling software correctly estimates the modes of motion during a rockfall.

- Similar ranges of rotational velocity before ground impact were observed in most models for both sets of coefficients of restitution.

- The laboratory-based coefficients of restitution reproduce more realistic bounce heights compared to the default coefficients. However, the rotational velocities and runout distances after ground impact were overestimated in all simulations.

The research conducted as part of this thesis showed that the measured three-axis acceleration data could be used to calculate resultant acceleration magnitudes. Resultant accelerations were used to estimate impact forces, useful in the design of protective structures, especially at less inclined slopes. In addition, the measured rotational velocity data can be used to calculate the rotational kinetic energy of a falling block accurately with known moments of inertia.

The findings of this study confirm that rockfall events are unpredictable and require further investigation and kinetic energy estimates from the perspective of the falling rock for safer and more economical protective designs. The physical motions described by bouncing and rolling phenomena are the least understood by rockfall studies, given the significant number of variables regarding impact conditions and rock characteristics. Therefore, the increasing demand for more realistic modeling input parameters is associated with public safety as a primary factor and saves time and resources, redirecting to a higher number of medium-to-high hazard rock cuts.

There is an increasing need to estimate coefficients of restitution capable of realistically predicting the dispersion of falling rocks in typical surfaces, and the Smart Rock can be considered a promising tool for accurate energy assessments and consequent hazard mitigation. Observations from this experimental research have demonstrated that similar block sizes can experience significant ranges of motion depending on the slope conditions, primarily controlled by the slope angle and/or presence of launch features. Therefore, the protective design of rockfall events must

303

primarily account for the slope conditions and alternatives to attenuate potential damage upon impact. Catchment ditch widths and geometries, and other safety measures must be engineered to stop falling blocks considering the slope angle and expected type of motion at a specific site.

9.3. Future work

Future work using the Smart Rock technology will be conducted at the University of New Hampshire and at the University Gustave Eiffel (Lyon, France) in collaboration with the New Hampshire Department of Transportation.

Field assessments with the Smart Rock sensors will be conducted in New Hampshire and the French Alpine region using Smart Rock and Measuring-While-Drilling (MWD) technologies to characterize properties of falling blocks and the in-place soil and rock conditions respectively. SRs will be used to quantify impact acceleration and block rotation and thus assess rock bouncing behavior and expected runout. MWD measurements will be used to characterize the in-place formation and the mechanical properties of impact surfaces. Methods to evaluate catchment ditches in the field will be developed.

In addition to the field experiments, an instrumented, small- and medium-scale experimental campaign under controlled conditions will be conducted. Several rockfall influencing parameters, including block and impact surface characteristics, and falling block kinematics, will be assessed. The objective is to evaluate different impact conditions and use the experimental data to determine modeling aspects that require better qualification.

Further analysis of the Smart Rock data in these field experiments will include a more independent assessment of the sensor data with limited reliance on video. Relevant aspects of rockfall motion, such as acceleration, rotation, and runout, will be compared using functional

forms incorporating multiple factors that can influence rockfall behavior, including block and slope characteristics.

Two- and three-dimensional rockfall modeling will be performed and calibrated based on field observations and measurements from both SR and MWD. Current modeling limitations will be assessed, and comparisons between field and model trajectories, endpoint locations, and rockfall motion will be established. Error percentages of rock kinematics and runout distances will be estimated for models compared with test series in the field, performed to evaluate rockfall repeatability of a same test block on a given slope profile.

Results from field and laboratory rockfalls and surface characterization with MWD are expected to improve the accuracy and reliability of existing software packages. The outcomes of this research will be implemented in rockfall protection systems in both France and New Hampshire.

LIST OF REFERENCES

Ansari, M. K., Ahmad, M., Singh, R., and Singh, T. N. (2015). Correlation between Schmidt hardness and coefficient of restitution of rocks. *Journal of African Earth Sciences*, *104*, 1-5.

Apostolov, A. (2016). Development and testing of motion tracking "Smart Rock" devices for geotechnical applications. (Master's thesis). University of New Hampshire, Durham, NH.

Apostolov, A. and Benoît, J. (2017). Motion Tracking "Smart Rock" Device for the Study of Landslide and Debris Flow Mechanisms. *North American Symposium on Landslides. Roanoke*, VA, June 4-8.

Arndt, B., & Arpin, B. (2016). Proposed Rock Slope and Rockfall Design Procedures and Methods for Evaluating Rockfall Sites within a Corridor. *In 67th Highway Geology Symposium*, July.

Arpaz, E. (2015). Determination of restitution coefficients for various granite samples. *Arabian Journal of Geosciences*, 8(7), 5285-5294.

Arpin, B., and Arndt, B. (2016). Comparison of 2D and 3D rockfall modeling for rockfall mitigation design. *In 67th Highway Geology Symposium*, July.

Asteriou, P., Saroglou, H., and Tsiambaos, G. (2012). Geotechnical and kinematic parameters affecting the coefficients of restitution for rock fall analysis. *International Journal of Rock Mechanics and Mining Sciences*, 54, 103-113.

Asteriou, P., and Tsiambaos, G. (2016). Empirical model for predicting rockfall trajectory direction. *Rock Mechanics and Rock Engineering*, 49(3), 927-941.

Azzoni, A., and de Freitas, M. H. (1995). Experimentally gained parameters, decisive for rock fall analysis. *Rock mechanics and rock engineering*, 28(2), 111-124.

Azzoni, A., La Barbera, G., and Zaninetti, A. (1995). Analysis and prediction of rockfalls using a mathematical model. *International journal of rock mechanics and mining sciences & Geomechanics* (Vol. 32, No. 7, pp. 709-724).

Bar, N., Nicoll, S., and Pothitos, F. (2016, September). Rock fall trajectory field testing, model simulations and considerations for steep slope design in hard rock. *In Proceedings of the*

First Asia Pacific Slope Stability in Mining Conference (pp. 457-466). Australian Centre for Geomechanics.

Basson, F. R. P. (2012, January). Rigid body dynamics for rock fall trajectory simulation. *In 46th US Rock Mechanics/Geomechanics Symposium*. American Rock Mechanics Association.

Basson, F.R.P., Humphreys, R., Temmu, A. (2013). *Coefficient of restitution for rigid body dynamics modelling from onsite experimental data*. In P.M. Dight (ed), Slope Stablity 2013. Australian Centre for Geomechanics, Perth, ISBN 978-0-9870937-5-2.

Bourrier, F., Dorren, L., Nicot, F., Berger, F., and Darve, F. (2009). Toward objective rockfall trajectory simulation using a stochastic impact model. *Geomorphology*, 110(3-4), 68-79.

Bourrier, F., Berger, F., Tardif, P., Dorren, L., and Hungr, O. (2012). Rockfall rebound: comparison of detailed field experiments and alternative modelling approaches. *Earth Surface Processes and Landforms*, 37(6), 656-665.

Bunce, C. M., Cruden, D. M., and Morgenstern, N. R. (1997). Assessment of the hazard from rock fall on a highway. *Canadian Geotechnical Journal*, 34(3), 344-356.

Caviezel, A., Christen, M. Buhler, Y. and Bartelt, P (2017). Calibration methods for numerical rockfall models based on experimental data. *6th Interdisciplinary Workshop on Rockfall Protection*. May, Barcelona, Spain.

Caviezel, A., and Gerber, W. (2018). Brief Communication: Measuring rock decelerations and rotation changes during short-duration ground impacts. *Natural Hazards and Earth System Sciences*, 18(11), 3145-3151.

Chai S., Yacoub, T., Charbonneau, K., and Curran, J.H. (2013). The effect of rigid body impact mechanics on tangential coefficient of restitution. *GeoMontréal 2013*.

Chau, K. T., Wong, R. H. C., and Lee, C. F. (1998). Rockfall problems in Hong Kong and some new experimental results for coefficients of restitution. *International Journal of Rock Mechanics and Mining Sciences*, 35(4-5), 662-663.

Chau, K. T., Wong, R. H. C., and Wu, J. J. (2002). Coefficient of restitution and rotational motions of rockfall impacts. *International Journal of Rock Mechanics and Mining Sciences*, 39(1), 69-77.

Chau, K. T., Wong, R. H. C., Liu, J., and Lee, C. F. (2003). Rockfall hazard analysis for Hong Kong based on rockfall inventory. *Rock Mechanics and Rock Engineering*, 36(5), 383-408.

Crosta, G.B., Agliardi, F., Frattini, P., and Lari, S. (2015). *Key issues in rock fall modeling, hazard and risk assessment for rockfall protection*. In Lollino, G. et al., (eds), Engineering Geology for Society and Territory¸ Vol. 2, Switzerland: Springer International Publishing. DOI: 10.1007/978-3-319-09057-3_4

Dadashzadeh, N., Duzgun, H.S.B., Yesiloglu-Gultekin, N., and Bilgin, A. (2014). Comparison of lumped mass and rigid body rockfall simulation models for the Mardin Castle, Turkey. *48th US Rock Mechanics/Geomechanics Symposium*. ARMA 14-7177. Minneapolis, MN, 1-4 June.

Descoeudres, F. (1997). Aspects géomécaniques des instabilités de falaises rocheuses et des chutes de blocs. *Publications de la société suisse de mécanique des sols et des roches*, 135, 3-11. In French.

Dorren, L. K. A., Berger, F., and Putters, U. S. (2006). Real-size experiments and 3-D simulation of rockfall on forested and non-forested slopes. *Natural Hazards and Earth System Sciences*, 6(1), 145-153.

Dorren, L. K. A., Domaas, U., Kronholm, K., and Labiouse, V. (2011). Methods for predicting rockfall trajectories and runout zones. In: S. Lambert & F. Nicot (eds.). *Rockfall engineering*. ISTE Ltd. / John Wiley & Sons Inc.: pp. 143 - 173.

Dias, G. P., and Barroso, E. V. (2006). Determinação experimental do coeficiente de restituição normal de rochas: aplicação na previsão do alcance de blocos em encostas. *Anuário do Instituto de Geociências*, 29(2), 149-167. In Portuguese.

Disenhof, C. R. (2018). Investigation of Surface Models and the Use of a Smart Rock for Rockfall Modeling. (Master's thesis). University of New Hampshire, Durham, NH.

Duffy, J. D., and Turner, A.K. (2012). "Conducting Field-Test Experiments." In Turner, A.K. and Schuster, R.L. (Eds). *Rockfall Characterization and Control* (pp. 407-441). Washington, D.C.: Transportation Research Board.

Evans, S. G., and Hungr, O. (1993). The assessment of rockfall hazard at the base of talus slopes. *Canadian geotechnical journal*, 30(4), 620-636.

Ferrari, F., Giani, G. P., and Apuani, T. (2013). Towards the comprehension of rockfall motion, with the aid of in situ tests. *Italian Journal of Engineering Geology and Environment*, 2013(TOPIC1), 163–171.

Ferrari, F., Giacomini, A., and Thoeni, K. (2016). Qualitative rockfall hazard assessment: a comprehensive review of current practices. *Rock Mechanics and Rock Engineering*, 49(7), 2865-2922.

Ferrari, F., Giacomini, A., Thoeni, K., and Lambert, C. (2017). Qualitative evolving rockfall hazard assessment for highwalls. *International Journal of Rock Mechanics and Mining Sciences*, 98, 88-101.

Fornaro, M., D. Peila, and M. Nebbia. (1990). Block falls on rock slopes: application of a numerical simulation program to some real cases. *Proceedings of the 6th International Concress, International Association of Engineering Geology*, Amsterdam, Netherlands (D.D. Price, ed.), Balkema, Rotterdam, Netherlands, pp. 2173 – 2180.

Garcia, B. S. (2019). Analyse des mécanismes d'interaction entre un bloc rocheux et un versant de propagation: application à l'ingénierie (Doctoral dissertation). Université Grenoble Alpes, Grenoble, France.

Ghana, M. F. A., Simon, N., & Lai, G. T. (2019, June). Coefficient of restitution of limestone determined from normal drop laboratory test. *In AIP Conference Proceedings* (Vol. 2111, No. 1, p. 060014). AIP Publishing LLC.

Giacomini, A., Thoeni, K., Lambert, C., Booth, S., and Sloan, S. W. (2012). Experimental study on rockfall drapery systems for open pit highwalls. *International Journal of Rock Mechanics and Mining Sciences*, 56, 171-181.

Giani, G. P., Giacomini, A., Migliazza, M., and Segalini, A. (2004). Experimental and theoretical studies to improve rock fall analysis and protection work design. *Rock Mechanics and Rock Engineering*, 37(5), 369-389.

Gomes, G. J. C. (2009). Avaliação do perigo relacionado à queda de blocos em rodovias (Master's thesis). Federal University of Ouro Preto. MG, Brazil. In Portuguese.

Gullison, M. (2013). Analysis of Smart Rock data from debris flow experimentation. (Master's thesis). University of New Hampshire, Durham, NH.

Harding, M. (2011). Design and development of a debris flow tracking "Smart Rock". (Master's thesis). University of New Hampshire, Durham, NH.

Harding, M. J., Fussell, B. K., Gullison, M. A., Benoît, J., and de Alba, P. A. (2014). Design and testing of a debris flow 'smart rock'. *Geotechnical Testing Journal*, 37(5), 769-785.

Heidenreich, B. (2004). Small- and Half- Scale Experimental Studies of Rockfall Impacts on Sandy Slopes. (Doctoral thesis). École Polytechnique Fédérale de Lausanne, Lausanne, Switzerland.

Heidenreich, B., and Labiouse, V. (2004). Small-scale experimental studies of rockfall impacts on granular slopes. *Rivista Italiana di Geotecnica*, 38(2), 80-91.

Higgins, J.D., and Andrew, R. D. (2012). "Rockfall types and causes." In Turner, A.K. and Schuster, R.L. (Eds). *Rockfall Characterization and Control* (pp. 21-55). Washington, D.C.: Transportation Research Board.

Japan Road Association. (1983). *Rockfall Handbook*. Maruzen Publisher, Tokyo. In Japanese.

Khetwal, S. S. (2017). Rockfall Modelling Technical Report. Report submitted to the Colorado School of Mines.

Labiouse, V., and Descoeudres, F. (1999). Possibilities and difficulties in predicting rockfall trajectories. *In Proc. of the Joint Japan-Swiss Scientific Seminar on Impact Load by Rock Falls and Design of Protection Structures*, Kanazawa, Japan (pp. 29-36).

Labiouse, V., and Heidenreich, B. (2009). Half-scale experimental study of rockfall impacts on sandy slopes. *Natural Hazards and Earth System Sciences*, 9(6), 1981-1993.

Leonhardt, P. M. (2001). Acceleration levels of dropped objects. Endevco Corporation.

Li, L. P., Sun, S. Q., Li, S. C., Zhang, Q. Q., Hu, C., and Shi, S. S. (2016). Coefficient of restitution and kinetic energy loss of rockfall impacts. *KSCE Journal of Civil Engineering*, 20(6), 2297-2307.

Nelson, G.S. and Snowden, T.D. (2010). Physics Calculations Related to Falling Objects. *Fact Sheet: Nelson & Associates*. doi: 10.13140/RG.2.1.3596.5522

Peng, B. (2000). Rockfall Trajectory Analysis – Parameter Determination and Application (Master's thesis). University of Canterbury, Christchurch, New Zealand.

Pfeiffer, T. J., and Bowen, T. D. (1989). Computer simulation of rockfalls. *Bulletin of the association of Engineering Geologists*, 26(1), 135-146.

Pfeiffer, T. J., and Higgins, J. D. (1990). Rockfall hazard analysis using the Colorado rockfall simulation program. *Transportation Research Record*, (1288).

Pierson, L.A., and Van Vickle, R. (1993). Rockfall Hazard Rating System – Participants' Manual. FHWA-SA-93-057, U.S. Department of Transportation.

Pierson, L.A., Gullison, C.F., and Chassie, R.G. (2001). Rockfall Catchment Area Design Guide. Report FHWA-OR-RD-02-04m, Oregon Department of Transportation, Dec. 2001.

Pierson, L.A., and Turner, A.K. (2012). "Implementation of Rock Slope Management Systems." In Turner, A.K. and Schuster, R.L. (Eds). Rockfall Characterization and Control (pp. 73-112). Washington, D.C.: Transportation Research Board.

Rocscience. Coefficient of restitution table. RocFall Help. Accessed October 2020. https://www.rocscience.com/help/rocfall/baggage/rn_rt_table.htm

Ritchie, A. (1963). Evaluation of Rockfall and its Control. Highway Research Board, N.17, 13-28.

Saeidi, S., Gratchev, I., Kim, D. H., and Chung, M. (2014). Evaluation of restitution coefficients concerning surface roughness. *In 23rd Australasian Conference on the Mechanics of Structures and Materials* (ACMSM23) Byron Bay, Australia (pp. 1-6).

Singh, P. K., Kainthola, A., Panthee, S., and Singh, T. N. (2016). Rockfall analysis along transportation corridors in high hill slopes. *Environmental Earth Sciences*, 75(5), 441.

Sneed, E.D., and Folk, R.L. (1958). Pebbles in the Lower Colorado River, Texas a study in particle morphogenesis. The Journal of Geology, Vol. 66 No. 2, pp 114-150.

Spadari, M., Giacomini, A., Buzzi, O., Fityus, S., and Giani, G. P. (2012). In situ rockfall testing in New South Wales, Australia. *International Journal of Rock Mechanics and Mining Sciences*, 49, 84-93.

Turner, A.K., and Duffy, J.D. (2012a). "Evaluation of Rockfall Mechanics." In Turner, A.K. and Schuster, R.L. (Eds). *Rockfall Characterization and Control* (pp. 285-333). Washington, D.C.: Transportation Research Board.

Turner, A.K., and Duffy, J.D. (2012b). "Modeling and Prediction of Rockfall." In Turner, A.K. and Schuster, R.L. (Eds). *Rockfall Characterization and Control* (pp. 334-406). Washington, D.C.: Transportation Research Board.

Turner, A.K., and Jayaprakash, G. P. (2012). "Introduction." In Turner, A.K. and Schuster, R.L. (Eds). *Rockfall Characterization and Control* (pp. 3-20). Washington, D.C.: Transportation Research Board.

Ushiro, T., Kusumoto, M., Shinohara, S., and Kinoshita, K. (2006). And experimental study related to rock fall movement mechanism (in Japanese). *J. Japan Society of Civil Engineers*, Series F., V. 62 No. 2, 377-386.

Wang, Y., Jiang, W., Cheng, S., Song, P., and Mao, C. (2018). Effects of the impact angle on the coefficient of restitution in rockfall analysis based on a medium-scale laboratory test. *Natural Hazards and Earth System Sciences*, 18(11), 3045-3061.

Wu, S. S. (1985). Rockfall evaluation by computer simulation. *Transportation research record*, *1031*, Transportation research Board, National Research Council, Washington, D.C., 1-5.

Wyllie, D.C. (2015). *Rock Fall Engineering*. New York, NY: CRC Press, Taylor & Francis Group.

APPENDIX A:

COEFFICIENTS OF RESTITUTION DATABASE

Table A.1. Summary of laboratory methodologies to determine restitution coefficients under different definitions.

Authors	Method	Sample retrieving	Material	Details	COR_{VN} Mean	COR_{VN} SD	COR_{VT} Mean	COR_{VT} SD	COR_E Mean	COR_E SD	COR_{TE} Mean	COR_{TE} SD
Wu (1985)	Rocks of different shapes (round to flat) and sizes (20 to 45 cm) were dropped in a wood platform (3.0 x 3.7 m).	Not mentioned	Rock on wood	Wood platform adjusted at 45° (other angles not included)	0.38	0.13	0.69	0.13				
Peng (2000)	Rock specimens from different locations and rock slabs (2.5 - 5.0 cm thickness) were used as impact surfaces. The dropped rocks were polished to a quasi-spherical shape. The spheres bounced five times, and the coefficient of restitution was calculated for each bounce. Experiments were recorded at 200 fps. Drop height not specified.	Not mentioned	Granite		0°: 0.51 12°: 0.67 22°: 0.71 46°: 0.68		0°: - 12°: 0.71 22°: 0.60 46°: 0.69					
			Basalt		0°: 0.49 12°: 0.48 23°: 0.45 46°: 0.53		0°: - 12°: 0.76 23°: 0.58 43° 0.61					
			Diorite		0°: 0.50 12°: 0.25 23°: 0.27 46°: 0.37		0°: - 12°: 0.67 23°: 0.49 46°: 0.67					
			Schist		0°: 0.58 10°: 0.56 20°: 0.6		0°: - 10°: 0.61 20°: 0.75					
			Gneiss		0°: 0.50		0°: -					
			Marble		0°: 0.30 12°: 0.34 22°: 0.34 46°: 0.52		0: - 12°: 0.50 22°: 0.50 46°: 0.75					
			Sandstone		0°: 0.39 12°: 0.46 22°: 0.40 46°: 0.52		0°: - 12°: 0.50 22°: 0.67 46°: 0.56					
			Limestone		0°: 0.54 10°: 0.18 20°: 0.25 46°: 0.40		0°: - 10°: 0.44 20°: 0.60 46°: 0.53					
			Steel		0°: 0.39 10°: 0.42 20°: 0.31 46°: 0.42		0°: - 10°: 0.64 20°: 0.72 46°: 0.65					

Table A.1 (cont.). Summary of laboratory methodologies to determine restitution coefficients under different definitions.

Authors	Method	Sample retrieving	Material	Details	COR_{VN}		COR_{VT}		COR_E		COR_{TE}	
					Mean	SD	Mean	SD	Mean	SD	Mean	SD
Peng (2000)	Same procedure as previous, but using rough rock blocks as impact surfaces. Rock blocks were dropped. Drop heights: 0, 0.6, 1.0, 1.5, 2.0, 2.5 m.	New Zealand	Basalt		0°: 0.18 40°: 0.29	0°: 0.05 40°: 0.03	0°: - 40°: 0.73	0°: - 40°: 0.07				
			Greywacke		0°: 0.73 40°: 0.26	0°: 0.01 40°: 0.07	0°: - 40°: 0.83	0°: - 40°: 0.03				
			Limestone		0°: 0.12 40°: 0.21	0°: 0.04 40°: 0.02	0°: - 40°: 0.62	0°: - 40°: 0.09				
	Same procedure on typical surfaces. Rock spheres and blocks dropped. 1.5m drop height. All impact surfaces were contained in a timber tray (30 x 60 x 10 cm).	New Zealand	Coarse sand	Rock sphere	0°: 0.00 20°: 0.19		0°: - 20°: -0.01					
			Gravel	Rock sphere	0°: 0.06 20°: 0.14		0°: - 20°: 0.31					
			Rock debris: limestones and basalts, angular fragments, 0.5 - 2 cm, compacted bed	Rock sphere	0°: 0.07 20°: 0.16		0°: - 20°: 0.61					
				Rock block	0°: 0.10 20°: 0.17		0°: - 20°: 0.67					
			Rock debris: paving materials, compacted bed	Rock sphere	0°: 0.09 20°: 0.15		0°: - 20°: 0.58					
				Rock block	0°: 0.08 20°: 0.15		0°: - 20°: 0.57					
			Soil: loess, compacted bed	Rock sphere	0°: 0.10 20°: 0.17		0°: - 20°: 0.35					
				Rock block	0°: 0.12 20°: 0.23		0°: - 20°: 0.61					
Chau et al. (2002)	Spherical boulders and impact surfaces made of plaster. The spheres are released in free fall and impact the surface positioned at different angles. Boulders released with slope apparatus. High-speed camera, 222 fps. Small scale.	Fabricated	Dental plaster, different concentrations	6.05g, 18.35mm diameter sphere, 6 - 10 tests	10°: 0.42 20°: 0.46 30°: 0.43 40°: 0.47 50°: 0.44 60°: 0.56 70°: 0.61		10°: 0.86 20°: 0.79 30°: 0.78 40°: 0.76 50°: 0.75 60°: 0.81 70°: 0.87		10°: 0.44 20°: 0.51 30°: 0.54 40°: 0.61 50°: 0.64 60°: 0.75 70°: 0.84		10°: 0.19 20°: 0.26 30°: 0.30 40°: 0.37 50°: 0.41 60°: 0.57 70°: 0.71	

Table A.1 (cont.). Summary of laboratory methodologies to determine restitution coefficients under different definitions.

Authors	Method	Sample retrieving	Material	Details	COR_{VN}		COR_{VT}		COR_E		COR_{TE}	
					Mean	SD	Mean	SD	Mean	SD	Mean	SD
Chau et al. (2002)	Spherical boulders and impact surfaces made of plaster. The spheres are released in free fall and impact the surface positioned at different angles. Boulders released with slope apparatus. High-speed camera, 222 fps. Small scale.	Fabricated	Dental plaster, different concentrations	153.64g, 60mm diameter sphere, 6 - 10 tests	10º: 0.45 20º: 0.37 30º: 0.47 40º: 0.45 50º: 0.43 60º: 0.45 70º: 0.48		10º: 0.83 20º: 0.83 30º: 0.67 40º: 0.66 50º: 0.70 60º: 0.86 70º: 0.98		10º: 0.47 20º: 0.46 30º: 0.53 40º: 0.55 50º: 0.60 60º: 0.78 70º: 0.93		10º: 0.22 20º: 0.21 30º: 0.28 40º: 0.30 50º: 0.33 60º: 0.36 70º: 0.40	
				204.33, 60mm diameter sphere, 6 - 10 tests	10º: 0.36 20º: 0.37 30º: 0.37 40º: 0.41 50º: 0.43 60º: 0.53 70º: 0.56		10º: 0.65 20º: 0.71 30º: 0.70 40º: 0.69 50º: 0.84 60º: 0.91 70º: 0.95		10º: 0.37 20º: 0.43 30º: 0.48 40º: 0.55 50º: 0.70 60º: 0.83 70º: 0.92		10º: 0.14 20º: 0.18 30º: 0.23 40º: 0.30 50º: 0.49 60º: 0.69 70º: 0.84	
Dias and Barroso (2006)	Granitic gneiss sphere, 30 mm diameter. Impact upon surfaces, impact times recorded with a microphone. Drop heights: 5, 10, 15, 20, 25, and 30 cm.	Rio de Janeiro, Brazil	Granitic gneiss	3 drop tests at each drop height.	0.7							
Asteriou et al. (2012)	Cubic rocks with smoothened edges (2 to 3 cm side) dropped on 5 cm thick and 15 cm long impact surfaces embedded in plaster. Two releasing mechanisms: blocks released with a vacuum pump (free fall), and an inclined tube (parabolic trajectory). Video recording at 250 fps, 2D analysis.	Greece	Sandstone	0.85 m drop height, 10 tests, free fall.					0.66	0.09		
				38 tests, parabolic drop.	0º: 0.69 15º: 0.62 30º: 0.77 45º: 0.77	0º: 0.12 15º: 0.16 30º: 0.12 45º: 0.12	0º: 1.10 15º: 0.94 30º: 0.86 45º: 0.93	0º: 0.44 15º: 0.10 30º: 0.07 45º: 0.04	0º: 0.74 15º: 0.73 30º: 0.83 45º: 0.91	0º: 0.05 15º: 0.08 30º: 0.05 45º: 0.04		
			Marble	0.60 to 1.4 m drop heights, 57 tests, free fall.					0.51	0.06		
				0.85 m drop height, 10 tests, free fall.					0.5	0.07		
				26 tests, parabolic drop.	0º: 0.50 15º: 0.53 30º: 0.73 45º: 0.88	0º: 0.12 15º: 0.16 30º: 0.23 45º: 0.08	0º: 1.26 15º: 0.78 30º: 0.74 45º: 0.83	0º: 0.33 15º: 0.18 30º: 0.04 45º: 0.04	0º: 0.63 15º: 0.65 30º: 0.73 45º: 0.84	0º: 0.05 15º: 0.07 30º: 0.06 45º: 0.04		

Table A.1 (cont.). Summary of laboratory methodologies to determine restitution coefficients under different definitions.

Authors	Method	Sample retrieving	Material	Details	COR_{VN} Mean	COR_{VN} SD	COR_{VT} Mean	COR_{VT} SD	COR_E Mean	COR_E SD	COR_{TE} Mean	COR_{TE} SD
Asteriou et al. (2012)	Cubic rocks with smoothened edges (2 to 3 cm side) dropped on 5 cm thick and 15 cm long impact surfaces, embedded in plaster. Two releasing mechanisms: blocks released with a vacuum pump (free fall) and an inclined tube (parabolic trajectory). Video recording at 250 fps, 2D analysis.	Greece	Limestone	0.89 m drop height, 8 tests, free fall.					0.5	0.05		
			Schist	0.85 m drop height, 8 tests, free fall.					0.38	0.04		
			Marl	0.89 m drop height, 8 tests, free fall.					0.36	0.03		
			Marl	30 tests total, parabolic drop.	0°: 0.25 15°: 0.36 30°: 0.54 45°: 0.88	0°: 0.04 15°: 0.08 30°: 0.07 45°: 0.19	0°: 1.63 15°: 0.91 30°: 0.68 45°: 0.74	0°: 0.25 15°: 0.10 30°: 0.06 45°: 0.10	0°: 0.53 15°: 0.61 30°: 0.63 45°: 0.77	0°: 0.02 15°: 0.03 30°: 0.03 45°: 0.09		
Basson et al. (2012)	Ten rocks between 0.35 and 2.08 kg were manually dropped 10 times from a height of 1.4m onto four horizontal surfaces: pit floor, haul road, catch berm, and hard rock. Slow-motion video recording. Zero rebound heights were assumed as 1 mm.	Boddington, Australia	Pit floor						0.003			
			Haul road						0.085			
			Catch berm						0.003			
			Hard rock						0.12			
Saeidi et al. (2014)	Two rocks were used as surfaces, whose inclinations were adjusted with plaster. Falling rock: round-shaped specimen, about 30g weight. Rock released manually. High-speed camera, 200 fps. Small scale.	Brisbane, Australia	Greywacke	Surface 1 0.7m drop height 0°: 12 tests 20°: 29 tests 30°: 29 tests	20°: 0.31 30°: 0.40	20°: 0.12 30°: 0.16	20°: 1.04 30°: 0.71	20°: 0.41 30°: 0.43	0°: 0.40 20°: 0.48 30°: 0.54	0°: 0.11 20°: 0.12 30°: 0.14		
				Surface 1 1.1m drop height 0°: 19 tests 20°: 32 tests 30°: 26 tests	20°: 0.25 30°: 0.33	20°: 0.12 30°: 0.18	20°: 0.83 30°: 0.77	20°: 0.61 30°: 0.21	0°: 0.35 20°: 0.40 30°: 0.50	0°: 0.15 20°: 0.16 30°: 0.12		

Table A.1 (cont.). Summary of laboratory methodologies to determine restitution coefficients under different definitions.

Authors	Method	Sample retrieving	Material	Details	COR_{VN} Mean	SD	COR_{VT} Mean	SD	COR_E Mean	SD	COR_{TE} Mean	SD
Saeidi et al. (2014)	Two rocks were used as surfaces, whose inclinations were adjusted with plaster. Falling rock: round-shaped specimen, about 30g weight. Rock released manually. High-speed camera, 200 fps. Small scale.	Brisbane, Australia	Greywacke	Surface 2 0.7m drop height 0°: 22 tests 20°: 23 tests 30°: 28 tests	20°: 0.38 30°: 0.32	20°: 0.11 30°: 0.14	20°: 0.93 30°: 1.00	20°: 0.41 30°: 0.28	0°: 0.41 20°: 0.49 30°: 0.59	0°: 0.13 20°: 0.10 30°: 0.08		
				Surface 2 1.1m drop height 0°: 22 tests 20°: 18 tests 30°: 26 tests	20°: 0.35 30°: 0.34	20°: 0.13 30°: 0.13	20°: 1.11 30°: 0.81	20°: 0.36 30°: 0.30	0°: 0.39 20°: 0.52 30°: 0.52	0°: 0.08 20°: 0.09 30°: 0.11		
Arpaz (2015)	A steel ball (2.5 g and 6 mm diameter) was dropped from 50cm high onto horizontal, flat granite surfaces (15 x 10 x 2 cm). A microphone detects the sound of the ball. The ball fell and bounced inside a glass tube to ensure vertical trajectories and a single impact point. The times between impacts were measured, and a COR value was found for each impact until the ball stopped. The bounce heights were determined from the measured flight periods between impacts.	Brazil	Amapa						0.83	0.05		
		Spain	Azul Platino						0.86	0.05		
		Finland	Baltic Brown						0.89	0.04		
		Italy	Bianco Sardo						0.83	0.07		
		Norway	Blue Pearl						0.83	0.08		
		Brazil	Cafe Imperial						0.91	0.05		
		Brazil	Campao Bonito						0.93	0.05		
		Finland	Carmen Red						0.93	0.05		
		Ukraine	Coral Mist						0.90	0.05		
		Spain	Crema Perla						0.88	0.05		
		Brazil	Giallo Fiorito						0.72	0.08		
		Brazil	Green Butterfly						0.84	0.07		
		Brazil	Green Marinace						0.89	0.06		
		India	Jet Black						0.87	0.04		
		India	Kashmir White						0.87	0.04		
		India	Multicolor						0.90	0.04		
		Zimbabwe	Nero Zimbabwe						0.90	0.05		
		Italy	Rosa Beta						0.88	0.07		
		Spain	Rosa Minho						0.88	0.04		
		Spain	Rosa Porino						0.88	0.05		
		Spain	Rosavel						0.86	0.04		
		Brazil	San Francisco Imperial						0.85	0.04		
		Russia	Santiago Red						0.91	0.06		
		India	Tan Brown						0.91	0.04		
		Brazil	Vermont						0.81	0.05		

Table A.1 (cont.). Summary of laboratory methodologies to determine restitution coefficients under different definitions.

Authors	Method	Sample retrieving	Material	Details	COR_{VN}		COR_{VT}		COR_E		COR_{TE}	
					Mean	SD	Mean	SD	Mean	SD	Mean	SD
Ansari et al. (2015)	Falling rock: rock balls (cut and grinded, 4 to 5 cm), 7 steel balls (1.5, 2.0, 3.0, 3.5, 4.0, 4.5 and 5.0 cm diameter) for comparative analysis. Impact surfaces: rock and steel slabs (at least 5 cm thickness), polished, smooth and flat, and clamped to a tilt test apparatus to measure the slope angles. Drop height: 1m. High-speed camera, 150fps.	Natural rocks retrieved at different locations, locations not mentioned	Basalt		0.33							
			Granite		0.42							
			Sandstone		0.29							
			Limestone		0.41							
			Marble		0.43							
			Steel		0.34							
Asteriou and Tsiambaos (2016)	Concrete blocks (3 cm side cubes and 4 cm diameter spheres). Adjustable release mechanism released rocks at an angle at the impact surface, which was also made of concrete with high-strength cement grout, 5 cm thick and 15 cm long. Video recording at 60 fps from two angles. 590 tests.	Fabricated	Concrete with high-strength cement grout	Cubes	0.59	0.05	1.04	0.05	0.78	0.02		
				Spheres	0.2	0.1	0.85	0.15	0.45	0.1		
Wang et al. (2018)	Spherical limestone polyhedrons (10 and 20 cm diam., natural rock, edges not smoothed), dropped using a release device. Surface: C25 concrete slab (1.2 x 0.5 x 0.15 m) at different angles, supported by a compacted gravely soil ramp. Infrared cameras to capture trajectories. 3 tests at each condition.	Three Gorges area, China	Limestone on concrete	1.2 kg, 10 cm diameter rock, 2.5m drop height.	30º: 0.42 45º: 0.53 60º: 0.76 75º: 1.00	30º: 0.09 45º: 0.04 60º: 0.06 75º: 0.11	30º: 0.80 45º: 0.82 60º: 0.69 75º: 0.53	30º: 0.03 45º: 0.09 60º: 0.03 75º: 0.03	30º: 0.56 45º: 0.72 60º: 0.70 75º: 0.56	30º: 0.04 45º: 0.05 60º: 0.03 75º: 0.02	30º: 0.36 45º: 0.57 60º: 0.59 75º: 0.44	30º: 0.05 45º: 0.07 60º: 0.04 75º: 0.02
				1.2 kg, 10cm diameter rock, 3.5m drop height.	30º: 0.38 45º: 0.52 60º: 0.88 75º: 1.11	30º: 0.04 45º: 0.02 60º: 0.11 75º: 0.27	30º: 0.92 45º: 0.78 60º: 0.70 75º: 0.65	30º: 0.08 45º: 0.08 60º: 0.12 75º: 0.19	30º: 0.59 45º: 0.69 60º: 0.74 75º: 0.67	30º: 0.04 45º: 0.06 60º: 0.08 75º: 0.17	30º: 0.39 45º: 0.52 60º: 0.64 75º: 0.58	30º: 0.04 45º: 0.08 60º: 0.10 75º: 0.21
				1.2, kg 10 cm diameter rock, 4.5m drop height.	30º: 0.39 45º: 0.58 60º: 0.53 75º: 1.68	30º: 0.03 45º: 0.07 60º: 0.17 75º: 0.30	30º: 0.88 45º: 0.82 60º: 0.70 75º: 0.49	30º: 0.04 45º: 0.06 60º: 0.02 75º: 0.08	30º: 0.57 45º: 0.67 60º: 0.67 75º: 0.57	30º: 0.01 45º: 0.04 60º: 0.02 75º: 0.04	30º: 0.37 45º: 0.50 60º: 0.51 75º: 0.45	30º: 0.02 45º: 0.05 60º: 0.03 75º: 0.05

Table A.1 (cont.). Summary of laboratory methodologies to determine restitution coefficients under different definitions.

Authors	Method	Sample retrieving	Material	Details	COR_{VN} Mean	COR_{VN} SD	COR_{VT} Mean	COR_{VT} SD	COR_E Mean	COR_E SD	COR_{TE} Mean	COR_{TE} SD
Wang et al. (2018)	Falling rock: spherical limestone polyhedrons (10 and 20 cm diameters, customized natural rock, edges not smoothed), dropped using a release device. Surface: C25 concrete slab (1.2 x 0.5 x 0.15 m) at different angles, supported by a compacted gravely soil ramp. Medium-scale. Infrared cameras to capture trajectories. 3 tests at each condition.	Three Gorges area, China	Limestone on concrete	10 kg, 20 cm diameter rock, 2.5 m drop height.	30º: 0.40 45º: 0.56 60º: 0.76 75º: 0.79	30º: 0.01 45º: 0.03 60º: 0.08 75º: 0.07	30º: 0.87 45º: 0.73 60º: 0.72 75º: 0.67	30º: 0.03 45º: 0.02 60º: 0.02 75º: 0.13	30º: 0.58 45º: 0.66 60º: 0.73 75º: 0.71	30º: 0.02 45º: 0.02 60º: 0.03 75º: 0.09	30º: 0.38 45º: 0.53 60º: 0.65 75º: 0.65	30º: 0.02 45º: 0.04 60º: 0.06 75º: 0.09
				10 kg, 20 cm diameter rock, 3.5 m drop height.	30º: 0.31 45º: 0.49 60º: 0.74 75º: 1.08	30º: 0.03 45º: 0.05 60º: 0.13 75º: 0.21	30º: 0.89 45º: 0.70 60º: 0.66 75º: 0.64	30º: 0.11 45º: 0.05 60º: 0.04 75º: 0.04	30º: 0.54 45º: 0.62 60º: 0.68 75º: 0.69	30º: 0.03 45º: 0.04 60º: 0.05 75º: 0.11	30º: 0.34 45º: 0.46 60º: 0.56 75º: 0.59	30º: 0.05 45º: 0.05 60º: 0.11 75º: 0.15
				10 kg, 20 cm diameter rock, 4.5 m drop height.	30º: 0.37 45º: 0.47 60º: 0.64 75º: 1.17	30º: 0.03 45º: 0.09 60º: 0.12 75º: 0.18	30º: 0.85 45º: 0.86 60º: 0.63 75º: 0.62	30º: 0.05 45º: 0.04 60º: 0.10 75º: 0.16	30º: 0.55 45º: 0.72 60º: 0.63 75º: 0.68	30º: 0.04 45º: 0.04 60º: 0.07 75º: 0.12	30º: 0.34 45º: 0.56 60º: 0.49 75º: 0.58	30º: 0.05 45º: 0.05 60º: 0.11 75º: 0.15
Ghana et al. (2019)	Normal drop test. Square block (15cm sides and 5cm thickness) acting as a surface. Two surface types: one natural and one smooth and clean. Falling block: cube, 2cm in size, edges smoothed. Drop tower with vacuum to perform free fall with minimum rotation experiments. High-speed camera, 240 fps. Small scale.	Gunung Panjang, Ipoh, Malaysia	Limestone	0.5 m drop height, smooth surface - 25 tests	0.403							
				0.5 m drop height, natural surface - 25 tests	0.286							
				1.0 m drop height, smooth surface - 25 tests	0.377							
				1.0 m drop height, natural surface - 25 tests	0.253							

Table A.2. Published coefficients of restitution and friction (Heidenreich, 2004, adapted).

Authors	COR_{VN}	COR_{VT}	COR_E	COR_{TE}	COR_I	COR_{VT}	COR_E	COR_{TE}
Habib (1977)	0.75-0.80							Based on experience in Italy
	0.50-0.60							Based on experience in Norway
Piteau and Claton (1977)	0.80-0.90	0.65-0.75						Solid rock
	0.50-0.80	0.45-0.65						Detrital material mixed with large rock boulders
	0.40-0.50	0.35-0.45						Compact detrital material mixed with small boulders
	0.20-0.40	0.20-0.30						Grass covered slopes
Wu (1985)	0.20-0.80	0.50-0.75						Rock on rock or wood platform
Heierli (1985)	0.95		0.9					Rock on rock or wood platform
	0.55		0.3					Gravel layer (35 cm)
	0.45		0.2					Gravel layer (70 cm)
	0.45		0.2					Debris
Bozzolo and Pamini (1986)				0.7				Rock at a slope angle of 44°
				0.55				Debris at a slope angle of 57°
Descoeudres and Zimmermann (1987)					0.4	0.5		Vineyard slopes
					0.85	0.5		Rock slopes
Hoek (1987)	0.53	0.99						Clean hard bedrock
	0.4	0.9						Asphalt roadway
	0.35	0.85						Bedrock outcrops with hard surface, large boulders
	0.32	0.82						Talus cover
	0.32	0.8						Talus cover with vegetation
	0.3	0.8						Soft soil, some vegetation
Urciuoli (1988)	0.05-0.35	0.5-1.00	0.02-1.00					Rock block impacting limestone
	~0	0.24						Debris fan
Gerber (1995)	0.17-0.43	0.45-0.88						Rock (limestone)
Ushiro et al. (2000)	0.10-0.40	0.71						Undefined materials

320

Table A.2 (cont.). Published coefficients of restitution and friction (Heidenreich, 2004, adapted).

Authors	COR_{VN}	COR_{VT}	COR_E	COR_{TE}	COR_I	μ	μr	Remarks
Pfeiffer and Bowen (older versions of CRSP) (1989)	0.37-0.42	0.87-0.92						Smooth, hard surface as paving rock
	0.33-0.37	0.83-0.87						Bedrock or boulders with little soil or vegetation
	0.30-0.33	0.83-0.87						Talus with little vegetation
	0.30-0.33	0.80-0.83						Talus with some vegetation
	0.28-0.32	0.80-0.83						Soft soil slope with little vegetation
	0.28-0.32	0.78-0.82						Vegetated soil slope
Giani, Barbierei et al. (1992, 1988)	0.5	0.95						Bedrock
	0.35	0.85						Bedrock covered by large blocks
	0.3	0.7						Debris formed by uniform distributed elements
	0.25	0.55						Soil covered by vegetation
Azzoni et al. (1995)						0.3 m³	1.2 m³	
			0.75-0.90			0.40-0.45	0.4	Rock (limestone)
			0.55-0.60			0.50-0.60	0.4	Fine angular debris and earth (compacted)
			0.35-0.45			0.70-0.80	0.60-0.70	Fine angular debris and earth (soft)
			0.45-0.50			0.60-0.70	0.50-0.60	Medium angular debris with angular rock fragments
			0.40-0.50			0.70-1.00		Medium angular debris with scattered trees
			0.55-0.70			0.65-1.20	0.60-0.80	Coarse angular debris with angular rock fragments
			0.50-0.60			0.55-0.65	0.45-0.50	Earth with grass and some vegetation
			<0.20			0.85		Ditch with mud
			0.50-0.65			0.50-0.65		Flat surface of artificially compacted ground
			0.75			0.40-0.45		Road
Kamijo (2000)	0.10-0.35							Vertical impact of a 220kg rock on hard surface
	0.1							Vertical impact of a 800kg rock on hard surface

Table A.2 (cont.). Published coefficients of restitution and friction (Heidenreich, 2004, adapted).

Authors	COR_{VN}	COR_{VT}	COR_E	COR_{TE}	COR_I	μ	μr	Remarks
Jones et al. (values gathered by program calibration for CRSP 4.0) (2000)	0.60-1.00	0.90-1.00						Smooth hard surface and paving
	0.15-0.30	0.75-0.95						Bedrock and boulder fields
	0.12-0.20	0.65-0.95						Talues and firm soil slopes
	0.10-0.20	0.50-0.80						Soft soil slopes
Budetta and Santo (evaluated by program calibration) (1994)	0.2	0.53						Rock
Kobayashi et al. (1990)							0.64	Rock slope also covered with trees
							0.38	Rock
							0.53	Scattered sagebrush, grass, few other boulders
							0.33	Rock
Hungr and Evans (1988)	0.5	0.8						Sparsely forested slope covered by a veneer of very fine weathered talus derived from weak schistose
	0.5	0.8						Limestone on bare uniform talus slope formed of basalt fragments
	0.7	0.9						Rectangular boulder of metamorphosed tuff on bare rock and a steep snow covered shelf
Robotham at al.	0.32	0.71						Limestone face
	0.3	0.62						Partially vegetated limestone scree
	0.32	0.71						Uncovered limestone blast pile
	0.25	0.49						Vegetated covered limestone pile
	0.28	0.84						Chalk face
	0.27	0.6						Vegetated chalk scree

Table A.3. Summary of field methodologies to determine restitution coefficients under different definitions.

Authors	Method	Sample retrieving	Material	Details	COR_{VN}		COR_{VT}		COR_E		COR_{TE}	
					Mean	SD	Mean	SD	Mean	SD	Mean	SD
Azzoni and de Freitas, Azzoni et al. (1995)	Prismatic (1.2 m³) and spherical (0.3 m³) blocks dropped from two slopes. Slope A: 45 m tall, 60 m long, approximately 50º with sections between 30º and 65º. Limestone, fine angular debris, fine-medium angular debris. Slope B: 40m tall, 60m long, approximately 40º. Fine angular debris, medium angular debris, coarse angular debris.	Strozza, Italy	Limestone								0.75-0.90	
			Fine angular debris and earth, compacted (gravel and cobbles, diam. < 20 cm)								0.55-0.60	
			Fine angular debris and earth, soft								0.35-0.45	
			Medium angular debris with angular rock fragments (20 - 40 cm diam.)								0.45-0.50	
			Medium angular debris with scattered trees								0.40-0.50	
			Coarse angular debris with angular rock fragments (40 - 120 cm diam.)								0.55-0.70	
			Earth with grass and some vegetation								0.50-0.60	
			Ditch with mud								<0.20	
			Yard (flat surface of artificially compacted ground)								0.50-0.65	
			Road								0.75	

Table A.3 (cont.). Summary of field methodologies to determine restitution coefficients under different definitions.

Authors	Method	Sample retrieving	Material	Details	COR_{VN}		COR_{VT}		COR_E		COR_{TE}	
					Mean	SD	Mean	SD	Mean	SD	Mean	SD
Giani el al. (2002)	43 rocks with volumes varying between 0.01 and 0.6 m^3 were dropped from a rock slope and laterally video recorded at 10 fps.	Parma, Italy	Well-graded debris with soil and low growth vegetation		0.52	0.09	0.79	0.03				
Giani et al. (2004)	40 rocks with volumes varying between 0.1 to 4.5 m^3	Lepontine Alps, Italy	Debris		0.25	0.26	0.47	0.1				
Asteriou et al. (2012)	Local rocks were roughly shaped into cubes and dropped by hand onto a local rock used as impact surface (7m x 3m area). Recorded laterally.	Greece	Marble	29 tests	0.94	1.04	0.85	0.1	0.75	0.15		
Giacomini et al. (2012)	Field. 40m drop height, 70deg angle. Concrete blocks, 30cm in largest dimension, 44.5kg. 2 sites, site 1 with drapery, site 2 no drapery.	New South Wales, Australia	Sandstone	Site 1: 2 tests	1.14	0.2	0.4	0.15				
			Mudstone	Site 1: 5 tests Site 2: 2 tests	0.61 0.59	0.16 0.09	0.78 0.52	0.11 0.08				
			Mudstone debris	Site 1: 1 tests	0.11	-	0.8	-				
			Coal	Site 2: 1 tests	0.41	-	0.64	-				
			Sandstone/Mudstone	Site 1: 6 tests Site 2: 10 tests	0.71 0.61	0.33 0.29	0.83 0.75	0.11 0.17				

Table A.3 (cont.). Summary of field methodologies to determine restitution coefficients under different definitions.

Authors	Method	Sample retrieving	Material	Details	COR_{VN} Mean	COR_{VN} SD	COR_{VT} Mean	COR_{VT} SD	COR_{E} Mean	COR_{E} SD	COR_{TE} Mean	COR_{TE} SD
Giacomini et al. (2012)	Field. 40m drop height, 70deg angle. Concrete blocks, 30cm in largest dimension, 44.5kg. 2 sites, site 1 with drapery, site 2 no drapery.	New South Wales, Australia	Mudstone/sandstone	Site 1: 4 tests	0.93	0.42	0.63	0.1				
			Debris	Site 1: 5 tests Site 2: 4 tests	0.22 0.13	0.08 0.05	0.40 0.15	0.13 0.13				
Bar et al. (2016)	Rocks were manually pushed (20 to 40 kg) or released with a lever (60 to 300 kg). Equipment assisted rock drops using a telescoping handler to lift and drop rocks between 1,000 and 6,500 kg. Rockfalls were conducted on bench face angles of 50º, 60º, 70º, and 80º, with multiple benches below for travel paths. Rock shapes: square, triangle, rhombus, pentagon, and hexagon.	Not mentioned	Bench floor (all data)		0.3	0.06	0.62	0.12				
			Bench floor (weathered rock)		0.24	0.06	0.57	0.11				
			Bench floor (fresh rock)		0.31	0.05	0.63	0.12				
			Bench face (all data)		0.4	0.06	0.84	0.07				
			Sandstone bench face		0.38	0.06	0.83	0.08				
			Siltstone bench face		0.44	0.06	0.81	0.06				

APPENDIX B:

FIELD ROCKFALL TRAJECTORIES AND SMART ROCK DATA OUTPUT

B.1. Dover, NH

Field Rockfall — Reference Rock, Dover/NH

SR number: 5. Date: 25-May-2020.

Mass: 5.21 kg. I_{XX}: 0.018 kg.m^2. I_{YY}: 0.011 kg.m^2. I_{ZZ}: 0.018 kg.m^2.

Width (X): 0.12 m. Length (Y): 0.2 m. Height (Z): 0.12 m. Shape: Compact Elongated.

Runout distance: not measured.

Drop height: not measured. Altimeter hoisting: 9.2 m.
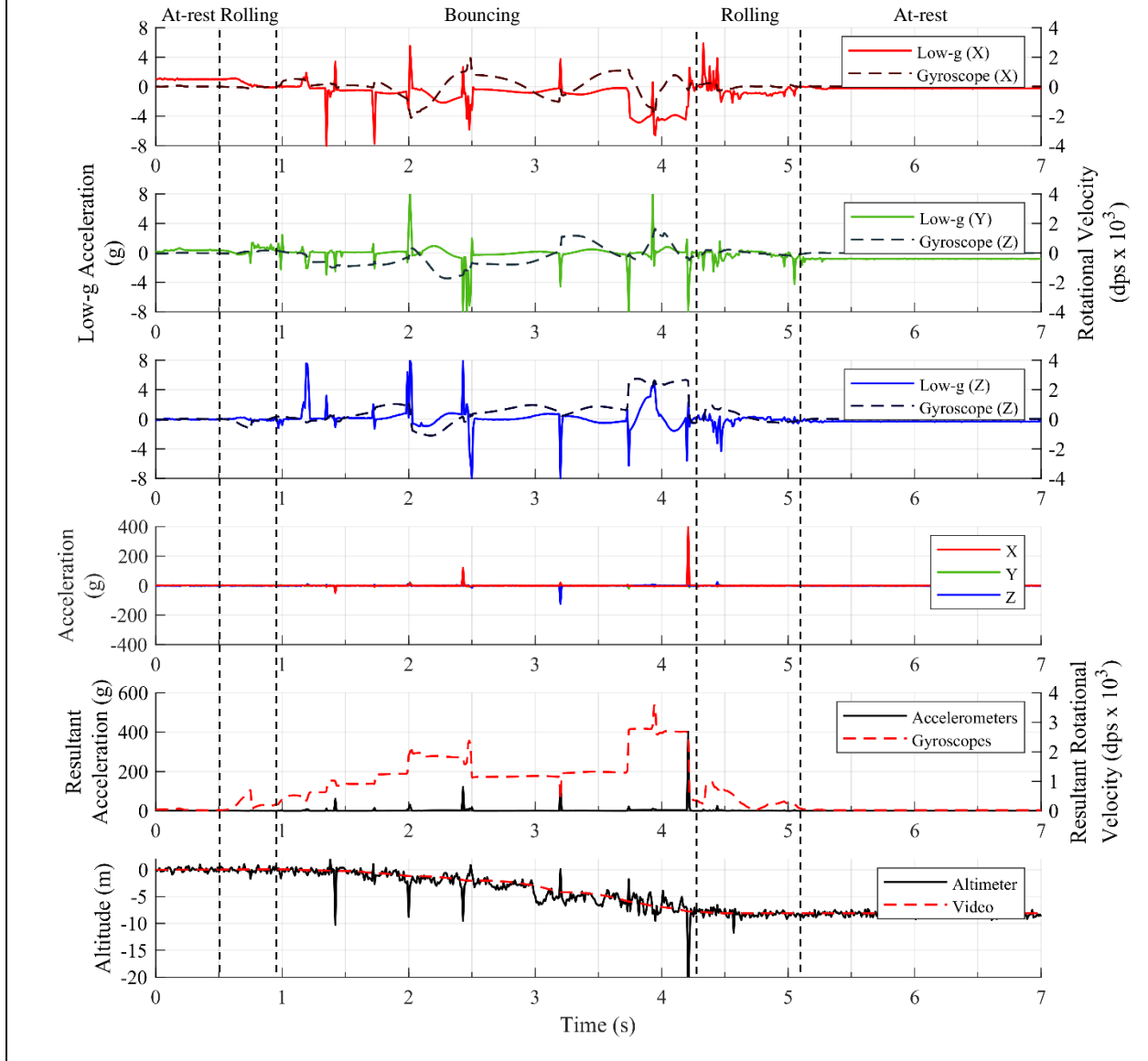
Figure B.1. Smart Rock test data: reference rock (SR 5), Dover NH.

Field Rockfall — Reference Rock, Dover/NH

SR number: 4. Date: 25-May-2020.

Mass: 5.21 kg. I_{XX}: 0.018 kg.m^2. I_{YY}: 0.011 kg.m^2. I_{ZZ}: 0.018 kg.m^2.

Width (X): 0.12 m. Length (Y): 0.2 m. Height (Z): 0.12 m. Shape: Compact Elongated.

Runout distance: not measured.

Drop height: not measured. Altimeter hoisting: 9.2 m.
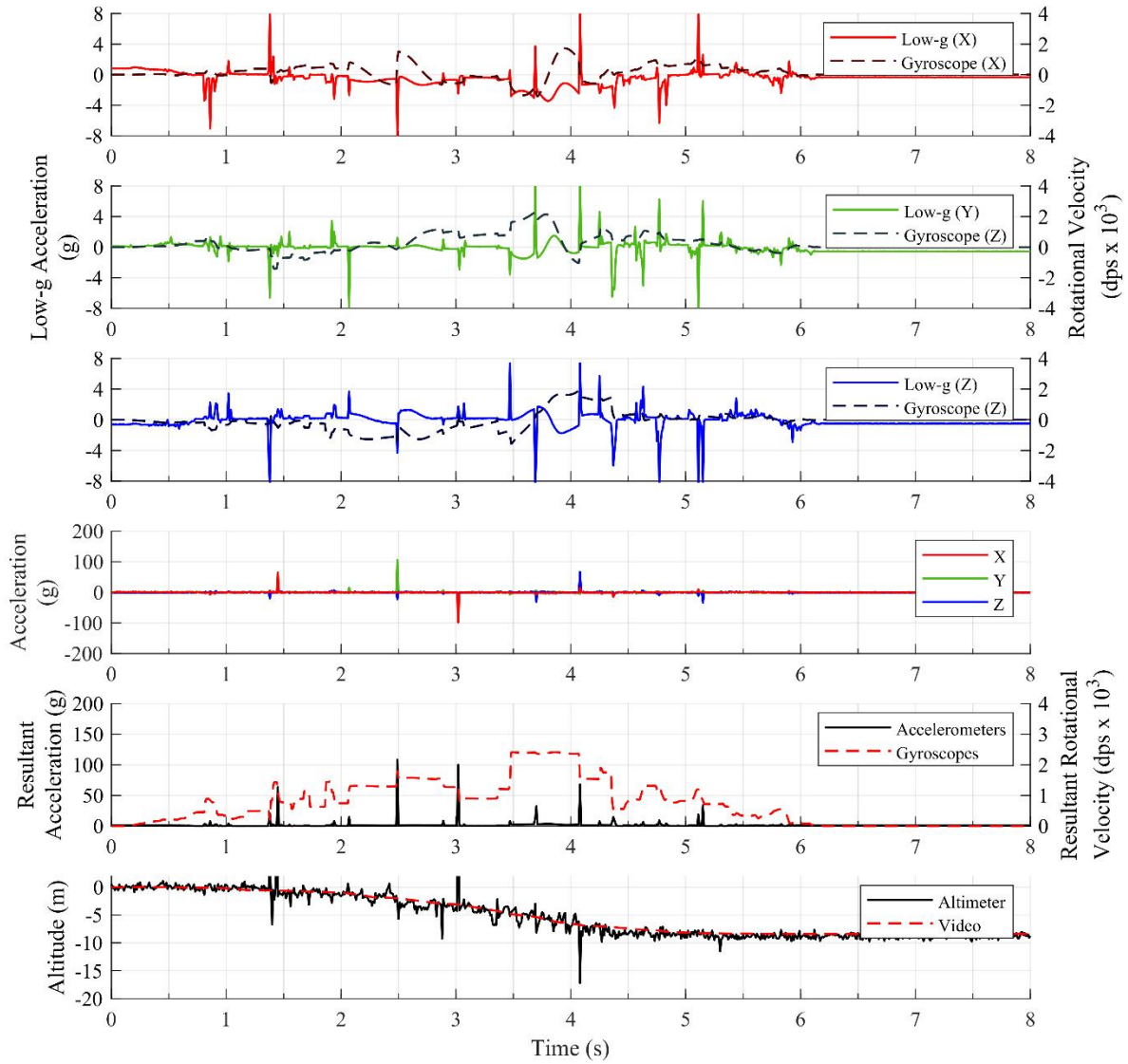
Figure B.2. Smart Rock test data: reference rock (SR 4), Dover NH.

Field Rockfall — Reference Rock, Dover/NH

SR number: 6. Date: 25-May-2020.

Mass: 5.21 kg. I_{XX}: 0.018 kg.m^2. I_{YY}: 0.011 kg.m^2. I_{ZZ}: 0.018 kg.m^2.

Width (X): 0.12 m. Length (Y): 0.2 m. Height (Z): 0.12 m. Shape: Compact Elongated.

Runout distance: not measured.

Drop height: not measured. Altimeter hoisting: 9.2 m.
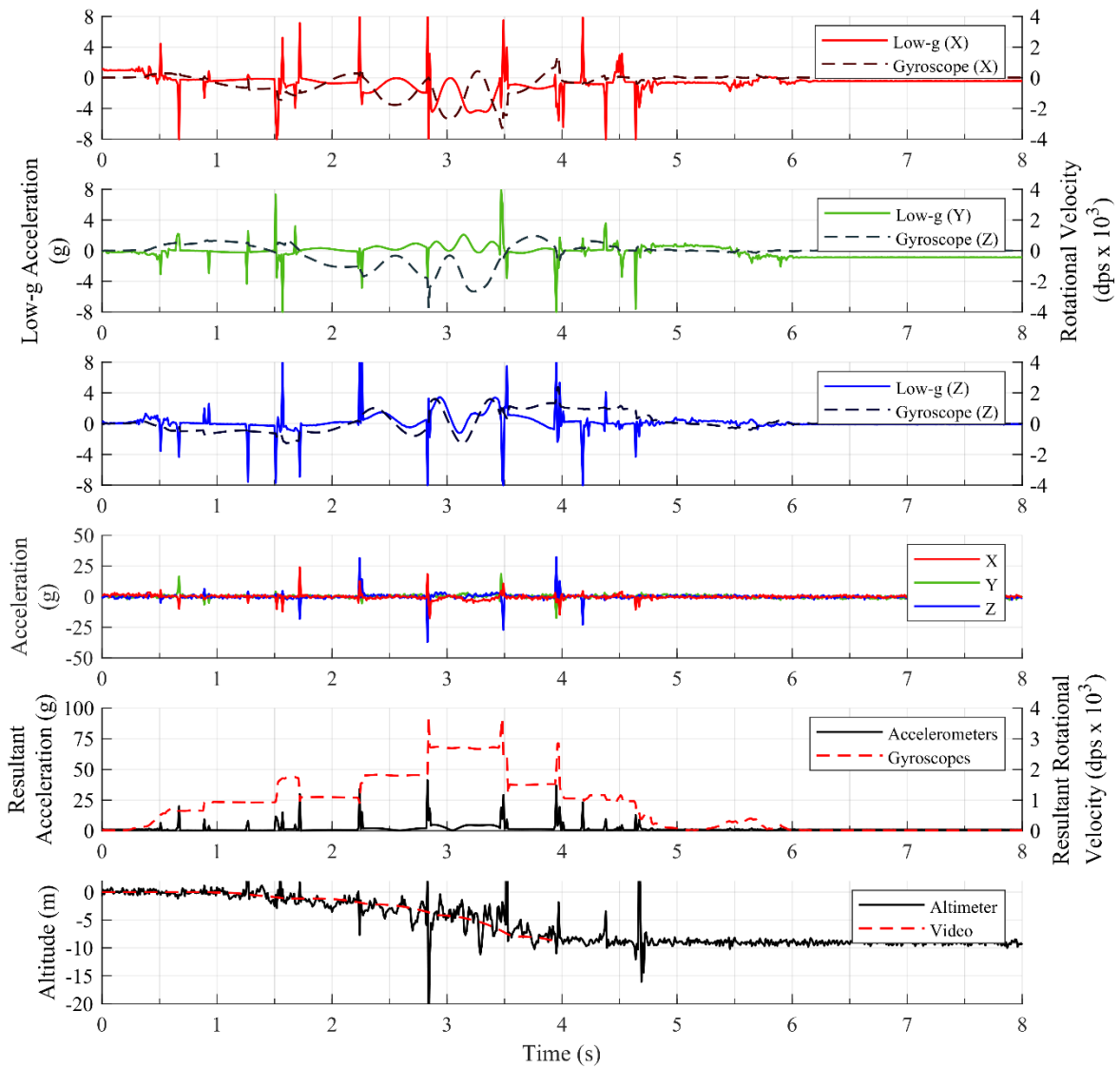
Figure B.3. Smart Rock test data: reference rock (SR 6), Dover NH.

329
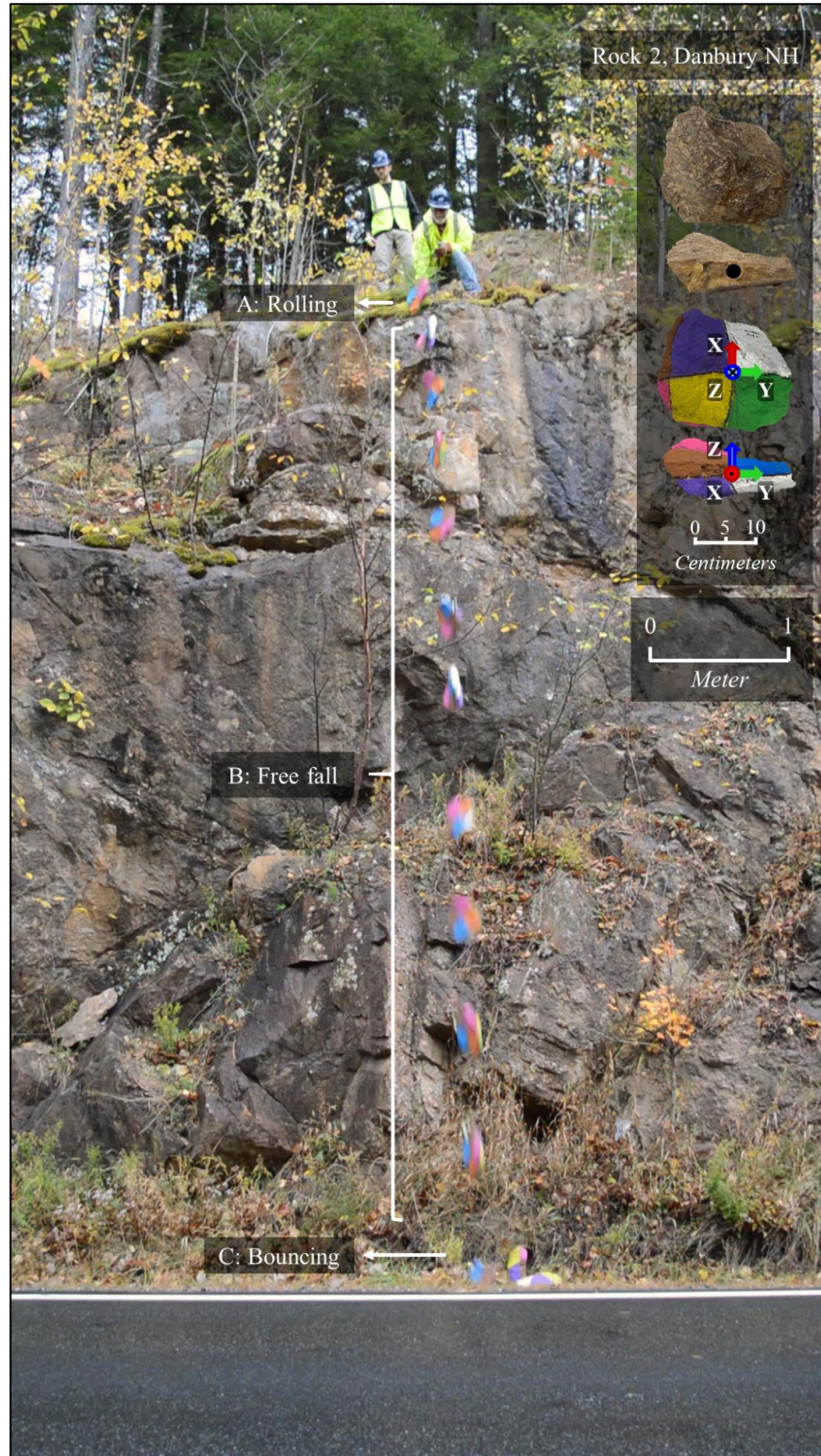
B.2. Danbury, NH

Figure B.4. Rockfall trajectory: rock 2, Danbury NH.

Field Rockfall — Rock 2, Danbury/NH

SR number: 3. Date: 16-Oct-2020.

Mass: 7.38 kg. I_{XX}: 0.036 kg.m^2. I_{YY}: 0.029 kg.m^2. I_{ZZ}: 0.056 kg.m^2.

Width (X): 0.25 m. Length (Y): 0.22 m. Height (Z): 0.07 m. Shape: Platy.

Runout distance: 1 m from slope toe.

Drop height: 7.3 m. Altimeter hoisting: 11.1 m.
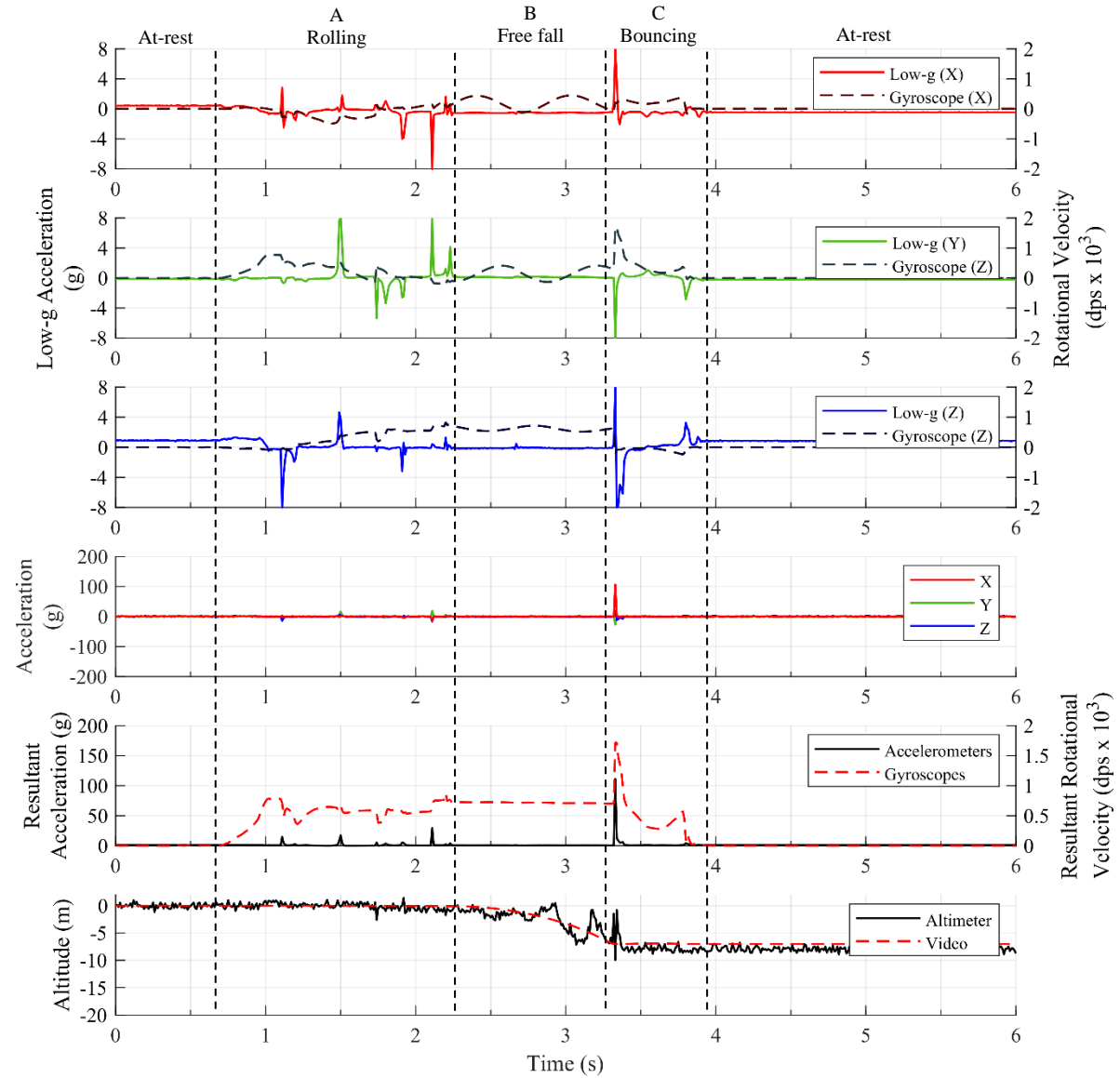
Figure B.5. Smart Rock data: rock 2, Danbury NH.

331
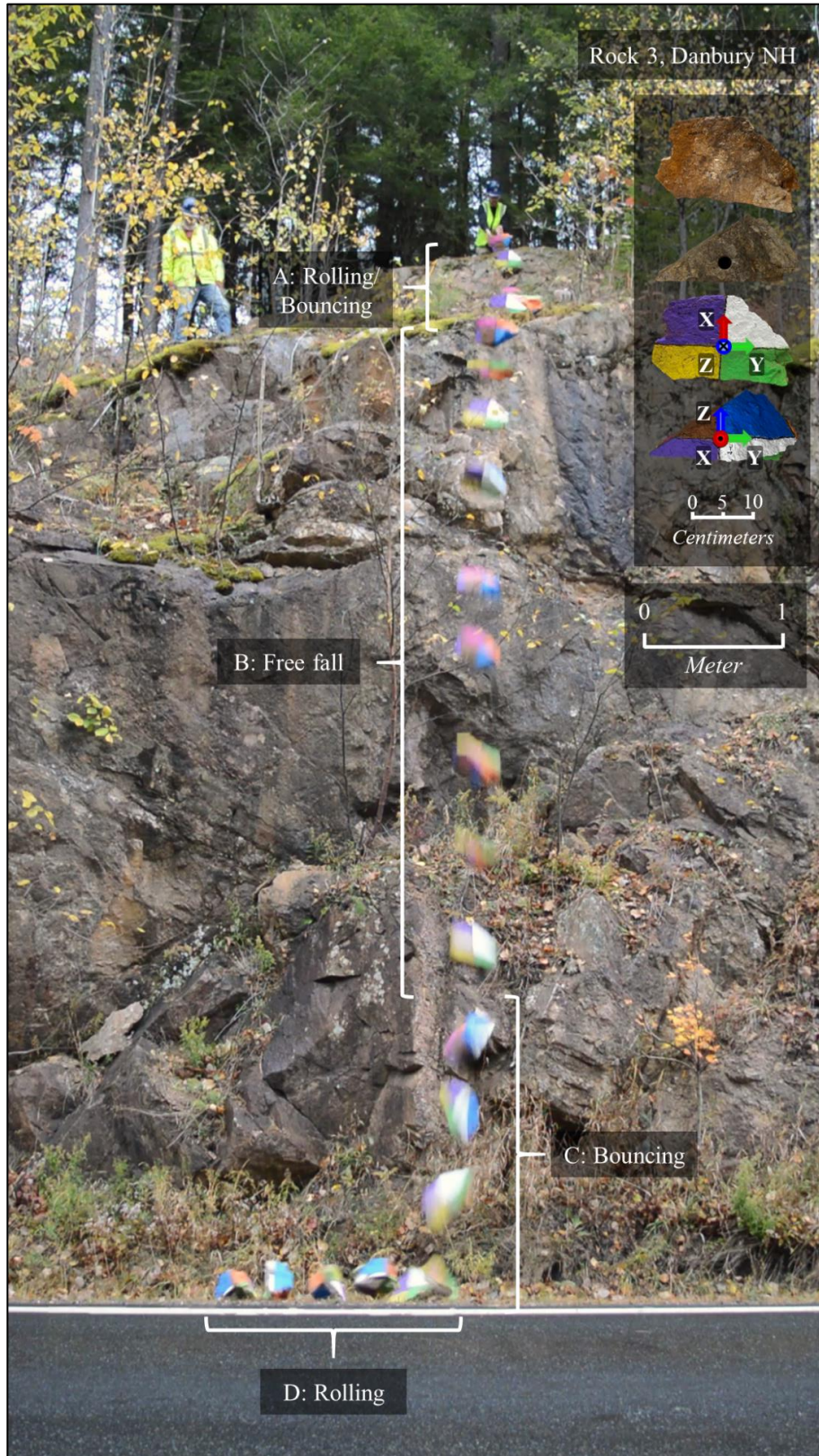
Figure B.6. Rockfall trajectory: rock 3, Danbury NH.

Field Rockfall — Rock 3, Danbury/NH

SR number: 1. Date: 16-Oct-2020.

Mass: 12.23 kg. I_{XX}: 0.081 kg.m^2. I_{YY}: 0.049 kg.m^2. I_{ZZ}: 0.101 kg.m^2.

Width (X): 0.22 m. Length (Y): 0.28 m. Height (Z): 0.1 m. Shape: Bladed.

Runout distance: 1 m from slope toe.

Drop height: 10.6 m. Altimeter hoisting: 12.3 m.
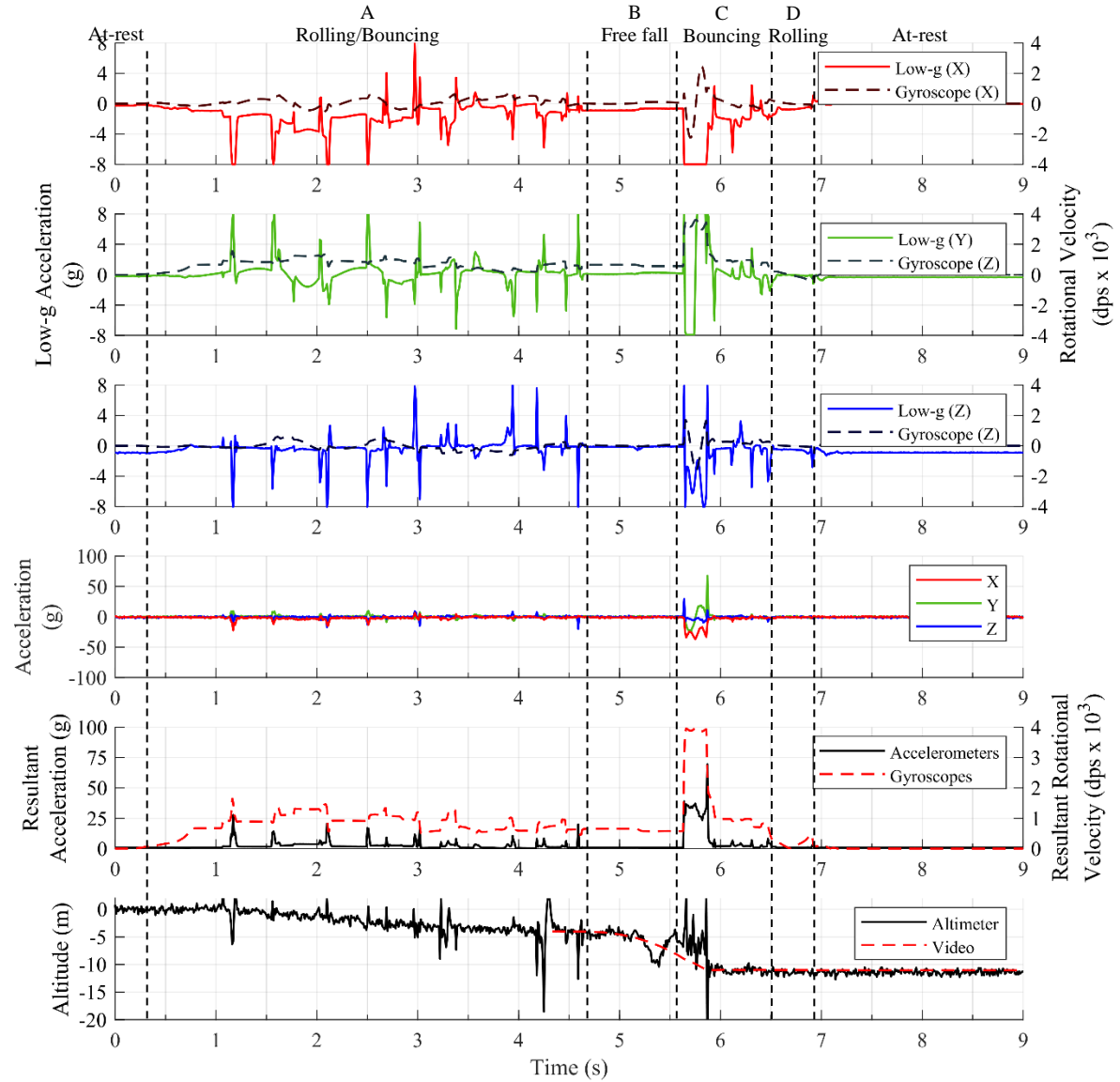
Figure B.7. Smart Rock data: rock 3, Danbury NH.

333
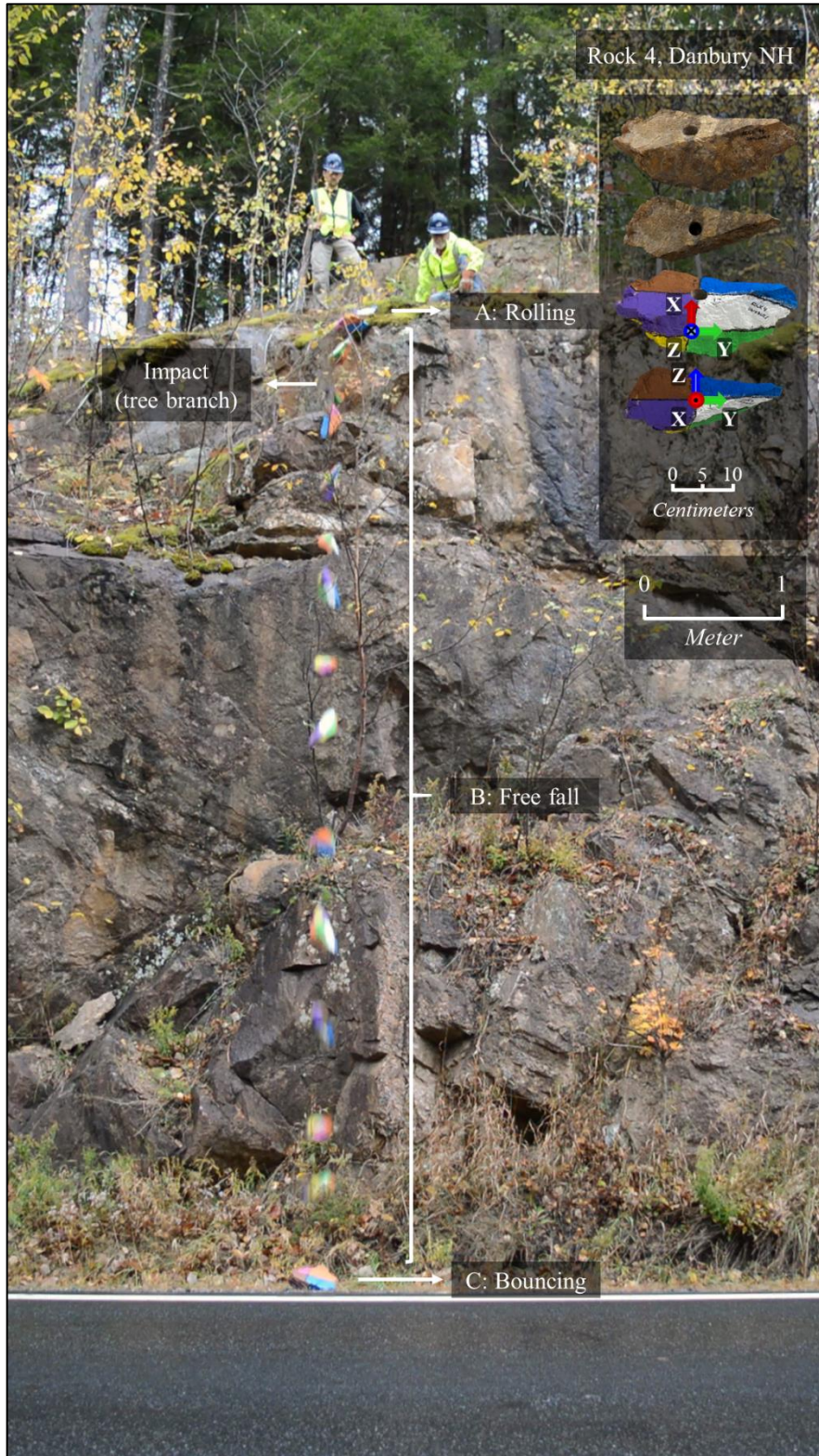
Figure B.8. Rockfall trajectory: rock 4, Danbury NH.

Field Rockfall — Rock 4, Danbury/NH

SR number: 4. Date: 16-Oct-2020.

Mass: 4.48 kg. I_{XX}: 0.025 kg.m^2. I_{YY}: 0.007 kg.m^2. I_{ZZ}: 0.022 kg.m^2.

Width (X): 0.1 m. Length (Y): 0.29 m. Height (Z): 0.09 m. Shape: Elongated.

Runout distance: 1.2 m from slope toe.

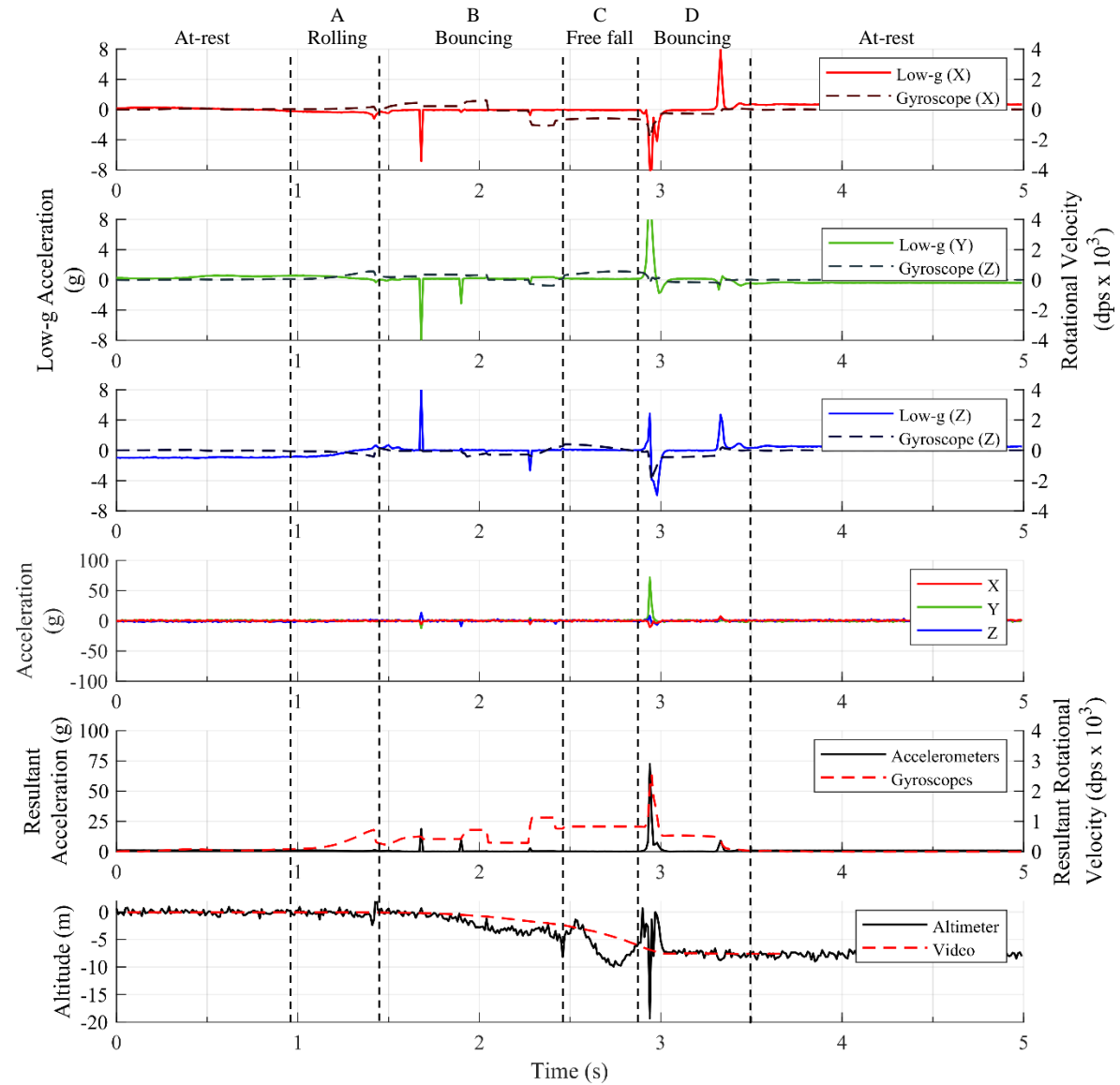Drop height: 7.3 m. Altimeter hoisting: 11.3 m.
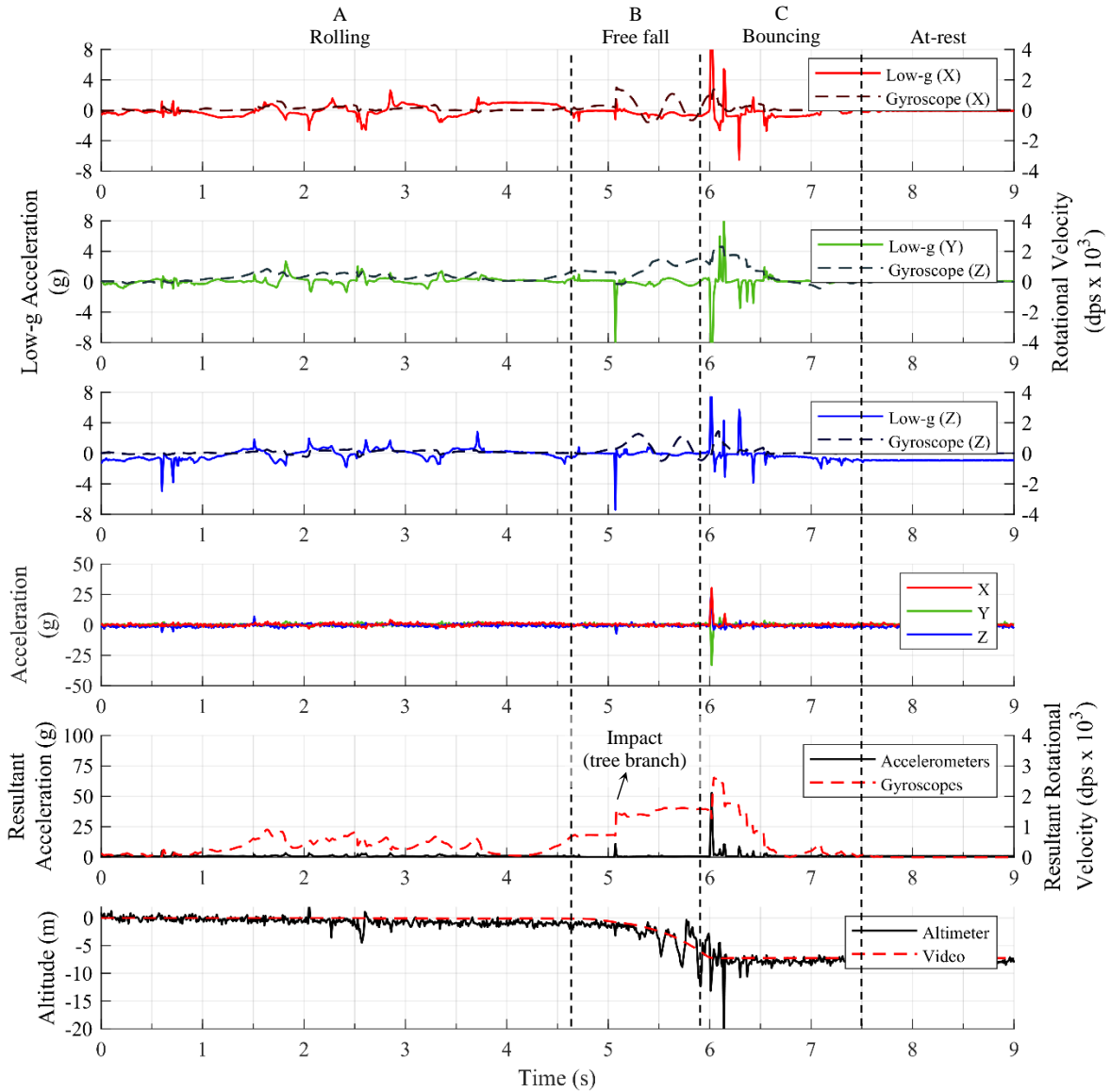
Figure B.9. Smart Rock data: rock 4, Danbury NH.

335
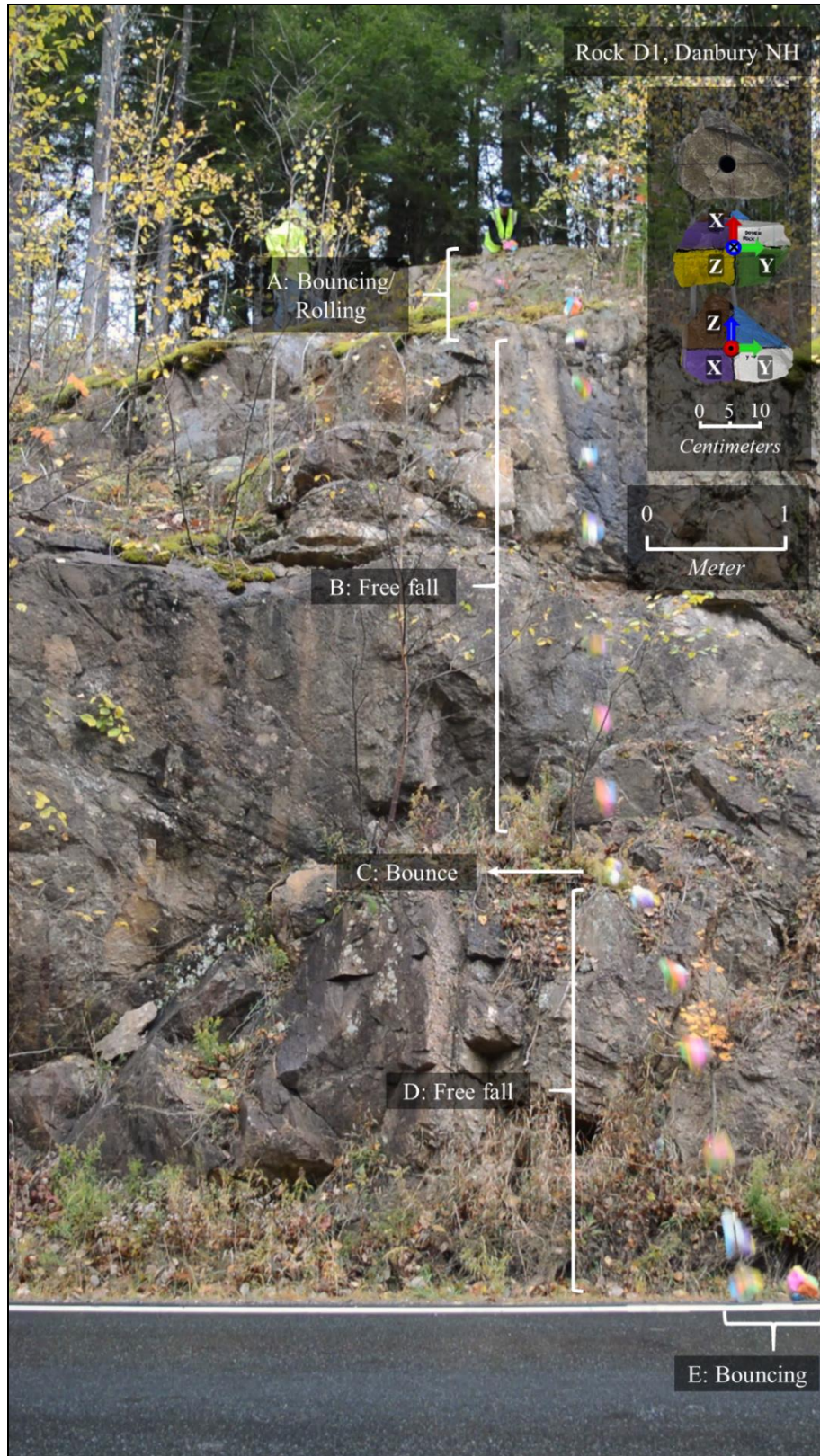
Figure B.10. Rockfall trajectory: rock D1, Danbury NH.

Figure B.11. Smart Rock data: rock D1, Danbury NH.
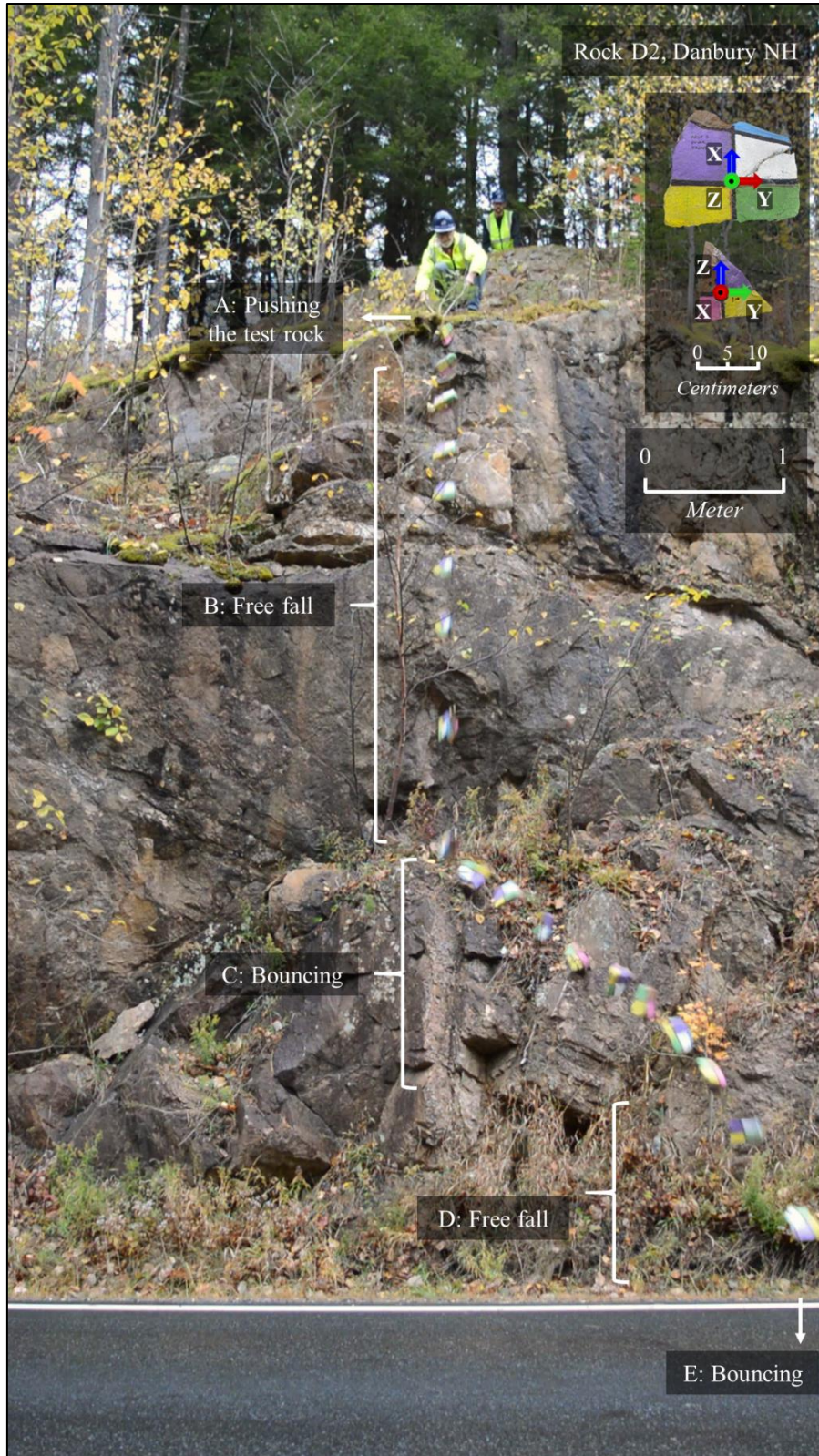
Figure B.12. Rockfall trajectory: rock D2, Danbury NH.

Field Rockfall — Rock D2, Danbury/NH

SR number: 5. Date: 16-Oct-2020.

Mass: 3.65 kg. I_{XX}: 0.006 kg.m^2. I_{YY}: 0.012 kg.m^2. I_{ZZ}: 0.012 kg.m^2.

Width (X): 0.18 m. Length (Y): 0.1 m. Height (Z): 0.13 m. Shape: Compact.

Runout distance: 1.8 m from slope toe.
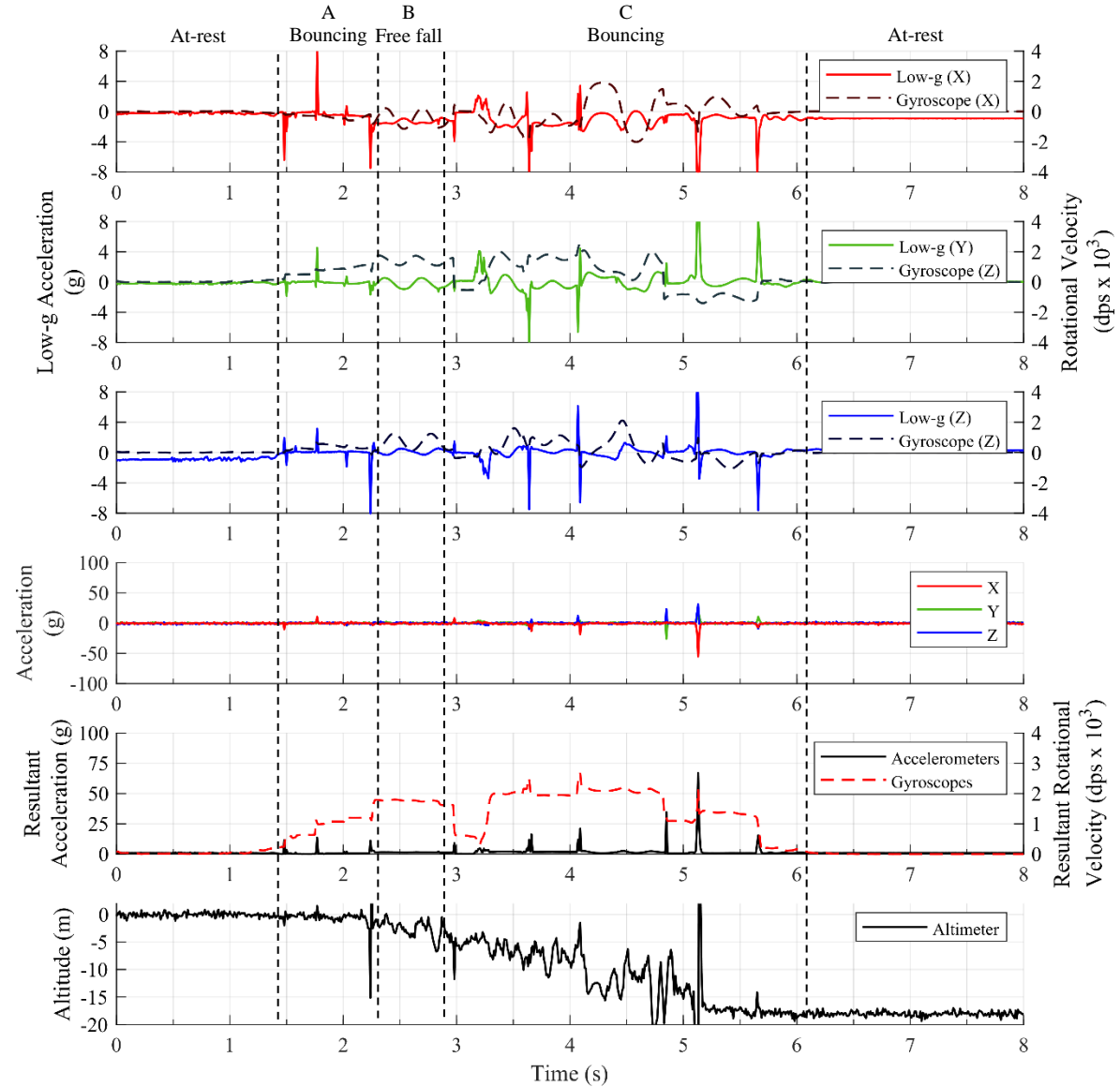
Drop height: 7.3 m. Altimeter hoisting: 10.8 m.
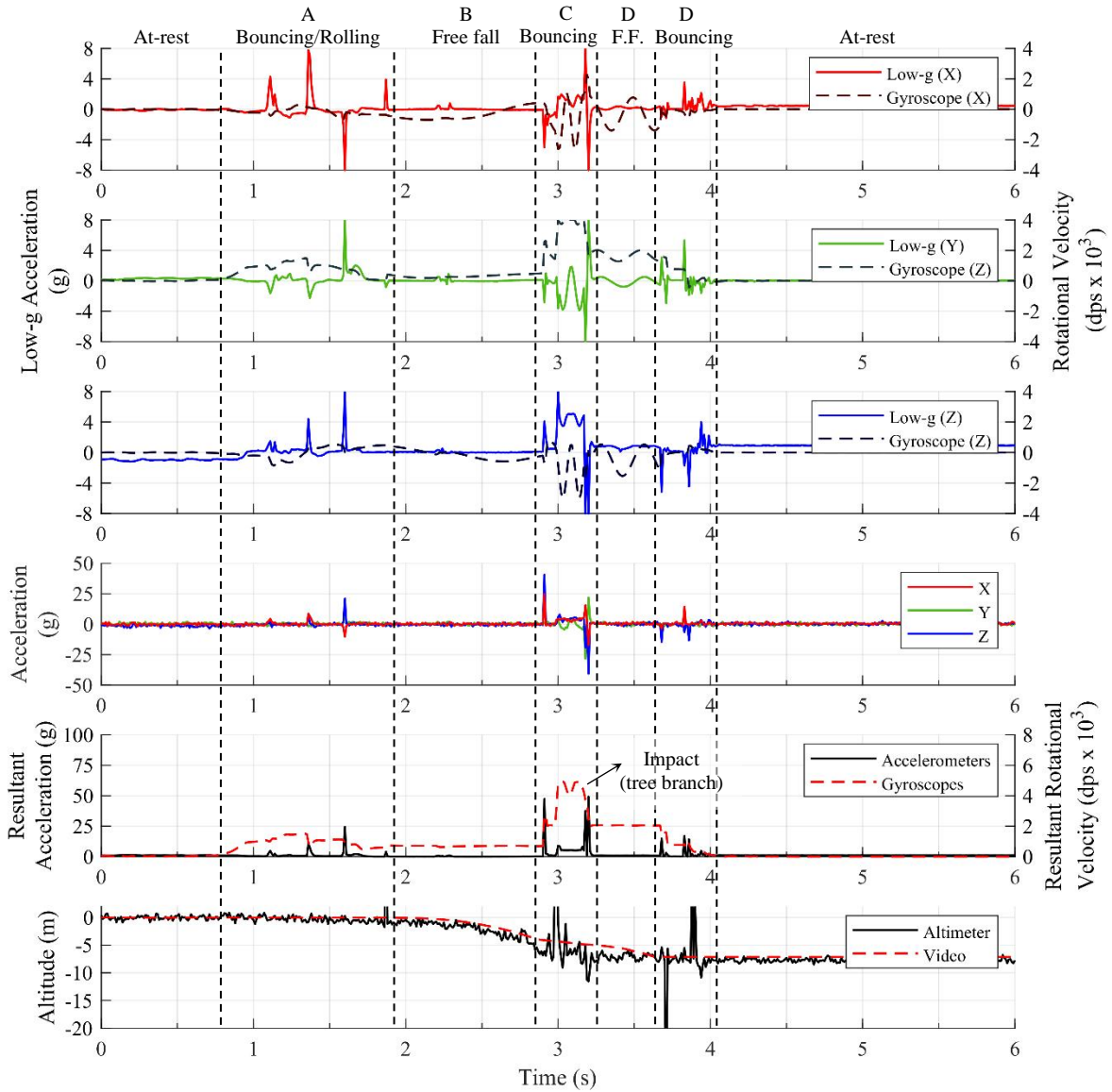
Figure B.13. Smart Rock data: rock D2, Danbury NH.
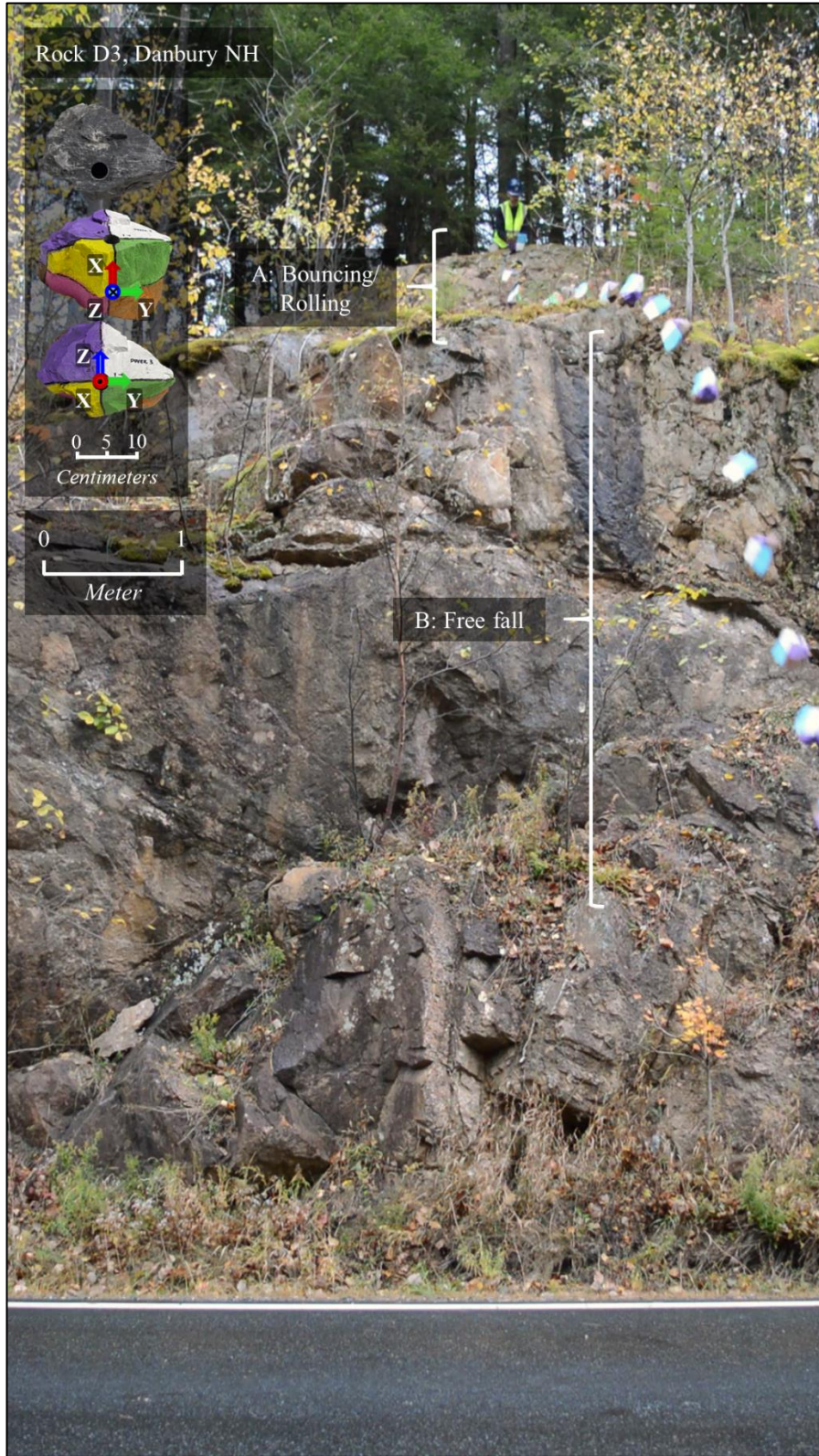
Figure B.14. Rockfall trajectory: rock D2, Danbury NH.

Field Rockfall — Rock D3, Danbury/NH

SR number: 4. Date: 16-Oct-2020.

Mass: 12.37 kg. I_{XX}: 0.065 kg.m^2. I_{YY}: 0.051 kg.m^2. I_{ZZ}: 0.077 kg.m^2.

Width (X): 0.22 m. Length (Y): 0.23 m. Height (Z): 0.15 m. Shape: Compact Platy.

Runout distance: 0.3 m from slope toe.
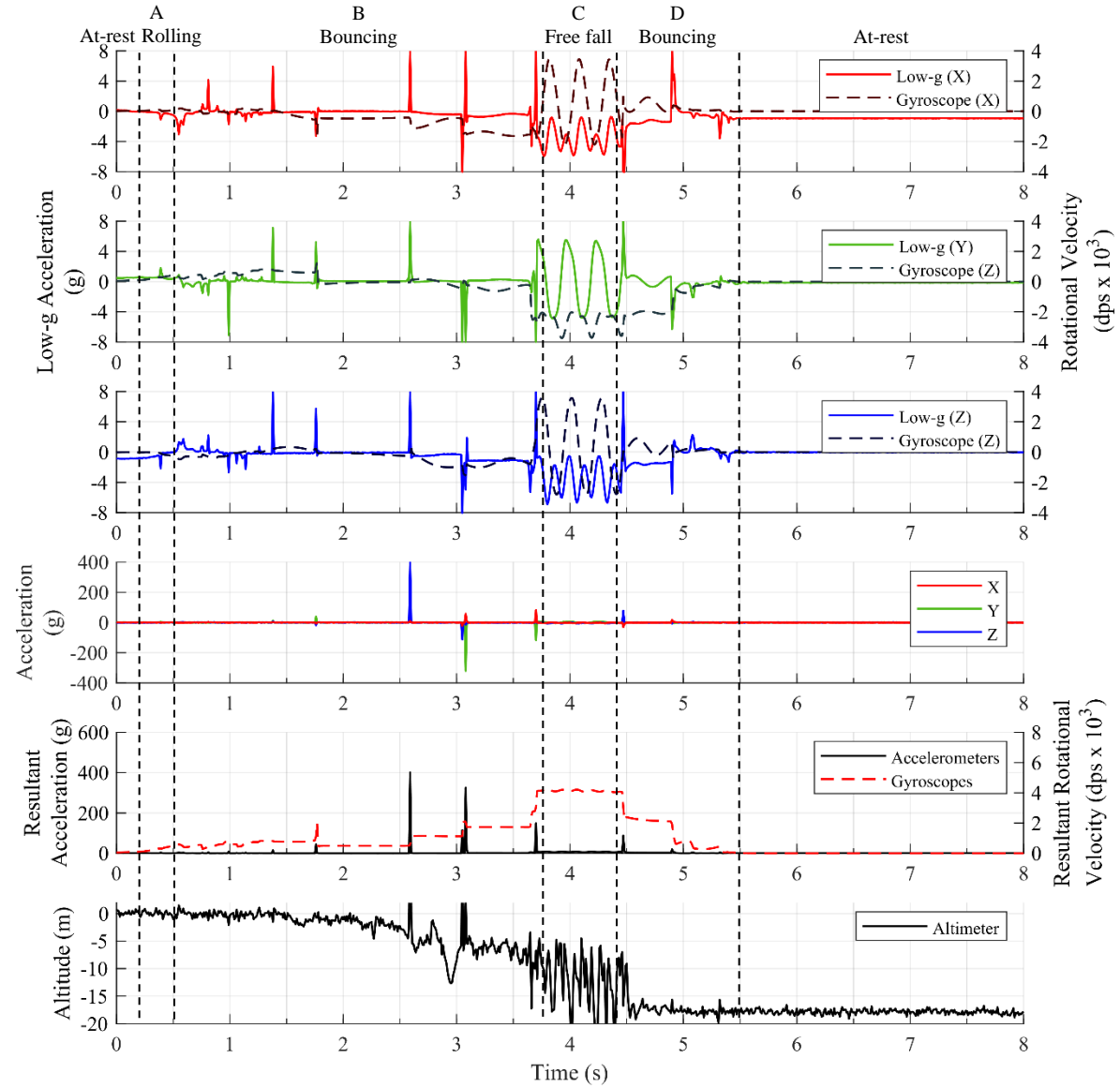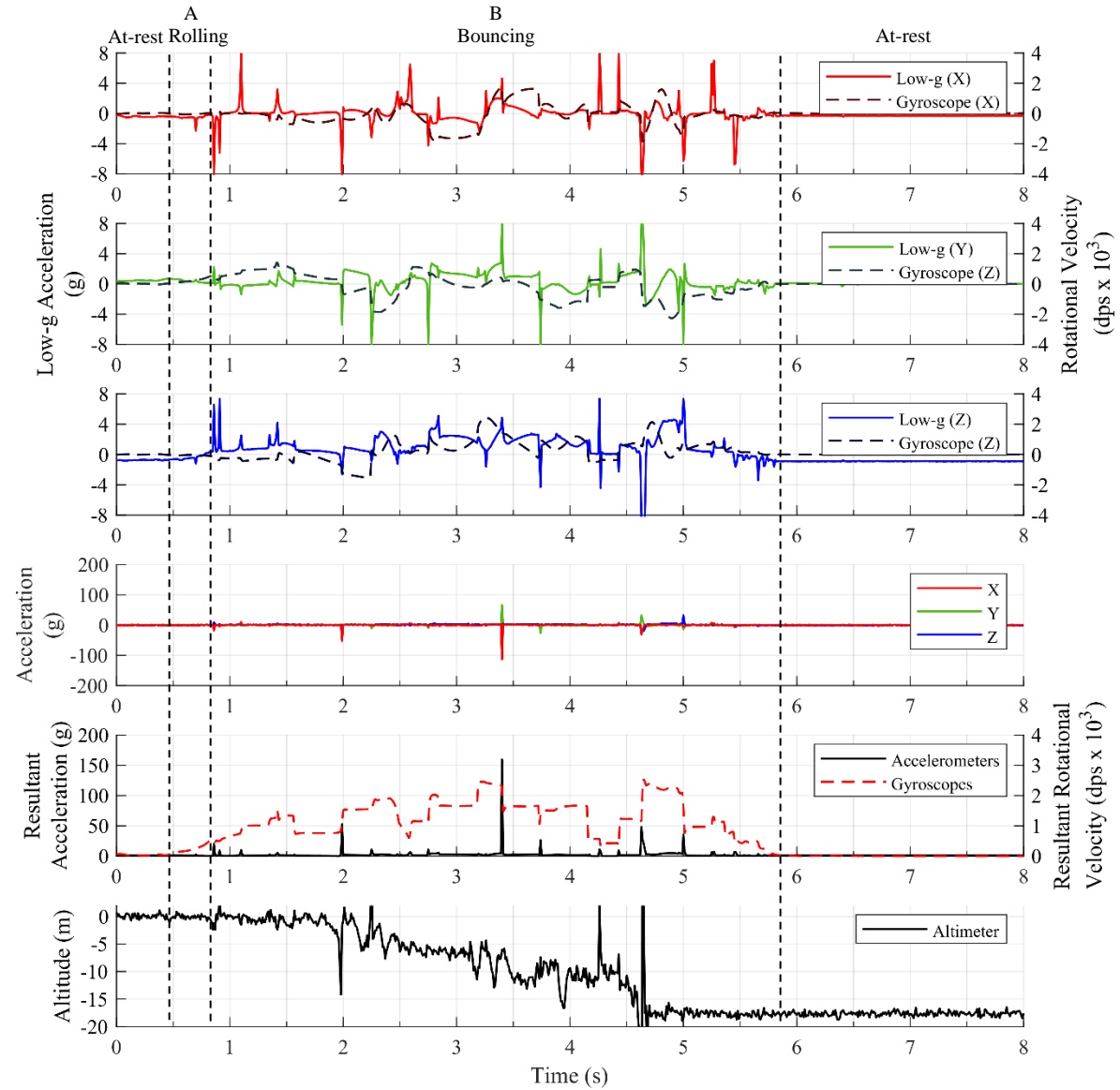
Drop height: 10.6 m. Altimeter hoisting: 10.6 m.
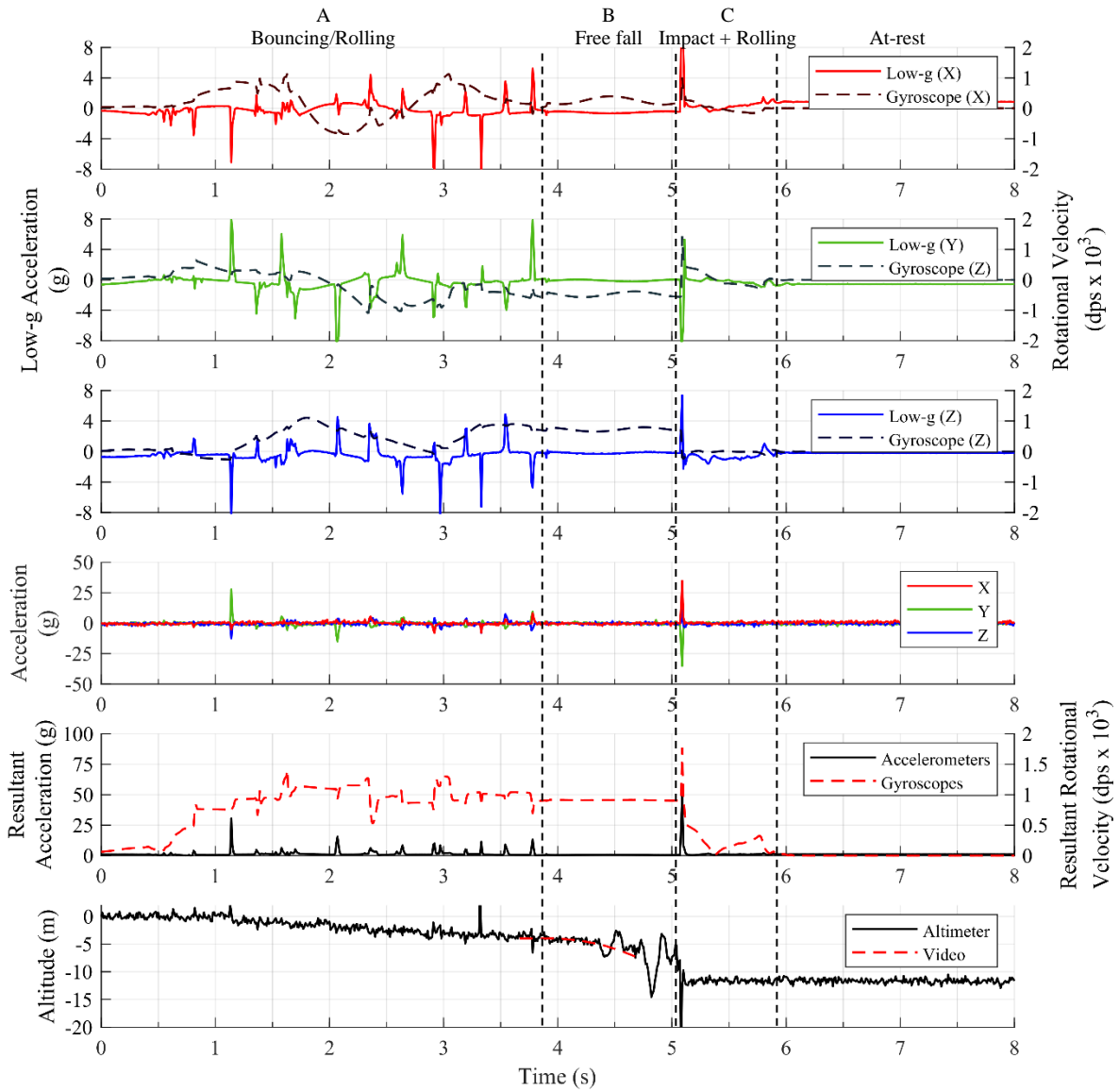
Figure B.15. Smart Rock data: rock D3, Danbury NH.

341
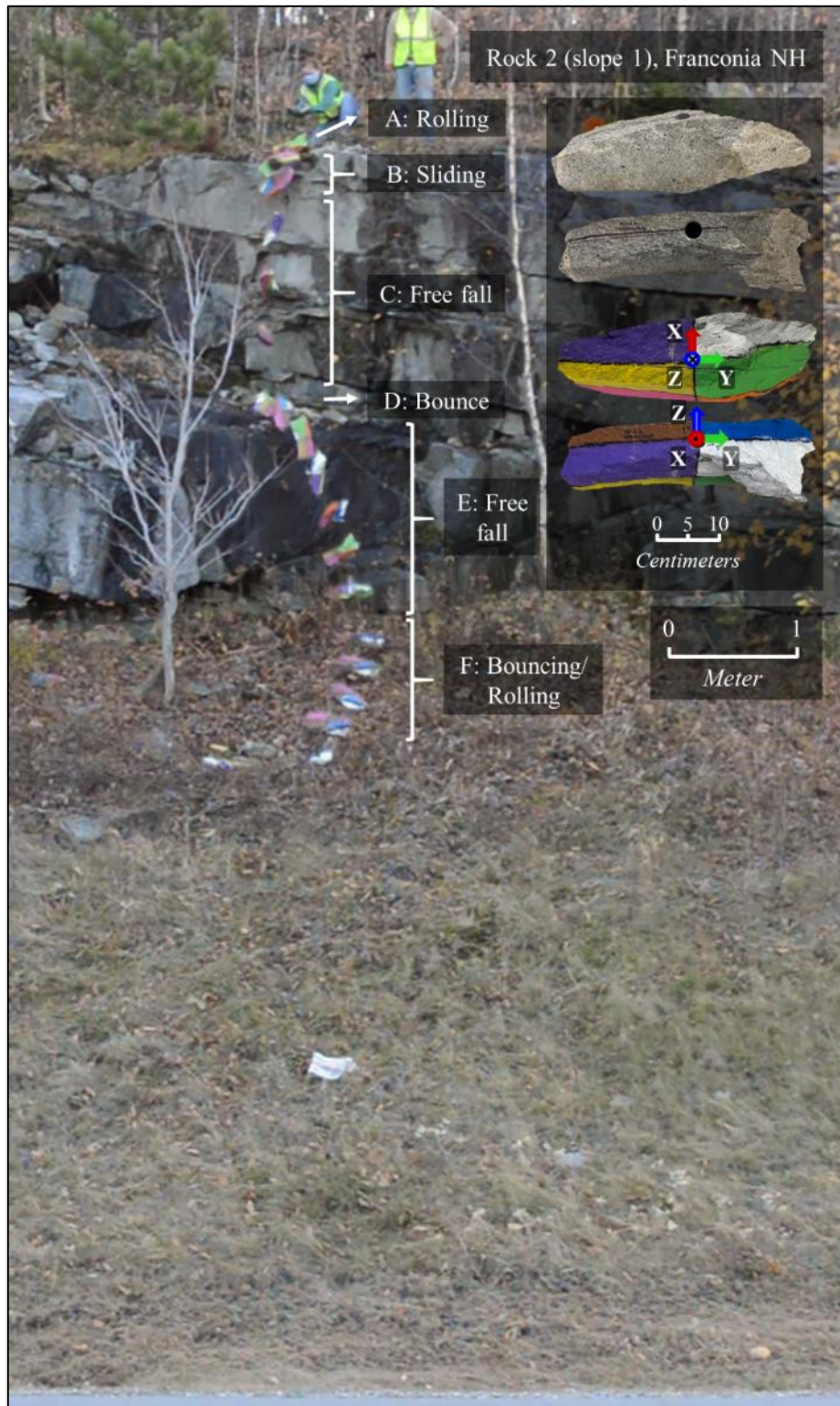
B.3. Franconia, NH

Figure B.16. Rockfall trajectory: rock 2 (slope 1), Franconia NH.

Field Rockfall — Rock 2 (slope 2), Franconia/NH

SR number: 5. Date: 23-Oct-2020.

Mass: 7.37 kg. I_{XX}: 0.034 kg.m^2. I_{YY}: 0.021 kg.m^2. I_{ZZ}: 0.032 kg.m^2.

Width (X): 0.18 m. Length (Y): 0.23 m. Height (Z): 0.19 m. Shape: Compact.

Runout distance: 1.8 m from slope toe.
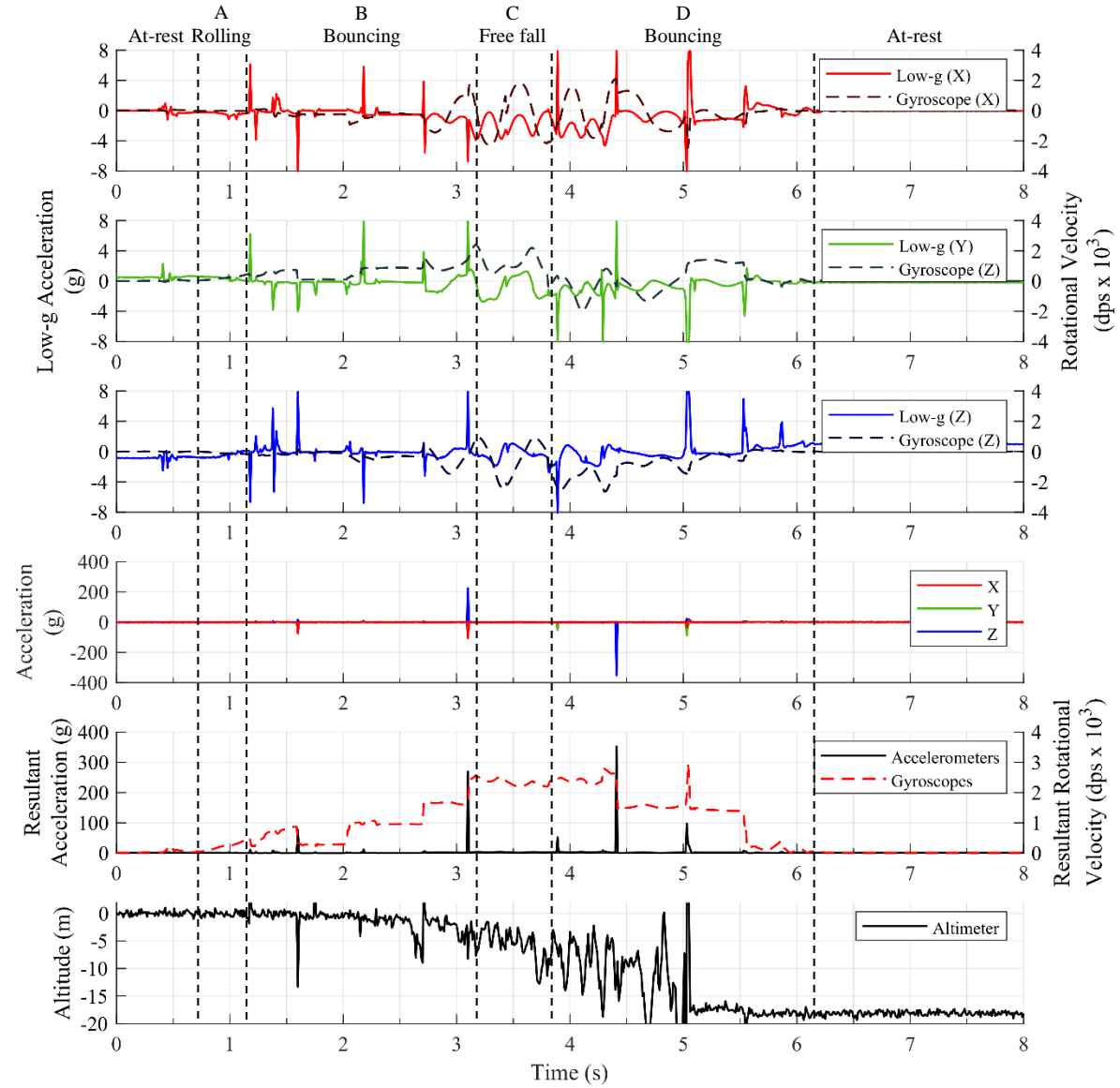
Drop height: 9.6 m. Altimeter hoisting: 11.9 m.
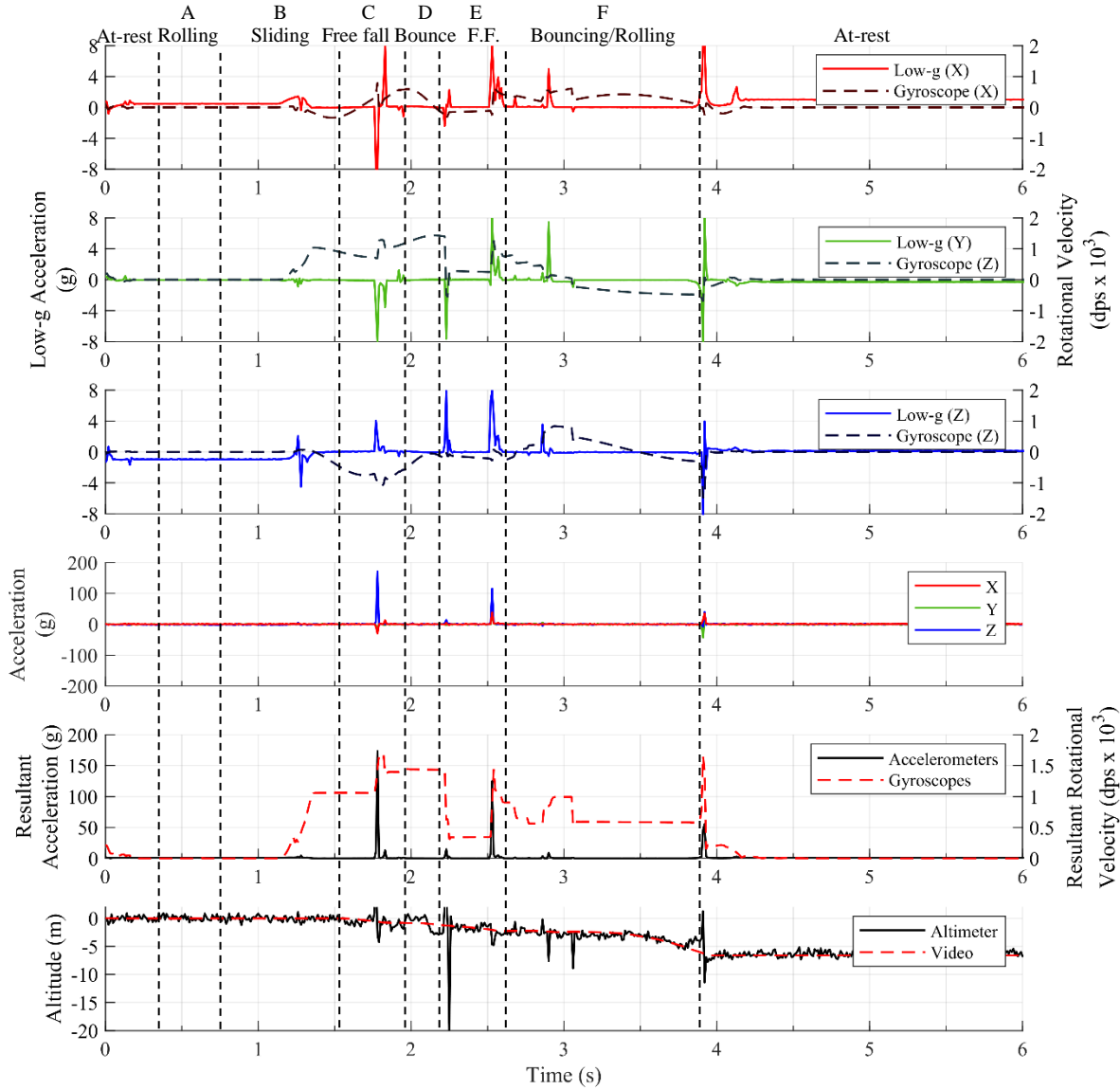
Figure B.17. Smart Rock data: rock 2 (slope 1), Franconia NH.

343
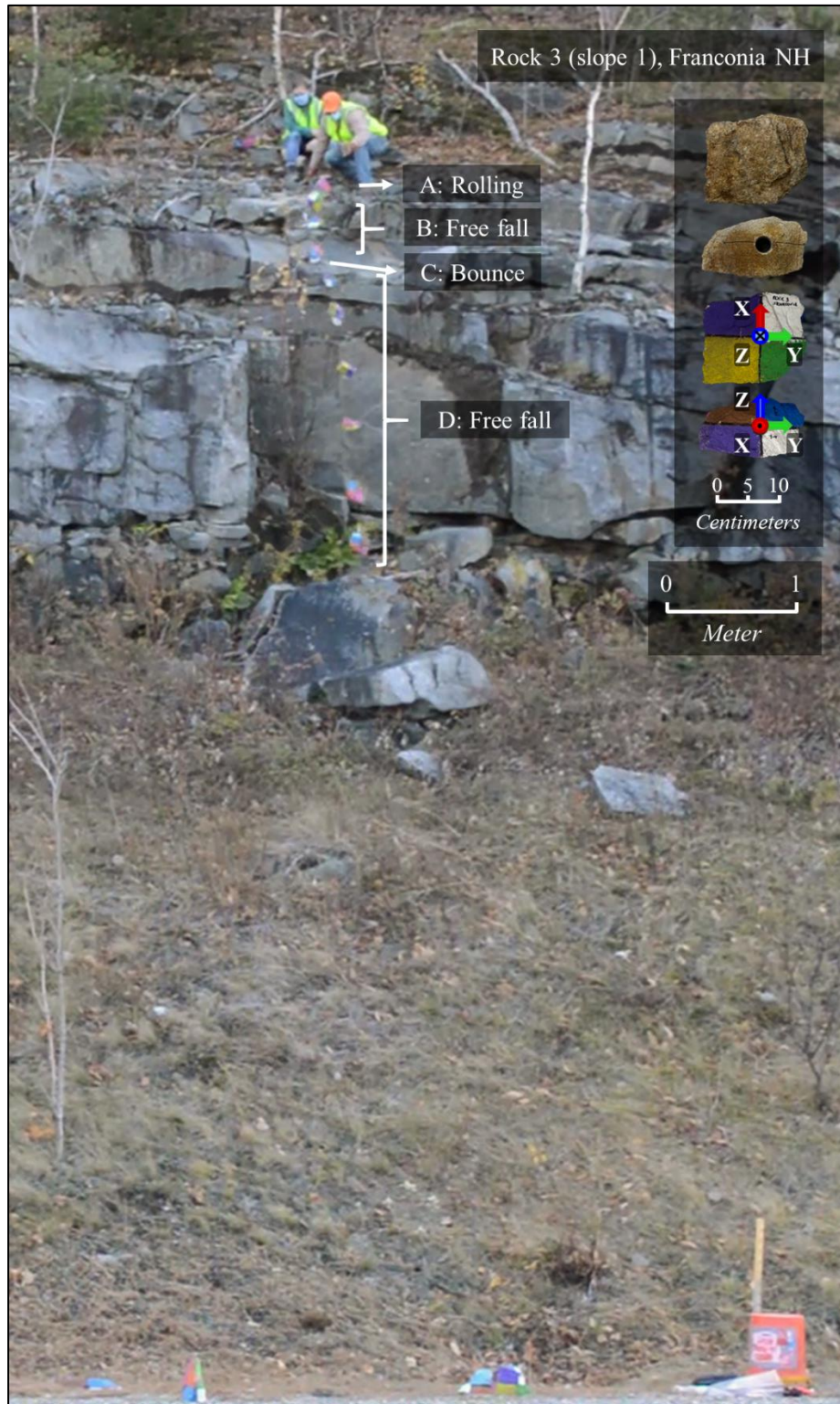
Figure B.18. Rockfall trajectory: rock 3 (slope 1), Franconia NH.

Field Rockfall — Rock 3 (slope 1), Franconia/NH

SR number: 3. Date: 23-Oct-2020.

Mass: 3.75 kg. I_{XX}: 0.009 kg.m^2. I_{YY}: 0.007 kg.m^2. I_{ZZ}: 0.013 kg.m^2.

Width (X): 0.1 m. Length (Y): 0.18 m. Height (Z): 0.14 m. Shape: Compact.

Runout distance: 0 m from slope toe.
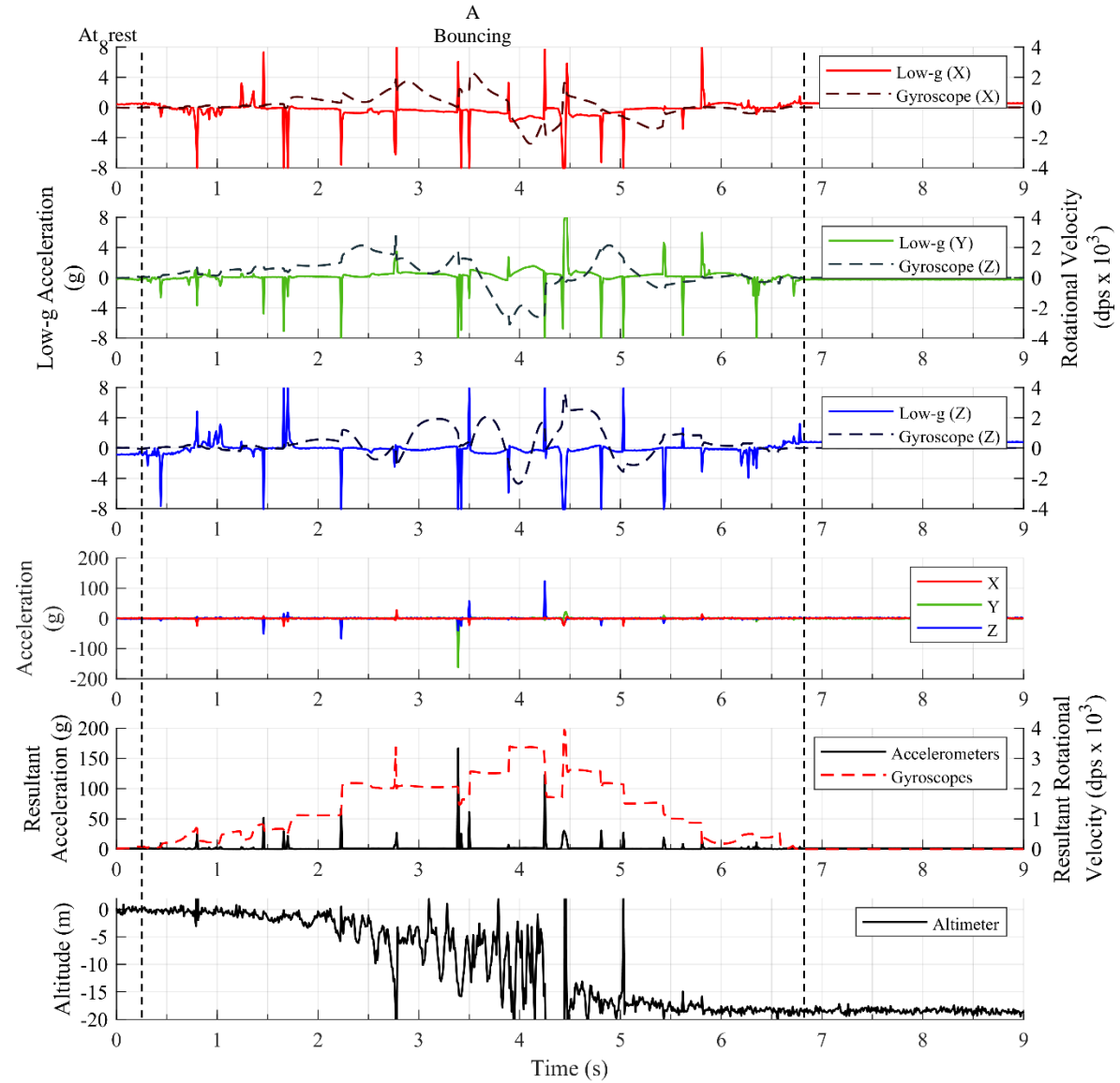
Drop height: 9.3 m. Altimeter hoisting: 11.4 m.
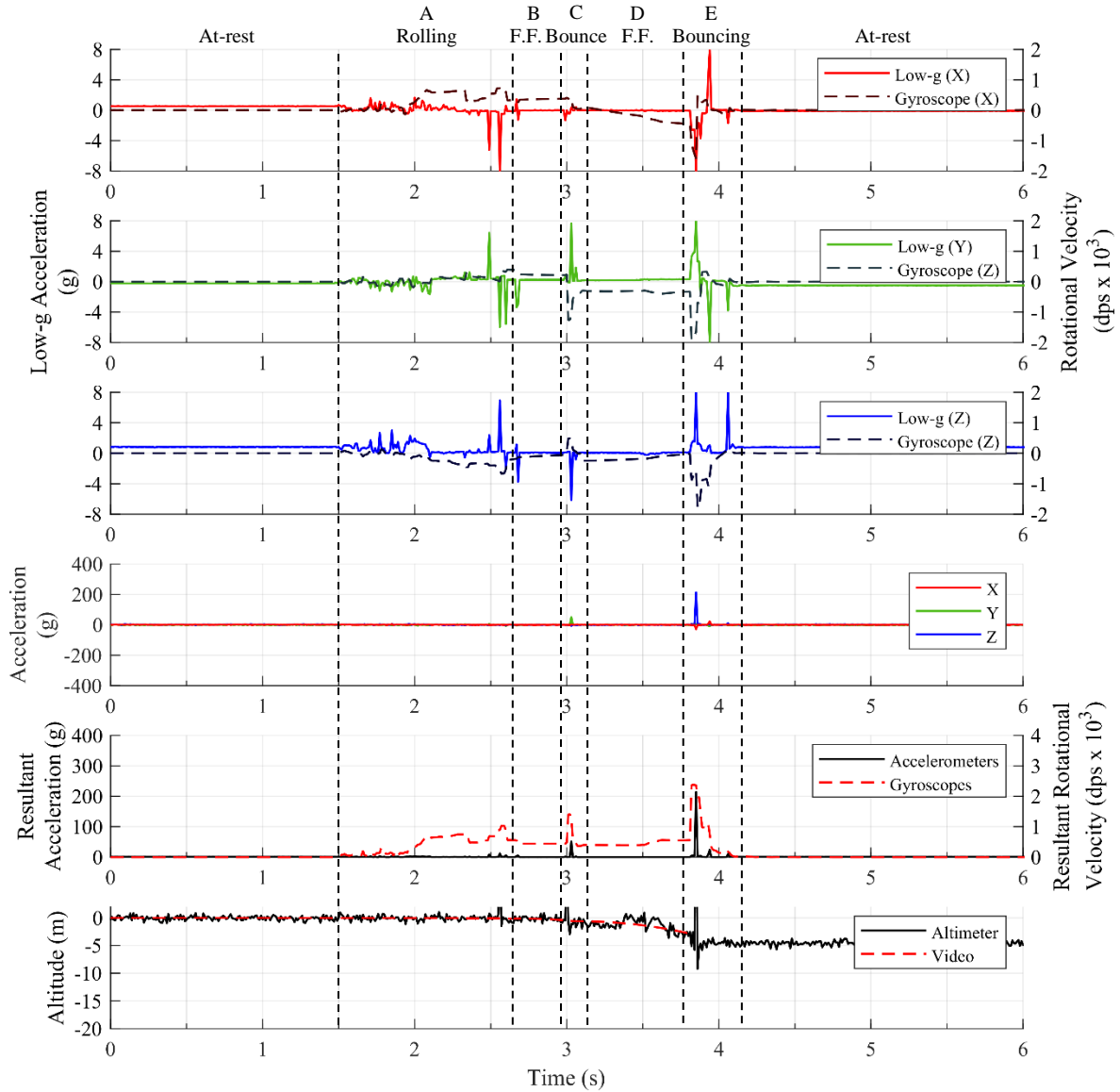
Figure B.19. Smart Rock data: rock 3 (slope 1), Franconia NH.

Figure B.20. Rockfall trajectory: rock 4 (slope 1), Franconia NH.

Field Rockfall — Rock 4 (slope 1), Franconia/NH

SR number: 1. Date: 23-Oct-2020.

Mass: 4.18 kg. I_{XX}: 0.013 kg.m^2. I_{YY}: 0.007 kg.m^2. I_{ZZ}: 0.015 kg.m^2.

Width (X): 0.1 m. Length (Y): 0.2 m. Height (Z): 0.1 m. Shape: Elongated.

Runout distance: 1.9 m from slope toe.

Drop height: 9.6 m. Altimeter hoisting: 11 m.
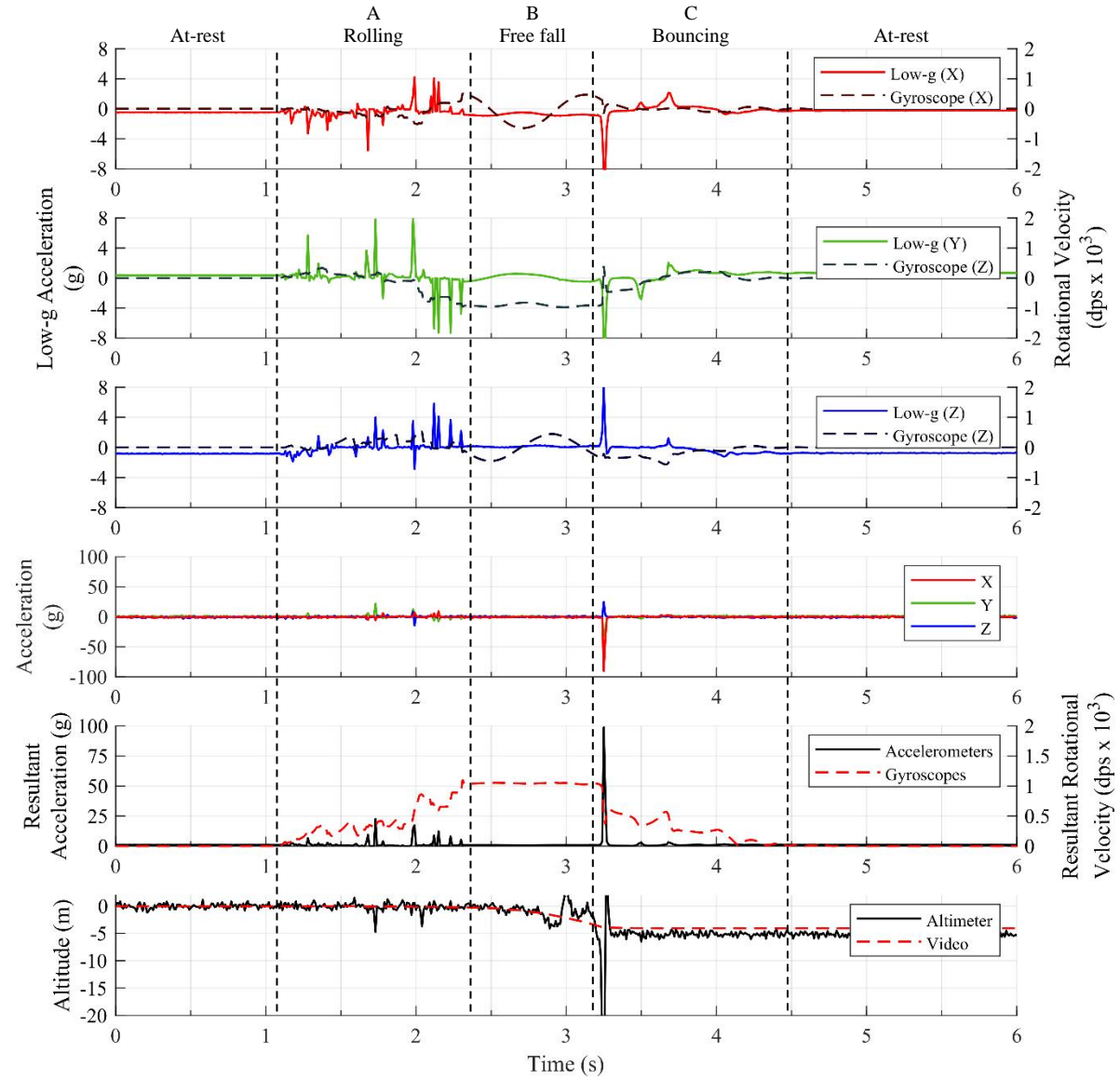
Figure B.21. Smart Rock data: rock 4 (slope 1), Franconia NH.

347
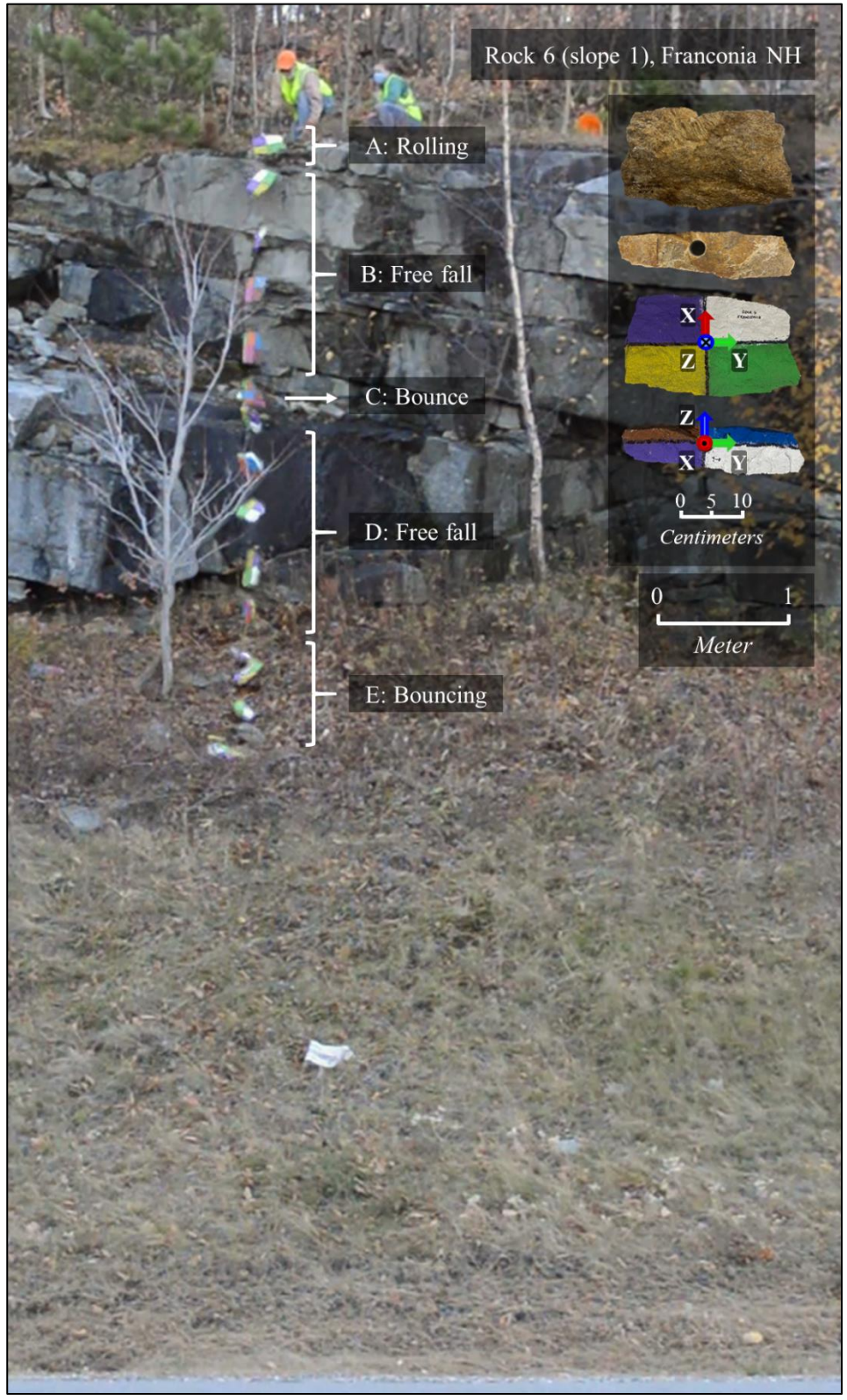
Figure B.22. Rockfall trajectory: rock 6 (slope 1), Franconia NH.

Figure B.23. Rockfall trajectory: rock 7 (slope 1), Franconia NH.

Field Rockfall — Rock 7 (slope 1), Franconia/NH

SR number: 4. Date: 23-Oct-2020.

Mass: 9.01 kg. I_{XX}: 0.081 kg.m^2. I_{YY}: 0.022 kg.m^2. I_{ZZ}: 0.069 kg.m^2.

Width (X): 0.1 m. Length (Y): 0.34 m. Height (Z): 0.2 m. Shape: Compact Elongated.

Runout distance: 1.3 m from slope toe.

Drop height: 9.3 m. Altimeter hoisting: 10.7 m.
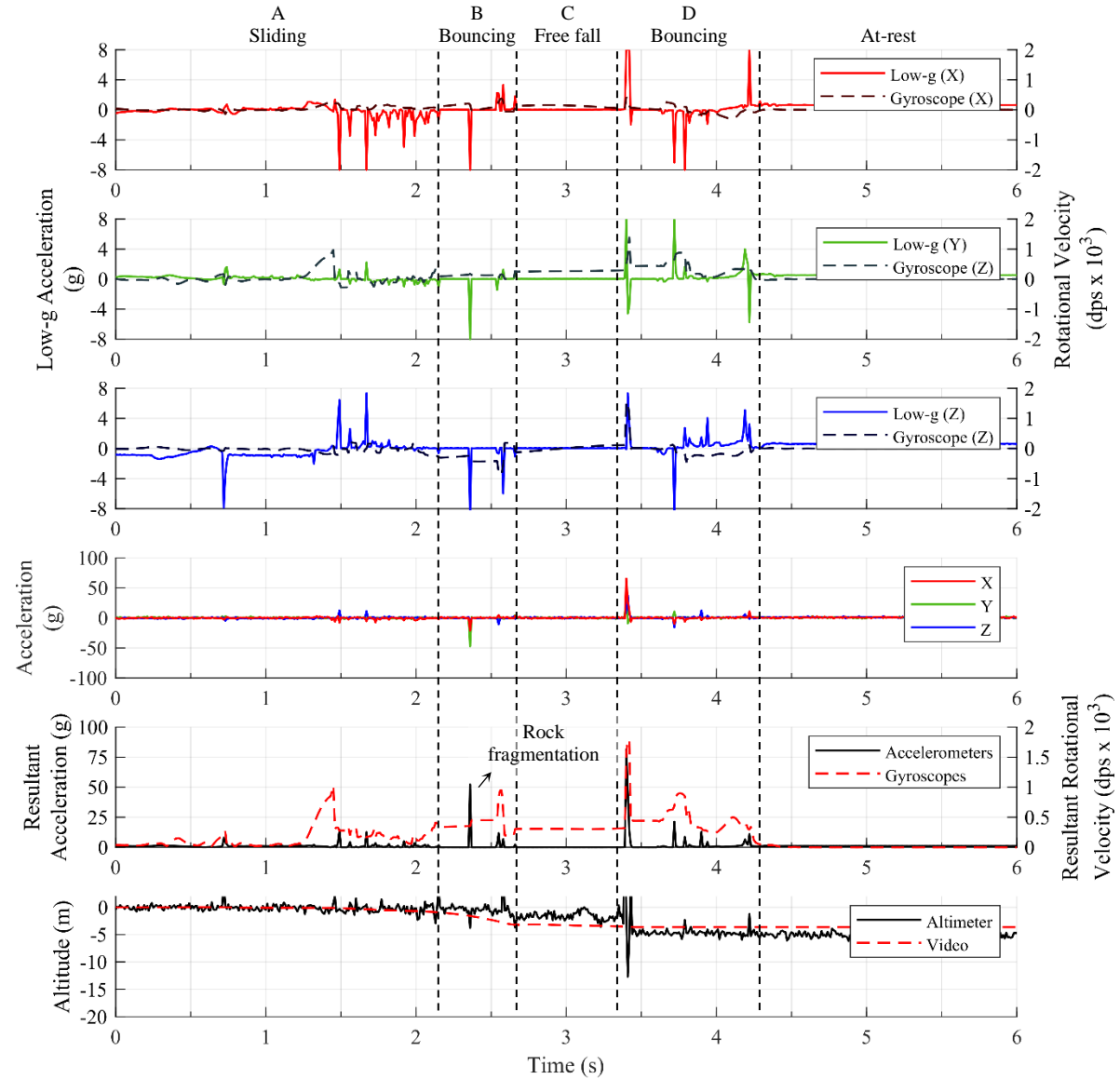

Figure B.24. Smart Rock data: rock 7 (slope 1), Franconia NH.

350
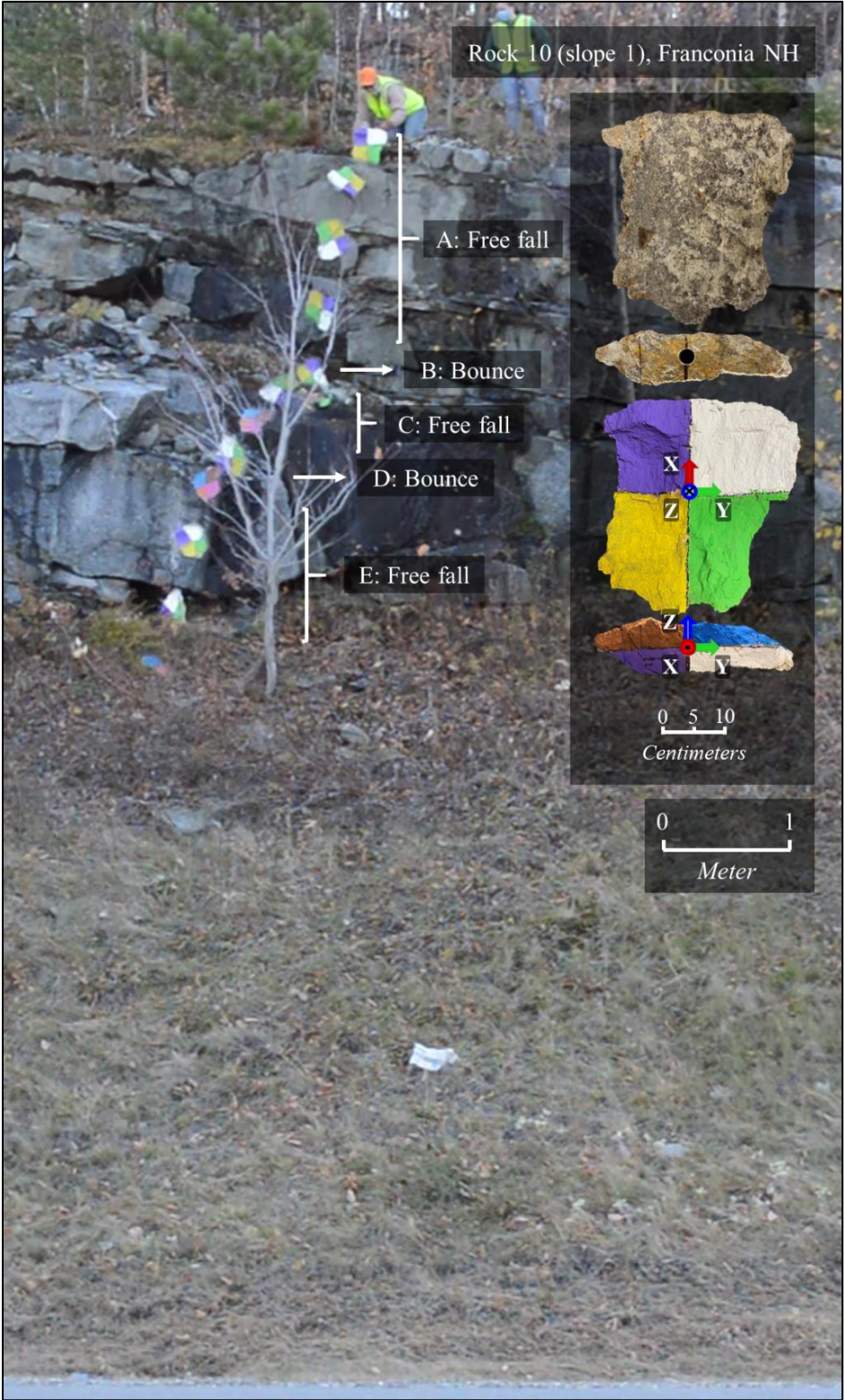
Figure B.25. Rockfall trajectory: rock 10 (slope 1), Franconia NH.

Field Rockfall — Rock 10 (slope 1), Franconia/NH

SR number: 1. Date: 23-Oct-2020.

Mass: 9.38 kg. I_{XX}: 0.026 kg.m^2. I_{YY}: 0.041 kg.m^2. I_{ZZ}: 0.062 kg.m^2.

Width (X): 0.34 m. Length (Y): 0.32 m. Height (Z): 0.08 m. Shape: Very Platy.

Runout distance: 0.8 m from slope toe.

Drop height: 9.6 m. Altimeter hoisting: 11.1 m.
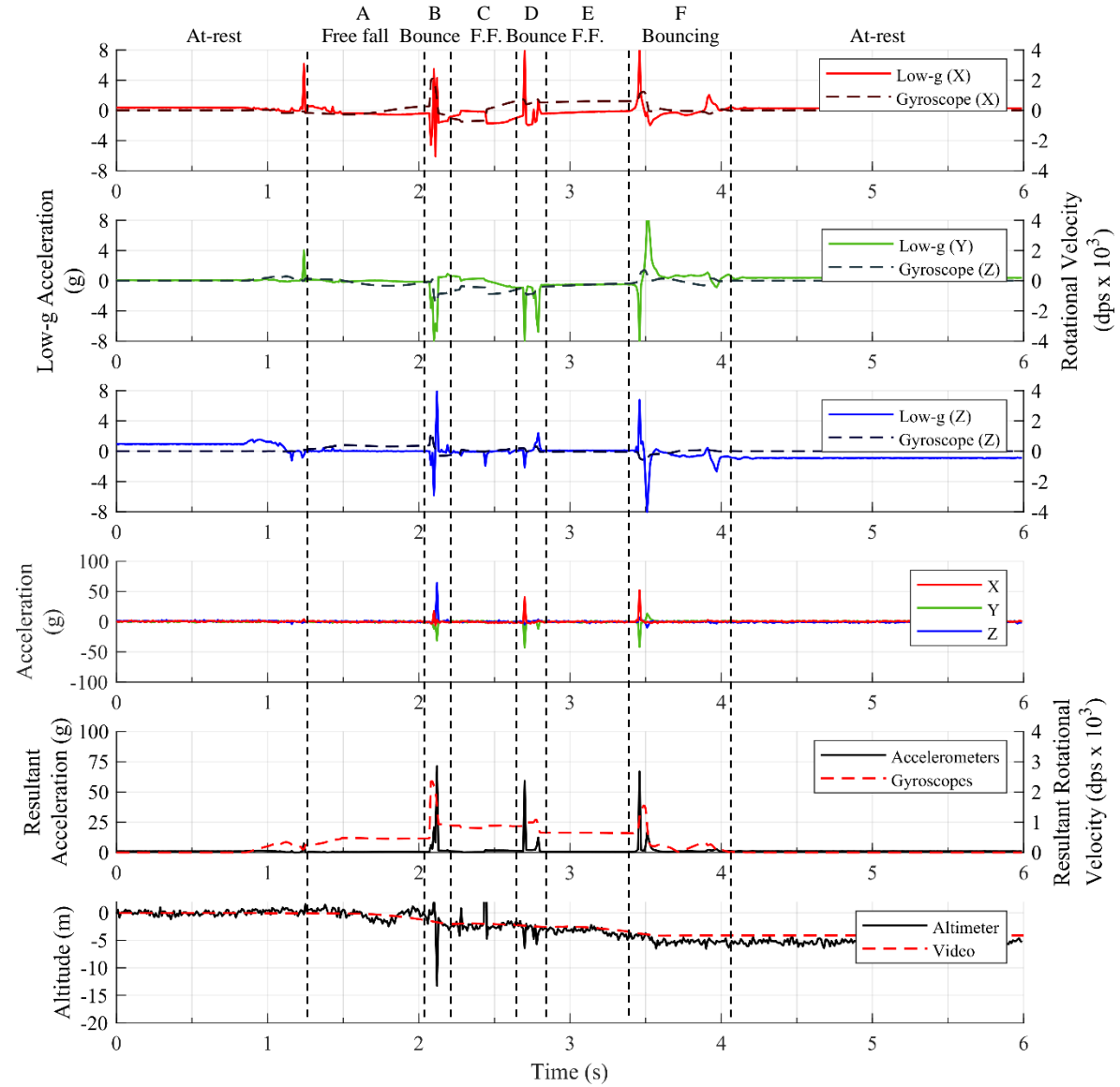
Figure B.26. Smart Rock data: rock 10 (slope 1), Franconia NH.
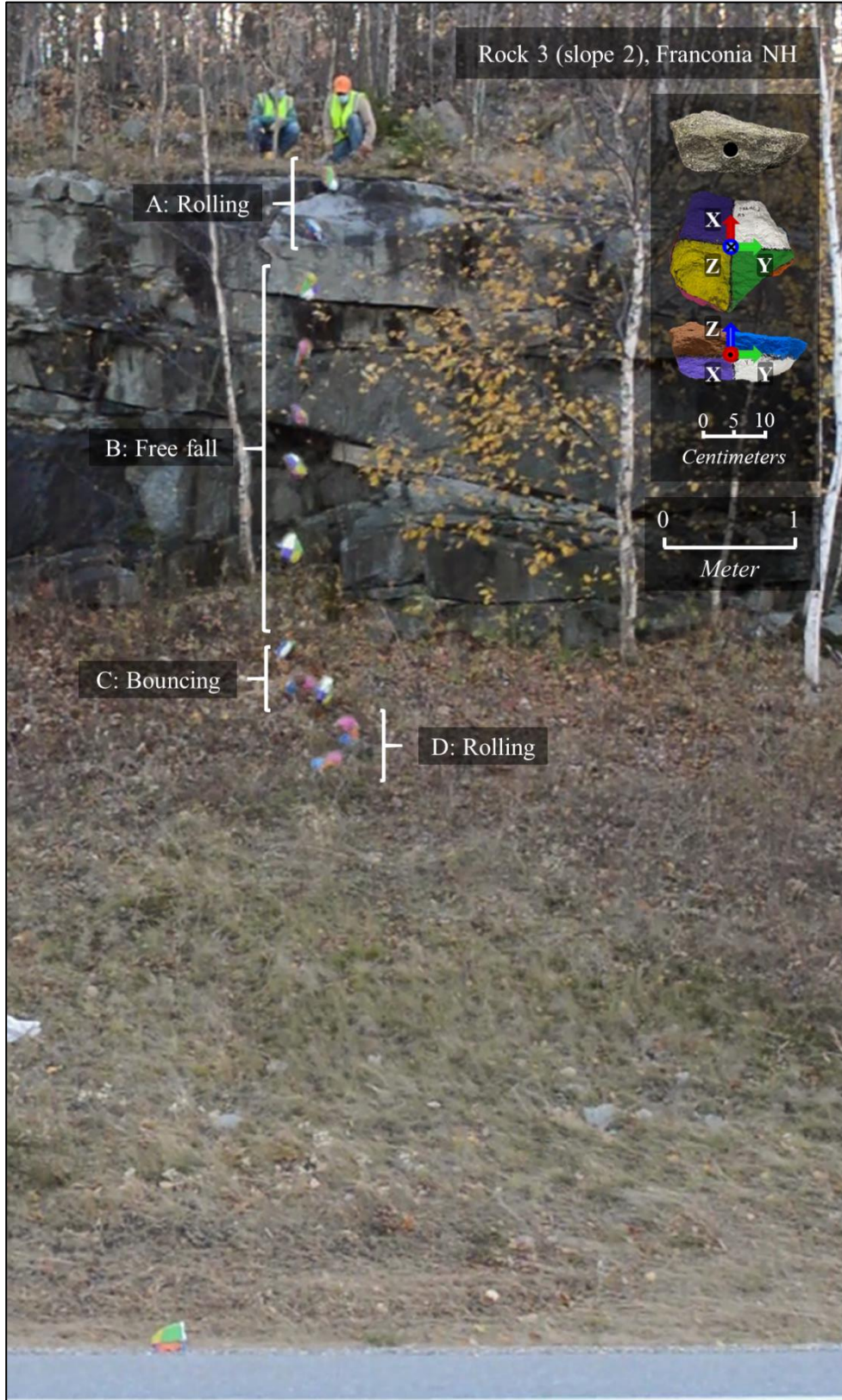
Figure B.27. Rockfall trajectory: rock 3, (slope 2), Franconia NH.

Field Rockfall — Rock 3 (slope 2), Franconia/NH

SR number: 4. Date: 23-Oct-2020.

Mass: 9.14 kg. I_{XX}: 0.039 kg.m^2. I_{YY}: 0.034 kg.m^2. I_{ZZ}: 0.063 kg.m^2.

Width (X): 0.24 m. Length (Y): 0.28 m. Height (Z): 0.08 m. Shape: Very Platy.

Runout distance: 3.8 m from slope toe.

Drop height: 9.6 m. Altimeter hoisting: 11 m.
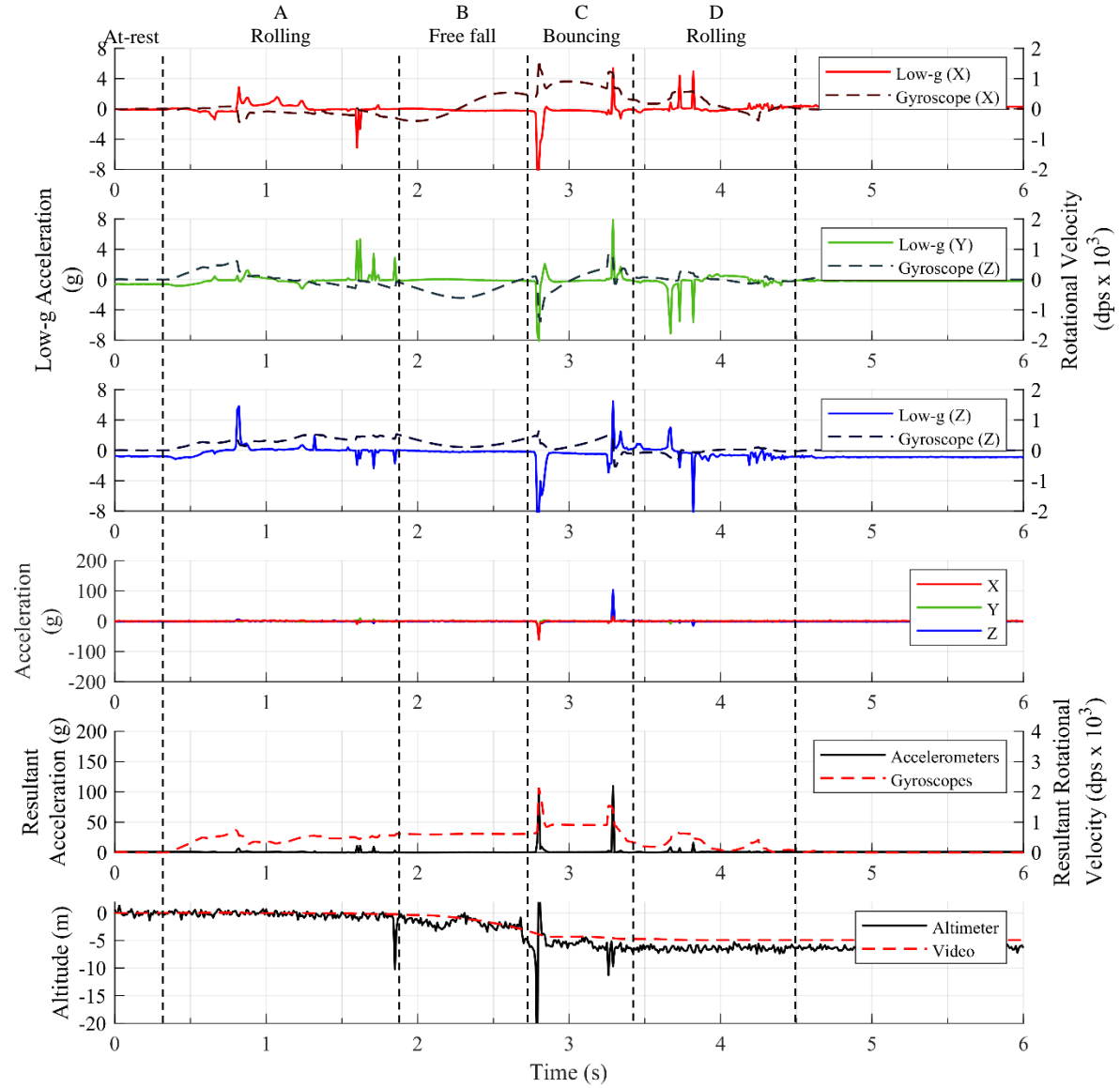
Figure B.28. Smart Rock data: rock 3, (slope 2), Franconia NH.

354
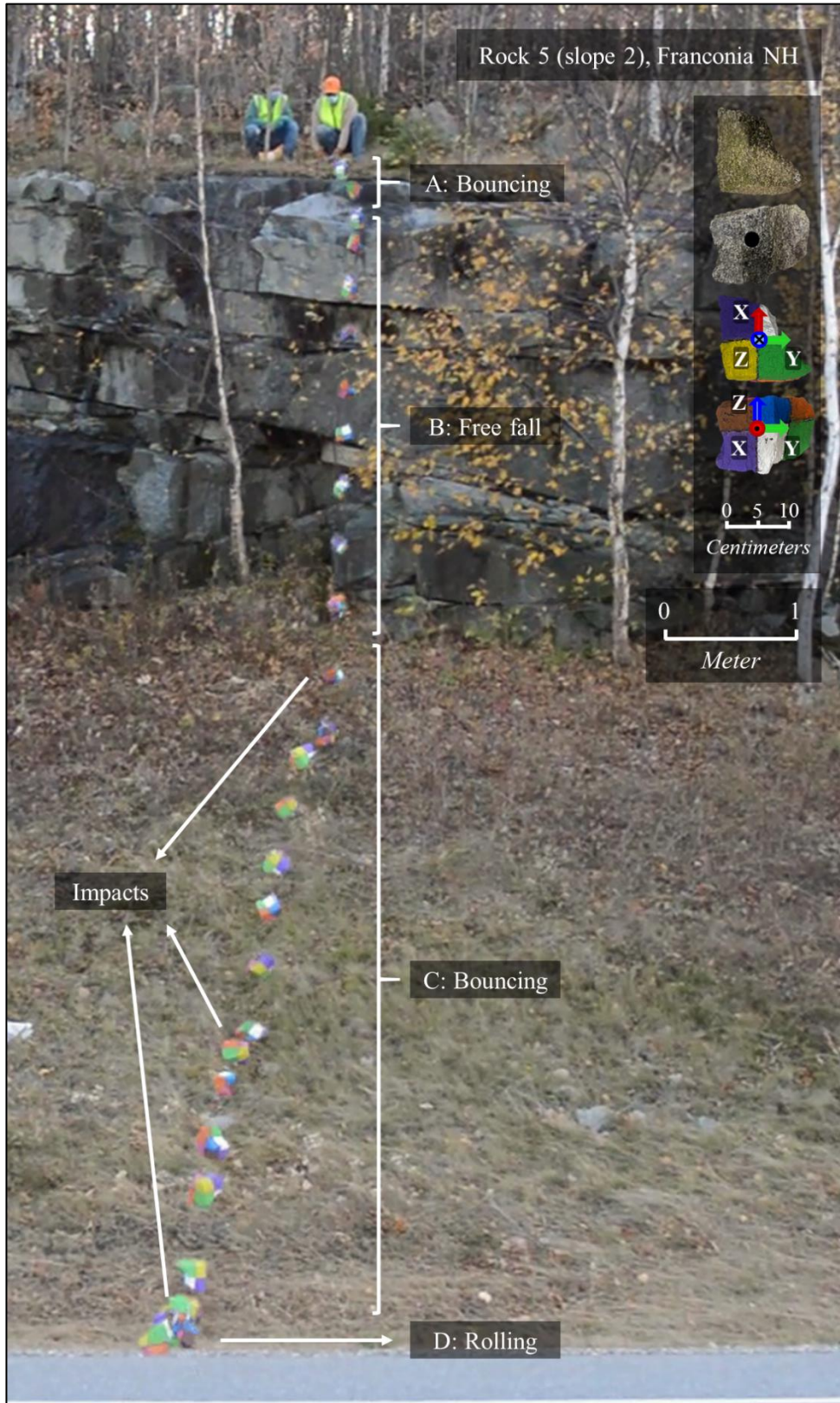
Figure B.29. Rockfall trajectory: rock 5, (slope 2), Franconia NH.

Field Rockfall — Rock 5 (slope 2), Franconia/NH

SR number: 3. Date: 23-Oct-2020.

Mass: 4.88 kg. I_{XX}: 0.014 kg.m^2. I_{YY}: 0.013 kg.m^2. I_{ZZ}: 0.015 kg.m^2.

Width (X): 0.15 m. Length (Y): 0.12 m. Height (Z): 0.11 m. Shape: Compact.

Runout distance: 0.2 m from road shoulder.

Drop height: 9.6 m. Altimeter hoisting: 11.1 m.
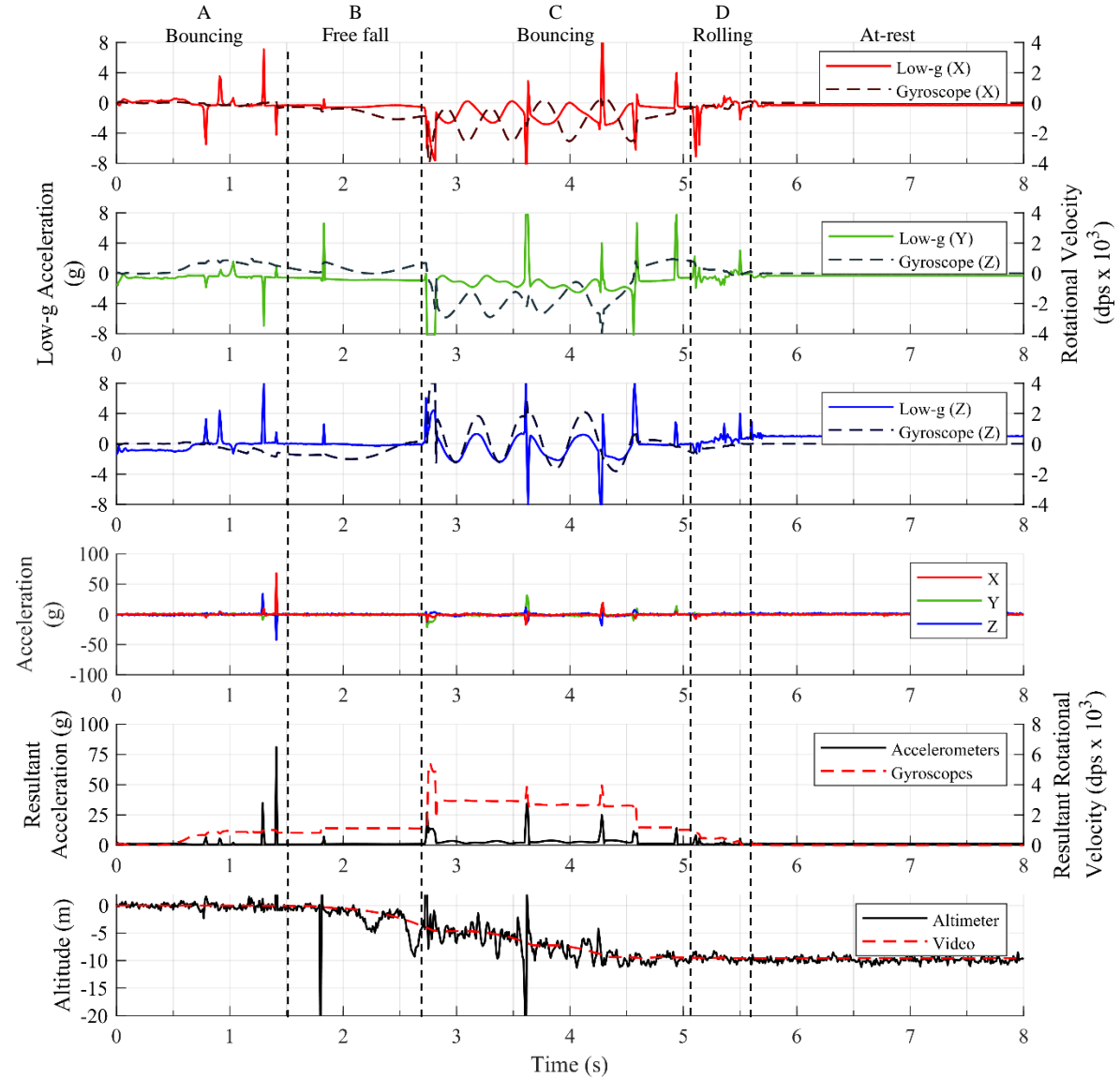
Figure B.30. Smart Rock data: rock 5, (slope 2), Franconia NH.
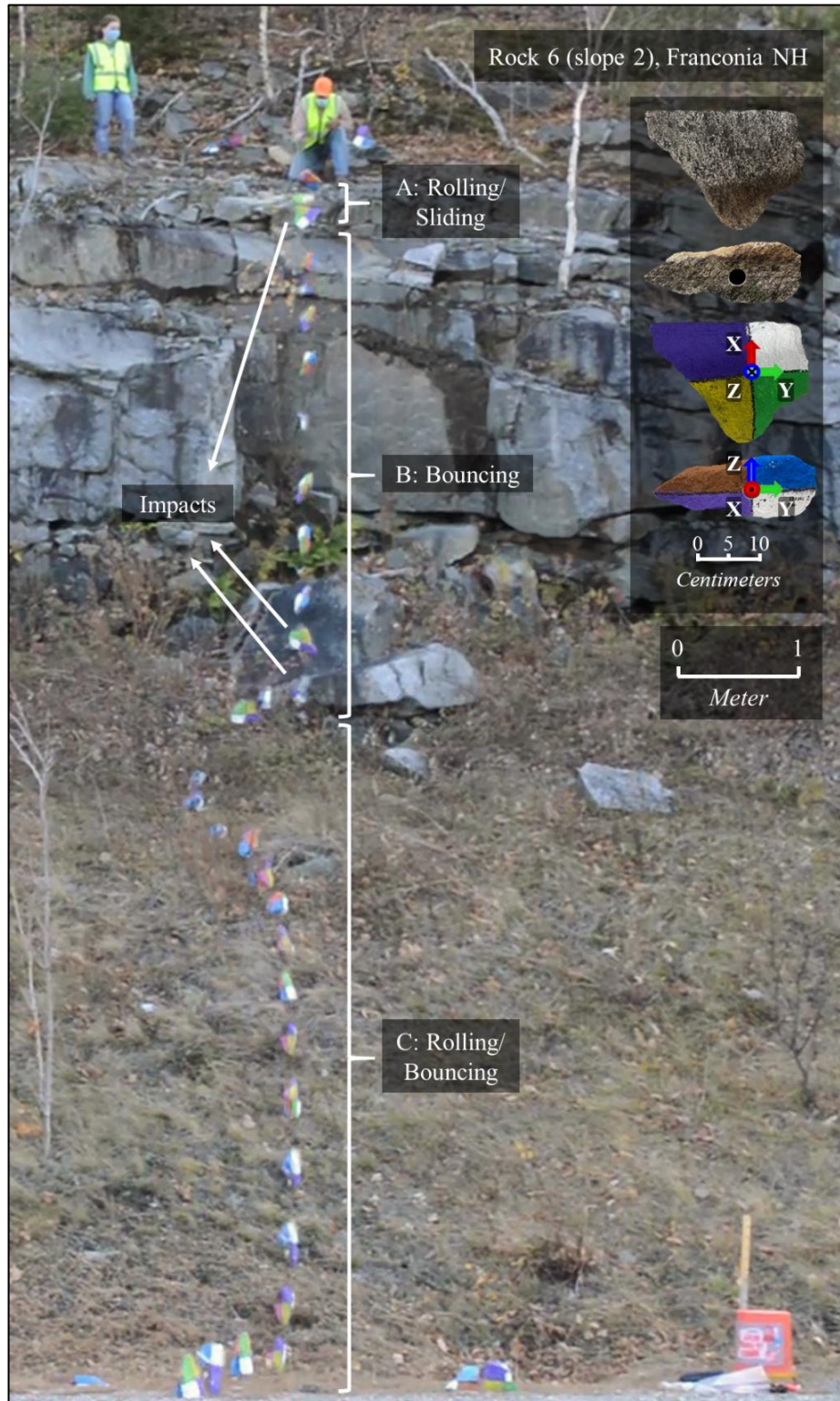
Figure B.31. Rockfall trajectory: rock 6, (slope 2), Franconia NH.

Field Rockfall — Rock 6 (slope 2), Franconia/NH

SR number: 1. Date: 23-Oct-2020.

Mass: 5.5 kg. I_{XX}: 0.019 kg.m^2. I_{YY}: 0.015 kg.m^2. I_{ZZ}: 0.029 kg.m^2.

Width (X): 0.2 m. Length (Y): 0.24 m. Height (Z): 0.09 m. Shape: Platy.

Runout distance: 1.4 m from road shoulder.

Drop height: 9.3 m. Altimeter hoisting: 10.7 m.
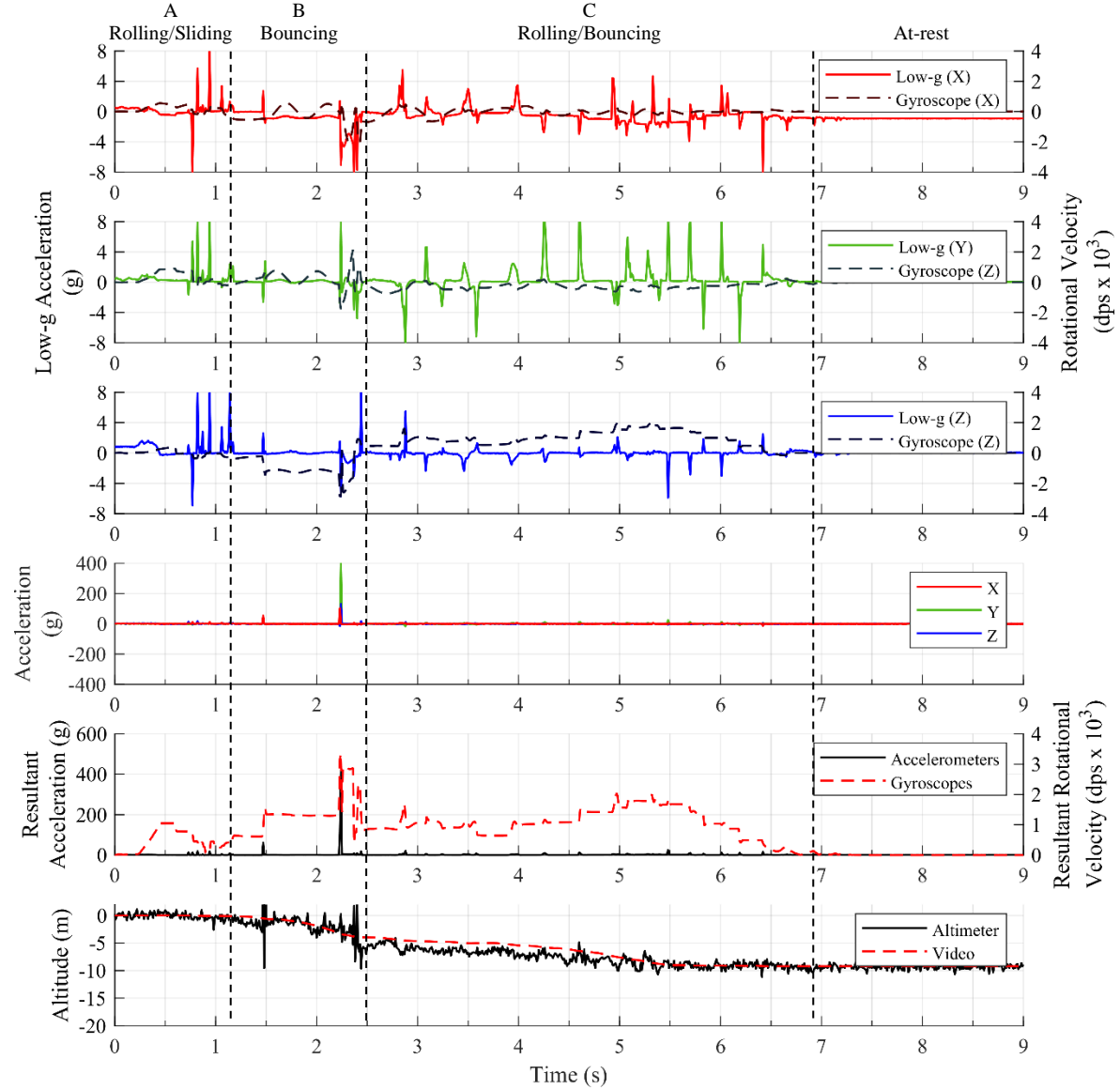
Figure B.32. Smart Rock data: rock 6, (slope 2), Franconia NH.

358

B.4. Franklin, NH

B.4.1. Franklin 1, NH
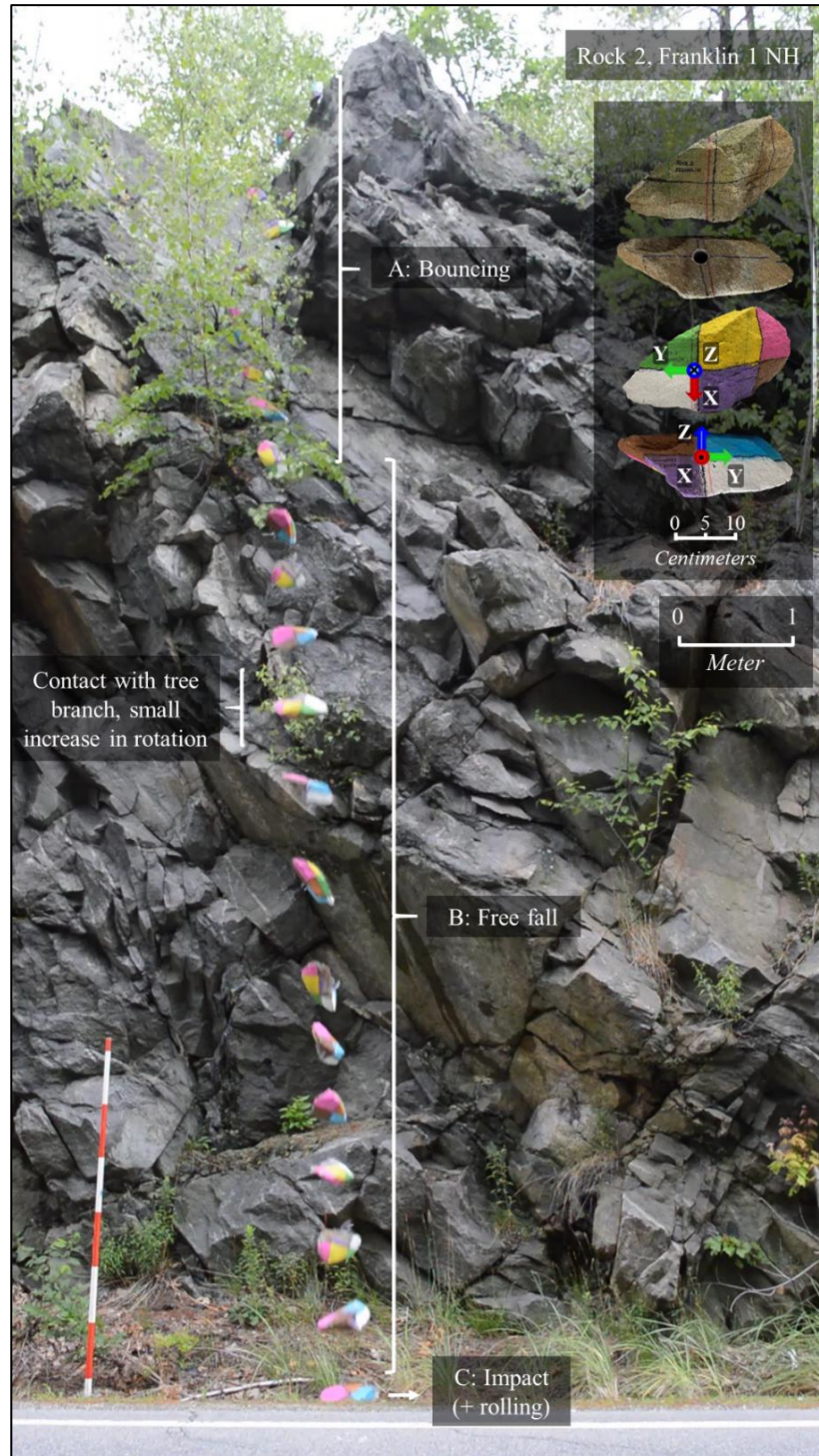
Figure B.33. Smart Rock data: rock 2, Franklin 1 NH.

Field Rockfall — Rock 2, Franklin 1/NH

SR number: 5. Date: 15-Jul-2020.

Mass: 8.44 kg. I_{XX}: 0.056 kg.m^2. I_{YY}: 0.03 kg.m^2. I_{ZZ}: 0.064 kg.m^2.

Width (X): 0.16 m. Length (Y): 0.24 m. Height (Z): 0.09 m. Shape: Bladed.

Runout distance: 1.1 m from slope toe.

Drop height: 12.5 m. Altimeter hoisting: 11.8 m.
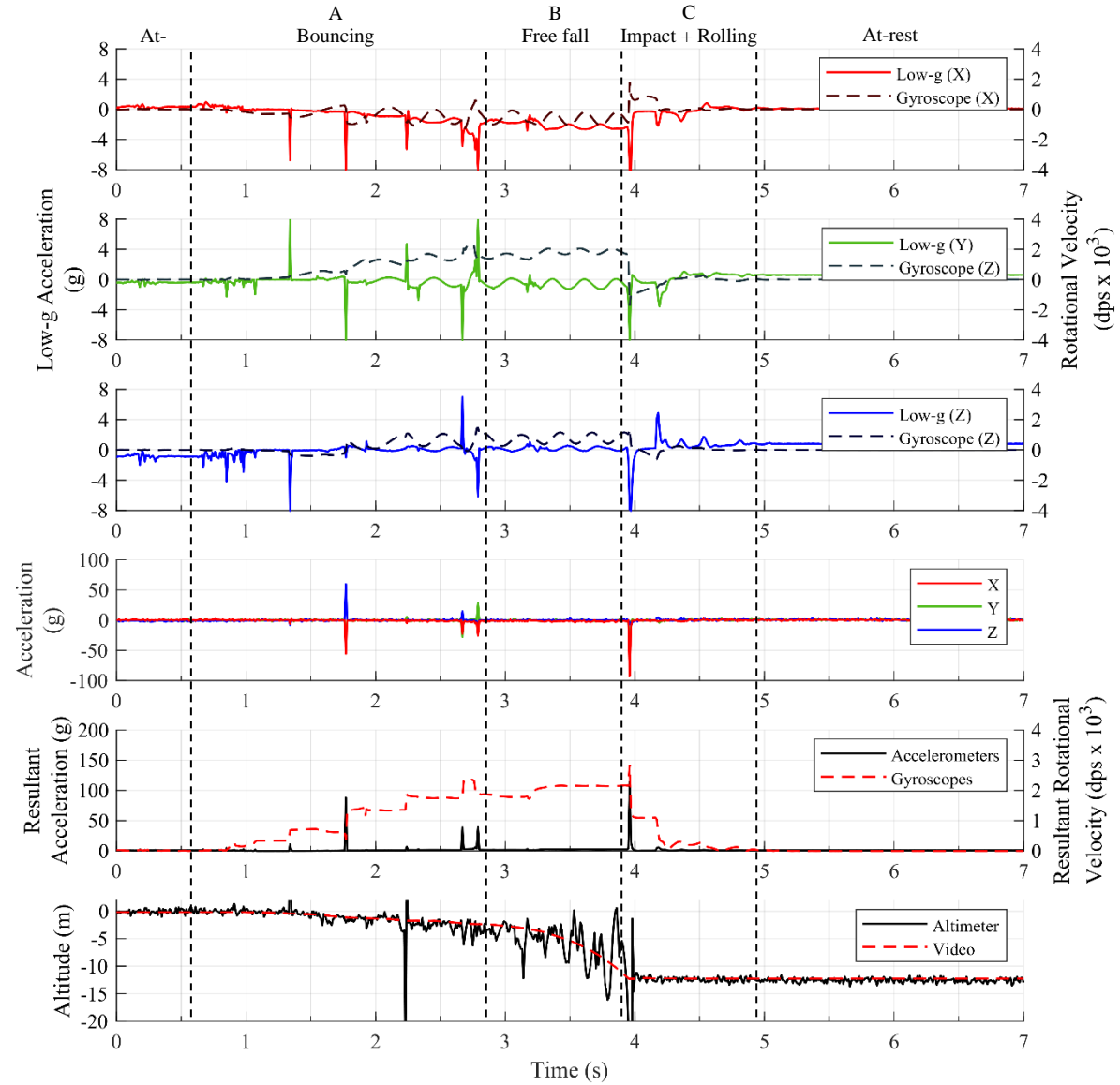
Figure B.34. Rockfall trajectory: rock 2, Franklin 1 NH.

360

Figure B.35. Rockfall trajectory: rock 3, Franklin 1 NH.

Field Rockfall — Rock 3, Franklin 1/NH

SR number: 3. Date: 15-Jul-2020.

Mass: 9.45 kg. I_{XX}: 0.057 kg.m^2. I_{YY}: 0.028 kg.m^2. I_{ZZ}: 0.053 kg.m^2.

Width (X): 0.14 m. Length (Y): 0.25 m. Height (Z): 0.17 m. Shape: Compact Elongated.

Runout distance: 8.1 m from slope toe.

Drop height: 12.5 m. Altimeter hoisting: 11.6 m.
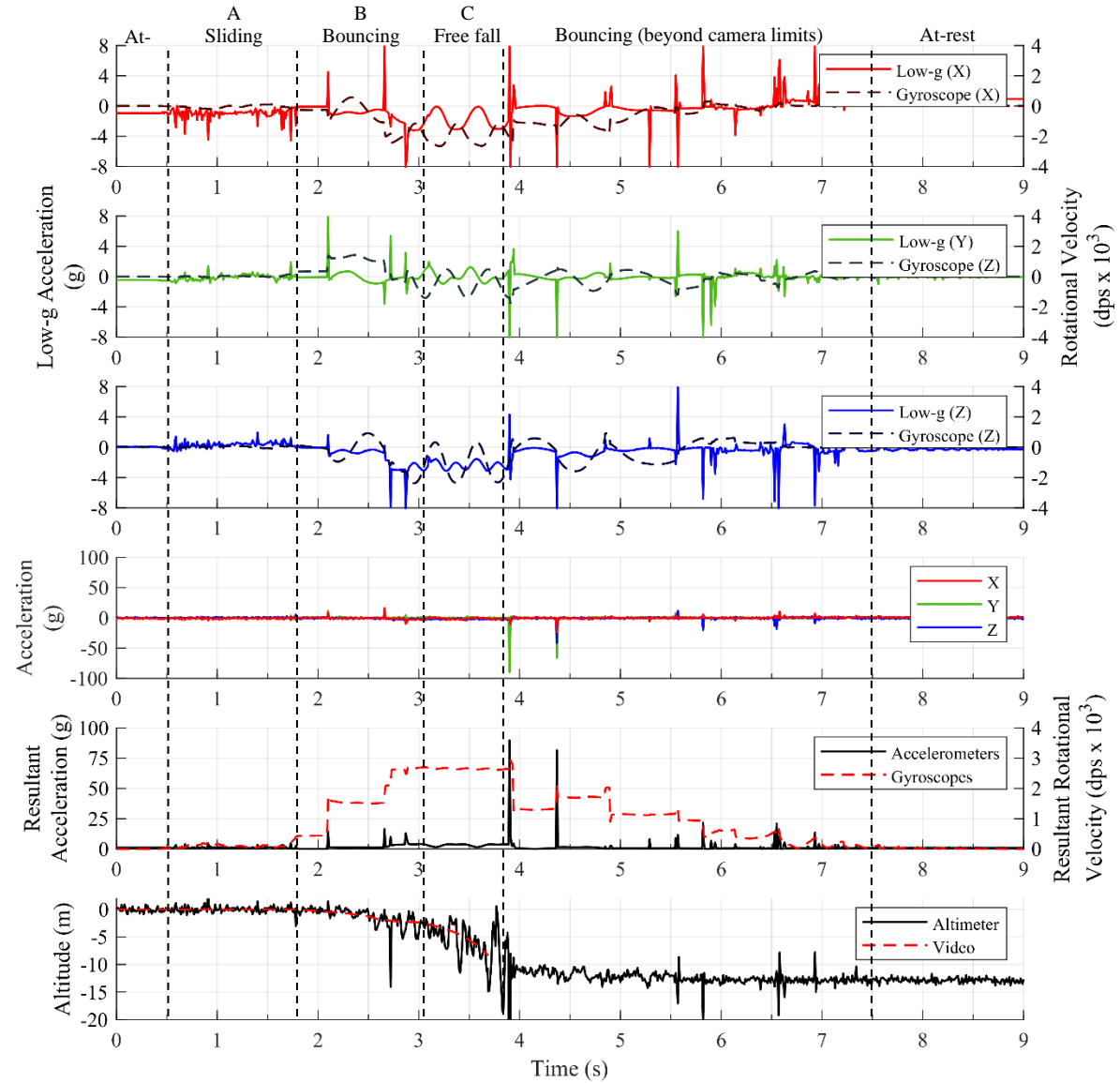

Figure B.36. Smart Rock data: rock 3, Franklin 1 NH.
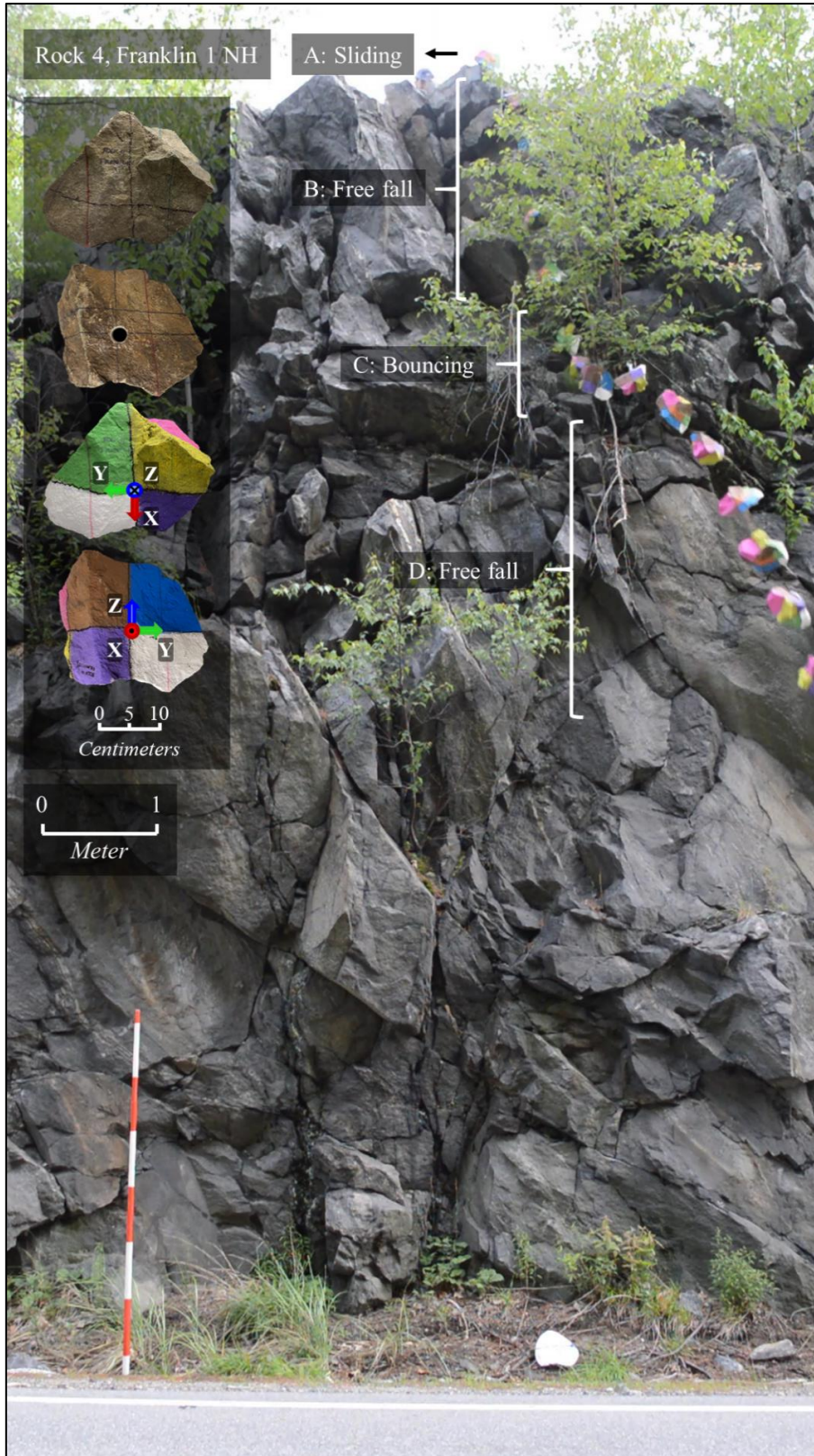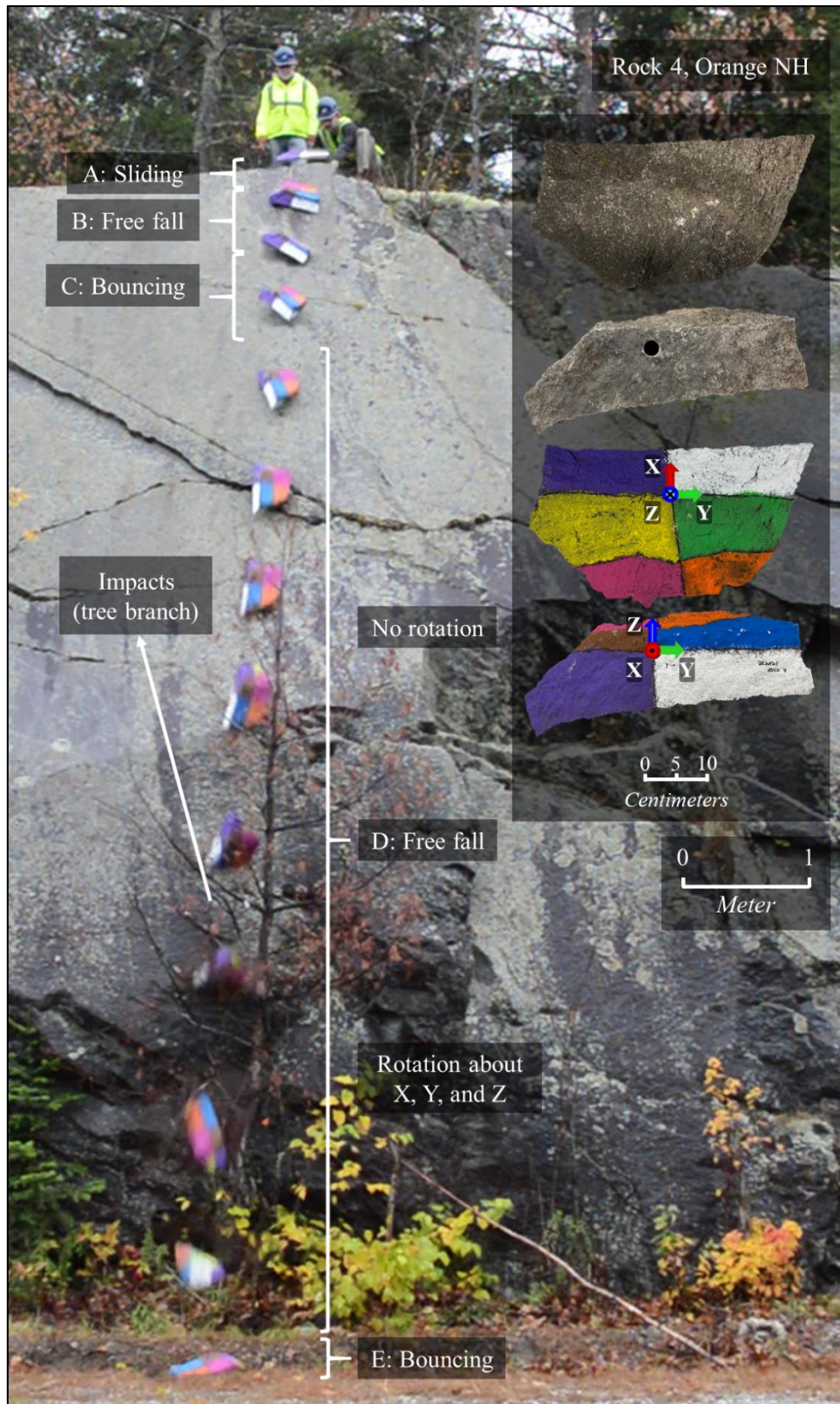
Figure B.36. Rockfall trajectory: rock 4, Franklin 1 NH.

Figure B.37. Smart Rock data: rock 4, Franklin 1 NH.

364

Figure B.38. Rockfall trajectory: rock 8, Franklin 1 NH.

Figure B.39. Smart Rock data: rock 8, Franklin 1 NH.

Figure B.40. Rockfall trajectory: rock 9, Franklin 1 NH.

Field Rockfall — Rock 9, Franklin 1/NH

SR number: 5. Date: 15-Jul-2020.

Mass: 10.52 kg. I_{XX}: 0.062 kg.m^2. I_{YY}: 0.049 kg.m^2. I_{ZZ}: 0.053 kg.m^2.

Width (X): 0.16 m. Length (Y): 0.21 m. Height (Z): 0.25 m. Shape: Compact.

Runout distance: 11.2 m from slope toe.

Drop height: 11.5 m. Altimeter hoisting: 11.2 m.
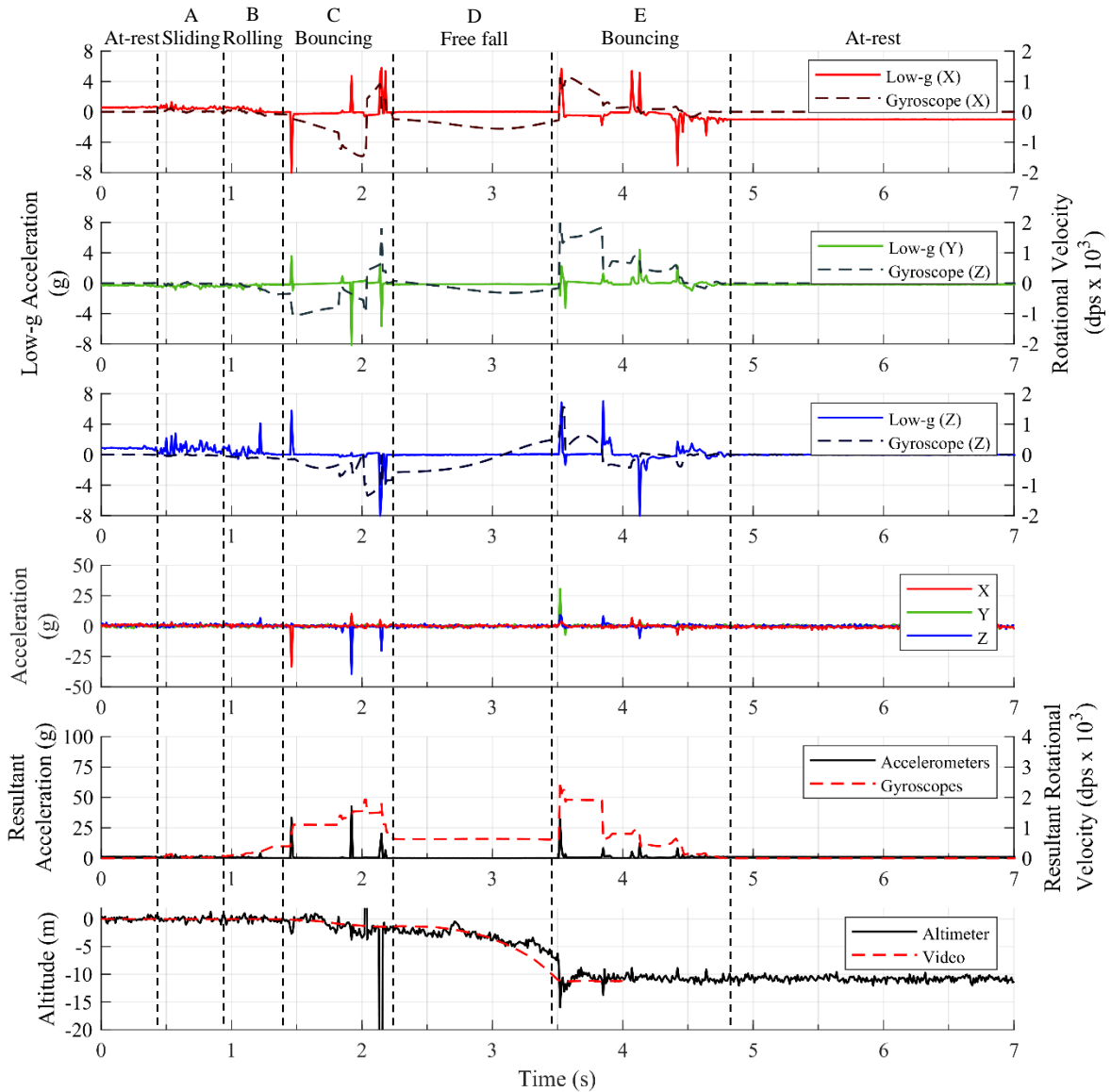
Figure B.41. Smart Rock data: rock 9, Franklin 1 NH.

B.4.2. Franklin 2, NH

Figure B.42. Rockfall trajectory: rock 1, Franklin 2 NH.

Field Rockfall — Rock 1, Franklin 2/NH

SR number: 1. Date: 15-Jul-2020.

Mass: 9.39 kg. I_{XX}: 0.055 kg.m^2. I_{YY}: 0.023 kg.m^2. I_{ZZ}: 0.06 kg.m^2.

Width (X): 0.13 m. Length (Y): 0.34 m. Height (Z): 0.15 m. Shape: Elongated.

Runout distance: 3.5 m from slope toe.
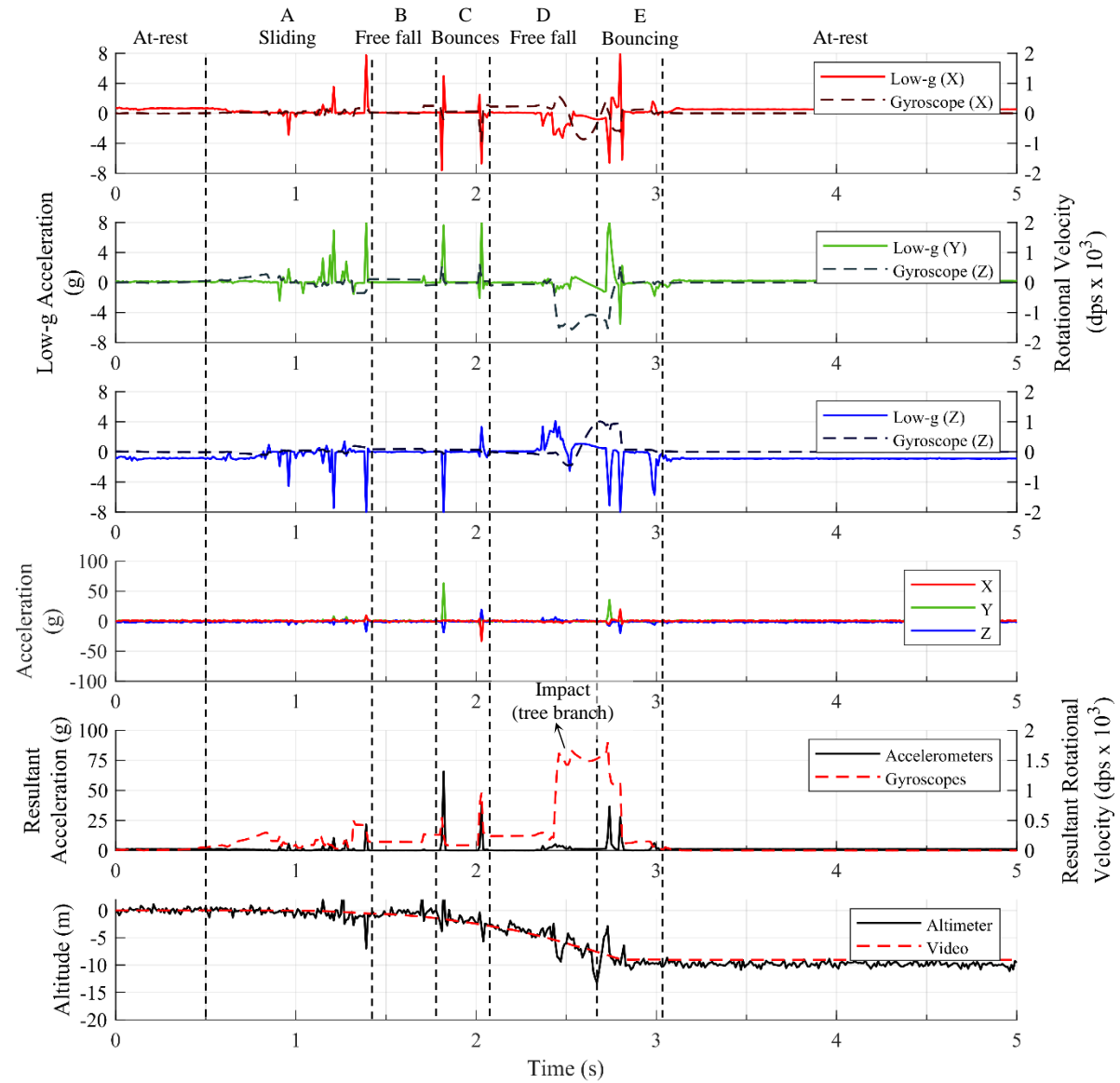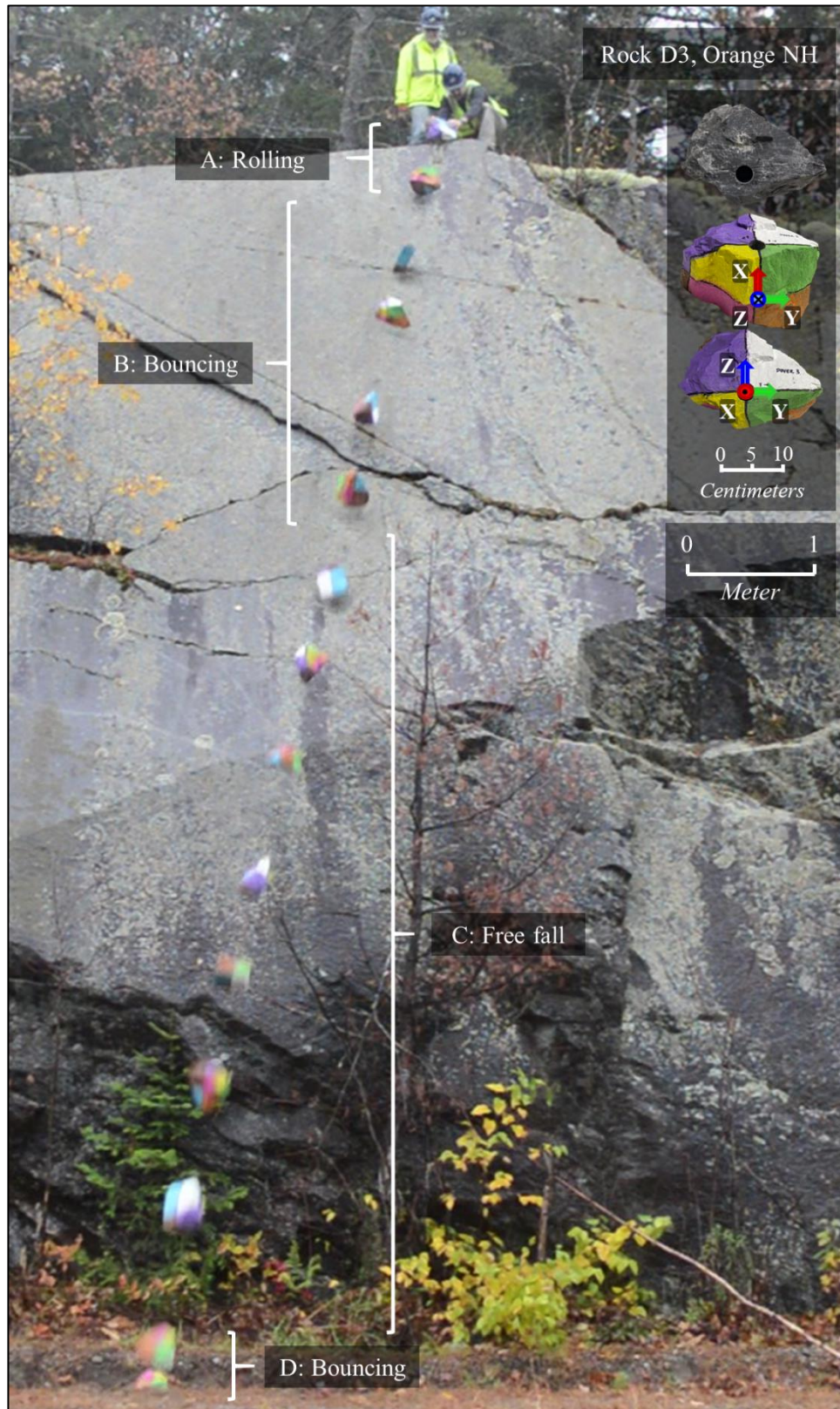
Drop height: 9.9 m. Altimeter hoisting: 10.7 m.
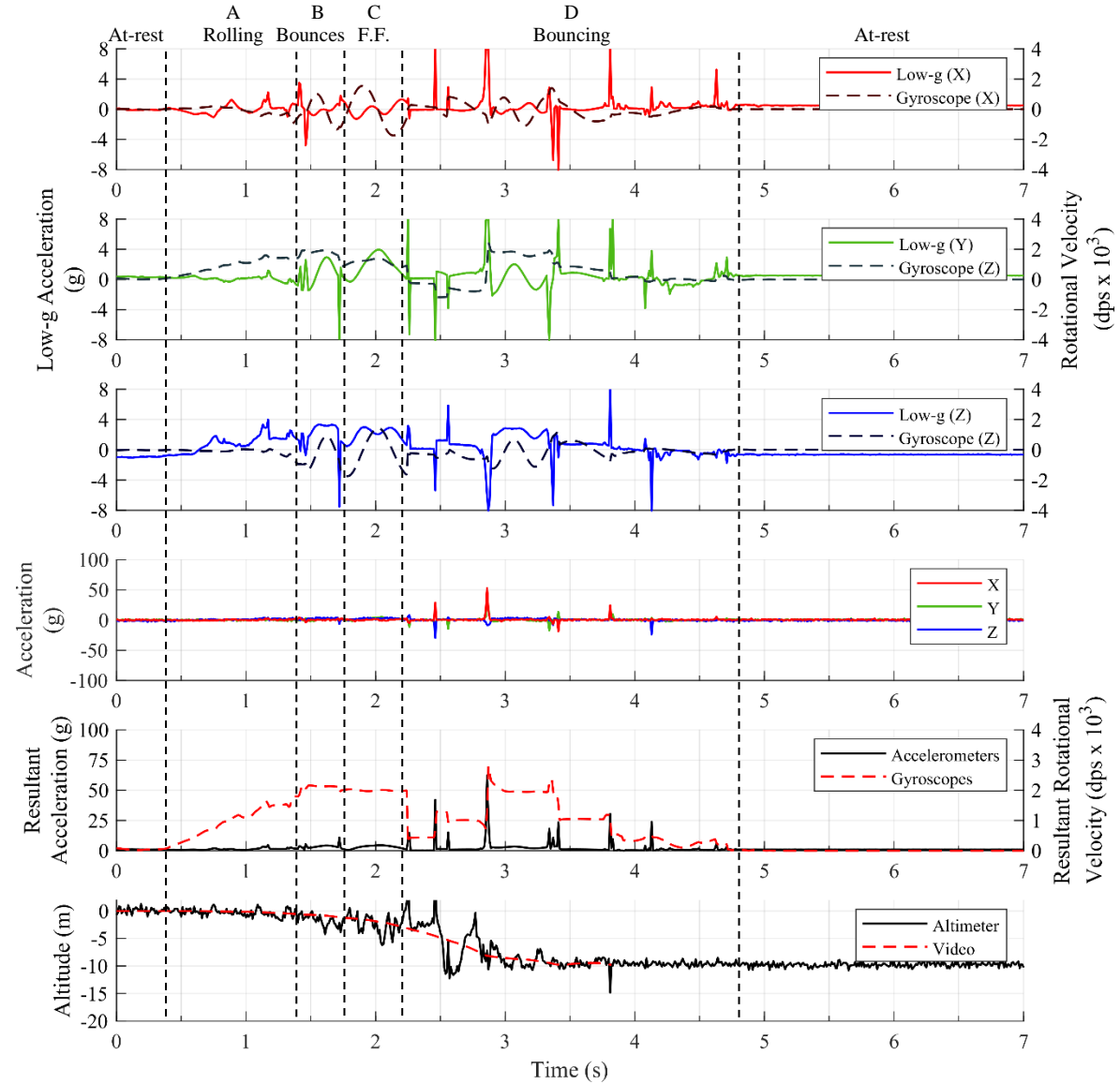
Figure B.43. Smart Rock data: rock 1, Franklin 2 NH.
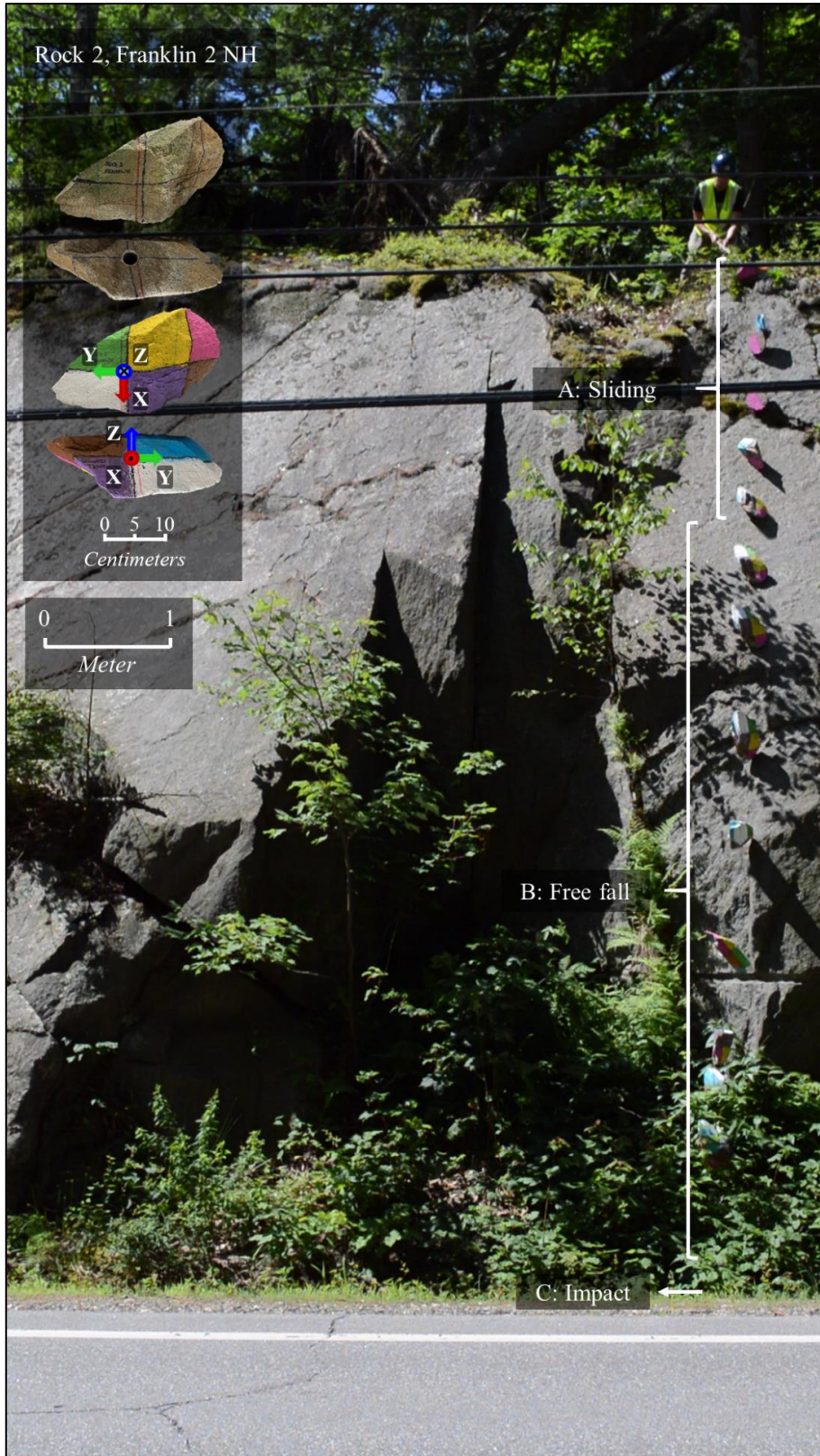
Figure B.44. Rockfall trajectory: rock 2, Franklin 2 NH.

Figure B.45. Rockfall trajectory: rock 3, Franklin 2 NH.
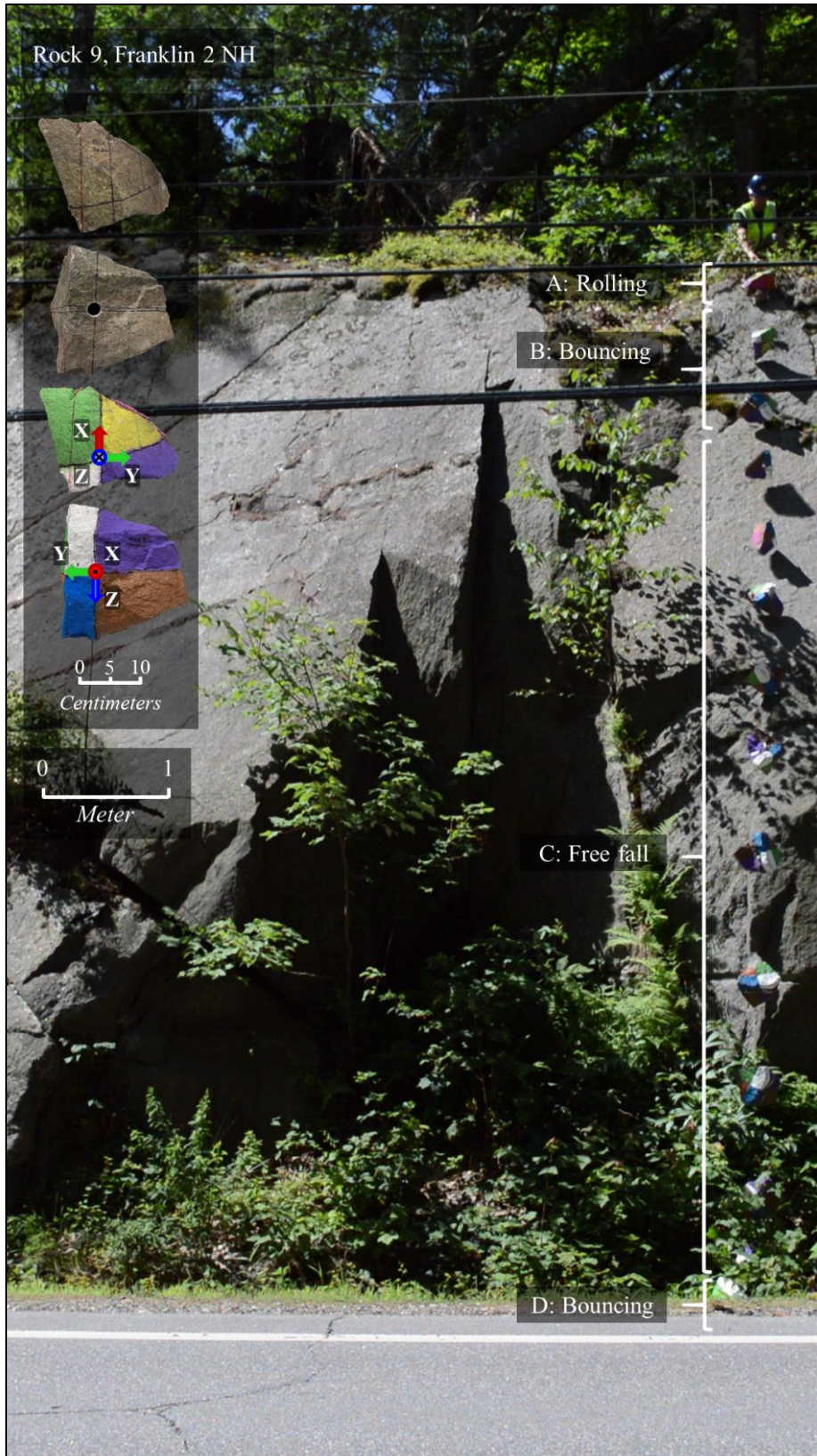
Figure B.46. Rockfall trajectory: rock 9, Franklin 2 NH.

Field Rockfall — Rock 9, Franklin 2/NH

SR number: 5. Date: 15-Jul-2020.

Mass: 10.52 kg. I_{XX}: 0.062 kg.m^2. I_{YY}: 0.049 kg.m^2. I_{ZZ}: 0.053 kg.m^2.

Width (X): 0.16 m. Length (Y): 0.21 m. Height (Z): 0.25 m. Shape: Compact.

Runout distance: 1.5 m from slope toe.

Drop height: 7.8 m. Altimeter hoisting: 7.8 m.

Figure B.47. Smart Rock data: rock 9, Franklin 2 NH.

B.4.3. Franklin 3, NH

Figure B.48. Smart Rock data: rock 2, Franklin 3 NH.

Field Rockfall — Rock 3, Franklin 3/NH

SR number: 1. Date: 15-Jul-2020.

Mass: 9.45 kg. I_{XX}: 0.057 kg.m^2. I_{YY}: 0.028 kg.m^2. I_{ZZ}: 0.053 kg.m^2.

Width (X): 0.14 m. Length (Y): 0.25 m. Height (Z): 0.17 m. Shape: Compact Elongated.

Runout distance: 3 m from slope toe.

Drop height: 18.2 m. Altimeter hoisting: 17.1 m.

Figure B.49. Smart Rock data: rock 3, Franklin 3 NH.

Field Rockfall — Rock 4, Franklin 3/NH

SR number: 4. Date: 15-Jul-2020.

Mass: 11.35 kg. I_{XX}: 0.067 kg.m^2. I_{YY}: 0.042 kg.m^2. I_{ZZ}: 0.055 kg.m^2.

Width (X): 0.18 m. Length (Y): 0.22 m. Height (Z): 0.16 m. Shape: Compact.

Runout distance: 3.2 m from slope toe.
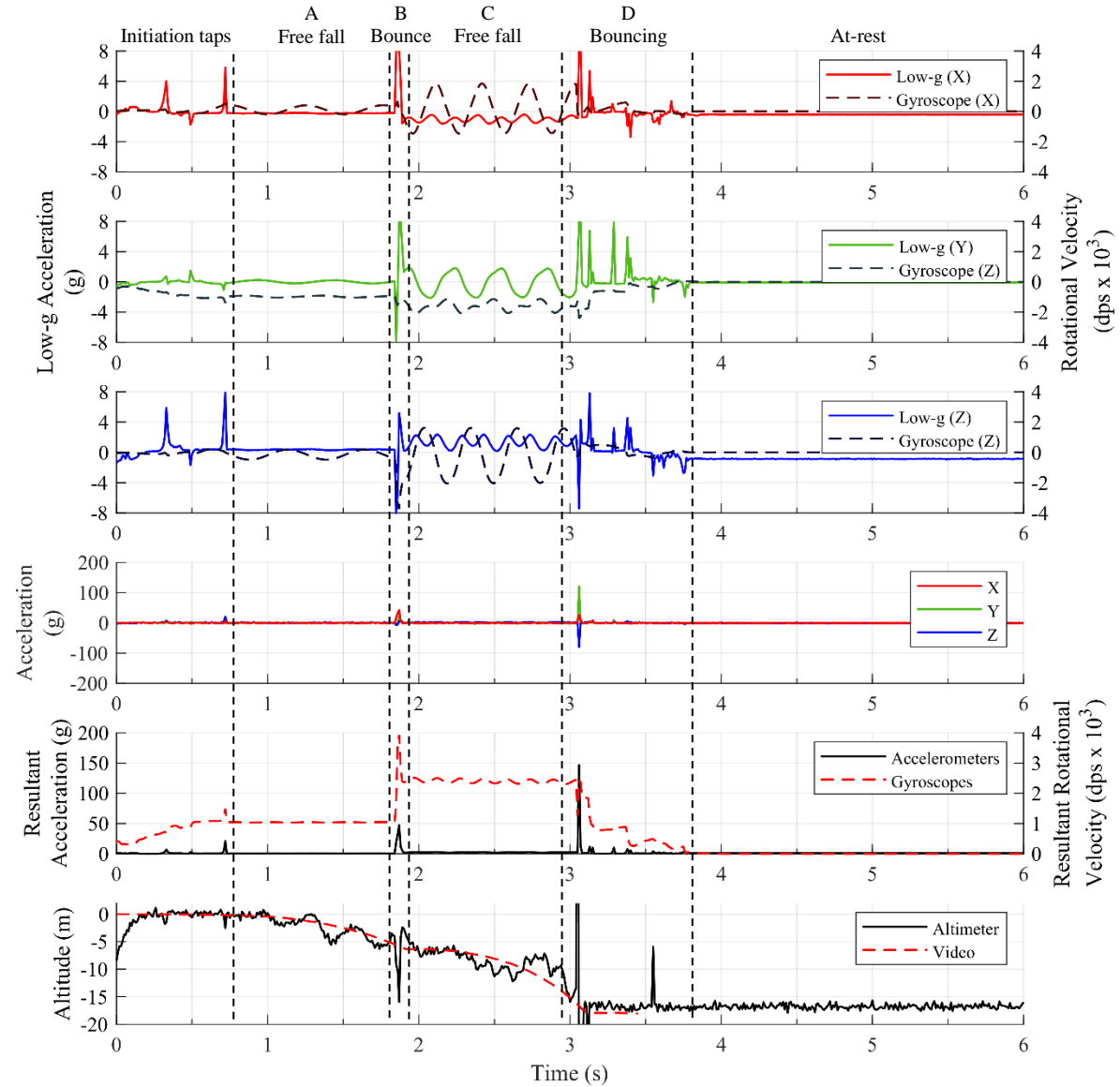
Drop height: 18.2 m. Altimeter hoisting: 17.6 m.

Figure B.50. Smart Rock data: rock 4, Franklin 3 NH.

Figure B.51. Smart Rock data: rock 8, Franklin 3 NH.

Field Rockfall — Rock 9, Franklin 3/NH

SR number: 3. Date: 15-Jul-2020.

Mass: 10.52 kg. I_{XX}: 0.062 kg.m^2. I_{YY}: 0.049 kg.m^2. I_{ZZ}: 0.053 kg.m^2.

Width (X): 0.16 m. Length (Y): 0.21 m. Height (Z): 0.25 m. Shape: Compact.

Runout distance: 7.6 m from slope toe.

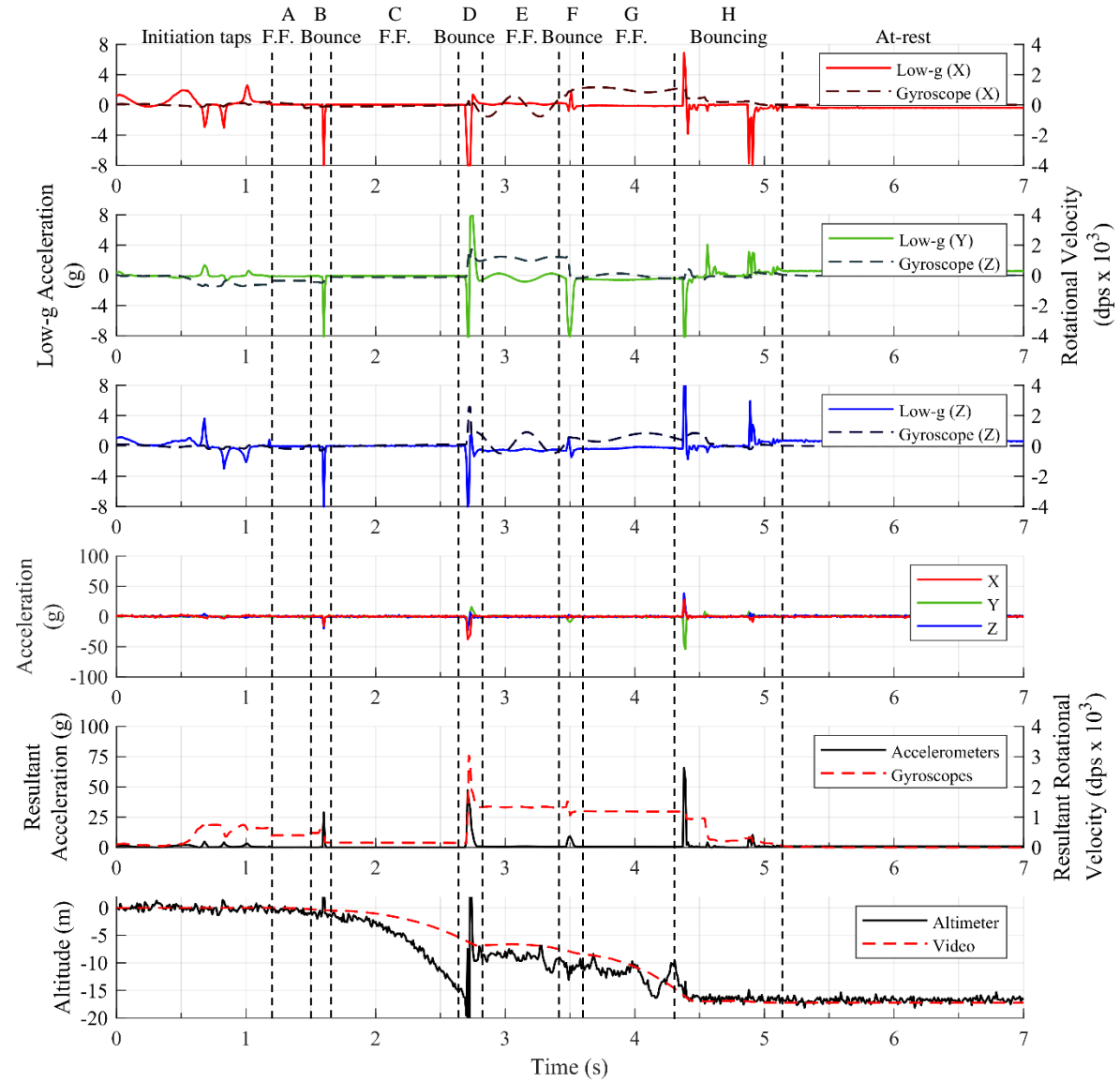Drop height: 18.2 m. Altimeter hoisting: 18.5 m.

Figure B.52. Smart Rock data: rock 9, Franklin 3 NH.

B.5. Keene, NH
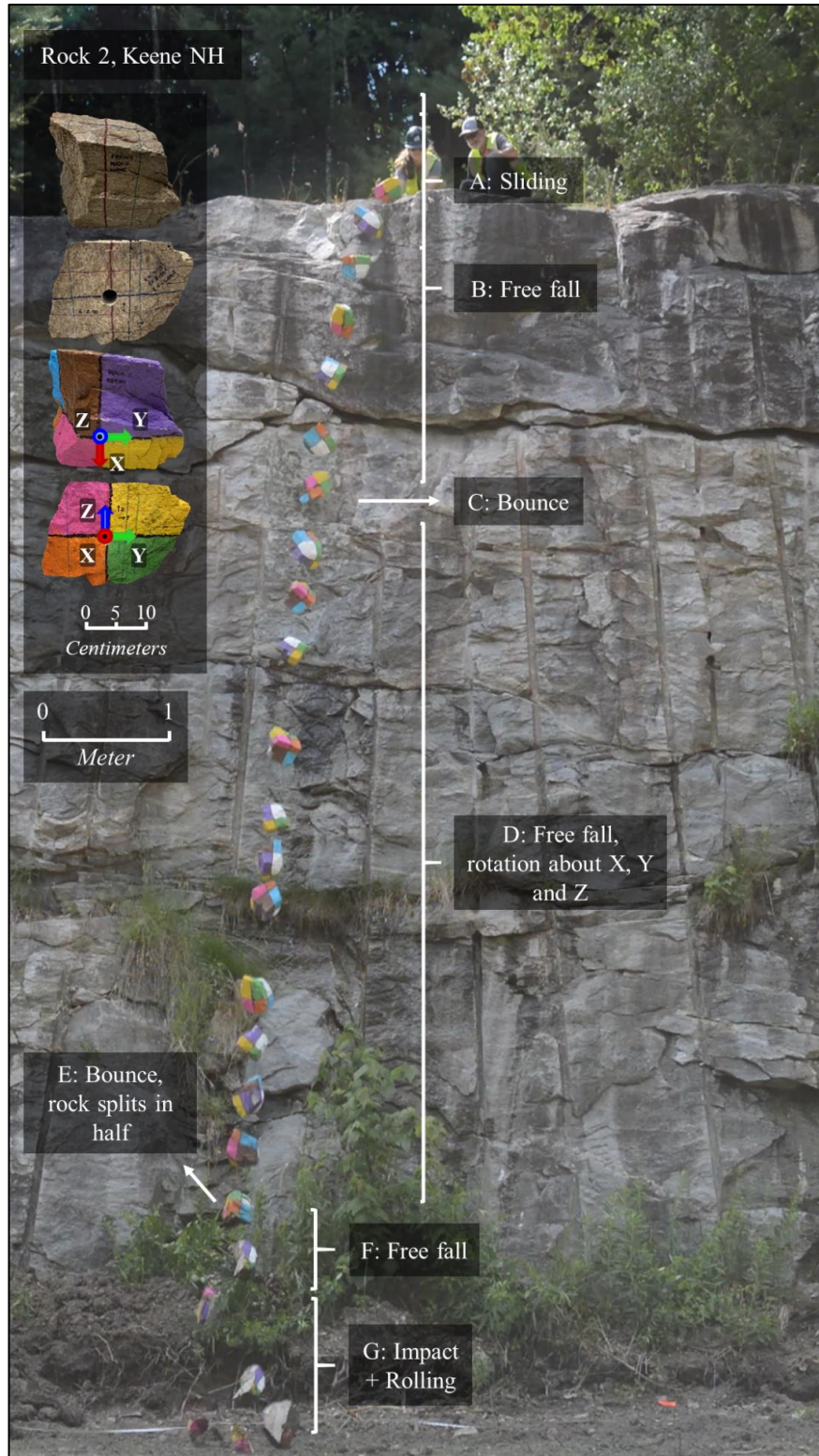
Figure B.53. Rockfall trajectory: rock 2, Keene NH.
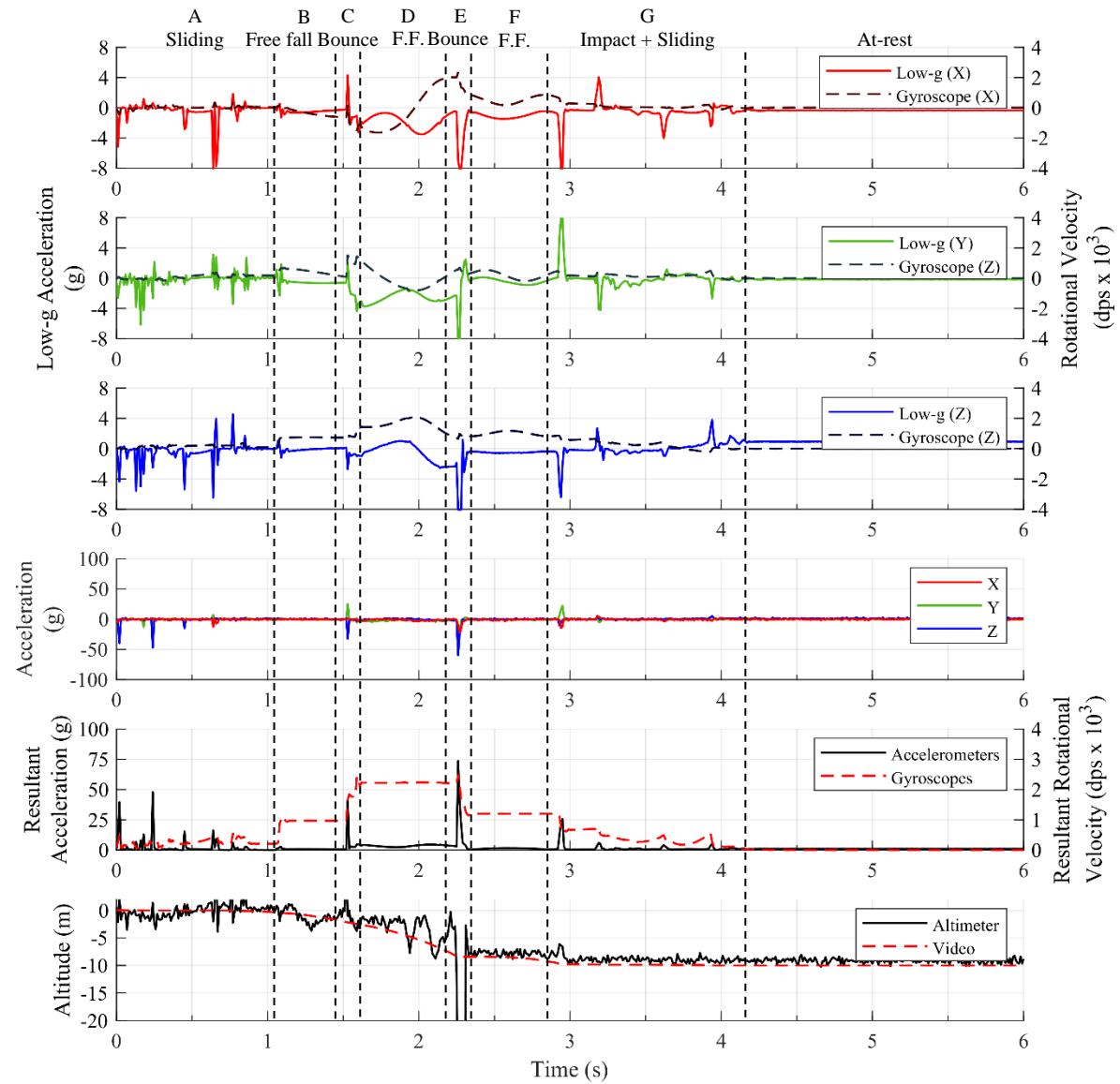
Figure B.54. Smart Rock data: rock 2, Keene NH.

Rock 3, Keene NH

A: Sliding

B: Bouncing

C: Sliding

0 5 10
Centimeters

0 1
Meter

Figure B.55. Rockfall trajectory: rock 3, Keene NH.

Field Rockfall — Rock 3, Keene/NH

SR number: 5. Date: 23-Jun-2020.

Mass: 16.21 kg. I_{XX}: 0.128 kg.m^2. I_{YY}: 0.072 kg.m^2. I_{ZZ}: 0.162 kg.m^2.

Width (X): 0.25 m. Length (Y): 0.32 m. Height (Z): 0.33 m. Shape: Compact.

Runout distance: 0 m from slope toe.

Drop height: 9.6 m. Altimeter hoisting: 9 m.
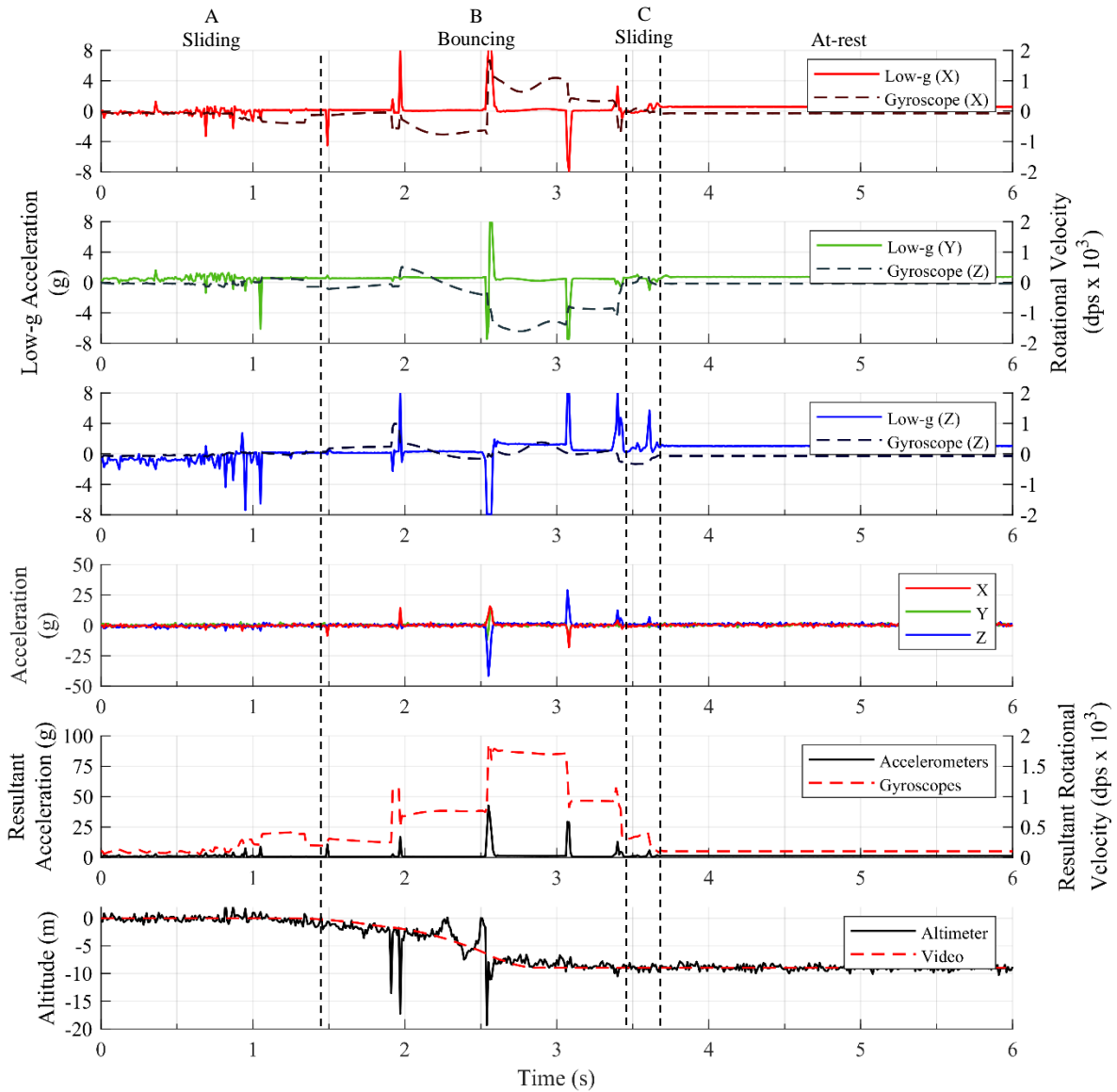
Figure B.56. Smart Rock data: rock 3, Keene NH.
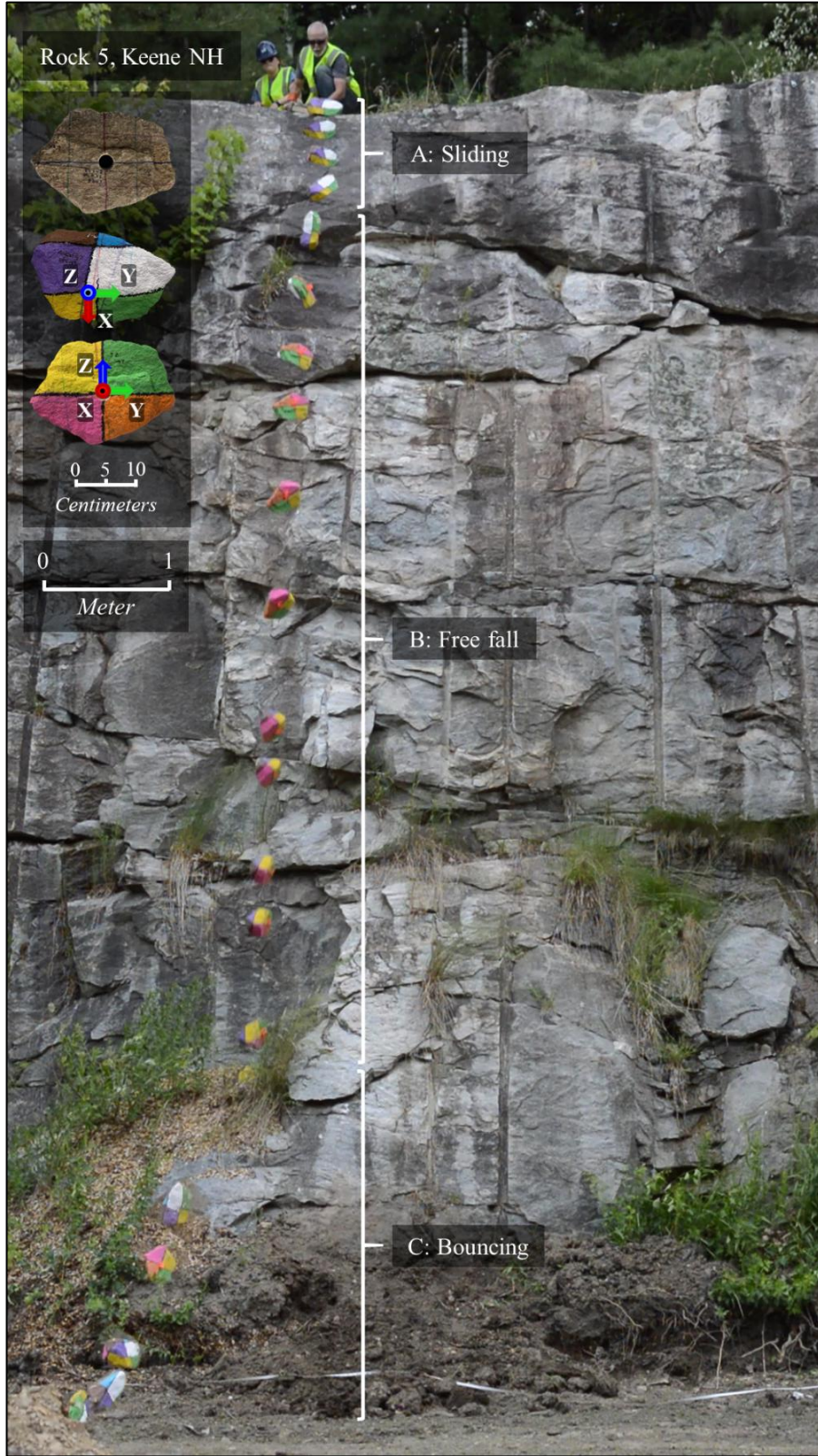
Figure B.57. Rockfall trajectory: rock 5, Keene NH.

Field Rockfall — Rock 5, Keene/NH

SR number: 5. Date: 23-Jun-2020.

Mass: 7.66 kg. I_{XX}: 0.043 kg.m^2. I_{YY}: 0.038 kg.m^2. I_{ZZ}: 0.018 kg.m^2.

Width (X): 0.13 m. Length (Y): 0.27 m. Height (Z): 0.19 m. Shape: Compact.

Runout distance: 1.1 m from slope toe.
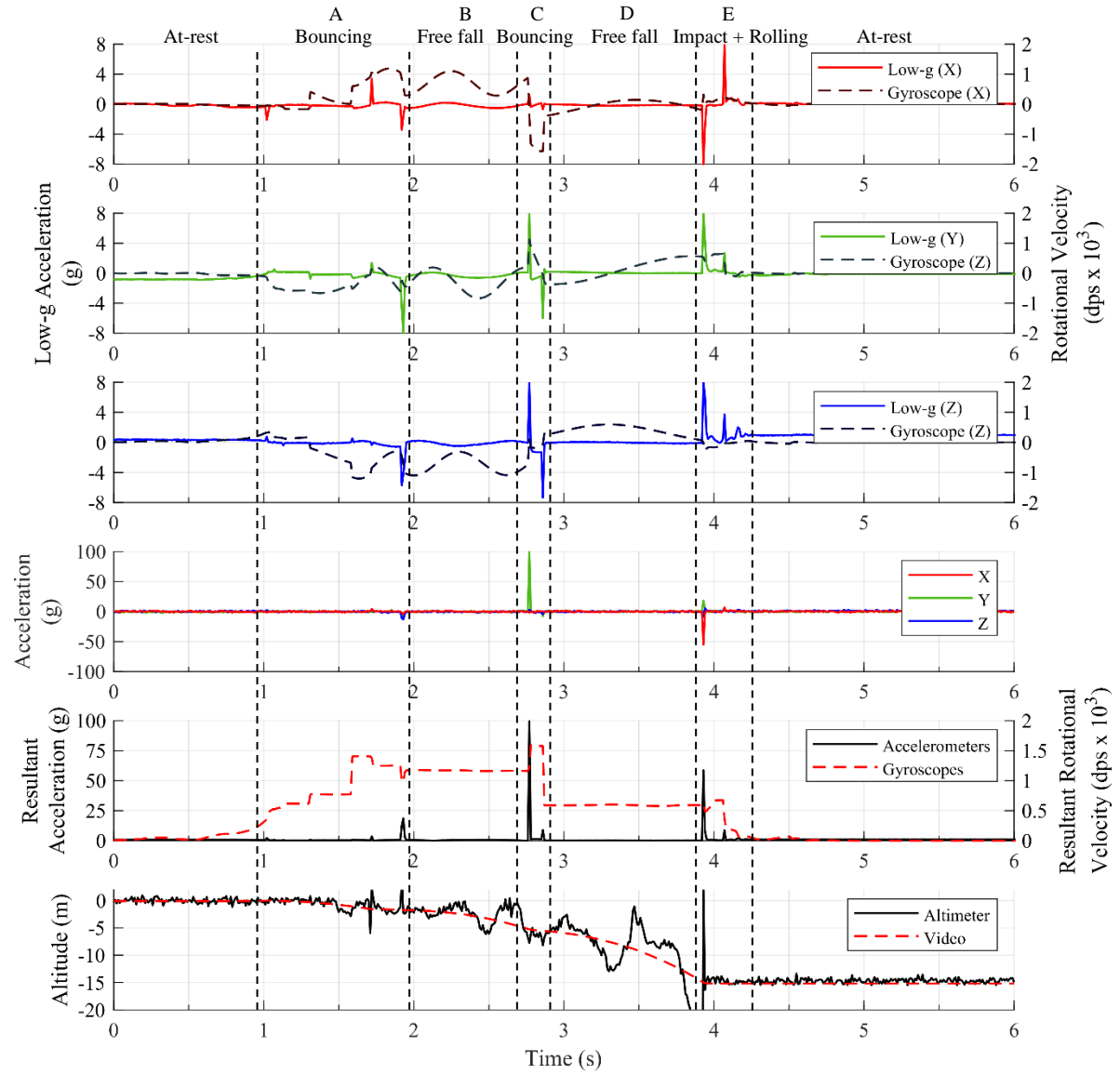
Drop height: 9.9 m. Altimeter hoisting: 9.4 m.
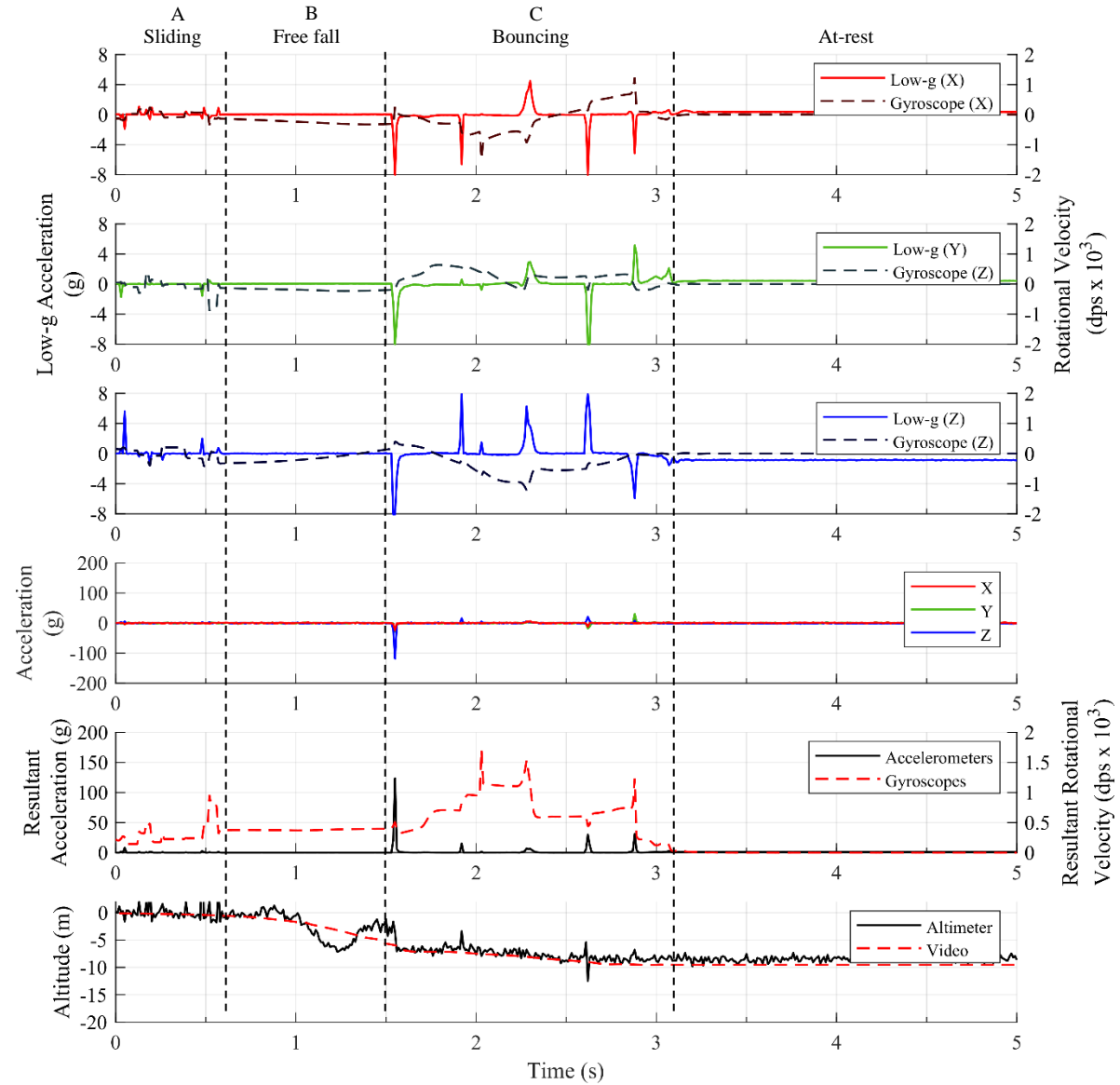
Figure B.58. Smart Rock data: rock 5, Keene NH.
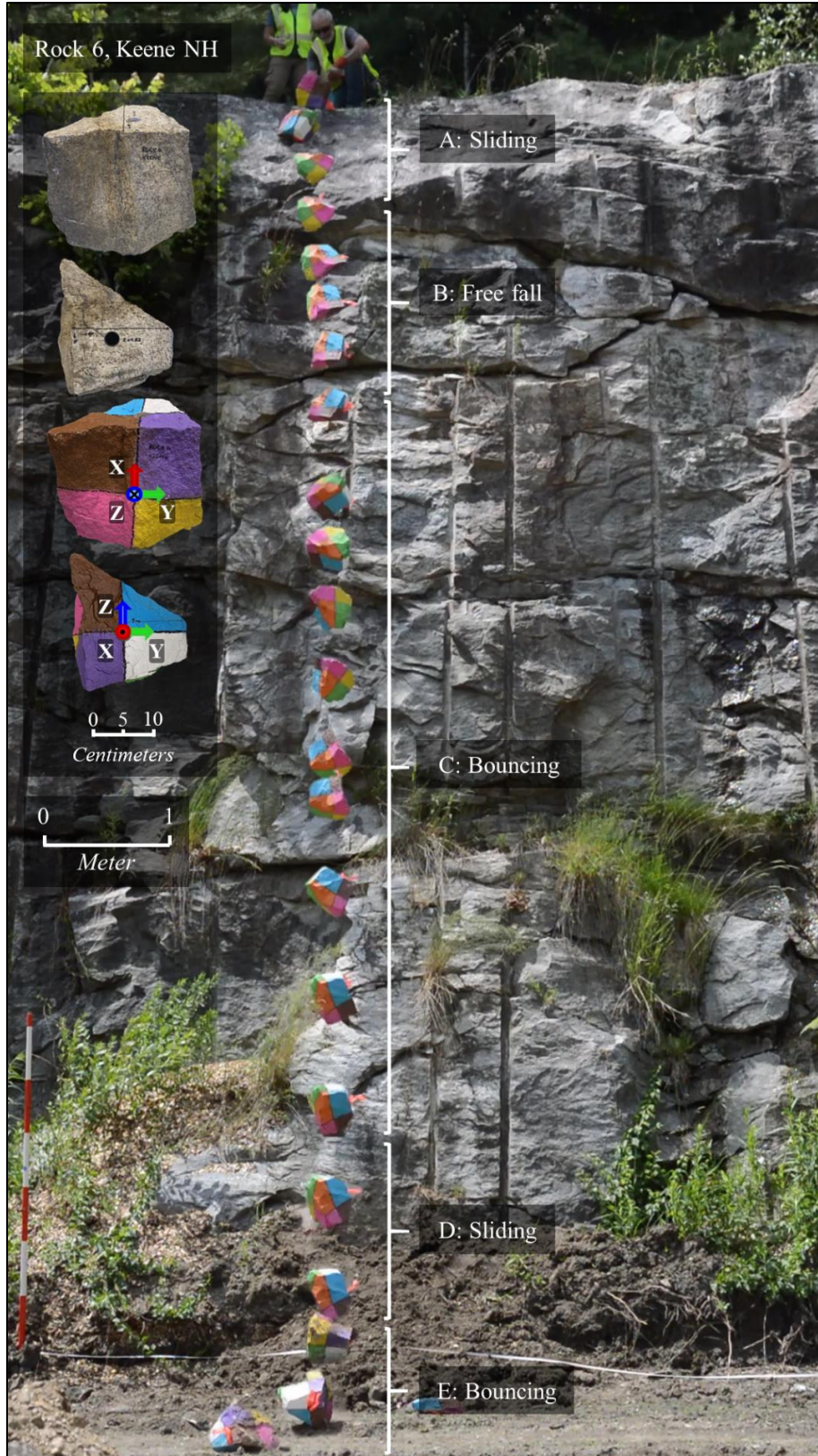
Figure B.59. Rockfall trajectory: rock 6, Keene NH.

Field Rockfall — Rock 6, Keene/NH

SR number: 1. Date: 23-Jun-2020.

Mass: 20.81 kg. I_{XX}: 0.144 kg.m^2. I_{YY}: 0.148 kg.m^2. I_{ZZ}: 0.146 kg.m^2.

Width (X): 0.17 m. Length (Y): 0.24 m. Height (Z): 0.24 m. Shape: Compact.

Runout distance: 3 m from slope toe.

Drop height: 9.9 m. Altimeter hoisting: 9.7 m.
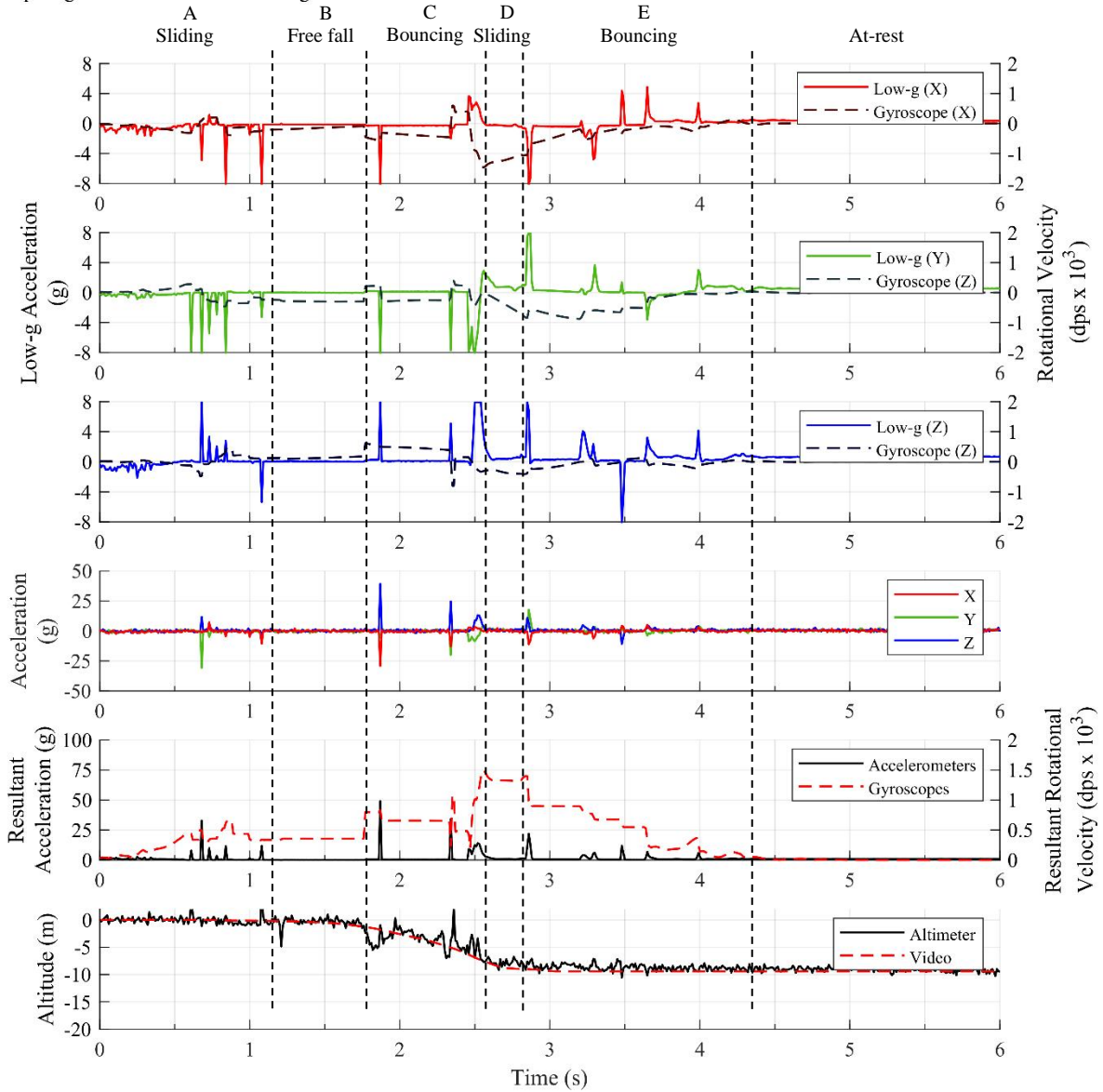

Figure B.60. Smart Rock data: rock 6, Keene NH.
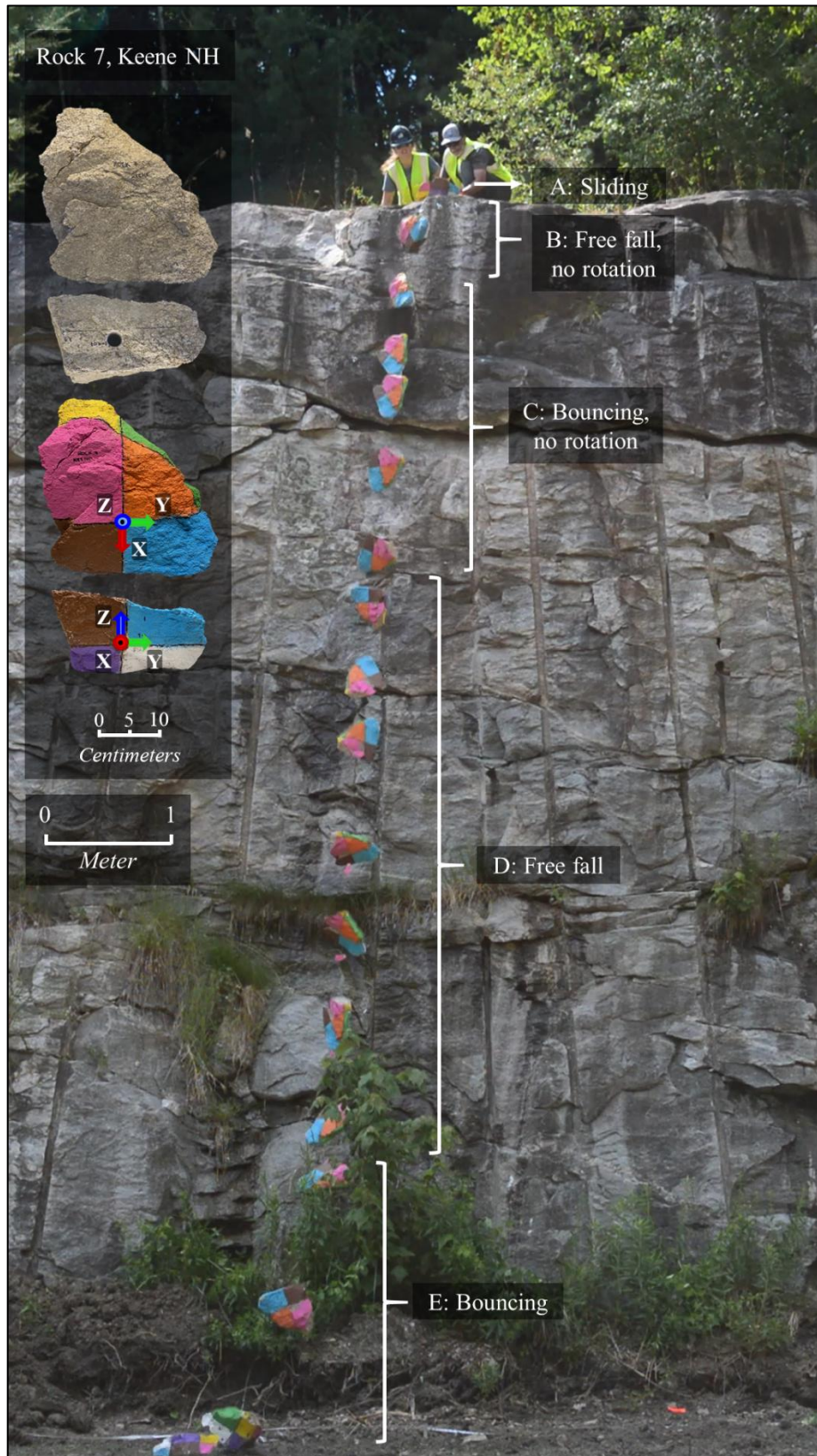
Figure B.61. Rockfall trajectory: rock 7, Keene NH.

Field Rockfall — Rock 7, Keene/NH

SR number: 5. Date: 23-Jun-2020.

Mass: 13.54 kg. I_{XX}: 0.075 kg.m^2. I_{YY}: 0.066 kg.m^2. I_{ZZ}: 0.118 kg.m^2.

Width (X): 0.27 m. Length (Y): 0.27 m. Height (Z): 0.13 m. Shape: Platy.

Runout distance: 2.4 m from slope toe.

Drop height: 9.6 m. Altimeter hoisting: 9.6 m.
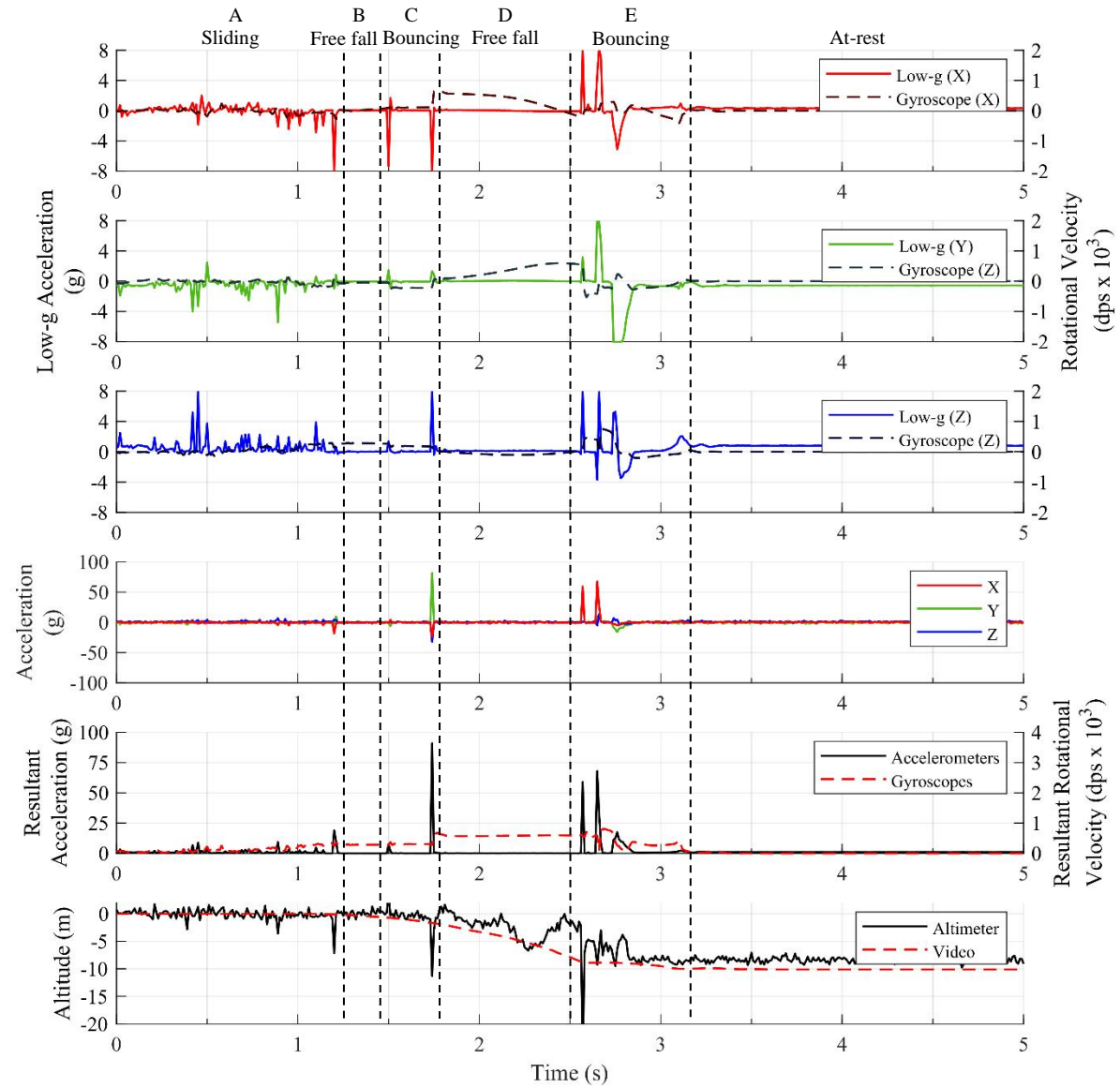
Figure B.62. Smart Rock data: rock 7, Keene NH.

389
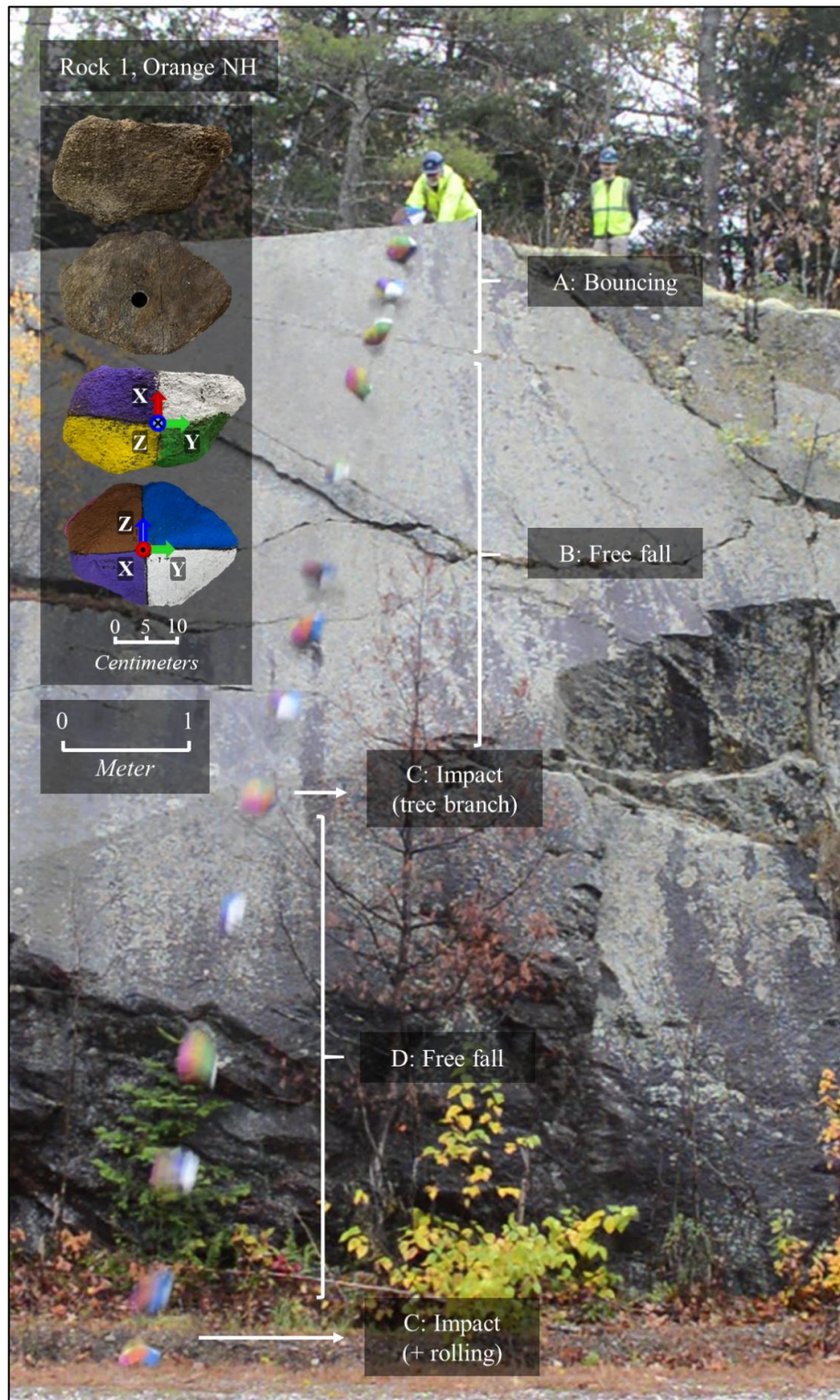
B.6. Orange, NH

Figure B.63. Rockfall trajectory: rock 1, Orange NH.
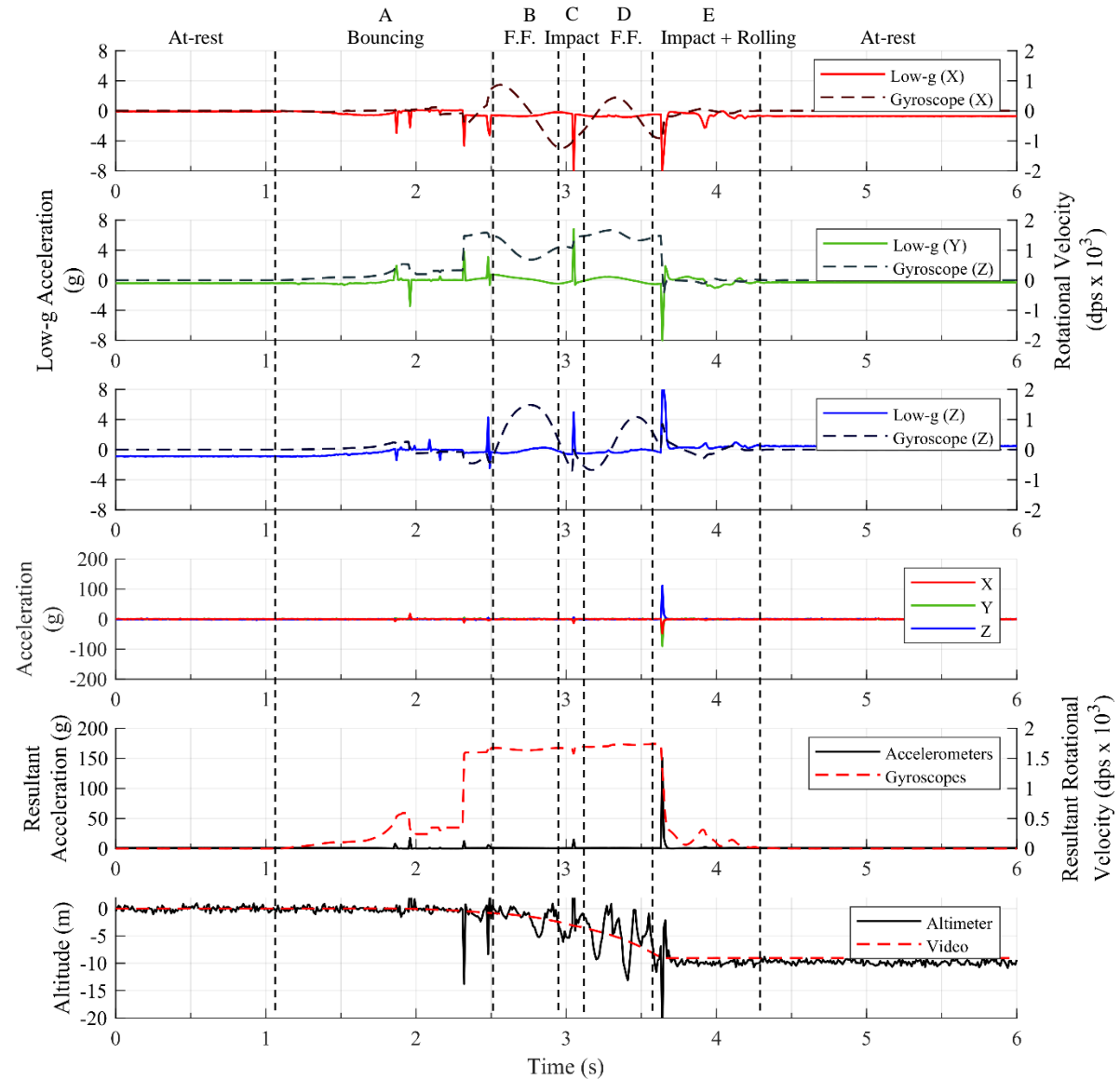
Figure B.64. Smart Rock data: rock 1, Orange NH.
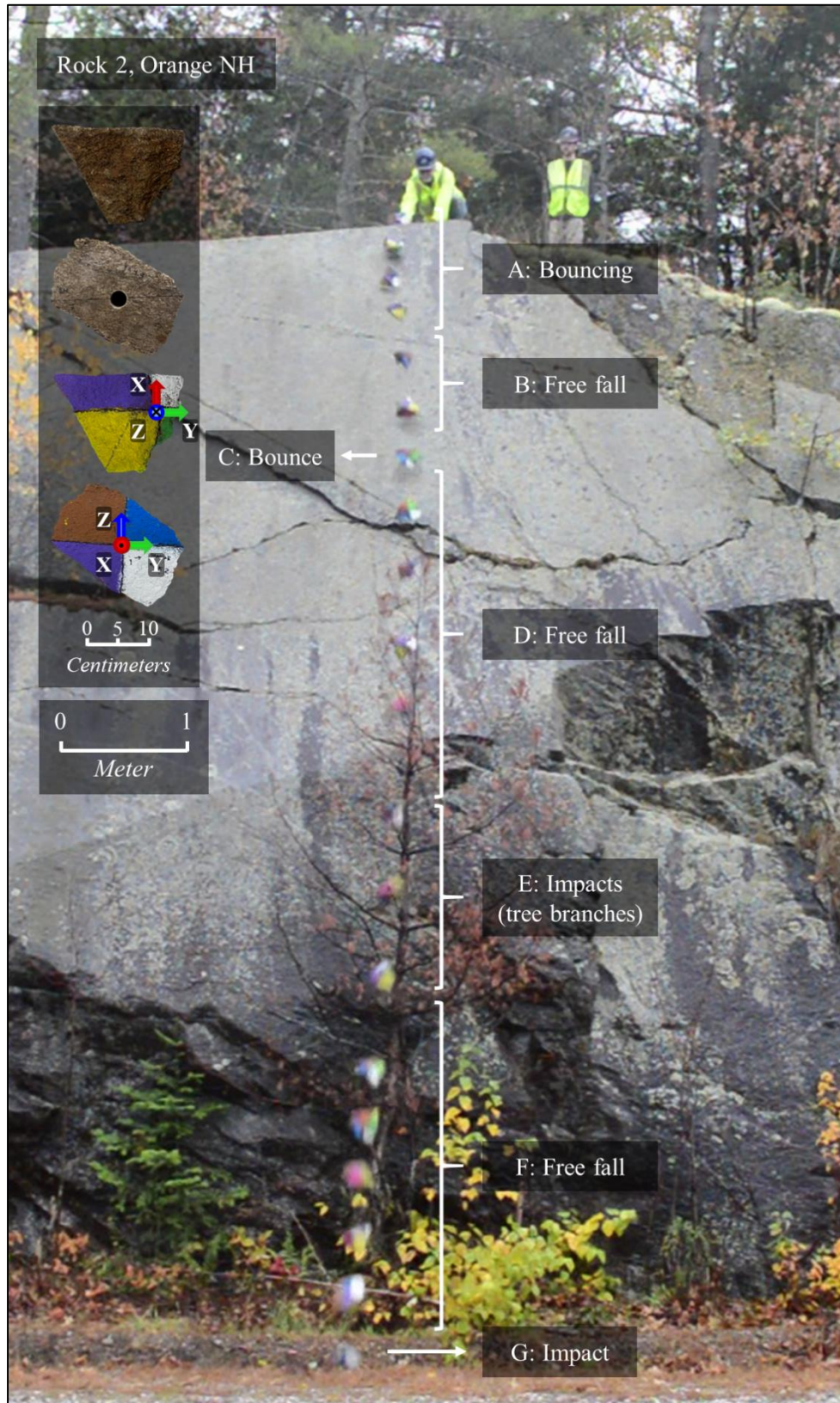
Figure B.65. Rockfall trajectory: rock 2, Orange NH.

Field Rockfall — Rock 2, Orange/NH

SR number: 4. Date: 16-Oct-2020.

Mass: 10.39 kg. I_{XX}: 0.03 kg.m^2. I_{YY}: 0.027 kg.m^2. I_{ZZ}: 0.028 kg.m^2.

Width (X): 0.17 m. Length (Y): 0.19 m. Height (Z): 0.15 m. Shape: Compact.

Runout distance: 1.8 m from slope toe.

Drop height: 9.1 m. Altimeter hoisting: 9.6 m.
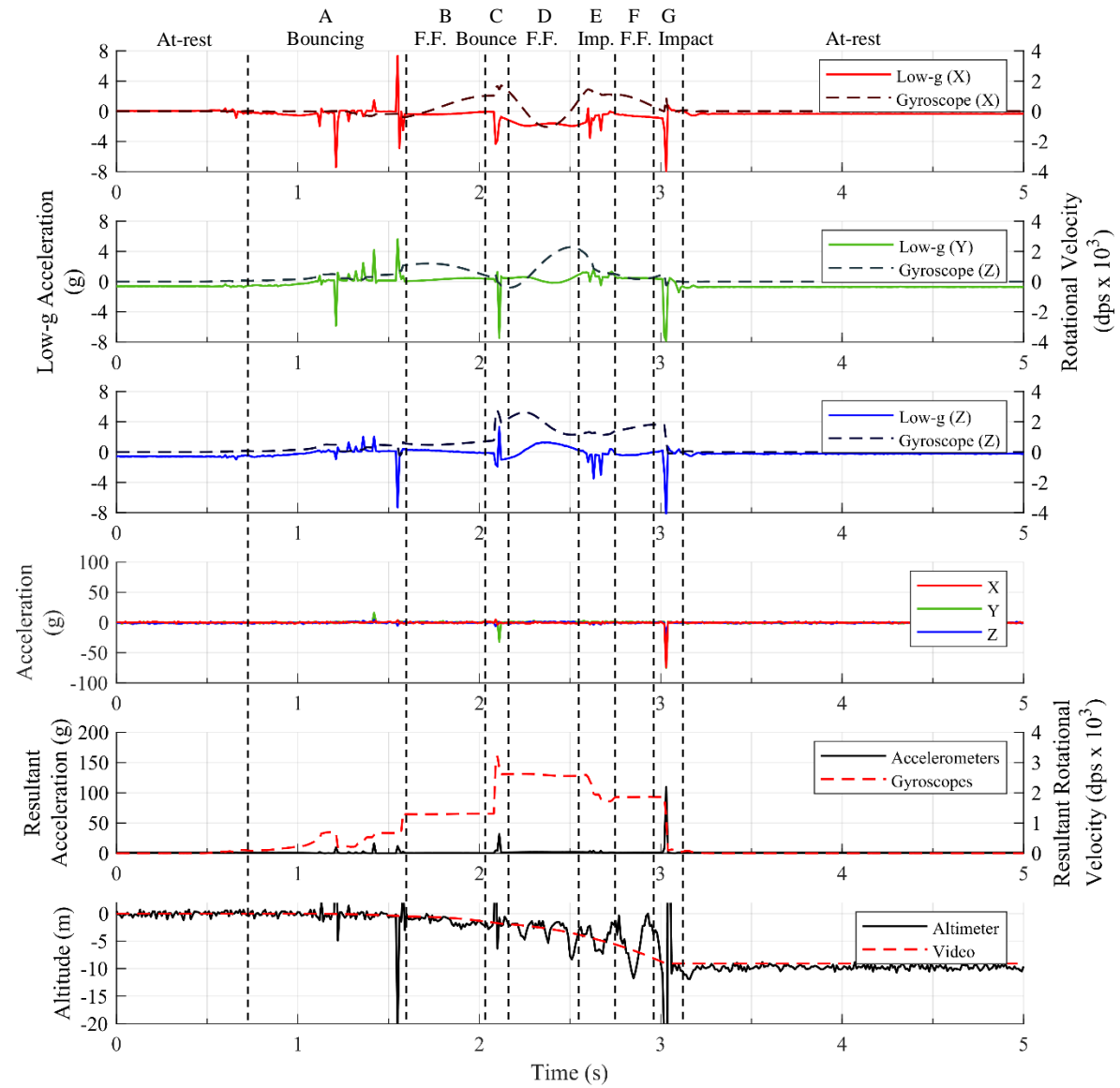
Figure B.66. Smart Rock data: rock 2, Orange NH.

Figure B.67. Rockfall trajectory: rock 4, Orange NH.

Field Rockfall — Rock 4, Orange/NH

SR number: 5. Date: 16-Oct-2020.

Mass: 18.06 kg. I_{XX}: 0.271 kg.m^2. I_{YY}: 0.084 kg.m^2. I_{ZZ}: 0.284 kg.m^2.

Width (X): 0.2 m. Length (Y): 0.36 m. Height (Z): 0.13 m. Shape: Elongated.

Runout distance: 1.6 m from slope toe.

Drop height: 9.1 m. Altimeter hoisting: 8.8 m.

Figure B.68. Smart Rock data: rock 4, Orange NH.

Rock D2, Orange NH

A: Sliding

B: Bouncing

0   5   10
Centimeters

0   1
Meter

C: Free fall

D: Bouncing

Figure B.69. Rockfall trajectory: rock D2, Orange NH.

Figure B.70. Rockfall trajectory: rock D3, Orange NH.

Field Rockfall — Rock D3, Orange/NH

SR number: 4. Date: 16-Oct-2020.

Mass: 12.37 kg. I_{XX}: 0.065 kg.m^2. I_{YY}: 0.051 kg.m^2. I_{ZZ}: 0.077 kg.m^2.

Width (X): 0.22 m. Length (Y): 0.23 m. Height (Z): 0.15 m. Shape: Compact Platy.

Runout distance: 2.5 m from slope toe.

Drop height: 9.1 m. Altimeter hoisting: 9 m.
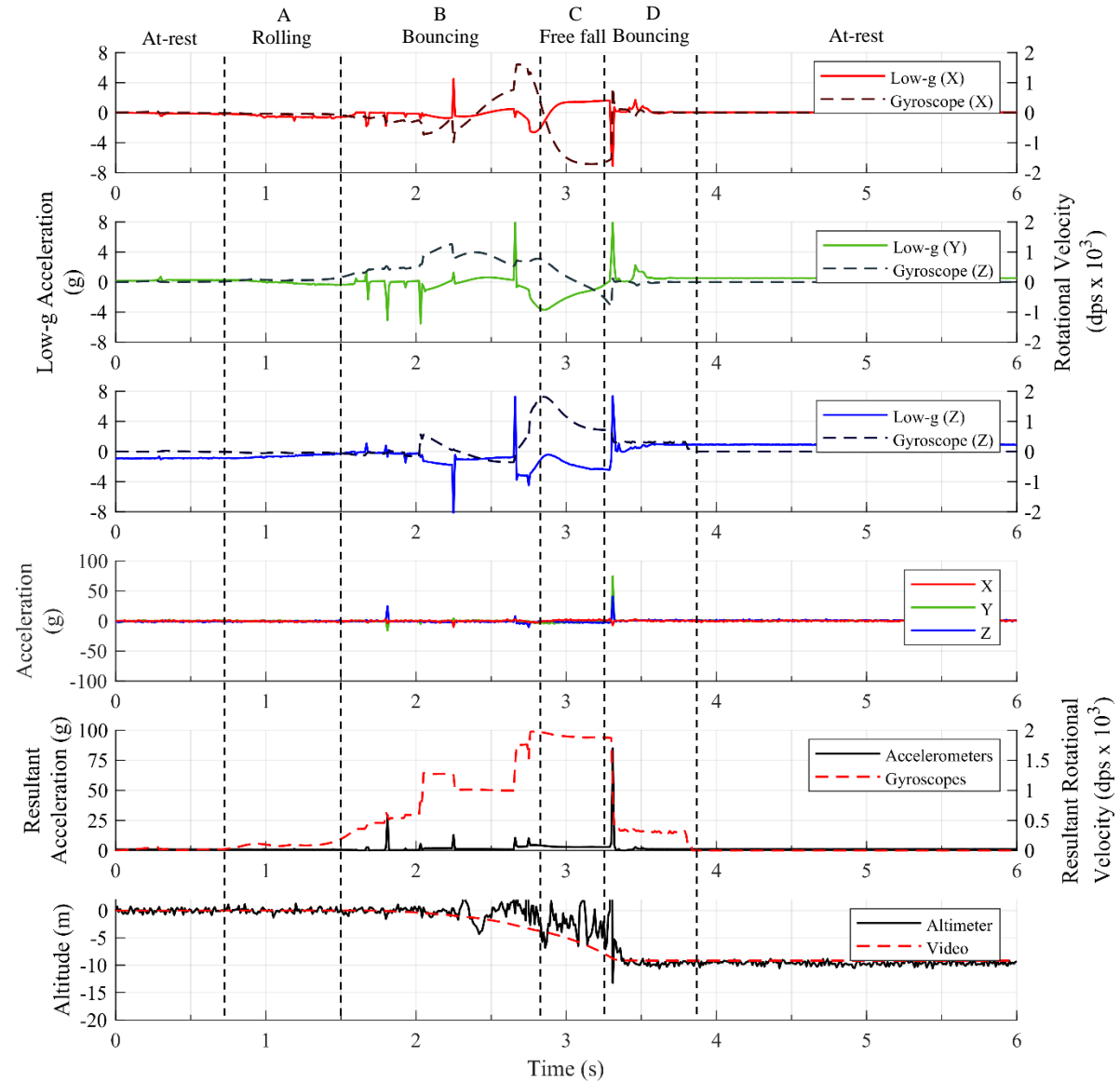
Figure B.71. Smart Rock data: rock D3, Orange NH.

B.7. Townshend, VT
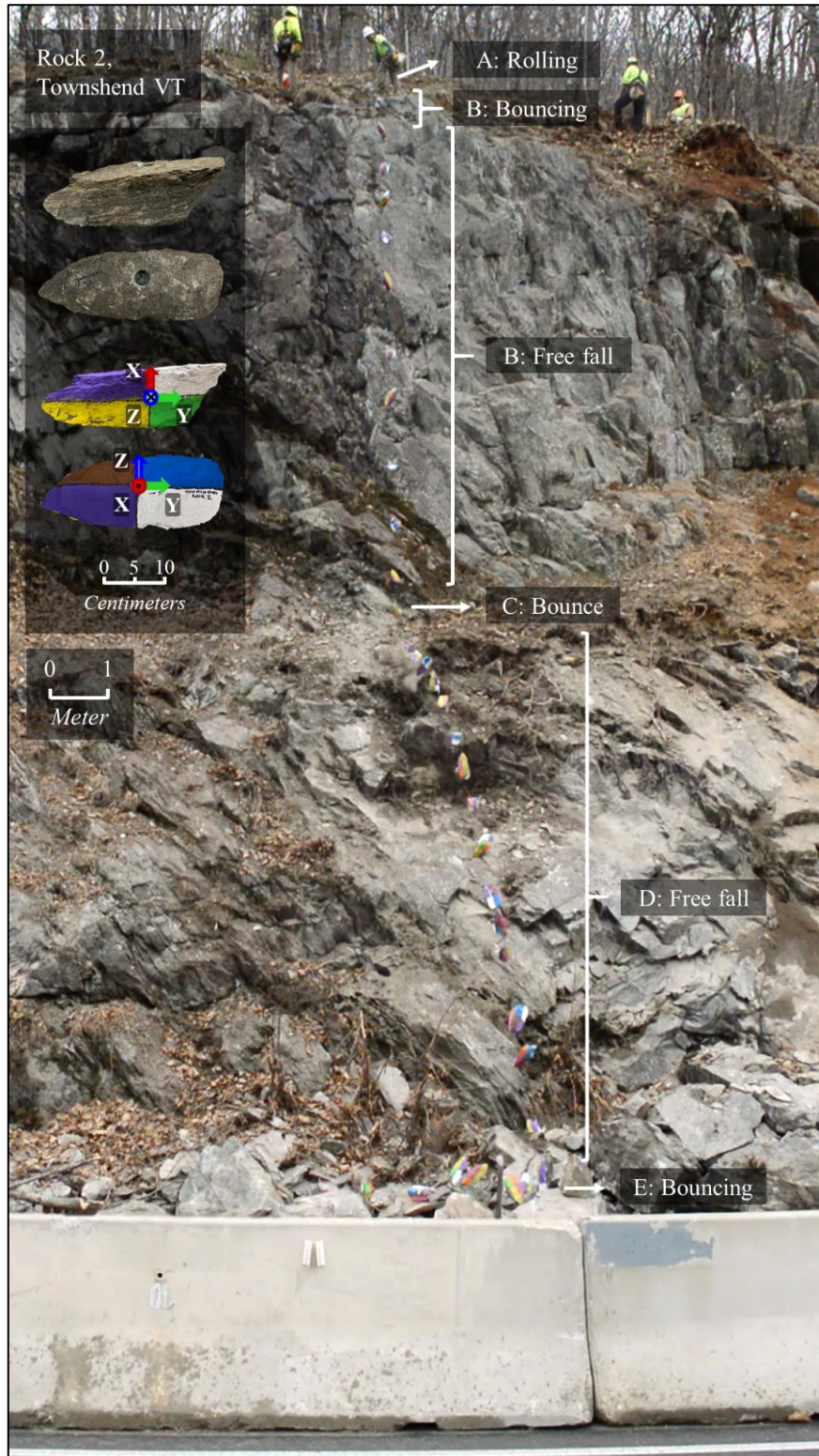
Figure B.72. Rockfall trajectory: rock 2, Townshend VT.

Field Rockfall — Rock 2, Townshend/VT

SR number: 5. Date: 11-Nov-2020.

Mass: 5.85 kg. I_{XX}: 0.032 kg.m^2. I_{YY}: 0.009 kg.m^2. I_{ZZ}: 0.03 kg.m^2.

Width (X): 0.1 m. Length (Y): 0.29 m. Height (Z): 0.12 m. Shape: Elongated.

Runout distance: 3.2 m from slope toe.

Drop height: 19 m. Altimeter hoisting: 17 m.
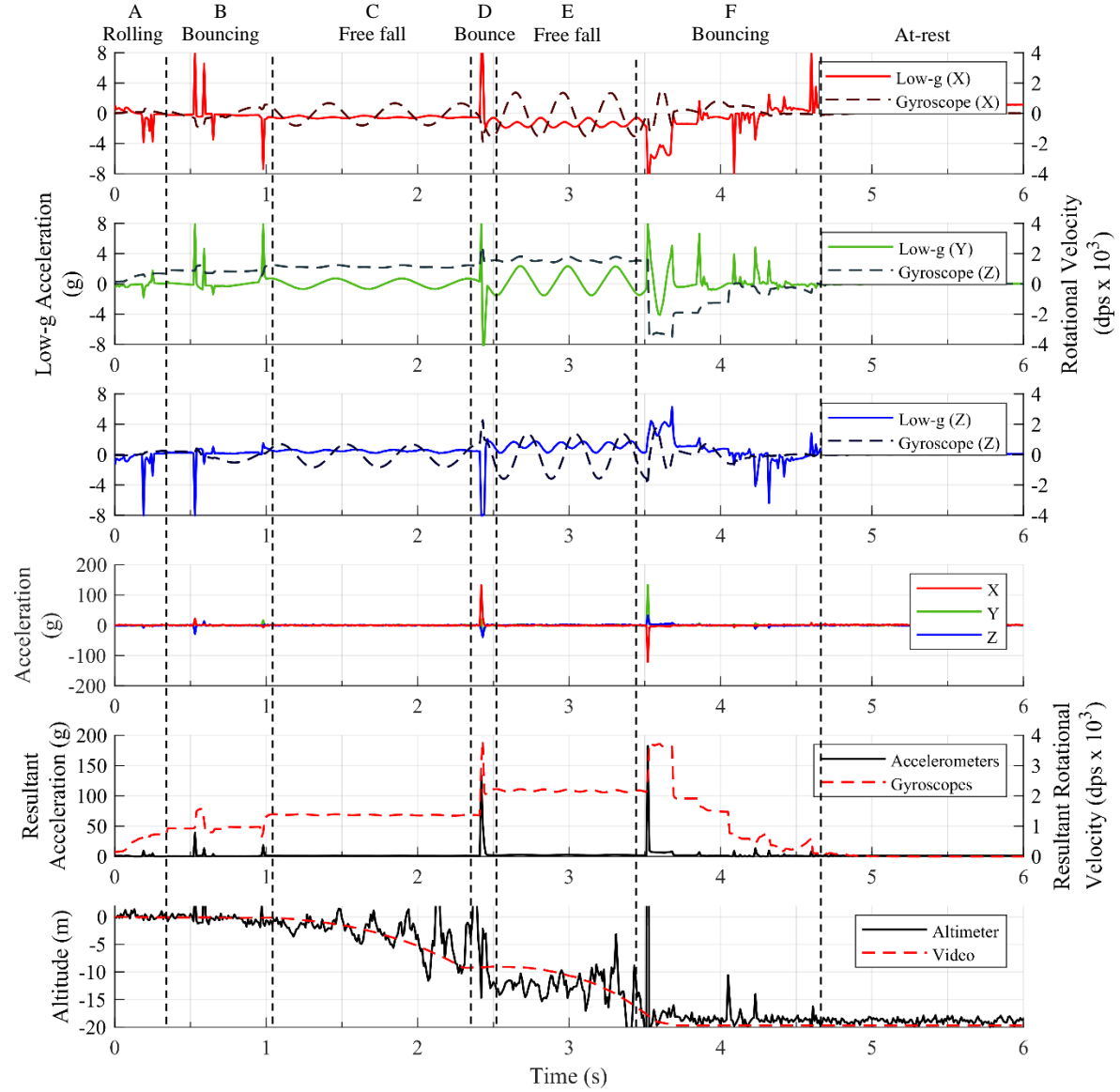
Figure B.73. Smart Rock data: rock 2, Townshend VT.
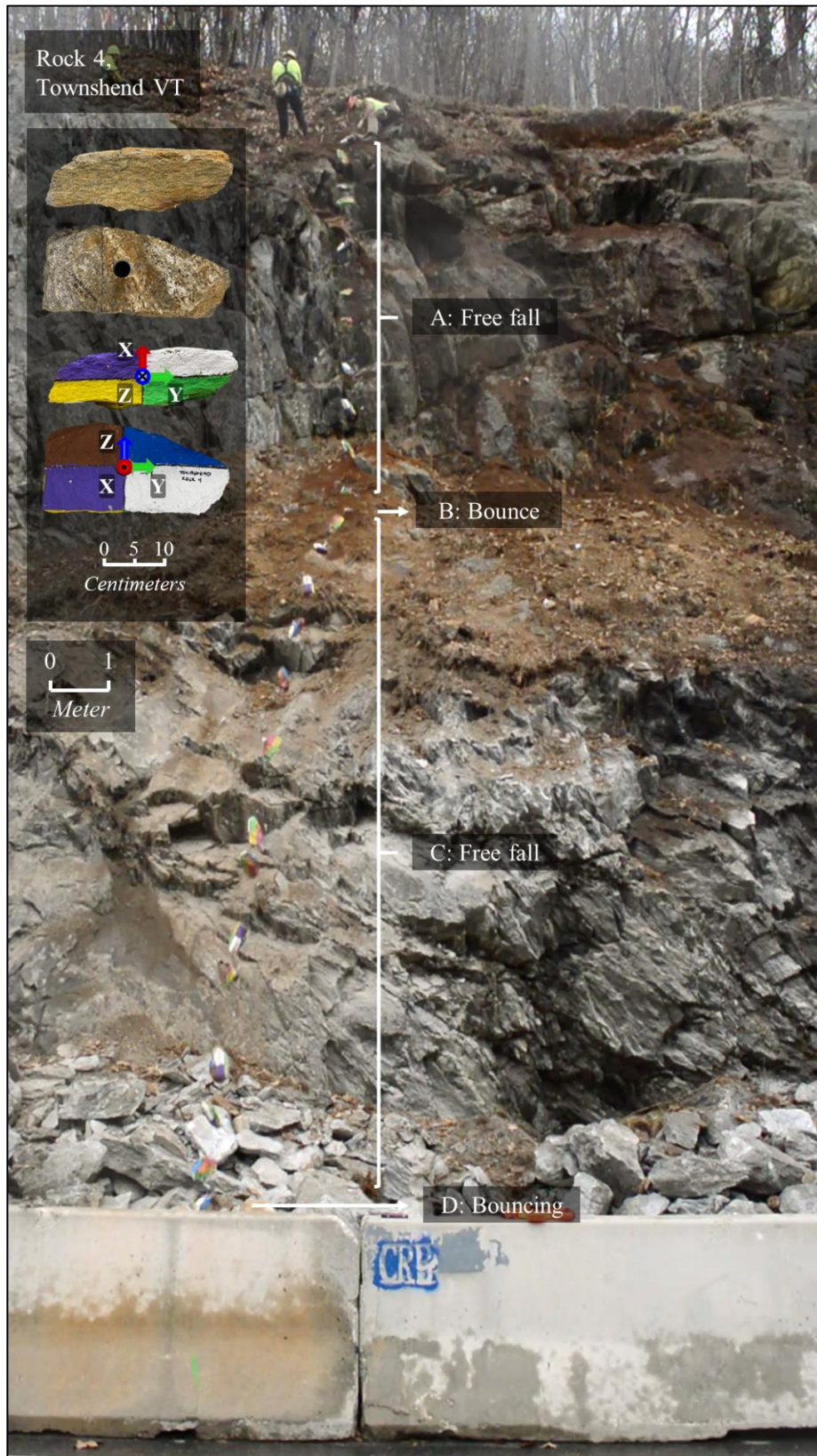
Figure B.74. Rockfall trajectory: rock 4, Townshend VT.

Figure B.75. Smart Rock data: rock 4, Townshend VT.
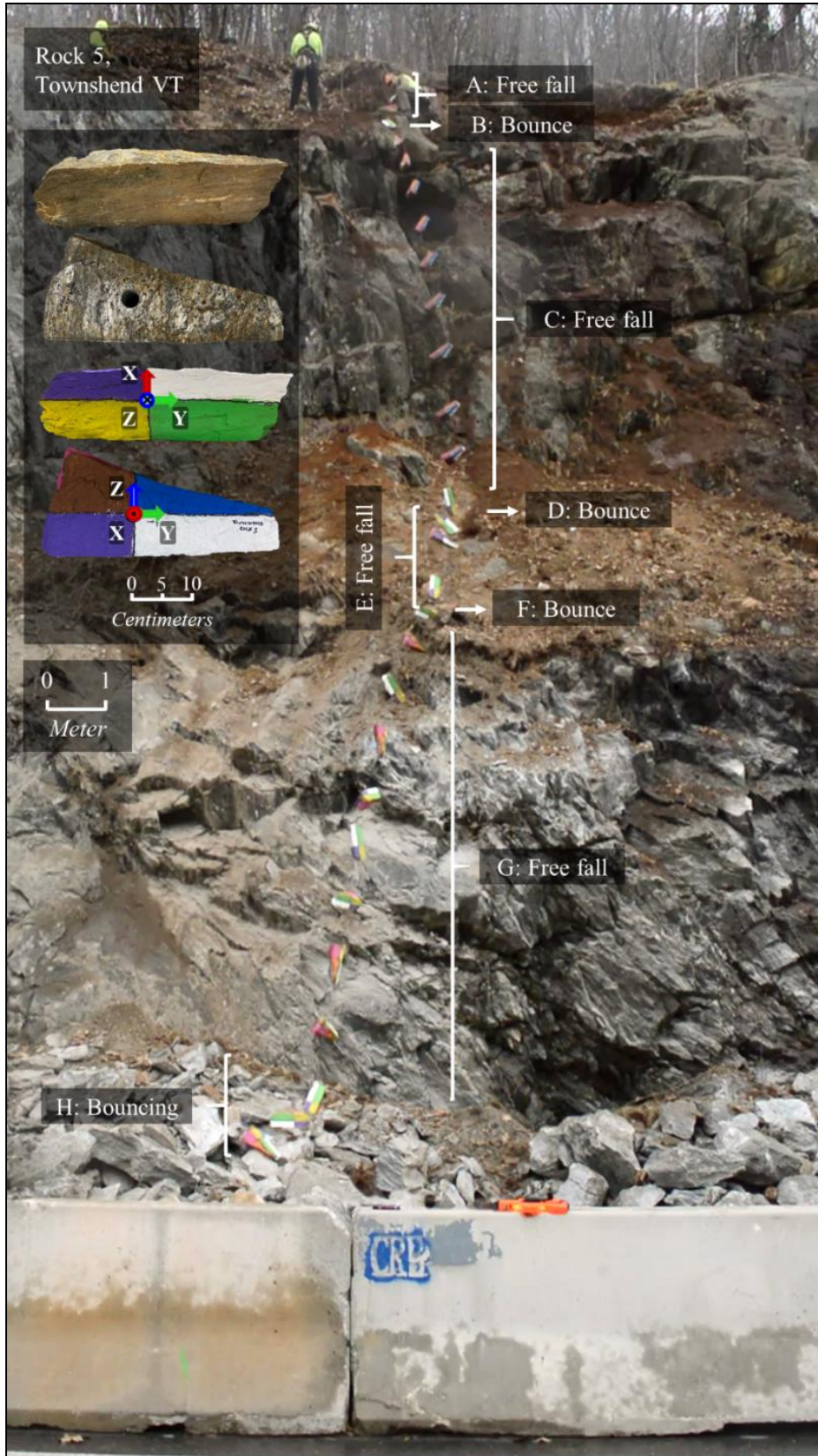
Figure B.76. Rockfall trajectory: rock 5, Townshend VT.

Figure B.77. Smart Rock data: rock 5, Townshend VT.

B.8. Warner, NH
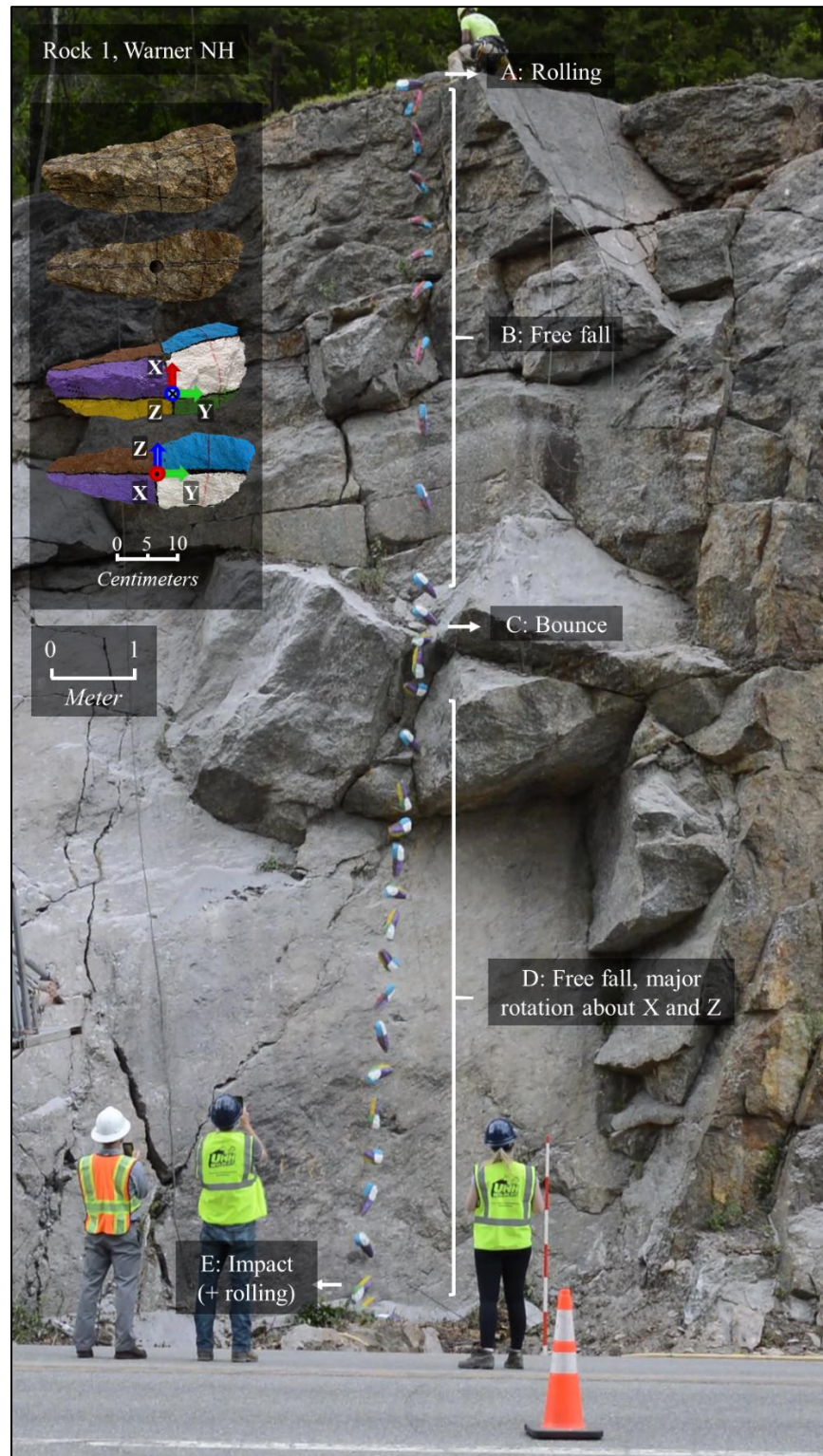
Figure B.78. Rockfall trajectory: rock 1, Warner NH.

Field Rockfall — Rock 1, Warner/NH

SR number: 4. Date: 02-Jun-2020.

Mass: 8.66 kg. I_{XX}: 0.081 kg.m^2. I_{YY}: 0.015 kg.m^2. I_{ZZ}: 0.08 kg.m^2.

Width (X): 0.1 m. Length (Y): 0.39 m. Height (Z): 0.11 m. Shape: Very Elongated.

Runout distance: 0 m from slope toe.

Drop height: 15.2 m. Altimeter hoisting: 15.1 m.
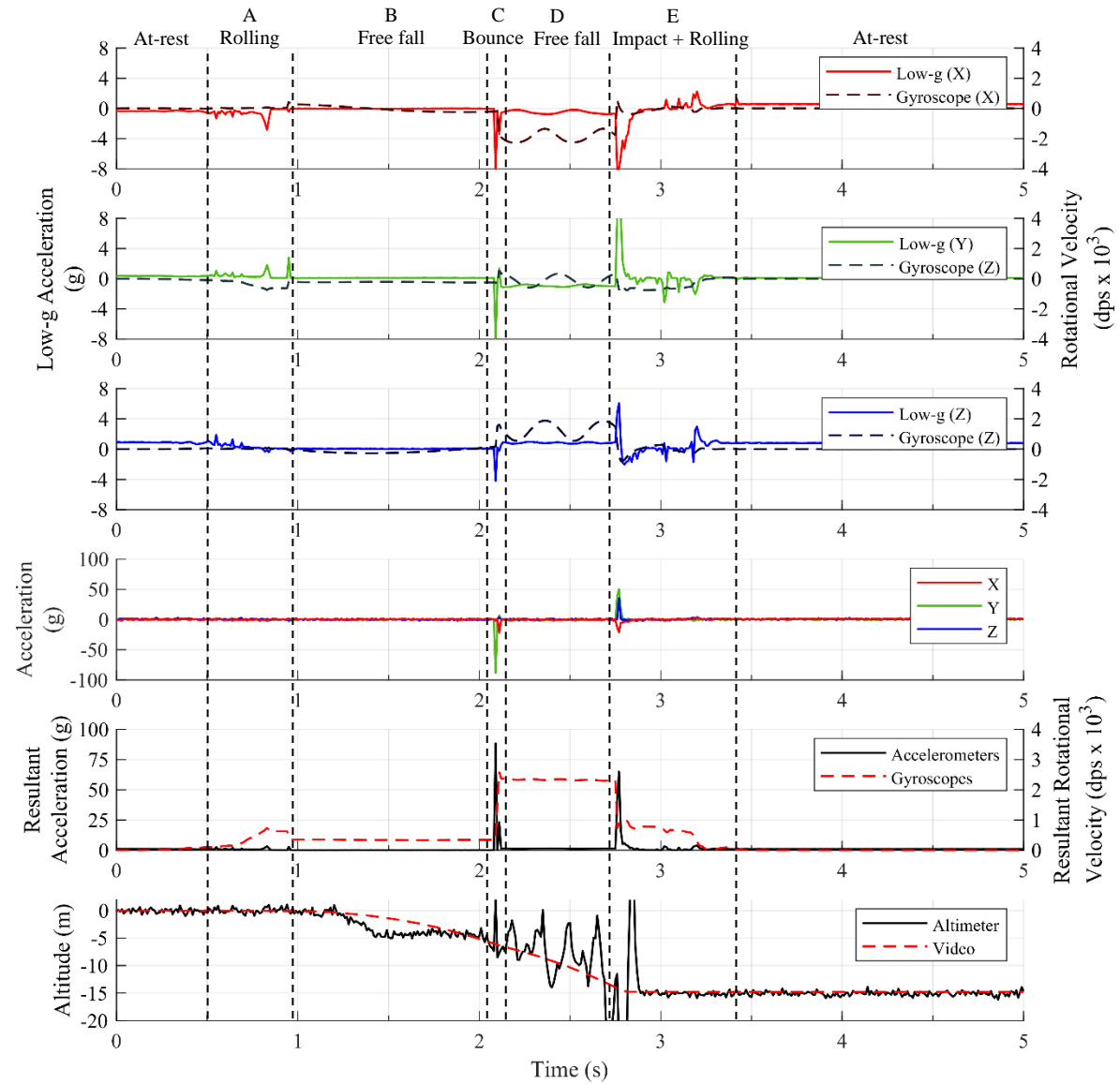
Figure B.79. Smart Rock data: rock 1, Warner NH.
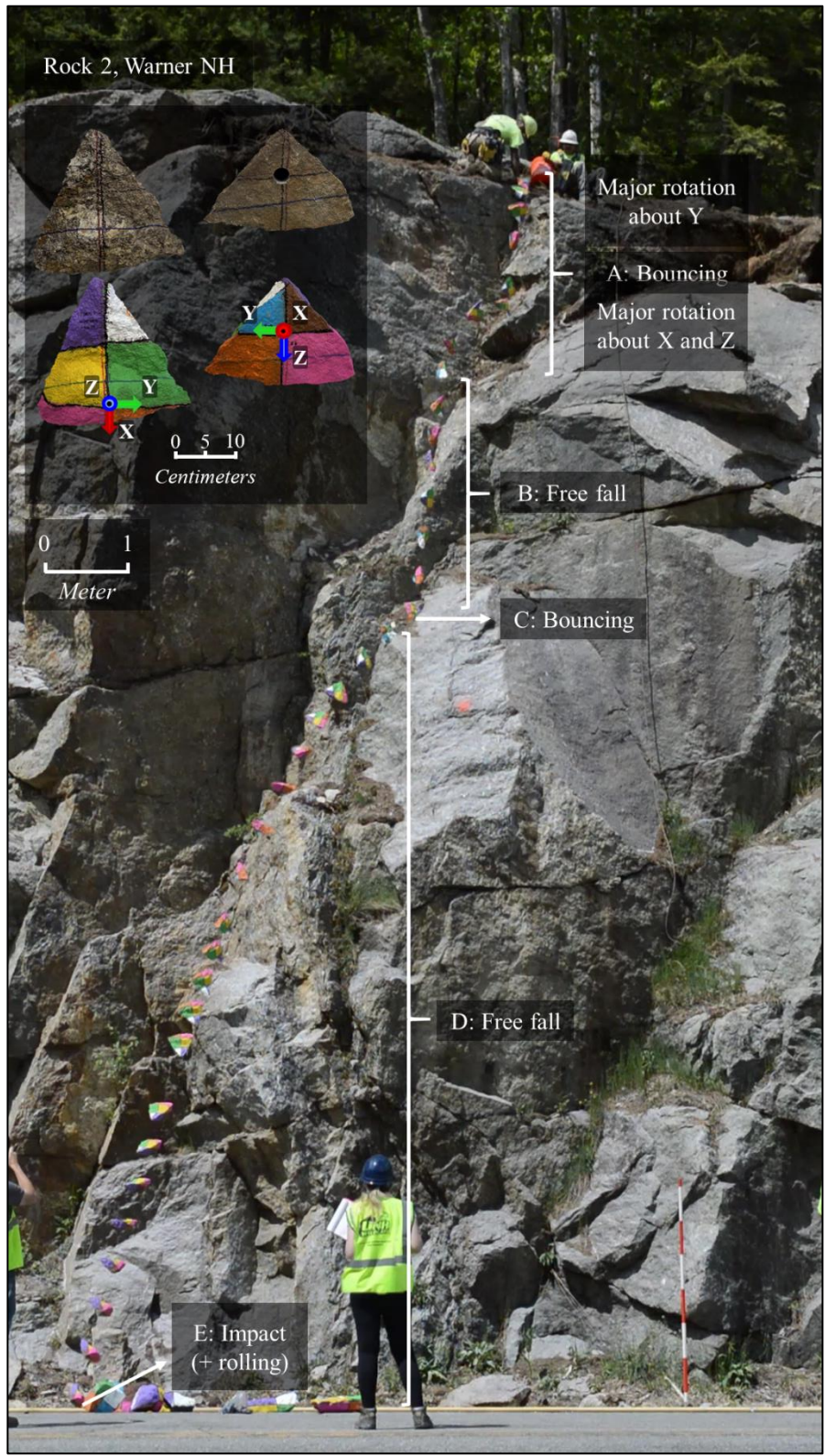
Figure B.80. Rockfall trajectory: rock 2, Warner NH.

Figure B.81. Smart Rock data: rock 2, Warner NH.
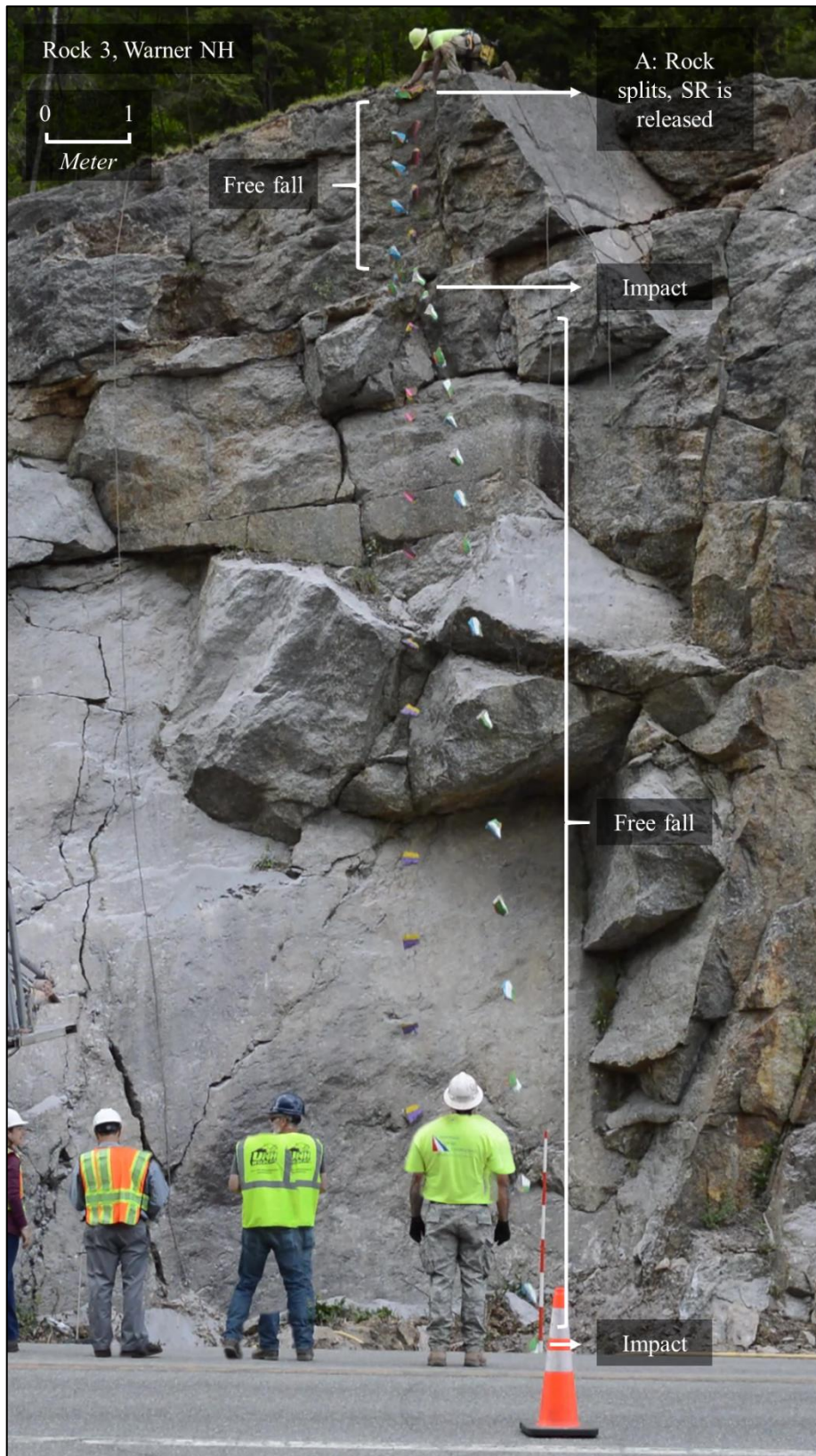
Figure B.82. Rockfall trajectory: rock 3, Warner NH.

Field Rockfall — Rock 3, Warner/NH

SR number: 5. Date: 02-Jun-2020.

Mass: 6.67 kg. I_{XX}: NaN kg.m^2. I_{YY}: NaN kg.m^2. I_{ZZ}: NaN kg.m^2.

Width (X): 0.07 m. Length (Y): 0.26 m. Height (Z): 0.12 m. Shape: Elongated.

Runout distance: 1.5 m from slope toe.
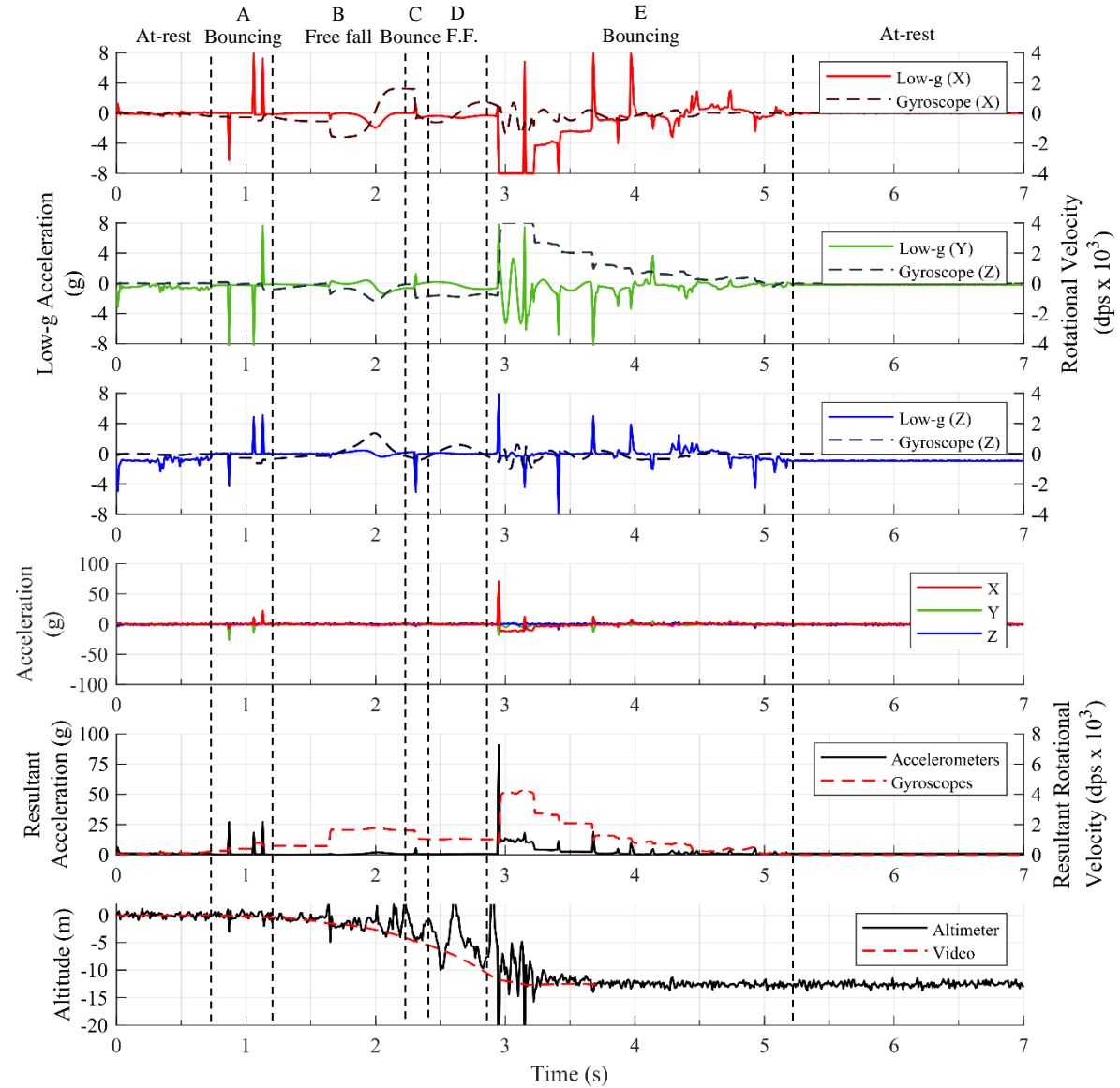
Drop height: 15.2 m. Altimeter hoisting: 15 m.
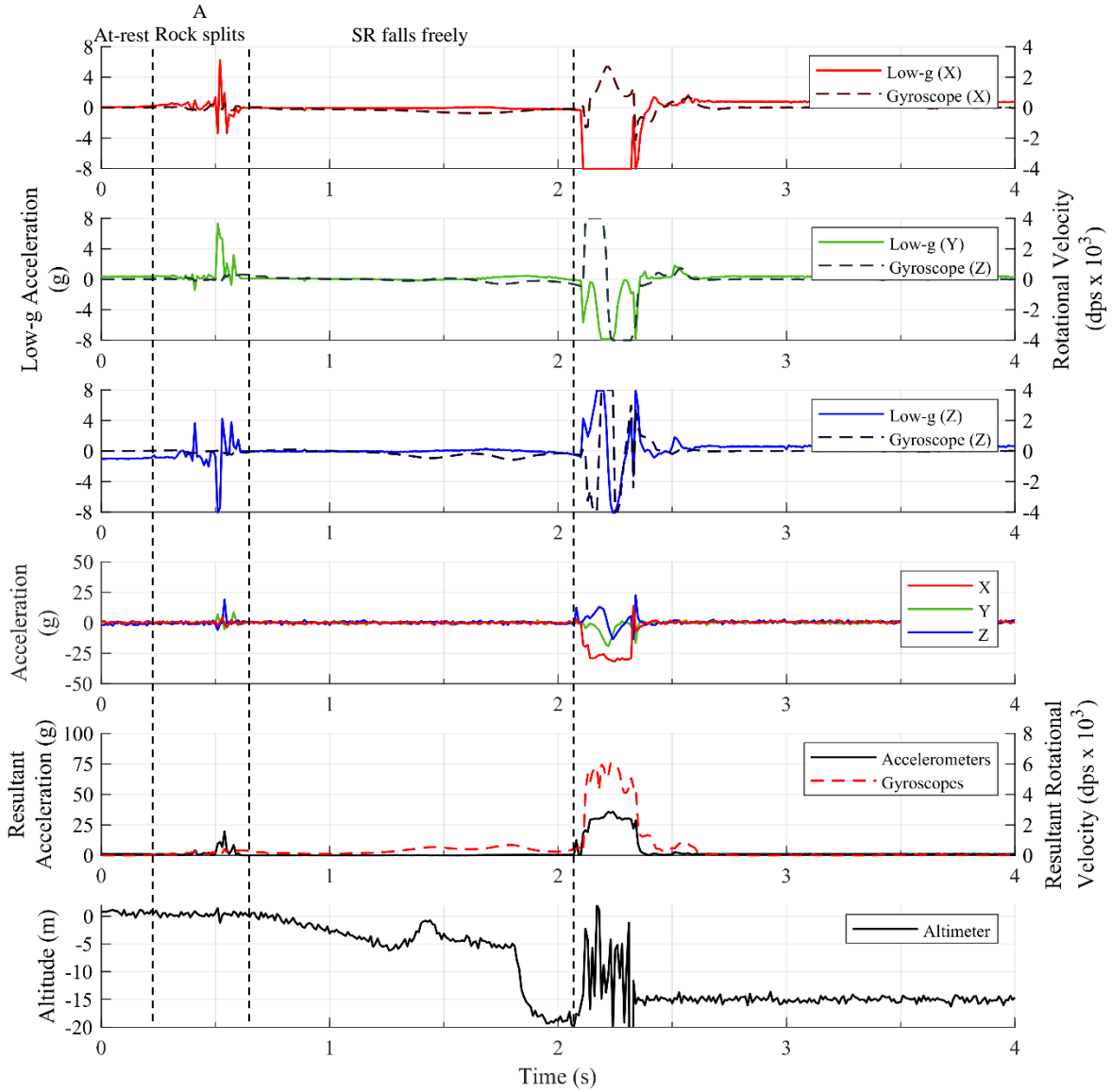

Figure B.83. Smart Rock data: rock 3, Warner NH.
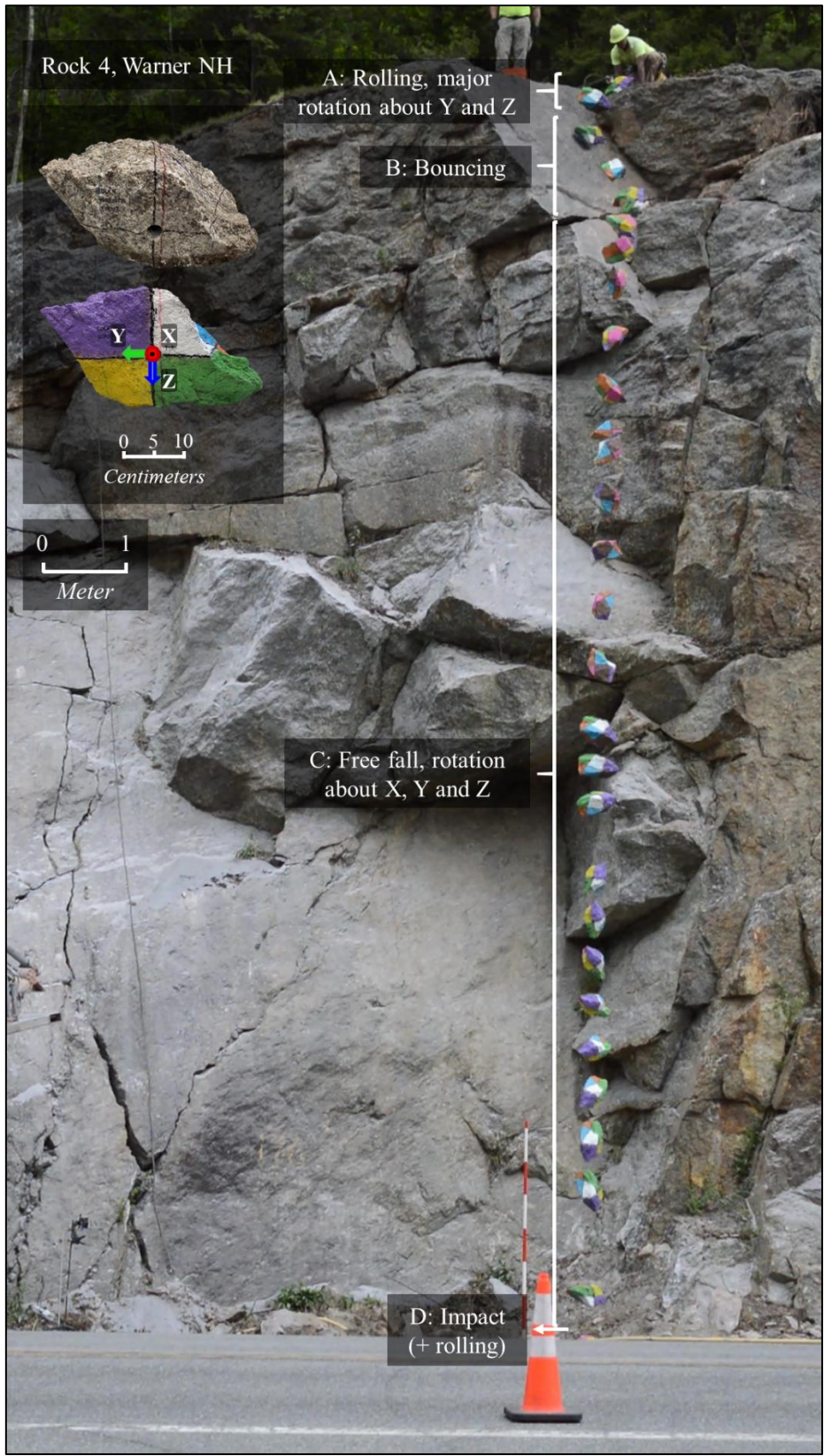
Figure B.84. Rockfall trajectory: rock 4, Warner NH.

411
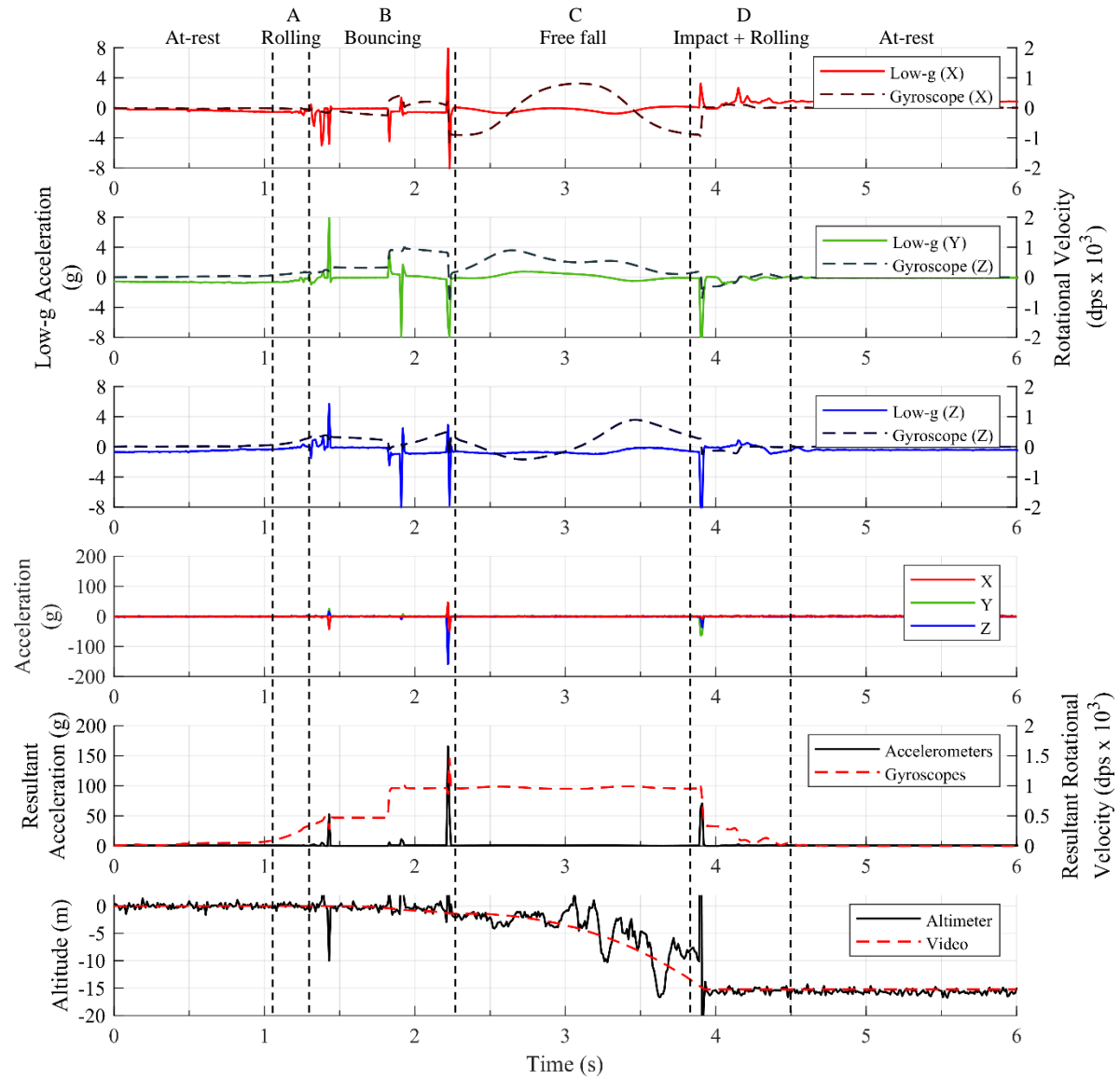
Figure B.85. Smart Rock data: rock 4, Warner NH.
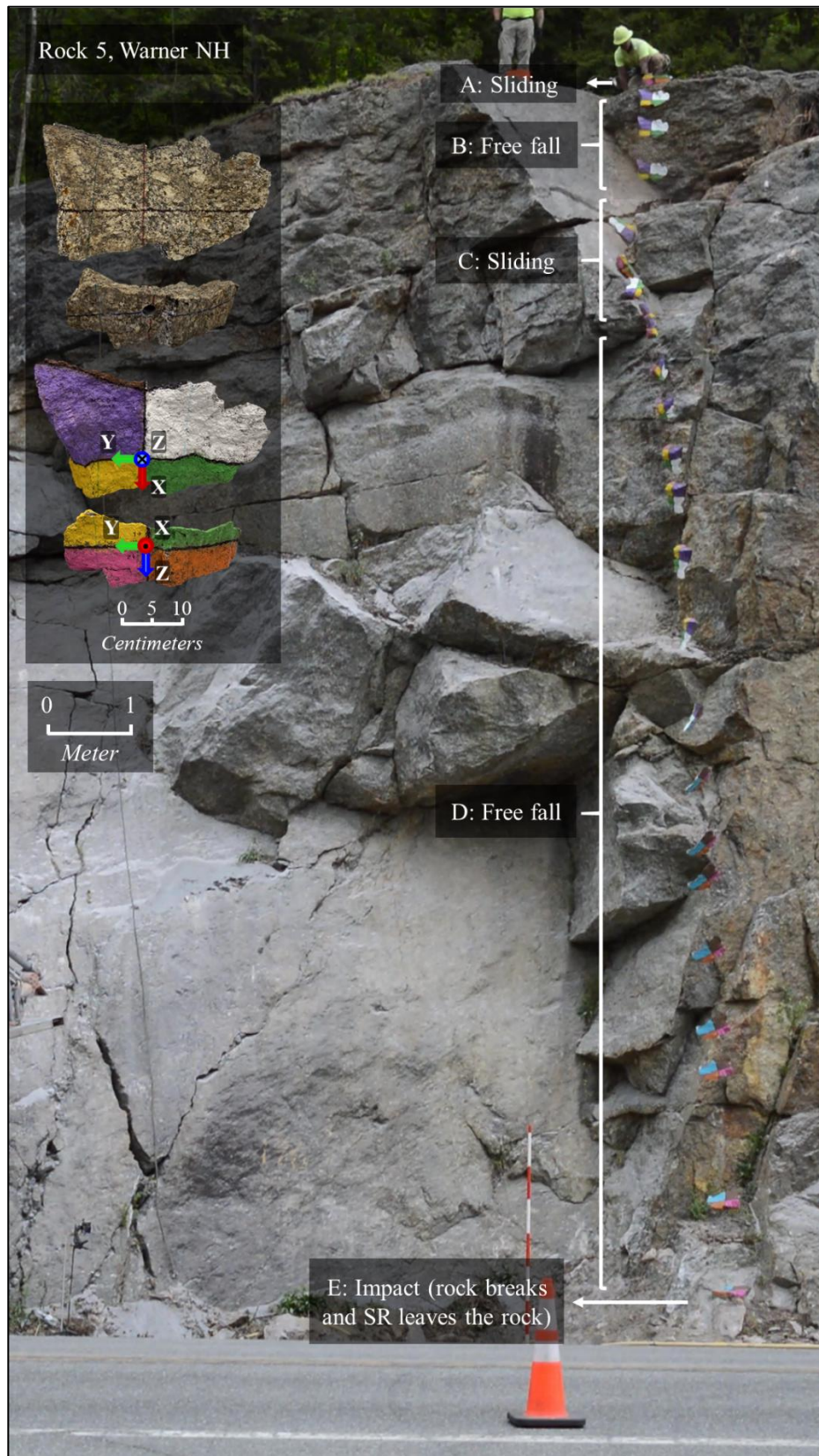
Figure B.86. Rockfall trajectory: rock 5, Warner NH.

413

Field Rockfall — Rock 5, Warner/NH

SR number: 3. Date: 02-Jun-2020.

Mass: 10.45 kg. I_{XX}: 0.111 kg.m^2. I_{YY}: 0.027 kg.m^2. I_{ZZ}: 0.129 kg.m^2.

Width (X): 0.16 m. Length (Y): 0.35 m. Height (Z): 0.07 m. Shape: Very Elongated.

Runout distance: 1.7 m from slope toe.

Drop height: 15.2 m. Altimeter hoisting: 15.5 m.
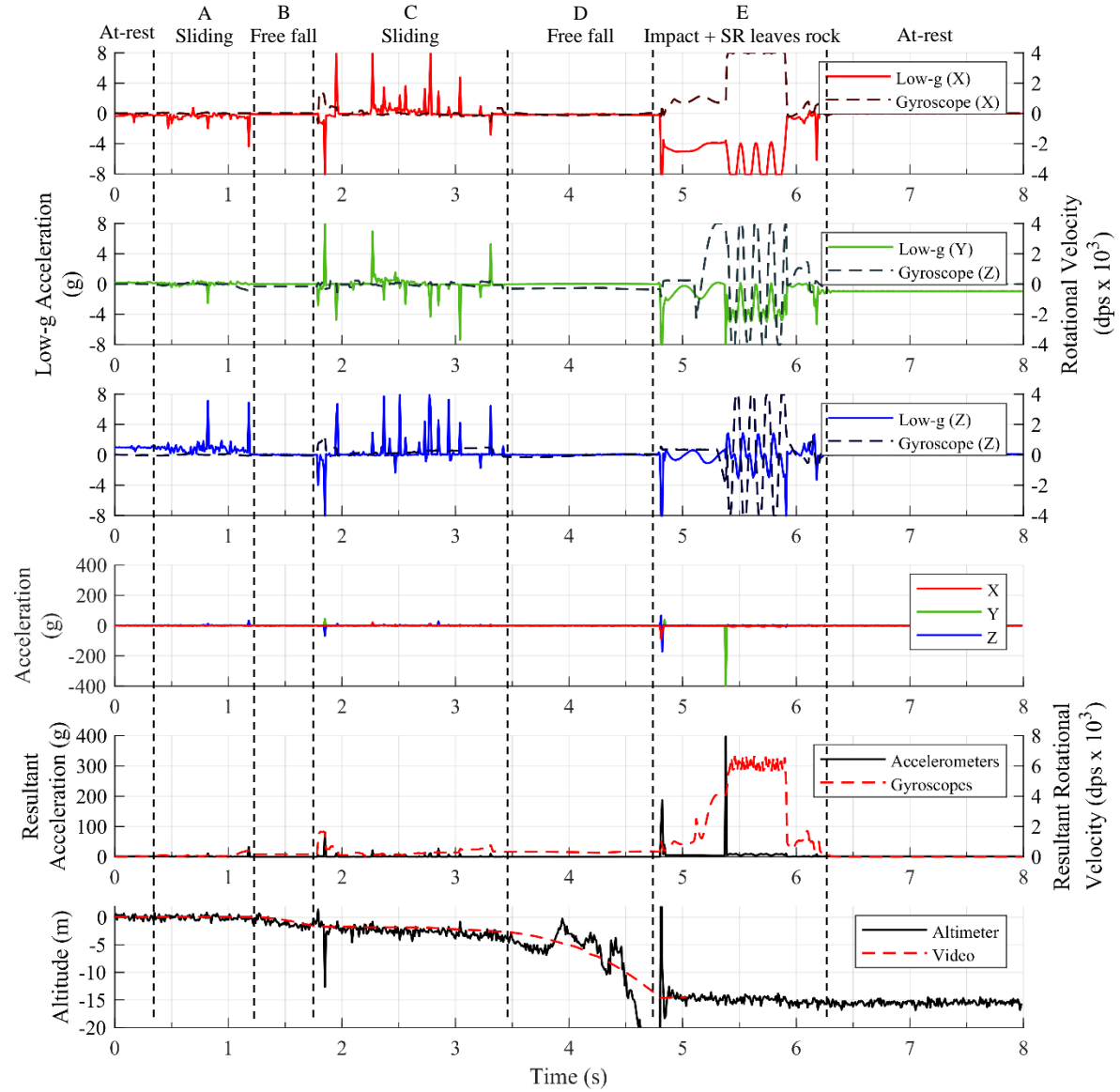
Figure B.87. Smart Rock data: rock 5, Warner NH.

414

B.9. Windham, NH

Figure B.88. Rockfall trajectory: rock 1, Windham NH.

Field Rockfall — Rock 1, Windham/NH

SR number: 1. Date: 29-Oct-2020.

Mass: 5.09 kg. I_{XX}: 0.015 kg.m^2. I_{YY}: 0.011 kg.m^2. I_{ZZ}: 0.019 kg.m^2.

Width (X): 0.16 m. Length (Y): 0.2 m. Height (Z): 0.09 m. Shape: Bladed.

Runout distance: 4.4 m from slope toe.

Drop height: 11.2 m. Altimeter hoisting: 11.1 m.
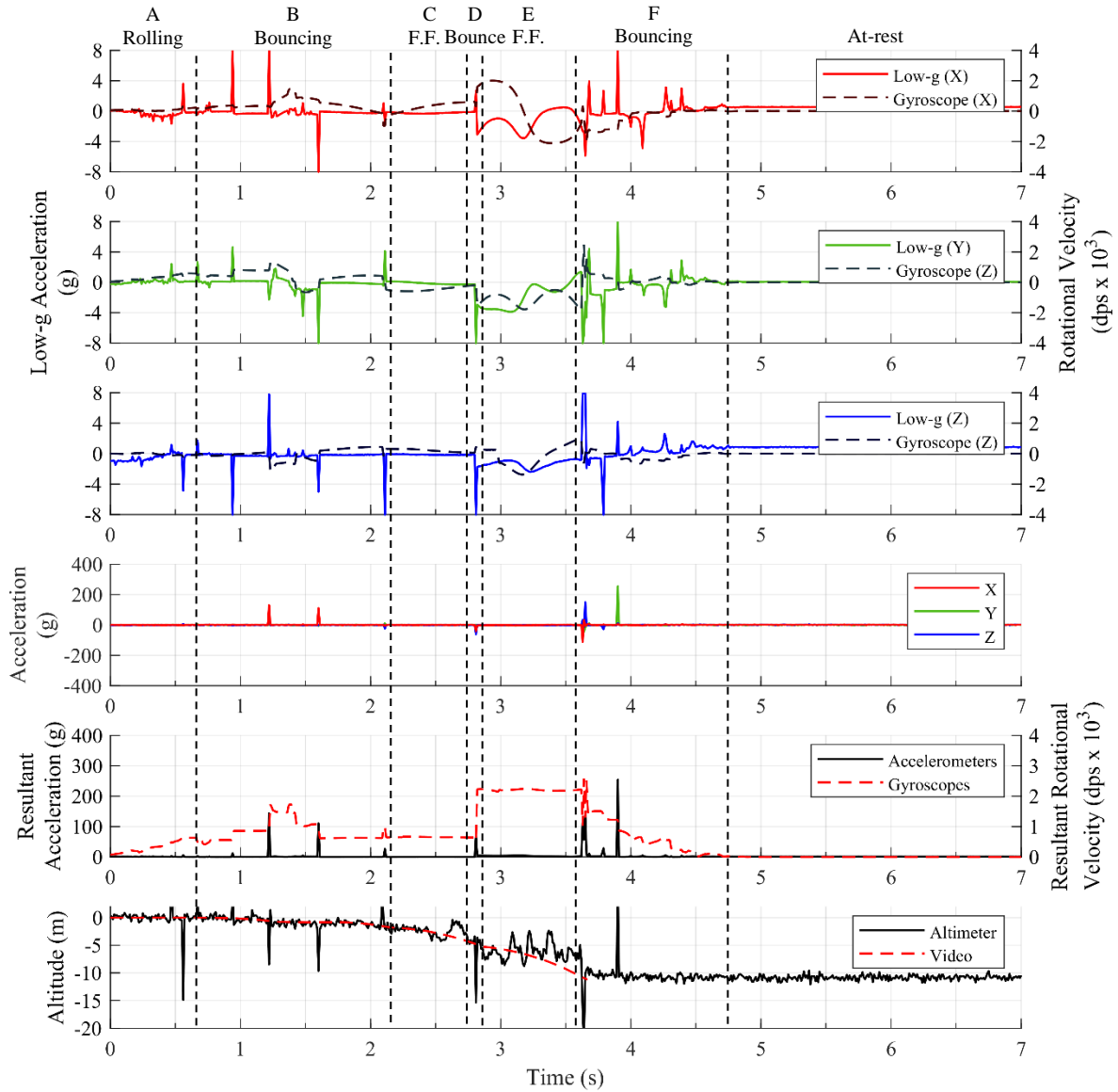
Figure B.89. Smart Rock data: rock 1, Windham NH.
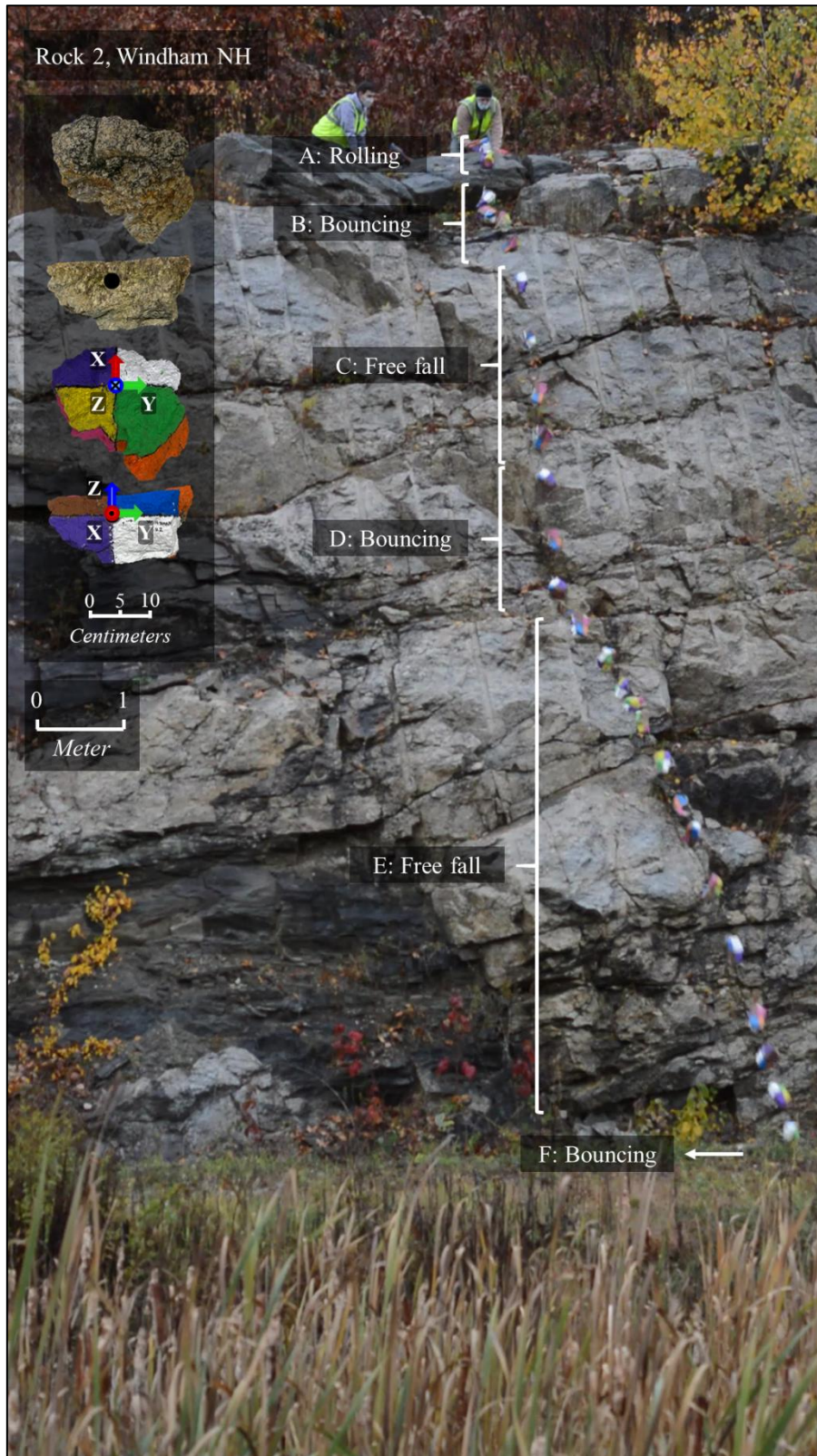
Figure B.90. Rockfall trajectory: rock 2, Windham NH.

417
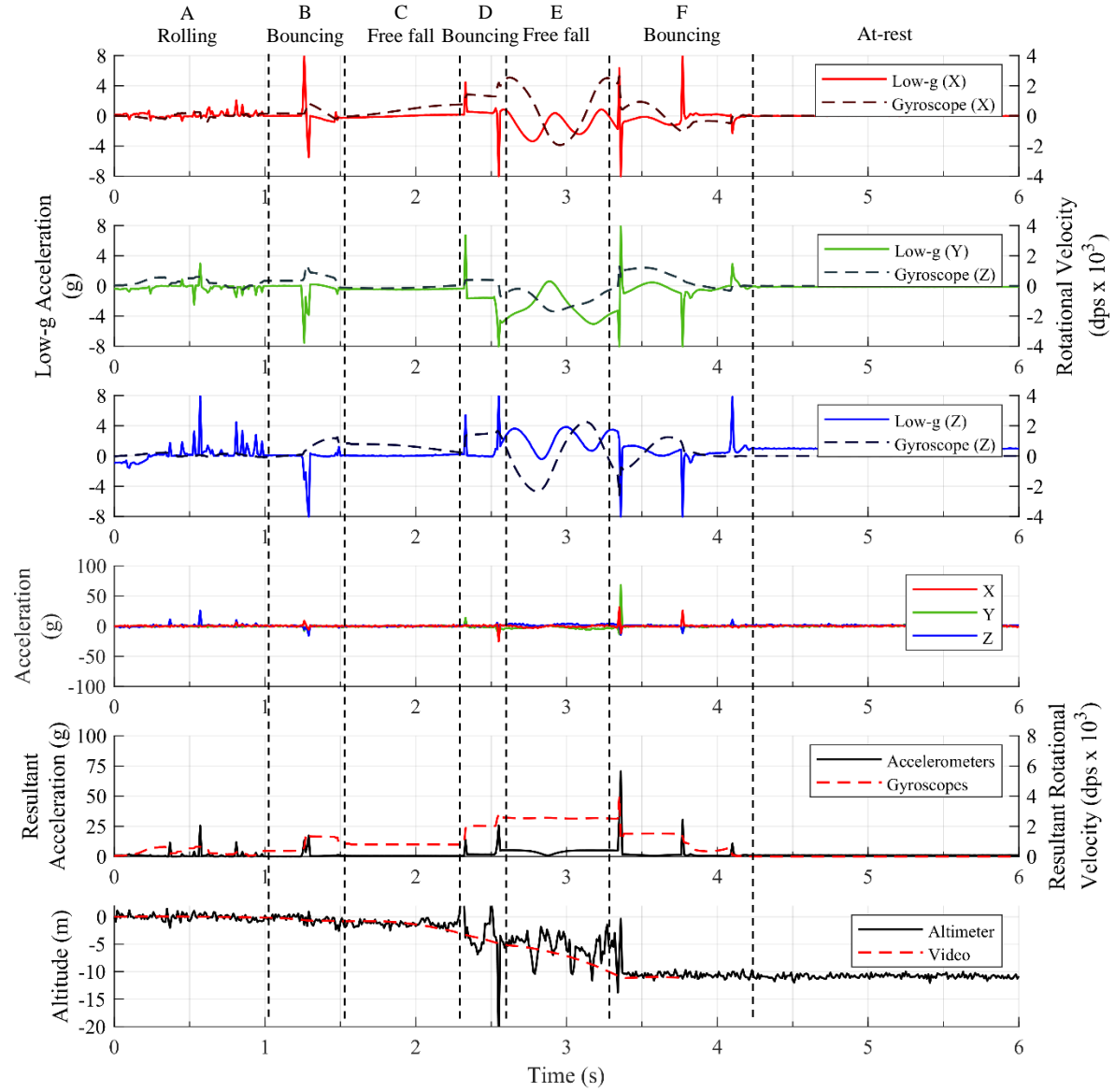
Figure B.91. Smart Rock data: rock 2, Windham NH.
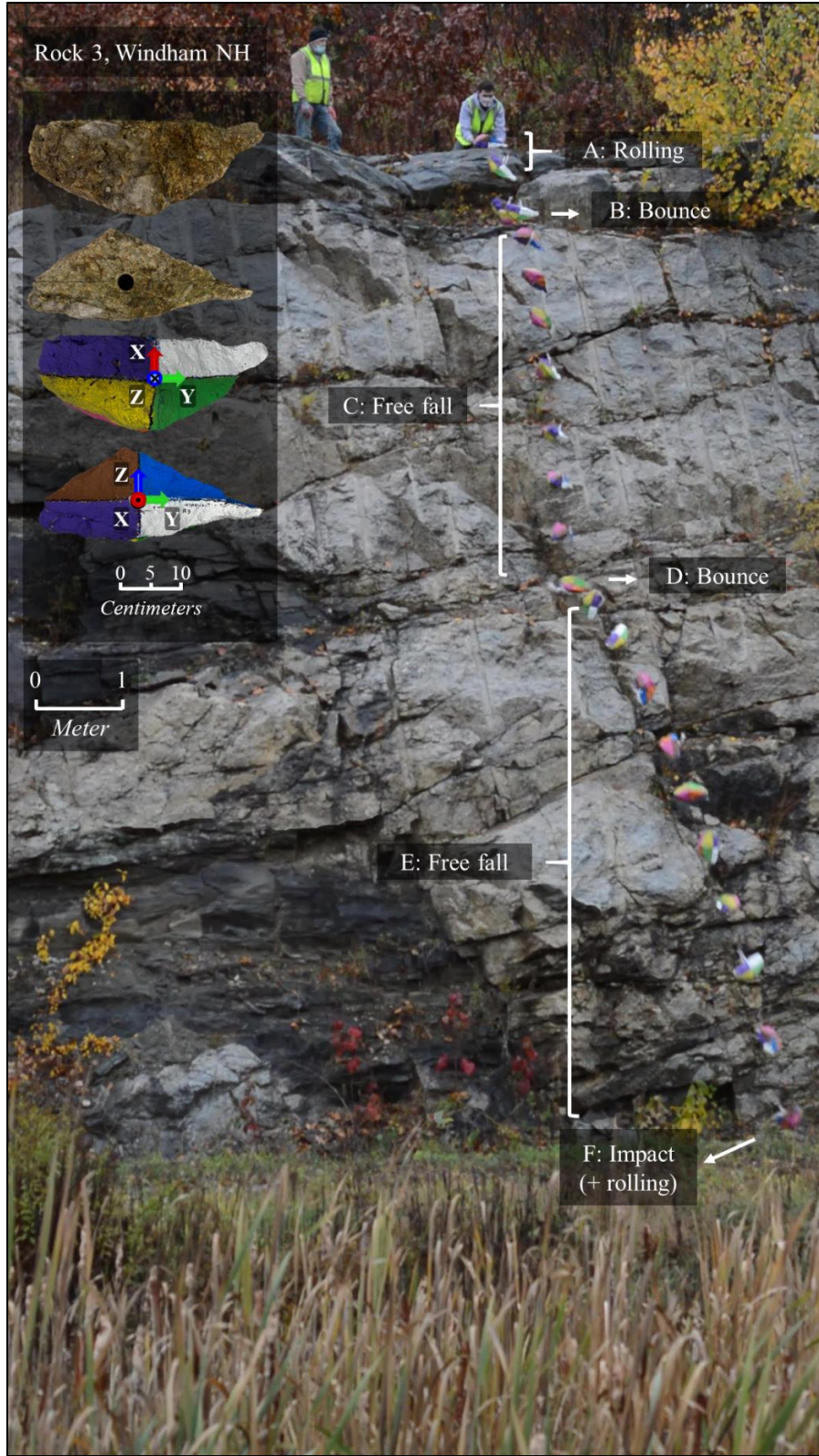
Figure B.92. Rockfall trajectory: rock 3, Windham NH.
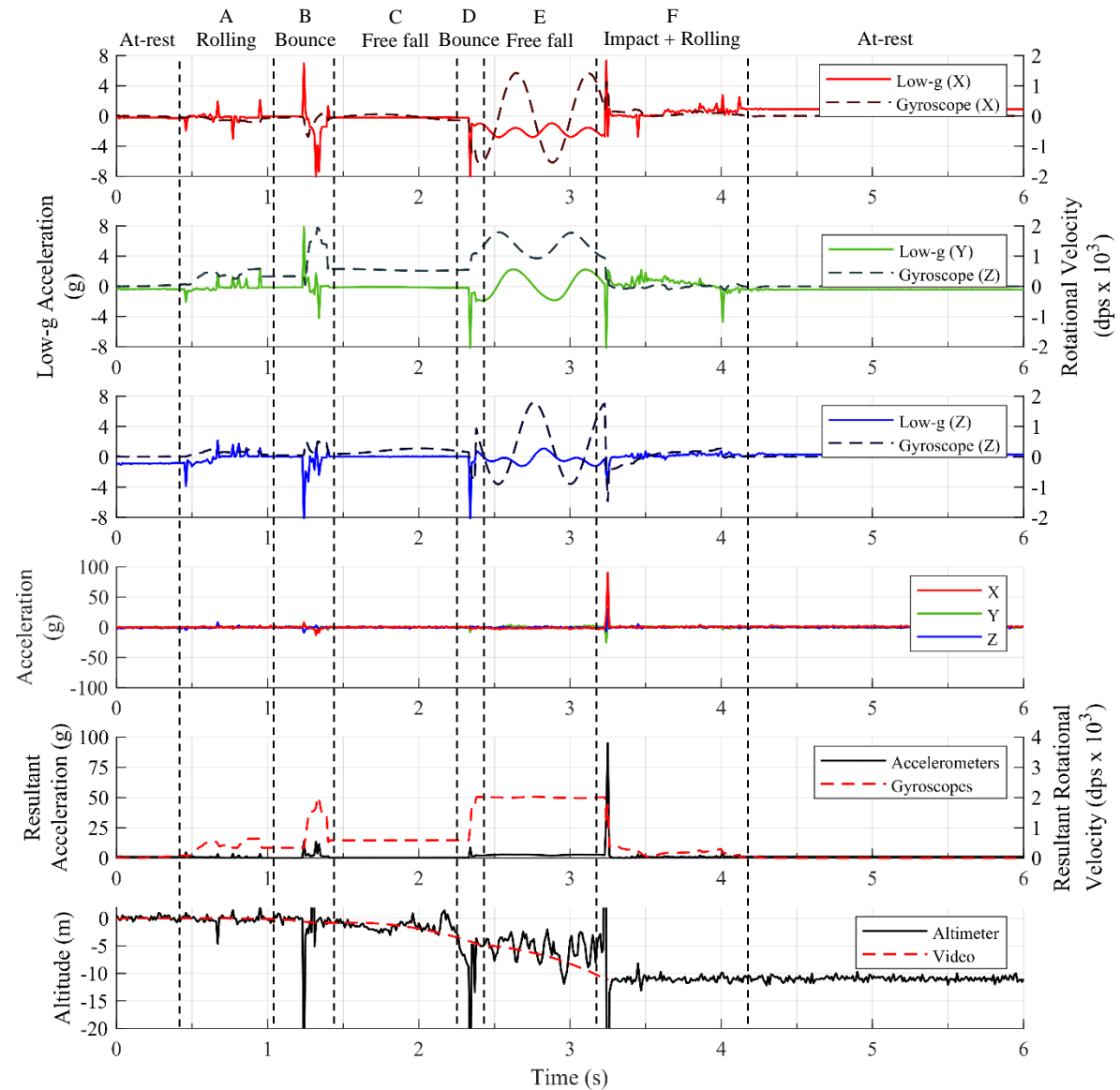
Figure B.93. Smart Rock data: rock 3, Windham NH.
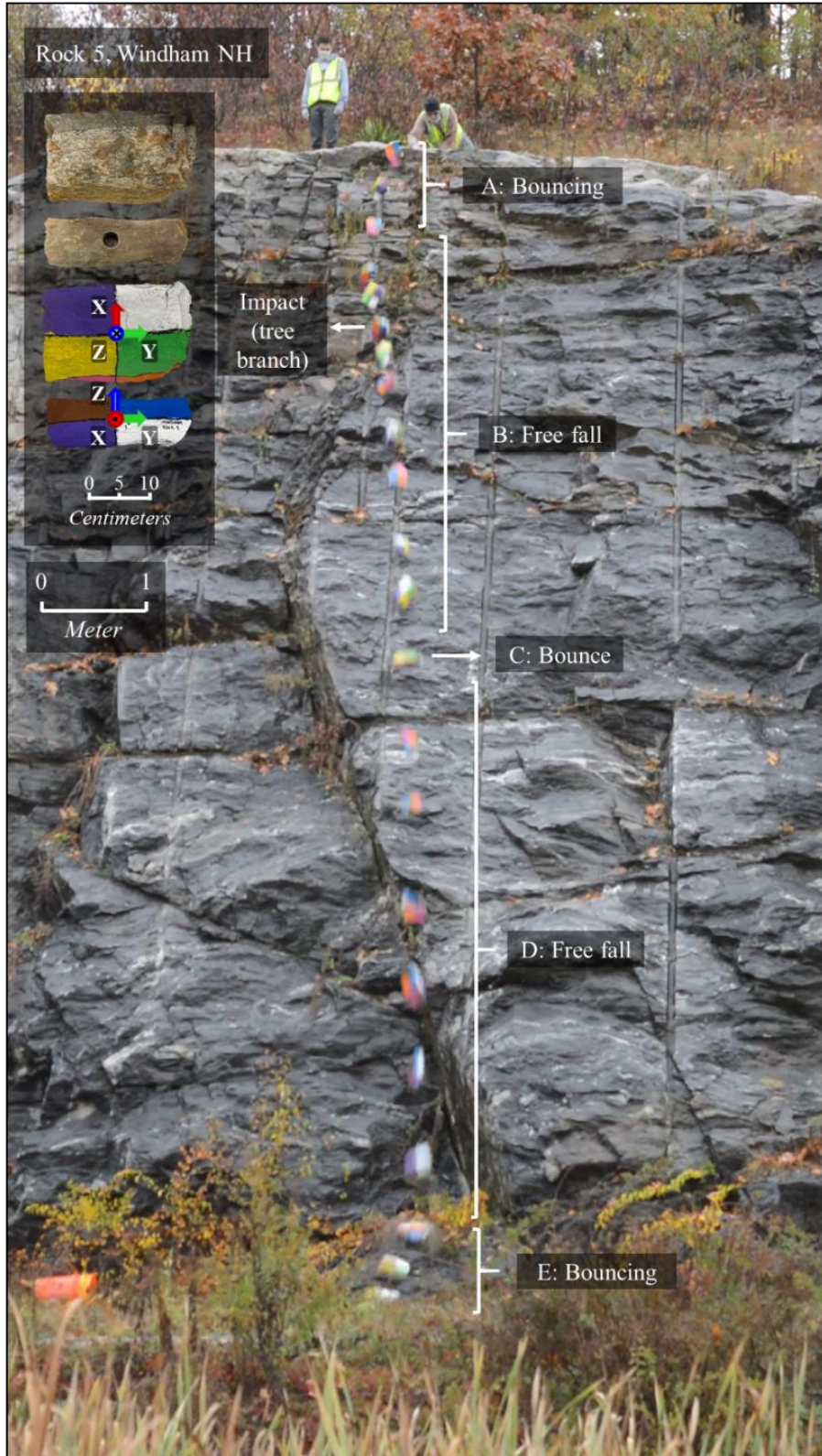
Figure B.94. Rockfall trajectory: rock 5, Windham NH.

Figure B.95. Smart Rock data: rock 5, Windham NH.
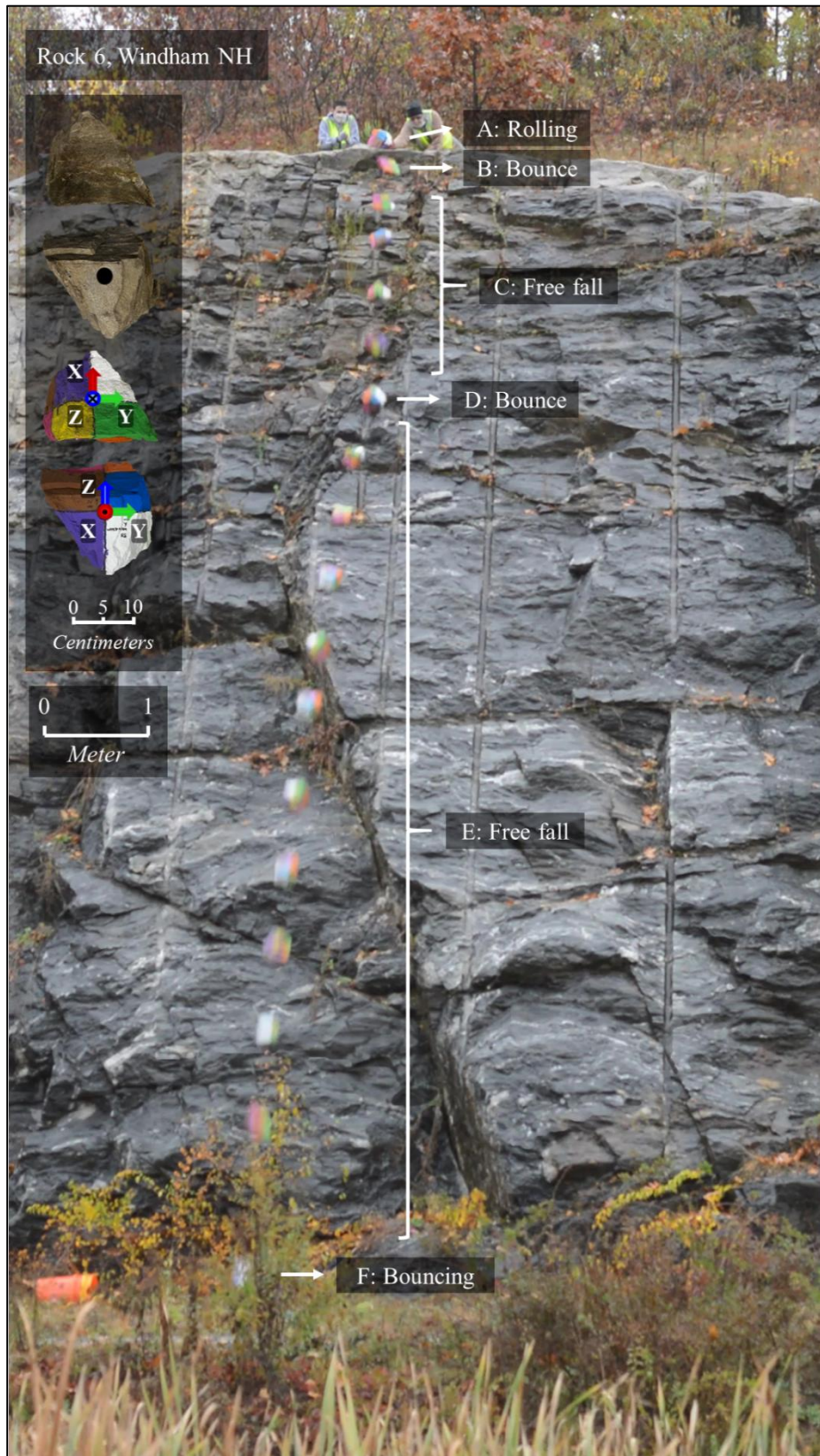
Figure B.96. Smart Rock data: rock 6, Windham NH.

423

Field Rockfall — Rock 6, Windham/NH

SR number: 4. Date: 29-Oct-2020.

Mass: 10.4 kg. I_{XX}: 0.052 kg.m^2. I_{YY}: 0.043 kg.m^2. I_{ZZ}: 0.051 kg.m^2.

Width (X): 0.17 m. Length (Y): 0.21 m. Height (Z): 0.22 m. Shape: Compact.

Runout distance: 1.9 m from slope toe.

Drop height: 12.6 m. Altimeter hoisting: 12.4 m.
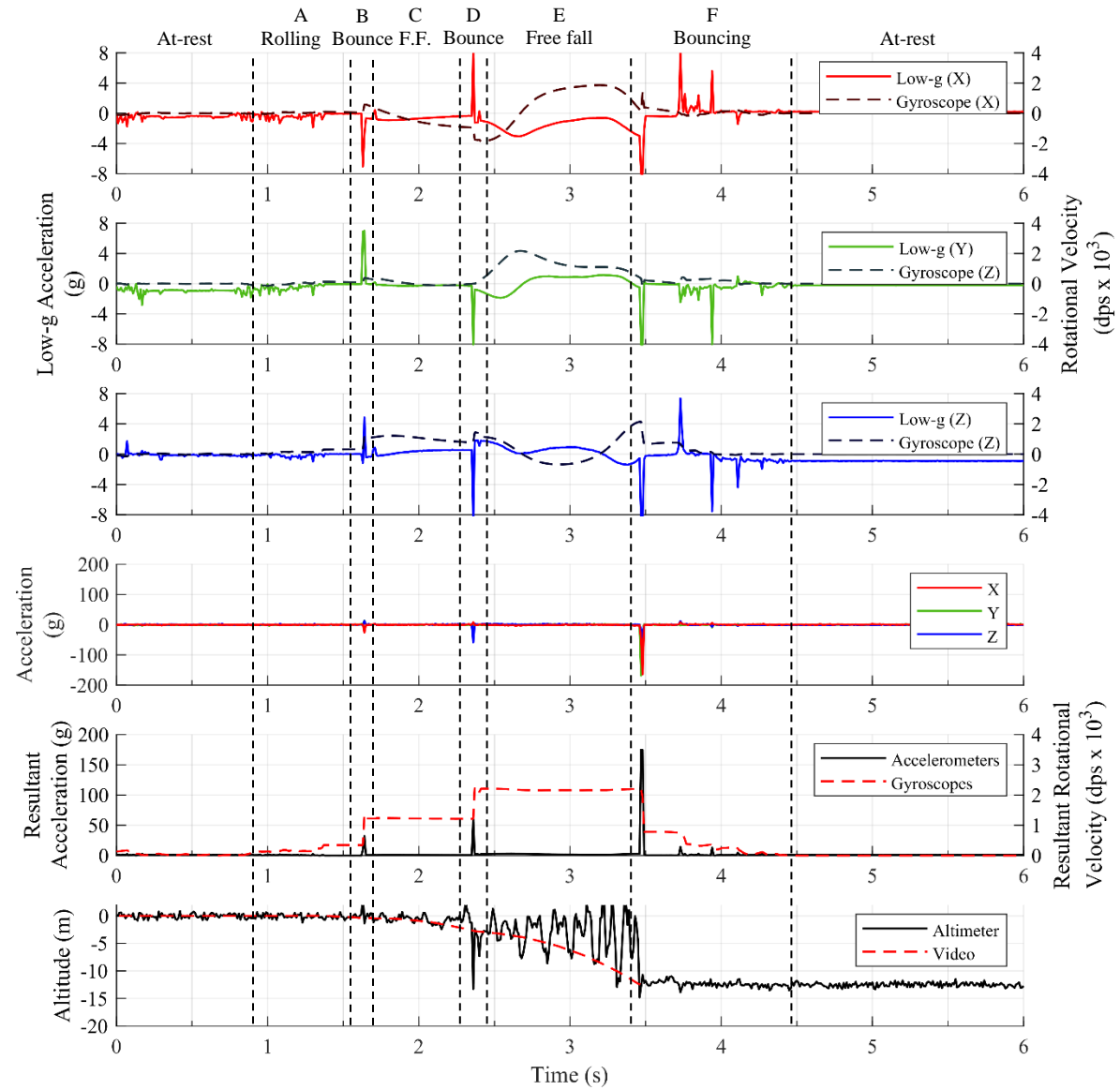
Figure B.97. Smart Rock data: rock 6, Windham NH.

APPENDIX C:

SMART ROCK DATA OUTPUT OF LABORATORY EXPERIMENTS

C.1. Tests on sand

C.1.1. Cubic block

Laboratory test — Cubic block — Sand (0º slope), test 1

SR number: 6. Date: 25-Feb-2021.

Mass: 1.096 kg. I_{XX}: 0.001 kg.m^2. I_{YY}: 0.0011 kg.m^2. I_{ZZ}: 0.0012 kg.m^2.

Width (X): 0.086 m. Length (Y): 0.074 m. Height (Z): 0.072 m. Shape: Compact.
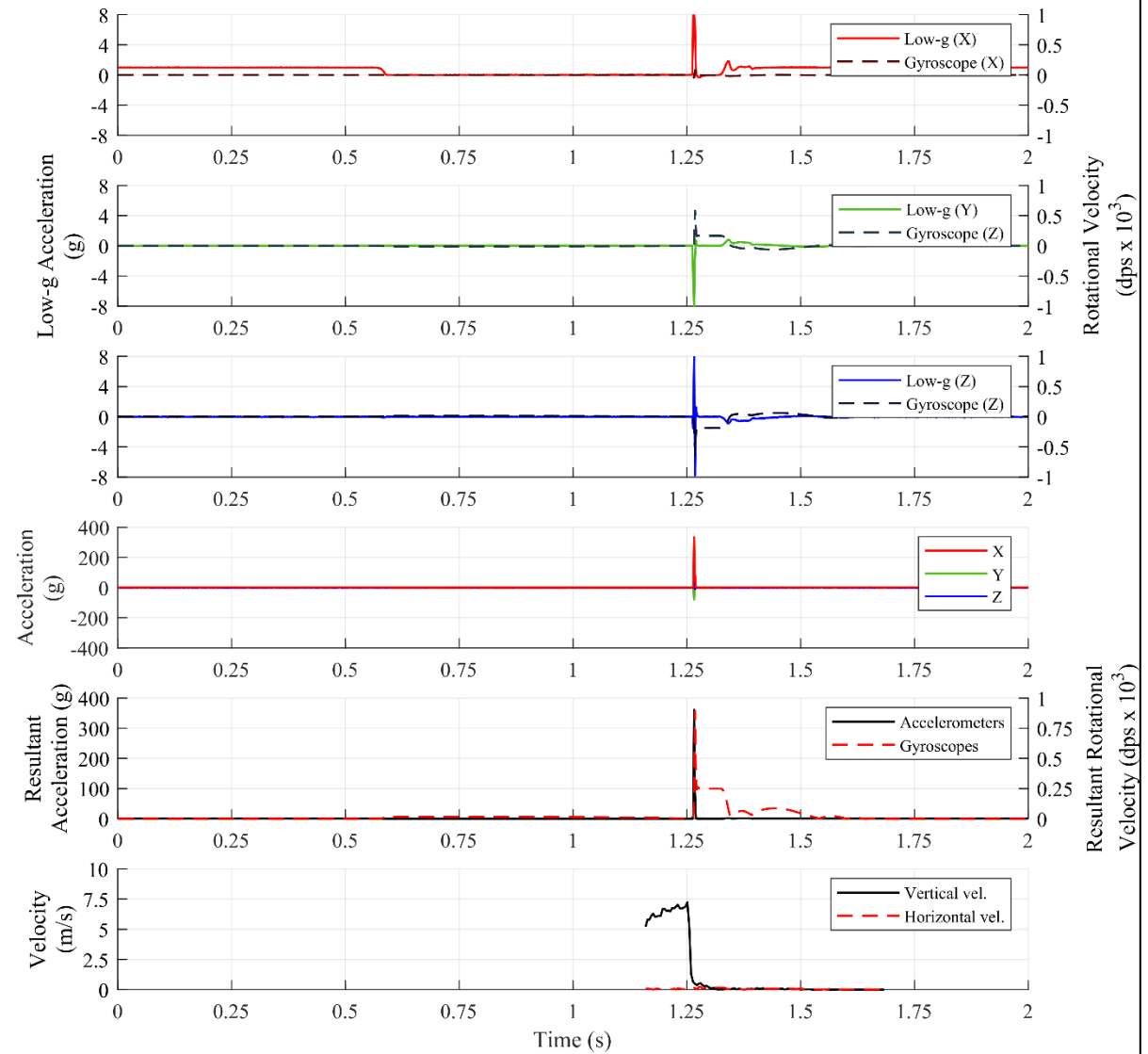
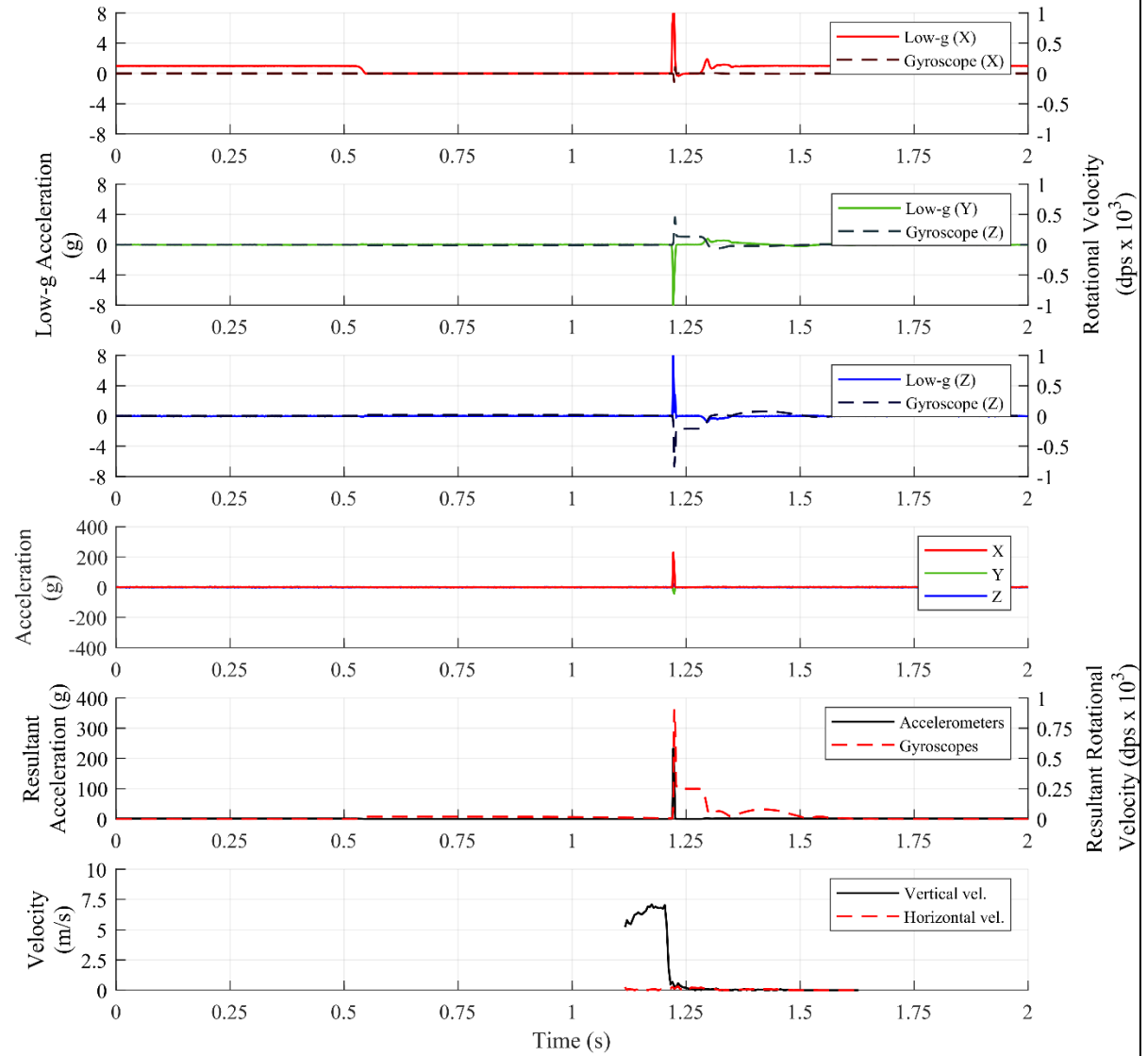Embedment depth: 10.6 mm.

Drop height: 2.2 m.
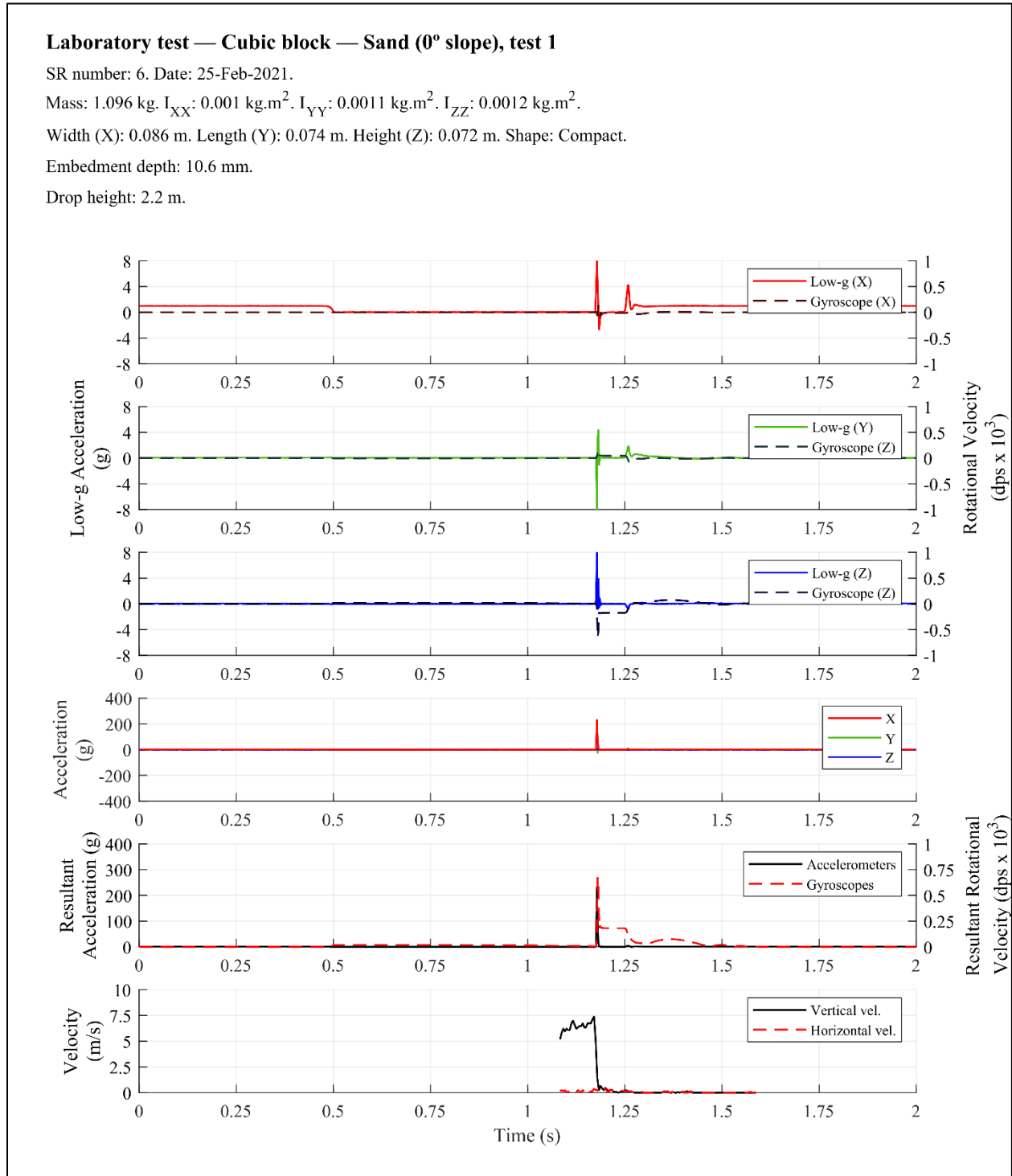
Figure C.1. Smart Rock data: test 1, cubic block, tests on sand.

Laboratory test — Cubic block — Sand (0º slope), test 2

SR number: 6. Date: 25-Feb-2021.

Mass: 1.096 kg. I_{XX}: 0.001 kg.m^2. I_{YY}: 0.0011 kg.m^2. I_{ZZ}: 0.0012 kg.m^2.

Width (X): 0.086 m. Length (Y): 0.074 m. Height (Z): 0.072 m. Shape: Compact.
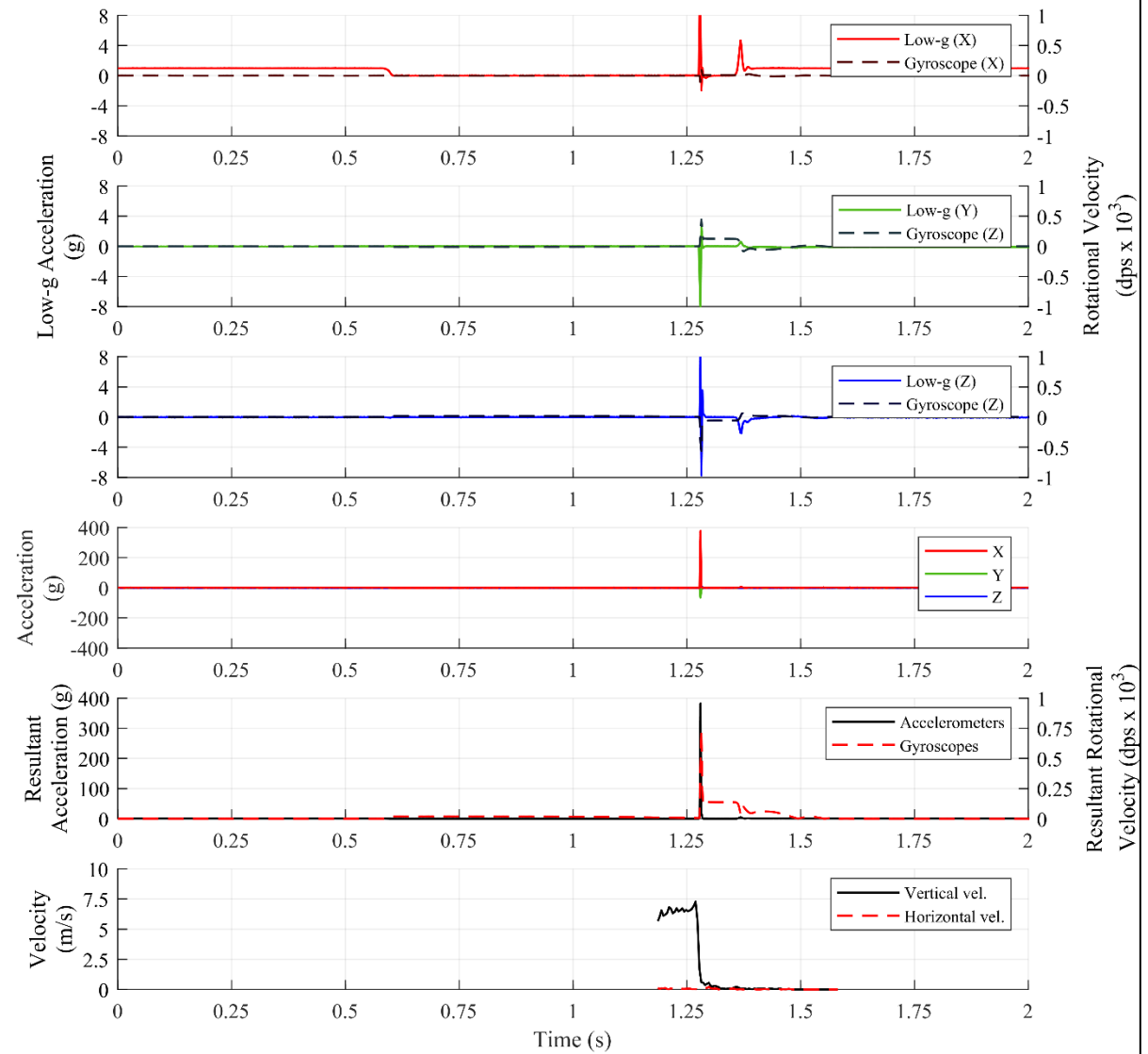
Embedment depth: 12.1 mm.
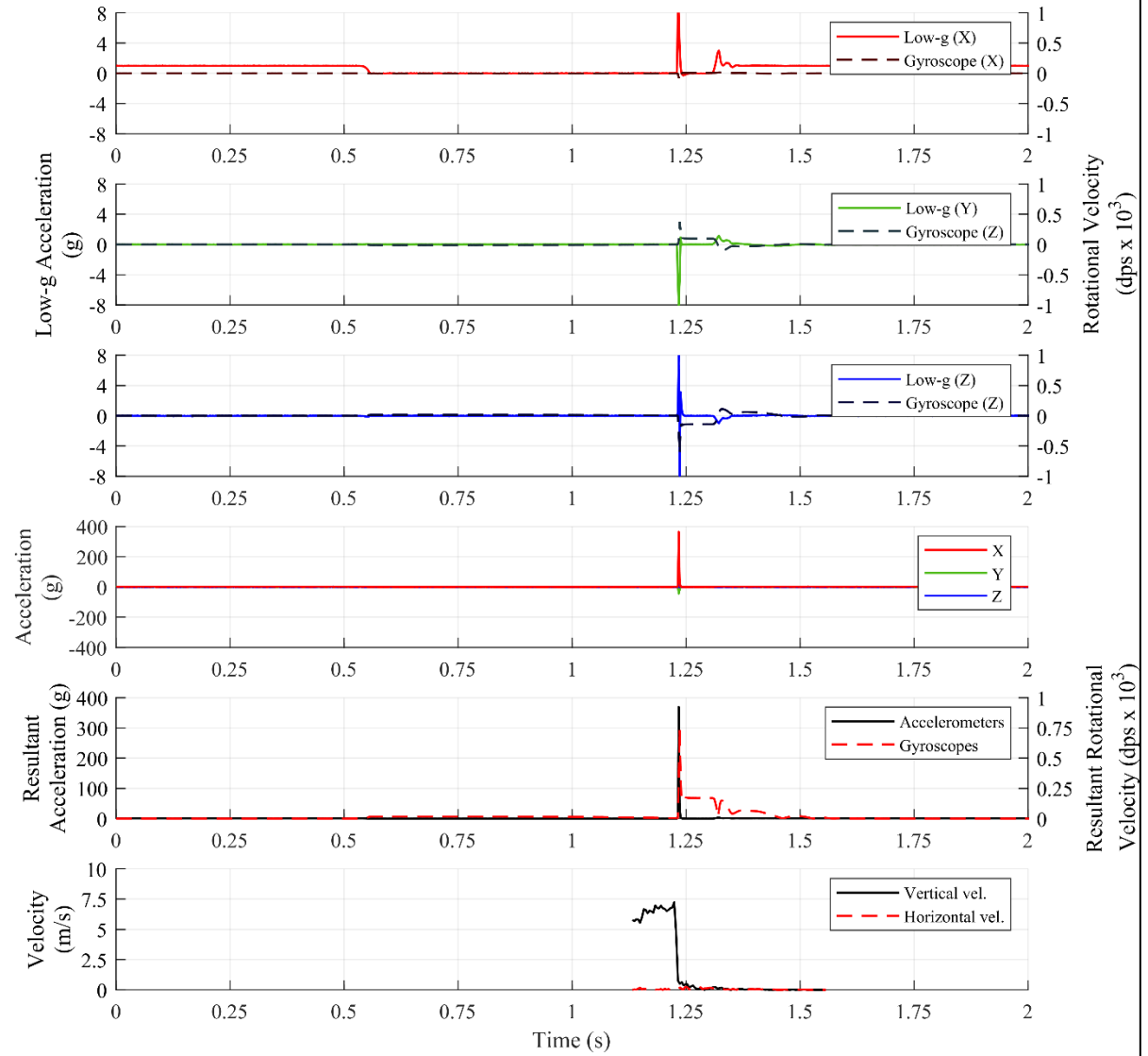
Drop height: 2.2 m.
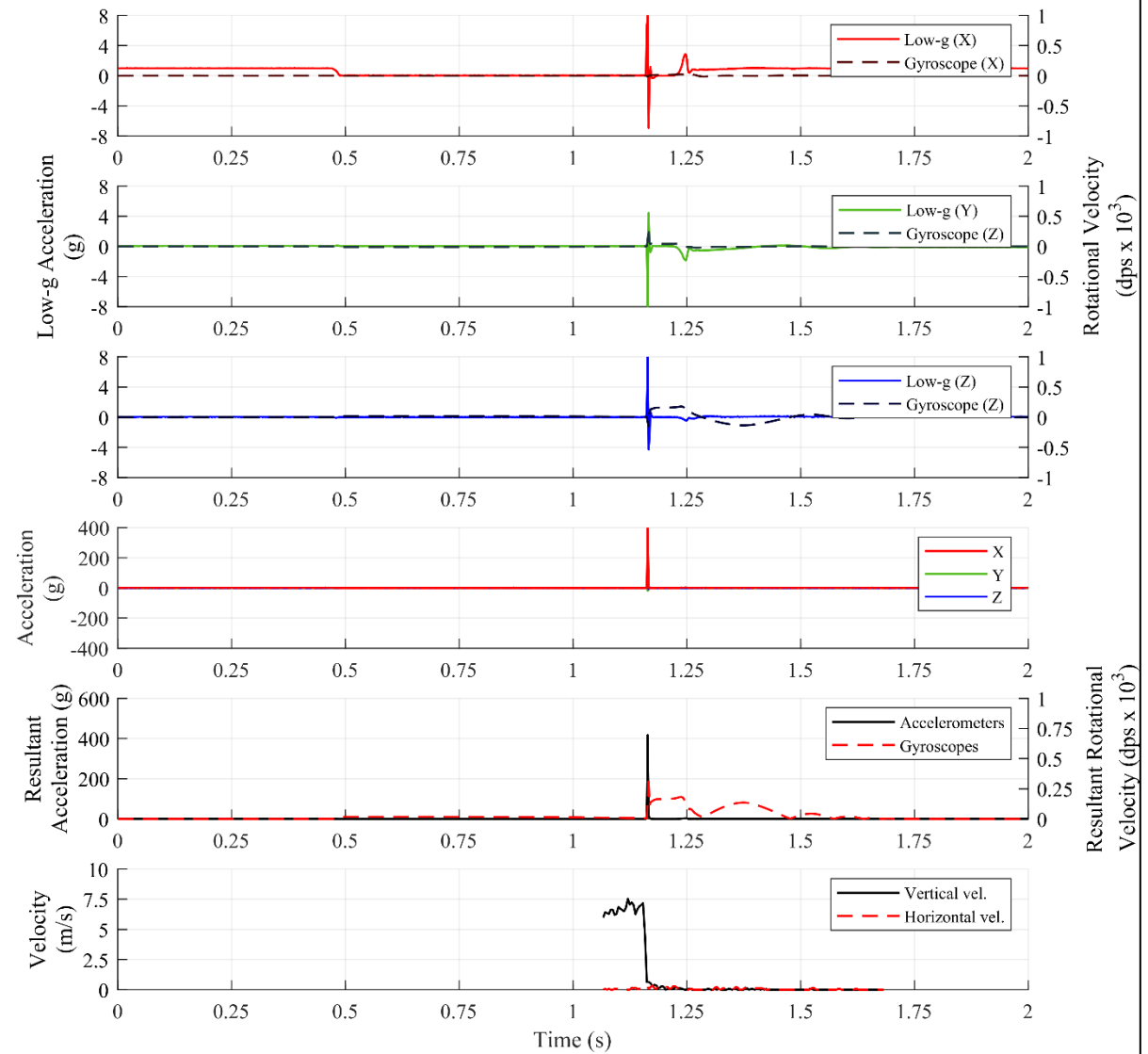
Figure C.2. Smart Rock data: test 2, cubic block, tests on sand.

Laboratory test — Cubic block — Sand (0º slope), test 3

SR number: 6. Date: 25-Feb-2021.

Mass: 1.096 kg. I_{XX}: 0.001 kg.m^2. I_{YY}: 0.0011 kg.m^2. I_{ZZ}: 0.0012 kg.m^2.

Width (X): 0.086 m. Length (Y): 0.074 m. Height (Z): 0.072 m. Shape: Compact.

Embedment depth: 12 mm.

Drop height: 2.2 m.
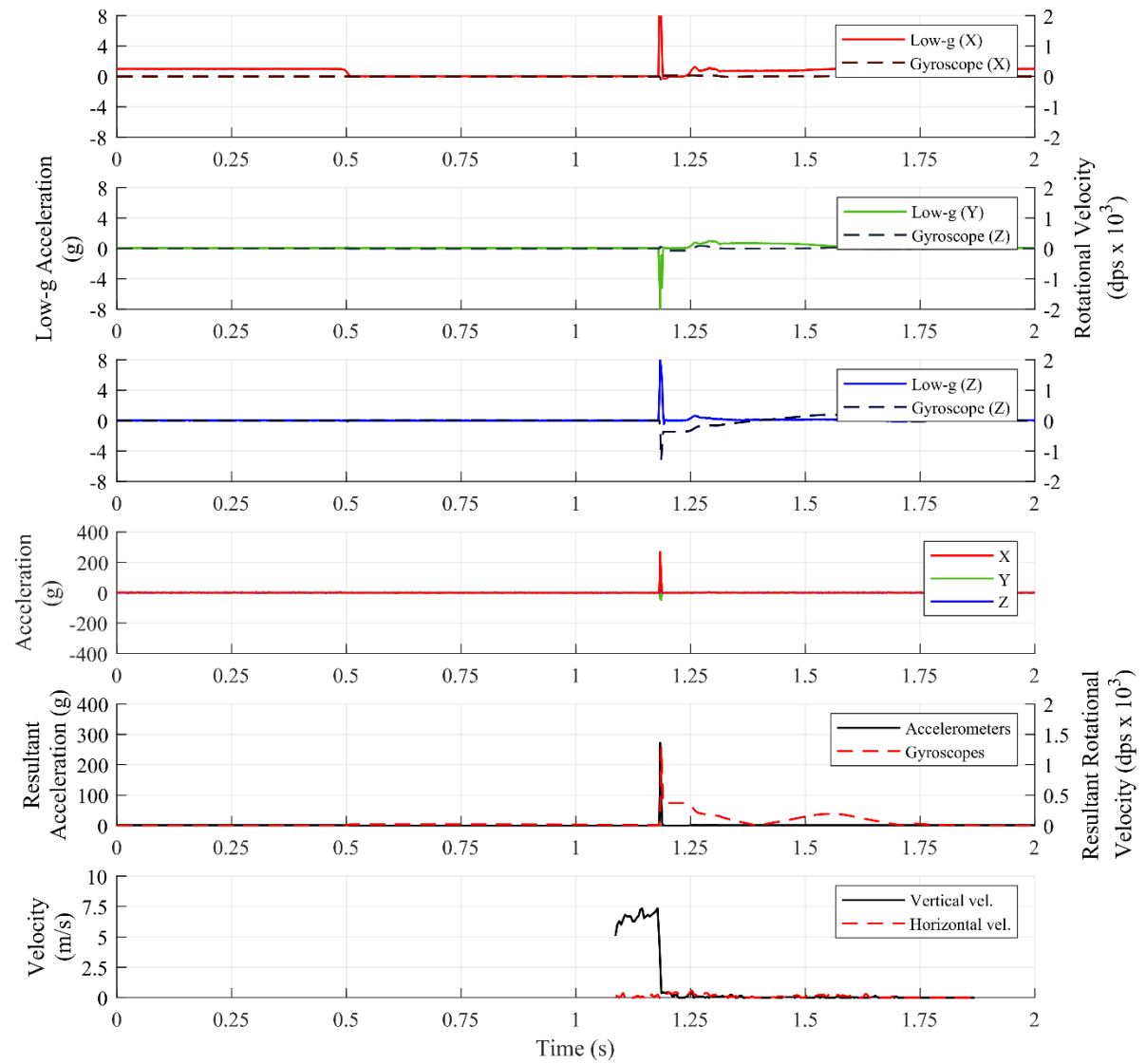
Figure C.3. Smart Rock data: test 3, cubic block, tests on sand.

Figure C.4. Smart Rock data: test 4, cubic block, tests on sand.

429

Figure C.5. Smart Rock data: test 5, cubic block, tests on sand.

Laboratory test — Cubic block — Sand (0º slope), test 6

SR number: 2. Date: 25-Feb-2021.

Mass: 1.096 kg. I_{XX}: 0.001 kg.m². I_{YY}: 0.0011 kg.m². I_{ZZ}: 0.0012 kg.m².

Width (X): 0.086 m. Length (Y): 0.074 m. Height (Z): 0.072 m. Shape: Compact.
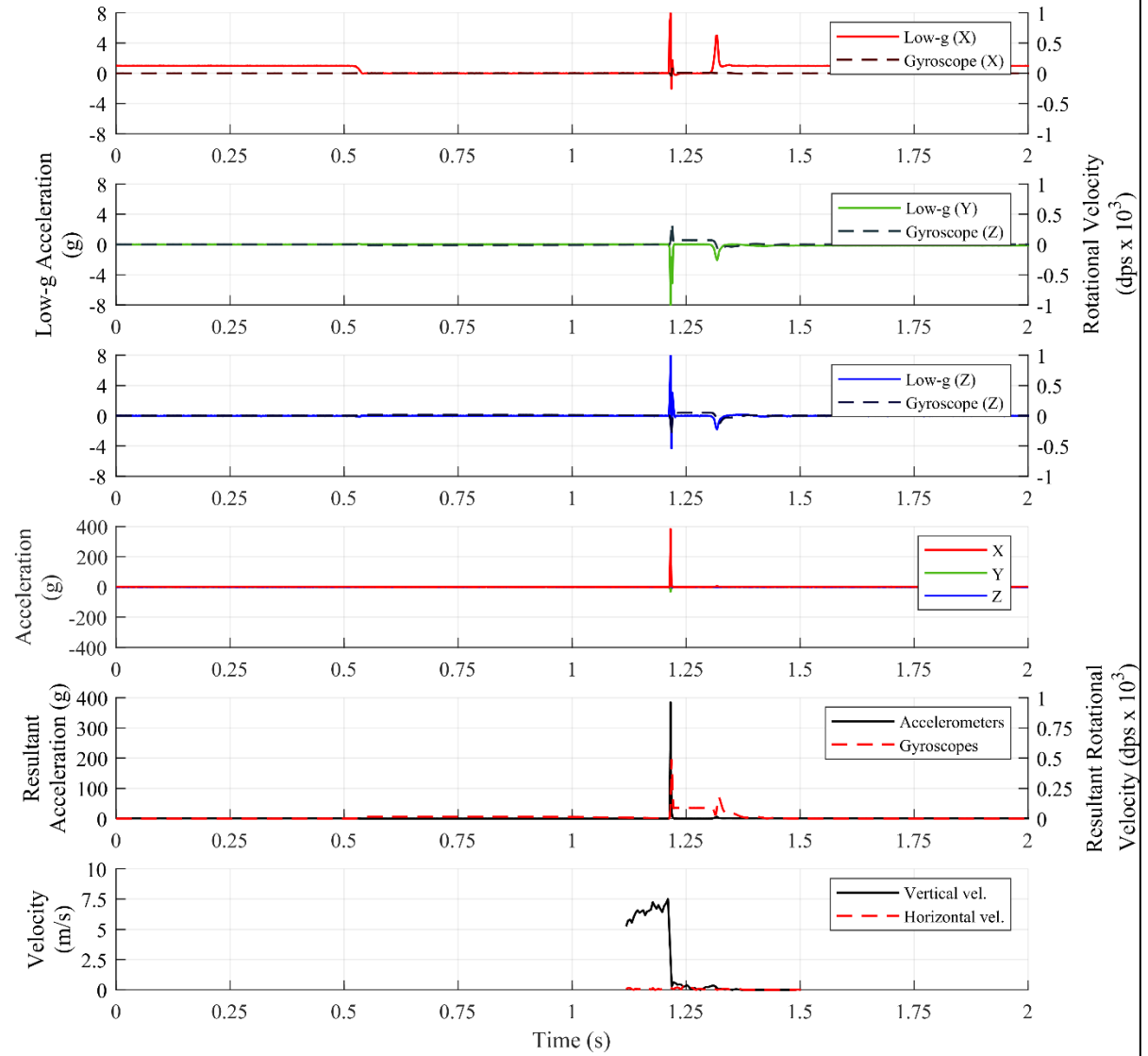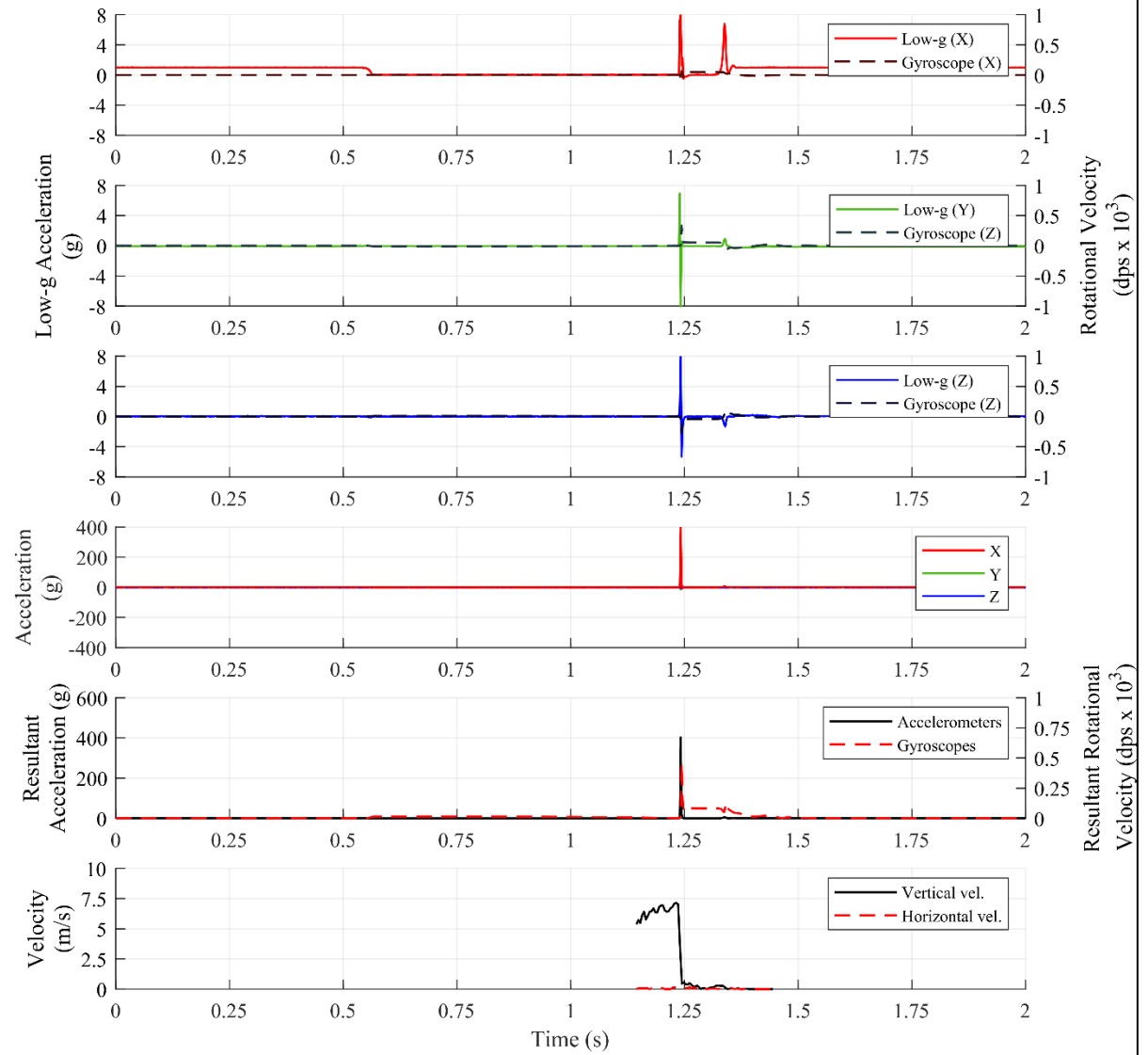
Embedment depth: 12.5 mm.

Drop height: 2.2 m.

Figure C.6. Smart Rock data: test 6, cubic block, tests on sand.

Laboratory test — Cubic block — Sand (0° slope), test 7

SR number: 2. Date: 25-Feb-2021.

Mass: 1.096 kg. I_{XX}: 0.001 kg.m^2. I_{YY}: 0.0011 kg.m^2. I_{ZZ}: 0.0012 kg.m^2.

Width (X): 0.086 m. Length (Y): 0.074 m. Height (Z): 0.072 m. Shape: Compact.

Embedment depth: 7.76 mm.

Drop height: 2.2 m.

Figure C.7. Smart Rock data: test 7, cubic block, tests on sand.

432

Laboratory test — Cubic block — Sand (0º slope), test 8

SR number: 2. Date: 25-Feb-2021.

Mass: 1.096 kg. I_{XX}: 0.001 kg.m^2. I_{YY}: 0.0011 kg.m^2. I_{ZZ}: 0.0012 kg.m^2.

Width (X): 0.086 m. Length (Y): 0.074 m. Height (Z): 0.072 m. Shape: Compact.
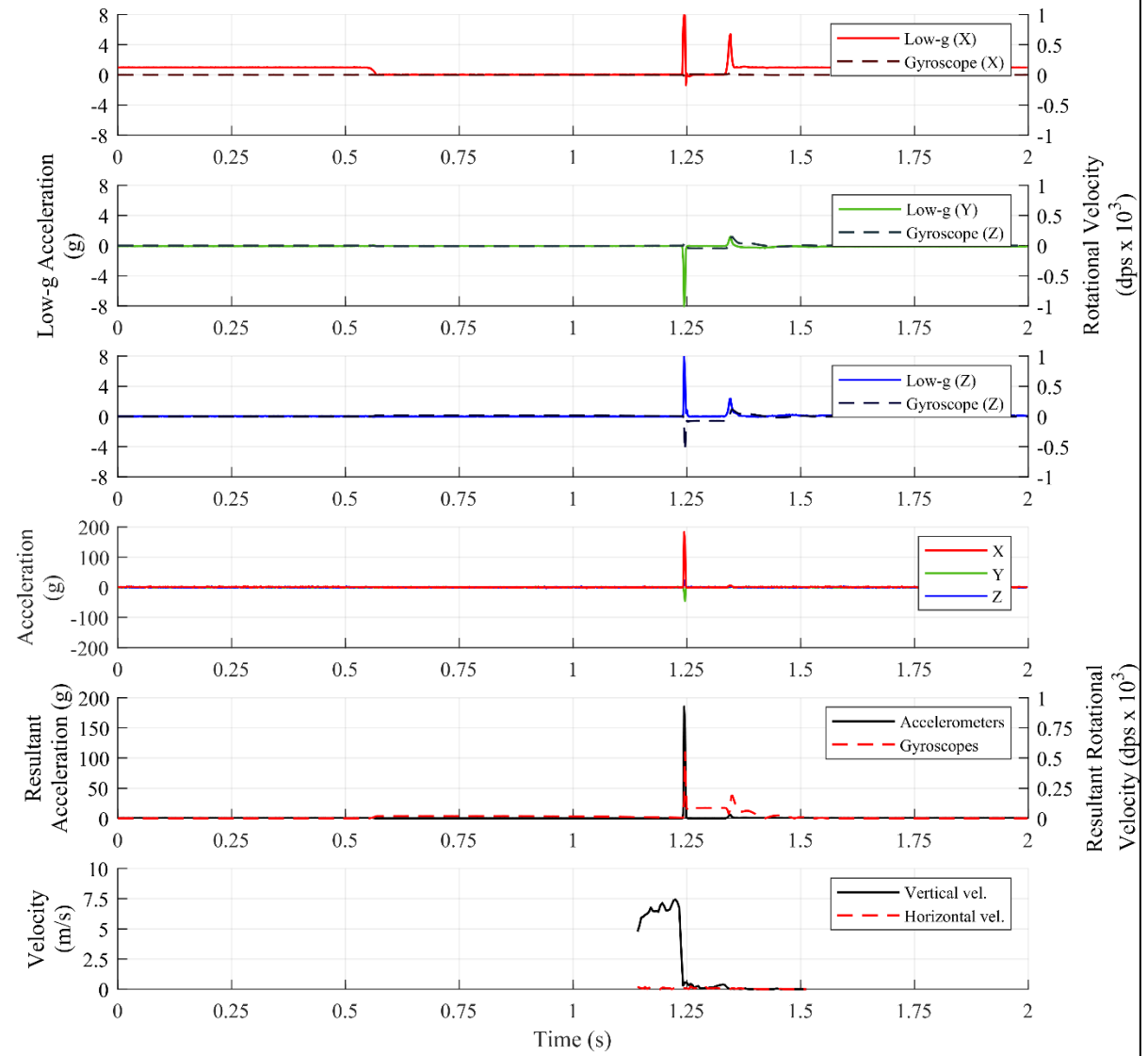
Embedment depth: 13.7 mm.

Drop height: 2.2 m.

Figure C.8. Smart Rock data: test 8, cubic block, tests on sand.

Laboratory test — Cubic block — Sand (0° slope), test 9

SR number: 6. Date: 25-Feb-2021.

Mass: 1.096 kg. I_{XX}: 0.001 kg.m^2. I_{YY}: 0.0011 kg.m^2. I_{ZZ}: 0.0012 kg.m^2.

Width (X): 0.086 m. Length (Y): 0.074 m. Height (Z): 0.072 m. Shape: Compact.

Embedment depth: 13.1 mm.

Drop height: 2.2 m.

Figure C.9. Smart Rock data: test 9, cubic block, tests on sand.

434

Laboratory test — Cubic block — Sand (0º slope), test 10

SR number: 6. Date: 25-Feb-2021.

Mass: 1.096 kg. I_{XX}: 0.001 kg.m^2. I_{YY}: 0.0011 kg.m^2. I_{ZZ}: 0.0012 kg.m^2.

Width (X): 0.086 m. Length (Y): 0.074 m. Height (Z): 0.072 m. Shape: Compact.

Embedment depth: 12.1 mm.

Drop height: 2.2 m.

Figure C.10. Smart Rock data: test 10, cubic block, tests on sand.
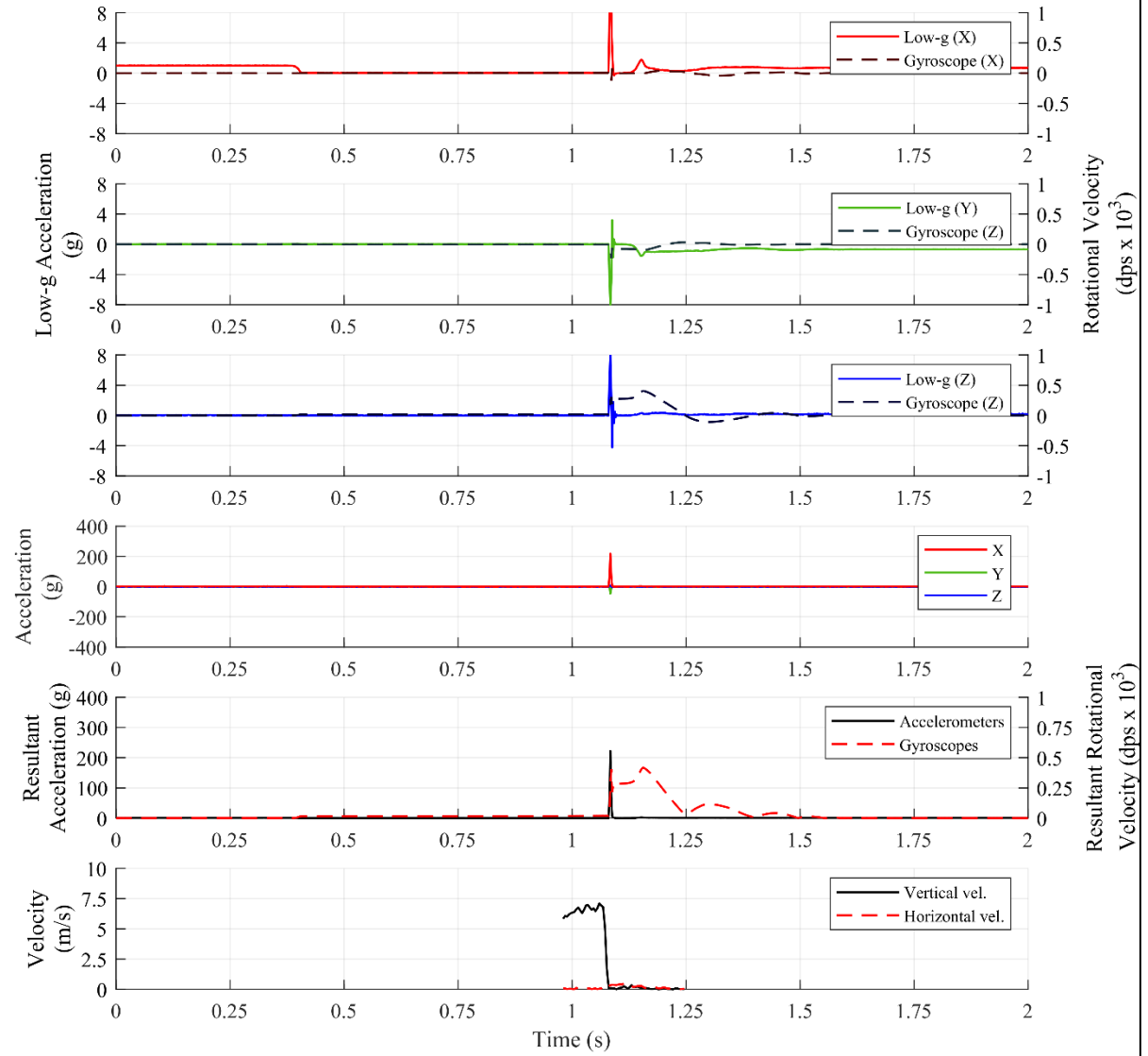
C.1.2. Cuboctahedron block
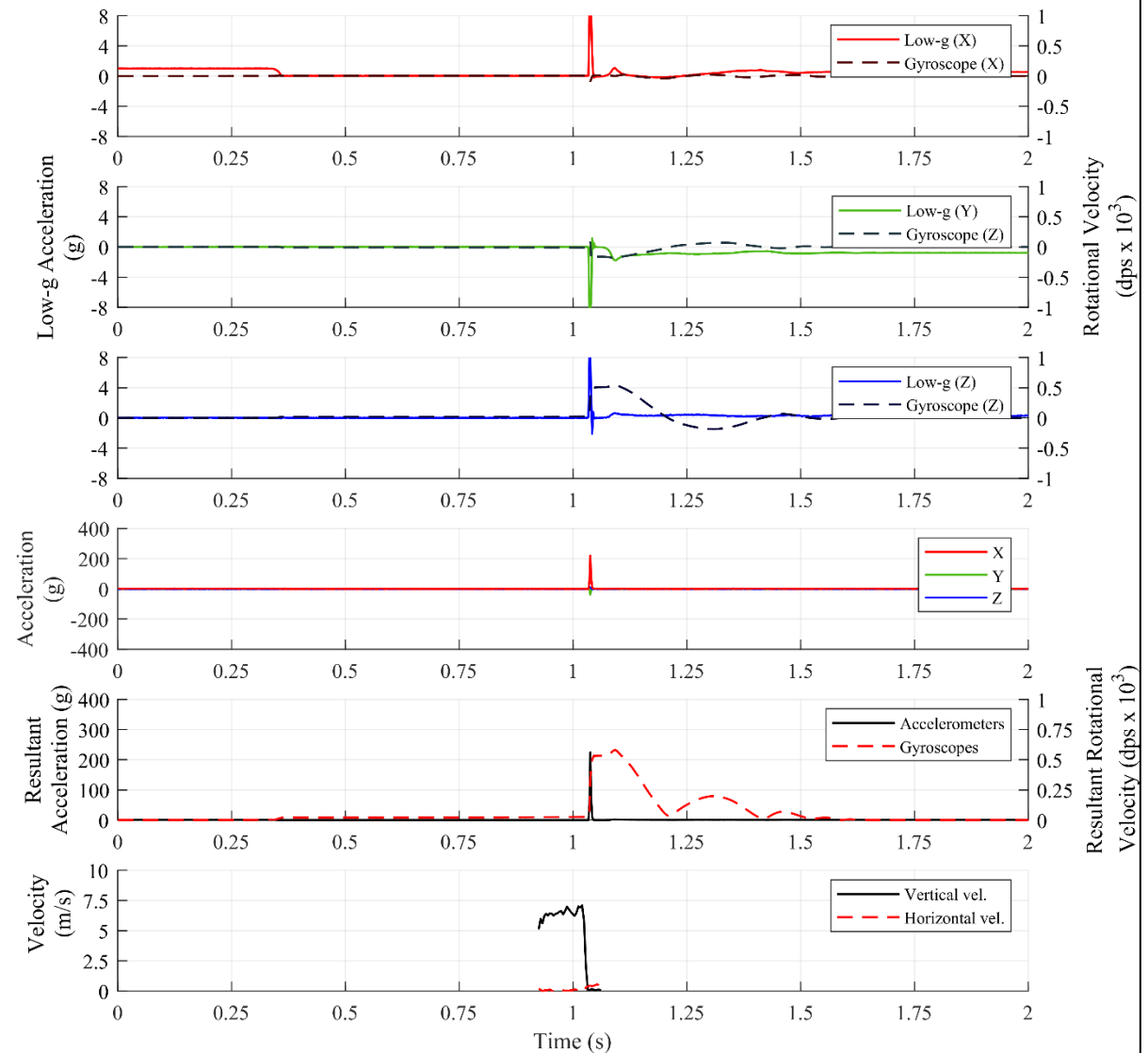
Figure C.11. Smart Rock data: test 1, cuboctahedron block, tests on sand.

Laboratory test — Cuboctahedron — Sand (0° slope), test 2

SR number: 6. Date: 23-Mar-2021.

Mass: 0.79 kg. I_{XX}: 0.0005 kg.m^2. I_{YY}: 0.0006 kg.m^2. I_{ZZ}: 0.0006 kg.m^2.

Width (X): 0.086 m. Length (Y): 0.074 m. Height (Z): 0.072 m. Shape: Compact.
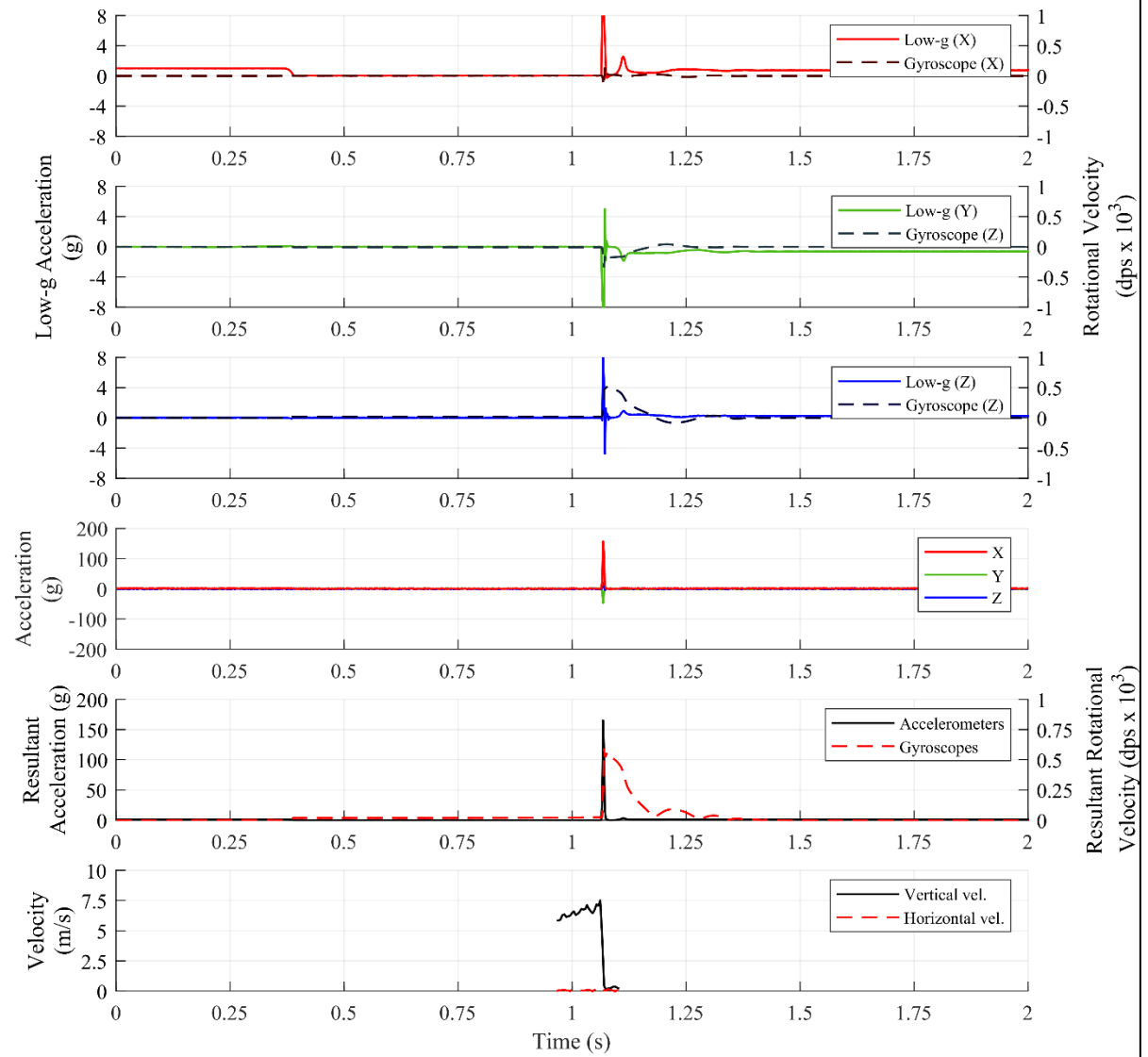
Embedment depth: 24.9 mm.

Drop height: 2.2 m.

Figure C.12. Smart Rock data: test 2, cuboctahedron block, tests on sand.

437

Laboratory test — Cuboctahedron — Sand (0º slope), test 3

SR number: 6. Date: 23-Mar-2021.

Mass: 0.79 kg. I_{XX}: 0.0005 kg.m^2. I_{YY}: 0.0006 kg.m^2. I_{ZZ}: 0.0006 kg.m^2.

Width (X): 0.086 m. Length (Y): 0.074 m. Height (Z): 0.072 m. Shape: Compact.

Embedment depth: 25.8 mm.

Drop height: 2.2 m.

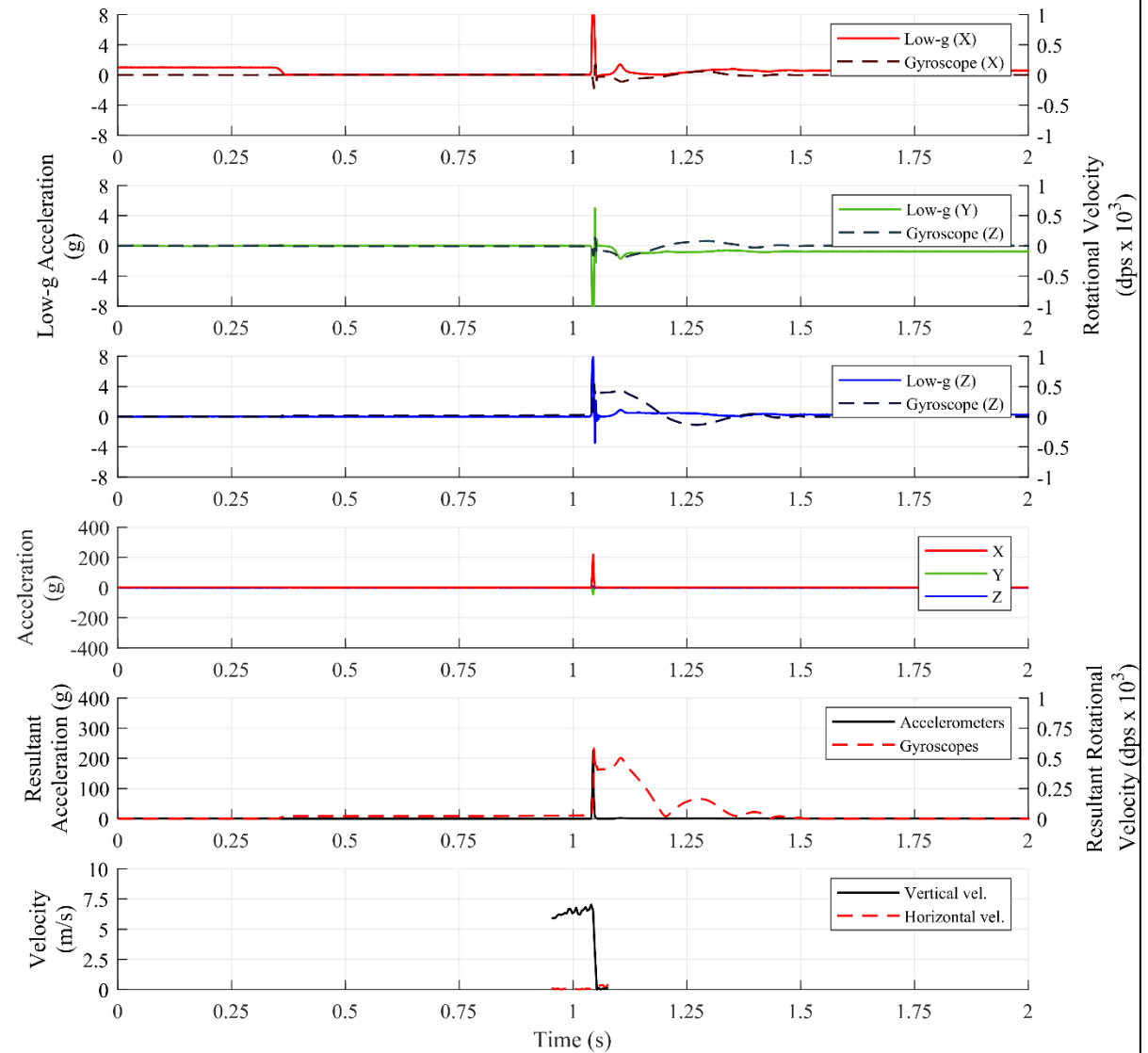Figure C.13. Smart Rock data: test 3, cuboctahedron block, tests on sand.

Figure C.14. Smart Rock data: test 4, cuboctahedron block, tests on sand.

Laboratory test — Cuboctahedron — Sand (0° slope), test 5

SR number: 6. Date: 23-Mar-2021.

Mass: 0.79 kg. I_{XX}: 0.0005 kg.m^2. I_{YY}: 0.0006 kg.m^2. I_{ZZ}: 0.0006 kg.m^2.

Width (X): 0.086 m. Length (Y): 0.074 m. Height (Z): 0.072 m. Shape: Compact.
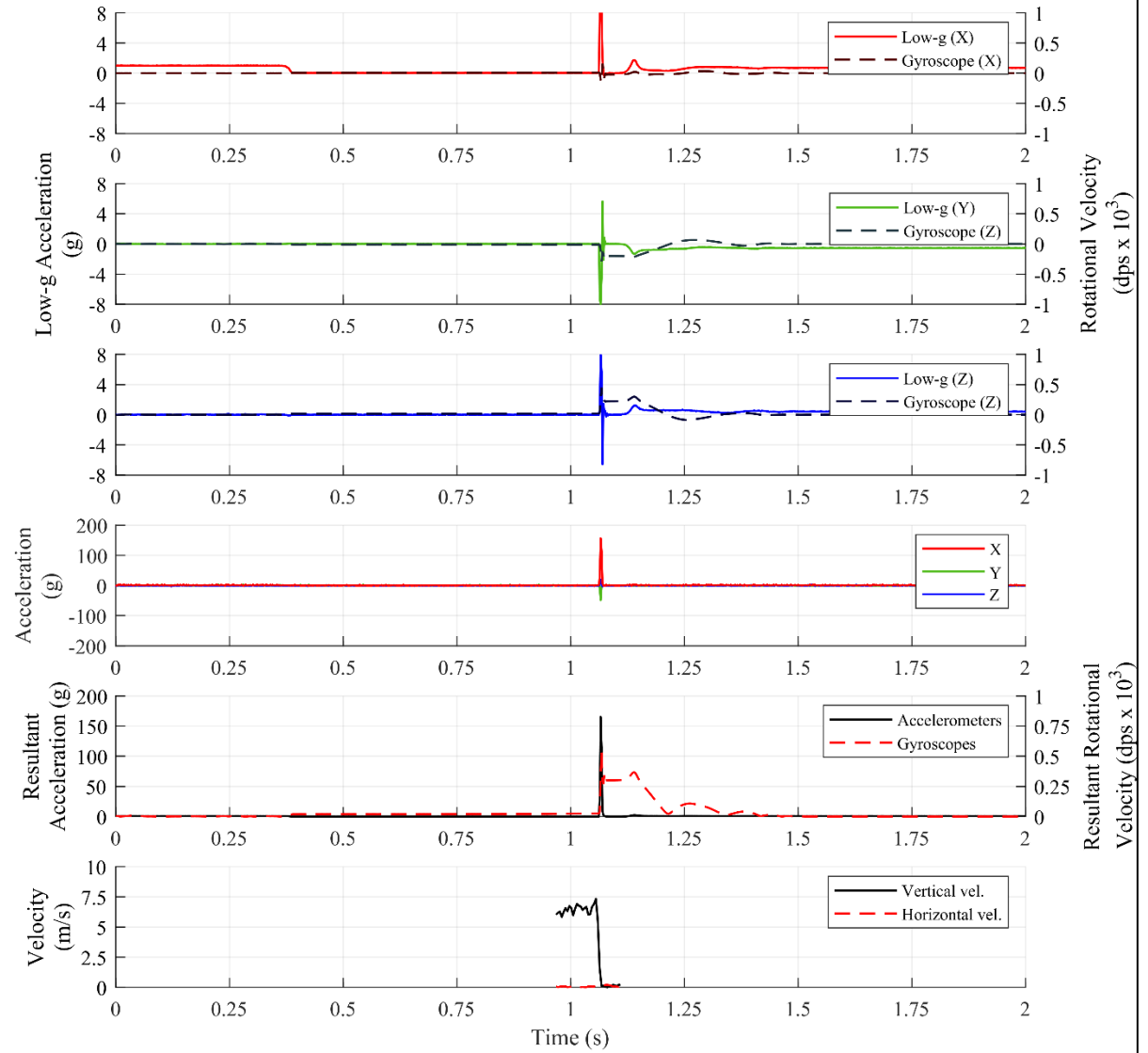
Embedment depth: 23.2 mm.

Drop height: 2.2 m.

Figure C.15. Smart Rock data: test 5, cuboctahedron block, tests on sand.

Laboratory test — Cuboctahedron — Sand (0º slope), test 6

SR number: 6. Date: 23-Mar-2020.

Mass: 0.79 kg. I_{XX}: 0.0005 kg.m^2. I_{YY}: 0.0006 kg.m^2. I_{ZZ}: 0.0006 kg.m^2.

Width (X): 0.086 m. Length (Y): 0.074 m. Height (Z): 0.072 m. Shape: Compact.
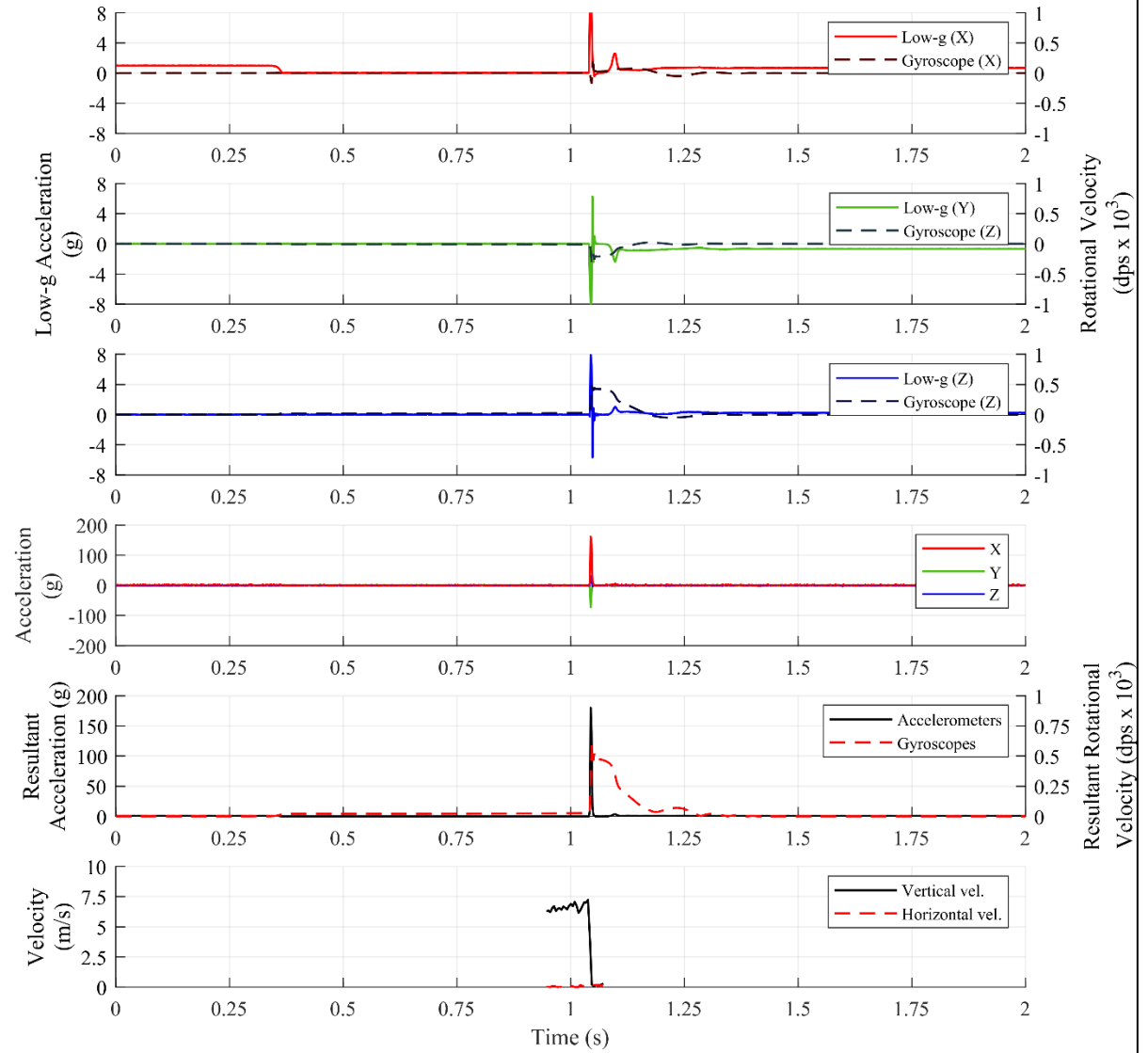
Embedment depth: 25.7 mm.

Drop height: 2.2 m.

Figure C.16. Smart Rock data: test 6, cuboctahedron block, tests on sand.

441

Laboratory test — Cuboctahedron — Sand (0° slope), test 7

SR number: 2. Date: 23-Mar-2021.

Mass: 0.79 kg. I_{XX}: 0.0005 kg.m^2. I_{YY}: 0.0006 kg.m^2. I_{ZZ}: 0.0006 kg.m^2.

Width (X): 0.086 m. Length (Y): 0.074 m. Height (Z): 0.072 m. Shape: Compact.

Embedment depth: 26.4 mm.
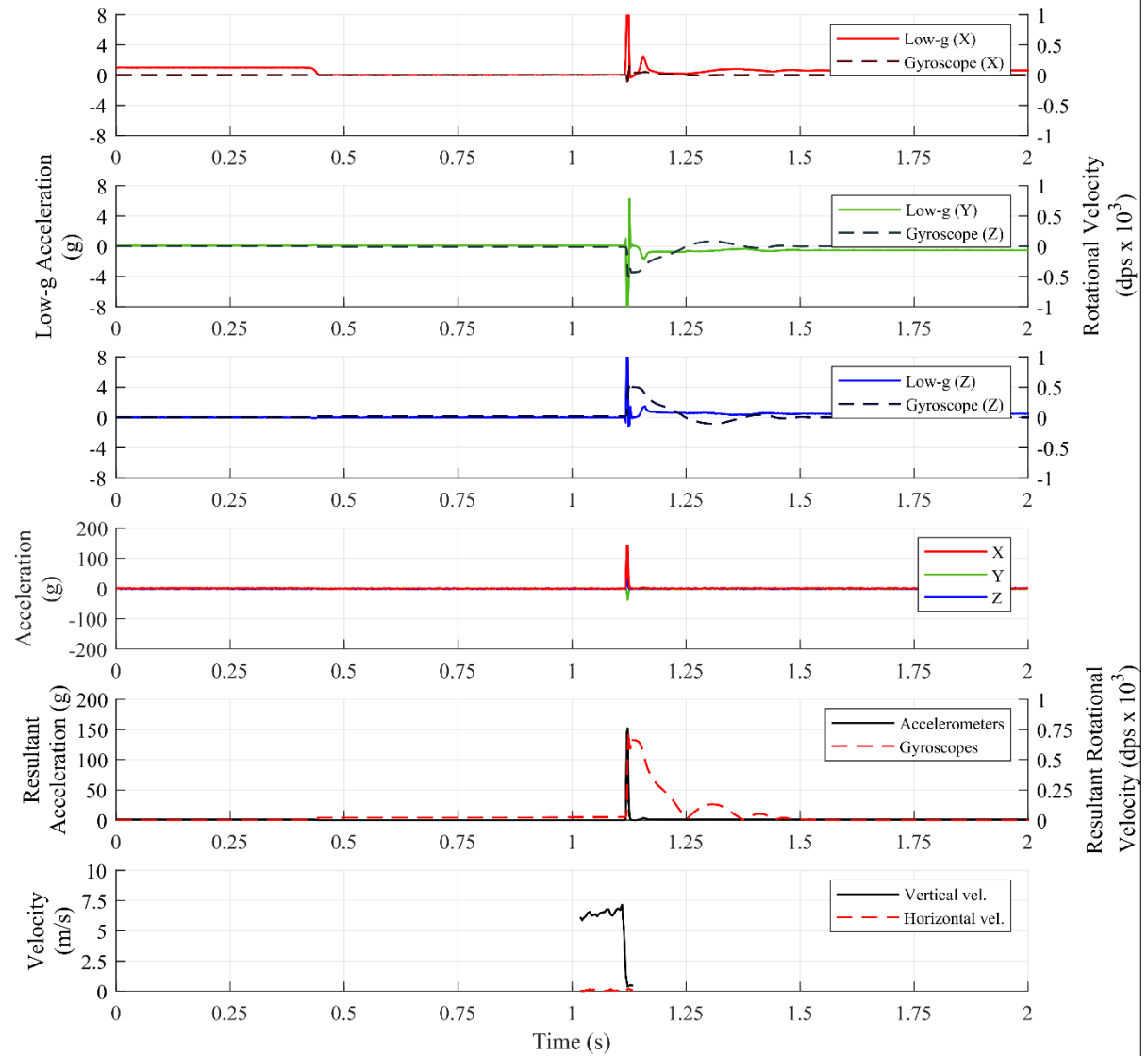
Drop height: 2.2 m.

Figure C.17. Smart Rock data: test 7, cuboctahedron block, tests on sand.

442

Laboratory test — Cuboctahedron — Sand (0º slope), test 8

SR number: 2. Date: 23-Mar-2021.

Mass: 0.79 kg. I_{XX}: 0.0005 kg.m^2. I_{YY}: 0.0006 kg.m^2. I_{ZZ}: 0.0006 kg.m^2.

Width (X): 0.086 m. Length (Y): 0.074 m. Height (Z): 0.072 m. Shape: Compact.

Embedment depth: 23.53 mm.
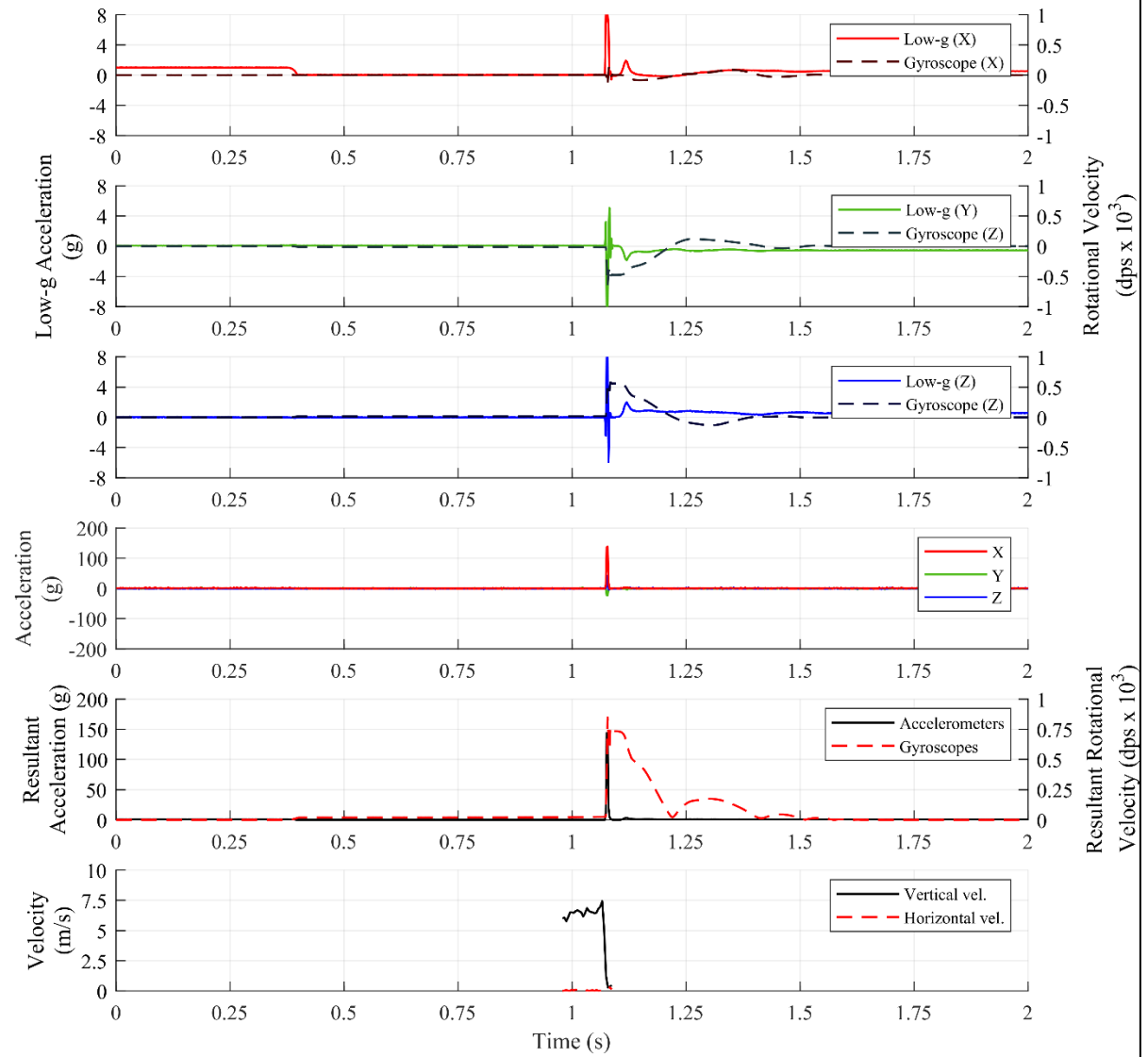
Drop height: 2.2 m.

Figure C.18. Smart Rock data: test 8, cuboctahedron block, tests on sand.

Laboratory test — Cuboctahedron — Sand (0° slope), test 9

SR number: 2. Date: 23-Mar-2021.

Mass: 0.79 kg. I_{XX}: 0.0005 kg.m^2. I_{YY}: 0.0006 kg.m^2. I_{ZZ}: 0.0006 kg.m^2.

Width (X): 0.086 m. Length (Y): 0.074 m. Height (Z): 0.072 m. Shape: Compact.

Embedment depth: 25.9 mm.
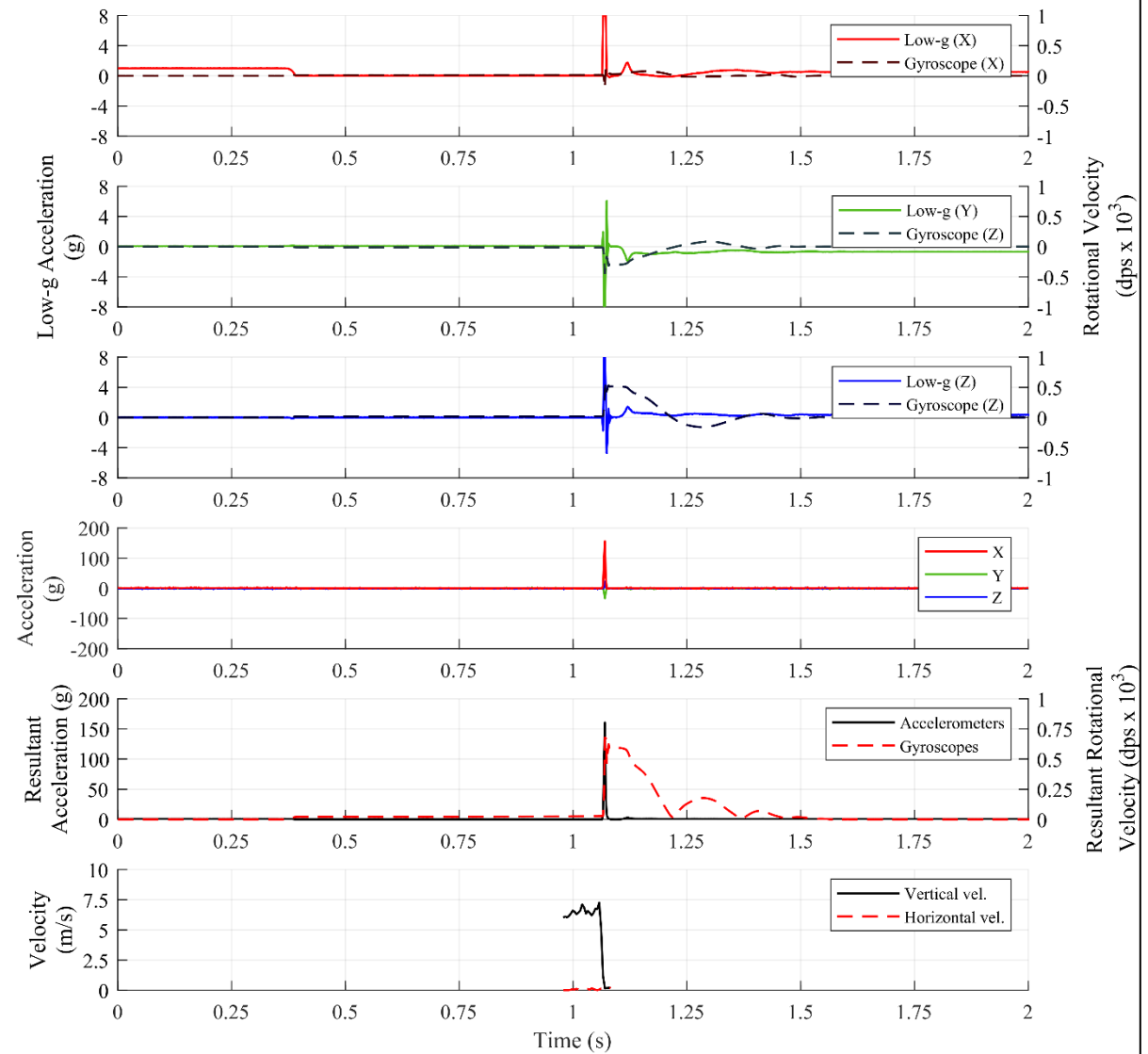
Drop height: 2.2 m.

Figure C.19. Smart Rock data: test 9, cuboctahedron block, tests on sand.

Laboratory test — Cuboctahedron — Sand (0° slope), test 10

SR number: 2. Date: 23-Mar-2021.

Mass: 1.096 kg. I_{XX}: 0.001 kg.m^2. I_{YY}: 0.0011 kg.m^2. I_{ZZ}: 0.0012 kg.m^2.

Width (X): 0.086 m. Length (Y): 0.074 m. Height (Z): 0.072 m. Shape: Compact.
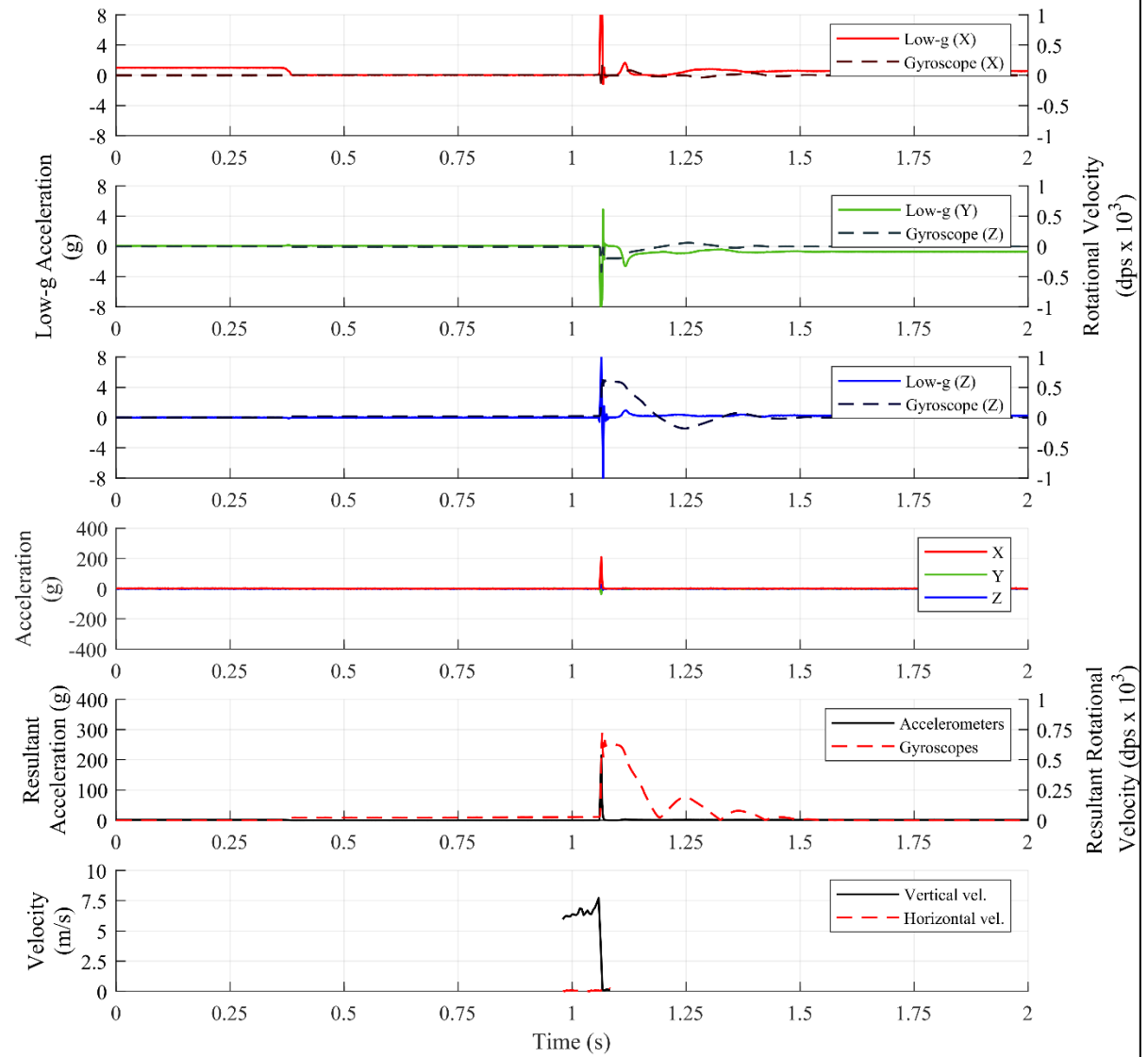
Embedment depth: 24.7 mm.

Drop height: 2.2 m.

Figure C.20. Smart Rock data: test 10, cuboctahedron block, tests on sand.

C.2. Tests on rock

Laboratory test — Cuboctahedron — Rock (0º slope), test 1

SR number: 6. Date: 05-Apr-2021.

Mass: 0.79 kg. I_{XX}: 0.0005 kg.m^2. I_{YY}: 0.0006 kg.m^2. I_{ZZ}: 0.0006 kg.m^2.

Width (X): 0.086 m. Length (Y): 0.074 m. Height (Z): 0.072 m. Shape: Compact.
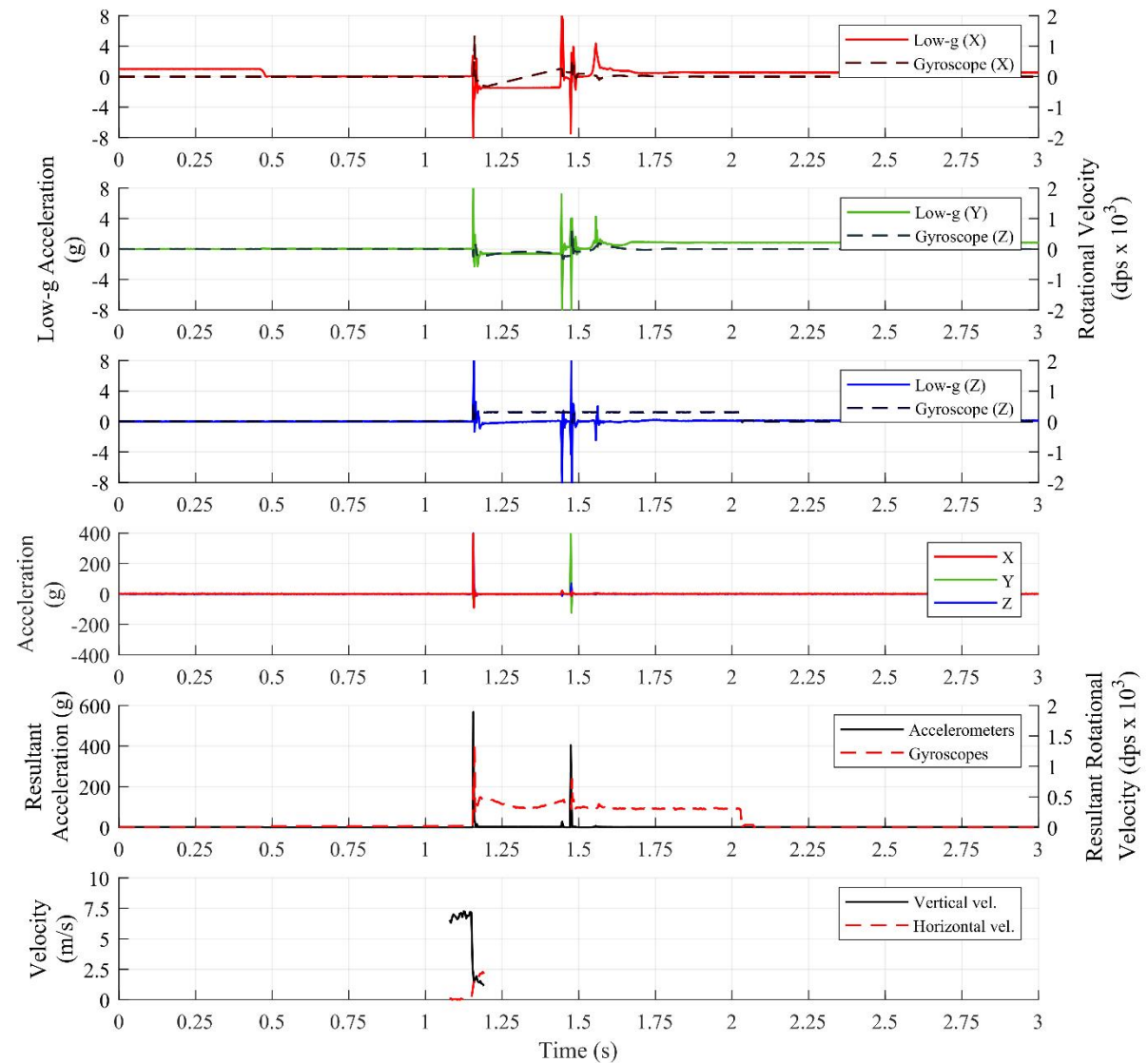
Embedment depth: 0 mm.

Drop height: 2.2 m.

Figure C.21. Smart Rock data: test 1, cuboctahedron block, tests on sand.

Laboratory test — Cuboctahedron — Rock (0° slope), test 2

SR number: 2. Date: 05-Apr-2021.

Mass: 0.79 kg. I_{XX}: 0.0005 kg.m^2. I_{YY}: 0.0006 kg.m^2. I_{ZZ}: 0.0006 kg.m^2.

Width (X): 0.086 m. Length (Y): 0.074 m. Height (Z): 0.072 m. Shape: Compact.
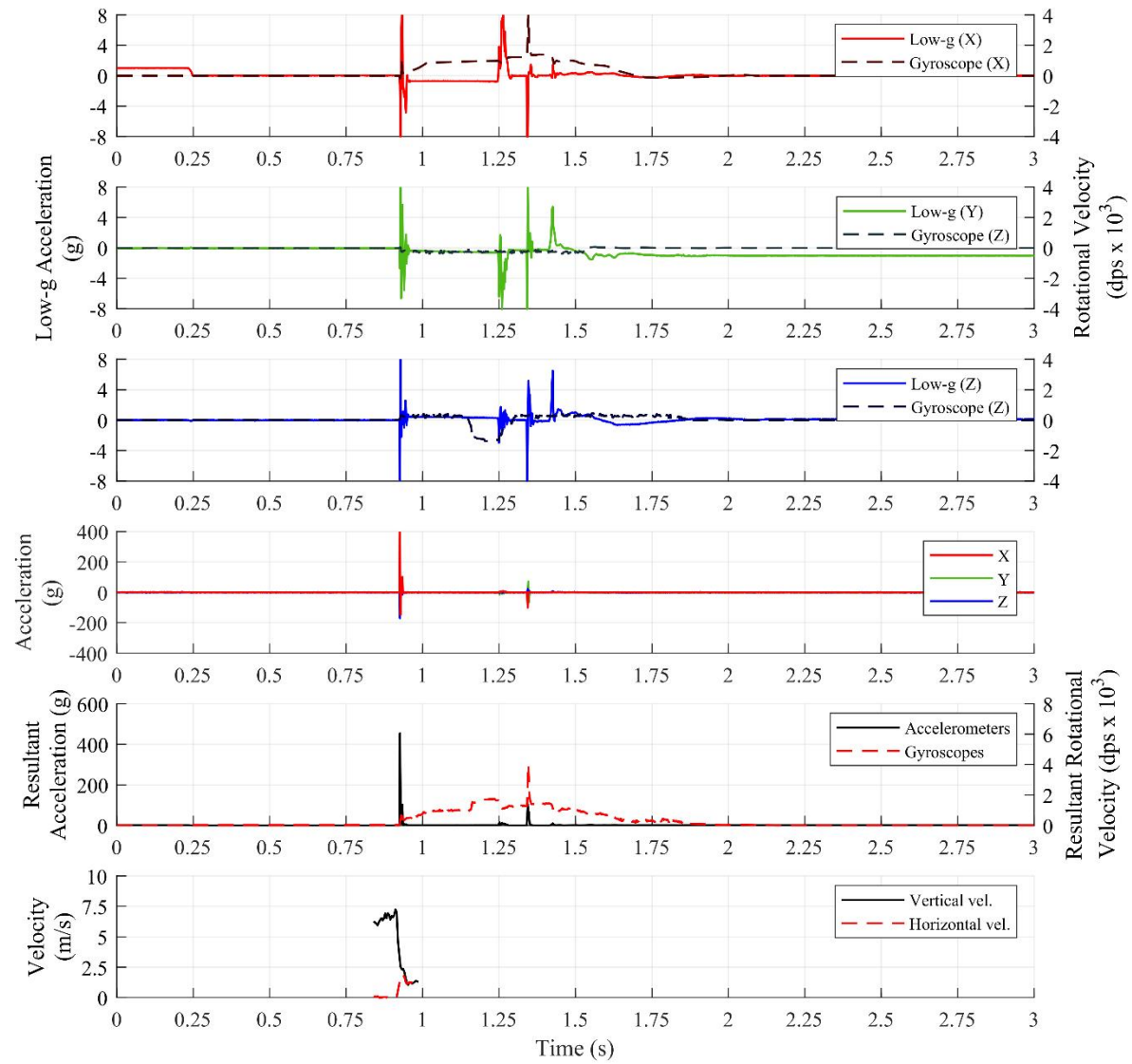
Embedment depth: 0 mm.

Drop height: 2.2 m.

Figure C.22. Smart Rock data: test 2, cuboctahedron block, tests on sand.

Laboratory test — Cuboctahedron — Rock (0º slope), test 3

SR number: 2. Date: 05-Apr-2021.

Mass: 0.79 kg. I_{XX}: 0.0005 kg.m^2. I_{YY}: 0.0006 kg.m^2. I_{ZZ}: 0.0006 kg.m^2.

Width (X): 0.086 m. Length (Y): 0.074 m. Height (Z): 0.072 m. Shape: Compact.
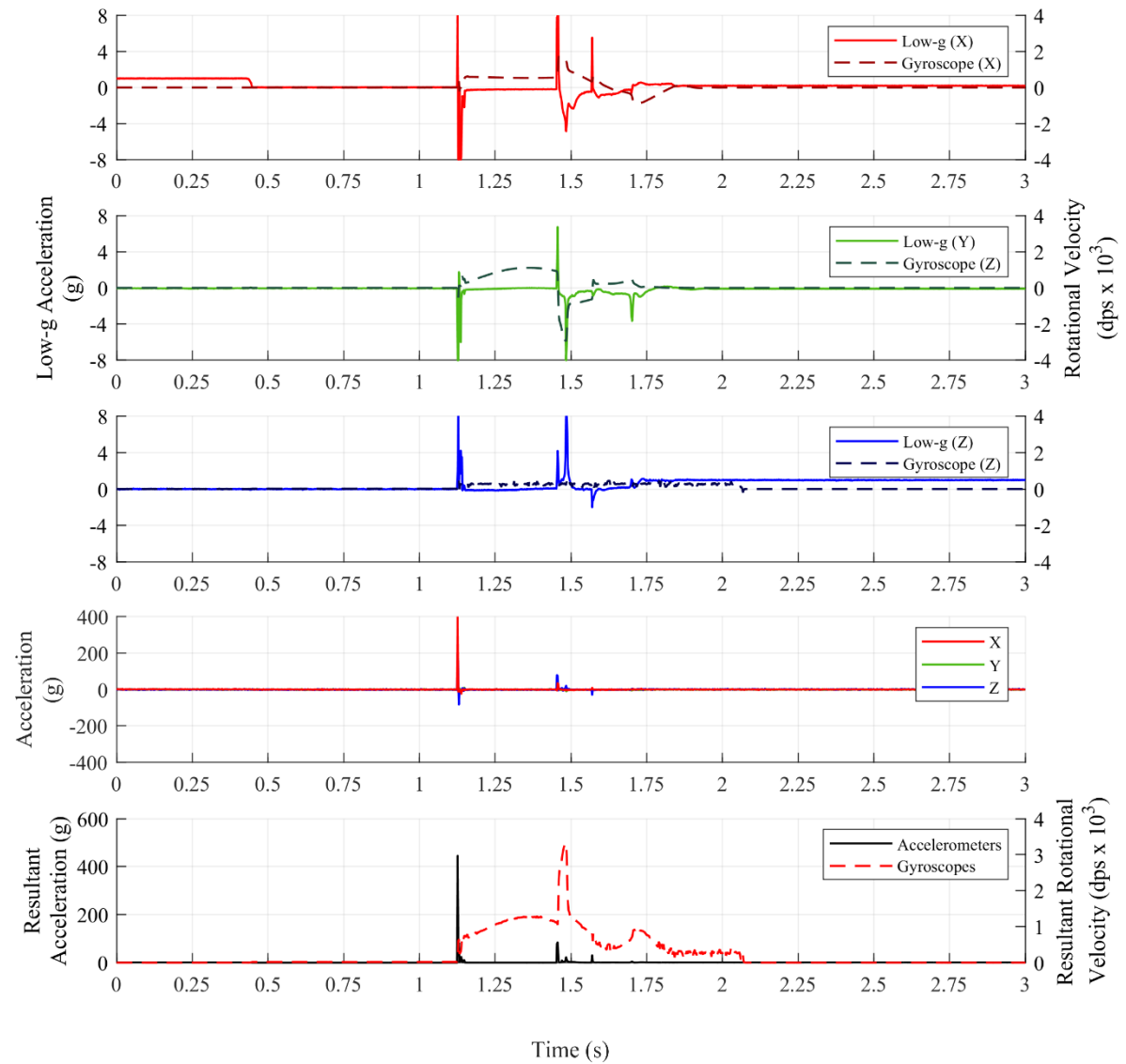
Embedment depth: 0 mm.

Drop height: 2.2 m.

Figure C.23. Smart Rock data: test 3, cuboctahedron block, tests on sand.